

nature

THE INTERNATIONAL WEEKLY JOURNAL OF SCIENCE

Shape-shifting
nanosensors use
NMR to probe
beyond the reach
of light **PAGE 73**

SEEING IN THE DARK

HEALTH SCIENCES

STAUNCH THE FLOW

Fewer blood transfusions
could save more lives

PAGE 24

CLIMATE POLICY

CHANGE IPCC'S REMIT

Add social science
to advisory mix

PAGE 27

HISTORY OF SCIENCE

NEW - WORLD ORDER

The birth of natural history
in North America

PAGE 30

NATURE.COM/NATURE

2 April 2015 £10

Vol. 520, No. 7545



9 770028 083095

THIS WEEK

EDITORIALS

STEPS New boots help you to walk this way **p.6**

WORLD VIEW End the war on cancer and move on **p.7**



CONSERVATION Spread the funds around to save species **p.9**

Communication breakdown

A policy change that could discourage UK government scientists from talking to the media is a backwards step. All researchers need to speak up to put science on the political agenda.

The United Kingdom dissolved its Parliament this week, with politicians now dispatched from the centre of political power in London's Westminster to fight for their constituency seats ahead of the general election on 7 May. The work of the government, and government scientists, continues. But many have been unsettled by a controversial change in their working conditions, which could prevent how freely they can discuss their work with journalists.

On 16 March, the Civil Service Code was amended to state that all UK civil servants require “ministerial authorisation for any contact with the media”. There is some confusion over who exactly this applies to, but it could affect thousands of scientists, including those who work directly for government departments and those in arms-length agencies such as the Met Office.

Critics made comparisons with the situation in Canada, where scientists have complained about a perceived muzzling by their government. In a letter of protest sent to the UK government last week, the heads of the Science Media Centre, an influential London charity that connects scientists and journalists; the Association of British Science Writers; and the UK science-communications network Stemptra warned that the rule change would discourage many scientists from talking to the media.

It is unclear how much of a difference the rule change will make — even to the scientists concerned and their employers. After seeking clarification from the government, the Met Office — home to world-renowned climate-research unit the Hadley Centre — was told it is “business as usual” and that its researchers could, as before, still speak to the media “under the guidance” of the press office.

Even before the rule change, many scientists directly employed by government departments were quick to tell journalists “you’ll have to go through the press office”. And senior figures are unlikely to be deterred from speaking out, as Chris Smith, head of the Environment Agency, did in 2014 when he rebutted government criticism of his team’s response to severe UK floods. Yet Fiona Fox, chief executive of the Science Media Centre and a signatory to the letter, says that she has “concrete evidence” that some scientists have already turned down media interviews as a result of the policy change. Unfortunately, it will be near-impossible to gauge its true impact, because we will never know how many people decide not to talk to the press as a result of it.

Any block on transparency and openness is a step backwards. The government that takes over after the general election should clarify what it wants from its scientists, and how the rule change alters that. It should consider an exemption for researchers talking to the media about their work in acknowledged areas of public interest, such as climate or health.

What the next government will look like — and what its attitude to science will be — is remarkably unclear. As we discuss on page 16, the United Kingdom is in a state of political flux. The two historically heavyweight political parties, left-wing Labour and right-wing Conservative, are roughly tied in the polls. The traditional third-place party, the Liberal Democrats, has been bleeding support.

This has boosted a following for outsider parties such as the Green Party and the UK Independence Party, which opposes membership in the European Union. Regionally focused groups such as the Scottish National Party are also expected to make gains.

These traditionally smaller parties could end up holding the balance of power in the next Parliament, whether they end up as part of a formal coalition government or in a looser arrangement

“Any block on transparency and openness is a step backwards.”

to support a minority government. Given the uncertainties, *Nature* has scrutinized the science policies of the minor parties. Science is unlikely to be a priority should any of them sit down to negotiate a share of power (with the possible exception of the climate-focused Greens). But their policies could end up determining how much money flows to research, and how it does so.

Government funding for science is at a crunch point in the United Kingdom. Amid years of austerity, the science budget has been held stable behind a ‘ring fence’. For the outgoing coalition government of Conservatives and Liberal Democrats, this is a sign of its support for research. But it has meant the pain of budgets eroded by inflation. Many researchers think that more money is needed, but the current political debate is heavy with talk of more cutbacks.

Science was high on the agenda during and after the last election in 2010, with a prominent campaign springing up in support of research spending. Such statements seem more muted in 2015. Scientists in the United Kingdom should find their voices again. And governments should not muzzle them. ■

Tree cheers

The world must follow Brazil’s lead and do more to protect and restore forests.

When deforestation in the Brazilian Amazon started to fall a decade ago, many scientists and environmentalists attributed the drop to unrelated trends in global commodities markets, which briefly depressed agricultural production in 2005–06. The assumption was that a developing country such as Brazil could not possibly assert control over its domain, and that farmers and ranchers would soon return to their old habits. But they didn’t. Production recovered and then increased, while the rate of deforestation continued to fall. Brazil proved the sceptics wrong, and in doing so it changed the global conversation on forests, food and rural development.

As we explore in a News Feature on page 20, the drop in deforestation

is down to a number of factors, including government policies and corporate efforts to clean up beef and soya-bean supply chains. Academics are still dissecting out cause and effect, trying to understand what worked where and how to help other countries to follow suit.

The first major factor is that in 2004 the Brazilian government decided to take the issue seriously. Harnessing its satellite-monitoring system, the government mounted sustained enforcement campaigns in areas where deforestation was rampant. It worked to root out corruption within the ranks of its environmental law enforcement agency by, for example, rotating teams among regions to prevent the kind of long-term relationships that enable bribery. It also designated new public land for permanent protection, engaged banks that provide agricultural loans, and increased pressure on local governments, which stepped up their own campaigns.

But the government did not act alone. Capitalizing on publicly available satellite data, environmental groups put a spotlight on the international corporations that trade in beef and soya beans. Most of the major players in both industries buckled under public pressure and signed agreements to halt purchases of the products from recently cleared land; new research suggests that these moratoria are changing the way landowners do business. Industrial-scale deforestation in the Amazon has been driven by global demand for protein, be it beef or soya beans, which often serve as a feedstock for chicken and pork. But globalization can also be a force for good when consumers and businesses raise their standards.

Brazil has created a portfolio of tools that other countries can study as they seek to minimize deforestation. But what comes next is less clear. No one has identified a simple recipe for sustainable rural development, and chopping down forests remains a profitable affair among criminal land speculators. Solving these problems will require extra

effort as well as money, and this at a time when Brazil is struggling to stave off outright recession.

Global policy-makers created a mechanism under the United Nations Framework Convention on Climate Change to help with such efforts. Dubbed REDD, for reducing emissions from deforestation and forest degradation, this pay-for-performance system is based on the carbon that is locked up in trees. Developing countries that document reduced deforestation and thus carbon dioxide emissions — or an expansion of forests — are eligible for payments from wealthy countries. Norway has already committed US\$1 billion to Brazil, which is dispersing the money for a range of government initiatives as well as research and policy experiments.

The challenge internationally is to ramp up funding for forest conservation and restoration, which is the easiest way to pull large amounts of carbon dioxide out of the atmosphere. Countries have already committed more than \$7.5 billion to the cause, and many governments and companies have made forest pledges. At a UN summit last September, a host of countries joined businesses, environmental groups and indigenous organizations in signing the New York Declaration on Forests, which calls for a halving of deforestation by 2020 and to end it by 2030. The document also calls for the restoration of 350 million hectares of forests and other landscapes globally by 2030. These are admirable goals, but further investments, particularly from the private sector, are needed if the world is to meet them.

Brazil is still writing its story in the Amazon, but its experience shows the potential for rapid progress. It also holds lessons for activists, businesses and governments: foremost among them is that it takes all three to tango. It's a complicated dance, but one the world must learn. ■

“Brazil’s experience shows the potential for rapid progress.”

Walking 2.0

A passive device that augments calf muscles improves on natural selection’s best effort.

Given that scientists can probe the secrets of matter and gaze into the depths of the cosmos, it is a wonder that we still have anything to learn about something as seemingly simple as the way we walk. Yet how and why humans evolved to walk on two legs — a feat that many take for granted — remains an active field of research. Not least because no one has yet managed to build a humanoid robot with the natural grace and poise of, say, someone walking to the post office, let alone with that of an Olympic athlete or catwalk model.

Armchair scenarios to explain how humans became bipedal turn up occasionally as submissions to this journal. Yet most fail to account for the manifold adaptations that humans require to assume the posture that most toddlers do without thinking.

Every part of our bodies is adapted to bipedality. Every nerve is tuned, every muscle responsive to the merest twitch of feedback required to keep something so intrinsically unstable vertical and in motion, and all without conscious thought.

This instability is key: the more unstable the object, the more manoeuvrable it is. Imagine the control systems that would be needed for a child to fly a modern fighter jet, and you begin to grasp the scale of the problem.

This explains why *Nature* is proud to publish a report this week that some readers might at first glance dismiss as quotidian engineering rather than pure science (S. H. Collins *et al.* *Nature* <http://dx.doi.org/10.1038/nature14288>; 2015). The authors have created a mechanical boot fitted with a disarmingly simple spring-loaded device that augments the force of the wearer’s calf muscles, reducing the metabolic

cost of walking by about 7%.

That might not sound like much, until one considers two remarkable things. First, the device is completely passive — it has no batteries and consumes no external power. Second, given that we assume that adaptations produced by evolution tend to the optimal, it is amazing that an improvement of this amount is even possible. Natural selection has honed human walking over millions of years, and yet there is still substantial room for improvement. Despite the way the phrase is sometimes used, natural selection is not a motive force for progressive improvement towards inevitable perfection, but an endless series of compromises as organisms adapt to new circumstances given the anatomies they have.

Humans come from a long line of creatures that mostly walked on all fours, supported by a horizontal backbone with vertebrae held under tension. Making the backbone vertical puts compressive loads on vertebrae, which can have painful consequences; lower back pain is the leading cause of worker absenteeism after the common cold, accounting for 15% of sick leaves and hundreds of millions of lost work days annually. Matters are even worse for pregnant women, and there is evidence that the spine has evolved further fixes to accommodate the enormous and sudden burden of carrying a fetus (K. K. Whitcome *et al.* *Nature* **450**, 1075–1078; 2007). So perhaps it is no surprise that there are still energy savings to be made, given that humans are products of evolution and not of conscious design. If we were going to be truly efficient at getting around, we would have evolved wheels.

A passive exoskeleton for the lower leg is a far cry from the commuter jet packs imagined in 1950s science fiction. Still, if one is inclined to dismiss a 7% saving as modest, one might easily imagine circumstances in which such a margin could mean all the difference between immobility and freedom. A passive device such as this might be just enough, say, to help a person with impaired mobility to get out of the house. A person for whom a trip to the post office might at present be as out of reach as a jet pack. ■

➔ **NATURE.COM**
To comment online,
click on Editorials at:
go.nature.com/xhunqy



Change the cancer conversation

The 'war on cancer' has run off course. Efforts must refocus on the best interests of patients, says Colin Macilwain.

When Angelina Jolie had a double mastectomy in 2013 after genetic tests revealed her susceptibility to certain cancers, she urged others to consider their own risk. Even more people will do so now, after the actress revealed that she has undergone a procedure to have her ovaries and Fallopian tubes removed as well. There is a positive effect to this, of course: greater awareness and reduced stigma can only help people with cancer.

But Jolie's story, of optimal diagnosis, advice and treatment, is not relevant to most people with cancer. Rather, it may serve to sustain unrealistic expectations that victory is pending in the 'war on cancer'.

Cancer, the rhetoric of this conflict holds, is an enemy that can be defeated with sufficient will and the right weapons. Unfortunately, like the 'wars' on drugs and terror, the war on cancer has become more about those doing the fighting and less about the best interests of those they are trying to serve.

It is surely time to concede defeat, or declare victory, or whatever — and build a more realistic and constructive approach to cancer prevention, treatment and care.

The most glaring failures of the war on cancer are burgeoning global costs and inconclusive progress on mortality rates. Collateral damage includes a misdirected biotechnology industry, misleading public debates on payment for exorbitant drug treatments, the self-interested promotion of unhelpful diagnostic tools, warped research priorities, mistreatment of patients (especially the elderly) and timid policy action on environmental causation.

The global war on cancer arguably began 44 years ago, with US President Richard Nixon's 1971 State of the Union address — although he did not actually invoke the phrase (see M. P. Coleman *J. Cancer Policy* 1, e31–e34; 2013).

The idea of turning defence against an enemy into a political patronage machine is much older. The Great Wall of China, for example, is anything but contiguous. Invaders could simply go through the gaps. But the wall was not built just to keep enemies out. It helped to keep the Chinese emperors in. In all such cases, fortifications end up being constructed primarily for the benefit of those who build them.

Take the biotech industry. Since its foundation, the search for cancer treatments has been at its core. That is because US health insurers (and, to a lesser extent, insurers and public-health providers elsewhere) will cough up silly money for treatments proven to prolong life by three to six months. The biotech model is largely predicated on the prospect of huge returns from cancer drugs.

That, in turn, leads to one of the most visible manifestations of the war on cancer in the United Kingdom: the public-relations battles to obtain payment for these drugs. Patient groups,

often industry-funded, unearth individual cases to put on front pages and press public agencies to approve payment for a treatment.

But the most bothersome facet of the fight is the state of doctor–patient interactions. To maintain the appearance of progress, and to meet key performance indicators, physicians are obliged to offer multiple approaches — such as chemotherapy and radiotherapy — to almost every patient. This is now extending into genetic testing and experimental therapies, such as stem-cell transplants. Much of this happens despite decidedly mixed evidence over whether patients really benefit. (Yes, some cancer survival rates are up, but that masks a complicated debate about how much of the increase is due to better and earlier diagnosis.)

Then there is the cancer-awareness industry. Corporations including the Ford Motor Company and American Airlines are now major sponsors of the Race for the Cure, the highest-profile US 'awareness' event. When these companies get credit for what was originally a grassroots anticancer action, something has gone badly wrong. Awareness focuses on tests and treatments, rather than on cause and prevention.

The cancer-research agenda is similarly skewed. The percentage of the US National Cancer Institute (NCI) budget that is devoted to prevention and control slipped from 11% in 2003 to 6% in 2013. Outcomes research — measuring the effectiveness of treatments — is neglected, in cancer as in other fields. Environmental-health research remains politically contentious and poorly funded.

Harold Varmus, who this week retires as director of the NCI, has called for the 'war on cancer' metaphor to be discarded. But it is still in wide-

spread use. And despite its weak track record, the war is a model that politicians are now in danger of adopting for another great health-care challenge for rich countries: neurodegenerative disease.

The area has had an upsurge of political interest of late, exemplified by the first Ministerial Conference on Global Action Against Dementia, held last month at the World Health Organization in Geneva, Switzerland. The wolves are already circling around neurodegenerative disease. The usual suspects — drug companies, equipment makers, university departments — all want a seat at the table. Policy-makers should be wary of them. The priority instead must be to improve quality of life. Despite the shiny promises of genetics and diagnostics, that in reality means more investment in the basics of shelter and care.

Otherwise, in 40 years' time, elderly and infirm people may be treated just as shabbily as they are now. And another Great Wall of special interests will be leaching off their pain. ■

Colin Macilwain writes about science policy from Edinburgh, UK.
e-mail: cfmworldview@googlemail.com

**AWARENESS
FOCUSES ON
TESTS AND
TREATMENTS,
RATHER THAN ON
CAUSE AND
PREVENTION.**

➔ **NATURE.COM**
Discuss this article
online at:
go.nature.com/jrqvbg

RESEARCH HIGHLIGHTS

Selections from the
scientific literature

ENVIRONMENTAL MICROBIOLOGY

Soil source for vine bacteria

The bacteria found on grapevines seem to come mostly from soil, a finding that could help researchers to understand how soil microbes influence the properties of wine made from the grapes.

Jack Gilbert at Argonne National Laboratory in Illinois and his colleagues took samples of soil and Merlot grapevines from five vineyards on Long Island, New York. They sequenced the bacterial genomes found in the soil and on the plants, and discovered that the bacterial communities on various plant parts were more similar to those in the soil around the roots than to each other. This suggests that the soil is a key bacterial reservoir for grapevines.

These grapevines seem to share a core microbial composition with those from California and from Bordeaux in France.

mBio 6, e02527-14 (2015)

BIOMECHANICS

Big tortoise shell makes flipping hell

The size and shape of a tortoise's shell influence how quickly the animal can right itself when it falls onto its back.

Ana Golubović of the University of Belgrade and her colleagues studied the Hermann's tortoise (*Testudo hermanni*; pictured), which lives in hilly, rocky habitats that often flips the animal onto its



back. The team measured the amount of time it took adult male and female tortoises to get back on their feet after being turned over.

They found that larger animals of both sexes spent more time righting themselves than smaller ones. Males that had larger plates along the rear edge of their shell — useful for adding stability during mating — also took longer to flip themselves back over.

A similar effect of shell shape on flipping may be found across other tortoise species, the researchers say.

Zool. Anz. 254, 99–105 (2015)



HUMAN EVOLUTION

Neanderthal freed from stone

A complete skeleton embedded in an Italian cave is that of an early Neanderthal.

Discovered in 1993 near Altamura in southern Italy, the remains (pictured) are coated in a thick layer of calcite, and the bones have been examined only while embedded. A team led by Giorgio Manzi at the Sapienza University of Rome got permission to cut out a small sample of a shoulder bone for laboratory study. Uranium–thorium dating of calcite layers surrounding

the bone suggests that the remains are between 128,000 and 187,000 years old. Mitochondrial DNA sequences from the bone matched those of other Neanderthals (*Homo neanderthalensis*).

The skeleton is the oldest Neanderthal from which DNA has been collected, the researchers say, making it a good candidate for further in-depth genetic analysis.

J. Hum. Evol. <http://dx.doi.org/10.1016/j.jhevol.2015.020.007> (2015)

PLANT SCIENCE

Potato gene guards against blight

A gene in a wild potato plant boosts the plant's resistance to the destructive potato-blight fungus.

For ten years, Vivianne Vleeshouwers of Wageningen University in the Netherlands and her colleagues combed the Andes — the ancestral home of the potato — for genes involved in defence against the fungus *Phytophthora infestans*. This organism caused the 1840s Irish potato famine and is still a common pathogen. They discovered that a wild

potato, *Solanum microdontum*, contains a gene encoding a protein called ELR that recognizes elicitin proteins, which are evolutionarily conserved in the fungus. ELR is an immune receptor that can trigger a defence response that kills infected leaf cells to slow the pathogen's spread.

The team transferred the gene to cultivated potato plants, where it conferred increased blight resistance. Using this gene could lead to more-durable blight resistance than other known resistance genes, the authors say. *Nature Plants* <http://dx.doi.org/10.1038/nplants.2015.34> (2015)

SOPRINTENDENZA ARCHEOLOGICA DELLA PUGLIA/
MUSEO ARCHEOLOGICO DI ALTAMURA

ZORANDIM/SHUTTERSTOCK

NEURODEVELOPMENT

Methylation makes the brain female

Normal development of the female rat brain requires active silencing of key male-associated genes during a critical period just before and after birth.

Bridget Nugent at the University of Maryland School of Medicine in Baltimore and her colleagues studied a region of the rat brain that differs significantly in males and females. They found that in females shortly after birth, there were more methyl groups attached to DNA in this brain region, reducing gene expression.

When they injected newborn females with a male hormone, the activity of an enzyme that adds methyl groups to DNA decreased. When they blocked the activity of this enzyme in female rats during the critical period after birth, the animals showed male-like gene expression and sexual behaviour.

Nature Neurosci. <http://dx.doi.org/10.1038/nn.3988> (2015)

CONSERVATION

More bang for the conservation buck

Conservation money directed at charismatic species could be used more effectively to save animals if it was applied in a more scientific manner.

Joseph Bennett at the University of Queensland in Brisbane, Australia, and his colleagues modelled the impact of more than NZ\$1 million (US\$765,000) in private funding given to protect 10 iconic bird species

in New Zealand, including the North Island brown kiwi (*Apteryx mantelli*; pictured).

If funding was directed at only the 10 species as originally assigned, an average of 1.4 further species would be effectively conserved, compared to a scenario in which there was no private funding. If the money was allocated in a way that benefited other endangered animals as well as the 10 flagship species, 2.8 extra species on average could be conserved. If the money was spread more widely to non-iconic but still-threatened New Zealand birds, an average of 3.3 more species could be saved.

Although private funding for such flagship species can generate vital conservation revenue, it should be spent carefully to maximize conservation benefits, the authors say.

Proc. R. Soc. B 282, 20142693 (2015)

HUMAN GENETICS

Iceland genomes reveal knockouts

More than 8,000 Icelanders carry a gene that is completely inactivated by mutations.

Patrick Sulem, Kari Stefansson and their colleagues at deCODE Genetics in Reykjavik sequenced the genomes of more than 2,600 Icelanders and used this to infer the genetics of another set of more than 100,000 people from Iceland. They found that 7.7% of this second set have low-frequency mutations that knock out both copies of at least one gene from a collection of almost 1,200 genes. Genes expressed in the brain and placenta were least likely to have lost their function. The most common type of knocked-out gene was involved in smell.

The next step is to study individuals with different gene knockouts to see

SOCIAL SELECTION

Popular articles on social media

Call for open-source health data

Open Humans, an online portal that encourages US citizens to share their DNA and other medical data with researchers, launched on 24 March. The announcement sparked discussion on social media that reflected both excitement and concerns over privacy. The website, run by New York University, the University of California in San Diego and Harvard Medical School in Boston, Massachusetts, is recruiting volunteers to provide personal health information for three research studies, with others potentially on the way. 'American gut' examines human gut microbiota, 'GoViral' profiles respiratory viruses, and the 'Harvard Personal Genome Project' collects genomic data. As Madeleine Ball, a geneticist at Harvard who is the principal investigator, wrote on Twitter: "Open source yourself to accelerate scientific discovery." Although some applauded the launch, others had reservations. "Putting #opensource to the ultimate test. Where do individuals draw the line btwn privacy & progress?" tweeted Ross Whippo, a marine ecologist at the Smithsonian Environmental Research Center in Edgewater, Maryland.

➔ NATURE.COM
For more on popular papers:
go.nature.com/bbebfq

what effects, if any, these mutations have on physiology and health.

Nature Genet. <http://dx.doi.org/10.1038/ng.3243> (2015)

CLIMATE CHANGE

Ice shelves shrink fast in Antarctica

The floating parts of Antarctica's ice sheets have been thinning at increasing rates since the mid-1990s, raising fears of ice-sheet collapse and of accelerating sea-level rise in a warming climate.

Fernando Paolo of the Scripps Institution of Oceanography in San Diego, California, and his colleagues analysed an 18-year record of observations from three satellite radar missions. They found that the loss of ice-shelf volume increased from about 25 cubic kilometres a year in 1994–2003 to more than 300 cubic kilometres each year in 2003–2012.

This thinning has been most drastic in West Antarctica, where some floating shelves have lost almost one-fifth of their

thickness in 18 years. If they continue to thin at current rates, these ice shelves will completely disappear within a century.

Science <http://doi.org/278> (2015)

ASTROPHYSICS

Zapped plasma emits sounds

Sound waves could be ringing across the surfaces of stars.

A team led by Ravindra Kumar of the Tata Institute of Fundamental Research in Mumbai, India, zapped a hot, dense cloud of plasma with an ultrafast laser and found that the rapid heating of the plasma generated acoustic oscillations with a frequency of roughly one trillion cycles per second.

The authors say that the plasma within stars could also be bunching up in such waves, as a natural consequence of the way plasma flows.

Phys. Rev. Lett. 115, 115001 (2015)

➔ NATURE.COM
For the latest research published by Nature visit:
www.nature.com/latestresearch



SEVEN DAYS

The news in brief

EVENTS

Space rock scoop

NASA plans to pluck a boulder off a larger asteroid and move it into orbit around the Moon for astronauts to visit. The decision on its controversial Asteroid Redirect Mission, announced on 25 March, rules out the possibility that a spacecraft would drag an entire asteroid into lunar space. NASA plans to launch a craft in December 2020, reach a yet-to-be-decided asteroid in 2022, and bring the rock back by 2025.

Livestock disease

A global campaign to eradicate a deadly livestock virus was launched this week at a meeting in Abidjan, Côte d'Ivoire. Pestes des petits ruminants threatens 80% of goats, sheep and other small ruminants worldwide, according to the Food and Agriculture Organization of the United Nations, which co-hosted the meeting with the World Organisation for Animal Health. The agencies hope to eradicate the disease by 2030.

LHC debris cleared

Workers at CERN have managed to clear a piece of metal debris responsible for delaying the restart of the Large Hadron Collider last week. On 30 March, engineers at Europe's particle-physics lab near Geneva, Switzerland, burned away the fragment, which had caused a short circuit in a diode box, using a controlled electrical discharge. The restart of the particle accelerator should be possible within days, says Paul Collier, head of beams at CERN.

POLICY

Antibiotic strategy

On 27 March, the White House released final details of its long-term national strategy to tackle

antibiotic-resistant bacteria. The plan, announced in September 2014, includes steps such as increasing surveillance for antimicrobial resistance at hospitals and providing incentives for drug companies to develop new antibiotics. President Barack Obama requested that US\$1.2 billion be set aside in the 2016 federal budget for initiatives to help curb antibiotic resistance.

Scientist gag fear

A rule change that could prevent UK government scientists from talking to the media without ministerial approval drew fire last week. In a 27 March letter to the UK government, Fiona Fox of the Science Media Centre in London joined with heads of the Association of British Science Writers and UK

science-communications network Stempa to protest against the change to the Civil Service Code. The letter warns that this could discourage scientists from talking to the media and might harm public understanding of science. Under the 16 March ruling, civil servants require "ministerial authorisation for any contact with the media". See page 5 for more.

FACILITIES

James Webb report

The James Webb Space Telescope, the successor to the Hubble Space Telescope due to launch in 2018, is at risk of falling behind schedule, says a 24 March report from the US Government Accountability Office (GAO). The famously over-budget, US\$8.8-billion

project, a collaboration between NASA, the Canadian Space Agency and the European Space Agency, was reorganized in 2011, and government auditors have kept a close eye on it since. Managers will be integrating and testing various parts of the telescope over the next 3.5 years. As time goes on and parts are joined together, project officials will be less able to accommodate slips in the schedule, the GAO warned.

RESEARCH

Anthrax attacked

The US Food and Drug Administration has approved a drug to treat people infected with anthrax (*Bacillus anthracis*) after inhaling spores, for instance in a



PATRICIO ROBLES GIL / SIERRA MADRE / MINDEN PICTURES / CORBIS

Mexico or Spain for telescope array

San Pedro Mártir in Mexico's Baja California peninsula (pictured) is a finalist for the Northern Hemisphere site of the Cherenkov Telescope Array (CTA). On 26 March, the CTA Consortium announced that it has narrowed down the five candidates to either San Pedro

Mártir or La Palma in Spain's Canary Islands, with a site in Arizona reserved as a back-up. The consortium will make its final decision in November. The roughly 100-telescope network at the CTA's Northern and Southern Hemisphere sites will detect high-energy γ -rays.

BILL INGALLS/NASA

bioterror attack. In 2011, the US government purchased the experimental drug from its maker, Cangene in Winnipeg, Canada, for the US Strategic National Stockpile. Cangene has since conducted studies on monkeys and rabbits, finding that between 36% and 70% of treated animals survived infection. The drug will no longer require emergency-use authorization, heralding faster treatment for those in need.

PEOPLE

Hawking trademark

Theoretical physicist Stephen Hawking at the University of Cambridge, UK, is trademarking his name. According to media reports this week, he has applied to the UK Intellectual Property Office to register his name and safeguard its commercial use. In an e-mail to *Nature*, a university spokesman wrote: "It's a personal matter for Professor Hawking and is not a university issue, but I understand that it is correct that he has taken measures to protect his name."

Twin in space

NASA astronaut Scott Kelly (pictured, left) and cosmonaut Mikhail Kornienko arrived at the International Space Station (ISS) on 28 March, beginning a year-long study



into how the human body responds to long-duration spaceflight. Kelly's identical twin, Mark (pictured, right), a retired astronaut, will provide an Earth-based control, undergoing the same battery of tests so that researchers can compare the differences between the twins. Kelly and Kornienko are joined on the ISS by cosmonaut Gennady Padalka, who will stay for six months, and is expected to break the record for most cumulative time in space, currently 803 days. See go.nature.com/ikjgp4 for more.

BUSINESS

Drug buyout

The world's largest generic drug maker is to pay US\$3.5 billion to buy Auspex, a company in La Jolla, California, that is developing drugs for nervous-system disorders. Teva, of Petach Tikva, Israel, which announced the deal

on 30 March, is betting on the success of Auspex's drug SD-809 (deutetrabenazine) to recoup its investment. SD-809 is under consideration for approval in the United States for treating involuntary movements associated with Huntington's disease, and is in late-stage clinical testing for a type of involuntary movement disorder called tardive dyskinesia.

AWARDS

Turing prize

The first US\$1-million A. M. Turing Award was scooped by Michael Stonebraker of the Massachusetts Institute of Technology in Cambridge on 25 March. The computer scientist was recognized for fundamental ideas on databases that underlie modern 'big data' applications — ideas he also put into practice by co-founding numerous start-up companies. This

year's award (formally named the 2014 award) from the Association for Computing Machinery is quadruple the amount of previous years, owing to a donation from Google. It is named after the British mathematician Alan Turing.

FUNDING

Impact costs

The United Kingdom's first attempt to assess the economic and societal impact of its research cost £57 million (US\$85 million), says an analysis published on 25 March. In 2014, UK universities produced almost 7,000 case studies outlining their research impacts as part of the Research Excellence Framework (REF), a five-yearly assessment used to allocate £1.6 billion in funding annually. RAND Europe, in Cambridge, UK, said that because impact accounts for 20% of the funding assessment, the £57-million price tag translated to a 'transaction cost' of just 3.5% — lower than the estimated administration costs for grants allocated by UK Research Councils.

Renewable energy

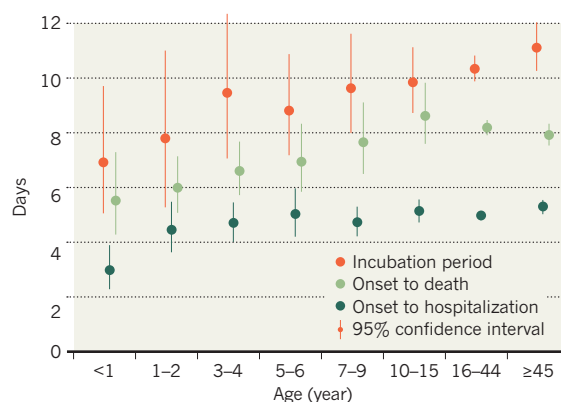
Global investment in renewable energy increased by 17% to US\$270 billion in 2014, the United Nations Environment Programme reported on 31 March. Led by China, the United States and Japan, the world added a record 103 gigawatts of capacity from renewables, which generated an estimated 9.1% of the world's electricity in 2014, up from 8.5% in 2013. The agency estimates that this reduced carbon dioxide emissions by roughly 1.3 gigatonnes — double the emissions from the global airline industry — compared with the CO₂ that would have been generated through fossil fuels. Solar and wind accounted for 92% of the total.

TREND WATCH

The Ebola virus infects fewer children than adults, but the disease progresses more quickly in children, according to a study of the current outbreak in West Africa (WHO Ebola Response Team *N. Engl. J. Med.* 372, 1274–1277; 2015). Young children had the highest case fatality rate, and also the quickest progression to death. The authors therefore recommend that children suspected to have Ebola should be referred and treated as early as possible.

EBOLA BY AGE

Incubation of the Ebola virus — and times from onset to hospitalization and to death — are shortest in young children.

SOURCE: WHO EBOLA RESPONSE TEAM *N. ENGL. J. MED.* 372, 1274–1277 (2015)

NATURE.COM

For daily news updates see:
www.nature.com/news

NEWS IN FOCUS

CLIMATE CHANGE How much global warming is too much? **p.14**

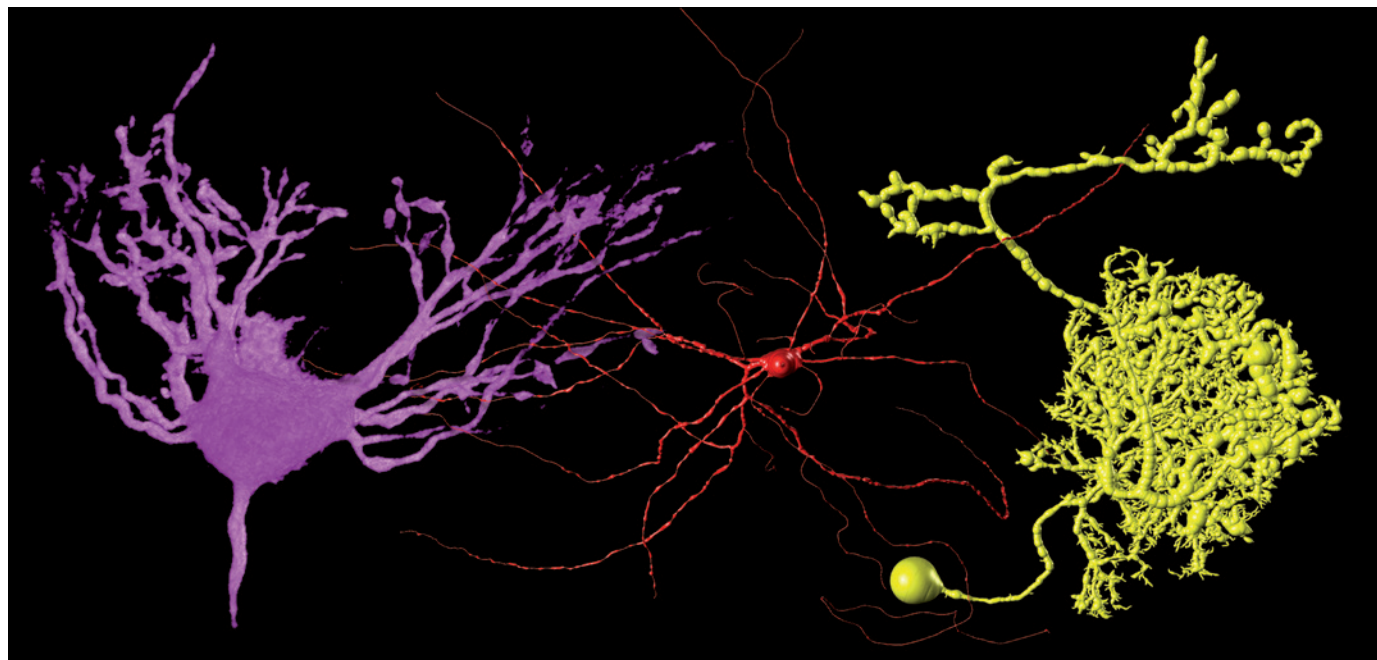
UK ELECTION Science policies of the potential kingmakers **p.16**

BIOTECHNOLOGY Gene-editing that comes in a smaller package **p.18**



MEDICINE Why less blood transfusions mean more lives saved **p.24**

ALLEN INSTITUTE FOR BRAIN SCIENCE



Brain cells from a chick (purple), turtle (red) and fruit fly (yellow) illustrate the diversity of neuron shapes.

NEUROSCIENCE

Neuron encyclopaedia fires up to reveal brain secrets

But effort to catalogue brain's building blocks may stoke disagreements over classification.

BY HELEN SHEN

An ambitious plan is afoot to build the world's largest public catalogue of neuronal structures. The BigNeuron project, announced on 31 March by the Allen Institute for Brain Science in Seattle, Washington, is designed to help researchers to simulate and understand the human brain. The project might also push neuroscientists to wrestle with fundamental — sometimes even emotional — questions about how to classify neurons.

It is the era of the mega-scale brain initiative: Europe's Human Brain Project aims to model the human brain in a supercomputer,

and the US BRAIN Initiative hopes to unravel how networks of neurons work together to produce thoughts and actions. Standing in the way of these projects is a surprising limitation. "We still don't know how many classes of neurons are in the brain," says neuroscientist Rafael Yuste at Columbia University in New York City.

BigNeuron aims to generate detailed descriptions of tens of thousands of individual neurons from various species, including fruit flies, zebrafish, mice and humans, and to suggest the best computer algorithms for extracting the finely branched shapes of these cells from microscopy data — a difficult and error-prone process.

Getting the details of the shapes right is crucial to accurately modelling the behaviour of neurons: their geometry helps to determine how they process and transmit information through electrical and chemical signals.

BigNeuron is not starting from scratch. Descriptions of neuron types date back to the Spanish neuroanatomist Santiago Ramón y Cajal, who in the late 1800s drew what he saw under the microscope. Stellate neurons are named after their starburst shape, and pyramidal neurons are recognizable by their pointed cell bodies.

But these definitions probably capture only a small slice of the diversity among the tens of millions of neurons in the mouse brain, ►

► or the tens of billions in the human one. “There are too many neurons in the brain, and we have only sampled a very, very small set,” says the Allen Institute’s Hanchuan Peng, who is leading the BigNeuron project.

A major bottleneck in cataloging more neurons has been extracting the three-dimensional structure from a stack of hundreds or thousands of two-dimensional microscope images. Neurons often turn sharply, loop back on themselves and cross over each other. So tracking all the branches can be tricky, both for humans and for machines. A simple neuron might take a few days to reconstruct by hand; a more complex cell could take months.

Computers tend not to trace neurons as well as people can, but some programs can tackle a tough case in just a few hours. Their success depends on the input data and on experimental conditions.

To make it possible to characterize thousands of neurons, the first phase of BigNeuron is to figure out which algorithms are best for specific jobs. Over the next few months, code developers will be invited to submit their best

reconstruction algorithms and neuroscientists their imaging data. Next, supercomputers will run the algorithms on the contributed data. The various reconstructions will be compared against each other and, where available, against human reconstructions, which are still considered the ‘gold standard’. All the data and algorithms will be made open-access.

The Human Brain Project, the Wellcome Trust in London and the Janelia Farm Research Campus in Ashburn, Virginia, are among those who have pledged to sponsor meetings and workshops for BigNeuron. Oak Ridge National Laboratory in Tennessee and Lawrence Berkeley National Laboratory in California will join the Human Brain Project in contributing supercomputing resources. The Allen Institute has no formal estimates yet of the project’s cost.

By 2016, project organizers hope to have a massive, annotated database of neuron morphologies. But Yuste thinks that BigNeuron will magnify another major challenge: researchers will have to agree on where to draw the boundaries between cell types.

Researchers generally agree on some neuron types, such as the chandelier cell. Other classes are not so clear, including the classic pyramidal cells, which make up about 80% of neurons in the cerebral cortex. Some researchers have proposed that the category actually encompasses many different types, whereas others see a single class of somewhat heterogeneous cells.

Egos are at stake, too, because several cell types are named after the researchers who described them. “People are very emotional about this,” Yuste says.

The problem, says Yuste, is that neuronal taxonomy has historically been based largely on qualitative descriptions and subjective assessment of microscope images. As imaging technologies and automated analysis algorithms improve, they will provide more-detailed data and quantitative measures to classify cells.

“I guarantee there are going to be new neurons that no one has ever described before, and neuron types that people have previously described that are going to get blown away,” says Yuste. ■

CLIMATE CHANGE

Global-warming limit of 2°C hangs in the balance

Panel creates scientific baseline for debate about climate reparations.

BY JEFF TOLLEFSON

In preparation for international climate talks in Paris this December, a scientific panel has completed a technical evaluation of the meeting’s official goal — to keep the global average temperature within 2°C of pre-industrial levels. Scheduled for release as soon as 3 April, the panel’s report will assess prospects for meeting this goal as well as impacts on environment and society that are likely to occur well before that threshold is breached, feeding into a potentially explosive debate about whether the target should be set even lower.

“We have provided a substantive basis for the political discussion,” says Andreas Fischlin, an ecological modeller at the Swiss Federal Institute of Technology in Zurich and co-facilitator of the process.

The 2°C goal encountered intense opposition when it was formally adopted in Cancún, Mexico, in 2010. Led by low-lying island nations and many of the poorest countries — which are likely to be hit hardest by rising seas and extreme weather — a solid majority of nations

in the United Nations Framework Convention on Climate Change called for a formal review into whether the goal should be lowered to 1.5°C. The bulk of support for the 2°C goal comes from wealthier industrialized nations, which can more easily adapt to the changing climate.

For many poor countries, the debate is about social justice, says Petra Tschakert, a geographer at Pennsylvania State University in University Park who participated in the process. Scientifically, Tschakert says, a goal of 1.5°C is clearly more protective of vulnerable populations. But developing countries recognize that meeting the 2°C goal, let alone 1.5°C, will be exceedingly difficult on the basis of current emissions trends. What they seek, she says, is a benchmark that they can use in Paris to fight for ‘loss and damages’ — monetary compensation paid by the biggest greenhouse-gas emitters to the poorer countries most harmed by warming.

“The science tells us that 1.5°C might be considerably better.”

“The real question is whether or not the high-income countries, the big polluting countries, are willing to pay loss and damages to countries that bear the brunt of the impacts,” she says. “Vulnerable countries have no other leverage within this political process.”

The history of the 2°C goal extends back four decades. At the time, researchers argued that it would be wise to keep Earth’s average temperature below the upper bound of the 10°C range that has prevailed naturally over the past few hundred thousand years. It has become increasingly clear, however, that temperatures are destined to soar well beyond anything that humans have ever witnessed. Even if countries keep to the emissions pledges they have made up to now, climate models predict that the world is on track for about 3°C of warming this century.

At the same time, a growing body of research suggests that ecological and economic impacts are already occurring with the 0.8°C of warming that has already occurred. These impacts will increase in severity as temperatures rise. Damage to coral reefs and Arctic ecosystems, as well as more extreme weather, can all be expected well



Austria's Pasterze Glacier has retreated hundreds of metres since nations began debating limiting warming to 2 °C.

ROBERT WALLIS/PANOS

before the 2°C threshold is reached, Fischlin says. But the panel had a hard time pinning down specific benefits that would accrue if warming were limited to 1.5°C.

"The science tells us that 1.5°C might be considerably better," Fischlin says. "But the uncertainties are often so large that they do not warrant a robust finding which would distinguish between those two worlds."

Some researchers argue that the international community should adopt more meaningful measures such as atmospheric carbon dioxide concentration, which has steadily risen in the past half-century in association with a rise in emissions, from about 320 parts per million to 400 parts per million.

"There's been a very strong incentive for governments to make bold claims about long-term

goals that they cannot deliver on," says David Victor, a political scientist at the University of California, San Diego. "If you start setting goals in terms of emissions, you get closer to what real governments and firms have control over."

Victor acknowledges that it may be politically impossible to get rid of the temperature target this year, but he says that negotiators are at least talking about another long-term goal: bringing net emissions to zero later this century. This would require drastic reductions in industrial greenhouse-gas emissions as well as reforestation and other land-use strategies that can pull carbon out of the atmosphere.

Fischlin says that the review should help to clarify one thing for policy-makers: over the short term, there is little practical difference between a 1.5°C world and a 2°C world. In both cases, governments must take immediate and aggressive action to start to steer the global emissions curve away from its upward trajectory. Some modest good news on that front came on 13 March, when the International Energy Agency in Paris announced that carbon emissions remained flat in 2014, the first time that has happened outside an economic recession.

"The big question now is whether we are going to start turning things around," Fischlin says. "This is more important than the precise details of the long-term goal." ■



Nicola Sturgeon, leader of the Scottish National Party and First Minister of Scotland.

UK ELECTION

Upstart parties set out science plans

What the rising influence of historically minor parties means for research policy.

BY ELIZABETH GIBNEY AND DANIEL CRESSEY

The UK general election on 7 May is uncertain on many fronts — not least in terms of what it means for science. Instead of the usual three-horse race between the two biggest parties, Labour and Conservative, and the Liberal Democrats (the country's historical 'third party'), it is likely that no one party will gain a majority, triggering a hung Parliament. As a result, a clutch of historically minor parties have a real chance of holding the balance of power — either as part of a formal coalition or by offering support to a minority government.

In a sign of the changing times, on 2 April, the leaders of seven parties are scheduled to participate in a televised debate; at the last general election, the debates featured just three parties.

So far in the run-up to the election, science has not featured prominently in the policies of any party. At a debate on 11 March at the Houses of Parliament, organized by the Society of Biology, representatives of the Conservatives, Labour and Liberal Democrats were all clear on the need to increase investment in science. However, only the Liberal Democrats, who are very unlikely to gain a majority, could commit to retaining the government's ring-fenced budget for research — a pot of

£4.6 billion (US\$6.8 billion) in annual funding.

Anne Glover, a molecular and cell biologist at the University of Aberdeen in Scotland and former scientific adviser to the European Union, says that the smaller parties might do well to prioritize investment in science to project an appealing message to voters. "It's a very positive thing, in an environment where there's a lot of negative campaigning," she says.

In the event of a hung Parliament, even minor parties that do not enter a formal coalition with the Labour or Conservative parties could still "greatly influence" policies, says Vernon Bogdanor, who studies government and politics at King's College London. "In some ways, you're stronger outside the government because you can bring the government down."

In a poll of *Nature* readers (see 'The science vote'), 74% — unsurprisingly — said that candidates' attitudes to science would affect their vote.

Nature outlines how three of the minority parties most likely to wield power would influence science.

GREEN PARTY

As the name suggests, the Greens have a lot to say about the

natural world. But with a philosophy rooted in environmentalism, the party presents a mixed bag for research: it has pledged to try to increase government spending on science, but also to curb animal research, nuclear power and the commercial use of genetically modified (GM) organisms.

The party's science spokesman, James Abbott, says that its opposition to all forms of animal research is not anti-science. "The Green Party approach to science is based on both evidence and ethics," he says. "So we understand that animal experiments can be used in medicine, but disagree that that justifies pain and suffering to animals." But Wendy Jarrett, chief executive of the London-based Understanding Animal Research group, which lobbies for scientists who work with animals, says that the Greens' policies would be a "disaster for science". "They are premised on a number of misapprehensions, such as that there are ready alternatives to using animals," she says. She fears that much medical research would relocate out of the United Kingdom if the Greens were to succeed in curbing animal research.

Other Green policies may sit better with scientists. Abbott notes that the party set a target for government science spending at 1% of gross domestic product, equal to that suggested by a group of academic bodies in February (the current science budget is smaller). The Greens also say that curbing global warming is a priority — and that they support government investment in renewable energy. But Peter Knight, emeritus professor of physics at Imperial College London and former president of the Institute of Physics in London, fears that if the Greens have greater influence in government, nuclear power could fall lower on the government agenda, which would make it hard for the United Kingdom to achieve its carbon dioxide reduction goals.

Abbott notes that the party is not against nuclear fusion — a technique that would fuse, instead of split, atoms to generate power. Nor does it oppose the use of GM organisms in research laboratories. However, the party vehemently opposes growing GM crops on a commercial scale, until its concerns about safety and the influence of large companies can be assuaged. "We think science plays an absolutely crucial role in society," says Abbott, "but what we're about is making sure that's done in an ethical framework."

The Green Party has one Member of Parliament in the outgoing government, and is targeting 11 more seats in the general election. The party says that it would not take part in a formal coalition government.

Natalie Bennett,
Green Party leader.



CHRISTOPHER FURLONG/GETTY



UKIP leader Nigel Farage.

UKIP

Best known for its goal to remove the United Kingdom from the European Union and introduce stricter policies on immigration, the UK Independence Party (UKIP) has an iffy record on science. Traditionally climate-sceptic, it attracted ridicule when a party member asked in a debate, “What happens when the renewable energy runs out?” — but later she said that she meant ‘renewable-energy subsidies’.

Ahead of the election, UKIP has found a more rational voice in parliamentary candidate Julia Reid, currently a Member of the European Parliament and UKIP’s science spokeswoman.

Reid has a PhD in pharmacology and is formerly a researcher at the Royal United Hospital in Bath. Although she is sceptical that climate change is man-made, UKIP’s policies on other issues seem crafted to appeal to scientifically minded voters. UKIP would scrap university tuition fees for science, mathematics and engineering students. And Reid told *Nature* that she is keen to see a “return to research for research’s sake” — although if the party had its way and the United Kingdom left Europe, it would also lose some €2 billion (US\$3 billion) annually in grants from the European Union’s Horizon 2020 research programme.

Reid has also reassured scientists that the party’s proposals on immigration consist of a points system that would prioritize highly skilled workers, such as scientists. But no academic that *Nature* spoke to was convinced. “Even if you were eligible for a points scheme, the rhetoric of ‘not welcome here’ would deter people from applying,” says David Price, vice-provost at University College London. Anything that deters foreigners from studying in the country would also be damaging to the higher-education ecosystem overall, he adds, because the financial health of UK universities relies on fees from international students, who pay much more than do domestic students.

SCOTTISH NATIONAL PARTY

On immigration, the Scottish National Party (SNP) could not differ more from UKIP. “Scotland has a clear economic rationale for growing

our population,” says an SNP spokesperson. The party sees immigration as a way to strengthen the Scottish economy, by growing the working-age population, she says. It would also support the reintroduction of a post-study work visa for international students, which was scrapped by the current UK government, an action that is widely blamed for a drop in university applications from abroad.

The SNP is likely to prove chief among the kingmakers. After narrowly losing a referendum on Scottish independence in September last year, its support is booming, while Labour support in Scotland has collapsed. That means the SNP might get as many as 50 of the 650 parliamentary seats in the House of Commons (it has just 6) and beat even the Liberal Democrats, now in fourth place according to most polls. Although the left-leaning SNP says that it would not work with the Conservatives, it is willing to work with Labour. But a point of friction would arise over the renewal of the United Kingdom’s nuclear deterrent, the Trident submarines based on Scotland’s west coast. The SNP is vehemently

against the plans and the issue would be “fundamental” for the party in the event of no outright majority after May’s election, says the spokesperson.

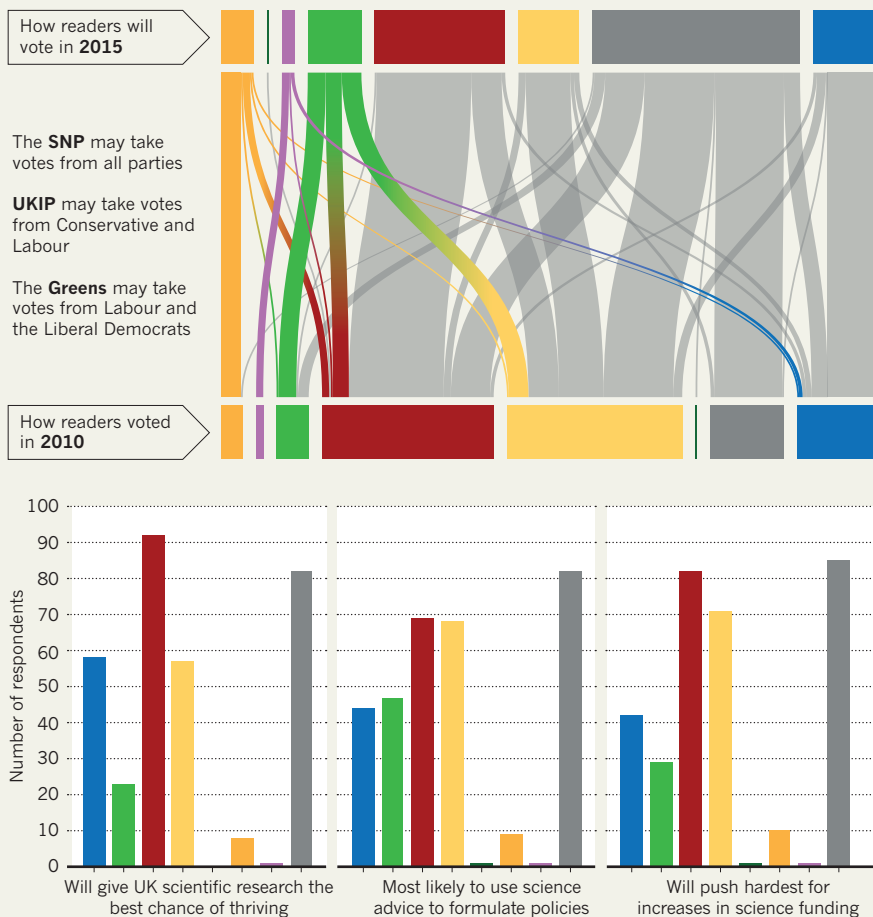
The SNP is the only one of these three minor parties to have held any power, having run the partially autonomous Scottish government since 2007. “I felt that the SNP really understood the value of science, both in terms of economic value and the value in evidence-based policy making,” says Glover, who was chief scientific adviser to the Scottish government from 2006 to 2011. The party has championed Scotland’s ‘research pools’, which encourage collaboration between institutions, as well as innovation centres that bring together academia and industry. Both are widely praised by Scottish scientists (see *Nature* 513, 151–152; 2014). By 2020, the SNP ambitiously aims for Scotland to generate an amount of energy from renewable sources that is equal to its electricity needs. Like the Greens, the SNP does not support building nuclear-power stations. ■ [SEE EDITORIAL P.5](#)

THE SCIENCE VOTE

Nature polled 321 of its readers about the 7 UK parties scheduled to appear in the first televised debate of the general-election campaign. Here we show how the support for each party has changed compared with the last election — and how readers rate the parties on science issues.

NATURE.COM For an interactive version, see go.nature.com/ey2qv7

■ SNP
 ■ UKIP
 ■ Labour
 ■ Conservatives
 ■ Plaid Cymru
 ■ Greens
 ■ Liberal Democrats
 ■ None, other or don't know



Mini enzyme moves gene editing closer to the clinic

Discovery expands potential CRISPR toolbox for treating genetic diseases in humans.

BY HEIDI LEDFORD

A tweak to a technique that edits DNA with pinpoint precision has boosted its ability to correct defective genes in people. Called CRISPR, the method is already used in the lab to insert and remove genome defects in animal embryos. But the genetic instructions for the machinery on which CRISPR relies — a gene-editing enzyme called Cas9 and RNA molecules that guide it to its target — are simply too large to be efficiently ferried into most of the human body's cells.

This week, researchers report a possible way around that obstacle: a Cas9 enzyme that is encoded by a gene about three-quarters the size of the one currently used. The finding, published on 1 April in *Nature*, could open the door to new treatments for a host of genetic maladies (F. A. Ran *et al.* *Nature* <http://dx.doi.org/10.1038/nature14299>; 2015).

"There are thousands of diseases in humans associated with specific genetic changes," says David Liu, a chemical biologist at Harvard University in Cambridge, Massachusetts, who was not involved in the latest study. "A fairly large fraction of those have the potential to be addressed using genome editing."

Genome editing has generated controversy, with unconfirmed reports of its use in human embryos. Some scientists have expressed concern that the technique might be used by fertility doctors to edit the genes of human embryos before its safety is established (see also E. Lanphier *et al.* *Nature* **519**, 410–411; 2015). That concern is exacerbated by the fact that changes made by the procedure in embryos would be passed to all subsequent generations without giving anyone affected the opportunity to consent

(see *Nature* **519**, 272; 2015). But in the non-reproductive cells of children and adults, where intergenerational issues are not a concern, researchers and companies are already racing to develop CRISPR as a clinical tool.

The ethics of that pursuit may be more straightforward, but its execution can be harder than using CRISPR in embryos. An embryo consists of a small number of cells that give rise to a human. To edit the genome at that stage is simply a matter of injecting the necessary CRISPR components into a few cells. An adult human, however, is a mix of trillions of cells assembled into many different tissues. Researchers fret over how to target the CRISPR machinery to the specific cells where defective genes are disrupting physiological processes.

"You can have the most optimal gene-editing system in the world, but if you can't deliver it to the proper cell type, it's irrelevant," says Nessim Bermingham, chief executive of Intellia Therapeutics in Cambridge, Massachusetts, which aims to bring genome editing to the clinic. "We're spending a tremendous amount of time working on it."

SNUG FIT

Gene-therapy researchers often harness a virus called AAV to shuttle foreign genes into mature human cells. However, most laboratories use a gene encoding the Cas9 protein that is too large to fit in the snug confines of the AAV genome alongside the extra sequences necessary for Cas9 function.

Feng Zhang of the Broad Institute of MIT and Harvard in Cambridge, Massachusetts, and his colleagues decided to raid bacterial genomes for a solution, because the CRISPR system is derived from a process that bacteria use to snip unwanted DNA sequences out of their genomes. Zhang's team analysed genes encoding more than 600 Cas9 enzymes from hundreds of bacteria in search of a smaller version that could be packaged in AAV and delivered to mature cells.

The gene encoding Cas9 in *Staphylococcus aureus* — a bacterium best known for causing skin infections and food poisoning — was more than 1,000 DNA letters smaller than the one for the commonly used Cas9. The researchers packed it into AAV along with RNAs that would target the enzyme to modify a cholesterol regulatory gene in the liver. Within a week of injecting mice with the modified virus, the team found that more than 40% of liver cells contained the modified gene.

"It's a terrific addition to the set of tools that genome engineers have at their disposal," says Liu. He has been developing ways to transport the larger Cas9 protein, bound to its guide RNAs, into cells without relying on a virus. Bermingham says that he expects labs to develop multiple delivery mechanisms that are tailored to individual tissues.

For now, biomedical engineer Charles Gersbach of Duke University in Durham, North Carolina, is eager to use the smaller Cas9 enzyme in mice to try to correct mutations associated with Duchenne muscular dystrophy, a devastating human disease that strikes 1 in 3,500 boys worldwide. Perhaps this will be the method that carries CRISPR into the clinic, he says, but it is too soon to tell. "It's a rapidly developing field," he says. "There are a lot of things that just haven't been tried yet." ■

"It's a terrific addition to the set of tools that genome engineers have at their disposal."


**MORE
ONLINE**

NEUROSCIENCE AND SOCIETY



Children's brains and cognitive ability are affected by poverty
go.nature.com/fkgghf

MORE STORIES

- Struggle to confirm archaeological damage in Iraq
go.nature.com/lq5lcl
- Psychiatric trials halted at University of Minnesota
go.nature.com/6kfeuu
- Concern over payment for 'fast-track' review
go.nature.com/tj3nkw

CORRECTIONS

The News Feature 'Eyes on the ocean' (*Nature* **519**, 280–282; 2015) used an earlier version of the name of the Pew Charitable Trusts. And the News Feature 'Biotech boot camp' (*Nature* **519**, 402–405; 2015) should have said that Steve Blank was involved in eight technology companies — he didn't launch all eight.



Battle for the Amazon

Brazil has waged a successful war on tropical deforestation, and other countries are trying to follow its lead. But victory remains fragile.

BY JEFF TOLLEFSON

Oziel Alves da Silva reins his horse to a stop near the edge of a pasture, and adjusts a baseball cap that has done little to protect his leathery skin from the tropical sun. Keeping an eye out for his herd, he surveys his 274-hectare ranch located in the eastern Amazonian state of Pará. Where he once dreamed of a vast open field covered with grasses and cattle, he sees nothing but palm trees that he cannot cut down.

The 39-year-old rancher is one of thousands of Brazilian landowners stymied by a historic campaign to halt the destruction of the world's largest rainforest. He was fined 720,000 reais (US\$230,000) and banned from selling cattle after trying to clear this field in 2009. Now Alves da Silva is once again operating legally, and he has little hope of expanding his pasture and increasing his herd. Along with many fellow ranchers

in the county of Brasil Novo, he has stopped cutting down trees and is trying to make peace with the law.

"We came together and decided we needed to change," he says.

Over the past decade, while the world has been busy haggling over future commitments to reduce greenhouse-gas emissions, Brazil has lowered its carbon dioxide output more than any other country through a historic effort to slow forest loss. The deforestation rate here last year was roughly 75% below the average for 1996 to 2005 — just shy of Brazil's pledge to achieve an 80% reduction by 2020. The country has managed this feat while increasing the amount of food it produces, much of it for export to a growing and hungry world.

Brazil's experience suggests that humanity has a chance to control agricultural expansion and preserve the planet's most diverse ecosystems. If other countries follow suit by protecting and expanding forests, which lock carbon up in trees and soils, they could slow the growth of global CO₂ emissions and buy the world some time to solve the thornier problem of curbing emissions from cars, power plants and industrial facilities.

"There is no question that Brazil has made a fundamental departure from the past," says Achim Steiner, executive director of the United Nations Environment Programme. "And it has given credence to the notion that forest conservation may be an important mechanism for international cooperation on climate."

Although Brazil's downward trend in deforestation has been evident for nearly a decade, it is only in the past couple of years that researchers have pieced together how the country put the brakes on an epidemic of illegal development that has eliminated roughly 20% of the Brazilian Amazon over the past half century. Even today, the story varies depending on who is telling it. This is what drew me to the Brazilian Amazon for two months last year. I travelled throughout the region, talking to scientists, ranchers, politicians, loggers and members of indigenous tribes — all with the aim of understanding how Brazil altered its environmental trajectory and where it goes from here.

Various factors conspired to curtail deforestation. The federal government designated areas in the Amazon basin for protection, cracked down on ranchers, farmers and land speculators, and put pressure on

Brazilian soldiers investigate illegally deforested land in 2009 in Pará state in the eastern Amazon.



The team promptly burned the camp to the ground, putting an end to that operation — at least for the moment.

The culprits that IBAMA encounters on the ground are often bit players, but the government is also investigating criminals higher up the chain, who make money by speculating on illegally cleared land. After I left, last August, the agency cracked down on a crime syndicate in Pará, arresting 22 people. And in February, IBAMA announced the arrest of the “largest deforester of the Amazon”: Ezequiel Castanha, a businessman in Novo Progresso who allegedly headed the syndicate and had spent months on the run. Officials say that deforestation in the region has dropped by 65% since August.

The basic outline of this enforcement strategy emerged in 2004 under former environment minister Marina Silva, a lifelong environmentalist and candidate in last year’s presidential elections. As minister, Silva tackled deforestation by strengthening IBAMA and bringing other government agencies on board. One key change she made was instituting a sophisticated system to root out corruption within IBAMA.

In parallel, the environmental group Greenpeace increased public pressure on companies by documenting the link between soya-bean farming and deforestation in media campaigns in Brazil and internationally, which pushed supermarket chains and food companies such as McDonald’s to declare a boycott on the purchase of illegally farmed soya. All of these changes helped to push the country’s major exporters to sign a moratorium in 2006, banning the purchase of soya beans from recently cleared land. Two years later, IBAMA published a blacklist of counties with the highest deforestation rates. Areas on the list faced increased enforcement by IBAMA, and landowners encountered tighter standards when they tried to take out agricultural loans. Brasil Novo was on the inaugural list, and IBAMA quickly descended on ranchers such as Alves da Silva.

Brasil Novo has since reduced its deforestation rate and is one of the latest counties to make it off the blacklist, but it was a hard road, says Zelma Campos, the region’s secretary of the environment. At a public meeting on land regulation in May last year, Campos told me that all ranchers — even law-abiding ones — had trouble marketing

local governments, while environmentalists ramped up campaigns against companies that were exporting beef, leather and soya beans from illegally cleared land. States and communities recognized that their economies were at risk, which drove them to develop their own policies (see ‘How fish and condoms can save the forest’).

Brazil’s success thus far offers potential lessons for other tropical countries where deforestation is on the rise, but the situation in the Amazon remains precarious. Enforcement has increased, but the basic factors driving deforestation — including poverty and the profitability of agricultural land — have not changed. Although the rate of land clearing in Brazil last year fell to its second lowest level since 1988, it had spiked in 2013, and some scientists expect another increase in 2015.

“Brazilians do not want deforestation,” climate scientist Carlos Nobre told me when I visited him in Brasília, where he was finishing his term as secretary for research and development at the Ministry of Science. But clearing and planting new land remains the primary force for economic growth in the Amazon, he says. “We do not yet have an alternative model.”

INCENDIARY MEASURES

The battle against illegal deforestation in Brazil starts with satellite images of the land surface. Since 1988, researchers have been compiling high-resolution maps of the forest cover each year. They obtain low-resolution images more frequently to spot fresh openings in the forest. Over the past decade, scientists have begun providing real-time information to Brazil’s environmental enforcement agency, the Brazilian Institute of Environment and Renewable Natural Resources (IBAMA).

In June last year, I joined an IBAMA team and its heavily armed police escort as they launched raids in southwestern Pará, which remains a hotbed for deforestation. We spent hours barrelling down shoddy roads in search of fresh clearings seen on satellite imagery. One day, the team interrogated landowners, searched homes and confiscated guns and chainsaws, but did not find the suspicious spot. A second outing in a different area looked like it was going to end the same way, but towards evening the crew found a couple of trails off the road. We hiked 50 metres through the underbrush and the sky opened up over a field of felled trees. On the other side of the road was an encampment, complete with a large tarpaulin-covered A-frame, hammocks and a propane stove.

“If we are successful in implementing this, it’s going to be a revolution.”

their beef when the blacklist came out. As a result, the local economy shrank and the tax base contracted, which undermined public services. Eventually, Brasil Novo’s only slaughterhouse was shut down. “No one wants to invest in a municipality with environmental problems,” explained Campos.

But this was just the beginning. In 2009, a 27-year-old federal prosecutor named Daniel Azeredo filed a lawsuit against various ranchers and 11 of the largest slaughterhouse operators in Pará, the state with the most deforestation in the Amazon. He warned major purchasers of beef and leather — including the supermarket chain Walmart, McDonald’s and the Adidas clothing company — that they could be held accountable for marketing illegal products. Greenpeace mounted another international public-relations campaign, and the cattle industry in Pará briefly ground to a halt.

For Azeredo, the fundamental problem was that nobody knew who owned what, which enabled outlaws to rule with violence. In a series of legal settlements, he pushed companies and local governments to support a rural land registry in Pará that was designed to help resolve conflicts over land ownership and allow the government to formally license agricultural operations. Greenpeace followed up by pushing major slaughterhouses into signing a moratorium — like the soya-bean



A condom factory in Acre uses sustainably collected latex.

HOW FISH AND CONDOMS CAN SAVE THE FOREST

Acre state is trying to build an economy that does not threaten the Amazon.

Music blared as hundreds of people gathered last September for the opening of a fish-food factory in Brazil's Acre state. Some ventured into the afternoon sunlight for a tour of the fish ponds while VIPs visited the facility, which was built with the help of Danish engineers. Nearby, construction was under way on a fish-processing plant.

Once finished, the US\$32-million complex could make Acre, on the border with Peru and Bolivia, a national powerhouse in aquaculture. Just as importantly for the state, which joined industry partners to invest in the facility, the plant could provide a source of protein that is an alternative to beef raised in cleared rainforest.

Acre is a role model at a time when governments are looking for sustainable forms of development. The aquaculture complex is the latest in a series of green investments by the governing Workers' Party, which has long put forest protection and social justice on top of its agenda.

"Acre really is the leader," says Steve Schwartzman, an anthropologist with the Environmental Defense Fund in Washington DC who has been working in the state since the 1980s. Although Acre remains relatively poor, Schwartzman says that agricultural production there is increasing, basic measures of social well-being are on the rise and economic development is growing faster than in neighbouring states. "Clearly they are doing something right."

In many ways, Acre is the birthplace of the modern Brazilian socio-environmental movement, begun by workers who tapped rubber trees and tried to stop ranchers from clearing land. Chico Mendes, leader of the rubber-tapper union, was murdered in 1988, but his colleagues went on to dominate state politics. One of them, Marina Silva, transformed Brazil's forest policy as environment minister from 2003 to 2008.

Building on its history, Acre's initial investment was in rubber, which can be sustainably harvested by rural residents. The state built a now-famous natural-latex condom factory in 2008, and offered subsidies to communities that produced the rubber. It also set up facilities to process and market Brazil nuts, another sustainable commodity. And it advanced its own system for mapping forests, calculating emissions and selling carbon credits for verified reductions in emissions from deforestation.

The German Development Bank has already bought nearly 16 million euros' (US\$17.5 million) worth of carbon credits from Acre. The state is also pursuing a deal with California that would allow businesses there to purchase credits.

Governor Tião Viana says that Acre has pursued an environmental vision, but it needs to show a return. Without sufficient investment from governments or companies, Viana says, the state's experiment will hit a wall as coffers dry up. "We need to do this together," he says. "We aren't looking for favours, we are looking for investments." **J.T.**

companies had three years earlier — on the purchase of beef from recently deforested lands.

The upshot is that the land registry has expanded from around 500 properties in 2009 to more than 112,000 today, covering 62% of the private land in the state. Deforestation in Pará has dropped by more than 57% over the same period (see 'Food and forests').

"This was huge," says Paul Barreto, a senior scientist with the Amazon Institute of People and the Environment, an environmental group based in Pará's capital, Belém. "The lawsuit was against the big companies but in the end it brought along everyone."

In 2012, faced with rural protests over the new enforcement regime, the Brazilian Congress revised its forest code. The new law scaled back various forest protections and let some landowners off the hook for past deforestation, but it also created a national land registry that was designed to serve as the basis for federal land management.

The move has triggered its own controversies. The soya-bean industry says that because the federal registry will enable the government to improve monitoring of landowners, the 2006 moratorium on sales is now unnecessary. But environmentalists argue that the registry is not ready. The debate has intensified questions about what caused the drop in deforestation, and what should come next.

FORCES IN THE FOREST

Scientists have been looking into these questions, trying to pick apart the factors that influence deforestation. In a study published last year, a research team confirmed suspicions that broader economic forces — which reduced agricultural profitability a decade ago — deserve partial credit for the initial drop in deforestation (D. Nepstad *et al. Science* **344**, 1118–1123; 2014). But deforestation rates remained low even when the economics improved; stricter enforcement and initiatives such as the moratoria seem to be why.

"It's basically a diffusion of different instruments, some of which have gained traction," says lead author Daniel Nepstad, a tropical ecologist who heads the Earth Innovation Institute, an advocacy group based in San Francisco, California. "It's impossible to quantify any of these factors individually, but they are all pushing in the right direction."

Holly Gibbs, a geographer at the University of Wisconsin–Madison, says it is possible to identify some of the more successful policies. She and her colleagues found that deforestation was higher in areas not covered by the soya-bean moratorium, including on properties that are already on the federal land registry (H. K. Gibbs *et al. Science* **347**, 377–378; 2015). Unpublished results suggest that the beef moratorium has had a similar effect on ranchers, who fear being banned from markets if they clear land.

"These moratoria are really leading to huge changes on the ground in Brazil," says Gibbs, and that raises questions about what will happen if the soya-bean moratorium is lifted as scheduled next year.

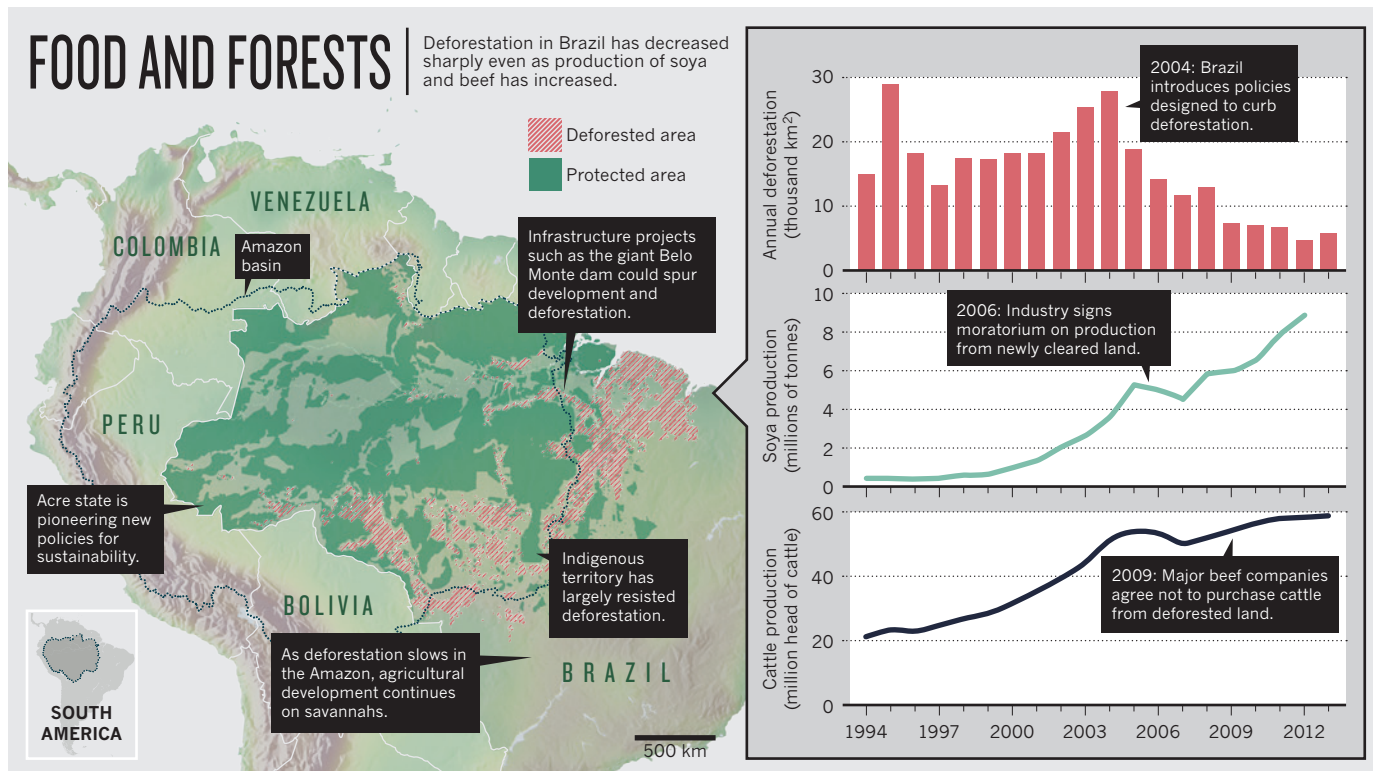
Brazilian officials nonetheless see the registry as the foundation for a new brand of land management. Government researchers are working on a monitoring system to classify and track different kinds of land use across the entire country as a complement to the national land registry. This could lead to an unprecedented capacity to track, study and promote better land use nationwide, they say.

"If we are successful in implementing this, it's going to be a revolution," says Francisco Oliveira, who heads the forest enforcement programme at the Ministry of the Environment in Brasília.

Even if the registry is successful, a fundamental challenge remains. It is cheaper for landowners — and more profitable for rogue speculators — to slash and burn forest than to rejuvenate soils and replant fallowed fields. Brazil is looking for ways to tilt the balance by improving and expanding operations on tracts of land that have already been cleared, using an influx of money designated for forest protection. In 2008, Norway agreed to pay \$1 billion if Brazil successfully reduced deforestation and thus CO₂ emissions. It was the world's first large-scale demonstration of

NATURE.COM

For a narrated slideshow on the Amazon, see: go.nature.com/kqjwyd



a strategy called REDD (Reducing Emissions from Deforestation and Forest Degradation). And Norwegian officials visited Brazil last month to talk about a second investment.

Brazil has dispersed more than \$150 million so far for projects on issues such as agricultural productivity, biodiversity research and land-use planning. But relatively little money has gone to landowners or programmes that noticeably benefit them. “The farmers are sort of sitting there bewildered, because they are not getting the incentives they were promised,” Nepstad says.

He is working with major soya-bean and beef companies, as well as government officials, on an approach that would help farmers by rewarding those who meet key standards instead of punishing them for poor performance. Landowners in counties that reduce deforestation could get easier access to low-interest loans, for instance. This approach could also involve direct payments to counties and landowners.

Brazil’s experience could inform the rollout of an international REDD programme created in 2013 under the United Nations Framework Convention on Climate Change. Although it is a shadow of the plan that many had imagined, the basic idea remains the same: industrialized nations pay for carbon to be maintained or increased in trees and soils through better forest management.

This approach has received more than \$7 billion from countries such as Norway, Germany, the United Kingdom and the United States. Much of that money has been invested in projects that are intended to demonstrate the idea and help governments to improve their forest-monitoring expertise. Last year, Brazil became the first country to submit its baseline forest assessment documenting deforestation to the United Nations. In December, five other countries announced their own submissions.

Initial payments could begin as early as 2017. Although there are no current provisions for long-term funding, negotiators hope to secure money in a treaty that nations plan to sign in Paris this year. Brazil is hoping for some of that cash but is not counting on it; officials say that they will continue to focus on domestic efforts.

International attention is shifting now to Indonesia, which is clearing more forest than any other country. Norway has committed \$1 billion to the country if the government can demonstrate reductions in deforestation and emissions. Environmentalists are also transferring their

experience in Brazil to Indonesia, and have extracted promises to tackle deforestation from various international corporations that are active in the palm-oil industry there.

Scepticism remains about whether these strategies will succeed in Indonesia, which is building a monitoring and enforcement programme from scratch. But Nepstad points out that a decade ago, nobody would have believed Brazil was about to turn a corner. “There are seeds of what we saw in Brazil ten years ago in Indonesia today,” Nepstad says.

FUTURE OF THE FOREST

Despite a decade of progress, the future of the Amazon rainforest remains uncertain. Some lawmakers want to scale back protected areas, and President Dilma Rousseff is encouraging investments in ports and hydroelectric dams, which could trigger more deforestation. Added to that is concern over the impacts of climate change, which threatens both the rainforest and existing crops.

Paulo Moutinho, former executive director of the Amazon Environmental Research Institute in Brasilia, fears that the government is overlooking more obvious solutions, such as designating more land for permanent protection. “It’s stupid,” he says, “but there’s a sense in Brasilia that we have too much protected area.”

Others are more sanguine. Back in Pará, Azeredo told me that Brazil’s march towards law and order on the frontier is slowly paying off. With a little persistence, he says, the beef industry could achieve a reasonable level of compliance in several years’ time. “We are creating a system of governance,” he says. “Before, we didn’t even know where to start.”

This is a message that ranchers such as Alves da Silva seem to have taken to heart. “Every day that passes, government enforcement is going to increase,” he says. “It’s only going to get harder to break the law.”

With little hope of expanding his operation, Alves da Silva concentrates on the herd at hand. He ropes and vaccinates a pair of newborn calves and then finishes for the day. As the light fades, we mount our horses and set off through his pasture. Behind us, the silhouette of the forest looms large. ■

Jeff Tollefson writes for *Nature* in New York and reported from Brazil on a fellowship funded by the Alicia Patterson Foundation.



SAVE BLOOD, SAVE LIVES

Transfusions are one of the most overused treatments in modern medicine, at a cost of billions of dollars. Researchers are working out how to cut back.

BY EMILY ANTHES

In 2009, a major California hospital was looking for ways to cut costs. Stanford Hospital and Clinics was on track that year to purchase nearly US\$6.8 million worth of blood for transfusions. But a growing body of evidence was suggesting that physicians could often forego the procedure.

So, beginning in July 2010, whenever a clinician used the hospital's computerized ordering system to request blood, it would call up the patient's most recent lab results. If the numbers indicated that she or he should be healthy enough to get by without a transfusion,

an alert would pop onto the screen gently reminding the doctor of the guidelines and requesting further justification for the order.

The results, detailed in two papers published in the past 18 months^{1,2}, were dramatic. The number of red-blood-cell transfusions dropped by 24% between 2009 and 2013, representing an annual savings of \$1.6 million in purchasing costs alone. And as transfusion rates fell, so did mortality, average length of stay and the number patients who needed to be readmitted within 30 days of a transfusion. By simply asking doctors to think twice about transfusions, the hospital had not only reduced

costs, but also improved patient outcomes.

Transfusions are common procedures, at least in developed nations. In 2011, US doctors transfused 21 million units of blood and blood products; in the United Kingdom, the number was nearly 3 million. But although transfusions can be lifesaving, they are often unnecessary and are sometimes even harmful. "I think we were kind of brainwashed into thinking that blood saves lives, and the more you give the better," says Steven Frank, an anaesthesiologist and director of the blood-management programme at the Johns Hopkins Health System in Baltimore, Maryland. "We've gone 180 degrees, and

PHOTOGRAPH BY GREG WHITE

now we think that less is more.”

Scientists are now recommending a more conservative approach to transfusions. But changing decades of established medical practice is not easy. Even when guidelines are clear, evidence suggests that clinicians often fail to follow them. “Weaning doctors off their love affair with blood is going to be harder than we think,” says Ian Roberts, director of the Clinical Trials Unit at the London School of Hygiene & Tropical Medicine.

TRANSFUSION TRIGGERS

Significant blood loss — as well as conditions ranging from leukaemia to vitamin deficiencies — can leave body tissues starved of oxygen. Transfusions of red blood cells collected from compatible donors are designed to reverse this state. (Some patients may receive transfusions of other blood components, such as platelets, which help with clotting, but red-cell transfusions are by far the most common.)

Scientists and doctors have experimented with transfusion since at least the seventeenth century, but the procedure did not become routine until the early 1900s, after researchers found that there were different blood groups and learned how to store donated blood. Blood banking really took off during the Second World War. In Britain, collection teams travelled around the country, tapping citizens’ arms to help soldiers on the front lines. “Will you help by giving a little of your blood?” a 1944 poster implored. “The lives of our wounded depend upon it.” By the end of the war, more than 750,000 people had heeded the call, some donating seven or eight times.

In the decades since, appeals for blood have become common, particularly in times of war or disaster. But transfusions were widely adopted without rigorous scientific scrutiny. At the time, randomized controlled trials were not standard, and the rationale for transfusion seemed obvious. “I think people took blood for granted,” Roberts says. “They thought ‘Well, if people are losing blood then they must need blood.’”

In the 1980s and 1990s, a confluence of factors sparked interest in cutting back. The discovery of the blood-borne hepatitis C and HIV raised concerns about the safety of transfusions. The resulting expansion of testing for infectious diseases increased the cost of collection, and toughened screening standards contributed to a decline in donations. Some clinicians began to wonder if they could get by with less.

In 1994, a team of Canadian researchers launched a study to evaluate how patients would respond to more sparing use of blood. Doctors typically decide whether to do a transfusion by measuring a patient’s level of haemoglobin, the protein inside red blood cells that binds to oxygen. The World Health Organization defines a healthy haemoglobin level as 13 grams per decilitre (g dL⁻¹) of blood or higher in men, and 12 g dL⁻¹ in women. Historically, doctors would consider a transfusion when a patient’s

haemoglobin fell below 10 g dL⁻¹, a trigger that was proposed in a 1942 paper³.

The Canadian team, led by epidemiologist and critical-care specialist Paul Hébert, put this widely used threshold to the test. The researchers randomly assigned 838 intensive-care patients to two groups: those in one group would receive a transfusion if their haemoglobin levels fell below 10 g dL⁻¹, and the other if their levels dropped under 7 g dL⁻¹.

After 30 days, all the people in the first group had received a transfusion, each receiving an average of 5.6 units of red blood cells (a unit is

“WEANING DOCTORS OFF THEIR LOVE AFFAIR WITH BLOOD IS GOING TO BE HARDER THAN WE THINK.”

the amount extracted from around 500 mL of donated blood). Patients in the more restrictive group got just 2.6 units, on average, and one-third of the group received no blood at all.

Yet the probability of death remained the same in both groups. And when the researchers analysed two subgroups of patients — those under 55 years old and those with milder illnesses — they found that the restrictive approach had actually reduced mortality.

“When we saw the results, the first thing I asked the statistician was, ‘Are you sure the group assignment was correct?’” recalls Hébert, who is now at the University of Montreal in Canada. “And then we proceeded to check all of our results because, frankly, we didn’t believe it.”

The team published its results in the *New England Journal of Medicine*⁴ in 1999. It was just one trial, but it got people’s attention, says Lawrence Tim Goodnough, director of the transfusion medicine programme and transfusion services at Stanford University Medical Center. “Everybody saw that and said, ‘We need to redo this in other clinical settings.’”

Between 2007 and 2014, at least six more large, randomized trials were published^{5–10}, each comparing restrictive guidelines to liberal ones. These trials enrolled patients with a wide variety of conditions — septic shock, traumatic brain injuries, gastrointestinal bleeding — as well as children in intensive care, adults undergoing cardiac surgery and older adults having hip surgery. All six studies revealed that patients fare just as well, and sometimes better, when doctors use lower haemoglobin thresholds.

RISKY MEDICINE

Researchers are now trying to understand why transfusions do not always have their intended benefits. It could be that haemoglobin levels are not a good proxy for what doctors really

care about, which is whether enough oxygen is actually being delivered to tissues. Or it could be that the blood people are receiving is not doing its job properly.

Fresh red cells are flexible, and flow easily through the body’s tiniest capillaries. But after a few weeks in a blood bank, their membranes stiffen. The cells change shape, become stickier and cling more tightly to oxygen. These changes, known as the storage lesion, could make red blood cells less effective. “This may explain why the so-called ‘gift of life’ isn’t translating into benefit for patients,” Goodnough says. Research has yielded contradictory findings as to whether the storage lesion actually worsens patient outcomes, but the results of a large randomized trial are expected later this year.

Transfusions not only have uncertain benefits, they also have risks. They can transmit infectious diseases, overwhelm the heart and injure the lungs. They can also wreak havoc on the immune system. “Blood is analogous to a liquid organ transplant,” Frank says. “It’s foreign tissue from another person.” Doctors can prevent most catastrophic immune responses by ensuring that donor and recipient are compatible for the proteins or carbohydrates known as antigens that characterize the ABO and Rh blood types. But blood cells contain many other antigens, and incompatibilities can spark immune reactions that range from mild to fatal.

Paradoxically, transfusions can dampen the immune response and leave patients more vulnerable to infection, although the mechanism behind this remains uncertain.

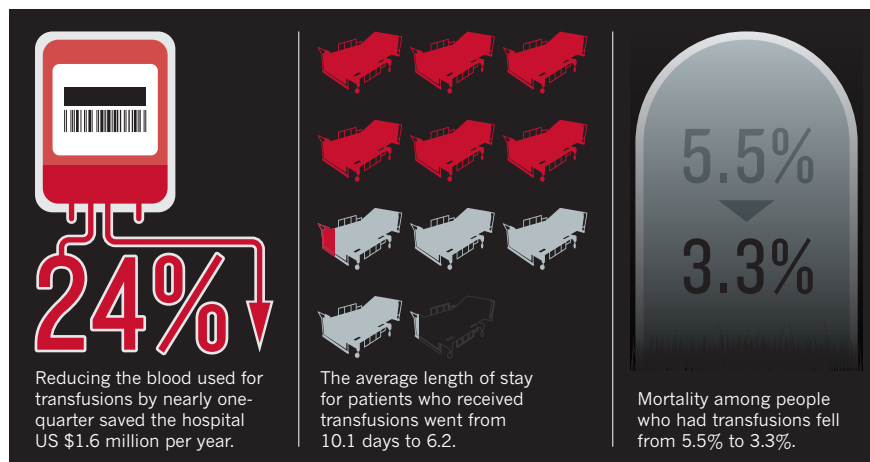
These risks may have gone unnoticed because they are not easy to observe in the course of day-to-day practice. Many people who receive transfusions are already critically ill, and infections are not uncommon in hospitals. The elevated risk that accompanies transfusions becomes apparent only when scientists analyse large patient populations.

For some patients, of course — especially those who are rapidly losing a lot of blood — transfusions are lifesaving. In a study published last year¹¹, Roberts and his colleagues found that transfusions were beneficial only to those with the most severe injuries — they actually increased mortality in people with mild injuries. And where the line should be drawn is not completely settled: there have not yet been any large, randomized trials examining whether lower thresholds are appropriate for patients having heart attacks or strokes, for example. In January, scientists unexpectedly found that liberal transfusion strategies yield better outcomes in people having surgery for cancer¹². The complexities of individual ailments and risk factors means that doctors still need to exercise their clinical judgement when deciding whether to prescribe a transfusion.

Nevertheless, experts say, it is evident that many patients have been getting unnecessary transfusions. As Roberts puts it: “There

DOCTOR'S ORDERS

By simply reminding doctors of the current guidelines when they order blood, a California hospital was able to save money and lives.



are some patients who will die without transfusions and there are some that will die because of transfusion.”

A CLINICAL EVOLUTION

The conservative approach is starting to gain acceptance among clinicians. More and more medical associations and professional organizations now recommend haemoglobin thresholds of around 7 g dL^{-1} to 8 g dL^{-1} — and hospitals are implementing strategies to reduce the odds that a patient will need a transfusion in the first place. Doctors are administering iron supplements to people with anaemia who are scheduled for elective surgery, minimizing the amount of blood drawn for laboratory tests and using ‘cell salvage’ techniques that collect and then re-infuse the blood a patient loses during surgery. Many of these measures have long been used to treat Jehovah’s Witnesses, who object to transfusions on religious grounds; now they are being applied to the broader population.

“We’re seeing more and more countries coming on board, asking for help in setting up patient blood-management programmes,” says Aryeh Shander, executive medical director of the Institute for Patient Blood Management and Bloodless Medicine and Surgery at Englewood Hospital and Medical Center in New Jersey.

The Netherlands has been at the cutting edge. In 2000, it adopted a transfusion threshold of 6.4 g dL^{-1} for otherwise healthy patients, and at least one blood bank reported a 12% decline in transfusions by 2009. And changes to blood-management programmes, new clinical guidelines and a shift towards less-invasive surgical techniques have led to declines in many other countries. In the United Kingdom, for example, the demand for red blood cells dropped by one-fifth between 1999 and 2012. And in the United States, the number of transfused units of whole blood and red blood cells fell by 8% between 2008 and 2011, the latest year for which

data are available. The AABB, formerly known as the American Association of Blood Banks, predicts that statistics to be released later this year will show a further 10% drop. Since 2001, the proportion of US hospitals that have had to cancel elective surgery because of a blood shortage has also steadily fallen.

Few believe that it is time for donors to stop rolling up their sleeves. There may still be shortages in some regions or in the aftermath of major disasters, and doctors anticipate an ongoing need for certain blood types and components, such as platelets, which do not last long in storage.

But there is still plenty of room to reduce demand, says AABB chief executive Miriam Markowitz. A 2011 audit¹³ of more than 9,000 UK transfusions, for example, found that more than half were potentially avoidable.

Merely changing clinical recommendations may not be enough. “Most people don’t pay attention to guidelines,” says Victor Ferraris, a cardiothoracic surgeon at the University of Kentucky in Lexington. And that may be particularly true when the guidelines seem to contradict first-hand observations. “Surgeons are very, very experience-oriented,” Ferraris says. “Every surgeon who’s ever lived has seen someone’s life saved by a blood transfusion.”

A study¹⁴ published last October illustrates the challenge. When scientists surveyed doctors working at two intensive-care units at Johns Hopkins Hospital, the vast majority of the clinicians reported that the ideal transfusion threshold was 7 g dL^{-1} . But the hospital’s electronic medical records revealed that 84% of patients in one unit and 92% in the other received transfusions before their haemoglobin levels fell that low. Some of the doctors deemed their patients too ill for the lower triggers and that the evidence did not apply to them, says David Murphy, the study’s first author and a critical-care specialist at Emory University in

Atlanta, Georgia. He and his colleagues also found that although doctors generally knew the recommended thresholds, many nurses did not. Nor did the units have a standardized approach, and caregivers rarely discussed the transfusion strategy for individual patients. “If you have ambiguity regarding what we should do for a patient, this greatly influences the likelihood of being able to deliver the right care,” Murphy says.

It is possible to overcome these problems, as the Stanford study showed (see ‘Doctor’s orders’). In the year before the computerized alerts began, just over half of transfusions were done on patients with haemoglobin levels of greater than 8 g dL^{-1} . By 2013, that proportion had fallen below 30%. “The fall-off was very immediate and it’s been sustained,” says Goodnough, who was the first author on the two papers^{1,2} that reported the results.

He thinks that the simple intervention succeeded for multiple reasons. For one thing, doctors may change their behaviour when they think that they are being watched. But the alerts also reminded clinicians about the guidelines, and provided links to the relevant literature. They also forced doctors to slow down and think, rather than defaulting to reflexive and long-ingrained standard procedure.

Finally, they may have provided an opening for caregivers to discuss the needs of individual patients. “Maybe the intern, who was ordering the blood because they were told to, goes back to the team and says, ‘I have to give a reason,’ and then they discuss it,” Goodnough says. The clinicians might decide to order the blood anyway, of course. Or they might stop, consider the evidence, and come to agree with what Goodnough believes is its clear message. “The safest blood transfusion,” he says, “is the one not given.” ■

Emily Anthes is a science journalist in New York City.

- Goodnough, L. T. et al. *Transfusion* **54**, 1358–1365 (2014).
- Goodnough, L. T. et al. *Transfusion* **54**, 2753–2759 (2014).
- Adams, R. C. & Lundy, J. S. *Anesthesiology* **3**, 603–607 (1942).
- Hébert, P. C. et al. *N. Engl. J. Med.* **340**, 409–417 (1999).
- Lacroix, J. et al. *N. Engl. J. Med.* **356**, 1609–1619 (2007).
- Hajjar, L. A. et al. *J. Am. Med. Assoc.* **304**, 1559–1567 (2010).
- Carson, J. L. et al. *N. Engl. J. Med.* **365**, 2453–2462 (2011).
- Villanueva, C. et al. *N. Engl. J. Med.* **368**, 11–21 (2013).
- Robertson, C. S. et al. *J. Am. Med. Assoc.* **312**, 36–47 (2014).
- Holst, L. B. et al. *N. Engl. J. Med.* **371**, 1381–1391 (2014).
- Perel, P. et al. *PLoS Med.* **11**, e1001664 (2014).
- de Almeida, J. P. et al. *Anesthesiology* **122**, 29–38 (2015).
- National Comparative Audit of Blood Transfusion: Part 1 Audit of Use of Blood in Adult Medical Patients (2011); available at go.nature.com/yubguj
- Murphy, D. J. et al. *Transfusion* **54**, 2658–2667 (2014).

SOURCE: REF 2

COMMENT

HISTORY Celebrating Mark Catesby, cataloguer of North America's wildlife **p.30**



BRAIN A compelling exploration of memory and forgetting **p.32**

ANTHROPOLOGY DNA analysis of palm-tree transplant supports Aboriginal myth **p.33**

LAB LIFE Discovery “evokes a special kind of ecstasy — it is almost like falling in love” **p.33**

ILLUSTRATION BY DAVID PARKINS



Embed the social sciences in climate policy

David G. Victor calls for the IPCC process to be extended to include insights into controversial social and behavioural issues.

The Intergovernmental Panel on Climate Change (IPCC) is becoming irrelevant to climate policy. By seeking consensus and avoiding controversy, the organization is suffering from the streetlight effect — focusing ever more attention on a well-lit pool of the brightest climate science. But the insights that matter are out in the darkness, far from the places that the natural sciences alone can illuminate.

With the ink barely dry on the IPCC's

latest reports, scientists and governments are planning reforms for the next big assessment^{1,2}. Streamlining the review and writing processes could, indeed, make the IPCC more nimble and relevant. But decisions made at February's IPCC meeting in Nairobi showed that governments have little appetite for change.

The basic report-making process and timing will remain intact. Minor adjustments such as greater coverage of cross-cutting

topics and more administration may make the IPCC slower. Similar soul searching, disagreement, indecision and trivial procedural tweaks have followed each of the five IPCC assessments over the past 25 years³.

This time needs to be different. The IPCC must overhaul how it engages with the social sciences in particular (see go.nature.com/vp7zgm). Fields such as sociology, political science and anthropology are central to understanding how people and

► societies comprehend and respond to environmental changes, and are pivotal in making effective policies to cut emissions and collaborate across the globe.

The IPCC has engaged only a narrow slice of social-sciences disciplines. Just one branch — economics — has had a major voice in the assessment process. In Working Group III, which assesses climate-change mitigation and policy, nearly two-thirds of 35 coordinating lead authors hailed from the field, and from resource economics in particular. The other social sciences were mostly absent. There was one political scientist: me. Among the few bright spots in that report compared with earlier ones is greater coverage of behavioural economics and risk analysis. In Working Group II, which assesses impacts and adaptation, less than one-third of the 64 coordinating lead authors were social scientists, and about half of those were economists.

Bringing the broader social sciences into the IPCC will be difficult, but it is achievable with a strategy that reflects how the fields are organized and which policy-relevant questions these disciplines know well. It will require big reforms in the IPCC, and the panel will have to relinquish part of the assessment process to other organizations that are less prone to paralysis in the face of controversy.

TUNNEL VISION

The IPCC walks a wavering line between science, which requires independence, and diplomacy, which demands responsiveness to government preference. Although scientists supply and hone the material for reports, governments have a say in all stages of assessment: they adopt the outline for each chapter, review drafts and approve the final reports.

Such tight oversight creates incentives for scientists to stick to the agreed scope and strip out controversial topics. These pressures are especially acute in the social sciences because governments want to control statements about social behaviour, which implicate policy. This domain covers questions such as which countries will bear the costs of climate change; schemes for allocating the burden of cutting emissions; the design of international agreements; how voters respond to information about climate policy; and whether countries will go to war over climate-related stress. The social sciences can help to provide answers to these questions, key for effective climate policy. In practice, few of these insights are explored much by the IPCC.

The narrowness of what governments will allow the IPCC to publish is particularly evident in the summary for policy-makers produced at the end of each assessment.

“Insights such as which policies work (or fail) in practice are skirted.”

Governments approve this document line-by-line with consensus. Disagreements range from those over how to phrase concepts such as a ‘global commons’ that requires collective action to those about whole graphs, which might present data in ways that some governments find inconvenient.

For example, during the approval of the summary from Working Group III last April, a small group of nations vetoed graphs that showed countries’ emissions grouped according to economic growth. Although this format is good science — economic growth is the main driver of emissions — it is politically toxic because it could imply that some countries that are developing rapidly need to do more to control emissions⁴.

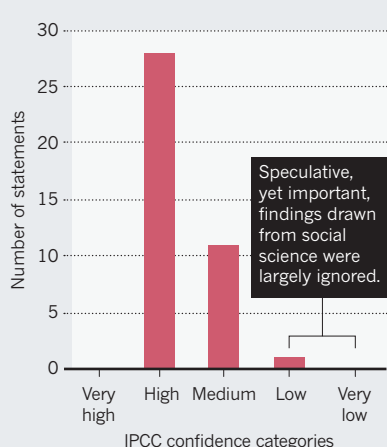
CONTEXT DEPENDENT

The big problem with the IPCC’s output is not the widely levelled charge that it has become too policy prescriptive or is captivated by special interests⁵. Its main affliction is pabulum — a surfeit of bland statements that have no practical value for policy. Abstract, global numbers from stylized, replicable models get approved because they do not implicate any country or action. Insights such as which policies work (or fail) in practice are skirted. Caveats are buried or mangled.

Readers of the Working Group III summary for policy-makers might learn, for instance, that annual economic growth might decrease by just 0.06 percentage points by 2050 if governments were to adopt policies that cut emissions in line with the widely discussed goal of 2 °C above pre-industrial levels⁶. They would have to wade through dense tables to realize that only a fraction of the models say that the goal is achievable, and through the main report to learn that the small cost arises only under simplified assumptions that are far from messy reality.

CONFIDENCE BIAS

Statements that made the cut for the IPCC Working Group III’s summary for policy-makers were mostly those assigned high degrees of confidence.



That said, the social sciences are equally culpable. Because societies are complex and are in many ways harder to study than cells in a petri dish, the intellectual paradigms across most of the social sciences are weak. Beyond a few exceptions — such as mainstream economics — the major debates in social science are between paradigms rather than within them.

Consider the role of international law. Some social scientists treat law like a contract; others believe that it works mainly through social pressures. The first set would advise policy-makers to word climate deals precisely — to include targets and timetables for emissions cuts — and to apply mechanisms to ensure that countries honour their agreements. The second group would favour bold legal norms with clear focal points — striving for zero net emissions, for example⁷. Each approach could be useful in the right context.

Multiple competing paradigms make it hard to organize social-science knowledge or to determine which questions and methods are legitimate. Moreover, the incentives within the social sciences discourage focusing on particular substantive topics such as climate change — especially when they require interdisciplinary collaboration. In political science, for example, research on political mobilization, administrative control and international cooperation among other specialities are relevant. Yet no leading political-science department has a tenured professor who works mainly on climate change⁸.

The paradigm problem need not be paralysing. Social scientists should articulate why different intellectual perspectives and contexts lead to different conclusions. Leading researchers in each area can map out disagreement points and their relevance.

Climate scientists and policy-makers should talk more about how disputes are rooted in different values and assumptions — such as about whether government institutions are capable of directing mitigation. Such disputes help to explain why there are so many disagreements in climate policy, even in areas in which the facts seem clear⁹.

Unfortunately, the current IPCC report structure discourages that kind of candour about assumptions, values and paradigms. It focuses on known knowns and known unknowns rather than on deeper and wider uncertainties. The bias is revealed in how the organization uses official language to describe findings — half of the statements in the Working Group III summary were given a ‘high confidence’ rating (see ‘Confidence bias’).

WIDER VISTA

Building the social sciences into the IPCC and the climate-change debate more generally is feasible over the next assessment cycle, which starts in October and runs to 2022, with efforts on the following three fronts.

SOURCE: REF.6



The solar-powered Barefoot College in Rajasthan, India, trains rural villagers in how to install, build and repair solar technologies.

First, the IPCC must ask questions that social scientists can answer. If the panel looks to the social-sciences literature on climate change, it will find little. But if it engages the fields on their own terms it will find a wealth of relevant knowledge — for example, about how societies organize, how individuals and groups perceive threats and respond to catastrophic stresses, and how collective action works best.

As soon as the new IPCC leadership is chosen later this year, the team should invite major social-sciences societies such as the American Political Science Association, the American and European societies of international law, the American Sociological Association and the Society for Risk Analysis to propose relevant topics that they can assess and questions they can answer. Multidisciplinary scientific organizations in diverse countries — such as the Royal Society in London and the Third World Academy of Sciences — would round out the picture, because social-sciences societies tend to be national and heavily US-based.

These questions should guide how the IPCC scopes its next reports. The agency should also ask such societies to organize what they know about climate by discipline — how sociology examines issues related to the topic, for example — and feed that into the assessment.

Second, the IPCC must become a more attractive place for social-science and humanities scholars who are not usually involved in the climate field and might find IPCC involvement daunting. The IPCC process is dominated by insiders who move from assessment to assessment and are tolerant of

the crushing rounds of review and layers of oversight that consume hundreds of hours and require travel to the corners of the globe. Practically nothing else in science service has such a high ratio of input to output. The IPCC must use volunteers' time more efficiently.

Third, all parties must recognize that a consensus process cannot handle controversial topics such as how best to design international agreements or how to govern the use of geoengineering technologies. For these, a parallel process will be needed to address the most controversial policy-relevant questions.

This supporting process should begin with a small list of the most important questions that the IPCC cannot handle on its own. A network of science academies or foundations sympathetic to the UN's mission could organize short reports — drawing from IPCC assessments and other literature — and manage a review process that is truly independent of government meddling. Oversight from prominent social scientists, including those drawn from the IPCC process, could give the effort credibility as well as the right links to the IPCC itself.

The list of topics to cover in this parallel mechanism includes how to group countries in international agreements — beyond the crude kettling adopted in 1992 that split the world into industrialized nations and the rest. The list also includes which kinds of policies have had the biggest impact on emissions, and how different concepts of justice and ethics could guide new international agreements that balance the burdens of mitigation and adaptation. There will also need to be a sober re-assessment of policy goals when it becomes clear that stopping

warming at 2 °C is no longer feasible¹⁰.

The IPCC has proved to be important — it is the most legitimate body that assesses the climate-related sciences. But it is too narrow and must not monopolize climate assessment. Helping the organization to reform itself while moving contentious work into other forums is long overdue. ■

David Victor is professor of international relations and director of the Laboratory on International Law and Regulation, University of California, San Diego, USA. He is also chairman of the Global Agenda Council on Governance for Sustainability at the World Economic Forum.
e-mail: david.victor@ucsd.edu

1. IPCC. *Future Work of the IPCC: Chairman's Vision Paper on the Future of the IPCC* (IPCC, 2015).
2. IPCC. *Future Work of the IPCC: Consideration of the Recommendations by the Task Group on Future Work of the IPCC* (IPCC, 2015).
3. Committee to Review the Intergovernmental Panel on Climate Change. *Climate Change Assessments: Review of the Processes and Procedures of the IPCC* (InterAcademy Council, 2010).
4. Victor, D. G., Gerlagh, R. & Baiocchi, G. *Science* **345**, 34–36 (2014).
5. Hulme, M. et al. *Nature* **463**, 730–732 (2010).
6. IPCC. *Summary for Policymakers in Climate Change 2014: Mitigation of Climate Change. Contribution of Working Group III to the Fifth Assessment Report of the Intergovernmental Panel on Climate Change* (eds Edenhofer, O. et al.) (Cambridge Univ. Press, 2014).
7. Hafner-Burton, E. M., Victor, D. G. & Lupu, Y. *Am. J. Intl Law* **106**, 47–97 (2012).
8. Keohane, R. O. *PS: Political Sci. & Politics* **48**, 19–26 (2015).
9. Hulme, M. *Why We Disagree About Climate Change: Understanding Controversy, Inaction and Opportunity* (Cambridge Univ. Press, 2009).
10. Victor, D. G. & Kennel, C. F. *Nature* **514**, 30–31 (2014).



Mark Catesby's depiction of *Catalpa bignonioides* and the orchard oriole (*Icterus spurius*).

HISTORY OF SCIENCE

Revelations of a wild continent

Linda Lear praises a study of one of the first naturalists to document North America's flora and fauna.

The mid-eighteenth century was the heyday of natural history. Scientists were redrawing the world map, discovering land bridges between continents and documenting new species of flora and fauna. Members of Britain's elite Royal Society, such as physician and collector Hans Sloane, were particularly interested in the classification of these species, as were many in the broader scientific community,

including those at the Chelsea Physic Garden in London who were tasked with evaluating and classifying specimens. Documenting the natural world became a consuming passion.

In July 1747, Mark Catesby (1682/3–1749), a largely self-taught naturalist, presented the final sections of a massive study to the Royal Society. Two decades in the making, *The Natural History of Carolina, Florida and the Bahama Islands* was the first comprehensive

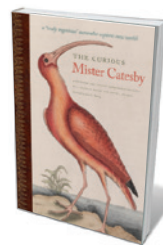
account of North American flora and fauna ever published. It comprised more than 200 hand-coloured etchings based on hundreds of preparatory drawings and notes, with descriptions of each in English and French. Royal Society secretary Cromwell Mortimer hailed them as “the most magnificent work I know since the Art of printing has been discovered”.

Now, the splendid anthology *The Curious Mister Catesby* shows that this praise was not exaggerated. Marking the tercentenary of Catesby's first visit to America in 1712–19, this comprehensive, lavishly illustrated work illuminates the many ways in which Catesby changed how the natural world was perceived and portrayed, suggesting for the first time a dynamic ecological relationship between flora and fauna. Edited by botanist Charles Nelson and David Elliott, executive director of the Catesby Commemorative Trust, it contains reproductions of paintings, engravings, photographs and maps, as well as essays by 25 scholars in fields from art history to the study of molluscs.

Although no likeness of Catesby exists and little is known about him, his evident dedication to documenting nature's marvels marks him as an ambitious and innovative plantsman, an inquisitive natural scientist and an artist of talent and energy. His friend Emanuel Mendez da Costa, an English botanist, drew him as “tall, meagre ... and of a silent disposition; but when he contracted a friendship was communicative, and affable”. Catesby was elected to the Royal Society in 1734, and in 1747 he completed an appendix to his *Natural History*, which included 20 extra drawings of species hitherto unknown to Britain, such as the silky camellia, *Stewartia malacodendron*.

Catesby sailed to Williamsburg, Virginia, in 1712, to collect botanical specimens for an illustrated natural history. His explorations of the Tidewater region in eastern Virginia and the wilderness east of the Appalachian Mountains were partially supported by horticultural patrons in London, eager for a supply of hardy North American species, and by like-minded colonial botanists.

He returned to London in 1719 with a collection of seeds, including those of the passion flower *Passiflora lutea*. The specimens so interested naturalists such as William Sherard that Catesby was able to raise funds for a second trip, arriving in Charleston (then Charles Town), South Carolina, in 1722. He explored perhaps as far as northeastern Georgia (then



The Curious Mister Catesby: A “Truly Ingenious” Naturalist Explores New Worlds

EDITED BY E. CHARLES NELSON AND DAVID J. ELLIOTT
Univ. Georgia Press: 2015.

SYLVIA BACON/CATESBY COMMEMORATIVE TRUST

part of Spanish Florida) more systematically than before, visiting each region in every season. Native American guides helped to carry his paints, mostly fast-drying watercolours and gouache, as well as boxes of specimens, drawings and field notes; they also saved him from venomous snakes and alligator-filled swamps, and shot game for food.

At the end of 1725, Catesby spent time in the Bahamas painting fishes, then returned to London. Unable to afford to hire a copper-plate engraver, he mastered the technique himself, with the help of French artist Joseph Goupy. He planned 100 etchings, mainly of birds, for Volume I; another 100 would comprise a second volume, showing fishes, crustaceans, reptiles, amphibians, insects, a few mammals and a handful of plants.

Catesby found birds the most beautiful of fauna. He was among the first to show associations between plants and animals, for example in his painting of the Greater Antillean bullfinch (*Loxia violacea*) with the poison-wood tree *Metopium toxiferum*. He contributed significantly to the understanding of avian migration, a topic of heated debate at a time when many believed that birds vanished in winter to hibernate in some form of suspended animation. Catesby argued in his paper 'Of Birds of Passage' (M. Catesby *Phil. Trans.* 44, 435–444; 1746) that birds fly to

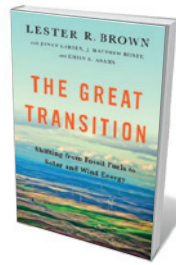


'The Bull Frog' — *Lithobates catesbeianus*.

warmer climates in winter, spurred by seasonal changes and availability of food.

An estimated 200 copies of Catesby's two volumes were printed, with hand-coloured engraved plates. These and two later editions were avidly sought by natural scientists and plant collectors. In 1768, King George III bought Catesby's original 263 watercolour field studies; they are now part of the British Royal Collection. Sadly, Catesby's achievements were diminished by the souring of

Books in brief



The Great Transition: Shifting from Fossil Fuels to Solar and Wind Energy

Lester R. Brown with Janet Larsen, J. Matthew Roney and Emily E. Adams
W. W. NORTON (2015)

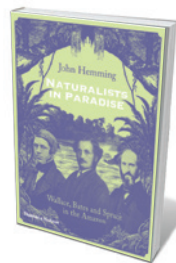
This lucid overview of world energy is surprisingly devoid of gloom. With colleagues at the Earth Policy Institute in Washington DC, environmental analyst Lester Brown suggests that the hold of fossil fuels is finally weakening. Wind and solar power are poised to fill the gap, driven by falling prices and increased environmental awareness. This treatise depicts future energy supply and generation systems that are radically different from today's, and far superior.



Rain: A Natural and Cultural History

Cynthia Barnett CROWN (2015)

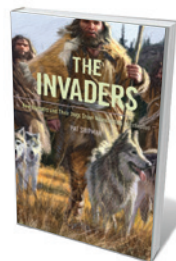
In this romp through rain from pre-history to now, journalist Cynthia Barnett shows how entwined all Earth (and most human) systems are with this life-giving and life-taking precipitation. From droughts that devastated ancient civilizations and floods that drown settlements today, to the rain that inspired cultural offerings such as music from Bo Diddley and Frédéric Chopin, Barnett shows that rain is to be respected and celebrated. She looks at the science of deluge, both whimsical — a rain of frogs in Britain in 1954 — and disastrous, including acid rain and catastrophic flooding.



Naturalists in Paradise: Wallace, Bates and Spruce in the Amazon

John Hemming THAMES AND HUDSON (2015)

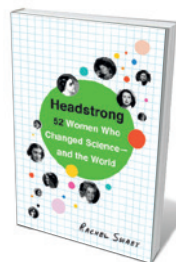
Nineteenth-century biology often seems to have involved as much adventuring as academia. Geographer John Hemming finds a wonderful tale in the Amazonian sojourn of co-discoverer of evolution Alfred Russel Wallace and his fellow nature-watchers, entomologist Henry Walter Bates and botanist Richard Spruce. Hemming shows how the challenges and triumphs of their time in this haven of biodiversity shaped these naturalists, and how they in turn shaped science through specimen collection and papers. An excellent addition to the slew of biographies of eminent Victorians.



The Invaders: How Humans and Their Dogs Drove Neanderthals to Extinction

Pat Shipman BELKNAP PRESS (2015)

Are humans the ultimate invasive species? So contends anthropologist Pat Shipman — and Neanderthals, she opines, were among our first victims. The relationship between *Homo sapiens* and *Homo neanderthalensis* is laid out cleanly, along with genetic and other evidence. Shipman posits provocatively that the deciding factor in the triumph of our ancestors was the domestication of wolves. Perhaps more troubling is the concept of early humans as invaders, rather than just another species finding its way.



Headstrong: 52 Women Who Changed Science — and the World

Rachel Swaby BROADWAY (2015)

A cursory glance at gender balance across science will show that women have still not gained equality. Journalist Rachel Swaby aims to present a comprehensive set of role models for the next generation, who should claim this parity. She ranges from seventeenth-century naturalist Maria Sibylla Merian to astronaut Sally Ride. But cramming 52 awe-inspiring researchers into just over 200 pages reduces them to career bullet points, shorn of context. These women, and those who will follow them, deserve more. [Daniel Cressley](#)



Catesby's rendition of *Eretmochelys imbricata*, the hawksbill sea turtle.

► relations between the United States and Britain after the American War of Independence (1775–83). As US artists and naturalists such as Alexander Wilson, William Bartram and John James Audubon became popular, the British pioneer — whose pre-Linnean classifications were by then outmoded — was largely forgotten. There were so few copies of Catesby's volumes in existence by the mid-nineteenth century that his work was rarely seen, further contributing to his obscurity.

The Curious Mister Catesby will stand for many years as the best critical analysis of his work, and of the groundbreaking natural science that his curiosity inspired. ■

Linda Lear is a historian of the American environment, an authority on Rachel Carson and author of *Beatrix Potter: The Extraordinary Life of a Victorian Genius*. e-mail: linda@lindalear.com

SYLVIA BACON/CATESBY COMMEMORATIVE TRUST

NEUROSCIENCE

Total recall, welcome oblivion

Alison Abbott enjoys a collection of essays on memory and forgetting.

Historian of psychology Douwe Draaisma knows well how to weave science, history and literature into irresistible tales. *Forgetting*, his latest collection of essays around the theme of memory, is — like his successful *Nostalgia Factory* (Yale University Press, 2013) — hard to put down.

His vivid tour through the history of memory-repression theories brings home how dangerous and wrong, yet persistent, were the ideas of Sigmund Freud and his intellectual heirs. Freud thought that traumatic memories and shameful thoughts could be driven from the consciousness, but not forgotten. They would simmer in the unconscious, influencing behaviour. He maintained that forcing them out with psychoanalysis, and confronting patients with them, would be curative.

Draaisma relates the case of an 18-year-old whom Freud dubbed Dora, diagnosed in 1900 with 'hysteria'. Dora's family refused to believe that the husband of her father's mistress had made sexual advances to her. Among other absurdities, Freud told Dora that her nervous cough reflected her repressed desire to fellate the man. Dora broke off the therapy, which Freud saw as proof of his theory. He thought that patients will naturally resist reawakening painful thoughts.

What Dora did not buy, plenty of others did. Psychoanalysis boomed, becoming lucrative. Its principles

► **NATURE.COM**
For more on science in culture, see:
[nature.com/
booksandarts](http://nature.com/booksandarts)



**Forgetting:
Myths, Perils and
Compensations**
DOUWE DRAAISMA,
TRANSLATED BY LIZ
WATERS
Yale Univ. Press: 2015.

now know from studies of post-traumatic stress disorder that traumatic memories are impossible to repress. They flood into the conscious mind in horrifying flashbacks.

Still, as Draaisma shows, theories of memory repression remain stubbornly attractive. We learn that revered Canadian neurosurgeon Wilder Penfield contributed to their longevity. During surgery for epilepsy, he electrically stimulated points on the surface of conscious patients' brains, and asked the patients what they felt. He was one of the first to map the functions of the sensory and motor cortices. His cartoon of a homunculus with body parts in proportion to the brain space dedicated to them — big lips, for example, and huge hands on spindly arms — is a neuroscience icon.

More controversial was his reading of

another experiment. When Penfield stimulated the temporal lobe, his patients reported flashes of dream-like sensations such as the sound of a carnival; he interpreted these as memory traces. He thought that nothing was truly forgotten, and that buried memories could be reactivated. This concept of total recall resonated for a long time in the public imagination. Recent interpretations of his work, however, debunk the idea that he had picked up true memory traces. Fewer than 10% of people experienced any sensation during temporal-lobe stimulation, and of those that did, the actual words recorded in their notes rarely corresponded to things that could be real memories. As Draaisma drolly notes, Penfield's patients reported nothing worthy of repression anyway. Only "snippets of respectable but humdrum lives ... no incestuous desires, no masturbation fantasies".

In another essay, the patient H. M. (Henry Molaison), who was unable to lay down fresh memories after experimental epilepsy surgery, gets a new biography revealing the misdemeanours of his surgeon. Elsewhere, Draaisma muses on aides-memoires such as photographs, and techniques for forgetting. However, one or two essays show the strains of stretching the formula of memory-related essays to the margin of the theme, where the impact is less important or interesting. ■

Alison Abbott is Nature's senior European correspondent.

Correspondence

Aboriginal myth meets DNA analysis

DNA analysis of the Australian outback's only palm tree, *Livistona mariae*, indicates that it originated from seeds brought from the north of the country — a finding backed up by a recently unearthed Aboriginal myth. This neatly illustrates how traditional ecological knowledge might inform modern research.

Known as the cabbage palm and found only in Palm Creek, *L. mariae* (pictured) diverged between 7,000 and 31,000 years ago from its relative *Livistona rigida*, found 1,000 kilometres to the north (see *Nature* **483**, 248; 2012). Because these dates overlap with human occupancy, the study concluded that the seeds could have been transported south and planted in central Australia (T. Kondo *et al. Proc. R. Soc. B* <http://doi.org/2w6>; 2012).

The Aboriginal myth came to our attention through a 2013 translation of an 1895 text by German anthropologist and missionary Carl Strehlow (see go.nature.com/kxfyvn). He wrote of a visit to Palm Creek: “There are beautiful 40 to 50 feet high palms here surrounded by gum trees and acacias and the herbs and flowers at their base release a sharp smell. How this palm got into the interior of Australia has not been established yet by science.” Strehlow relates that, according to traditional local beliefs, “the gods from the high north brought the seeds to this place a long time ago”.

David M. J. S. Bowman
University of Tasmania, Australia.
Jason Gibson *Museum Victoria, Melbourne, Victoria, Australia.*
Toshiaki Kondo *Hiroshima University, Japan.*
david.bowman@utas.edu.au

US Congress replies on NSF scrutiny

As chairman of the US House Committee on Science, Space, and Technology, I do not



believe that you do justice to the committee's efforts to better understand how the US National Science Foundation (NSF) spends US\$7 billion dollars of taxpayers' money (*Nature* **519**, 138–139; 2015).

The NSF is not “caught between the scientists it serves and the lawmakers it answers to”. The money is not the NSF's or the scientists': it is the people's. Congress has a responsibility to ensure that the money is spent wisely and in the national interest.

As you point out, NSF director France Córdova has voiced her support for my proposal that research should be in the national interest if it is to be funded by the NSF. At a recent hearing of the House science committee, she declared the proposal to be “very similar and compatible with NSF's internal guidelines” (see go.nature.com/oywlbd).

Significant progress has also been made on the need for extra transparency and accountability at the NSF. Its new policy acknowledges the need for the agency to communicate clearly and describe research grant awards in non-technical terms. **Lamar Smith** *House of Representatives, Washington DC, USA.*
tx21ima@mail.house.gov

Evaluate risks of coating reservoirs

The environmental effects of chemical films that reduce evaporation of water from reservoirs should be properly evaluated before the films are applied on a large scale (*Nature* **519**, 18–19; 2015).

For example, when these films are driven by waves towards the shoreline (F. R. Crow and

A. L. Mitchell *Water Resources Res.* **11**, 493–495; 1975), they could accumulate in soils and sediments and then enter biological concentration processes, disrupting ecosystems (C. Franke *et al. Chemosphere* **29**, 1501–1514; 1994). The film coating reduces the water's surface tension, interfering with floating plants, pollen transport and insect egg-laying. It has a heating effect that could alter flux between water layers, disturbing solutes and habitats.

Hydrophobic airborne pollutants, including particles of black carbon, will be attracted to the films, potentially changing the surface's reflectivity (albedo) and contributing to climate change.

We should learn from previous ill-judged large-scale chemical applications and ensure that the necessary safety tests and regulatory measures are in place first.

Guohe Huang *North China Electric Power University, Beijing, China.*

Yao Yao *University of Regina, Saskatchewan, Canada.*
huang@iseis.org

Laboratory work is 'like falling in love'

Kevan Martin's obituary of neuroscientist Vernon Mountcastle (*Nature* **518**, 304; 2015) nicely conveys the intensity of his passion for experimental work. This was eloquently expressed in a letter he sent to me on his retirement from the bench.

Mountcastle wrote: “I miss laboratory work in a way that is difficult to describe. It has always been my heart's joy, and my own experience has always been that even the most trivial original discovery of one's own evokes a special kind of ecstasy — it is almost like falling in love for the first time, all over again!”

Oliver Sacks *New York University School of Medicine, New York, USA.*
mail@oliversacks.com

PLD3 and sporadic Alzheimer's disease risk

ARISING FROM C. Cruchaga *et al.* *Nature* **505**, 550–554 (2014); doi:10.1038/nature12825

Recently, Cruchaga *et al.* described the association of rare variants in the phospholipase D3 gene (*PLD3*) with the risk of developing Alzheimer's disease¹; this observation resulted from a strategy based on whole exome sequencing of late-onset Alzheimer's disease familial forms. A missense substitution, Val232Met (rs145999145), was reported to co-segregate with Alzheimer's disease in two families and was further associated with Alzheimer's disease risk; in addition to Val232Met, two other *PLD3* variants, Ala442Ala (rs4819) and Met6Arg, were reported to be nominally associated with Alzheimer's disease risk. We were not able to replicate the association of these variants with the risk of sporadic Alzheimer's disease in a large case–control study. Our data suggest that *PLD3* is at best a minor genetic risk factor of sporadic Alzheimer's disease. There is a Reply to this Brief Communication Arising by Cruchaga, C. & Goate, A. M. *Nature* **520**, <http://dx.doi.org/10.1038/nature14037> (2015).

We aimed to replicate the association between *PLD3* variants and Alzheimer's disease risk in a French case–control study of 2,083 cases (age = 75.6 ± 9.1 years, age at onset = 72.8 ± 10.1 years, 35% male) and 6,536 controls (age = 79.0 ± 7.0 years, 39.4% male)². Direct real-time KASPar (Kbioscience allele-specific polymerase chain reaction) assay was used to genotype the three previously reported rare variants, while genome-wide association study (GWAS) data were used to evaluate other potential signals within the *PLD3* locus and to adjust all analyses for population substructure. Met6Arg was found to be not polymorphic in our French population; for the other variants the genotyping success rate was >99%.

The Val232Met variant was not associated with Alzheimer's disease risk in our data set ($P = 0.58$; Table 1). Cruchaga *et al.*¹ reported a decrease in the methionine allele frequency with age in controls, leading to a subsequent increase in Alzheimer's disease risk associated with this allele in the oldest¹. However, using the same age strata as reported in Cruchaga *et al.*¹, we did not observe any age-dependent variation in the methionine allele frequency in our controls (>65 years, 0.5%; >70 years, 0.4%; >75 years, 0.5%). The other proposed *PLD3* risk variant, Ala442Ala (rs4819), did not show any significant association with Alzheimer's disease risk ($P = 0.10$; Table 1). Of note, we calculated that our study was well adapted to detect (>90%) a similar increased risk (odds ratio ≥ 2) described by Cruchaga *et al.*¹ (assuming an α level of 0.05).

For further assessment of the potential association of the *PLD3* locus with Alzheimer's disease risk in our GWAS data set, we analysed 147 imputed single nucleotide polymorphisms (SNPs) (minor allele frequency >0.005 and an $R^2 > 0.3$; 1K genome reference panel, December 2010) in the genomic region encompassing *PLD3* (±20 kb). Eighteen SNPs exhibited only marginal nominal association with Alzheimer's disease risk ($0.01 < P < 0.05$). This is in line with GWAS meta-analysis results from the International Genomics of Alzheimer's Project (IGAP; stage 1 including 17,008 cases and 37,154 controls): in this study none of the SNPs in the *PLD3* region met our criteria for follow-up genotyping ($P < 0.001$) and were thus not analysed³.

Additional analyses using genome-wide haplotype data generated from our GWAS data set did not reveal any haplotypes encompassing *PLD3* that nominally associated with Alzheimer's disease risk⁴. Finally, a recent 'burden' analysis in IGAP did not detect genome-wide/suggestive signals within this locus⁵.

The analysis of a large French case–control study does not confirm any association between rare and common variants in *PLD3* with sporadic Alzheimer's disease risk, in accordance with other observations both in familial and sporadic Alzheimer's disease (see accompanying Comments by Hooli *et al.*⁶ and Heilmann *et al.*⁷). However, further investigations will be required to confirm whether or not *PLD3* is a genetic susceptibility factor for Alzheimer's disease.

Jean-Charles Lambert¹, Benjamin Grenier-Boley¹, Céline Bellenguez¹, Florence Pasquier², Dominique Campion³, Jean-François Dartigues⁴, Claudine Berr⁵, Christophe Tzourio⁶ & Philippe Amouyel¹

¹INSERM, U744, Université Lille 2, Institut Pasteur de Lille, Lille 59000, France.

email: jean-charles.lambert@pasteur-lille.fr

²CNR-MAJ, Centre Hospitalier Régional Universitaire de Lille, Université Lille 2, Lille 59000, France.

³CNR-MAJ, INSERM, U1079, Rouen University Hospital, Rouen 76031, France.

⁴Inserm U897, Victor Segalen University, Bordeaux 33076, France.

⁵INSERM, U1061, Faculty of Medicine, Hôpital La Colombière, Montpellier 34093, France.

⁶INSERM, U708, Victor Segalen University, Bordeaux, France.

Received 15 July; accepted 16 October 2014.

- Cruchaga, C. *et al.* Rare coding variants in the phospholipase D3 gene confer risk for Alzheimer's disease. *Nature* **505**, 550–554 (2014).
- Lambert, J. C. *et al.* Genome-wide association study identifies variants at CLU and CR1 associated with Alzheimer's disease. *Nature Genet.* **41**, 1094–1099 (2009).
- Lambert, J. C. *et al.* Meta-analysis of 74,046 individuals identifies 11 new susceptibility loci for Alzheimer's disease. *Nature Genet.* **45**, 1452–1458 (2013).
- Lambert, J. C. *et al.* Genome-wide haplotype association study identifies the *FRMD4A* gene as a risk locus for Alzheimer's disease. *Mol. Psychiatry* **18**, 461–470 (2013).
- Escott-Price, V. *et al.* Gene-wide analysis detects two new susceptibility genes for Alzheimer's disease. *PLoS ONE* **9**, e94661 (2014).
- Hooli, B. V. *et al.* *PLD3* gene variants and Alzheimer's disease. *Nature* **520**, <http://dx.doi.org/10.1038/nature14040> (2015).
- Heilmann, S. *et al.* *PLD3* in non-familial Alzheimer's disease. *Nature* **520**, <http://dx.doi.org/10.1038/nature14039> (2015).

Author Contributions Data analyses: J.-C.L., B.G.-B., C.B.; sample collection: F.P., D.C., J.-F.D., C.B., C.T.; manuscript writing: J.-C.L., P.A.

Competing Financial Interests Declared none.

doi:10.1038/nature14036

Table 1 | Association of *PLD3* SNPs with Alzheimer's disease risk in a French case–control study

SNP	rs number	MAF in controls	MAF in cases	Allelic OR (CI 95%)	P (Fisher's test)	Logistic OR (CI 95%)*	P*
Val232Met	rs145999145	0.0041	0.0045	1.09 (0.64–1.87)	0.78	1.17 (0.67–2.04)	0.58
Ala442Ala	rs4819	0.0151	0.0123	0.81 (0.59–1.11)	0.22	0.76 (0.55–1.05)	0.10

MAF, minor allele frequency; OR, odds ratio.

*Additive model adjusted for age, gender and principal components.

PLD3 variants in population studies

ARISING FROM C. Cruchaga *et al.* *Nature* **505**, 550–554 (2014); doi:10.1038/nature12825

Cruchaga *et al.*¹ reported that rare genetic variants in phospholipase D3 (*PLD3*) are associated with increased Alzheimer's disease risk, and showed that *PLD3* is involved in amyloid- β precursor protein processing and is overexpressed in brain tissue from Alzheimer's disease patients; however, the key variant *PLD3* Val232Met did not pass genome-wide significance. This observation raises questions whether the genetic association of *PLD3* with Alzheimer's disease replicates. We associated *PLD3* Val232Met with Alzheimer's disease in three large population-based studies and three case-control studies. In total, we performed a meta-analysis of results from 1,914 Alzheimer's disease cases and 8,021 controls of European descent; furthermore, we searched for other coding *PLD3* variants in sequence data of 1,067 Alzheimer's disease cases and 1,553 controls. There is a Reply to this Brief Communication Arising by Cruchaga, C. & Goate, A. M. *Nature* **520**, <http://dx.doi.org/10.1038/nature14037> (2015).

Carrier frequencies of the *PLD3* Val232Met variant in controls ranged from 0.34% to 1.42%, consistent with 0–1.17% reported by Cruchaga *et al.*¹ (Table 1). Likewise, the frequencies of *PLD3* Val232Met in cases ranged from 0.66% to 2.19% compared to 0.7–2.6% (ref. 1). We note that the range of carrier frequencies overlaps between cases and controls, such that in some population-based cohorts, the carrier frequency in controls (for example, 1.28% in Framingham Heart Study (FHS)) is higher than that of cases in other cohorts (for example, 0.68% in Age, Gene/Environment Susceptibility-Reykjavik Study (AGES)). Within each cohort frequencies of Val232Met were higher in cases than controls (Table 1), but in none of the populations was the case carrier frequency for Val232Met significantly increased. However, pooled analyses showed a 1.94-fold increased risk of Alzheimer's disease for carriers compared to non-carriers (odds ratio (OR) 1.94, adjusted for age and sex, 95% confidence interval = 1.05–3.57), which was marginally significant ($P = 0.03$) (Table 1). Notably, the crude ORs often differed considerably from the age- and sex-adjusted estimates. With the exception of Alzheimer's Disease Neuroimaging Initiative (ADNI), the ORs were higher after adjustment for age and sex, suggesting that many asymptomatic carriers were relatively young compared to cases and that age needs to be controlled for in the analyses as a putative confounder.

We further associated other coding variants in *PLD3* with Alzheimer's disease and performed a gene-based test using sequence data from two studies encompassing 1,067 Alzheimer's disease cases and 1,553 controls^{2,3}. We performed a meta-analysis on the results of whole genome sequence data of the ADNI study, 499 Alzheimer's disease cases and 293 controls, with results of a combined cohort of 568 Dutch Alzheimer's

disease cases and 1,260 Dutch controls. We observed 21 rare polymorphic coding variants and 1 splice site variant. Of the 20 observed *PLD3* variants detected by Cruchaga *et al.*¹, we observed 9 (S63G, P76A, V232M, N284S, C300Y, A442A, G452E, D447G and R488C). Five variants showed the same direction of effect as seen by Cruchaga *et al.*¹. *PLD3* Ala442Ala was one of the variants that showed the same direction of effect (OR 1.24, 95% confidence interval = 0.74–2.06, $P = 0.41$). After correcting the P value for multiple testing, none of the variants observed in our study conferred a significant increase in Alzheimer's disease risk. Furthermore, gene-based analysis did not show significant association of *PLD3* variants with Alzheimer's disease risk (optimized sequence kernel association test (SKAT-O) $P = 0.61$ and burden test OR 1.27, 95% confidence interval = 0.85–1.9, $P = 0.24$).

In conclusion, the carrier frequencies of *PLD3* Val232Met in our data set are consistent with those reported by Cruchaga *et al.*¹ and we show a nominally significant association of *PLD3* Val232Met with Alzheimer's disease. This is in contrast to findings presented in three accompanying Comments^{4–6}. However, in contrast to Cruchaga *et al.*¹ we found no significant association of other *PLD3* variants with Alzheimer's disease in the single variant or gene-based analyses. Therefore, in our analyses *PLD3* does not yet meet the criteria proposed by ref. 7 to be implicated in Alzheimer's disease. Thus, our data do not strongly support an important contribution of rare *PLD3* variants in the aetiology of Alzheimer's disease. The most notable findings in our study are the need to control for age as a confounder in rare variant analyses and the high variability of the frequency of *PLD3* Val232Met across populations. The latter finding highlights the need for careful matching of cases and controls for ethnic background when investigating rare variants.

Methods

Data from RS², FHS⁸ and AGES⁹ studies were genotyped on the Illumina exome chip¹⁰. Amsterdam Dementia cohort³, Alzheimer Center Erasmus MC and RS underwent whole-exome sequencing at Center for Biomix, Rotterdam. RS exome sequence and exome chip data partially overlapped, genotypes were concordant, and non-overlapping samples were used in *PLD3* Val232Met analysis. As covariates gender and age at onset for Alzheimer's disease cases or the date of last examination/censoring for cognitively healthy controls were used. GRIP¹¹ was imputed using the Dutch specific reference panel (imputation quality (R^2) = 0.74)^{12,13}. Subjects aged below 55 years were excluded. The R-package 'seqMeta' (version seqMeta_1.4) was used for meta-analysis of single variant score test and gene-based test.

Data used in preparation of this article were obtained from the Alzheimer's Disease Neuroimaging Initiative (ADNI) database (<http://adni.loni.usc.edu>). As such, the investigators within the ADNI contributed to the design and implementation

Table 1 | Association of *PLD3* Val232Met with Alzheimer's disease

Cohort	Cases			Controls			Overall carrier frequency (%)	Crude OR	OR (95% CI)	P value
	Carriers (n)	Non-carriers (n)	Carrier frequency (%)	Carriers (n)	Non-carriers (n)	Carrier frequency (%)				
AGES	1	145	0.68	12	2,371	0.50	0.51	1.36	3.18 (0.17–58.73)	0.44
Dutch Alzheimer centres	3	451	0.66	4	609	0.65	0.66	1.01	1.55 (0.25–9.38)	0.64
GRIP	2	109	1.80	14	975	1.42	1.45	1.28	1.58 (0.25–9.91)	0.62
RS	6	470	1.26	23	2,389	0.95	1.00	1.33	1.43 (0.51–4.03)	0.49
ADNI	7	492	1.40	1	292	0.34	1.01	4.15	2.94 (0.63–13.8)	0.17
FHS	5	223	2.19	17	1,314	1.28	1.41	1.73	2.63 (0.71–9.70)	0.15
Combined	24	1,890	1.25	71	7,950	0.89	0.96	1.53	1.94 (1.05–3.57)	0.03

Odds Ratios (OR) and P values from score tests are shown adjusted for age and sex, based on a logistic regression model. Crude ORs were calculated using carrier frequencies of cases and controls. Combined crude OR is the Mantel-Haenszel estimate of the pooled crude ORs (95% CI 0.91–2.57 and two-sided P value = 0.11). AGES, Age, Gene/Environment Susceptibility-Reykjavik Study. Framingham Heart Study (FHS) and Rotterdam Study (RS) were genotyped on the Illumina exome chip version 1.0. Genetic Research in Isolated Populations (GRIP) subjects were imputed. Dutch Alzheimer centres encompass whole-exome sequence data of Alzheimer's disease cases from Amsterdam Dementia Cohort, Alzheimer Center Rotterdam MC and controls from RS (not genotyped on the exome chip). Alzheimer's Disease Neuroimaging Initiative (ADNI) samples are whole-genome sequenced.

of ADNI and/or provided data but did not participate in analysis or writing of this report. A complete listing of ADNI investigators can be found at http://adni.loni.usc.edu/wp-content/uploads/how_to_apply/ADNI_Acknowledgement_List.pdf.

Sven J. van der Lee¹, Henne Holstege^{2,3}, Tsz Hang Wong⁴, Johanna Jakobsdottir⁵, Joshua C. Bis⁶, Vincent Chouraki^{7,8}, Jeroen G. J. van Rooij⁹, Megan L. Grove¹⁰, Albert V. Smith^{5,11}, Najaf Amin¹, Seung-Hoan Choi^{7,12}, Alexa S. Beiser^{7,12}, Melissa E. Garcia¹³, Wilfred F. J. van IJcken¹⁴, Yolande A. L. Pijnenburg², Eva Louwersheimer², Rutger W. W. Brouwer¹⁴, Mirjam C. G. N. van den Hout¹⁴, Edwin Oole¹⁴, Gudny Eiriksdottir⁵, Daniel Levy^{7,8,15}, Jerome I. Rotter¹⁶, Valur Emilsson^{5,17}, Christopher J. O'Donnell^{7,15}, Thor Aspelund^{5,18}, Andre G. Uitterlinden^{1,9,19}, Lenore J. Launer¹³, Albert Hofman¹, Eric Boerwinkle^{10,20}, Bruce M. Psaty^{6,21,22}, Anita L. DeStefano^{7,12}, Philip Scheltens², Sudha Seshadri^{7,8}, John C. van Swieten^{2,4}, Vilmundur Gudnason^{5,11}, Wiesje M. van der Flier^{2,23}, M. Arfan Ikram^{1,4,24} & Cornelia M. van Duijn¹

¹Department of Epidemiology, Erasmus Medical Center, Rotterdam 3000 CA, The Netherlands.

email: c.vanduijn@erasmusmc.nl

²Alzheimer Center, Department of Neurology, VU University Medical Center, Neuroscience Campus Amsterdam, Amsterdam 1081 HZ, The Netherlands.

³Department of Clinical Genetics, VU University Medical Center, Neuroscience Campus Amsterdam, Amsterdam 1081 HZ, The Netherlands.

⁴Department of Neurology, Erasmus Medical Center, Rotterdam 3000 CA, The Netherlands.

⁵Icelandic Heart Association, Kopavogur 201, Iceland.

⁶Cardiovascular Health Research Unit, Department of Medicine, University of Washington, Seattle, Washington 98101, USA.

⁷National Heart, Lung and Blood Institute Framingham Heart Study, Framingham, Massachusetts 01702-5827, USA.

⁸Boston University School of Medicine, Boston, Massachusetts 02118, USA.

⁹Department of Internal Medicine, Erasmus Medical Center, Rotterdam 3000 CA, The Netherlands.

¹⁰School of Public Health, Human Genetics Center, University of Texas Health Science Center at Houston, Houston, Texas 77030, USA.

¹¹Faculty of Medicine, University of Iceland, Reykjavik 101, Iceland.

¹²Department of Biostatistics, Boston University School of Public Health, Boston, Massachusetts 02118, USA.

¹³Laboratory of Epidemiology and Population Sciences, National Institute on Aging, Bethesda, Maryland 20892, USA.

¹⁴Center for Biomics, Erasmus Medical Center, Rotterdam 3000 CA, The Netherlands.

¹⁵National Heart, Lung, and Blood Institute, Intramural Research Program, National Institutes of Health, Bethesda, Maryland 20892, USA.

¹⁶Institute for Translational Genomics and Population Sciences, Los Angeles BioMedical Research Institute at Harbor-UCLA Medical Center, Torrance, California 90502, USA.

¹⁷Faculty of Pharmaceutical Sciences, University of Iceland, Reykjavik 101, Iceland.

¹⁸Centre for Public Health, University of Iceland, Reykjavik 101, Iceland.

¹⁹Netherlands Consortium on Health Aging and National Genomics Initiative, Leiden 2300 RC, The Netherlands.

²⁰Human Genome Sequencing Center, Baylor College of Medicine, Houston, Texas 77030, USA.

²¹Department of Epidemiology, University of Washington, Seattle, Washington 98101, USA.

²²Group Health Research Institute, Seattle, Washington 98101-1448, USA.

²³Department of Epidemiology & Biostatistics, VU University Medical Center, Neuroscience Campus Amsterdam, Amsterdam 1081 HZ, The Netherlands.

²⁴Departments of Radiology, Erasmus Medical Center, Rotterdam 3000 CA, The Netherlands.

Received 15 July; accepted 16 October 2014.

- Cruchaga, C. *et al.* Rare coding variants in the phospholipase D3 gene confer risk for Alzheimer's disease. *Nature* **505**, 550–554 (2014).
- Hofman, A. *et al.* The Rotterdam Study: 2014 objectives and design update. *Eur. J. Epidemiol.* **28**, 889–926 (2013).
- van der Flier, W. M. *et al.* Optimizing patient care and research: the amsterdam dementia cohort. *J. Alzheimers Dis.* **41**, 313–327 (2014).
- Heilmann, S. *et al.* PLD3 in non-familial Alzheimer's disease. *Nature* **520**, <http://dx.doi.org/10.1038/nature14039> (2015).
- Lambert, J.-C. *et al.* PLD3 and sporadic Alzheimer's disease risk. *Nature* **520**, <http://dx.doi.org/10.1038/nature14036> (2015).
- Hooli, B. V. *et al.* PLD3 gene variants and Alzheimer's disease. *Nature* **520**, <http://dx.doi.org/10.1038/nature14040> (2015).
- MacArthur, D. G. *et al.* Guidelines for investigating causality of sequence variants in human disease. *Nature* **508**, 469–476 (2014).
- Splansky, G. L. *et al.* The Third Generation Cohort of the National Heart, Lung, and Blood Institute's Framingham Heart Study: design, recruitment, and initial examination. *Am. J. Epidemiol.* **165**, 1328–1335 (2007).
- Harris, T. B. *et al.* Age, Gene/Environment Susceptibility-Reykjavik Study: multidisciplinary applied phenomics. *Am. J. Epidemiol.* **165**, 1076–1087 (2007).
- Grove, M. L. *et al.* Best practices and joint calling of the HumanExome BeadChip: the CHARGE Consortium. *PLoS ONE* **8**, e68095 (2013).
- Liu, F. *et al.* A genome-wide screen for late-onset Alzheimer disease in a genetically isolated Dutch population. *Am. J. Hum. Genet.* **81**, 17–31 (2007).
- Deelen, P. *et al.* Improved imputation quality of low-frequency and rare variants in European samples using the 'Genome of The Netherlands'. *Eur. J. Hum. Genet.* (2014).
- The Genome of the Netherlands Consortium. Whole-genome sequence variation, population structure and demographic history of the Dutch population. *Nature Genet.* **46**, 818–825 (2014).

Author Contributions Study design: C.M.v.D.; acquisition of phenotype and genotype data: H.H., T.H.W., J.G.J.v.R., A.V.S., S.-H.C., A.S.B., M.E.G., W.F.J.v.I.J., Y.A.L.P., E.L., R.W.B.B., M.C., G.N.v.d.H., E.O., G.E., D.L., J.I.R., V.E., C.J.O., T.A., A.G.U., L.J.L., A.H., E.B., B.M.P., A.L.D., P.S., S.S., J.C.v.S., V.G., W.M.v.d.F., M.A.I., C.M.v.D.; data analysis: S.J.v.d.L., H.H., T.H.W., J.J., J.C.B., V.C., N.A. The manuscript was drafted by S.J.v.d.L., N.A., M.A.I., C.M.v.D.; all authors reviewed the manuscript.

Competing Financial Interests Declared none.

doi:10.1038/nature14038

PLD3 in non-familial Alzheimer's disease

ARISING FROM C. Cruchaga *et al.* *Nature* **505**, 550–554 (2014); doi:10.1038/nature12825

Interest in the role of rare genetic variants in the aetiology of complex diseases such as Alzheimer's disease is increasing^{1,2}. Recently, Cruchaga *et al.*³ provided evidence supporting the role of rare variants in the phospholipase D3 (PLD3) gene in both familial late-onset Alzheimer's disease

(age at onset >65 years) and in non-familial Alzheimer's disease. In a follow-up study of 3,568 non-familial Alzheimer's disease cases and 3,867 controls of German or Spanish descent, we failed to replicate the latter finding. Our results therefore cast doubt on the aetiological

Table 1 | Association results for *PLD3* variants in the replication analysis

Sample	Status	<i>n</i>	Age in years (\pm s.d.)	Fem (%)	Pro76Ala			Val232Met			Ala442Ala			Burden test*		
					MAF (%)	OR (95% CI)	<i>P</i>	MAF (%)	OR (95% CI)	<i>P</i>	MAF (%)	OR (95% CI)	<i>P</i>	Prop. car. cases	Prop. car. ctrl	<i>P</i>
ACE	Cases	2,166	82.1 (\pm 7.7)	71.2	0.02	1.27	0.86	0.39	1.08 (0.57–	0.81	1.25	0.99 (0.70–	0.98	0.017	0.014	0.7
	Controls	2,754	54.4 (\pm 11.7)	64.5	0.02	(0.08–20.34)		0.36	2.07)		1.25	1.42)				
Sant Pau	Cases	461	76.8 (\pm 5.6)	64.7	0.11	0.39 (0.02–	0.49	0.54	∞	0.16	1.08	1.96 (0.43–	0.37	0.027	0.017	0.4
	Controls	180	72.1 (\pm 8.2)	45.3	0.28	6.25)		0			0.56	9.00)				
German	Cases	941	72.5 (\pm 8.7)	64.5	0.11	1.98 (0.18–	0.57	0.21	0.49 (0.15–	0.24	1.70	1.33 (0.78–	0.29	0.006	0.01	0.6
	Controls	933	90.0 (\pm 3.3)	63.5	0.05	21.9)		0.43	1.65)		1.29	2.26)				
Meta-analysis	Cases	3,568	79.0 (\pm 8.8)	68.6	0.06	1.45	0.65	0.36	1.01 (0.59–	0.97	1.35	1.09 (0.82–	0.55	0.015	0.013	1
	Controls	3,867	63.7 (\pm 18.3)	63.4	0.04	(0.32–6.46)		0.36	1.72)		1.23	1.46)				

Variants are shown with position on chromosome 19 indicated below. CI, confidence interval; Fem, proportion of females in the sample; MAF, minor allele frequency; *n*, number of individuals; OR, odds ratio; *P*, *P* value of the Armitage trend test; Prop. car. cases, proportion of carriers in cases; Prop. car. ctrl, proportion of carriers in controls; s.d., standard deviation. p.Met6Arg was monomorphic in all of the investigated samples.

*The collapsing regression test^{1,4} was used for the meta-analysis with 'originating centre' as covariate.

relevance of rare coding *PLD3* variants in non-familial Alzheimer's disease. There is a Reply to this Brief Communication Arising by Cruchaga, C. & Goate, A. M. *Nature* **520**, <http://dx.doi.org/10.1038/nature14037> (2015).

Four coding *PLD3* variants reported by Cruchaga *et al.*³ with *P* < 0.15 (p.Met6Arg, p.Pro76Ala, p.Val232Met and p.Ala442Ala) were genotyped in three independent non-familial Alzheimer's disease case-control samples using Sequenom's iPLEX assay. The two Spanish samples comprised: (1) 2,166 cases and 2,754 controls (Fundació ACE)⁴; and (2) 461 cases and 180 controls (St Pau Hospital)⁵. The German sample comprised 941 cases and 933 controls from three multicentre studies^{6–8}. All non-familial Alzheimer's disease cases fulfilled the National Institute of Neurological and Communicative Disorders and Stroke (NINCDS) and the Alzheimer's Disease and Related Disorders Association (ADDA) criteria, and all participants provided written informed consent. Association was tested using Armitage's test for allelic trend (INTERSNP⁹). In addition, a burden analysis was performed with the collapsing test COLL¹⁰.

In the Spanish and German samples, the variant p.Met6Arg was found to be monomorphic. No evidence for an association between non-familial Alzheimer's disease and any of the three polymorphic *PLD3* variants was found in the analyses of the three individual study samples or in the analysis of the combined sample (*P* > 0.05, Table 1). Interestingly, the power of our case-control study was sufficiently large to detect an odds ratio (OR) of 2 or larger, as reported by Cruchaga *et al.*³.

Since the association reported by Cruchaga *et al.*³ was mainly for late-onset Alzheimer's disease and was stronger in cases with a positive family history³, we stratified our samples according to: (1) age at onset (that is, \leq 65 or >65 years); and (2) family history (defined as the presence of at least one self-reported dementia case in the family). However, neither analysis generated evidence for association (*P* > 0.05). Similarly, the burden analysis revealed no significant differences between non-familial Alzheimer's disease cases and controls in terms of the occurrence of any of the four *PLD3* variants (*P* > 0.05, Table 1).

Our analyses in two European populations did not implicate rare *PLD3* coding variants in non-familial Alzheimer's disease susceptibility. This calls into question both their genetic epidemiological relevance in the investigated populations, and their importance in the pathogenesis of non-familial Alzheimer's disease. Although we cannot with certainty exclude a false-negative finding secondary to population stratification, this possibility seems unlikely for the following reasons: our findings are consistent with the negative findings reported from the French population in an accompanying Comment by Lambert *et al.*¹¹; and the allele frequencies obtained in the French controls were very similar to those obtained in our Spanish and German controls. Furthermore, a meta-analysis of 7,565 cases and 18,424 controls, which included

the present sample, did not reveal an association with p.Val232Met (see accompanying Comment by Hooli *et al.*¹²). Here, the power to detect an association was 96.6% at α = 0.05. In summary, these data suggest that our results are reliable.

Notably, our findings do not concur with those of the accompanying paper by van der Lee *et al.*¹³ who reported a significant association for p.Val232Met in their meta-analysis of six independent samples (1,914 non-familial Alzheimer's disease patients and 8,021 controls). However, the size of the individual samples was—at least in terms of the number of cases—small, and the participants had been recruited from various populations. Both the low frequency of p.Val232Met, and its varying frequency between their small investigated samples, render the van der Lee *et al.*¹³ result difficult to interpret. Although our results do not exclude the possibility that these *PLD3* variants are implicated in Alzheimer's disease patients with a strong family history of Alzheimer's disease, the accompanying Comment by Hooli *et al.*¹² found no evidence for this hypothesis in an investigation of 439 multiply affected Alzheimer's disease families.

In conclusion, our results in non-familial Alzheimer's disease cases from Spain and Germany provide no support for the hypothesis that rare *PLD3* variants are implicated in the aetiology of Alzheimer's disease. Clarification of the role of *PLD3* in Alzheimer's disease will require the investigation of further large samples from defined populations.

Stefanie Heilmann^{1,2}, Dmitriy Drichel³, Jordi Clarimon^{4,5}, Victoria Fernández⁶, André Lacour³, Holger Wagner⁷, Mathias Thelen⁷, Isabel Hernández⁶, Juan Fortea^{4,5}, Montserrat Alegret⁶, Rafael Blesa^{4,5}, Ana Mauleón⁶, Maitée Rosende Roca⁶, Johannes Kornhuber⁸, Oliver Peters⁹, Reinhard Heun⁷, Lutz Frölich¹⁰, Michael Hüll¹¹, Michael T. Heneka^{3,12}, Eckart Rütger¹³, Steffi Riedel-Heller¹⁴, Martin Scherer¹⁵, Jens Wiltfang¹³, Frank Jessen^{3,7,16}, Tim Becker^{3,17}, Lluís Tárraga⁶, Mercè Boada⁶, Wolfgang Maier^{3,7}, Alberto Lleó^{4,5}, Agustín Ruiz⁶, Markus M. Nöthen^{1,2} & Alfredo Ramirez^{1,7}

¹Institute of Human Genetics, University of Bonn, 53127 Bonn, Germany. email: alfredo.ramirez@ukb.uni-bonn.de

²Department of Genomics, Life & Brain Center, University of Bonn, 53127 Bonn, Germany.

³German Center for Neurodegenerative Diseases (DZNE), 53175 Bonn, Germany.

⁴Memory Unit, Neurology Department and Sant Pau Biomedical Research Institute, Hospital Santa Creu i Sant Pau, Autonomous University Barcelona, 08025 Barcelona, Spain.

⁵Center for Networking Biomedical Research in Neurodegenerative Diseases (CIBERNED), 28029 Madrid, Spain.

⁶Memory Clinic of Fundació ACE, Catalan Institute of Applied Neurosciences, 08028 Barcelona, Spain.

⁷Department of Psychiatry and Psychotherapy, University of Bonn, 53127 Bonn, Germany.

⁸Department of Psychiatry and Psychotherapy, University Clinic Erlangen, Friedrich-Alexander University Erlangen-Nürnberg, 91054 Erlangen, Germany.

⁹Department of Psychiatry, Charité University Medicine, 14050 Berlin, Germany.

¹⁰Department of Geriatric Psychiatry, Central Institute of Mental Health, Medical Faculty Mannheim, University of Heidelberg, 68159 Mannheim, Germany.

¹¹Centre for Geriatric Medicine and Section of Gerontopsychiatry and Neuropsychology, Medical School, University of Freiburg, 79106 Freiburg, Germany.

¹²Clinical Neuroscience Unit, Department of Neurology, University of Bonn, 53127 Bonn, Germany.

¹³Department of Psychiatry and Psychotherapy, University of Göttingen, 37075 Göttingen, Germany.

¹⁴Institute of Social Medicine, Occupational Health and Public Health, University of Leipzig, 04103 Leipzig, Germany.

¹⁵Department of Primary Medical Care, University Medical Centre Hamburg-Eppendorf, 20246 Hamburg, Germany.

¹⁶Department of Psychiatry and Psychotherapy, University of Cologne, 50937 Cologne, Germany.

¹⁷Institute for Medical Biometry, Informatics and Epidemiology, University of Bonn, 53127 Bonn, Germany.

Received 15 July; accepted 16 October 2014.

1. Guerreiro, R. *et al.* TREM2 variants in Alzheimer's disease. *N. Engl. J. Med.* **368**, 117–127 (2013).
2. Pottier, C. *et al.* High frequency of potentially pathogenic SORL1 mutations in autosomal dominant early-onset Alzheimer disease. *Mol. Psychiatry* **17**, 875–879 (2012).

3. Cruchaga, C. *et al.* Rare coding variants in the phospholipase D3 gene confer risk for Alzheimer's disease. *Nature* **505**, 550–554 (2014).
4. Ruiz, A. *et al.* Follow-up of loci from the International Genomics of Alzheimer's Disease Project identifies *TRIP4* as a novel susceptibility gene. *Transl. Psychiatr.* **4**, e358 (2014).
5. Ruiz, A. *et al.* Assessing the role of the TREM2 p.R47H variant as a risk factor for Alzheimer's disease and frontotemporal dementia. *Neurobiol. Aging* **35**, 444.e1–4 (2013).
6. Ramirez, A. *et al.* SUCLG2 identified as both a determinant of CSF Aβ1–42 levels and an attenuator of cognitive decline in Alzheimer's disease. *Hum. Mol. Genet.* (2014).
7. Kornhuber, J. *et al.* Early and differential diagnosis of dementia and mild cognitive impairment: design and cohort baseline characteristics of the German Dementia Competence Network. *Dement. Geriatr. Cogn. Disord.* **27**, 404–417 (2009).
8. Jessen, F. *et al.* Prediction of dementia in primary care patients. *PLoS ONE* **6**, e16852 (2011).
9. Herold, C., Steffens, M., Brockschmidt, F. F., Baur, M. P. & Becker, T. INTERSNP: genome-wide interaction analysis guided by a priori information. *Bioinformatics* **25**, 3275–3281 (2009).
10. Li, B. & Leal, S. M. Methods for detecting associations with rare variants for common diseases: application to analysis of sequence data. *Am. J. Hum. Genet.* **83**, 311–321 (2008).
11. Lambert, J.-C. *et al.* *PLD3* and sporadic Alzheimer's disease risk. *Nature* **520**, <http://dx.doi.org/10.1038/nature14036> (2015).
12. Hooli, B. V. *et al.* *PLD3* gene variants and Alzheimer's disease. *Nature* **520**, <http://dx.doi.org/10.1038/nature14040> (2015).
13. van der Lee, S. J. *et al.* *PLD3* variants in population studies. *Nature* **520**, <http://dx.doi.org/10.1038/nature14038> (2015).
14. Morris, A. P. & Zeggini, E. An evaluation of statistical approaches to rare variant analysis in genetic association studies. *Genet. Epidemiol.* **34**, 188–193 (2010).

Author Contributions Data collection: J.C., I.H., J.F., M.A., R.B., A.M., M.R.R., J.K., O.P., R.H., L.F., M.H., M.T.H., E.R., S.R.H., M.S., J.W., F.J., L.T., M.B., A.L.; experimental work: S.H., V.F., A.L., H.W., M.T.; project planning: Ag.R., Al.R., J.C., T.B., S.H., M.M.N.; data analysis: S.H., D.D., An.L., T.B., Al.R., J.C., Ag.R.; administrative, technical or material support: J.C., An.L., H.W., M.T., I.H., J.F., M.A., R.B., A.M., M.R.R., J.K., O.P., M.S., L.T., M.B., W.M., Al.L., Ag.R., Al.R.; critical revision of the manuscript for important intellectual content: S.H., D.D., J.C., V.F., An.L., H.W., M.T., I.H., J.F., M.A., R.B., A.M., M.R.R., J.K., O.P., R.H., L.F., M.H., M.T.H., E.R., S.R.H., M.S., J.W., F.J., T.B., L.T., M.B., W.M., Al.L., Ag.R., M.M.N., Al.R.; drafting of the manuscript: Al.R., M.M.N., S.H., T.B., D.D., Ag.R., J.C.; obtaining funding: W.M., M.M.N., F.J., M.S., M.B., L.T., Ag.R., T.B. and J.C.

Competing Financial Interests Declared none.

doi:10.1038/nature14039

Cruchaga & Goate reply

REPLYING TO J.-C. Lambert *et al.* *Nature* **520**, <http://dx.doi.org/10.1038/nature14036> (2015); S. J. van der Lee *et al.* *Nature* **520**, <http://dx.doi.org/10.1038/nature14038> (2015); S. Heilmann *et al.* *Nature* **520**, <http://dx.doi.org/10.1038/nature14039> (2015)

In a recent study we used a family-based study design followed by custom genotyping and sequencing in large case–control data sets. We found that several low-frequency variants, including Val232Met, in *PLD3* were enriched in Alzheimer's disease cases compared to controls¹. van der Lee *et al.*², Heilmann *et al.*³ and Lambert *et al.*⁴ independently attempted to replicate the association between the Val232Met variant and Alzheimer's disease risk in case–control data sets, population cohorts and family-based studies.

Replication of associations for low-frequency and rare variants presents some challenges related to statistical power and population stratification. Population stratification is especially important for low-frequency variants. Even populations from the same region have been shown to have significantly different minor allele frequencies (MAF) for low-frequency variants^{5,6} that can lead to both false-negative and false-positive results. It is currently unclear whether even principal component factors derived from genome-wide association studies (GWAS) are sufficient to correct for this potential problem⁶, but should be the minimum correction performed for low-frequency variant analyses. This problem of differences in population structure and genetic background can be clearly identified in the van der Lee *et al.*², Heilmann *et al.*³ and

Lambert *et al.*⁴ studies. The MAF for the Val232Met and other variants varies widely within the three studies; MAF in controls ranges from 0% to 1.42%. While some studies matched cases and controls by ethnic background and included principal components in the statistical analyses (van der Lee *et al.*² and Lambert *et al.*⁴), this was not the case for Heilmann *et al.*³: as shown in their Table 1, the MAF for *PLD3* Val232Met varies hugely by data set, indicating that the MAF is heavily dependent on the studied population, even within the same country. We have previously screened for the Val232Met variant in a case–control data set from the north-central region of Spain and observed an extremely low MAF (MAF = 0.002; *n* = 1,000; unpublished data), providing direct evidence for regional differences in MAF for this variant. Furthermore, in the absence of GWAS data, several important quality-control steps cannot be performed. First, in the Heilmann *et al.*³ study it is impossible to know whether the cases and controls were matched to correct for population stratification. Second, it is unclear whether Heilmann *et al.*³ can identify duplicates or cryptic relatedness in this study. As a result, it is not possible to determine whether these findings are real or just a problem of population stratification. A recent study using a southern German population replicated the association of *PLD3*

at the gene level with Alzheimer's disease⁷, suggesting that the findings from Heilmann *et al.*³ could be a false negative due to one or all of the problems described above.

Additionally, it is interesting that the adjusted regression in Lambert *et al.*⁴ and van der Lee *et al.*² generates a higher odds ratio (OR) than the non-adjusted, suggesting that some of the unaffected carriers of the Val232Met variant may be younger than the affected carriers, which would lead to a lower estimated OR. In both studies the OR for the Val232Met variant is in the predicted direction, and in the case of van der Lee *et al.*² they replicated the association of this variant ($P = 0.03$) with an OR (1.94, 95% confidence interval (CI) = 1.05–3.57) very similar to the initially reported OR (OR = 2.1). Furthermore, the same group found that the Val232Met variant was associated with proline and phosphatidylcholine plasma levels⁸, which have been recently identified as promising biomarkers for Alzheimer's disease⁹, further supporting the role of PLD3 in Alzheimer's disease.

Together, these data suggest that (1) different European populations exhibit different MAF for rare variants, and therefore it is extremely important to correct for population stratification, and (2) the relative risk for a specific variant varies by population/region.

In general, these studies suggest that the association of the PLD3 Val232Met variant is real although the OR may be lower than that initially reported.

C. Cruchaga and A. M. Goate prepared this Reply on behalf of all authors of ref. 1.

Carlos Cruchaga^{1,2} & Alison M. Goate^{1,2}

¹Department of Psychiatry, Washington University, St Louis, Missouri 63110, USA.

email: cruchagac@psychiatry.wustl.edu

²Hope Center Program on Protein Aggregation and Neurodegeneration, Washington University St Louis, Missouri 63110, USA.

1. Cruchaga, C. *et al.* Rare coding variants in the phospholipase D3 gene confer risk for Alzheimer's disease. *Nature* **505**, 550–554 (2014).
2. van der Lee, S. J. *et al.* PLD3 variants in population studies. *Nature* **520**, <http://dx.doi.org/10.1038/nature14038> (2015).
3. Heilmann, S. *et al.* PLD3 in non-familial Alzheimer's disease. *Nature* **520**, <http://dx.doi.org/10.1038/nature14039> (2015).
4. Lambert, J.-C. *et al.* PLD3 and sporadic Alzheimer's disease risk. *Nature* **520**, <http://dx.doi.org/10.1038/nature14036> (2015).
5. Moore, C. B. *et al.* Low frequency variants, collapsed based on biological knowledge, uncover complexity of population stratification in 1000 genomes project data. *PLoS Genet.* **9**, e1003959 (2013).
6. Mathieson, I. & McVean, G. Differential confounding of rare and common variants in spatially structured populations. *Nature Genet.* **44**, 243–246 (2012).
7. Schulte, E. C. *et al.* Excess of rare coding variants in PLD3 in late- but not earlyonset Alzheimer's disease. *Human Genome Var.* **2**, 14028 (2015).
8. van der Lee, S. J. *et al.* PLD3 associates to proline a proposed biomarker in Mapstone *et al.* *Alzheimers Dement.* **10**, P887–P888 (2014).
9. Mapstone, M. *et al.* Plasma phospholipids identify antecedent memory impairment in older adults. *Nature Med.* **20**, 415–418 (2014).

doi:10.1038/nature14037

QUANTUM PHYSICS

Two-atom bunching

The Hong–Ou–Mandel effect, whereby two identical quantum particles launched into the two input ports of a ‘beam-splitter’ always bunch together in the same output port, has now been demonstrated for helium-4 atoms. [SEE LETTER P.66](#)

LINDSAY J. LEBLANC

All particles, including photons, electrons and atoms, are described by a characteristic list of ‘quantum numbers’. For a pair of particles whose lists match, there is no way of telling them apart — they are perfectly indistinguishable. One of the more intriguing consequences of quantum mechanics arises from this indistinguishability, and was exemplified¹ in an experiment by Hong, Ou and Mandel (HOM) in the 1980s. The researchers showed that, although a single photon approaching an intersection along one of two input paths exits in one of two output paths with equal probability, identical pairs brought to the intersection simultaneously from different paths always exit together. On page 66 of this issue, Lopes *et al.*² now demonstrate this manifestation of two-particle quantum interference for two identically prepared — and thus indistinguishable — helium-4 atoms. The result provides an opportunity to extend advances made in quantum optics to the realm

of atomic systems, especially for applications in quantum information.

As a graduate student faced with finding a wedding present for my labmate, I decided that the HOM experiment was a fitting analogy to marriage: from two separate paths, this couple’s lives were intersecting and would continue along a single path together. Along with the formalism describing the effect tucked into the card, I gave them a glass ‘beam-splitter’ to represent a key ingredient in the optical demonstration of the effect: this glass cube could act as the intersection, at which half the light incident on any of the four polished faces is transmitted, with the remaining half being reflected; for single particles, the probabilities for transmission and reflection are both 50%. All HOM experiments require a ‘50:50 beam-splitting’ mechanism that sends quantum particles incident along one of two input paths to one of two output paths with a 50% probability (Fig. 1a).

Careful analysis shows that there must be a well-defined relationship between the

beam-splitter’s inputs and outputs that is demanded by energy conservation in the classical picture of the beam-splitter³, or by a property known as unitarity in the quantum view⁴: for classical waves, this relationship fixes the relative positions of the output waves’ peaks and valleys with respect to those of the input waves, whereas for quantum particles this relationship manifests as a relative ‘phase’ between the particles’ input and output wavefunctions. Although the probability of finding a particle in a particular output path depends only on the amplitude of its wavefunction, the phase is important when determining the output wavefunction, and corresponding output probability, for two or more particles.

If two particles enter such a 50:50 beam-splitter, naively one would expect one of four possible outcomes: two in which the particles exit along a path together, and two in which they exit along different paths (Fig. 1b). In these cases, the single-particle output-wavefunction phases accumulate in an overall output phase. The HOM result is a consequence of the

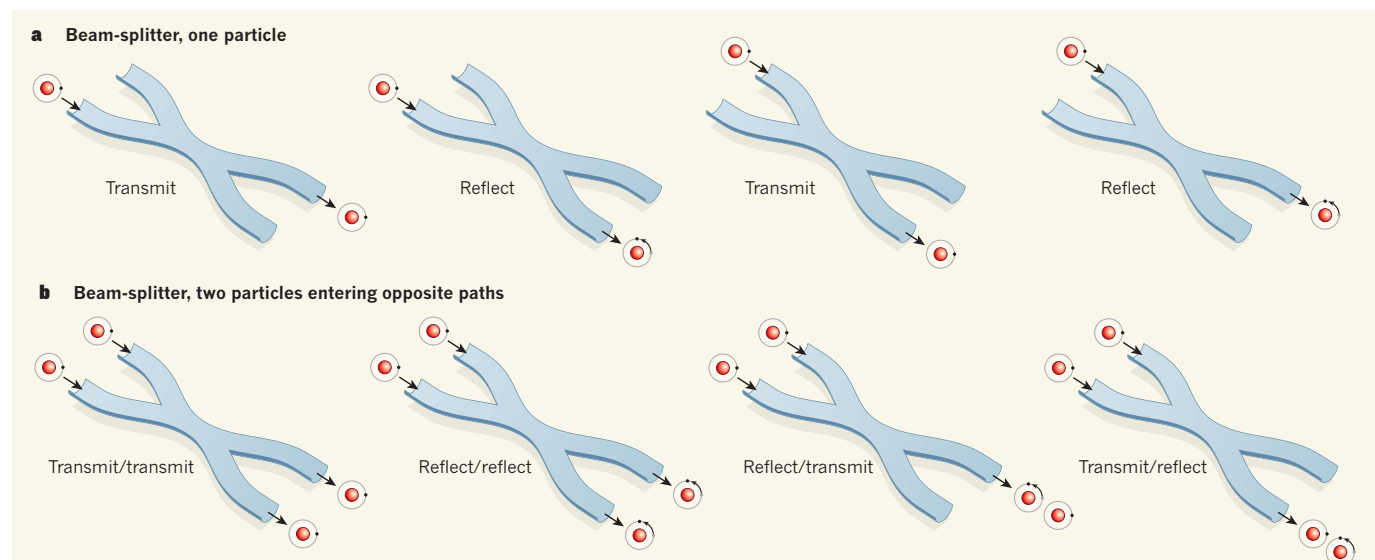


Figure 1 | Beam-splitter and quantum probabilities. Each beam-splitter (blue) is represented as two input paths (left) and two output paths (right); here we consider ‘50:50’ beam-splitters, for which the probability of each output is of equal magnitude. A particle is represented by a red circle, and its wavefunction’s phase by the position of the black dot on the grey circle. Individual phases cannot be measured directly. **a**, Possible outcomes for a single particle entering either of the input paths; the probabilities for particle transmission and

reflection are both 50%. In the case of reflection, the phase changes by 90°. **b**, For incoming particles at both inputs, there are four possible outcomes. However, the overall probability of the outcomes is determined by adding the individual probabilities using rules of quantum mechanics. For bosonic particles such as photons and helium-4 atoms, the subject of Lopes and colleagues’ study², the first two outcomes (transmit/transmit and reflect/reflect) cancel. The only outcomes remaining are the third and the fourth.

particles' indistinguishability, which means that there is no measurable difference between the two outcomes in which the particles exit along different paths. The overall output phases of these indistinguishable outcomes are opposite to each other, and when added together using quantum rules for bosons (particles with integer spin, a quantum property common to both photons and helium-4 atoms), these two possible outcomes interfere and cancel. The only outcomes remaining are those with two particles in a single output. As a result, simultaneous single-particle detections ('coincidence counts') at both outputs are forbidden.

Lopes *et al.* demonstrate two-particle quantum interference with helium-4 atoms. In their experiments, the atoms' paths are related to their speeds, which are manipulated by selectively transferring momentum to and from light in absorption and emission processes^{5,6}. First, the researchers prepared a 'twin pair' by removing from an atom reservoir indistinguishable atoms with different speeds. Second, they used light pulses to modify the atoms' momenta and cause the pair to meet; the atom in the first path travels with velocity v_1 and the atom in the second path with v_2 . A beam-splitting mechanism implemented reflection and transmission by changing the atoms' speeds with 50% probability from v_1 to v_2 and vice versa.

The atoms continued to travel until they hit a time-resolved, multipixel atom-counting detector, at which an atom with v_1 would arrive at a different time from one with v_2 . Lopes and colleagues prepared many twin pairs in a short interval and recorded the precise location and timing of the atoms' arrivals at the detector: a coincident count would be the measurement at a particular location of a particle at time t_1 followed by a measurement at t_2 . Although the researchers found that the arrivals from the many pairs were distributed in two time windows (corresponding to the two output paths), they found a striking lack of instances among these random outcomes when the time difference was exactly $t_2 - t_1$, indicating that the atoms from a twin pair must be exiting the beam-splitter with the same velocity. This 'anticorrelation' is the signature of a HOM experiment.

As in quantum-optics demonstrations of the HOM effect, the present result demonstrates that pairs of identical, 'quantum-entangled' particles have been produced. The unique capabilities of this apparatus, including the combination of condensed metastable helium-4 atoms and the atom-counting detector, offer a spatial and temporal resolution unavailable to others. Protocols for transmitting and processing quantum information, analogous to those used in optical systems, can now be implemented with new capabilities in atomic systems: atoms, unlike photons, may interact with one another, and because they have mass, their mechanical properties,

such as momentum, can be varied and used as experimental parameters.

Furthermore, because atoms can also be fermions (particles with half-integer spin, such as electrons), they could exhibit a quantum-interference effect that is the fermionic equivalent of the HOM effect⁴. Evidence for this mechanism has already been seen in electronic systems⁷. The bosonic HOM effect demonstrated here, and its fermionic counterpart, may offer new possibilities for implementing quantum-information protocols and for exploring the foundations of quantum physics. ■

Lindsay J. LeBlanc is in the Department of Physics, University of Alberta, Edmonton, Alberta T6G 2E1, Canada.
e-mail: lindsay.leblanc@ualberta.ca

1. Hong, C. K., Ou, Z. Y. & Mandel, L. *Phys. Rev. Lett.* **59**, 2044–2046 (1987).
2. Lopes, R. *et al. Nature* **520**, 66–68 (2015).
3. Ou, Z. Y. & Mandel, L. *Am. J. Phys.* **57**, 66 (1989).
4. Loudon, R. *Phys. Rev. A* **58**, 4904–4909 (1998).
5. Campbell, G. K. *et al. Phys. Rev. Lett.* **96**, 020406 (2006).
6. Bonneau, M. *et al. Phys. Rev. A* **87**, 061603 (2013).
7. Neder, I. *et al. Nature* **448**, 333–337 (2007).

CANCER

A piece of the p53 puzzle

An iron-dependent form of cell death called ferroptosis has been implicated as a component of the tumour-suppressor activity of p53, providing fresh insight into how this protein prevents cancer development. SEE ARTICLE P.57

KATHRYN T. BIEGING & LAURA D. ATTARDI

The gene that encodes the p53 tumour-suppressor protein is the most commonly mutated gene in human cancers¹. Indeed, p53 is inactivated in more than half of all cancers, reflecting the fact that it provides a crucial brake to cancer development, and that incapacitating p53 is often a requisite step for the emergence of cancer. However, despite years of research, our understanding of how p53 performs its job remains far from complete. In this issue, Jiang *et al.*² (page 57)

uncover a previously unknown role for p53 in regulating a type of cell death dubbed ferroptosis, completing one more piece of the p53 puzzle.

Conventionally, p53 is thought of as a sentinel for DNA damage. In this role as a guardian of the genome, p53 responds to DNA damage either by putting the brakes on proliferation, allowing cells to pause and repair damaged DNA before dividing, or by driving a form of cell suicide called apoptosis, both of which protect against the accumulation of mutant cells that have the potential to

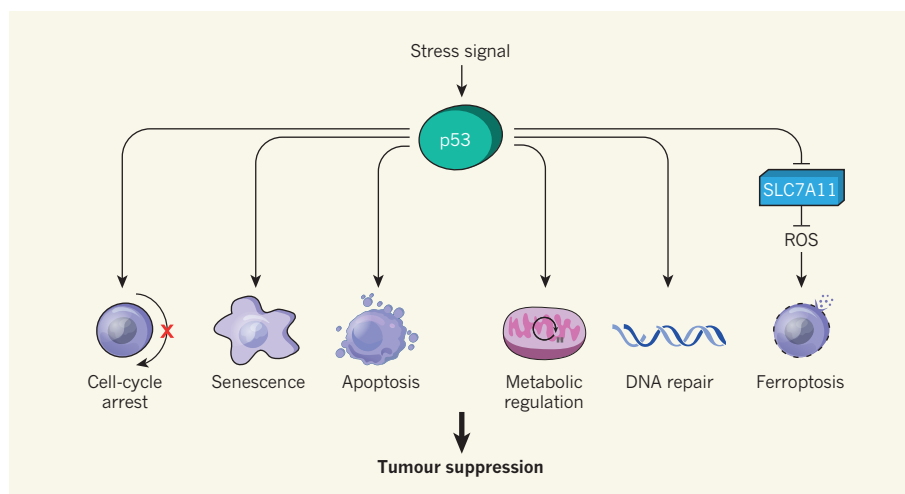


Figure 1 | The functions of p53 in tumour suppression. Activation of p53 in response to stress signals leads to diverse cellular responses. Conventionally, the tumour-suppressor activity of p53 has been attributed to its ability to induce cell-cycle arrest, senescence and a form of cell death called apoptosis in response to DNA damage or the expression of cancer-promoting genes. However, studies indicate that other p53-mediated activities, such as metabolic regulation or DNA repair, might be needed for tumour suppression, or might compensate when these classical functions are absent. Jiang *et al.*² show that p53 represses the target gene *SLC7A11* to promote the accumulation of reactive oxygen species (ROS), triggering a non-apoptotic form of cell death called ferroptosis that suppresses tumour growth.

fuel cancer development^{3,4}. The protein fulfils this responsibility in large part by serving as a transcription factor that, among its many target genes, modulates the expression of genes encoding proteins that inhibit cell division or induce apoptosis⁴.

Although this regulatory role as a guardian of the genome seems to account for p53's tumour-suppressor function, several studies have altered our thinking about how p53 represses cancer development. A set of papers (including one from the authors of the current study) provided pivotal evidence that p53-mediated apoptosis and proliferative arrest in response to DNA-damage signals are dispensable for tumour suppression^{5–7}. These studies illuminated the functions of p53 that are not essential for tumour suppression, but failed to definitively reveal which p53 functions are required. Jiang and colleagues' latest study sheds light on this issue.

The authors use a mutated form of p53 called p53^{3KR}, which carries alterations at several key sites in its DNA-targeting region. As such, p53^{3KR} has an impaired ability to activate many of p53's target genes, including those responsible for the protein's anti-proliferative and pro-apoptotic activity. The mutated protein nonetheless suppresses spontaneous tumour development in mice⁶ — but how? The authors embark on an unbiased quest to answer this question by searching for potential mediators of p53 tumour-suppressor function. They identify *SLC7A11* as a gene whose expression is repressed by both p53 and p53^{3KR}.

SLC7A11 is a cell-surface, amino-acid transporter protein that dampens the production of reactive oxygen species (ROS), which can wreak havoc in a cell by inducing damage⁸. In particular, by limiting ROS accumulation, *SLC7A11* inhibits ferroptosis, a form of non-apoptotic cell death triggered by the iron-dependent production of ROS⁹ (Fig. 1). Jiang *et al.* show that both p53 and p53^{3KR} can stimulate ferroptosis *in vitro* in response to the ferroptosis-activating agent erastin, and that this response can be inhibited by the overproduction of *SLC7A11*. This contrasts starkly with the inability of p53^{3KR} to regulate classical p53 functions, and suggests that the ability to induce ferroptosis could account for the function of p53^{3KR} in mice.

To test this hypothesis, the authors analyse mouse embryos carrying p53^{3KR} but lacking the protein Mdm2, an essential inhibitor of p53. These mutant embryos normally die as a result of hyperactive p53 signalling, but the authors show that inhibiting ferroptosis imparts some protection against this lethality. These experiments provide evidence that ferroptosis contributes to p53 activity *in vivo*, in this case promoting embryonic lethality.

Expanding this analysis to cancer development, Jiang and colleagues next show that overexpression of *SLC7A11* overcomes the tumour-suppressor effects of p53^{3KR} in

tumours transplanted into mice. This suggests that repression of *SLC7A11* transcription is necessary for p53^{3KR}-mediated tumour suppression, and, moreover, that p53^{3KR} suppresses tumour growth at least in part through ferroptosis. However, it remains unclear whether p53-mediated activation of ferroptosis is a front-line tumour-suppressive response or whether it primarily provides a back-up mechanism when other p53 functions are crippled, as in the p53^{3KR} mutant.

This study unveils a new pathway for p53-dependent tumour suppression. However, many questions remain. For instance, it is still unknown whether ferroptosis is a general mechanism that operates in all tumour types or whether it has a more selective function, suppressing cancers that originate from specific tissues. It is also not yet clear which p53-activating signals — such as expression of cancer-promoting genes or deprivation of nutrients — activate ferroptosis *in vivo*. The roles of other p53 target genes in ferroptosis must also be defined.

In the broader landscape, it will be imperative to determine which other p53-dependent processes contribute to tumour suppression and what their context dependencies may be¹⁰. Although DNA-damage-induced apoptosis and cell-cycle arrest have been deemed to be dispensable for tumour suppression, this

does not preclude a role for these responses in some settings. Finally, the finding that inducing ferroptosis by using an erastin analogue delays the growth of p53-expressing tumours in a mouse transplant model¹¹ suggests that activating ferroptosis may be a promising therapeutic strategy for treating tumours in which p53 activity is retained, a possibility that warrants further investigation. ■

Kathryn T. Bieging and Laura D. Attardi are in the Department of Radiation Oncology, Stanford University School of Medicine, Stanford, California 94305-5152, USA.

L.D.A. is also in the Department of Genetics, Stanford University School of Medicine, e-mail: attardi@stanford.edu

1. Freed-Pastor, W. A. & Prives, C. *Genes Dev.* **26**, 1268–1286 (2012).
2. Jiang, L. *et al.* *Nature* **520**, 57–62 (2015).
3. Lane, D. P. *Nature* **358**, 15–16 (1992).
4. Vousden, K. H. & Prives, C. *Cell* **137**, 413–431 (2009).
5. Brady, C. A. *et al.* *Cell* **145**, 571–583 (2011).
6. Li, T. *et al.* *Cell* **149**, 1269–1283 (2012).
7. Valente, L. J. *et al.* *Cell Rep.* **3**, 1339–1345 (2013).
8. Conrad, M. & Sato, H. *Amino Acids* **42**, 231–246 (2012).
9. Dixon, S. J. *et al.* *Cell* **149**, 1060–1072 (2012).
10. Bieging, K. T., Mello, S. S. & Attardi, L. D. *Nature Rev. Cancer* **14**, 359–370 (2014).
11. Yang, W. S. *et al.* *Cell* **156**, 317–331 (2014).

This article was published online on 18 March 2015.

BIODIVERSITY

Land use matters

A meta-analysis at a local scale reveals that land-use change has caused species richness to decline by approximately 8.1% on average globally, mainly as a result of large increases in croplands and pastures. [SEE ARTICLE P.45](#)

BRIAN MCGILL

The main effects humans have on our planet seem to manifest in factors of two: we have doubled the rate at which nitrogen enters the biosphere by using fertilizer; we have diverted half of the fresh water and half of all plant productivity for our own purposes; and we have modified about half of the planet's land^{1,2}. It is widely speculated that the last of these — modifying roughly 50% of all land — is the biggest human-caused threat to biodiversity, but this theory has never been comprehensively assessed. On page 45 of this issue, Newbold *et al.*³ describe an ambitious attempt to evaluate the global impact of land-use change on terrestrial biodiversity.

The authors assembled a data set of more than 380 previous studies comparing the biodiversity of sites with no human change (original or primary vegetation) with similar sites modified for human use. They combined

this data set with further data on the global land-use changes made by humans over the past 500 years⁴, and also with several predictions of how humans might modify land use over the next 100 years. The processes controlling biodiversity are highly scale-specific⁵, and most previous studies have focused either on extinctions at global scales or on the number of species in certain regions (and the latter is actually often increasing⁶). By contrast, Newbold *et al.* analysed their data at a local scale, typically smaller than a football field, which is more relevant to the way humans interact with nature.

The headline finding is that land-use change has caused the number of species (species richness) contained in these small plots of land to decline by 8.1% over 500 years when averaged across the globe. The authors also find a 10.7% decline in the number of individual organisms, with an additional decline in richness resulting from this loss of individuals rather



Figure 1 | Land conversions reduce species richness. Newbold *et al.*³ show that the greatest reductions in biodiversity resulting from land-use change occur when pristine vegetation is converted to cropland or pasture, such as has occurred next to the Iguazú National Park in Brazil.

than from an underlying biodiversity loss.

The study excels in providing details of where and why these losses occurred. Types of human modification that were evaluated include conversions to pasture, cropland, tree plantations, urbanization and secondary vegetation (land that was disturbed but allowed to regrow). The authors found that areas of secondary vegetation show little species loss, whereas land converted to pasture, cropland and urban areas show heavy loss (see Figure 1 in the paper³). Considering that the most common human land-use conversions are to secondary vegetation, cropland and pasture, it becomes clear that most of the impact on biodiversity has resulted from conversion of pristine vegetation to cropland and pasture (Fig. 1). As a result, most of the loss has occurred in the prairie steppes of North America and Eurasia, in heavily grazed subtropical dry areas, and in countries that have experienced rapid agricultural growth to support heavy population growth, such as Indonesia, India, Brazil and China (see Figure 3 of the paper³). However, the average 8.1% decline hides a lot of variability — for example, the authors find that low-intensity urban land use and moderate human densities (roughly speaking, suburbs) are actually associated with increased species richness.

Three other recent papers^{7–9} also assembled data from large numbers of studies at similar scales and over a variety of time periods, but these studies found that, on average, there has been no change in local species richness. The difference between these findings and those of Newbold *et al.* is quite small (0% over 3–260 years versus 8% over 500 years) relative to the uncertainty (the 95% error range in Newbold and colleagues' study is 3.5–12.9% species loss, not including uncertainties in land-use

change). However, the perceived qualitative difference will loom large in people's minds.

One possible explanation for the discrepancy is that different methods were used — two of the previous analyses^{7,8} used studies that tracked diversity on single pieces of land through time, which has the advantage of directly measuring the quantity of interest but the disadvantage of potentially introducing spatial sampling biases. But I suspect the main explanation is that Newbold *et al.* targeted a single human impact — land-use change — whereas the three other studies averaged across all forms of human impact. Some of these, such as increased fertilization and bringing about species invasions, can actually increase species richness (and might also explain the species increase in suburban regions found by Newbold and colleagues).

It would be odd if the negative effects of land-use change documented by Newbold *et al.* were exactly counterbalanced, such that the net effect of all types of human impacts averaged out to zero (at the local scale). Yet that might be the most parsimonious explanation for the results across these four studies. And it might not be so odd if ecological processes strongly regulate local species richness¹⁰. This would require rates of local extinction to increase when there are too many species, and arrival rates of locally novel species to increase when there are too few species, effectively pushing the system towards a 'set point' for species richness. There is good evidence for this in an island context¹¹, but more study of such processes is needed for mainland communities¹⁰.

Newbold and colleagues' study has two limitations that are worthy of comment. First, their compilation of the literature demonstrates the existence of publication

bias — studies showing positive effects were published less often than statistically likely. Newbold and colleagues have been careful to address this problem and I do not think it greatly affected their results. But it is a wake-up call that our literature on this topic is biased.

Second, their estimates of diversity loss focused on the endpoints of changes, such as urbanization versus pasture, without segregating the data on the basis of the land's starting point, such as grassland versus forest. It seems probable that there have been larger declines in species richness in land that started as forest than as grassland (because forests typically start with more species), but many of the conversions to pastures and croplands that drive the authors' results started as grasslands, not forests — this could lead to a bias in the results. As better data become available, future studies should unpack these nuances.

Despite these limitations, Newbold and colleagues' study is by far the best empirical demonstration to date that land-use change negatively affects local biodiversity on average, and effectively puts this question beyond debate. It also shows that the greatest negative impacts come from the introduction of cropland and pasture, both in areas of rapid population growth and in the breadbaskets of Eurasia and North America, rather than from urbanized land and harvested land that is allowed to regrow. This has clear implications for conservation policies and priorities.

The scenarios examined by the authors for the next 100 years suggest that average species richness will fall by a further 3.4% if there are no interventions into practices of land-use change. Yet they also show that, even within the range of what economists consider to be realistic mitigation scenarios, we have the ability to reverse trends in biodiversity loss and even to increase average local richness. This paper provides clear guidance for policymakers — the ball is now in their court. ■

Brian McGill is in the School of Biology and Ecology, and the Mitchell Center for Sustainability Solutions, University of Maine, Orono, Maine 04469, USA.
e-mail: mail@brianmcgill.org

1. Millennium Ecosystem Assessment. *Ecosystems and Human Well-Being* (World Resources Inst., 2005).
2. Vitousek, P. M., Mooney, H. A., Lubchenco, J. & Melillo, J. M. *Science* **277**, 494–499 (1997).
3. Newbold, T. *et al.* *Nature* **520**, 45–50 (2015).
4. Hurr, G. C. *et al.* *Clim. Change* **109**, 117–161 (2011).
5. McGill, B. J., Dornelas, M., Gotelli, N. J. & Magurran, A. E. *Trends Ecol. Evol.* **30**, 104–113 (2015).
6. Sax, D. F. & Gaines, S. D. *Trends Ecol. Evol.* **18**, 561–566 (2003).
7. Dornelas, M. *et al.* *Science* **344**, 296–299 (2014).
8. Vellend, M. *et al.* *Proc. Natl Acad. Sci. USA* **110**, 19456–19459 (2013).
9. Supp, S. R. & Ernest, S. K. M. *Ecology* **95**, 1717–1723 (2014).
10. Ernest, S. K. M., Brown, J. H., Thibault, K. M., White, E. P. & Goheen, J. R. *Am. Nat.* **172**, E257–E269 (2008).
11. MacArthur, R. H. & Wilson, E. O. *The Theory of Island Biogeography* (Princeton Univ. Press, 1967).

Preventing stars from eating their young

Researchers have found a mechanism that prevents newly forming giant-planet cores from spiralling in towards their parent stars. The result may explain why planets such as Saturn and Jupiter are where they are today. [SEE LETTER P.63](#)

MARTIN J. DUNCAN

Writing in this issue, Benítez-Llambay *et al.*¹ (page 63) report computer simulations that may throw light on why the Solar System and a substantial fraction of exoplanetary systems have gas-giant planets that are separated from their host stars by distances of at least Earth's distance from the Sun. Gas giants are planets such as Jupiter (Fig. 1) and Saturn, with masses tens to hundreds of times that of Earth and consisting mostly of gas.

In the widely accepted model of gas-giant formation (for a review, see ref. 2), an embryonic solid core forms in a disk of gas and dust that orbits a newly forming star. The embryo grows by colliding with, and thereby accreting, smaller solid bodies from the circumstellar disk. If it grows sufficiently quickly, it can reach a critical solid mass that is large enough — about 10 Earth masses — for it to undergo rapid accretion of the surrounding gas and to mature into a gas giant before the disk gas disperses (a process that takes 1 million to 10 million years).

For more than 30 years^{3,4}, it has been recognized that this scenario suffers from a potentially fatal flaw. The growing planetary embryo raises a gravitational wake in the gas disk that is predicted to exert a tidal torque on the planet and make it spiral towards the surface of the star much faster than it can grow. The spiralling occurs within about 100,000 years for an embryo of a few Earth masses. However, roughly 10–20% of exoplanetary systems and, of course, our own Solar System, have gas giants that are beyond 1 astronomical unit (AU) from their host stars⁵ (1 AU is the median Earth–Sun separation), so nature has apparently overcome this difficulty. Interest in the past few years has focused^{6,7} on the gravitational effects of the gas in the annulus around the planet's orbit, where the rotational speed of the gas is close to that of the embryo: the corotation region.

In their simulations of a solid planetary embryo orbiting in a gas disk, Benítez-Llambay *et al.* show that the energy released by the material in solid bodies that are accreting onto the growing embryo can substantially heat the gas in the corotation region near the

embryo and cause regions just behind and just ahead of the embryo's orbital path to expand and become under-dense. The region behind expands more than the region ahead (for reasons given below), and so the latter pulls the embryo forward more than the former pulls it back. This results in a positive contribution (which the authors call a “heating torque”) to the embryo's angular momentum that causes the embryo to migrate outward from the parent star and that can, under certain circumstances, overcome the negative contribution from the spiral wake.

Just what are those circumstances? The authors first show that the asymmetry in the heating and expansion of regions ahead of and behind the embryo is related to the fact that a parcel of gas in the disk that is at the same distance from the star as the embryo moves slightly more slowly in its circular orbit than the embryo, provided that the gas pressure decreases with increasing distances from the star. The gradient in the gas pressure helps to support the gas parcel in the same way that the vertical gradient in Earth's atmospheric pressure prevents the atmosphere from collapsing on our heads. In the stellar context, it means that the region in the gas disk that exactly corotates with the embryo is within the embryo's orbit. This causes the gas flow and heating to differ ahead of and behind the embryo. Thus, in most regions of the disk the heating torque is robustly positive.

However, the magnitude of the heating torque depends on the disk's opacity (which determines how far from the embryo the energy of accreted material is deposited), the rate at which material is accreted (which controls the rate at which energy is liberated and hence is linearly related to the heating torque), and the mass of the embryo. For embryo masses near one Earth mass, for which migration towards the star most threatens gas-giant formation, if the accretion rate doubles the embryo mass within about 60,000 years, the heating torque will overcome the tidal torque for the ‘standard’ values of the disk properties adopted by Benítez-Llambay and co-workers.

Therefore, the results suggest a bifurcation in embryo behaviour: disks in which embryo growth is rapid can go on to produce gas giants at or beyond 1 AU, whereas disks in which accretion of solids is slow may lead to ‘failed cores’, which migrate inward. The authors note that this bifurcation could explain the strong observed correlation in extrasolar systems between the abundance of heavy elements in the host star (elements, other than hydrogen and helium, that would be in the form of solids to be accreted) and the presence of gas giants beyond 1 AU from it.

Benítez-Llambay and colleagues' simulations are just a first attempt at modelling the complex coupling between the processes of hydrodynamics and of energy transfer that take place in the circumstellar-disk regions

NASA

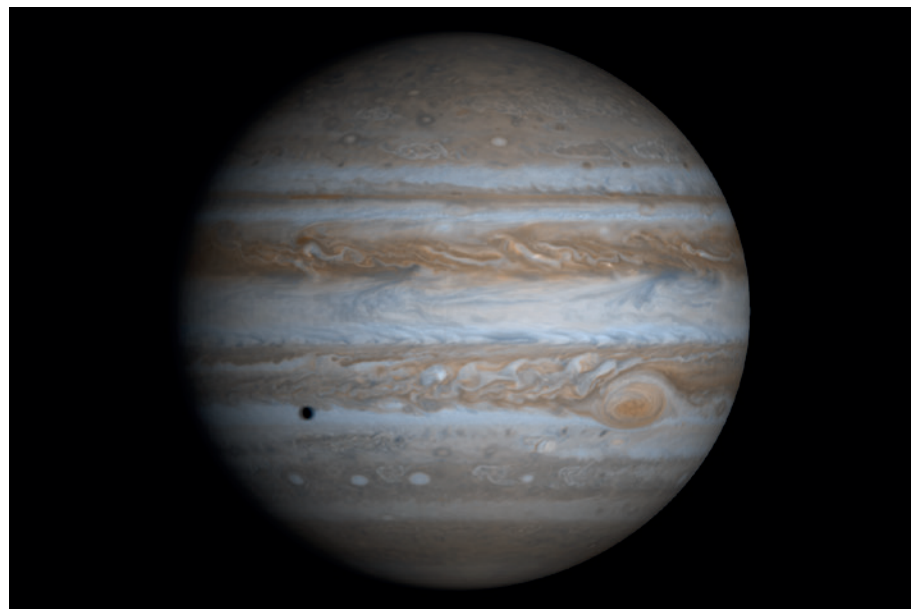


Figure 1 | Planet Jupiter. Benítez-Llambay *et al.*¹ describe computer simulations of a planetary embryo orbiting in a gas disk that may explain the distances of gas-giant planets such as Jupiter from their host stars. The tiny black feature is the shadow cast on the planet by its moon Europa.

near a growing planetary embryo. Further modelling is needed, especially in view of studies^{8,9} of the high accretion rates associated with pebble-sized objects in the presence of gas disks. Nonetheless, the authors' results underscore what has become increasingly apparent in the past decade — that the amazingly diverse nature of exoplanetary orbits and the structure of the planets on them force us to carefully examine our models of planet formation in an attempt to discern which of many complex and interrelated physical phenomena

are likely to be most significant in shaping planetary-system architectures. The present study may well contribute an important ingredient to the mix. ■

Martin J. Duncan is in the Department of Physics, Engineering Physics and Astronomy, Queen's University, Kingston, Ontario K7L 7N6, Canada.
e-mail: duncan@astro.queensu.ca

1. Benítez-Llambay, P., Masset, F., Koenigsberger, G. &

Szulágyi, J. *Nature* **520**, 63–65 (2015).
2. Levison, H. F., Thommes, E. & Duncan, M. J. *Astron. J.* **139**, 1297–1314 (2010).
3. Goldreich, P. & Tremaine, S. *Astrophys. J.* **241**, 425–441 (1980).
4. Ward, W. R. *Icarus* **126**, 261–281 (1997).
5. Howard, A. W. *Science* **340**, 572–576 (2013).
6. Baruteau, C. et al. Preprint at <http://arxiv.org/abs/1312.4293> (2013).
7. Paardekooper, S.-J., Baruteau, C. & Kley, W. *Mon. Not. R. Astron. Soc.* **410**, 293–303 (2011).
8. Ormel, C. W. & Klahr, H. H. *Astron. Astrophys.* **520**, A43 (2010).
9. Lambrechts, M. & Johansen, A. *Astron. Astrophys.* **544**, A32 (2012).

PLANT BIOLOGY

Coding in non-coding RNAs

The discovery of peptides encoded by what were thought to be non-coding — or 'junk' — regions of precursors to microRNA sequences reveals a new layer of gene regulation. These sequences may not be junk, after all. SEE LETTER P.90

PETER M. WATERHOUSE
& ROGER P. HELLENS

In plants and animals, microRNAs regulate the expression of many different genes¹. Such regulation is crucial in a variety of processes, including transitions through developmental stages and responses to environmental stresses. MicroRNAs (miRNAs) are short in sequence and are generated by enzymatic excision from precursor transcripts called primary miRNAs (pri-miRs), which until now had been assumed not to encode any proteins. But on page 90 of this issue, Laressergues *et al.*² provide convincing evidence to the contrary. They find that some pri-miRs encode peptides that enhance production of their miRNAs. This is the first report of a functional peptide being encoded by a pri-miR and provides a fresh perspective on the significance of pri-miR regions beyond those that directly give rise to miRNAs.

In the 1970s, as it started to become clear that the genomic regions that encode proteins (the genes) swim in a sea of non-protein-coding sequences, the idea of meaningless, or 'junk', DNA became a hot topic of discussion. Biologists are now well aware of introns, the sequences within genes that separate the coding regions (exons) and which are spliced out at the messenger-RNA level, as well as their notable regulatory roles. However, the term junk DNA has survived and is used loosely to describe genomic sequences between genes, giving them an implied lack of importance.

The debate about the usefulness of non-protein-coding DNA sequences continues to rage^{3,4}. However, within these intergenic regions of a genome are the sequences

that produce most plant and many animal pri-miRs. Clearly, these sequences are not useless. Yet the regions of a pri-miR that do not generate the miRNA or the highly structured adjacent sequences have suffered the similar fate of being largely ignored and possibly thought of as junk RNA lacking function.

Both plant and animal pri-miRs are transcribed from DNA in the nucleus by the enzyme RNA polymerase II (Fig. 1). The structured (fold-back) region of the transcript surrounding the miRNA sequence is recognized and processed by one of two enzymes —

Drosha or Dicer-like1. (In animals, Drosha extracts a short hairpin-like RNA known as pre-miR, which contains the miRNA sequence⁵. In plants, Dicer-like1 cuts out the miRNA in a duplex form⁶.) Next, transporter proteins export the excised sequences to the cytoplasm, where they are further processed before becoming competent to guide the RNA-induced silencing complex (RISC) in repressing target genes through either cleavage or translational repression of their mRNAs.

It is generally thought that the sequences of a pri-miR upstream and downstream of the foldback region are rapidly degraded after excision of the embedded miRNA. However, the initial pri-miR has the same characteristics as any mRNA produced by RNA polymerase II (specifically, alteration of its 5' end by a modification called capping, and addition of polyadenyl groups to its 3' end). It is therefore equipped with the signals for nuclear export, and for stability and translation in the cytoplasm. Nonetheless, the fate of any full-length pri-miR that escapes processing into an miRNA — in maize (corn), for example, such pri-miR sequences can range from 250 to 2,500 nucleotides long⁷ — and its capacity to encode a

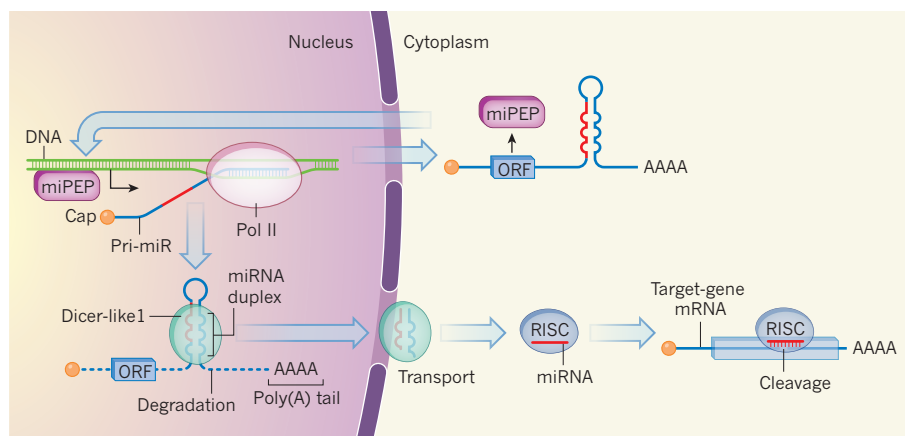


Figure 1 | MicroRNAs and their associated peptides. The precursors of plant microRNAs (miRNAs) are pri-miR sequences, which are transcribed from DNA by the enzyme RNA polymerase II (Pol II). They are then modified by capping and addition of a poly(A) tail. The miRNA duplexes are subsequently excised by the enzyme Dicer-like1 and transported to the cytoplasm; other parts of the pri-miR are degraded. After further processing, the resulting miRNA sequence guides repression of gene expression as part of the RISC complex. Laressergues *et al.*² report that some pri-miRs contain short open reading frame (ORF) sequences that can produce peptides (miPEP). The miPEPs enhance expression of the pri-miR, leading to more miRNA and so more effective cleavage of the target gene's messenger RNA. Such ORFs may avoid degradation as part of pri-miRs that might exit the nucleus without being processed by Dicer-like1.

peptide have been largely unnoticed or ignored.

Lauressergues and colleagues identified short open reading frames (ORFs) — sequences that can potentially encode proteins — in many different pri-miRs of two plant species. For five of them, they predicted the corresponding amino-acid sequences of the ORFs, synthesized the corresponding peptides and made specific antibodies against them. Using these antibodies, the authors showed that the ORFs are naturally translated in plants into peptides that they call miPEPs.

In the cases examined, the miPEPs had the same tissue distribution as their associated mature miRNAs and enhanced the expression and effectiveness of these miRNAs. Moreover, the miPEPs promoted the transcription of their corresponding pri-miR, rather than enhancing miRNA stability. This discovery reveals an unexpected function for at least part of the non-foldback pri-miR sequences and highlights yet another layer of gene regulation. It also raises questions about the existence and functions of other peptides potentially encoded by such short ORFs.

Genomic sequences with the potential to encode pri-miRs are constantly evolving in plants. They seem to arise from inverted duplications of whole or fragmented genes that lead to the production of hairpin-like RNAs⁸. If such RNAs produce useful miRNAs for gene regulation, they are refined into pri-miRs; if not, they erode away. This has led to the concept of ancient and recent miRNAs. Ancient miRNAs have sequences and functions that are conserved across many species, have survived for hundreds of millions of years, and seem destined to be essential for future plant evolution. Recent miRNAs are more species-specific and have much less assured functions and futures.

The miPEPs discovered in the present paper are associated with several families of miRNAs. If we put miR165 into the miR166 family (the two miRNAs differ by only one nucleotide), all seven of the miPEPs discovered in the present paper are associated with ancient miRNA families that are conserved across all flowering plants. Thus, they have all had the evolutionary time to create ORFs encoding functionally useful peptides. From this, it seems likely that yet-to-be-discovered miPEPs will be more prevalent in ancient miRNA families and that miPEPs in younger miRNA families may be detectably co-evolving with their associated miRNAs. It also seems possible that miPEPs are encoded in some animal pri-miRs.

The identification of further miPEPs, using bioinformatics alone, might not be easy. Five of the seven miPEPs identified by Lauressergues *et al.* are encoded in ORFs of fewer than 100 nucleotides. Sequences encoding potential peptides from ORFs of this size are often ignored or filtered out by automated genome-annotation programs, because the probability of their occurring by chance alone

increases exponentially as they get shorter.

Short yet functional peptide-encoding ORFs are also beginning to be discovered upstream of larger conventional protein-coding ORFs⁹, and many of these defy convention by having unusual start codons (sequences that initiate protein synthesis)¹⁰. The experimental discovery of miPEPs and other small peptides such as these raises an inconvenient question: are we missing a vast library of biologically important peptide signals because our bioinformatic analyses are not yet well enough designed to detect them? ■

Peter M. Waterhouse and Roger P. Hellens
are at the Queensland University of Technology
Centre for Tropical Crops and Biocommodities,
Brisbane, Queensland 4001, Australia.

e-mail: peter.waterhouse@qut.edu.au

1. Ameres, S. L. & Zamore, P. D. *Nature Rev. Mol. Cell Biol.* **14**, 475–488 (2013).
2. Lauressergues, D. *et al. Nature* **520**, 90–93 (2015).
3. Birney, E. *et al. Nature* **489**, 57–74 (2012).
4. Kellis, M. *et al. Proc. Natl Acad. Sci. USA* **111**, 6131–6138 (2014).
5. Carthew, R. W. & Sontheimer, E. J. *Cell* **136**, 642–655 (2009).
6. Fang, Y. & Spector, D. L. *Curr. Biol.* **17**, 818–823 (2007).
7. Zhang, L. *et al. PLoS Genet.* **5**, e1000716 (2009).
8. Cuperus, J. T., Fahlgren, N. & Carrington, J. C. *Plant Cell* **23**, 431–442 (2011).
9. Andrews, S. J. & Rothnagel, J. A. *Nature Rev. Genet.* **15**, 193–204 (2014).
10. Laing, W. A. *et al. Plant Cell* <http://dx.doi.org/10.1105/tpc.114.133777> (2015).

This article was published online on 25 March 2015.

ZOOLOGY

Here be dragons

Emerging evidence indicates that dragons can no longer be dismissed as creatures of legend and fantasy, and that anthropogenic effects on the world's climate may inadvertently be paving the way for the resurgence of these beasts.

**ANDREW J. HAMILTON, ROBERT M. MAY
& EDWARD K. WATERS**

Long considered to be the stuff of legend, dragons cross cultures and continents. Until recently, however, scant attention had been paid to the fact that the commonality in cultural representations of such creatures indicates something more sinister. From depictions in Ancient Greek literature and Slavic myth, to the dragons of the East or allusions in Zoroastrian scripture, the descriptions resonate. What if these legends were rooted in truth? The differences in appearance — some

lack wings, some have multiple heads and some seem not to breathe fire — once thought to reflect local traditions, can also readily be explained by speciation.

The 800th anniversary of the signing of *Magna Carta* in 1215 has sparked an unprecedented investigation of literary resources from the early medieval period. One such document, uncovered by chance under a pile of rusty candlesticks in a locked cupboard marked “*loste propertie*” in the depths of the University of Oxford’s Bodleian Library, provides strong evidence that the field of fantastical beasts requires urgent re-evaluation.



Figure 1 | Lizards of legend. Dragons have somehow wormed their way into the realm of fantasy, which belies the threat posed by them in the twenty-first century.

ANDERSON, WAYNE/PRIVATE COLLECTION/BRIDGEMAN IMAGES

Attributed to the monk Godfrey of Exmouth, the treatise discusses many verified aspects of English history but, crucially, proffers evidence that for millennia dragons have periodically been a scourge to civilizations (Fig. 1).

Further work has revealed that the early medieval period was a veritable paradise for dragons. This can be attributed to the period's unusually warm temperatures (Fig. 2) and an abundance of knights, the beasts' favourite combatant and food. It was also a time when wealth and status were measured in terms of gold and silver — the preferred nesting material for Western dragons. As result, the major needs for living, feeding and, crucially, relaxation were readily available to dragons, allowing populations to flourish. The roasting of flesh and the indiscriminate demolition of hovels and castles became commonplace.

As Godfrey of Exmouth attests, this was an era when humanity as a whole was fully aware of the existence of dragons and all other magical beings. It is likely that the persistent anti-social behaviour of dragons, and the failure of seemingly powerful magical beings to combat the scourge effectively, led to a deep-seated antipathy: witches became kindling, wizards who dared to imagine a heliocentric Universe suffered the indignity of trial and ridicule.

The combination of decreasing temperatures and a sharp decline in the number of knights saw the onset among dragons of The Great Sleep around the start of the fifteenth century. Such a phenomenon is well recognized: many ectothermic beasts enter a period of brumation (analogous to hibernation in endotherms) under adverse food and climatic conditions. The Great Sleep coincided with what is generally referred to as the Little Ice Age (Fig. 2). Historical records demonstrate that this period was a time of relative peace, at least with regard to dragon attacks. Many believed that dragons — the fire-breathing species, at any rate — had become extinct by the thirteenth or fourteenth century¹. This belief has further been extended to a perplexing level, whereby conventional opinion now holds that dragons, and indeed all other magical beings, are mere fantasy. Such a creed has been a blessing for dragons, because it spelt an end to the persecutions. Witches are now seen as crazy but harmless women, and wizards as senile old men with nothing better to do than wander around folk festivals in funny hats.

The calm was shaken briefly from 1586 to 1597 with The First Stir. Dragons behave no differently from other ectotherms in their brumation protocols, and they will periodically awaken from their slumber and check to see whether outside conditions justify ending the torpor. With their need to maintain extremely high temperatures in their buccal and nasal furnaces, it is crucially important for the fire-breathing species to ensure that the environmental conditions are energetically favourable before breaking their dormancy: there must be warmth and food. Fortunately, The First Stir coincided with the depths of the Little Ice Age

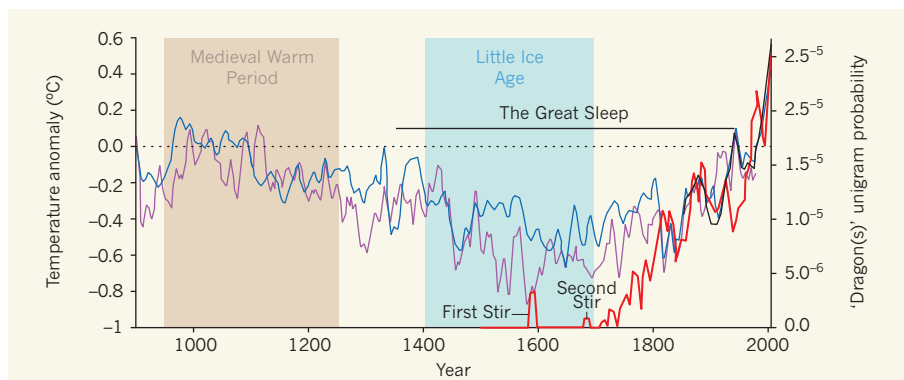


Figure 2 | The rise and fall and rise again of dragons. The relative frequency of 'dragons' in fictional literature (thick red line), as determined as a unigram probability⁴, with two historical reconstructions of Northern Hemisphere temperature (decadal smoothing) shown in blue⁵ and purple⁶. Global temperatures have been measured since 1855 (thick black line⁵). Temperature anomalies represent deviations from the 1961–90 reference period. The rising incidence of dragons in the literature correlates with rising temperatures, and suggests that these fire-breathing lizards are being sighted more frequently. As a result, the large-scale 'Third Stir' is deemed to be imminent.

and a bewildering lack of knights. Thus, the decision to return to slumber was made without hesitation. Although very few witnessed the awakenings, those who did (including some highly respected philosophers) were quick to record their astonishment in text (Fig. 2), but were immediately ridiculed by their peers and their writings relegated to the disrespected genre of fiction.

The Second Stir, 1680–90, although generally considered smaller than the first, produced similar results. Belief in dragons was virtually restricted to youngsters — who are readily ignored — and a handful of believing philosophers (scientists), who were acutely aware of how their predecessors had been ostracized a century earlier and so chose to remain mostly silent on sightings. This is reflected in the lower frequency of dragons in the literature in this stir compared with the first (Fig. 2).

The shift in societal views of dragons from reality to fantasy has been described by some as a kind of bewitchment. Newt Scamander² suggests that there was a deliberate policy among those of a 'magical' persuasion to hide the creatures. This is thought to have taken the form of casting a neurotransfer spell that translocates all information on magical phenomena held in the brain to a small lobe of the neocortex exclusively reserved for imaginative thought. As a result, any reported sightings are almost always done under the unconscious protection of fictitious communication. (This view has been challenged in the light of other cryptozoological phenomena such as the yeti or the Loch Ness monster, although the evidence remains inconclusive and proponents have largely been dismissed as unsuitable for responsible positions.)

It would have been expected that humanity's ignorance of the dragon situation would have been maintained were it not for a combination of events in the past few decades. First, the global economic downturn has led to a rise

in the search for 'buried' treasure, and hoards that serve as homes to resting dragons are an ideal way to bolster a failing economic policy. This strategy of 'quantitative thieving' is highly likely to provoke reprisals from slumbering dragons who awake to discover that their nests have been stripped bare.

To make matters worse, it seems that the 'block' on human awareness is occasionally failing, as evidenced in 1976 when a scientist (ironically, a knight and baron) published a non-fiction manuscript on dragons in *Nature*³. Sluggish action on global warming is set to compound the problem, and policies such as the restoration of knighthoods in Australia are likely to exacerbate the predicament yet further by providing a sustained and delicious food supply. It is now only a matter of time before The Third Stir takes place, and this, to borrow a phrase from Godfrey of Exmouth, will be the "bigge one". Climatic conditions are rapidly reaching an optimum for breeding dragons, and it is only a matter of time before the neurotransfer spell loses its efficacy completely. Further research into fireproof protective clothing is highly recommended — as is an avoidance of honorific titles. ■

Andrew J. Hamilton is at *The University of Melbourne and Federation University, Australia*. **Robert M. May** is at *the University of Oxford, UK*. **Edward K. Waters** is at *the University of Notre Dame Australia, Australia*. e-mails: andrewjh@unimelb.edu.au; robert.may@zoo.ox.ac.uk; edward.waters@nd.edu.au

- Hogarth, P. J. *Bull. Br. Ecol. Soc.* **7**, 2–5 (1976).
- Scamander, N. *Fantastic Beasts and Where to Find Them* (Bloomsbury, 2001).
- May, R. M. *Nature* **264**, 16–17 (1976).
- Michel, J.-B. et al. *Science* **331**, 176–182 (2011).
- Mann, M. E. et al. *Science* **326**, 1256–1260 (2009).
- Moberg, A. et al. *Nature* **433**, 613–617 (2005).

This article first appeared online on 1 April 2015; some of its content may merit a degree of scepticism.

Global effects of land use on local terrestrial biodiversity

Tim Newbold^{1,2*}, Lawrence N. Hudson^{3*}, Samantha L. L. Hill^{1,3}, Sara Contu³, Igor Lysenko⁴, Rebecca A. Senior^{1†}, Luca Börger⁵, Dominic J. Bennett^{4‡}, Argyrios Choimes^{3,4}, Ben Collen⁶, Julie Day^{4†}, Adriana De Palma^{3,4}, Sandra Díaz⁷, Susy Echeverria-Londoño³, Melanie J. Edgar³, Anat Feldman⁸, Morgan Garon⁴, Michelle L. K. Harrison⁴, Tamera Alhusseini⁴, Daniel J. Ingram^{4†}, Yuval Itescu⁸, Jens Kattge^{9,10}, Victoria Kemp⁴, Lucinda Kirkpatrick^{4†}, Michael Kleyer¹¹, David Laginha Pinto Correia³, Callum D. Martin⁴, Shai Meiri⁸, Maria Novosolov⁸, Yuan Pan⁴, Helen R. P. Phillips^{3,4}, Drew W. Purves², Alexandra Robinson⁴, Jake Simpson⁴, Sean L. Tuck¹², Evan Weiher¹³, Hannah J. White^{4†}, Robert M. Ewers⁴, Georgina M. Mace⁶, Jörn P. W. Scharlemann^{1,14} & Andy Purvis^{3,4}

Human activities, especially conversion and degradation of habitats, are causing global biodiversity declines. How local ecological assemblages are responding is less clear—a concern given their importance for many ecosystem functions and services. We analysed a terrestrial assemblage database of unprecedented geographic and taxonomic coverage to quantify local biodiversity responses to land use and related changes. Here we show that in the worst-affected habitats, these pressures reduce within-sample species richness by an average of 76.5%, total abundance by 39.5% and rarefaction-based richness by 40.3%. We estimate that, globally, these pressures have already slightly reduced average within-sample richness (by 13.6%), total abundance (10.7%) and rarefaction-based richness (8.1%), with changes showing marked spatial variation. Rapid further losses are predicted under a business-as-usual land-use scenario; within-sample richness is projected to fall by a further 3.4% globally by 2100, with losses concentrated in biodiverse but economically poor countries. Strong mitigation can deliver much more positive biodiversity changes (up to a 1.9% average increase) that are less strongly related to countries' socioeconomic status.

Biodiversity faces growing pressures from human actions, including habitat conversion and degradation, habitat fragmentation, climate change, harvesting and pollution¹. As a result, global assessments show that species' extinction risk is increasing on average while population sizes are declining^{1,2}. Such assessments have usually focused on data-rich vertebrates, so might not reflect broader biodiversity³. Furthermore, most have concentrated on the global status of species, whereas the long-term security of many ecosystem functions and services—especially in changing environments—is likely to depend upon local biodiversity^{4–6}. Average trends in local diversity remain unclear: analyses of temporal changes in assemblages have suggested no systematic change in species richness^{7,8}, but the available times-series data might under-represent transitions between land-use types⁹, and population time series suggest vertebrate populations have declined sharply in recent decades³.

Spatial comparisons provide an alternative source of evidence on how human pressures affect biodiversity, assuming that differences in pressures have caused observed biodiversity differences between otherwise matched sites^{10–12}. The prevalence of published spatial comparisons makes it possible to go beyond particular taxa or regions^{11,12} to develop global, taxonomically representative models. Furthermore, the willingness of

many researchers to share their raw data makes it possible to consider multiple aspects of biodiversity, rather than the single, simple metrics of most existing models¹⁰, which cannot capture all key aspects of diversity¹³.

We present the most geographically and taxonomically representative models to date of how several aspects of the composition and diversity of terrestrial assemblages respond to multiple human pressures. The explanatory variables in our models most directly measure land use and infrastructure, but might correlate^{14,15} with two other important pressures, harvesting and invasive species, for which comparable high-resolution spatial data are unavailable globally. We exclude climate change effects because they are not captured well by spatial comparisons. We use our models to infer past net changes in assemblages since the year 1500, project future changes over this century under different socioeconomic scenarios of land use, and relate projected national changes in local biodiversity to socioeconomic variables and natural biodiversity.

Our models of local within-sample species richness (hereafter 'richness'), rarefaction-based species richness (hereafter 'rarefied richness'), total abundance, compositional turnover and average organism size are

¹United Nations Environment Programme World Conservation Monitoring Centre, 219 Huntingdon Road, Cambridge CB3 0DL, UK. ²Computational Science Laboratory, Microsoft Research Cambridge, 21 Station Road, Cambridge CB1 2FB, UK. ³Department of Life Sciences, Natural History Museum, Cromwell Road, London SW7 5BD, UK. ⁴Department of Life Sciences, Imperial College London, Silwood Park, London SL5 7PY, UK. ⁵Department of Biosciences, College of Science, Swansea University, Singleton Park, Swansea SA2 8PP, UK. ⁶Department of Genetics, Evolution and Environment, Centre for Biodiversity and Environment Research, University College London, Gower Street, London WC1E 6BT, UK. ⁷Instituto Multidisciplinario de Biología Vegetal (CONICET-UNC) and FCEfYN, Universidad Nacional de Córdoba, Casilla de Correo 495, 5000 Córdoba, Argentina. ⁸Department of Zoology, Faculty of Life Sciences, Tel-Aviv University, 6997801 Tel Aviv, Israel. ⁹Max Planck Institute for Biogeochemistry, Hans Knöll Straße 10, 07743 Jena, Germany. ¹⁰German Centre for Integrative Biodiversity Research (iDiv) Halle-Jena-Leipzig, Deutscher Platz 5e, 04103 Leipzig, Germany. ¹¹Landscape Ecology Group, Institute of Biology and Environmental Sciences, University of Oldenburg, D-26111 Oldenburg, Germany. ¹²Department of Plant Sciences, University of Oxford, Oxford OX1 3RB, UK. ¹³Biology Department, University of Wisconsin—Eau Claire, Eau Claire, Wisconsin 54701, USA. ¹⁴School of Life Sciences, University of Sussex, Brighton BN1 9QG, UK. †Present addresses: Department of Animal and Plant Sciences, University of Sheffield, Alfred Denny Building, Western Bank, Sheffield S10 2TN, UK (R.A.S.); Department of Earth Science and Engineering, Imperial College London, London SW7 2AZ, UK and Institute of Zoology, Zoological Society of London, London NW1 4RY, UK (D.J.B.); College of Life and Environmental Sciences, Hatherly Laboratories, University of Exeter, Prince of Wales Road, Exeter EX4 4PS, UK (J.D.); School of Life Sciences, University of Sussex, Brighton BN1 9QG, UK (D.J.I.); School of Biological and Ecological Sciences, University of Stirling, Stirling FK9 4LA, UK (L.K.); School of Biological Sciences, Queen's University Belfast, 97 Lisburn Road, Belfast BT9 7BL, UK (H.J.W.).

*These authors contributed equally to this work.

based on among-site comparisons of ecological assemblage composition collated from the literature as part of the PREDICTS project¹⁶. The data set consisted of 1,130,251 records of abundance and 320,924 of occurrence or species richness at 11,525 sites (2–360 sites per study, median 15; Fig. 1a). These data, from 284 publications (see Methods), represent 26,953 species (1.4% of the number formally described¹⁷) and 13 of the 14 terrestrial biomes (Extended Data Fig. 1). Each site was

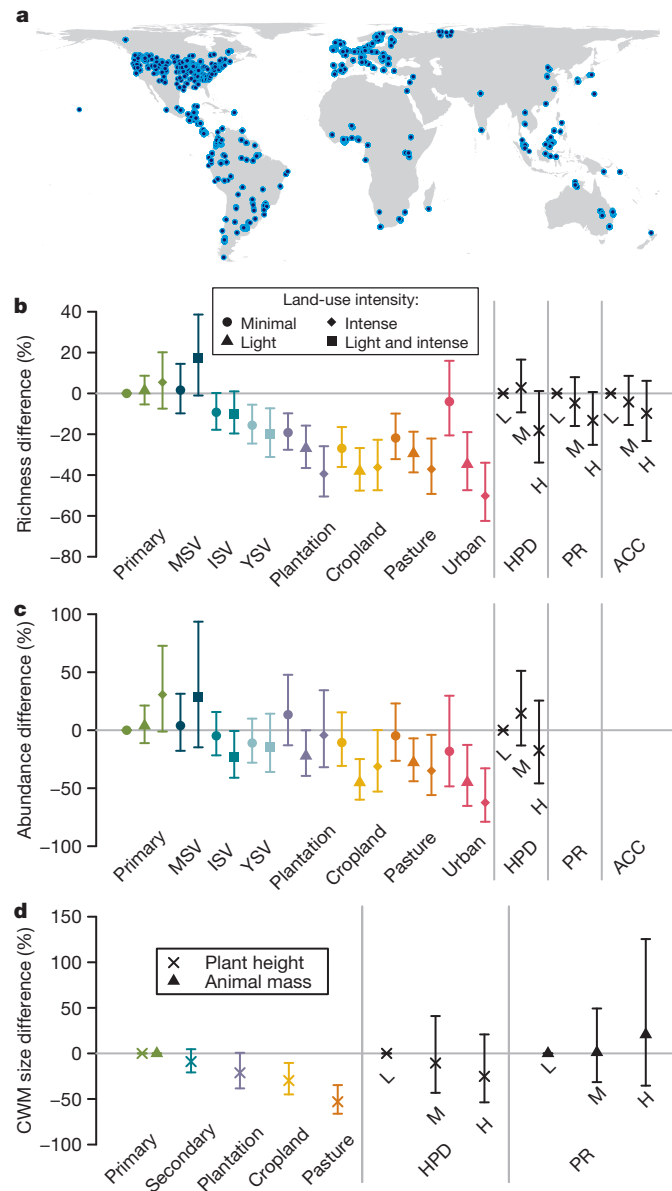


Figure 1 | Locations of sites and responses of four metrics of local diversity to human pressures. **a**, Sites used in the models. **b–d**, Responses⁴⁴ of richness (**b**), total abundance (**c**) and community-weighted mean (CWM) organism size—plant height (crosses) and animal mass (triangles)—(**d**) to anthropogenic variables. Error bars show 95% confidence intervals. Primary, primary vegetation; YSV, young secondary vegetation; ISV, intermediate secondary vegetation; MSV, mature secondary vegetation; plantation, plantation forest. Land-use intensity is categorized as minimal (circle), light (triangle), intense (diamond), or combined light and intense (square). HPD, human population density⁴⁵; PR, proximity to roads⁴⁶ (as $-\log(\text{distance to nearest road})$); and ACC, accessibility to humans⁴⁷ (as $-\log(\text{travel time to nearest major city})$), are shown as fitted effects from a model with no interactions between continuous effects and land use, at the lowest (L), median (M) and highest (H) values in the data set. Sample sizes are given in full in the Methods.

scored for six putative pressures: land use¹¹ and use intensity¹⁸, land-use history¹⁹, human population density²⁰, proximity to roads²¹ and accessibility from the nearest large town. Random effects in our models accounted for study-level differences in response variables and sampling methods, and for the within-study spatial arrangement of sites.

Effects of pressure on site-level diversity

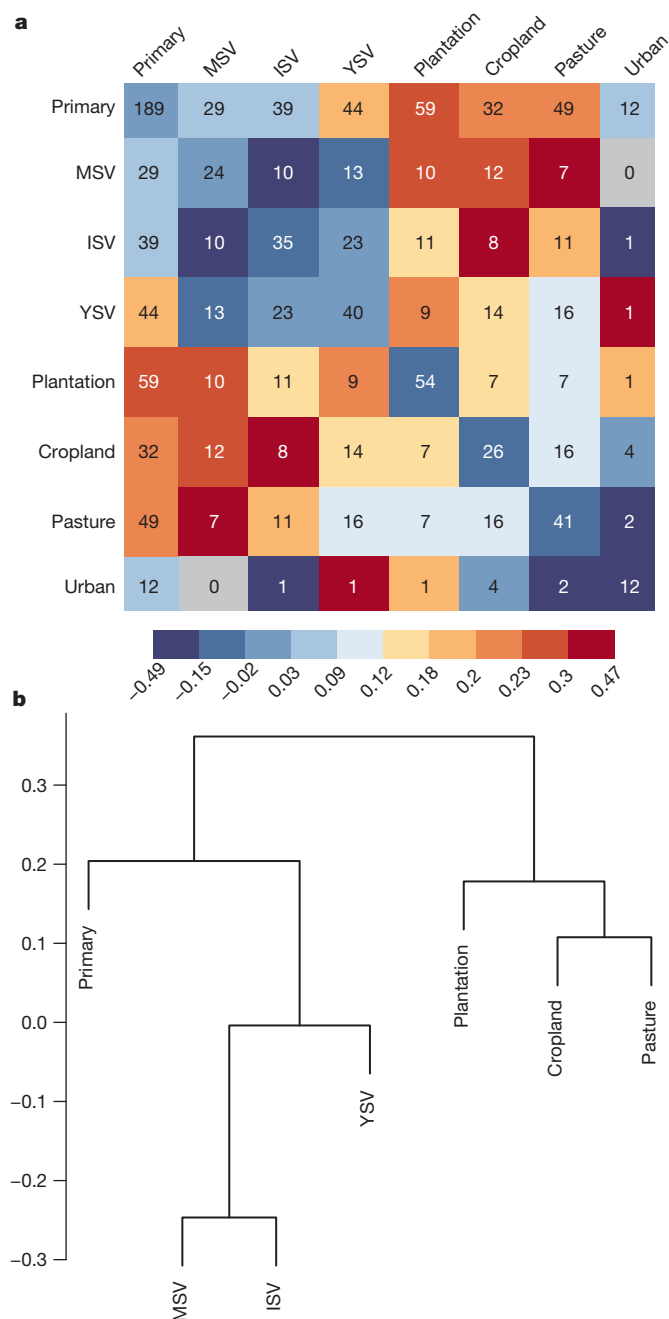
Local richness, rarefied richness and total abundance were most strongly influenced by land use and land-use intensity: they were substantially lower in most other land-use types than in primary vegetation, especially in intensively used areas (Fig. 1; see Supplementary Information for statistics and coefficient estimates). These results extend those of previous, geographically or taxonomically restricted, meta-analyses (for example, refs 11, 22). Other variables were weaker as main effects, but showed stronger effects in interaction (Extended Data Fig. 2) and were often significant overall (see Supplementary Information). Richness and total abundance tended to be slightly lower at the highest human population densities, and richness was lower nearer to roads and in more accessible sites (Fig. 1). Differences in richness were not driven solely by differences in abundance. Rarefied richness²³ (see Methods for details) showed weaker but mostly similar patterns, although the effects of variables other than land use and land-use intensity were not significant (Extended Data Fig. 3a, b). Under the worst combinations of pressures, our models estimated richness, rarefied richness and total abundance to be 76.5%, 40.3% and 39.5% lower, respectively, than in minimally affected sites. Effects of pressures on vertebrate, invertebrate and plant richness were statistically indistinguishable ($P > 0.05$; results not shown). The modelled coefficients were robust to efforts to correct for any publication bias (Extended Data Fig. 4). As with all studies based on data from the literature, unpublished data are almost unrepresented. Coefficients were also robust under cross-validation (Extended Data Fig. 3c, d), and the model residuals showed little spatial autocorrelation (Extended Data Fig. 5).

The importance of secondary vegetation for conservation is a hotly debated topic^{11,24,25}, and an important one, given that this land use will soon become the most widespread type²⁶. We find that the answer depends strongly on the secondary vegetation's maturity: early-stage communities tend to be less diverse than those in primary vegetation and are compositionally distinct, but these differences are much reduced in mature secondary vegetation (Figs 1 and 2; we caution though that not all data sources clearly distinguished mature secondary from primary vegetation). This successional rise in diversity accords with a recent meta-analysis of plant communities over time⁷.

Net changes in diversity provide an incomplete view of the effects of human activities on biodiversity because they ignore the replacement of original species by newcomers⁸. We therefore analysed how land use affects similarity in species composition between sites. Communities under the same land use were, as expected, the most similar (Fig. 2a). Across land uses, communities in primary vegetation were most like those in secondary vegetation, while plantation forest, pasture and cropland communities formed a different, human-dominated cluster (Fig. 2b).

Anthropogenic pressures can affect ecosystem functions and services more strongly than changes in species diversity would imply, if species' responses depend on their traits²⁷. Large size is often linked to species' declines^{28,29} and is important for some ecosystem processes³⁰. We combined abundance data with species' average sizes to calculate site-level community-weighted mean plant height and animal mass. As in local studies²⁹, mean plant height was lower in human-dominated land uses than in primary and secondary vegetation, and tended to decline with increasing human population density (Fig. 1d). Most field studies focused on particular plant taxa, so this difference does not simply reflect tree removal. Average animal mass did not change consistently with land use or human population density, but increased with proximity to roads (Fig. 1d).

Models like ours that substitute space for time ignore time lags in biotic changes, which can be important³¹. We also assume that land uses



are situated randomly within studies relative to sites' intrinsic suitability for biodiversity. Adding global data on other important pressures as they become available, and also incorporating climate change, will give a more complete picture of human effects on local biodiversity.

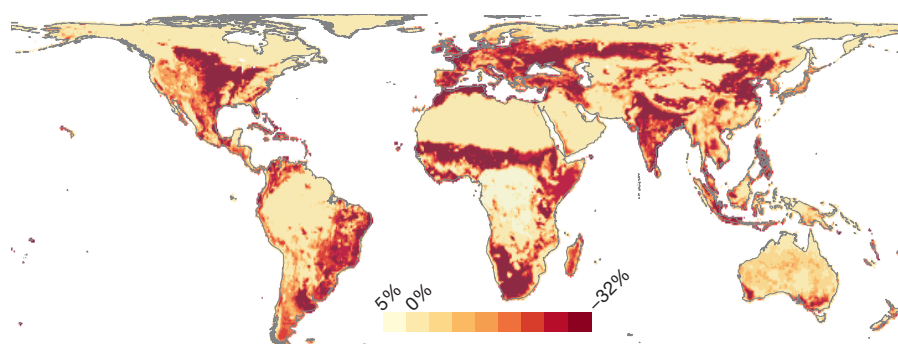


Figure 2 | Similarity in assemblage composition as a function of land use. **a**, Average dissimilarity of species composition ($1 - \text{Sørensen Index}$) between pairs of sites within and among land uses (shown relative to the similarity between pairs of primary-vegetation sites); blue and red colours indicate, respectively, more or less similar composition; numbers indicate numbers of studies within which comparisons could be made. **b**, Clustering of land-use types based on average compositional dissimilarity; urban sites were excluded owing to the small sample size.

Global effects on local diversity to date

By applying our model for within-sample species richness—the most widely used and understood biodiversity measure—to maps of current pressure variables¹⁰, we estimated the global pattern of net local changes to date in plot-level richness (Fig. 3; we did not estimate total richness within the $0.5^\circ \times 0.5^\circ$ grid cells). Human-dominated areas are inferred to have lost much more local diversity than have regions where more natural vegetation remains. The worst-affected cells showed a 31% reduction in average local richness—probably enough to alter ecosystem functioning substantially⁴. Local richness increased in 1.7% of cells (by $\leq 4.8\%$). Total abundance and, less strongly, rarefied richness showed broadly similar patterns (Extended Data Fig. 6).

We applied our models to global spatial estimates of how land use and human population changed from 1500–2005 (ref. 26) (see Methods) to infer the global history of local biodiversity change. Here we focus on within-sample species richness because of its wide use and easy interpretation. Our inferences incorporate uncertainty in model parameter estimates, but not in the trajectories of the pressures themselves (which have not been assessed³²) nor effects of changes in roads and accessibility, for which temporal estimates could not be obtained.

Richness is estimated to have declined most rapidly in the 19th and 20th centuries (Fig. 4), with other metrics showing similar responses (Extended Data Fig. 6). By 2005, we estimate that land use and related pressures had reduced local richness by an average of 13.6% (95% confidence interval (CI): 9.1–17.8%) and total abundance by 10.7% (95% CI: 3.8% gain to 23.7% reduction) compared with what they would have been in the absence of human effects. Approximately 60% of the decline in richness was independent of effects on abundance; average rarefied richness has fallen by 8.1% (95% CI: 3.5–12.9%). Although these confidence limits omit uncertainty in the projections of land use and other pressures, there is less uncertainty in estimates of current pressure levels than in changes over time³³.

Our inferences contrast with two recent analyses of community time series^{7,8}, which suggested no overall trend in local diversity, and with the Living Planet Index³, which, based on vertebrate population time series, reports a much more rapid decline in abundance than we infer. Although time series potentially provide a more direct view of temporal trends than our space-for-time approach, the available data might under-represent transitions between land-use types⁹. However, our approach may underestimate additions of species through climate change and species invasion (although accessibility and proximity to roads may partly capture the latter^{14,15}).

Figure 3 | Net change in local richness caused by land use and related pressures by 2000. Projections used an IMAGE reference scenario¹⁰. The baseline landscape was assumed to be entirely uninhabited, unused primary vegetation. Shown using a Lambert Cylindrical Equal-Area projection at $0.5^\circ \times 0.5^\circ$ resolution.

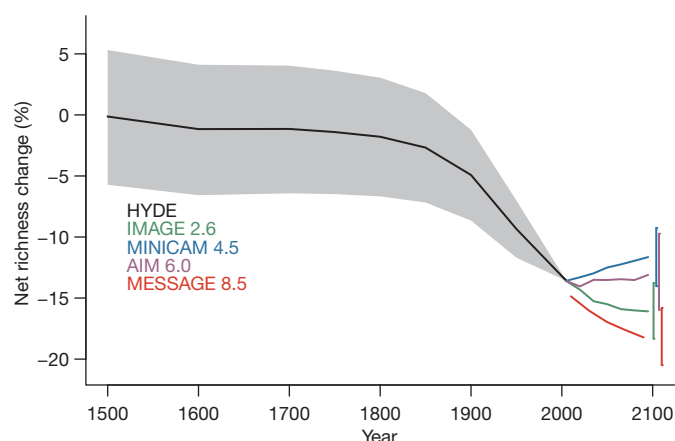


Figure 4 | Projected net change in local richness from 1500 to 2095. Future projections were based on the four RCP scenarios (Table 1). Historical (shading) and future (error bars) uncertainty is shown as 95% confidence intervals, rescaled to zero in 2005. The baseline for projections is a world entirely composed of uninhabited, unused primary vegetation; thus, the value at 1500 is not constrained to be zero because by then non-primary land uses were present (and in some regions widespread). The global average projection for MESSAGE 8.5 does not join the historical reconstruction because that scenario's human population projections start in 2010 and because human population and plantation forest extent have not been harmonized among scenarios.

Global and national projections to 2095

Global changes in local diversity from 2005 to 2095 were projected using estimated land use and human population from the four Intergovernmental Panel on Climate Change Representative Concentration Pathway (RCP) scenarios²⁶, which correspond to different intensities of global climate change (Table 1). Although these estimates have limitations³², they are the most consistent available, are widely used³⁴, and are consistent with the historical estimates²⁶. However, they—like all other global land-use projections—include no estimate of uncertainty; therefore, each of our projections must be viewed as the predicted biodiversity outcome under one particular set of land-use assumptions.

Projected net changes in average local diversity to 2095 vary widely among scenarios (Fig. 4 and Extended Data Fig. 6). The scenario with the least climate change (IMAGE 2.6) yields the second-worst outcome for biodiversity, because it assumes rapid conversion of primary vegetation, especially in the tropics, to crops and biofuels²⁶ (Table 1 and Extended Data Fig. 7). These projections do not imply that low-emission

scenarios must entail large losses of biodiversity, but instead reflect that scenario's mitigation strategy. Indeed, in MiniCAM 4.5 (where mitigation is through carbon markets, crop improvements and diet shifts, Table 1) average richness is projected to increase (though other diversity metrics respond more weakly, Extended Data Fig. 6). The worst biodiversity outcomes arise from the scenario with most climate change (MESSAGE 8.5) in which rapid human population growth drives widespread agricultural expansion (Table 1 and Extended Data Fig. 7). This scenario, which has been characterized as 'business-as-usual'³⁵, most closely matches recent trends in emissions³⁶ and gives the worst outcomes even though our projections omit direct climate effects on local assemblages.

The global projections hide wide regional and national variation (Fig. 5 and Extended Data Fig. 8). Projections for 2095 under business-as-usual (MESSAGE 8.5) are strongly inequitable, presenting serious challenges for both sustainable development and global conservation of biodiversity (Fig. 5a). Under this scenario, European and North American countries, typically with a high Human Development Index, low native biodiversity and widespread historical land conversion, are mostly projected to gain in local richness by 2095. More naturally biodiverse but less economically developed Southeast Asian and especially sub-Saharan African countries, with more natural and semi-natural habitat, will suffer the greatest losses (Fig. 5a and Extended Data Fig. 8f).

Such globally inequitable outcomes might be avoidable. The best scenario for biodiversity (MiniCAM 4.5; Fig. 4) yielded country-level outcomes that are relatively independent of Human Development Index, native species richness (Fig. 5b) and past changes (Extended Data Fig. 8e). For local richness, outcomes under MiniCAM4.5 were better than MESSAGE 8.5 for 93% of countries worldwide (Fig. 5c).

Under AIM 6.0, most Afrotropical countries are projected to gain in local richness but heavy losses are inferred for the Indo-Malay region (Extended Data Fig. 8). Projections under IMAGE 2.6 are spatially similar to those under MESSAGE 8.5. The land-use change caused by the biofuels-based strategy in IMAGE 2.6 is projected to have a major negative effect overall on terrestrial biodiversity (Extended Data Fig. 8).

Conclusions

Many assessments of the state of biodiversity have focused on global metrics such as rates of species extinction³⁷, but resilient delivery of ecosystem functions and services is more likely to depend on local diversity^{4–6}. Our models suggest land-use changes and associated pressures strongly reduce local terrestrial biodiversity, and we estimate global average reductions to date of 13.6% in within-sample species richness, 10.7% in total abundance and 8.1% in rarefaction-based species richness (Figs 3 and 4). Climate change, which we could not include in our

Table 1 | Key features of the four RCP scenarios

Scenario	Land use (see also Extended Data Fig. 7)	Climate and energy	Human population
IMAGE 2.6	Agriculture moves from developed to developing countries. Large increase in area of biofuel plantations. Urban extent assumed constant.	Increased energy efficiency. Increased use of carbon capture and storage, nuclear, renewable energy and biofuels. Approximately 1 °C temperature increase by 2100 compared to pre-industrial.	10.1 billion by 2100 (UN Medium variant, 2010)
MiniCAM 4.5	Carbon pricing leads to preservation of primary forest and expansion of secondary forest. Crop yield increases, improved agricultural efficiency and dietary shifts lead to decreases in cropland and pasture areas. Small increase in area of biofuel plantations. Urban extent assumed constant.	Decline in overall energy use. Decreased use of fossil fuels and increase in nuclear and renewable energy, and in carbon capture and storage. Moderate increase in use of biofuels, but limited by availability of biomass. Approximately 1.75 °C temperature increase by 2100.	Peaks above 9 billion around 2065, then declines to 8.7 billion by 2095.
AIM 6.0	Urban area increases owing to human population growth. Cropland area increases to meet food demand. Pasture area declines strongly.	Approximately 2.5 °C temperature increase by 2100.	9.1 billion by 2100 (UN Medium variant, 2004)
MESSAGE 8.5	Increasing crop yields and intensification account for much of the increased production required, but area of cropland and, to a lesser extent, pasture increases rapidly. Small increase in area of biofuel plantations. Urban area increases owing to increased population.	Small improvements in efficiency leading to high demand for energy. Conventional oil and gas become scarce, leading to shift in favour of unconventional and carbon-intensive fossil fuels. Moderate increase in use of biofuels. Approximately 4 °C increase in temperature by 2100.	12 billion by 2100.

Land-use and human population assumptions are detailed in ref. 26, energy assumptions in refs 40–42, and climate implications in ref. 43.

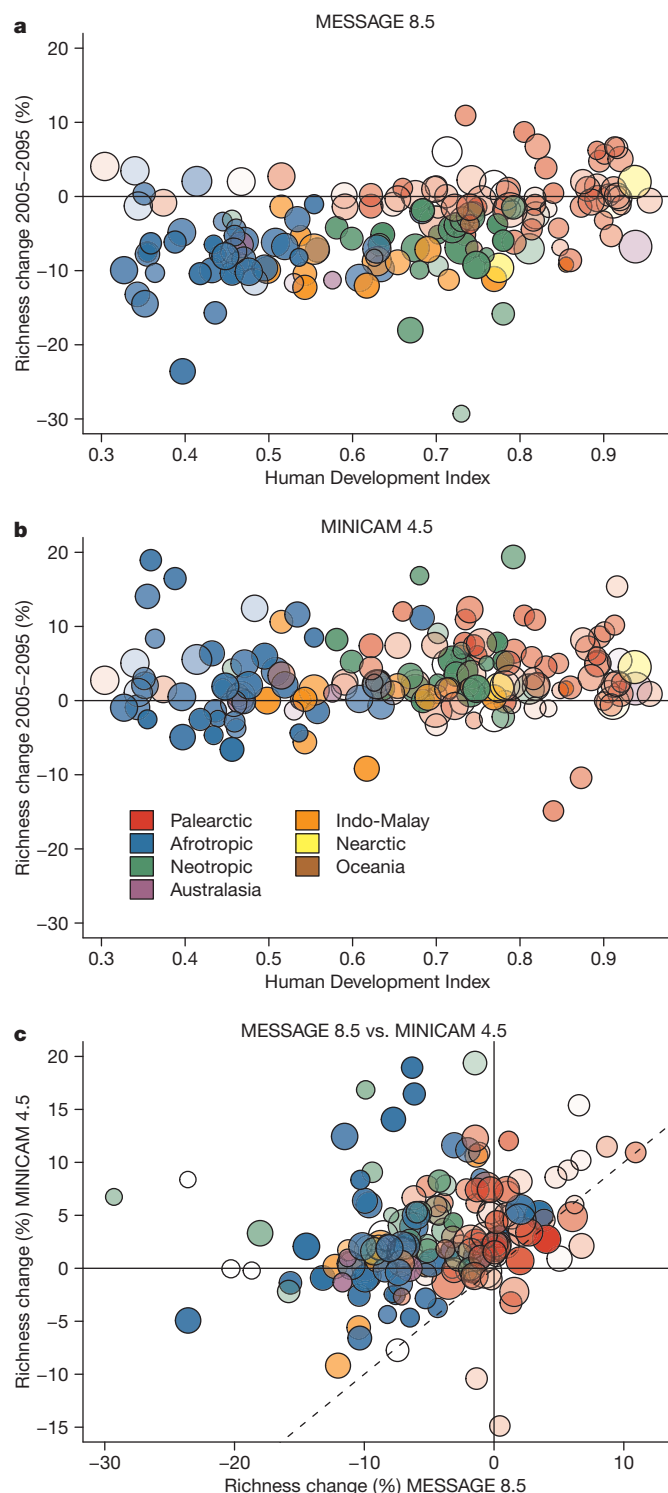


Figure 5 | Biodiversity projections at the country level. **a**, **b**, Country-level projections of average net local richness change between 2005 and 2095 under the worst (**a**, MESSAGE 8.5) and best (**b**, MiniCAM 4.5) RCP scenarios for biodiversity, shown in relation to countries' Human Development Index. Colours indicate biogeographic realms; colour intensity reflects natural vertebrate species richness (more intense colour represents higher richness); point diameter is proportional to (log) country area. **c**, Correlation between projected richness changes under the MiniCAM 4.5 and MESSAGE 8.5 scenarios, with dashed line showing equality; colours as in **a** and **b**; colour intensity is proportional to the Human Development Index (more intense colour represents higher index).

framework, is likely to exacerbate losses, especially under business-as-usual³⁸, although direct effects of climate change will increase local diversity in some regions⁸.

It is important to remember that the habitat conversion and associated changes that reduced local biodiversity had largely positive consequences for people; agricultural intensification underpinned many countries' development. However, benefits have not been shared equally among or within countries³⁹. Losses of local species richness exceeding 20% are likely to substantially impair the contribution of biodiversity to ecosystem function and services, and thus to human well-being⁴. We estimate that reductions in average plot-level species richness currently exceed this level for 28.4% of grid cells, increasing to 41.5% of cells by 2095 under business-as-usual (note that we do not estimate or project total richness across the cell). Importantly, our projections suggest that such widespread large losses are not inevitable. With concerted action and the right societal choices, global sustainability of local biodiversity may be an achievable goal.

Online Content Methods, along with any additional Extended Data display items and Source Data, are available in the online version of the paper; references unique to these sections appear only in the online paper.

Received 9 July 2014; accepted 12 February 2015.

- Tittensor, D. P. *et al.* A mid-term analysis of progress toward international biodiversity targets. *Science* **346**, 241–244 (2014).
- Pimm, S. L. *et al.* The biodiversity of species and their rates of extinction, distribution, and protection. *Science* **344**, 1246–1252 (2014).
- Collen, B. *et al.* Monitoring change in vertebrate abundance: the Living Planet Index. *Conserv. Biol.* **23**, 317–327 (2009).
- Hooper, D. U. *et al.* A global synthesis reveals biodiversity loss as a major driver of ecosystem change. *Nature* **486**, 105–108 (2012).
- Isbell, F. *et al.* High plant diversity is needed to maintain ecosystem services. *Nature* **477**, 199–202 (2011).
- Cardinale, B. J. *et al.* Biodiversity loss and its impact on humanity. *Nature* **486**, 59–67 (2012).
- Vellend, M. *et al.* Global meta-analysis reveals no net change in local-scale plant biodiversity over time. *Proc. Natl Acad. Sci. USA* **110**, 19456–19459 (2013).
- Dornelas, M. *et al.* Assemblage time series reveal biodiversity change but not systematic loss. *Science* **344**, 296–299 (2014).
- Cardinale, B. Overlooked local biodiversity loss. *Science* **344**, 1098 (2014).
- Alkemade, R. *et al.* GLOBIO3: a framework to investigate options for reducing global terrestrial biodiversity loss. *Ecosystems* **12**, 374–390 (2009).
- Gibson, L. *et al.* Primary forests are irreplaceable for sustaining tropical biodiversity. *Nature* **478**, 378–381 (2011).
- Mendenhall, C. D., Karp, D. S., Meyer, C. F. J., Hadly, E. A. & Daily, G. C. Predicting biodiversity change and averting collapse in agricultural landscapes. *Nature* **509**, 213–217 (2014).
- Pereira, H. M. *et al.* Essential biodiversity variables. *Science* **339**, 277–278 (2013).
- Weber, E. & Li, B. Plant invasions in China: what is to be expected in the wake of economic development? *Bioscience* **58**, 437–444 (2008).
- Clements, G. R. *et al.* Where and how are roads endangering mammals in Southeast Asia's forests? *PLoS ONE* **9**, e115376 (2014).
- Hudson, L. N. *et al.* The PREDICTS database: a global database of how local terrestrial biodiversity responds to human impacts. *Ecol. Evol.* **4**, 4701–4735 (2014).
- Chapman, A. D. *Numbers of Living Species in Australia and the World*. (Australian Biological Resources Study, 2009).
- Phalan, B., Onial, M., Balmford, A. & Green, R. E. Reconciling food production and biodiversity conservation: land sharing and land sparing compared. *Science* **333**, 1289–1291 (2011).
- Balmford, A. Extinction filters and current resilience: the significance of past selection pressures for conservation biology. *Trends Ecol. Evol.* **11**, 193–196 (1996).
- Newbold, T. *et al.* A global model of the response of tropical and sub-tropical forest biodiversity to anthropogenic pressures. *Proc. R. Soc. B* **281**, 20141371 (2014).
- Benítez-López, A., Alkemade, R. & Verweij, P. A. The impacts of roads and other infrastructure on mammal and bird populations: a meta-analysis. *Biol. Conserv.* **143**, 1307–1316 (2010).
- Murphy, G. E. P. & Romanuk, T. N. A meta-analysis of declines in local species richness from human disturbances. *Ecol. Evol.* **4**, 91–103 (2014).
- Magurran, A. E. *Measuring Biological Diversity*. (Wiley-Blackwell, 2004).
- Barlow, J. *et al.* Quantifying the biodiversity value of tropical primary, secondary, and plantation forests. *Proc. Natl Acad. Sci. USA* **104**, 18555–18560 (2007).
- Dent, D. H. & Wright, S. J. The future of tropical species in secondary forests: A quantitative review. *Biol. Conserv.* **142**, 2833–2843 (2009).
- Hurt, G. C. *et al.* Harmonization of land-use scenarios for the period 1500–2100: 600 years of global gridded annual land-use transitions, wood harvest, and resulting secondary lands. *Clim. Change* **109**, 117–161 (2011).
- Díaz, S. *et al.* Functional traits, the phylogeny of function, and ecosystem service vulnerability. *Ecol. Evol.* **3**, 2958–2975 (2013).

28. Cardillo, M. *et al.* Multiple causes of high extinction risk in large mammal species. *Science* **309**, 1239–1241 (2005).
29. Mayfield, M. M. *et al.* Differences in forest plant functional trait distributions across land-use and productivity gradients. *Am. J. Bot.* **100**, 1356–1368 (2013).
30. Séguin, A., Harvey, E., Archambault, P., Nozais, C. & Gravel, D. Body size as a predictor of species loss effect on ecosystem functioning. *Sci. Rep.* **4**, 4616 (2014).
31. Wearn, O. R., Reuman, D. C. & Ewers, R. M. Extinction debt and windows of conservation opportunity in the Brazilian Amazon. *Science* **337**, 228–232 (2012).
32. Harfoot, M. *et al.* Integrated assessment models for ecologists: the present and the future. *Glob. Ecol. Biogeogr.* **23**, 124–143 (2014).
33. Ellis, E. C. Anthropogenic transformation of the terrestrial biosphere. *Phil. Trans. R. Soc. A* **369**, 1010–1035 (2011).
34. Mora, C. *et al.* The projected timing of climate departure from recent variability. *Nature* **502**, 183–187 (2013).
35. Burrows, M. T. *et al.* Geographical limits to species-range shifts are suggested by climate velocity. *Nature* **507**, 492–495 (2014).
36. Oldfield, F. & Steffen, W. Anthropogenic climate change and the nature of Earth System science. *Anthr. Rev.* **1**, 70–75 (2014).
37. Pereira, H. M. *et al.* Scenarios for global biodiversity in the 21st century. *Science* **330**, 1496–1501 (2010).
38. Warren, R. *et al.* Quantifying the benefit of early climate change mitigation in avoiding biodiversity loss. *Nature Clim. Chang.* **3**, 678–682 (2013).
39. Millennium Ecosystem Assessment. *Ecosystems and Human Well-being: Biodiversity Synthesis*. (World Resources Institute, 2005).
40. van Vuuren, D. P. *et al.* RCP2.6: exploring the possibility to keep global mean temperature increase below 2°C. *Clim. Change* **109**, 95–116 (2011).
41. Thomson, A. M. *et al.* RCP4.5: a pathway for stabilization of radiative forcing by 2100. *Clim. Change* **109**, 77–94 (2011).
42. Riahi, K. *et al.* RCP 8.5—A scenario of comparatively high greenhouse gas emissions. *Clim. Change* **109**, 33–57 (2011).
43. Rogelj, J., Meinshausen, M. & Knutti, R. Global warming under old and new scenarios using IPCC climate sensitivity range estimates. *Nature Clim. Chang.* **2**, 248–253 (2012).
44. Bates, D., Maechler, M., Bolker, B. & Walker, S. lme4: Linear mixed-effects models using Eigen and S4. <http://cran.r-project.org/web/packages/lme4/> (2013).
45. Center for International Earth Science Information Network (CIESIN) Columbia University, International Food Policy Research Institute (IFPRI), The World Bank & Centro Internacional de Agricultura Tropical (CIAT). Global rural-urban mapping project, version 1 (GRUMPv1): population density grid. (NASA Socioeconomic Data and Applications Center (SEDAC), 2011). <http://dx.doi.org/10.7927/H4R20Z93> (Accessed 11 July 2012).
46. Center for International Earth Science Information Network (CIESIN) Columbia University & Information Technology Outreach Services (ITOS) University of Georgia. Global roads open access data set, version 1 (gROADSv1). (NASA Socioeconomic Data and Applications Center (SEDAC), 2013). <http://dx.doi.org/10.7927/H4VD6WCT> (Accessed 18 December 2013).
47. Nelson, A. *Estimated travel time to the nearest city of 50,000 or more people in year 2000*. <http://bioval.jrc.ec.europa.eu/products/gam/index.htm> (2008). (Accessed 14 July 2014).

Supplementary Information is available in the online version of the paper.

Acknowledgements We thank all the many researchers who have made their data available to us; S. Butchart and Birdlife International for sharing bird body-size data; F. Gilbert for hoverfly body-size data; the IMAGE, HYDE, MESSAGE and MiniCAM teams, especially R. Alkemade, M. Bakkenes and A. Thomson for sharing additional data from their integrated assessment models; D. Tittensor for statistical advice; C. Sleep and S. Patlola at the Natural History Museum in London for IT support with the database; members of the GARD initiative (<http://www.gardinitiative.org/index.html>) for help with estimating the reptile species richness map; K. Jones, J. Tylianakis, M. Crawley and E. J. Milner-Gulland for discussion, N. Burgess for comments on a draft of the paper. We also thank C. D. Thomas and two anonymous reviewers for very helpful comments on the manuscript. This study is part of the PREDICTS (Projecting Responses of Ecological Diversity in Changing Terrestrial Systems) project, which is supported by the UK Natural Environment Research Council (NERC, grant number: NE/J011193/1), the Biotechnology and Biological Sciences Research Council (grant number: BB/F017324/1) a Hans Rausing PhD scholarship. The study was also supported by the TRY initiative on plant traits, whose database is maintained at Max-Planck-Institute for Biogeochemistry, Jena, Germany, and which is supported by DIVERSITAS, IGBP, the Global Land Project, NERC, the French Foundation for Biodiversity Research, and GIS 'Climat, Environnement et Société' France. This is a contribution from the Imperial College Grand Challenges in Ecosystem and the Environment Initiative.

Author Contributions T.N., L.N.H., S.L.L.H., S.C., I.L., B.C., D.W.P., R.M.E., G.M.M., J.P.W.S. and A.P. designed the project and this study; T.N., L.N.H., I.L., R.A.S., L.B., J.P.W.S. and A.P. performed the analyses; T.N., L.N.H., S.L.L.H., S.C., D.J.B., A.C., B.C., J.D., A.D.P., S.E.-L., M.G., M.L.K.H., T.A., D.J.I., V.K., L.K., D.L.P.C., C.D.M., Y.P., H.R.P.P., A.R., J.S., H.J.W. and A.P. collated the assemblage composition data; T.N., L.N.H., S.L.L.H., S.C., A.D.P., I.L., H.R.P.P., J.P.W.S. and A.P. designed the data-collection protocols and database; R.A.S., S.D., M.J.E., A.F., Y.I., J.K., M.K., S.M. and E.W. made substantial contributions to the trait data used in the analyses and S.L.T. to the site-level environmental data; R.A.S., A.F., Y.I., S.M., and M.N. generated the maps of species richness used in the model projections; T.N., L.N.H. and A.P. wrote the manuscript with contributions from G.M.M., L.B., D.W.P., R.M.E., A.D.P., H.R.P.P., S.L.L.H., R.A.S., B.C., S.D., A.F., Y.I., J.K., M.K., S.M., J.P.W.S. and S.L.T.; T.N. and L.N.H. contributed equally to the study.

Author Information Reprints and permissions information is available at www.nature.com/reprints. The authors declare no competing financial interests. Readers are welcome to comment on the online version of the paper. Correspondence and requests for materials should be addressed to T.N. (Tim.Newbold@unep-wcmc.org).

METHODS

Data collation. Between March 2012 and April 2014 we collated among-site comparisons of ecological assemblage composition from published studies (or from unpublished datasets where the methods have been published) examining the effect of human activities on more than one named taxon. A full description of how the data set was assembled and curated is presented elsewhere¹⁶. We define sites to be in the same study if they were sampled using the same methodology and the data were reported in the same paper; therefore, some publications contain multiple studies. After six months of broad searching, we targeted efforts towards under-represented taxa, habitat types, biomes and regions. We accepted data only from published or in-press papers, or data collected using a published methodology, and we required that the data providers agreed to our making their data publicly available at the end of the PREDICTS (Projecting Responses of Ecological Diversity In Changing Terrestrial Systems) project in 2015. We accepted data only where abundance, occurrence or richness had been measured at two or more sampling locations and/or times, and where all sites were sampled using the same sampling procedure and with either the same effort or site-specific data on effort. We used geographical coordinates preferentially from the paper or supplied by data providers; but where coordinates were not thus available, we geo-referenced them from maps in the papers. The final data set came from 378 studies^{48–329} and two unpublished datasets (M. E. Hanley, 2005 and 2011) that were collected with published methods¹⁴⁶.

Studies compared from 2 to 360 sites (median = 15; 82% had ≥ 5 sites); most sampled species from multiple families but fewer than half sampled multiple orders. Over 70% of sites were from studies that sampled entire communities within a taxonomic group rather than a target list of species. Removing studies having a target list did not substantially alter model coefficients (results not shown) and increased the projected global net average loss of local species richness until 2005 by 0.6%. Sites varied in the maximum linear extent sampled (median 106 m; inter-quartile range 50 m to 354 m). Model coefficients for the approximately 50% of studies that reported maximum linear extent were robust to its inclusion in the models (results not shown).

The great majority of listed taxa were species level, although many could not be given explicit species identifications (for example, morpho-species)¹⁶; henceforth we refer to distinct taxa in our data set as species. We matched taxonomic names given in the source paper to the Catalogue of Life 2013 Annual Checklist (COL)³³⁰, obtaining the full taxonomic classification. In order to relate the taxonomic names to species-level trait databases, we generated, for each taxon, a 'best-guess' Latin binomial as: (a) the taxon name from COL if the COL query returned a species-level identification; (b) the first two words of the text returned by the COL query if this was a sub-species designation; (c) the first two words of the taxon name in the source publication if the COL query returned neither a species or sub-species name, and the taxon name in the source publication contained two or more words. Taxa that met none of these criteria were not matched to trait data, but were included in the calculation of richness and total abundance, and for estimating turnover in community composition among sites.

The resulting data set contained data for 26,953 species at 11,525 sites. For many high-diversity taxa, the database contains data for more than 1% of the number of species thought to have been formally described (Extended Data Fig. 1a). The distribution of sites among major biomes is roughly proportional to the amount of terrestrial net primary productivity (NPP) fixed within each biome (Extended Data Fig. 1b).

Site-level composition and diversity. We computed four site-level biodiversity metrics: within-sample species richness, total abundance, rarefaction-based richness and community-weighted mean organism size. These were calculated as follows.

Within-sample species richness was calculated as the number of differently-named taxa recorded at a given site in a standardised sampling unit (a measure also known as species density³³¹). We gave precedence to the author's classification of species, even where a search of global databases revealed potential synonymies, because only certain taxonomic groups could be reliably matched to accepted taxonomies.

This measure of richness is appropriate for conservation questions but among-site differences could be due to effects on numbers of individuals as well as to changes in the shape of the species accumulation curve³³¹. We therefore also calculated rarefaction-based species richness by taking 1,000 random samples of n individuals from each site, where n is the smallest total number of individuals recorded at any site within its study, and calculating the mean species richness across samples. This index could only be calculated for sites where, in addition to the criteria above being met, abundance was recorded as number of individuals. Rarefied species richness was rounded to the nearest integer for analysis with Poisson errors.

Total abundance was calculated as the sum of the measures of abundance of all taxa at a site; we were thus unable to estimate abundance for sites where only species occurrence or overall richness or diversity had been recorded (17% of sites). Some abundance metrics—those not reported as densities per unit time, distance, area or volume sampled—were sensitive to sampling effort. When a study reported any

of these metrics and sampling effort varied among sites within a study, we corrected the raw abundance measurements for the sampling effort expended at each sampling location and time. This was done by rescaling the sampling efforts within each study so that the most heavily sampled site had a value of one (to prevent introducing additional heterogeneity into the modelled values), and then dividing the raw abundance measurements by this relative sampling effort.

Community-weighted mean organism size was calculated as the arithmetic mean of log-transformed height of plants (available for 4,235 species in our data set) or the log-transformed body mass or volume of vertebrates, beetles and hoverflies (5,236 species) present at a site, weighted by abundance³³². Plant height data were taken from the TRY database³³³; for 61 species where plant vegetative height data were unavailable, we estimated it from generative height from a regression across the 2,554 species with estimates of both traits ($R^2 = 0.91$). Data on vertebrate body mass were taken from the PanTHERIA database for mammals³³⁴, from BirdLife International's World Bird Database for birds, and from a wide range of published and grey-literature sources for amphibians^{335–381}. Length data for reptiles were taken from published^{382,383} and unpublished (S. Meiri and A. Feldman, unpublished data) sources, and converted to estimates of body mass using published length-mass allometries^{384,385}. Arthropod size data (beetles and hoverflies) were collated from published sources^{386,387}. Beetle length and amphibian snout-vent length values were raised to the power three so that they had the same dimensionality as the other animal size measures. For both plant height and vertebrate body mass, missing values were interpolated as the average values for congeners, since both of these traits are strongly conserved phylogenetically (Pagel's $\lambda = 0.98, 0.997, 0.93, 0.89$ for plant height, vertebrate body mass, beetle body length and hoverfly thorax volume, respectively).

Human pressure data. While many human pressures can affect local biodiversity, we focus on those that can be obtained for sites around the world and for which, as far as possible, spatiotemporal data are available for 1500–2095; this focus enables us to use our statistical models as a basis for projecting responses through time. Each site was assigned to one of eight land-use classes based on the description of the habitat given in the source paper (see Extended Data Table 1 for definitions): primary vegetation, secondary vegetation (subdivided into mature, intermediate or young secondary vegetation), plantation forest, cropland, pasture and urban¹⁶. These classes were selected to match the land-use classification adopted in the Intergovernmental Panel on Climate Change Representative Concentration Pathways scenarios²⁶ to facilitate the projection of our models onto these scenarios. Sites were also assigned to a level of human intensity of use (minimal, light or intense) within each major land-use class, also based on the description of the habitat in the source paper (see Extended Data Table 1 for definitions). The factors that determined this level depended on the land-use class (for example, bushmeat extraction and limited logging in primary and secondary vegetation, or stocking density and chemical inputs in pasture; Extended Data Table 1). Sites that could not be classified for land-use and use intensity were excluded from the analyses. The final dataset contained the following numbers of sites in each land use and land-use intensity level: primary vegetation, minimal use, 1,546 (from 183 studies); light use, 860 (76 studies); intense use, 449 (33 studies); mature secondary vegetation, minimal use, 198 (52 studies); light/intense use, 213 (23 studies); intermediate secondary vegetation, minimal use, 404 (55 studies); light/intense use, 269 (30 studies); young secondary vegetation, minimal use, 431 (50 studies); light/intense use, 331 (34 studies); plantation forest, minimal use, 356 (47 studies); light use, 402 (42 studies); intense use, 238 (29 studies); cropland, minimal use, 427 (45 studies); light use, 632 (43 studies); intense use, 703 (36 studies); pasture, minimal use, 525 (43 studies); light use, 434 (52 studies); intense use, 174 (23 studies); and urban, minimal use, 174 (23 studies); light use, 244 (26 studies); intense use, 195 (18 studies).

We overlaid our sites with available global data sets to obtain site-level estimates of human population density⁴⁵, distance to the nearest road⁴⁶ and estimated travel time to nearest population centre with greater than 50,000 inhabitants⁴⁷. For distance to nearest road, the map of roads was first projected onto a Berhmann equal-area projection. These operations were carried out using Python code implemented using the *arcpy* Python module in ArcMap version 10.0 (ref. 388). In the main figures, the inverses of distance to roads and travel time to major population centre (proximity to roads and accessibility) were presented so that high values corresponded to higher hypothesized human effect. To estimate the history of human use of the landscapes within which sites were located, we calculated the number of years since the 30-arc-second grid cell containing each site became 30% covered by human land uses (cropland, pasture and urban), according to the HYDE model³⁸⁹. Co-linearity among variables describing anthropogenic change was low; the highest correlation was between land use and human population density (Pearson $R^2 = 0.31$).

Modelling site-level diversity, composition and turnover. The response of site-level diversity to the measures of anthropogenic change was modelled using generalized linear mixed effects models, implemented in the *lme4* package version

1.0–5 (ref. 44) in R version 3.0.2 (ref. 390). We first compared candidate random-effects structures using the full candidate fixed-effects structure³⁹¹. Random-intercept terms considered in all models were the identity of the study from which data were taken, to account for study-level differences in the response variables and sampling methods used, and—within study—the spatial block in which the site was located, to account for the spatial arrangement of sites. For models of species richness (within-sample and rarefied), we also fitted an observation-level random effect (that is, site identity) to account for the overdispersion present³⁹². We also considered random slopes, with respect to study, of each of the main fixed effects (land use, land-use intensity, human population density, distance to nearest road, travel time to nearest major city and time since the landscape was majority converted to human uses). Random effects were retained or discarded based on the models' Akaike Information Criterion values.

Once the best random-effects structure had been selected, we performed backward stepwise model simplification to select the best fixed-effects structure (see Supplementary Information)³⁹¹. Human population density, distance to roads, travel time to nearest major city and time since major human use of the landscape were log transformed in the analyses, with a value of 1 added to human population density, travel time to nearest major city and time since major landscape conversion to deal with zero values. These four variables were fitted as continuous effects, with quadratic polynomials for human population, distance to roads and travel time to nearest major city, and as a linear effect for time since human landscape conversion. For variables fitted as quadratic polynomials, we also tested linear effects during the backward stepwise model selection. All continuous variables were rescaled before analysis so that values ranged between zero and one. Interaction terms were tested first, and then removed to test the main effects. All main effects that were part of significant interaction terms were retained in the final models regardless of their significance as main effects. For the model of community-weighted mean body mass and plant height, because the number of sites with data was smaller than for the other metrics, only land use (excluding urban sites, which were few), human population density and distance to roads, and no interactions, were fitted (for the model of plant height, sample sizes in each land use were: primary vegetation, 634 sites; secondary vegetation, 851 sites; plantation forest, 222 sites; cropland, 72 sites; pasture, 412 sites; and for the model of animal mass: primary vegetation, 1728 sites; secondary vegetation, 805 sites; plantation forest, 602 sites; cropland, 641 sites; pasture, 440 sites). The decision whether or not to retain terms was based on likelihood ratio tests. The coefficient estimates of the best models are shown in Fig. 1b–d and Extended Data Fig. 2, and the formulae and statistical results are shown in the Supplementary Information. To test for spatial autocorrelation in the residuals of the final best models, we calculated Moran's *I* values and associated *P* values, separately for each study considered in the models, using the *spdep* package version 0.5–68 (ref. 393) in R; the distribution of *P* values across studies was used as an indication of whether spatial autocorrelation was likely to cause a problem. This revealed that the residuals showed little spatial autocorrelation (Extended Data Fig. 5). We used cross validation to assess the robustness of model parameter estimates, first based on dividing the studies randomly into ten equal-sized sets and dropping each set in turn (Extended Data Fig. 3c), and second based on leaving out the studies from each biome in turn (Extended Data Fig. 3d).

Publication bias is a potential problem for any large-scale synthesis of data from many publications. In standard meta-analyses, funnel plots³⁹⁴ can be used to test for any relationship between standard error and effect size, as a bias in effect sizes at high standard error towards more positive or more negative effects indicates a likely effect of publication bias. Creating funnel plots for our data was more complicated because ours was a site-level analysis of raw diversity estimates rather than a traditional meta-analysis. Instead we generated individual models relating diversity to land use for each study that sampled at least two sites within each of at least two land-use types. We focused on land use because: (a) there were a small number of sites included in most within-study models; and (b) the original studies focused on effects of land use, not generally on land-use intensity, human population density or distance to roads, and thus any effect of publication bias would likely be seen in the land-use coefficients. Funnel plots were generated by plotting, for each land-use type, the estimated model coefficients against the associated standard errors (Extended Data Fig. 4). There were some indications of an effect of publication bias, with less certain coefficient estimates tending to have more negative estimates for some of the land uses (Extended Data Fig. 4). However, study-level random slopes of human-dominated land uses tended to be more negative for studies that sampled more sites (Extended Data Fig. 4). It is important to emphasize that in a site-level analysis like ours, studies with fewer sites have less weight in the models. Modelled coefficient estimates were generally robust to the removal of these studies (Extended Data Fig. 4). Basing projections on coefficient estimates from models where small studies were excluded led to a less than 1% change in the estimated global richness values (results not shown). As with all studies based on data from the literature, we underrepresent unpublished data.

To model turnover of species composition between pairs of sites, we calculated average dissimilarity²³ in the lists of present species ($1 - \text{Sørensen index}$) between all pairs of sites within each study. For this analysis, we were only able to consider studies with more than one site in at least one of the land-use types considered. Once compositional similarity had been calculated for every pair of sites within each study, the average compositional similarity was calculated for every pair of land-use types considered within each study (including comparisons between sites in the same land-use type). Finally, the average compositional similarity was calculated for each pair of land-use types across all studies. To visualize the clustering of different land-use types in terms of community composition, we performed a hierarchical complete-linkage cluster analysis on the compositional dissimilarity (that is, $1 - \text{similarity}$) matrix, using the *hclust* function in R version 3.0.2 (ref. 390). To test whether differences in the average geographic distance between pairs of sites in different land-use combinations affected these results, we correlated average compositional similarity with average distance between sites, for all pairwise combinations of land use (including comparisons of a land-use type with itself). Correlations between average distance and average community similarity were only very weakly negative ($R^2 = 0.001$), suggesting they do not strongly distort the comparisons of community composition. However, the fact that some land uses tend to occur more closely together than others could influence the diversity patterns seen in our models, if some land uses are typically close to high-diversity habitats and so are more likely to benefit from dispersal. For example, sites in secondary vegetation and plantation forest were closer, on average, to primary vegetation sites than were those in cropland, pasture and urban (average distances to sites in primary vegetation were: other primary vegetation sites = 7.38 km; mature secondary vegetation = 4.4 km; intermediate secondary vegetation = 3.9 km; young secondary vegetation = 6.9 km; plantation forest = 4.2 km; cropland = 16.4 km; pasture = 10.1 km; and urban = 11.4 km). Accounting for distance in such already complex models is not computationally tractable. In making the projections, we therefore implicitly assume that the average distances will not change (that is, that secondary vegetation and plantation forests will remain closer to primary vegetation than cropland, pasture and urban habitats).

Projecting the models onto spatial estimates of anthropogenic variables. We projected the best overall models of richness (within-sample and rarefied), abundance and community-weighted mean organism size onto estimates of land use, land-use intensity and human population density at $0.5^\circ \times 0.5^\circ$ resolution, using historical estimates for 1500 to 2005, and four RCP scenarios of future changes (IMAGE 2.6, MiniCAM 4.5, AIM 6.0 and MESSAGE 8.5; the names refer to the integrated assessment models used and the numbers to the amount of radiative forcing assumed in 2100)³⁹⁵. In the absence of global projections, proximity to roads and accessibility were omitted from our projections.

Estimates of land use for both the historical reconstruction and the future scenarios were taken from the harmonized land-use data accompanying the scenarios²⁶. Estimates of the stage of secondary vegetation (young, intermediate or mature) are not available directly in the RCP land-use data. However, these data contain estimates of the transition each year between secondary vegetation and all other land-use types. To convert this into an estimate of the proportion of secondary vegetation in each of the stages of maturity, we considered any transition to secondary vegetation to result in secondary vegetation of age zero. Each year, this age was then incremented by one. In the absence of better information, any transitions from secondary vegetation to any other land-use type were assumed to be drawn evenly from the ages currently represented. For the purposes of the projections, secondary vegetation was considered to be young until an age of 30 years, intermediate between 30 years and 100 years, and mature thereafter. We developed C# code to convert land-use transitions into estimates of the stage structure of secondary vegetation.

Gridded temporal estimates of human population density were directly available for the HYDE historical scenario and MESSAGE future scenario. Human population trajectories in the MiniCAM model were resolved only to the level of United Nations regions⁴¹; we therefore downsampled these to grid cells assuming no temporal change in the spatial pattern of relative population density within regions compared to present day patterns⁴⁵, which is the method used in other RCP-scenario land-use models lacking human population data resolved to grid cells²⁶. Gridded estimates of human population from the MESSAGE model were downloaded from <http://www.iiasa.ac.at/web-apps/ggi/GgiDb/>. For the scenarios for which human population projections were not available (IMAGE and AIM), we used country-level estimates from the 'medium' scenario of the United Nations population division³⁹⁶, which gives the closest global predictions of future human population to those assumed by IMAGE and AIM²⁶. These country-level estimates were downsampled to grid cells using the same method as for MiniCAM's regional projections.

Land-use intensity was an important explanatory variable in our models, but global maps of land-use intensity are not available. We therefore generated global

estimates of current land-use intensity based on a map of 'Global Land Systems'³⁹⁷, which divides coarse land-use types into sub-categories based on levels of cropland intensity, livestock densities and human population density. We mapped each Global Land Systems class onto one or more relevant combinations of our classes of land use and land-use intensity (Extended Data Table 2). The Global Land Systems data set has a spatial resolution of 5 arcmin. To calculate the proportion of each $0.5^\circ \times 0.5^\circ$ cell occupied by each land use and land-use intensity combination we calculated the proportion of 5-arcmin cells within each $0.5^\circ \times 0.5^\circ$ cell containing matching Global Land Systems categories (see legend of Extended Data Table 2 for details).

To generate past and future estimates of land-use intensity, we modelled the current proportion of each land-use type estimated to be under minimal, light or intense levels of intensity within each grid cell (one model for each intensity level), as a function of the prevalence of the land-use type within each cell and human population density, with the relationships allowed to vary among the 23 United Nations (UN) sub-regions (that is, we fitted interaction terms between UN sub-region and both the prevalence of each land-use type and human population density). UN sub-region data were taken from the world borders shapefile version 0.3 (http://thematicmapping.org/downloads/world_borders.php) and converted to a $0.5^\circ \times 0.5^\circ$ raster using ArcMap version 10.0 (ref. 388). The models were developed using generalized linear models with a binomial distribution of errors, implemented in the lme4 package version 1.0-5 (ref. 44) in R version 3.0.2 (ref. 390). The resulting models explained between 30.6% and 76.7% of the deviance in estimated current levels of intensity. Past and future land-use intensities were estimated by applying the models to the same past and future estimates of land use and human population density as above.

The scenarios gave the proportion of each grid cell estimated to be occupied by each combination of land use and land-use intensity. We did not attempt to resolve human population density within grid cells for our historical estimates or forecasts, thereby assuming it to be spatially (but not temporally) constant within each cell. The coefficients from the models of site-level diversity were thus applied to each combination of land use and intensity within each cell, with the same human population density estimate across all combinations. All predictions were expressed as a percentage net change compared with a baseline before human land-use effects on biodiversity, in which all land use was assumed to be primary vegetation of minimal intensity of use, and with a human population density of zero. Each cell's average value of net biodiversity change was calculated as the area-weighted mean value across all land uses and intensities. Global average values were calculated as mean values across all cells, weighted by cell area and an appropriate weighting factor to account for the fact that cells have different baseline levels of diversity. The weighting factors applied were: terrestrial vertebrate species richness in the case of richness, and net primary production (NPP) in the case of total abundance. No weighting factor was applied for projections of community-weighted mean plant height. Terrestrial vertebrate species richness was estimated by overlaying extent-of-occurrence range maps for mammals, birds, amphibians and reptiles, using Python code written by ourselves and implemented in ArcMap version 10.0 (ref. 388). Data on NPP were estimates of potential NPP (that is, in the absence of human effects) from the Lund-Postdam-Jena (LPJ) Dynamic Global Vegetation Model³⁹⁸.

The 95% confidence intervals around the projected values of biodiversity for each combination of pressure variables were estimated based on uncertainty in the modelled coefficients. We were unable to conduct multi-model averaging to account for uncertainty in the structure of the models (that is, projections were based only on the final best model) because applying such complex mixed-effects models, based on such large data sets, to multiple scenarios of human pressure at a global scale was intractable both in terms of time and computer-memory requirements. We were also unable to account for uncertainty in the trajectories of the human pressure variables, because uncertainty estimates are not available for any of the variables considered.

To estimate average biodiversity change in individual countries, we intersected the gridded projections with the world borders shapefile (see above) using the extract function in the raster package version 2.2-12 (ref. 399) in R version 3.0.2 (ref. 390). Mean values across the cells associated with each country were calculated, weighted by cell area. To interpret the outcomes for countries in terms of their natural biodiversity, we related the country-level projections to estimates of average natural vertebrate species richness (see above). To interpret the outcomes for countries in terms of their socio-economic status, we related the projections to estimates of the Human Development Index, which is an indicator of education, life expectancy, wealth and standard of living (<https://data.undp.org/>).

48. Aben, J., Dorenbosch, M., Herzog, S. K., Smolders, A. J. P. & Van Der Velde, G. Human disturbance affects a deciduous forest bird community in the Andean foothills of central Bolivia. *Bird Conserv. Int.* **18**, 363–380 (2008).

49. Adum, G. B., Eichhorn, M. P., Oduro, W., Ofori-Boateng, C. & Rodel, M. O. Two-stage recovery of amphibian assemblages following selective logging of tropical forests. *Conserv. Biol.* **27**, 354–363 (2013).
50. Aguilar Barquero, V. & Jiménez Hernández, F. Diversidad y distribución de palmas (Arecaceae) en tres fragmentos de bosque muy húmedo en Costa Rica. *Rev. Biol. Trop.* **57**, 83–92 (2009).
51. Alberta Biodiversity Monitoring Institute (ABMI). The raw soil arthropods dataset and the raw trees & snags dataset from Prototype Phase (2003–2006) and Rotation 1 (2007–2012). (2013).
52. Alcalá, E. L., Alcalá, A. C. & Dolino, C. N. Amphibians and reptiles in tropical rainforest fragments on Negros Island, the Philippines. *Environ. Conserv.* **31**, 254–261 (2004).
53. Alcayaga, O. E., Pizarro-Araya, J., Alfaro, F. M. & Cepeda-Pizarro, J. Spiders (Arachnida, Araneae) associated to agroecosystems in the Elqui Valley (Coquimbo Region, Chile). *Revista Colombiana De Entomología* **39**, 150–154 (2013).
54. Ancrenaz, M., Goossens, B., Gimenez, O., Sawang, A. & Lackman-Ancrenaz, I. Determination of ape distribution and population size using ground and aerial surveys: a case study with orang-utans in lower Kinabatangan, Sabah, Malaysia. *Anim. Conserv.* **7**, 375–385 (2004).
55. Arbeláez-Cortés, E., Rodríguez-Correa, H. A. & Restrepo-Chica, M. Mixed bird flocks: patterns of activity and species composition in a region of the Central Andes of Colombia. *Revista Mexicana De Biodiversidad* **82**, 639–651 (2011).
56. Armbricht, I., Perfecto, I. & Silverman, E. Limitation of nesting resources for ants in Colombian forests and coffee plantations. *Ecol. Entomol.* **31**, 403–410 (2006).
57. Arroyo, J., Iturrondobeitia, J. C., Rad, C. & Gonzalez-Carcedo, S. Oribatid mite (Acari) community structure in steppe habitats of Burgos Province, central northern Spain. *J. Nat. Hist.* **39**, 3453–3470 (2005).
58. Azhar, B. *et al.* The influence of agricultural system, stand structural complexity and landscape context on foraging birds in oil palm landscapes. *Ibis* **155**, 297–312 (2013).
59. Azpiroz, A. B. & Blake, J. G. Avian assemblages in altered and natural grasslands in the northern Campos of Uruguay. *Condor* **111**, 21–35 (2009).
60. Baeten, L. *et al.* Early trajectories of spontaneous vegetation recovery after intensive agricultural land use. *Restor. Ecol.* **18**, 379–386 (2010).
61. Baeten, L., Hermy, M., Van Daele, S. & Verheyen, K. Unexpected understorey community development after 30 years in ancient and post-agricultural forests. *J. Ecol.* **98**, 1447–1453 (2010).
62. Báldi, A., Batáry, P. & Erdős, S. Effects of grazing intensity on bird assemblages and populations of Hungarian grasslands. *Agric. Ecosyst. Environ.* **108**, 251–263 (2005).
63. Banks, J. E., Sandvik, P. & Keesecker, L. Beetle (Coleoptera) and spider (Araneae) diversity in a mosaic of farmland, edge, and tropical forest habitats in western Costa Rica. *Pan-Pac. Entomol.* **83**, 152–160 (2007).
64. Barlow, J. *et al.* Quantifying the biodiversity value of tropical primary, secondary, and plantation forests. *Proc. Natl Acad. Sci. USA* **104**, 18555–18560 (2007).
65. Bartolommei, P., Mortelliti, A., Pezzo, F. & Puglisi, L. Distribution of nocturnal birds (Strigiformes and Caprimulgidae) in relation to land-use types, extent and configuration in agricultural landscapes of Central Italy. *Rendiconti Lincei-Scienze Fisiche E Naturali* **24**, 13–21 (2013).
66. Basset, Y. *et al.* Changes in Arthropod assemblages along a wide gradient of disturbance in Gabon. *Conserv. Biol.* **22**, 1552–1563 (2008).
67. Bates, A. J. *et al.* Changing bee and hoverfly pollinator assemblages along an urban-rural gradient. *PLoS ONE* **6**, (2011).
68. Baur, B. *et al.* Effects of abandonment of subalpine hay meadows on plant and invertebrate diversity in Transylvania, Romania. *Biol. Conserv.* **132**, 261–273 (2006).
69. Berg, A., Ahnre, K., Ockinger, E., Svensson, R. & Soderstrom, B. Butterfly distribution and abundance is affected by variation in the Swedish forest-farmland landscape. *Biol. Conserv.* **144**, 2819–2831 (2011).
70. Bernard, H., Fjeldsa, J. & Mohamed, M. A case study on the effects of disturbance and conversion of tropical lowland rain forest on the non-volant small mammals in north Borneo: management implications. *Mammal Study* **34**, 85–96 (2009).
71. Berry, N. J. *et al.* The high value of logged tropical forests: lessons from northern Borneo. *Biodivers. Conserv.* **19**, 985–997 (2010).
72. Bicknell, J. & Peres, C. A. Vertebrate population responses to reduced-impact logging in a neotropical forest. *For. Ecol. Manage.* **259**, 2267–2275 (2010).
73. Bihn, J. H., Verhaagh, M., Braendle, M. & Brandl, R. Do secondary forests act as refuges for old growth forest animals? Recovery of ant diversity in the Atlantic forest of Brazil. *Biol. Conserv.* **141**, 733–743 (2008).
74. Billeter, R. *et al.* Indicators for biodiversity in agricultural landscapes: a pan-European study. *J. Appl. Ecol.* **45**, 141–150 (2008).
75. Bôçon, R. *Riqueza e abundância de aves em três estágios sucessionais da floresta ombrófila densa submontana, Antonina, Paraná*. PhD thesis, Universidade Federal do Paraná (2010).
76. Borges, S. H. Bird assemblages in secondary forests developing after slash-and-burn agriculture in the Brazilian Amazon. *J. Trop. Ecol.* **23**, 469–477 (2007).
77. Boutin, C., Baril, A. & Martin, P. A. Plant diversity in crop fields and woody hedgerows of organic and conventional farms in contrasting landscapes. *Agric. Ecosyst. Environ.* **123**, 185–193 (2008).
78. Bouyer, J. *et al.* Identification of ecological indicators for monitoring ecosystem health in the trans-boundary W Regional park: a pilot study. *Biol. Conserv.* **138**, 73–88 (2007).
79. Bragagnolo, C., Nogueira, A. A., Pinto-da-Rocha, R. & Pardini, R. Harvestmen in an Atlantic forest fragmented landscape: evaluating assemblage response to habitat quality and quantity. *Biol. Conserv.* **139**, 389–400 (2007).

80. Brearley, F. Q. Below-ground secondary succession in tropical forests of Borneo. *J. Trop. Ecol.* **27**, 413–420 (2011).
81. Brito, I., Goss, M. J., de Carvalho, M., Chatagnier, O. & van Tuinen, D. Impact of tillage system on arbuscular mycorrhiza fungal communities in the soil under Mediterranean conditions. *Soil Tillage Res.* **121**, 63–67 (2012).
82. Brunet, J. *et al.* Understory succession in post-agricultural oak forests: habitat fragmentation affects forest specialists and generalists differently. *For. Ecol. Manage.* **262**, 1863–1871 (2011).
83. Buczkowski, G. Extreme life history plasticity and the evolution of invasive characteristics in a native ant. *Biol. Invasions* **12**, 3343–3349 (2010).
84. Buczkowski, G. & Richmond, D. S. The effect of urbanization on ant abundance and diversity: a temporal examination of factors affecting biodiversity. *PLoS ONE* **7**, (2012).
85. Buddle, C. M. & Shorthouse, D. P. Effects of experimental harvesting on spider (Araneae) assemblages in boreal deciduous forests. *Can. Entomol.* **140**, 437–452 (2008).
86. Buscardo, E. *et al.* The early effects of afforestation on biodiversity of grasslands in Ireland. *Biodivers. Conserv.* **17**, 1057–1072 (2008).
87. Cabra-García, J., Bermúdez-Rivas, C., Osorio, A. M. & Chacón, P. Cross-taxon congruence of alpha and beta diversity among five leaf litter arthropod groups in Colombia. *Biodivers. Conserv.* **21**, 1493–1508 (2012).
88. Cáceres, N. C., Napoli, R. P., Casella, J. & Hannibal, W. Mammals in a fragmented savannah landscape in south-western Brazil. *J. Nat. Hist.* **44**, 491–512 (2010).
89. Cagle, N. L. Snake species distributions and temperate grasslands: a case study from the American tallgrass prairie. *Biol. Conserv.* **141**, 744–755 (2008).
90. Calviño-Cancela, M., Rubido-Bará, M. & van Etten, E. J. B. Do eucalypt plantations provide habitat for native forest biodiversity? *For. Ecol. Manage.* **270**, 153–162 (2012).
91. Cameron, S. A. *et al.* Patterns of widespread decline in North American bumble bees. *Proc. Natl Acad. Sci. USA* **108**, 662–667 (2011).
92. Carrijo, T. F., Brandao, D., de Oliveira, D. E., Costa, D. A. & Santos, T. Effects of pasture implantation on the termite (Isoptera) fauna in the Central Brazilian Savanna (Cerrado). *J. Insect Conserv.* **13**, 575–581 (2009).
93. Carvalho, A. L. d., Ferreira, E. J. L., Lima, J. M. T. & de Carvalho, A. L. Floristic and structural comparisons among palm communities in primary and secondary forest fragments of the Raimundo Irineu Serra Environmental Protection Area - Rio Branco, Acre, Brazil. *Acta Amazon.* **40**, 657–666 (2010).
94. Castro, H., Lehsten, V., Lavorel, S. & Freitas, H. Functional response traits in relation to land use change in the Montado. *Agric. Ecosyst. Environ.* **137**, 183–191 (2010).
95. Castro-Luna, A. A., Sosa, V. J. & Castillo-Campos, G. Bat diversity and abundance associated with the degree of secondary succession in a tropical forest mosaic in south-eastern Mexico. *Anim. Conserv.* **10**, 219–228 (2007).
96. Center For International Forestry Research (CIFOR). Multidisciplinary Landscape Assessment — Cameroon. <http://www.cifor.org/mla> (2013).
97. Center For International Forestry Research (CIFOR). Multidisciplinary Landscape Assessment — Philippines. <http://www.cifor.org/mla> (2013).
98. Centro Agronómico Tropical de Investigación y Enseñanza (CATIE). *Unpublished data of reptilian and amphibian diversity in six countries in Central America* (Centro Agronómico Tropical de Investigación y Enseñanza (CATIE), 2010).
99. Cerezo, A., Conde, M. & Poggio, S. Pasture area and landscape heterogeneity are key determinants of bird diversity in intensively managed farmland. *Biodivers. Conserv.* **20**, 2649–2667 (2011).
100. Chapman, K. & Reich, P. Land use and habitat gradients determine bird community diversity and abundance in suburban, rural and reserve landscapes of Minnesota, USA. *Biol. Conserv.* **135**, 527–541 (2007).
101. Chauvat, M., Wolters, V. & Dauber, J. Response of collembolan communities to land-use change and grassland succession. *Ecography* **30**, 183–192 (2007).
102. Clarke, F. M., Rostant, L. V. & Racey, P. A. Life after logging: post-logging recovery of a neotropical bat community. *J. Appl. Ecol.* **42**, 409–420 (2005).
103. Cleary, D. F. *et al.* Diversity and community composition of butterflies and odonates in an ENSO-induced fire affected habitat mosaic: a case study from East Kalimantan, Indonesia. *Oikos* **105**, 426–448 (2004).
104. Cleary, D. F. *et al.* Burning and logging differentially affect endemic vs. widely distributed butterfly species in Borneo. *Divers. Distrib.* **12**, 409–416 (2006).
105. Cockle, K. L., Leonard, M. L. & Bodrati, A. A. Presence and abundance of birds in an Atlantic forest reserve and adjacent plantation of shade-grown yerba mate, in Paraguay. *Biodivers. Conserv.* **14**, 3265–3288 (2005).
106. Connop, S., Hill, T., Steer, J. & Shaw, P. Microsatellite analysis reveals the spatial dynamics of *Bombus humilis* and *Bombus sylvarum*. *Insect Conserv. Divers.* **4**, 212–221 (2011).
107. D'Aniello, B., Stanislaw, I., Bonelli, S. & Balletto, E. Haying and grazing effects on the butterfly communities of two Mediterranean-area grasslands. *Biodivers. Conserv.* **20**, 1731–1744 (2011).
108. Darvill, B., Knight, M. E. & Goulson, D. Use of genetic markers to quantify bumblebee foraging range and nest density. *Oikos* **107**, 471–478 (2004).
109. Davis, A. L. V. & Philips, T. K. Effect of deforestation on a southwest Ghana dung beetle assemblage (Coleoptera: Scarabaeidae) at the periphery of Ankara conservation area. *Environ. Entomol.* **34**, 1081–1088 (2005).
110. Davis, E. S., Murray, T. E., Fitzpatrick, U., Brown, M. J. F. & Paxton, R. J. Landscape effects on extremely fragmented populations of a rare solitary bee, *Colletes floralis*. *Mol. Ecol.* **19**, 4922–4935 (2010).
111. Dawson, J. *et al.* Bird communities of the lower Waria Valley, Morobe Province, Papua New Guinea: a comparison between habitat types. *Trop. Conserv. Sci.* **4**, 317–348 (2011).
112. Delabie, J. H. C. *et al.* Ants as biological indicators of Wayana Amerindian land use in French Guiana. *C. R. Biol.* **332**, 673–684 (2009).
113. Diekötter, T., Walther-Hellwig, K., Conradi, M., Suter, M. & Frank, R. Effects of landscape elements on the distribution of the rare bumblebee species *Bombus muscorum* in an agricultural landscape. *Biodivers. Conserv.* **15**, 57–68 (2006).
114. Domínguez, E., Bahamonde, N. & Muñoz-Escobar, C. Efectos de la extracción de turba sobre la composición y estructura de una turbera de *Sphagnum* explotada y abandonada hace 20 años, Chile. *Anales Instituto Patagonia (Chile)* **40**, 37–45 (2012).
115. Domínguez-Haydar, Y. & Armbrrecht, I. Response of ants and their seed removal in rehabilitation areas and forests at El Cerrejón coal mine in Colombia. *Restor. Ecol.* **19**, 178–184 (2011).
116. Dumont, B. *et al.* How does grazing intensity influence the diversity of plants and insects in a species-rich upland grassland on basalt soils? *Grass Forage Sci.* **64**, 92–105 (2009).
117. Dures, S. G. & Cumming, G. S. The confounding influence of homogenising invasive species in a globally endangered and largely urban biome: Does habitat quality dominate avian biodiversity? *Biol. Conserv.* **143**, 768–777 (2010).
118. Edenius, L., Mikusinski, G. & Bergh, J. Can repeated fertilizer applications to young Norway spruce enhance avian diversity in intensively managed forests? *Ambio* **40**, 521–527 (2011).
119. Elek, Z. & Lovei, G. L. Patterns in ground beetle (Coleoptera: Carabidae) assemblages along an urbanisation gradient in Denmark. *Acta Oecologica* **32**, 104–111 (2007).
120. Endo, W. *et al.* Game vertebrate densities in hunted and nonhunted forest sites in Manu National Park, Peru. *Biotropica* **42**, 251–261 (2010).
121. Faruk, A., Belabut, D., Ahmad, N., Knell, R. J. & Garner, T. W. J. Effects of oil-palm plantations on diversity of tropical anurans. *Conserv. Biol.* **27**, 615–624 (2013).
122. Farwig, N., Sajita, N. & Boehning-Gaese, K. Conservation value of forest plantations for bird communities in western Kenya. *For. Ecol. Manage.* **255**, 3885–3892 (2008).
123. Fayle, T. M. *et al.* Oil palm expansion into rain forest greatly reduces ant biodiversity in canopy, epiphytes and leaf-litter. *Basic Appl. Ecol.* **11**, 337–345 (2010).
124. Felton, A. M., Engstrom, L. M., Felton, A. & Knott, C. D. Orangutan population density, forest structure and fruit availability in hand-logged and unlogged peat swamp forests in West Kalimantan, Indonesia. *Biol. Conserv.* **114**, 91–101 (2003).
125. Fensham, R., Dwyer, J., Eyre, T., Fairfax, R. & Wang, J. The effect of clearing on plant composition in mulga (*Acacia aneura*) dry forest, Australia. *Austral Ecol.* **37**, 183–192 (2012).
126. Fermon, H., Waltert, M., Vane-Wright, R. I. & Muhlenberg, M. Forest use and vertical stratification in fruit-feeding butterflies of Sulawesi, Indonesia: impacts for conservation. *Biodivers. Conserv.* **14**, 333–350 (2005).
127. Ferreira, C. & Alves, P. C. *Impacto da implementação de medidas de gestão do habitat nas populações de coelho-bravo (Oryctolagus cuniculus algirus) no Parque Natural do Sudoeste Alentejano e Costa Vicentina*. (Centro de Investigação em Biodiversidade e Recursos Genéticos (CIBIO), 2005).
128. Fierro, M. M., Cruz-Lopez, L., Sanchez, D., Villanueva-Gutierrez, R. & Vandame, R. Effect of biotic factors on the spatial distribution of stingless bees (Hymenoptera: Apidae, Meliponini) in fragmented neotropical habitats. *Neotrop. Entomol.* **41**, 95–104 (2012).
129. Filgueiras, B., Iannuzzi, L. & Leal, I. Habitat fragmentation alters the structure of dung beetle communities in the Atlantic Forest. *Biol. Conserv.* **144**, 362–369 (2011).
130. Flaspohler, D. J. *et al.* Long-term effects of fragmentation and fragment properties on bird species richness in Hawaiian forests. *Biol. Conserv.* **143**, 280–288 (2010).
131. Fukuda, D., Tisen, O. B., Momose, K. & Sakai, S. Bat diversity in the vegetation mosaic around a lowland dipterocarp forest of Borneo. *Raffles Bull. Zool.* **57**, 213–221 (2009).
132. Furlani, D., Ficetola, G. F., Colombo, G., Ugurlucan, M. & De Bernardi, F. Deforestation and the structure of frog communities in the Humedale Terraba-Sierpe, Costa Rica. *Zoolog. Sci.* **26**, 197–202 (2009).
133. Garden, J. G., McAlpine, C. A. & Possingham, H. P. Multi-scaled habitat considerations for conserving urban biodiversity: native reptiles and small mammals in Brisbane, Australia. *Landscape Ecol.* **25**, 1013–1028 (2010).
134. Gardner, T. A., Hernandez, M. I. M., Barlow, J. & Peres, C. A. Understanding the biodiversity consequences of habitat change: the value of secondary and plantation forests for neotropical dung beetles. *J. Appl. Ecol.* **45**, 883–893 (2008).
135. Gheler-Costa, C., Vettorazzi, C. A., Pardini, R. & Verdade, L. M. The distribution and abundance of small mammals in agroecosystems of southeastern Brazil. *Mammalia* **76**, 185–191 (2012).
136. Giordani, P. Assessing the effects of forest management on epiphytic lichens in protected forests using different indicators. *Plant Biosyst.* **146**, 628–637 (2012).
137. Giordano, S. *et al.* Biodiversity and trace element content of epiphytic bryophytes in urban and extraurban sites of southern Italy. *Plant Ecol.* **170**, 1–14 (2004).
138. Golodets, C., Kigel, J. & Sternberg, M. Recovery of plant species composition and ecosystem function after cessation of grazing in a Mediterranean grassland. *Plant Soil* **329**, 365–378 (2010).
139. Gottschalk, M. S., De Toni, D. C., Valente, V. L. S. & Hofmann, P. R. P. Changes in Brazilian Drosophilidae (Diptera) assemblages across an urbanisation gradient. *Neotrop. Entomol.* **36**, 848–862 (2007).
140. Goulson, D. *et al.* Effects of land use at a landscape scale on bumblebee nest density and survival. *J. Appl. Ecol.* **47**, 1207–1215 (2010).
141. Goulson, D., Lye, G. C. & Darvill, B. Diet breadth, coexistence and rarity in bumblebees. *Biodivers. Conserv.* **17**, 3269–3288 (2008).

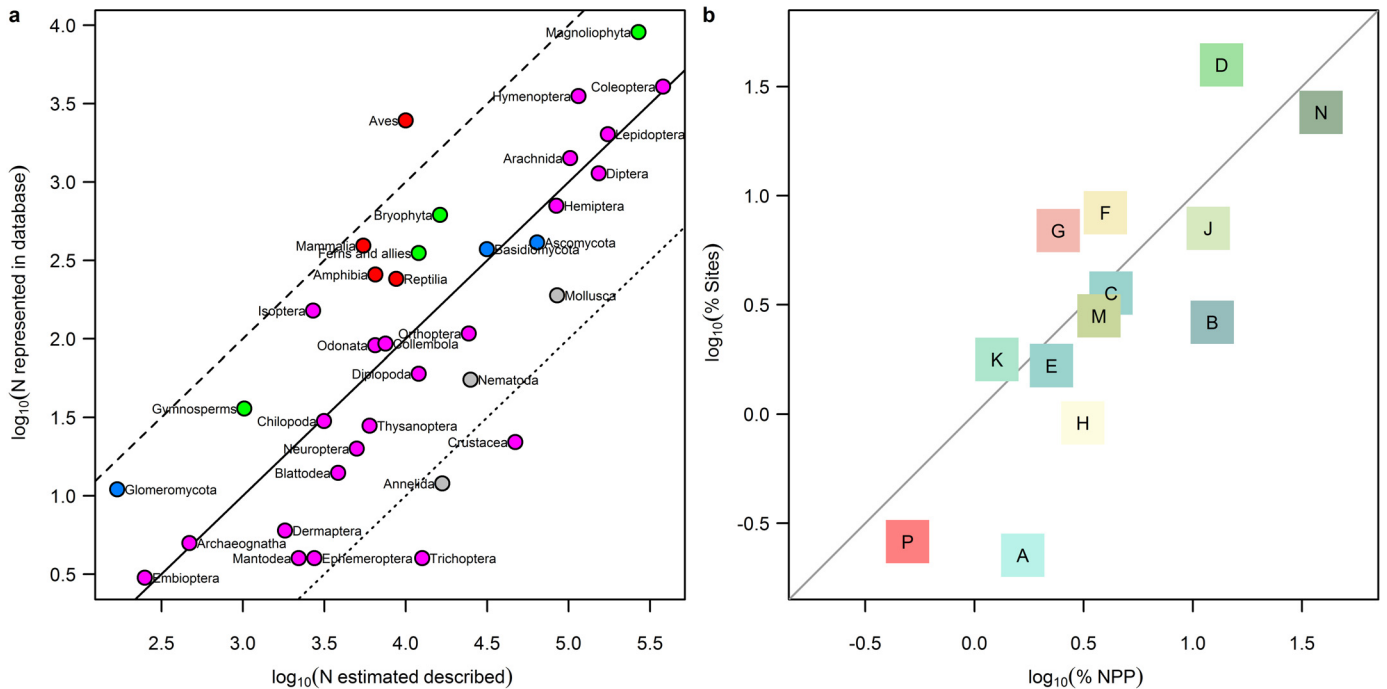
142. Gove, A. D., Majer, J. D. & Rico-Gray, V. Methods for conservation outside of formal reserve systems: the case of ants in the seasonally dry tropics of Veracruz, Mexico. *Biol. Conserv.* **126**, 328–338 (2005).
143. Grogan, J. *et al.* What loggers leave behind: impacts on big-leaf mahogany (*Swietenia macrophylla*) commercial populations and potential for post-logging recovery in the Brazilian Amazon. *For. Ecol. Manage.* **255**, 269–281 (2008).
144. Gu, W.-B., Zhen-Rong, Y. & Dun-Xiao, H. Carabid community and its fluctuation in farmland of salinity transforming area in the North China Plain: a case study in Quzhou County, Hebei Province. *Biodivers. Sci.* **12**, 262–268 (2004).
145. Gutierrez-Lamus, D. L. Composition and abundance of Anura in two forest types (natural and planted) in the eastern cordillera of Colombia. *Caldasia* **26**, 245–264 (2004).
146. Hanley, M. E. *et al.* Increased bumblebee abundance along the margins of a mass flowering crop: evidence for pollinator spill-over. *Oikos* **120**, 1618–1624 (2011).
147. Hanson, T. R., Brunsfeld, S. J., Finegan, B. & Waits, L. P. Pollen dispersal and genetic structure of the tropical tree *Dipteryx panamensis* in a fragmented Costa Rican landscape. *Mol. Ecol.* **17**, 2060–2073 (2008).
148. Hashim, N., Akmal, W., Jusoh, W. & Nasir, M. Ant diversity in a Peninsular Malaysian mangrove forest and oil palm plantation. *Asian Myrmecology* **3**, 5–8 (2010).
149. Hatfield, R. G. & LeBuhn, G. Patch and landscape factors shape community assemblage of bumble bees, *Bombus* spp. (Hymenoptera: Apidae), in montane meadows. *Biol. Conserv.* **139**, 150–158 (2007).
150. Hawes, J. *et al.* Diversity and composition of Amazonian moths in primary, secondary and plantation forests. *J. Trop. Ecol.* **25**, 281–300 (2009).
151. Helden, A. J. & Leather, S. R. Biodiversity on urban roundabouts—Hemiptera, management and the species-area relationship. *Basic Appl. Ecol.* **5**, 367–377 (2004).
152. Hernández, L., Delgado, L., Meier, W. & Duran, C. Empobrecimiento de bosques fragmentados en el norte de la Gran Sabana, Venezuela. *Interiencia* **37**, 891–898 (2012).
153. Herrmann, F., Westphal, C., Moritz, R. F. A. & Steffan-Dewenter, I. Genetic diversity and mass resources promote colony size and forager densities of a social bee (*Bombus pascuorum*) in agricultural landscapes. *Mol. Ecol.* **16**, 1167–1178 (2007).
154. Hietz, P. Conservation of vascular epiphyte diversity in Mexican coffee plantations. *Conserv. Biol.* **19**, 391–399 (2005).
155. Higuera, D. & Wolf, J. H. D. Vascular epiphytes in dry oak forests show resilience to anthropogenic disturbance, Cordillera Oriental, Colombia. *Caldasia* **32**, 161–174 (2010).
156. Hilje, B. & Aide, T. M. Recovery of amphibian species richness and composition in a chronosequence of secondary forests, northeastern Costa Rica. *Biol. Conserv.* **146**, 170–176 (2012).
157. Hoffmann, A. & Zeller, U. Influence of variations in land use intensity on species diversity and abundance of small mammals in the Nama Karoo, Namibia. *Belg. J. Zool.* **135**, 91–96 (2005).
158. Horgan, F. G. Invasion and retreat: shifting assemblages of dung beetles amidst changing agricultural landscapes in central Peru. *Biodivers. Conserv.* **18**, 3519–3541 (2009).
159. Hu, C. & Cao, Z. P. Nematode community structure under compost and chemical fertilizer management practice, in the north China plain. *Exp. Agric.* **44**, 485–496 (2008).
160. Hylander, K. & Weibull, H. Do time-lagged extinctions and colonizations change the interpretation of buffer strip effectiveness? – a study of riparian bryophytes in the first decade after logging. *J. Appl. Ecol.* **49**, 1316–1324 (2012).
161. Hylander, K. & Nemomissa, S. Complementary roles of home gardens and exotic tree plantations as alternative habitats for plants of the Ethiopian montane rainforest. *Conserv. Biol.* **23**, 400–409 (2009).
162. Ims, R. A. & Henden, J. A. Collapse of an arctic bird community resulting from ungulate-induced loss of erect shrubs. *Biol. Conserv.* **149**, 2–5 (2012).
163. Cubides, P. J. I. & Cardona, J. N. U. Anthropogenic disturbance and edge effects on anuran assemblages inhabiting cloud forest fragments in Colombia. *Natureza & Conservação* **9**, 39–46 (2011).
164. Ishitani, M., Kotze, D. J. & Niemela, J. Changes in carabid beetle assemblages across an urban-rural gradient in Japan. *Ecography* **26**, 481–489 (2003).
165. Jacobs, C. T., Scholtz, C. H., Escobar, F. & Davis, A. L. V. How might intensification of farming influence dung beetle diversity (Coleoptera: Scarabaeidae) in Maputo Special Reserve (Mozambique)? *J. Insect Conserv.* **14**, 389–399 (2010).
166. Johnson, M. F., Gómez, A. & Pinedo-Vasquez, M. Land use and mosquito diversity in the Peruvian Amazon. *J. Med. Entomol.* **45**, 1023–1030 (2008).
167. Jonsell, M. Old park trees as habitat for saproxylic beetle species. *Biodivers. Conserv.* **21**, 619–642 (2012).
168. Julier, H. E. & Roulston, T. H. Wild bee abundance and pollination service in cultivated pumpkins: farm management, nesting behavior and landscape effects. *J. Econ. Entomol.* **102**, 563–573 (2009).
169. Jung, T. S. & Powell, T. Spatial distribution of meadow jumping mice (*Zapus hudsonius*) in logged boreal forest of northwestern Canada. *Mamm. Biol.* **76**, 678–682 (2011).
170. Kapoor, V. Effects of rainforest fragmentation and shade-coffee plantations on spider communities in the Western Ghats, India. *J. Insect Conserv.* **12**, 53–68 (2008).
171. Kappes, H., Katzschnher, L. & Nowak, C. Urban summer heat load: meteorological data as a proxy for metropolitan biodiversity. *Meteorologische Zeitschrift* **21**, 525–528 (2012).
172. Kati, V., Zografou, K., Tzikali, E., Chitos, T. & Willemse, L. Butterfly and grasshopper diversity patterns in humid Mediterranean grasslands: the roles of disturbance and environmental factors. *J. Insect Conserv.* **16**, 807–818 (2012).
173. Katovai, E., Burley, A. L. & Mayfield, M. M. Understorey plant species and functional diversity in the degraded wet tropical forests of Kolombangara Island, Solomon Islands. *Biol. Conserv.* **145**, 214–224 (2012).
174. Kessler, M. *et al.* Tree diversity in primary forest and different land use systems in Central Sulawesi, Indonesia. *Biodivers. Conserv.* **14**, 547–560 (2005).
175. Kessler, M. *et al.* Alpha and beta diversity of plants and animals along a tropical land-use gradient. *Ecol. Appl.* **19**, 2142–2156 (2009).
176. Knight, M. E. *et al.* Bumblebee nest density and the scale of available forage in arable landscapes. *Insect Conserv. Divers.* **2**, 116–124 (2009).
177. Knop, E., Ward, P. I. & Wich, S. A. A comparison of orang-utan density in a logged and unlogged forest on Sumatra. *Biol. Conserv.* **120**, 183–188 (2004).
178. Kohler, F., Verhulst, J., van Klink, R. & Kleijn, D. At what spatial scale do high-quality habitats enhance the diversity of forbs and pollinators in intensively farmed landscapes? *J. Appl. Ecol.* **45**, 753–762 (2008).
179. Koivula, M., Hyrylainen, V. & Soininen, E. Carabid beetles (Coleoptera: Carabidae) at forest-farmland edges in southern Finland. *J. Insect Conserv.* **8**, 297–309 (2004).
180. Kolb, A. & Diekmann, M. Effects of environment, habitat configuration and forest continuity on the distribution of forest plant species. *J. Veg. Sci.* **15**, 199–208 (2004).
181. Körösi, Á., Batáry, P., Orosz, A., Rédei, D. & Báldi, A. Effects of grazing, vegetation structure and landscape complexity on grassland leafhoppers (Hemiptera: Auchenorrhyncha) and true bugs (Hemiptera: Heteroptera) in Hungary. *Insect Conserv. Divers.* **5**, 57–66 (2012).
182. Krauss, J., Klein, A. M., Steffan-Dewenter, I. & Tscharnkte, T. Effects of habitat area, isolation, and landscape diversity on plant species richness of calcareous grasslands. *Biodivers. Conserv.* **13**, 1427–1439 (2004).
183. Krauss, J., Steffan-Dewenter, I. & Tscharnkte, T. How does landscape context contribute to effects of habitat fragmentation on diversity and population density of butterflies? *J. Biogeogr.* **30**, 889–900 (2003).
184. Kumar, R. & Shahabuddin, G. Effects of biomass extraction on vegetation structure, diversity and composition of forests in Sariska Tiger Reserve, India. *Environ. Conserv.* **32**, 248–259 (2005).
185. Lachat, T. *et al.* Arthropod diversity in Lama forest reserve (South Benin), a mosaic of natural, degraded and plantation forests. *Biodivers. Conserv.* **15**, 3–23 (2006).
186. Lantschner, M. V., Rusch, V. & Hayes, J. P. Habitat use by carnivores at different spatial scales in a plantation forest landscape in Patagonia, Argentina. *For. Ecol. Manage.* **269**, 271–278 (2012).
187. Lantschner, M. V., Rusch, V. & Peyrou, C. Bird assemblages in pine plantations replacing native ecosystems in NW Patagonia. *Biodivers. Conserv.* **17**, 969–989 (2008).
188. Latta, S. C., Tinoco, B. A., Astudillo, P. X. & Graham, C. H. Patterns and magnitude of temporal change in avian communities in the Ecuadorian Andes. *Condor* **113**, 24–40 (2011).
189. Légaré, J.-P., Hébert, C. & Ruel, J.-C. Alternative silvicultural practices in irregular boreal forests: response of beetle assemblages. *Silva Fennica* **45**, 937–956 (2011).
190. Letcher, S. G. & Chazdon, R. L. Rapid recovery of biomass, species richness, and species composition in a forest chronosequence in northeastern Costa Rica. *Biotropica* **41**, 608–617 (2009).
191. Littlewood, N. A., Pakeman, R. J. & Pozsgai, G. Grazing impacts on Auchenorrhyncha diversity and abundance on a Scottish upland estate. *Insect Conserv. Divers.* **5**, 67–74 (2012).
192. Liu, Y. H., Axmacher, J. C., Wang, C. L., Li, L. T. & Yu, Z. R. Ground beetle (Coleoptera: Carabidae) assemblages of restored semi-natural habitats and intensively cultivated fields in northern China. *Restor. Ecol.* **20**, 234–239 (2012).
193. Lo-Man-Hung, N. F., Gardner, T. A., Ribeiro-Júnior, M. A., Barlow, J. & Bonaldo, A. B. The value of primary, secondary, and plantation forests for Neotropical epigeic arachnids. *J. Arachnol.* **36**, 394–401 (2008).
194. López-Quintero, C. A., Straatsma, G., Franco-Molano, A. E. & Boekhout, T. Macrofungi diversity in Colombian Amazon forests varies with regions and regimes of disturbance. *Biodivers. Conserv.* **21**, 2221–2243 (2012).
195. Louhaichi, M., Salkini, A. K. & Petersen, S. L. Effect of small ruminant grazing on the plant community characteristics of semiarid Mediterranean ecosystems. *Int. J. Agric. Bio.* **11**, 681–689 (2009).
196. Lucas-Borja, M. E. *et al.* The effects of human trampling on the microbiological properties of soil and vegetation in Mediterranean mountain areas. *Land Degrad. Dev.* **22**, 383–394 (2011).
197. Luja, V., Herrando-Perez, S., Gonzalez-Solis, D. & Luiselli, L. Secondary rain forests are not havens for reptile species in tropical Mexico. *Biotropica* **40**, 747–757 (2008).
198. Luskin, M. S. Flying foxes prefer to forage in farmland in a tropical dry forest landscape mosaic in Fiji. *Biotropica* **42**, 246–250 (2010).
199. MacSwiney, M. C. G., Vilchis, P. L., Clarke, F. M. & Racey, P. A. The importance of cenotes in conserving bat assemblages in the Yucatan, Mexico. *Biol. Conserv.* **136**, 499–509 (2007).
200. Maeto, K. & Sato, S. Impacts of forestry on ant species richness and composition in warm-temperate forests of Japan. *For. Ecol. Manage.* **187**, 213–223 (2004).
201. Magura, T., Horvath, R. & Tothmeresz, B. Effects of urbanization on ground-dwelling spiders in forest patches, in Hungary. *Landscape Ecol.* **25**, 621–629 (2010).
202. Mallari, N. A. D. *et al.* Population densities of understorey birds across a habitat gradient in Palawan, Philippines: implications for conservation. *Oryx* **45**, 234–242 (2011).
203. Malone, L. *et al.* Observations on bee species visiting white clover in New Zealand pastures. *J. Apic. Res.* **49**, 284–286 (2010).

204. Marín-Spiotta, E., Ostertag, R. & Silver, W. L. Long-term patterns in tropical reforestation: plant community composition and aboveground biomass accumulation. *Ecol. Appl.* **17**, 828–839 (2007).
205. Marshall, E. J. P., West, T. M. & Kleijn, D. Impacts of an agri-environment field margin prescription on the flora and fauna of arable farmland in different landscapes. *Agric. Ecosyst. Environ.* **113**, 36–44 (2006).
206. Martin, P. S., Gheler-Costa, C., Lopes, P. C., Rosalino, L. M. & Verdade, L. M. Terrestrial non-volant small mammals in agro-silvicultural landscapes of Southeastern Brazil. *For. Ecol. Manage.* **282**, 185–195 (2012).
207. Matsumoto, T., Itioka, T., Yamane, S. & Momose, K. Traditional land use associated with swidden agriculture changes encounter rates of the top predator, the army ant, in Southeast Asian tropical rain forests. *Biodivers. Conserv.* **18**, 3139–3151 (2009).
208. Mayfield, M. M., Ackerly, D. & Daily, G. C. The diversity and conservation of plant reproductive and dispersal functional traits in human-dominated tropical landscapes. *J. Ecol.* **94**, 522–536 (2006).
209. McFrederick, Q. S. & LeBuhn, G. Are urban parks refuges for bumble bees *Bombus* spp. (Hymenoptera: Apidae)? *Biol. Conserv.* **129**, 372–382 (2006).
210. McNamara, S., Erskine, P. D., Lamb, D., Chantalangsy, L. & Boyle, S. Primary tree species diversity in secondary fallow forests of Laos. *For. Ecol. Manage.* **281**, 93–99 (2012).
211. Meyer, B., Gaebeler, V. & Steffan-Dewenter, I. D. Patch size and landscape effects on pollinators and seed set of the horseshoe vetch, *hippocrepis comosa*, in an agricultural landscape of central Europe. *Entomol. Gen.* **30**, 173–185 (2007).
212. Meyer, B., Jauker, F. & Steffan-Dewenter, I. Contrasting resource-dependent responses of hoverfly richness and density to landscape structure. *Basic Appl. Ecol.* **10**, 178–186 (2009).
213. Micó, E., García-López, A., Brustel, H., Padilla, A. & Galante, E. Explaining the saproxylic beetle diversity of a protected Mediterranean area. *Biodivers. Conserv.* **22**, 889–904 (2013).
214. Milder, J. C. *et al.* Effects of farm and landscape management on bird and butterfly conservation in western Honduras. *Ecosphere* **1**, art2 (2010).
215. Miranda, M. V., Politi, N. & Rivera, L. O. Unexpected changes in the bird assemblage in areas under selective logging in piedmont forest in northwestern Argentina. *Ornitol. Neotrop.* **21**, 323–337 (2010).
216. Moreno-Mateos, D. *et al.* Effects of land use on nocturnal birds in a Mediterranean agricultural landscape. *Acta Ornithologica* **46**, 173–182 (2011).
217. Muchane, M. N. *et al.* Land use practices and their implications on soil macro-fauna in Maasai Mara ecosystem. *Int. J. Biodivers. Conserv.* **4**, 500–514 (2012).
218. Mudri-Stojnic, S., Andric, A., Jozan, Z. & Vujic, A. Pollinator diversity (Hymenoptera and Diptera) in semi-natural habitats in Serbia during summer. *Archives Bio. Sci.* **64**, 777–786 (2012).
219. Naidoo, R. Species richness and community composition of songbirds in a tropical forest-agricultural landscape. *Anim. Conserv.* **7**, 93–105 (2004).
220. Nakamura, A., Proctor, H. & Catterall, C. P. Using soil and litter arthropods to assess the state of rainforest restoration. *Ecol. Manage. Restor.* **4**, S20–S28 (2003).
221. Naoe, S., Sakai, S. & Masaki, T. Effect of forest shape on habitat selection of birds in a plantation-dominant landscape across seasons: comparison between continuous and strip forests. *J. For. Res.* **17**, 219–223 (2012).
222. Navarrete, D. & Halffter, G. Dung beetle (Coleoptera: Scarabaeidae: Scarabaeinae) diversity in continuous forest, forest fragments and cattle pastures in a landscape of Chiapas, Mexico: the effects of anthropogenic changes. *Biodivers. Conserv.* **17**, 2869–2898 (2008).
223. Navarro, I. L., Roman, A. K., Gomez, F. H. & Perez, H. A. Seasonal variation in dung beetles (Coleoptera: Scarabaeidae: Scarabaeinae) from Serrania de Coraza, Sucre (Colombia). *Revista Colombiana de Ciencia Animal* **3**, 102–110 (2011).
224. Neuschulz, E. L., Botzat, A. & Farwig, N. Effects of forest modification on bird community composition and seed removal in a heterogeneous landscape in South Africa. *Oikos* **120**, 1371–1379 (2011).
225. Nicolas, V., Barriere, P., Tapiero, A. & Colyn, M. Shrew species diversity and abundance in Ziama Biosphere Reserve, Guinea: comparison among primary forest, degraded forest and restoration plots. *Biodivers. Conserv.* **18**, 2043–2061 (2009).
226. Nielsen, A. *et al.* Assessing bee species richness in two Mediterranean communities: importance of habitat type and sampling techniques. *Ecol. Res.* **26**, 969–983 (2011).
227. Noreika, N. & Kotze, D. J. Forest edge contrasts have a predictable effect on the spatial distribution of carabid beetles in urban forests. *J. Insect Conserv.* **16**, 867–881 (2012).
228. Noreika, N. New records of rare species of Coleoptera found in Ukmergė district in 2004–2005. *New Rare Lithuanian Insect Species* **21**, 68–71 (2009).
229. Norfolk, O., Abdel-Dayem, M. & Gilbert, F. Rainwater harvesting and arthropod biodiversity within an arid agro-ecosystem. *Agric. Ecosyst. Environ.* **162**, 8–14 (2012).
230. Noriega, J. A., Realpe, E. & Fagua, G. *Diversidad de escarabajos coprofagos* (Coleoptera: Scarabaeidae) en un bosque de galería con tres estadios de alteración. *Universitas Scientiarum* **12**, 51–63 (2007).
231. Noriega, J. A., Palacio, J. M., Monroy-G, J. D. & Valencia, E. *Estructura de un ensamblaje de escarabajos coprofagos* (Coleoptera: Scarabaeinae) en tres sitios con diferente uso del suelo en Antioquia, Colombia. *Actualidades Biológicas (Medellin)* **34**, 43–54 (2012).
232. Nöske, N. M. *et al.* Disturbance effects on diversity of epiphytes and moths in a montane forest in Ecuador. *Basic Appl. Ecol.* **9**, 4–12 (2008).
233. Numa, C., Verdu, J. R., Rueda, C. & Galante, E. Comparing dung beetle species assemblages between protected areas and adjacent pasturelands in a Mediterranean savanna landscape. *Rangeland Ecol. Manag.* **65**, 137–143 (2012).
234. O'Connor, T. G. Influence of land use on plant community composition and diversity in Highland Sourveld grassland in the southern Drakensberg, South Africa. *J. Appl. Ecol.* **42**, 975–988 (2005).
235. O'Dea, N. & Whittaker, R. J. How resilient are Andean montane forest bird communities to habitat degradation? *Biodivers. Conserv.* **16**, 1131–1159 (2007).
236. Ofori-Boateng, C. *et al.* Differences in the effects of selective logging on amphibian assemblages in three West African forest types. *Biotropica* **45**, 94–101 (2013).
237. Oke, C. Land snail diversity in post extraction secondary forest reserves in Edo State, Nigeria. *Afr. J. Ecol.* **51**, 244–254 (2013).
238. Oke, C. O. & Chokor, J. U. The effect of land use on snail species richness and diversity in the tropical rainforest of south-western Nigeria. *Am. Sci.* **10**, 95–108 (2009).
239. Oliveira, D. E., Carrijo, T. F. & Brandão, D. Species composition of termites (Isoptera) in different Cerrado vegetation physiognomies. *Sociobiology* **60**, 190–197 (2013).
240. Osgathorpe, L. M., Park, K. & Goulson, D. The use of off-farm habitats by foraging bumblebees in agricultural landscapes: implications for conservation management. *Apidologie (Celle)* **43**, 113–127 (2012).
241. Otavo, S. E., Parrado-Rosselli, A. & Noriega, J. A. Scarabaeoidea superfamily (Insecta: Coleoptera) as a bioindicator element of anthropogenic disturbance in an Amazon national park. *Rev. Biol. Trop.* **61**, 735–752 (2013).
242. Otto, C. R. V. & Roloff, G. J. Songbird response to green-tree retention prescriptions in clearcut forests. *For. Ecol. Manage.* **284**, 241–250 (2012).
243. Paradis, S. & Work, T. T. Partial cutting does not maintain spider assemblages within the observed range of natural variability in Eastern Canadian black spruce forests. *For. Ecol. Manage.* **262**, 2079–2093 (2011).
244. Paritsis, J. & Aizen, M. A. Effects of exotic conifer plantations on the biodiversity of understory plants, epigeal beetles and birds in *Nothofagus dombeii* forests. *For. Ecol. Manage.* **255**, 1575–1583 (2008).
245. Parra-H, A. & Nates-Parra, G. Variation of the orchid bees community (Hymenoptera: Apidae) in three altered habitats of the Colombian "llano" piedmont. *Rev. Biol. Trop.* **55**, 931–941 (2007).
246. Pelegrin, N. & Bucher, E. H. Effects of habitat degradation on the lizard assemblage in the Arid Chaco, central Argentina. *J. Arid Environ.* **79**, 13–19 (2012).
247. Phalan, B., Onial, M., Balmford, A. & Green, R. Reconciling food production and biodiversity conservation: land sharing and land sparing compared. *Science* **333**, 1289–1291 (2011).
248. Pillsbury, F. C. & Miller, J. R. Habitat and landscape characteristics underlying anuran community structure along an urban-rural gradient. *Ecol. Appl.* **18**, 1107–1118 (2008).
249. Pineda, E. & Halffter, G. Species diversity and habitat fragmentation: frogs in a tropical montane landscape in Mexico. *Biol. Conserv.* **117**, 499–508 (2004).
250. Politi, N., Hunter, M., Jr & Rivera, L. Assessing the effects of selective logging on birds in Neotropical piedmont and cloud montane forests. *Biodivers. Conserv.* **21**, 3131–3155 (2012).
251. Poveda, K., Martinez, E., Kersch-Becker, M., Bonilla, M. & Tscharntke, T. Landscape simplification and altitude affect biodiversity, herbivory and Andean potato yield. *J. Appl. Ecol.* **49**, 513–522 (2012).
252. Power, E. F., Kelly, D. L. & Stout, J. C. Organic farming and landscape structure: effects on insect-pollinated plant diversity in intensively managed grasslands. *PLoS ONE* **7**, (2012).
253. Power, E. F. & Stout, J. C. Organic dairy farming: impacts on insect-flower interaction networks and pollination. *J. Appl. Ecol.* **48**, 561–569 (2011).
254. Presley, S. J., Willig, M. R., Wunderle, J. M., Jr & Saldanha, L. N. Effects of reduced-impact logging and forest physiognomy on bat populations of lowland Amazonian forest. *J. Appl. Ecol.* **45**, 14–25 (2008).
255. Proenca, V. M., Pereira, H. M., Guilherme, J. & Vicente, L. Plant and bird diversity in natural forests and in native and exotic plantations in NW Portugal. *Acta Oecologica* **36**, 219–226 (2010).
256. Quaranta, M. *et al.* Wild bees in agroecosystems and semi-natural landscapes. 1997–2000 collection period in Italy. *Bull. Insectology* **57**, 11–62 (2004).
257. Quintero, C., Laura Morales, C. & Adrian Aizen, M. Effects of anthropogenic habitat disturbance on local pollinator diversity and species turnover across a precipitation gradient. *Biodivers. Conserv.* **19**, 257–274 (2010).
258. Redpath, N., Osgathorpe, L. M., Park, K. & Goulson, D. Crofting and bumblebee conservation: The impact of land management practices on bumblebee populations in northwest Scotland. *Biol. Conserv.* **143**, 492–500 (2010).
259. Reid, J. L., Harris, J. B. C. & Zahawi, R. A. Avian habitat preference in tropical forest restoration in southern Costa Rica. *Biotropica* **44**, 350–359 (2012).
260. Reis, Y. T. & Canello, E. M. Termite (Insecta, Isoptera) richness in primary and secondary Atlantic Forest in southeastern Bahia. *Iheringia Serie Zoologia* **97**, 229–234 (2007).
261. Rey-Velasco, J. C. & Miranda-Esquivel, D. R. *Habitat modification in Andean forest: the response of ground beetles (Coleoptera: Carabidae) on the northeastern Colombian Andes*. BSc thesis, Universidad Industrial de Santander, (2010).
262. Ribeiro, D. B. & Freitas, A. V. L. The effect of reduced-impact logging on fruit-feeding butterflies in Central Amazon, Brazil. *J. Insect Conserv.* **16**, 733–744 (2012).
263. Richardson, B. A., Richardson, M. J. & Soto-Adames, F. N. Separating the effects of forest type and elevation on the diversity of litter invertebrate communities in a humid tropical forest in Puerto Rico. *J. Anim. Ecol.* **74**, 926–936 (2005).
264. Robles, C. A., Carmaran, C. C. & Lopez, S. E. Screening of xylophagous fungi associated with *Platanus acerifolia* in urban landscapes: biodiversity and potential biodeterioration. *Landsc. Urban Plan.* **100**, 129–135 (2011).

265. Rodrigues, M. M., Uchoa, M. A. & Ide, S. Dung beetles (Coleoptera: Scarabaeoidea) in three landscapes in Mato Grosso do Sul, Brazil. *Braz. J. Biol.* **73**, 211–220 (2013).
266. Römbke, J., Schmidt, P. & Höfer, H. The earthworm fauna of regenerating forests and anthropogenic habitats in the coastal region of Paraná. *Pesquisa Agropecu. Bras.* **44**, 1040–1049 (2009).
267. Romero-Duque, L. P., Jaramillo, V. J. & Perez-Jimenez, A. Structure and diversity of secondary tropical dry forests in Mexico, differing in their prior land-use history. *For. Ecol. Manage.* **253**, 38–47 (2007).
268. Rosselli, L. *Factores ambientales relacionados con la presencia y abundancia de las aves de los humedales de la Sabana de Bogotá*. PhD thesis, Universidad Nacional de Colombia, (2011).
269. Rousseau, L., Fonte, S. J., Tellez, O., van der Hoek, R. & Lavelle, P. Soil macrofauna as indicators of soil quality and land use impacts in smallholder agroecosystems of western Nicaragua. *Ecol. Indic.* **27**, 71–82 (2013).
270. Safian, S., Csontos, G. & Winkler, D. Butterfly community recovery in degraded rainforest habitats in the Upper Guinean forest zone (Kakum forest, Ghana). *J. Insect Conserv.* **15**, 351–359 (2011).
271. Sakchoowong, W., Nomura, S., Ogata, K. & Chanpaisaeng, J. Diversity of pselaphine beetles (Coleoptera: Staphylinidae: Pselaphinae) in eastern Thailand. *Entomol. Sci.* **11**, 301–313 (2008).
272. Saldana-Vazquez, R. A., Sosa, V. J., Hernandez-Montero, J. R. & Lopez-Barrera, F. Abundance responses of frugivorous bats (Stenodermatinae) to coffee cultivation and selective logging practices in mountainous central Veracruz, Mexico. *Biodivers. Conserv.* **19**, 2111–2124 (2010).
273. Samnegård, U., Persson, A. S. & Smith, H. G. Gardens benefit bees and enhance pollination in intensively managed farmland. *Biol. Conserv.* **144**, 2602–2606 (2011).
274. Santana, J., Porto, M., Gordinho, L., Reino, L. & Beja, P. Long-term responses of Mediterranean birds to forest fuel management. *J. Appl. Ecol.* **49**, 632–643 (2012).
275. Savage, J., Wheeler, T. A., Moores, A. M. A. & Taillefer, A. G. Effects of habitat size, vegetation cover, and surrounding land use on diptera diversity in temperate nearctic bogs. *Wetlands* **31**, 125–134 (2011).
276. Schmidt, A. C., Fraser, L. H., Carlyle, C. N. & Bassett, E. R. L. Does cattle grazing affect ant abundance and diversity in temperate grasslands? *Rangeland Ecol. Manag.* **65**, 292–298 (2012).
277. Schon, N. L., Mackay, A. D. & Minor, M. A. Soil fauna in sheep-grazed hill pastures under organic and conventional livestock management and in an adjacent ungrazed pasture. *Pedobiologia (Jena)* **54**, 161–168 (2011).
278. Schüepp, C., Herrmann, J. D., Herzog, F. & Schmidt-Entling, M. H. Differential effects of habitat isolation and landscape composition on wasps, bees, and their enemies. *Oecologia* **165**, 713–721 (2011).
279. Schüepp, C., Rittiner, S. & Entling, M. H. High bee and wasp diversity in a heterogeneous tropical farming system compared to protected forest. *PLoS ONE* **7**, (2012).
280. Scott, D. M. *et al.* The impacts of forest clearance on lizard, small mammal and bird communities in the arid spiny forest, southern Madagascar. *Biol. Conserv.* **127**, 72–87 (2006).
281. Sedlock, J. L. *et al.* Bat diversity in tropical forest and agro-pastoral habitats within a protected area in the Philippines. *Acta Chiropt.* **10**, 349–358 (2008).
282. Shafie, N. J., Sah, S. A. M., Latip, N. S. A., Azman, N. M. & Khairuddin, N. L. Diversity pattern of bats at two contrasting habitat types along Kerian River, Perak, Malaysia. *Trop. Life Sci. Res.* **22**, 13–22 (2011).
283. Shahabuddin, G. & Kumar, R. Effects of extractive disturbance on bird assemblages, vegetation structure and floristics in tropical scrub forest, Sariska Tiger Reserve, India. *For. Ecol. Manage.* **246**, 175–185 (2007).
284. Sheil, D. *et al.* *Exploring biological diversity, environment and local people's perspectives in forest landscapes: Methods for a multidisciplinary landscape assessment*. (Center for International Forestry Research (CIFOR), Jakarta, 2002).
285. Sheldon, F., Styring, A. & Hosner, P. Bird species richness in a Bornean exotic tree plantation: a long-term perspective. *Biol. Conserv.* **143**, 399–407 (2010).
286. Shuler, R. E., Roulston, T. H. & Farris, G. E. Farming practices influence wild pollinator populations on squash and pumpkin. *J. Econ. Entomol.* **98**, 790–795 (2005).
287. Silva, F. A. B., Costa, C. M. Q., Moura, R. C. & Farias, A. I. Study of the dung beetle (Coleoptera: Scarabaeidae) community at two sites: atlantic forest and clear-cut, Pernambuco, Brazil. *Environ. Entomol.* **39**, 359–367 (2010).
288. da Silva, P. G. *Espécies de Scarabaeinae (Coleoptera: Scarabaeidae) de fragmentos florestais com diferentes níveis de alteração em Santa Maria, Rio Grande do Sul*. MSc thesis, Universidade Federal de Santa Maria, (2011).
289. Slade, E. M., Mann, D. J. & Lewis, O. T. Biodiversity and ecosystem function of tropical forest dung beetles under contrasting logging regimes. *Biol. Conserv.* **144**, 166–174 (2011).
290. Smith-Pardo, A. & Gonzalez, V. H. Bee diversity (Hymenoptera: Apoidea) in a tropical rainforest succession. *Acta Biologica Colombiana* **12**, 43–55 (2007).
291. Sodhi, N. S. *et al.* Deforestation and avian extinction on tropical landbridge islands. *Conserv. Biol.* **24**, 1290–1298 (2010).
292. Sosa, R. A., Benz, V. A., Galea, J. M. & Poggio Herrero, I. V. *Efecto del grado de disturbio sobre el ensamble de aves en la reserva provincial Parque Luro, La Pampa, Argentina*. *Revista de la Asociación Argentina de Ecología de Paisajes* **1**, 101–110 (2010).
293. de Souza, V. M., de Souza, B. & Morato, E. F. Effect of the forest succession on the anurans (Amphibia: Anura) of the Reserve Catuaba and its periphery, Acre, southwestern Amazonia. *Revista Brasileira De Zoologia* **25**, 49–57 (2008).
294. Sridhar, H., Raman, T. R. S. & Mudappa, D. Mammal persistence and abundance in tropical rainforest remnants in the southern Western Ghats, India. *Curr. Sci.* **94**, 748–757 (2008).
295. St-Laurent, M. H., Ferron, J., Hins, C. & Gagnon, R. Effects of stand structure and landscape characteristics on habitat use by birds and small mammals in managed boreal forest of eastern Canada. *Can. J. For. Res.* **37**, 1298–1309 (2007).
296. Ström, L., Hylander, K. & Dynesius, M. Different long-term and short-term responses of land snails to clear-cutting of boreal stream-side forests. *Biol. Conserv.* **142**, 1580–1587 (2009).
297. Struebig, M. J., Kingston, T., Zubaid, A., Mohd-Adnan, A. & Rossiter, S. J. Conservation value of forest fragments to Palaeotropical bats. *Biol. Conserv.* **141**, 2112–2126 (2008).
298. Su, Z. M., Zhang, R. Z. & Qiu, J. X. Decline in the diversity of willow trunk-dwelling weevils (Coleoptera: Curculionoidea) as a result of urban expansion in Beijing, China. *J. Insect Conserv.* **15**, 367–377 (2011).
299. Sugiura, S., Tsuru, T., Yamaura, Y. & Makihara, H. Small off-shore islands can serve as important refuges for endemic beetle conservation. *J. Insect Conserv.* **13**, 377–385 (2009).
300. Summerville, K. S. Managing the forest for more than the trees: effects of experimental timber harvest on forest Lepidoptera. *Ecol. Appl.* **21**, 806–816 (2011).
301. Summerville, K. S., Conoan, C. J. & Steichen, R. M. Species traits as predictors of Lepidopteran composition in restored and remnant tallgrass prairies. *Ecol. Appl.* **16**, 891–900 (2006).
302. Sung, Y. H., Karraker, N. E. & Hau, B. C. H. Terrestrial herpetofaunal assemblages in secondary forests and exotic *Lophostemon confertus* plantations in South China. *For. Ecol. Manage.* **270**, 71–77 (2012).
303. Threlfall, C. G., Law, B. & Banks, P. B. Sensitivity of insectivorous bats to urbanization: implications for suburban conservation planning. *Biol. Conserv.* **146**, 41–52 (2012).
304. Tonietto, R., Fant, J., Ascher, J., Ellis, K. & Larkin, D. A comparison of bee communities of Chicago green roofs, parks and prairies. *Landsc. Urban Plan.* **103**, 102–108 (2011).
305. Turner, E. C. & Foster, W. A. The impact of forest conversion to oil palm on arthropod abundance and biomass in Sabah, Malaysia. *J. Trop. Ecol.* **25**, 23–30 (2009).
306. Tylanakis, J. M., Klein, A. M. & Tschamtker, T. Spatiotemporal variation in the diversity of hymenoptera across a tropical habitat gradient. *Ecology* **86**, 3296–3302 (2005).
307. Vanbergen, A. J., Woodcock, B. A., Watt, A. D. & Niemela, J. Effect of land-use heterogeneity on carabid communities at the landscape scale. *Ecography* **28**, 3–16 (2005).
308. Vassilev, K., Pedashenko, H., Nikolov, S. C., Apostolova, I. & Dengler, J. Effect of land abandonment on the vegetation of upland semi-natural grasslands in the Western Balkan Mts. Bulgaria. *Plant Biosyst.* **145**, 654–665 (2011).
309. Vázquez, D. P. & Simberloff, D. Ecological specialization and susceptibility to disturbance: conjectures and refutations. *Am. Nat.* **159**, 606–623 (2002).
310. Verboven, H. A. F., Brys, R. & Hermys, M. Sex in the city: reproductive success of *Digitalis purpurea* in a gradient from urban to rural sites. *Landsc. Urban Plan.* **106**, 158–164 (2012).
311. Verdasca, M. J. *et al.* Forest fuel management as a conservation tool for early successional species under agricultural abandonment: The case of Mediterranean butterflies. *Biol. Conserv.* **146**, 14–23 (2012).
312. Verdú, J. R. *et al.* Grazing promotes dung beetle diversity in the xeric landscape of a Mexican Biosphere Reserve. *Biol. Conserv.* **140**, 308–317 (2007).
313. Vergara, C. H. & Badano, E. I. Pollinator diversity increases fruit production in Mexican coffee plantations: the importance of rustic management systems. *Agric. Ecosyst. Environ.* **129**, 117–123 (2009).
314. Vergara, P. M. & Simonetti, J. A. Avian responses to fragmentation of the Maulino Forest in central Chile. *Oryx* **38**, 383–388 (2004).
315. Walker, T. R., Crittenden, P. D., Young, S. D. & Prystina, T. An assessment of pollution impacts due to the oil and gas industries in the Pechora basin, north-eastern European Russia. *Ecol. Indic.* **6**, 369–387 (2006).
316. Wang, Y., Bao, Y., Yu, M., Xu, G. & Ding, P. Nestedness for different reasons: the distributions of birds, lizards and small mammals on islands of an inundated lake. *Divers. Distrib.* **16**, 862–873 (2010).
317. Watling, J. I., Gerow, K. & Donnelly, M. A. Nested species subsets of amphibians and reptiles on Neotropical forest islands. *Anim. Conserv.* **12**, 467–476 (2009).
318. Weller, B. & Ganzhorn, J. U. Carabid beetle community composition, body size, and fluctuating asymmetry along an urban-rural gradient. *Basic Appl. Ecol.* **5**, 193–201 (2004).
319. Wells, K., Kalko, E. K. V., Lakim, M. B. & Pfeiffer, M. Effects of rain forest logging on species richness and assemblage composition of small mammals in Southeast Asia. *J. Biogeogr.* **34**, 1087–1099 (2007).
320. Williams, C. D., Sheahan, J. & Gormally, M. J. Hydrology and management of turloughs (temporary lakes) affect marsh fly (Sciomyzidae: Diptera) communities. *Insect Conserv. Divers.* **2**, 270–283 (2009).
321. Willig, M. R. *et al.* Phyllostomid bats of lowland Amazonia: effects of habitat alteration on abundance. *Biotropica* **39**, 737–746 (2007).
322. Winfree, R., Griswold, T. & Kremen, C. Effect of human disturbance on bee communities in a forested ecosystem. *Conserv. Biol.* **21**, 213–223 (2007).
323. Woinarski, J. C. Z. *et al.* Fauna assemblages in regrowth vegetation in tropical open forests of the Northern Territory, Australia. *Wildl. Res.* **36**, 675–690 (2009).
324. Woodcock, B. A. *et al.* The potential of grass field margin management for enhancing beetle diversity in intensive livestock farms. *J. Appl. Ecol.* **44**, 60–69 (2007).

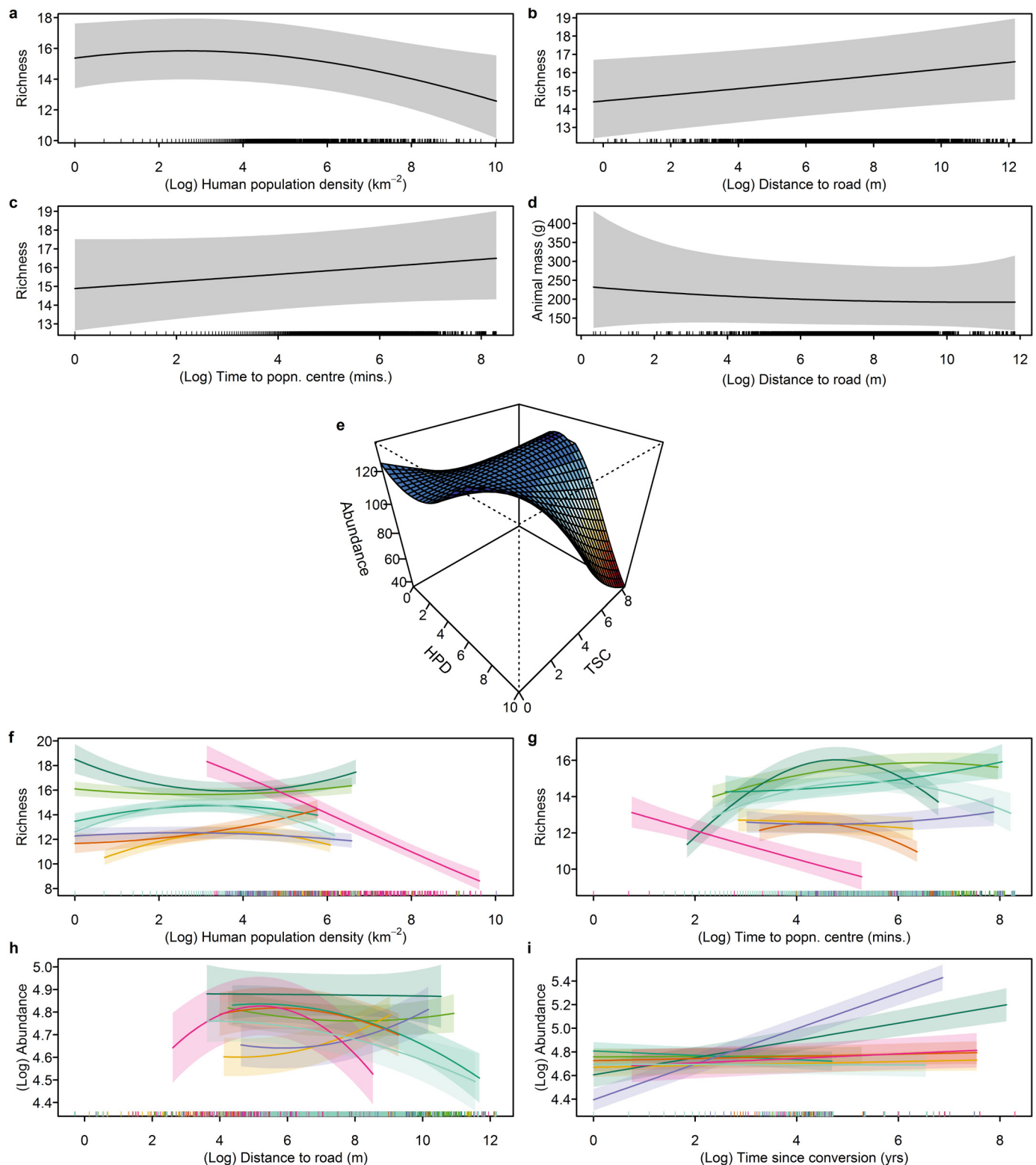
325. Wunderle, J. M., Henriques, L. M. P. & Willig, M. R. Short-term responses of birds to forest gaps and understory: an assessment of reduced-impact logging in a lowland Amazon forest. *Biotropica* **38**, 235–255 (2006).
326. Yoshikura, S., Yasui, S. & Kamijo, T. Comparative study of forest-dwelling bats' abundances and species richness between old-growth forests and conifer plantations in Nikko National Park, central Japan. *Mammal Study* **36**, 189–198 (2011).
327. Zaitsev, A. S., Chauvat, M., Pflug, A. & Wolters, V. Oribatid mite diversity and community dynamics in a spruce chronosequence. *Soil Biol. Biochem.* **34**, 1919–1927 (2002).
328. Zaitsev, A. S., Wolters, V., Waldhardt, R. & Dauber, J. Long-term succession of oribatid mites after conversion of croplands to grasslands. *Appl. Soil Ecol.* **34**, 230–239 (2006).
329. Zimmerman, G., Bell, F. W., Woodcock, J., Palmer, A. & Paloniemi, J. Response of breeding songbirds to vegetation management in conifer plantations established in boreal mixedwoods. *For. Chron.* **87**, 217–224 (2011).
330. Roskov, Y. et al. *Species 2000 & ITIS Catalogue of Life, 2013 Annual Checklist*. <http://catalogueoflife.org/annual-checklist/2013/> (2013).
331. Gotelli, N. J. & Colwell, R. K. Quantifying biodiversity: procedures and pitfalls in the measurement and comparison of species richness. *Ecol. Lett.* **4**, 379–391 (2001).
332. Violle, C. et al. Let the concept of trait be functional! *Oikos* **116**, 882–892 (2007).
333. Kattge, J. et al. TRY – a global database of plant traits. *Glob. Change Biol.* **17**, 2905–2935 (2011).
334. Jones, K. E. et al. PanTHERIA: a species-level database of life history, ecology, and geography of extant and recently extinct mammals. *Ecology* **90**, 2648 (2009).
335. Cooper, N., Bielby, J., Thomas, G. H. & Purvis, A. Macroecology and extinction risk correlates of frogs. *Glob. Ecol. Biogeogr.* **17**, 211–221 (2008).
336. AmphibiaWeb. <http://amphibiaweb.org/> (2013).
337. Sunyer, J., Páiz, G., Dehling, D. M. & Köhler, G. A collection of amphibians from Río San Juan, southeastern Nicaragua. *Herpetol. Notes* **2**, 189–202 (2009).
338. Zug, G. R. & Zug, P. B. The marine toad *Bufo marinus*: a natural history resumé of native populations. *Smithson. Contrib. Zool.* **284**, 1–58 (1979).
339. Amphibians & Reptiles of Peninsular Malaysia. <http://www.amphibia.my/> (2009).
340. Shahriza, S., Ibrahim, H. J. & Shahrul Anuar, M. S. The correlation between total rainfall and breeding parameters of white-lipped frog, *Rana labialis* (Anura: Ranidae) in Kedah, Malaysia. *Trop. Nat. Hist.* **10**, 131–139 (2010).
341. Bain, R. H. & Quang Truong, N. Three new species of narrow-mouth frogs (genus: *Microhyla*) from Indochina, with comments on *Microhyla annamensis* and *Microhyla palmipes*. *Copeia* **2004**, 507–524 (2004).
342. Su, M.-Y., Kam, Y.-C. & Fellers, G. M. Effectiveness of amphibian monitoring techniques in a Taiwanese subtropical forest. *Herpetol. J.* **15**, 73–79 (2005).
343. Matson, T. O. A morphometric comparison of gray treefrogs, *Hyla chrysoscelis* and *H. versicolor*, from Ohio. *Ohio J. Sci.* **90**, 98–101 (1990).
344. Ningombarn, B. & Bordoloi, S. Amphibian fauna of Loktak Lake, Manipur, India with ten new records for the state. *Zoos Print J.* **22**, 2688–2690 (2007).
345. Lance, S. L. & Wells, K. D. Are spring peeper satellite males physiologically inferior to calling males? *Copeia* **1993**, 1162–1166 (1993).
346. Da Silva, E. T., Dos Reis, E. P., Feio, R. N. & Filho, O. P. R. Diet of the invasive frog *Lithobates catesbeianus* (Shaw, 1802) (Anura: Ranidae) in Viçosa, Minas Gerais State, Brazil. *South Am. J. Herpetol.* **4**, 286–294 (2009).
347. Blomquist, S. M. & Hunter, M. L., Jr. A multi-scale assessment of habitat selection and movement patterns by northern leopard frogs (*Lithobates [Rana] pipiens*) in a managed forest. *Herpetol. Conserv. Biol.* **4**, 142–160 (2009).
348. Caramaschi, U. & da Cruz, C. A. G. Redescription of *Chiasmocleis albopunctata* (Boettger) and description of a new species of *Chiasmocleis* (Anura: Microhylidae). *Herpetologica* **53**, 259–268 (1997).
349. Brasileiro, C. A., Sawaya, R. J., Kiefer, M. C. & Martins, M. Amphibians of an open cerrado fragment in southeastern Brazil. *Biota Neotrop.* **5**, BN00405022005 (2005).
350. De Almeida Prado, C. P. *Estratégias reprodutivas em uma comunidade de anuros no pantanal, estado de Mato Grosso do Sul, Brasil*. PhD thesis, Universidade Estadual Paulista, 2003.
351. De Almeida Prado, C. P., Uetanabaro, M. & Lopes, F. S. Reproductive strategies of *Leptodactylus chaquensis* and *L. podicipinus* in the Pantanal, Brazil. *J. Herpetol.* **34**, 135–139 (2000).
352. De Carvalho, T. R., Giaretta, A. A. & Fature, K. G. A new species of *Hypsiboas* Wagler (Anura: Hylidae) closely related to *H. multifasciatus* Günther from southeastern Brazil. *Zootaxa* **2521**, 37–52 (2010).
353. Heyer, W. R. & Heyer, M. M. *Leptodactylus elenae* Heyer. *Cat. Am. Amphib. Reptil.* **742**, 1–5 (2002).
354. Heyer, W. R. Variation within the *Leptodactylus podicipinus-wagneri* complex of frogs (Amphibia: Leptodactylidae). *Smithson. Contrib. Zool.* **546**, (1994).
355. Jungfer, K.-H. & Hödl, W. A new species of *Osteocephalus* from Ecuador and a redescription of *O. lepieurii* (Dumeril & Bibron, 1841) (Anura: Hylidae). *Amphibia-Reptilia* **23**, 21–46 (2002).
356. Fouquet, A., Gaucher, P., Blanc, M. & Velez-Rodriguez, C. M. Description of two new species of *Rhinella* (Anura: Bufonidae) from the lowlands of the Guiana shield. *Zootaxa* **1663**, 17–32 (2007).
357. Lynch, J. D. A review of the leptodactylid frogs of the genus *Pseudopaludicola* in Northern South America. *Copeia* **1989**, 577–588 (1989).
358. González, C. E. & Hamann, M. I. Nematode parasites of two anuran species *Rhinella schneideri* (Bufonidae) and *Scinax acuminatus* (Hylidae) from Corrientes, Argentina. *Rev. Biol. Trop.* **56**, 2147–2161 (2008).
359. Pombal, J. P., Jr, Bilate, M., Gambale, P. G., Signorelli, L. & Bastos, R. P. A new miniature treefrog of the *Scinax ruber* clade from the cerrado of central Brazil (Anura: Hylidae). *Herpetologica* **67**, 288–299 (2011).
360. Ibáñez, R., Jaramillo, C. A. & Solís, F. A. Description of the advertisement call of a species without vocal sac: *Craugastor gollmeri* (Amphibia: Craugastoridae). *Zootaxa* **3184**, 67–68 (2012).
361. Hertz, A., Hauenschild, F., Lotzkat, S. & Köhler, G. A new golden frog species of the genus *Diasporus* (Amphibia, Eleutherodactylidae) from the Cordillera Central, western Panama. *Zookeys* **196**, 23–46 (2012).
362. Goldberg, S. R. & Bursey, C. R. Helminths from fifteen species of frogs (Anura, Hylidae) from Costa Rica. *Phyllomedusa* **7**, 25–33 (2008).
363. Bennett, W. O., Summers, A. P. & Brainerd, E. L. Confirmation of the passive exhalation hypothesis for a terrestrial caecilian, *Dermophis mexicanus*. *Copeia* **1999**, 206–209 (1999).
364. Anderson, M. T. & Mathis, A. Diets of two sympatric Neotropical salamanders, *Bolitoglossa mexicana* and *B. rufescens*, with notes on reproduction for *B. rufescens*. *J. Herpetol.* **33**, 601–607 (1999).
365. McCranie, J. R. & Wilson, L. D. Taxonomic changes associated with the names *Hyla spinipollex* Schmidt and *Ptychohyla merazi* Wilson and McCranie (Anura: Hylidae). *Southwest. Nat.* **38**, 100–104 (1993).
366. Barrio-Amorós, C. L., Guayasamin, J. M. & Hedges, S. B. A new minute Andean *Pristimantis* (Anura: Strabomantidae) from Venezuela. *Phyllomedusa* **11**, 83–93 (2012).
367. Arroyo, S. B., Serrano-Cardozo, V. H. & Ramírez-Pinilla, M. P. Diet, microhabitat and time of activity in a *Pristimantis* (Anura, Strabomantidae) assemblage. *Phyllomedusa* **7**, 109–119 (2008).
368. Savage, J. M. & Myers, C. Frogs of the *Eleutherodactylus biporcatus* group (Leptodactylidae) of Central America and northern South America, including rediscovered, resurrected, and new taxa. *Am. Mus. Novit.* **3357**, 1–48 (2002).
369. Simões, P. I. *Diversificação do complexo Allobates femoralis* (Anura, Dendrobatidae) em florestas da Amazônia brasileira: desvendando padrões atuais e históricos. PhD thesis, Instituto Nacional de Pesquisas da Amazônia, 2010.
370. Guayasamin, J. M., Ron, S. R., Cisneros-Heredia, D. F., Lamar, W. & McCracken, S. F. A new species of frog of the *Eleutherodactylus lacrimosus* assemblage (Leptodactylidae) from the western Amazon Basin, with comments on the utility of canopy surveys in lowland rainforest. *Herpetologica* **62**, 191–202 (2006).
371. Jared, C., Antoniazzi, M. M., Verdade, V. K. & Toledo, L. F. The Amazonian toad *Rhaebo guttatus* is able to voluntarily squirt poison from the paratoid macroglands. *Amphibia-Reptilia* **32**, 546–549 (2011).
372. Wollenberg, K. C., Veith, M., Noonan, B. P. & Lötters, S. Polymorphism versus species richness—systematics of large *Dendrobates* from the eastern Guiana Shield (Amphibia: Dendrobatidae). *Copeia* **2006**, 623–629 (2006).
373. Shepard, D. B. & Caldwell, J. P. From foam to free-living: ecology of larval *Leptodactylus labyrinthicus*. *Copeia* **2005**, 803–811 (2005).
374. Heyer, W. R., García-Lopez, J. M. & Cardoso, A. J. Advertisement call variation in the *Leptodactylus mystaceus* species complex (Amphibia: Leptodactylidae) with a description of a new sibling species. *Amphibia-Reptilia* **17**, 7–31 (1996).
375. Zimmermann, B. L. A comparison of structural features of calls of open and forest habitat frog species in the central Amazon. *Herpetologica* **39**, 235–246 (1983).
376. Bernarde, P. S. & Kokubum, M. N. D. C. Seasonality, age structure and reproduction of *Leptodactylus (Lithodytes) lineatus* (Anura, Leptodactylidae) in Rondônia state, southwestern Amazon, Brazil. *Iheringia Série Zool.* **99**, 368–372 (2009).
377. Campbell, J. A. & Clarke, B. T. A review of frogs of the genus *Otophryne* (Microhylidae) with the description of a new species. *Herpetologica* **54**, 301–317 (1998).
378. Kan, F. W. *Population dynamics, diet and morphological variation of the Hong Kong newt (Paramesotriton hongkongensis)*. MPhil thesis, The University of Hong Kong, 2010.
379. Stuart, B. L., Chuaynkern, Y., Chan-ard, T. & Inger, R. F. Three new species of frogs and a new tadpole from eastern Thailand. *Fieldiana Zool. New Ser.* **111**, 1–19 (2006).
380. Ao, J. M., Bordoloi, S. & Ohler, A. Amphibian fauna of Nagaland with nineteen new records from the state including five new records for India. *Zoos Print J.* **18**, 1117–1125 (2003).
381. Ohler, A. et al. Sorting out *Lalos*: description of new species and additional taxonomic data on megophryid frogs from northern Indochina (genus *Leptolalax*, Megophryidae, Anura). *Zootaxa* **3147**, 1–83 (2011).
382. Meiri, S. Evolution and ecology of lizard body sizes. *Glob. Ecol. Biogeogr.* **17**, 724–734 (2008).
383. Itescu, Y., Karraker, N. E., Raia, P., Pritchard, P. C. H. & Meiri, S. Is the island rule general? Turtles disagree. *Glob. Ecol. Biogeogr.* **23**, 689–700 (2014).
384. Meiri, S. Length-weight allometries in lizards. *J. Zool. (Lond.)* **281**, 218–226 (2010).
385. Feldman, A. & Meiri, S. Length-mass allometry in snakes. *Biol. J. Linn. Soc.* **108**, 161–172 (2013).
386. Edgar, M. *What can we learn from body length? A study in Coleoptera*. MRes thesis, Imperial College London, 2014.
387. Gilbert, F., Rotheray, G. E., Zafar, R. & Emerson, P. in *Phylogenetics Ecol.* 324–343 (Academic Press, 1994).
388. ESRI. ArcGIS Desktop: Release 10. (Environmental Systems Research Institute, 2011).
389. Klein Goldewijk, K., Beusen, A., Van Dreht, G. & De Vos, M. The HYDE 3.1 spatially explicit database of human-induced global land-use change over the past 12,000 years. *Glob. Ecol. Biogeogr.* **20**, 773–786 (2011).
390. R Core Team. *R: A Language and Environment for Statistical Computing*. <http://www.r-project.org> (R Foundation for Statistical Computing, 2013).

391. Zuur, A. F., Ieno, E. N., Walker, N. J., Saveliev, A. A. & Smith, G. M. *Mixed Effects Models and Extensions in Ecology with R*. (Springer, 2009).
392. Rigby, R. A., Stasinopoulos, D. M. & Akantziliotou, C. A framework for modelling overdispersed count data, including the Poisson-shifted generalized inverse Gaussian distribution. *Comput. Stat. Data Anal.* **53**, 381–393 (2008).
393. Bivand, R. spdep: spatial dependence: weighting schemes, statistics and models. R Package Version 0.5-68. <http://cran.r-project.org/web/packages/spdep> (2013).
394. Møller, A. P. & Jennions, M. D. Testing and adjusting for publication bias. *Trends Ecol. Evol.* **16**, 580–586 (2001).
395. van Vuuren, D. P. *et al.* The representative concentration pathways: an overview. *Clim. Change* **109**, 5–31 (2011).
396. United Nations Population Division. World Population Prospects: The 2010 Revision Population Database. <http://www.un.org/esa/population/> (2011).
397. van Asselen, S. & Verburg, P. H. Land cover change or land-use intensification: simulating land system change with a global-scale land change model. *Glob. Chang. Biol.* **19**, 3648–3667 (2013).
398. Haberl, H. *et al.* Quantifying and mapping the human appropriation of net primary production in earth's terrestrial ecosystems. *Proc. Natl Acad. Sci. USA* **104**, 12942–12947 (2007).
399. Hijmans, R. J. raster: Geographic data analysis and modeling. <http://cran.r-project.org/package=raster> (2014).
400. Olson, D. M. *et al.* Terrestrial ecoregions of the world: a new map of life on Earth. *Bioscience* **51**, 933–938 (2001).



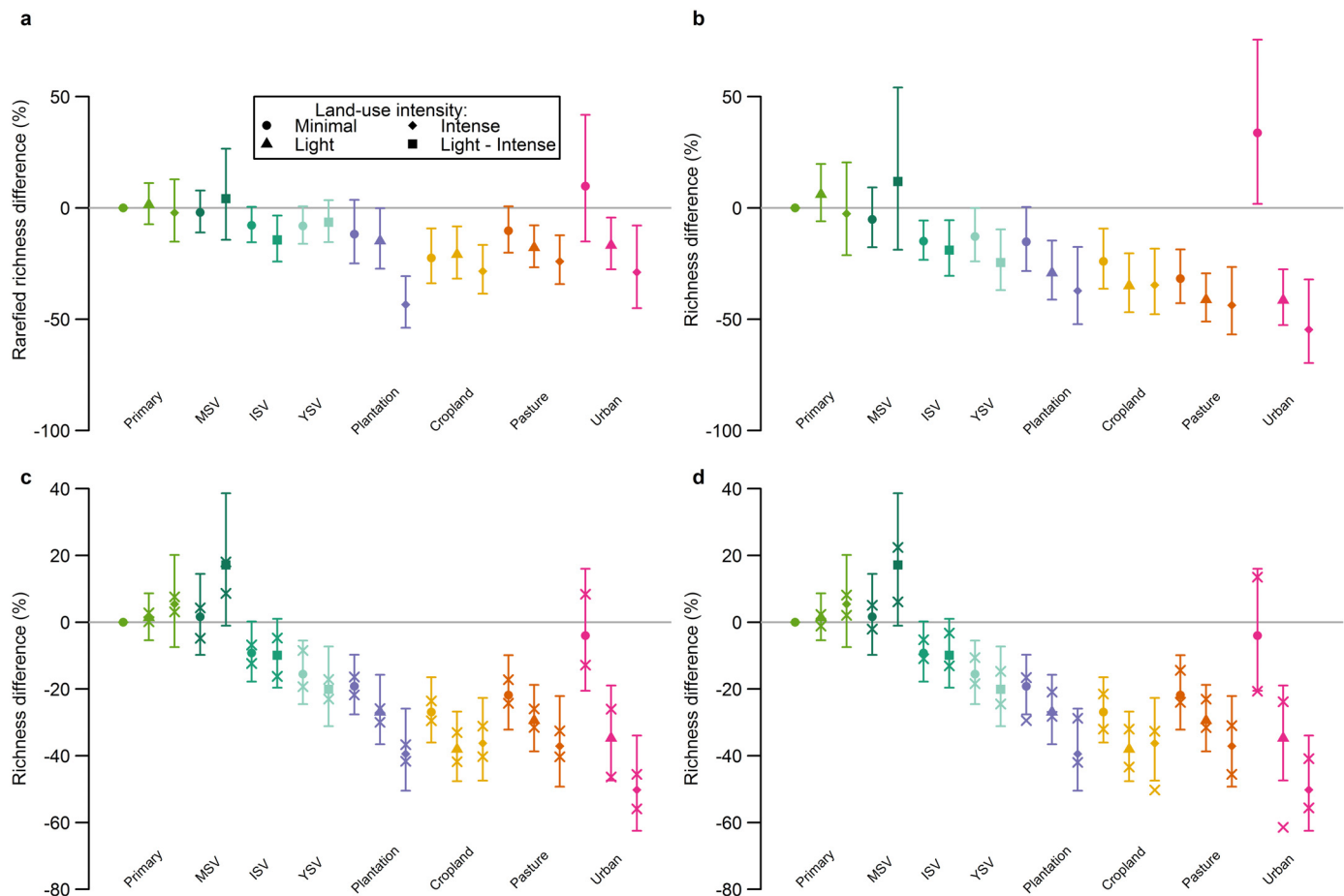
Extended Data Figure 1 | Taxonomic and geographic representativeness of the data set used. **a**, The relationship between the number of species represented in our data and the number estimated to have been described¹⁷ for 47 major taxonomic groups. Lines show (from bottom to top) 0.1%, 1% and 10% representation of described species in our data set; magenta, invertebrates; red, vertebrates; green, plants; blue, fungi; and grey, all other taxonomic groups. **b**, The relationship across biomes⁴⁰⁰ between the percentage of global terrestrial net primary production and the number of sites in our data set; A, tundra; B, boreal forests and taiga; C, temperate conifer forests; D, temperate

broadleaf and mixed forests; E, montane grasslands and shrublands; F, temperate grasslands, savannahs and shrublands; G, Mediterranean forests, woodlands and scrub; H, deserts and xeric shrublands; J, tropical and subtropical grasslands, savannahs and shrublands; K, tropical and subtropical coniferous forests; M, tropical and subtropical dry broadleaf forests; N, tropical and subtropical moist broadleaf forests; P, mangroves; note that the flooded grasslands and savannah biome is not represented in the data set; grey line shows a 1:1 relationship.



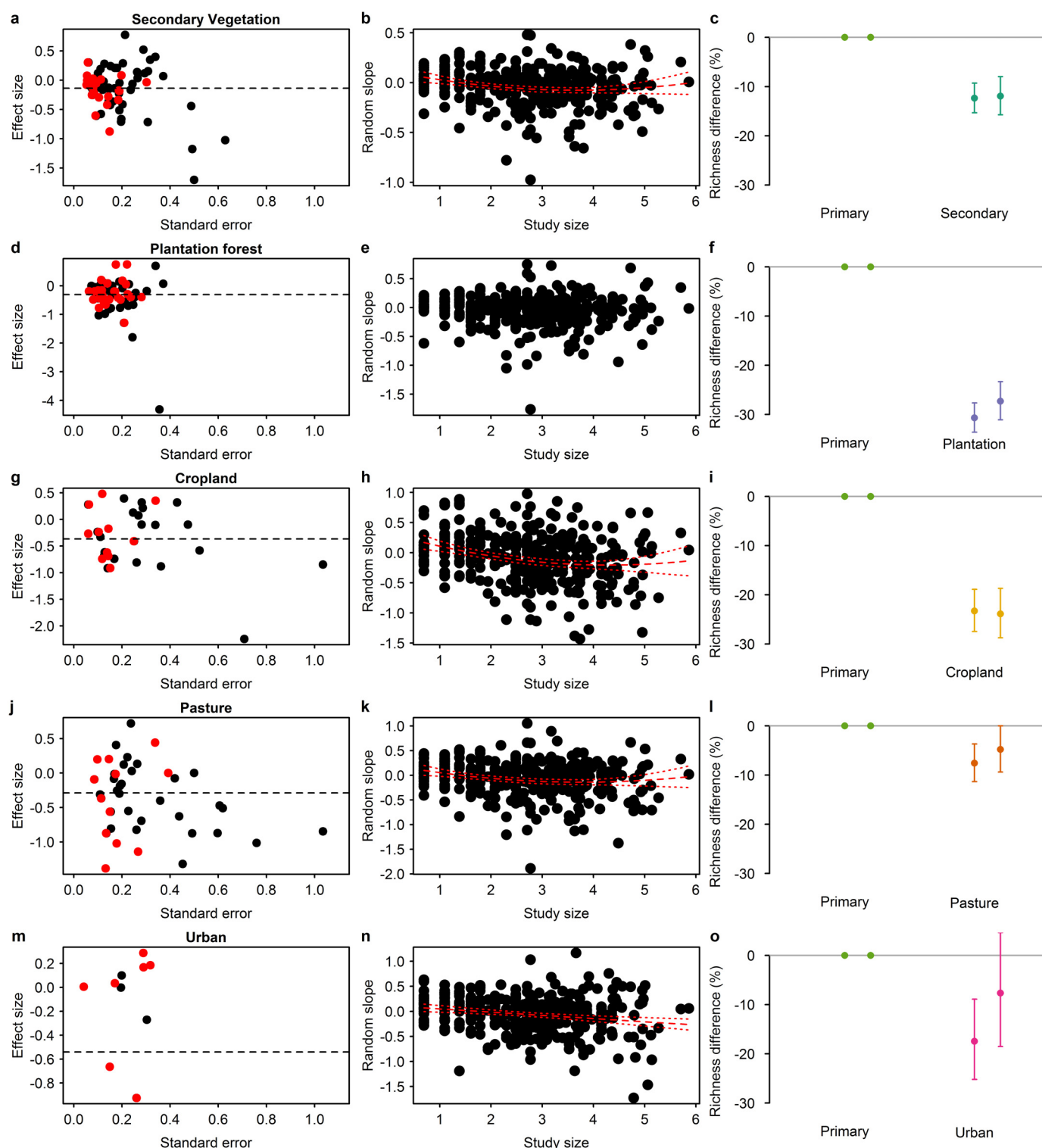
Extended Data Figure 2 | Detailed response of local diversity to human pressures. **a–i**, Modelled effects (controlling for land use and land-use intensity) of human population density (HPD), distance to nearest road, time since 30% conversion of a landscape to human uses (TSC) and time to nearest population centre with greater than 50,000 inhabitants (**a–d**), interactions between pairs of these variables (**e**), and interactions between the variables and land use (**f–i**) on site-level diversity. **a–c**, **f**, **g**, Within-sample species richness; **e**, **h**, **i**, total abundance; and **d**, community-weighted mean vertebrate body mass. Shaded polygons in **a–d** show 95% confidence intervals. For clarity,

shaded polygons in **f–i** are shown as $\pm 0.5 \times \text{s.e.m.}$ Confidence intervals in **e** are omitted. Rugs along the *x* axes in the line graphs show the values of the explanatory variables represented in the data set used for modelling. Only significant effects are shown. Note that distance to nearest road and travel time to major population centre measures are the raw (log-transformed) values fitted in the models rather than the proximity to roads and accessibility values (obtained as 1 minus the former values) presented in Fig. 1. Sample sizes are given in full in the Methods.



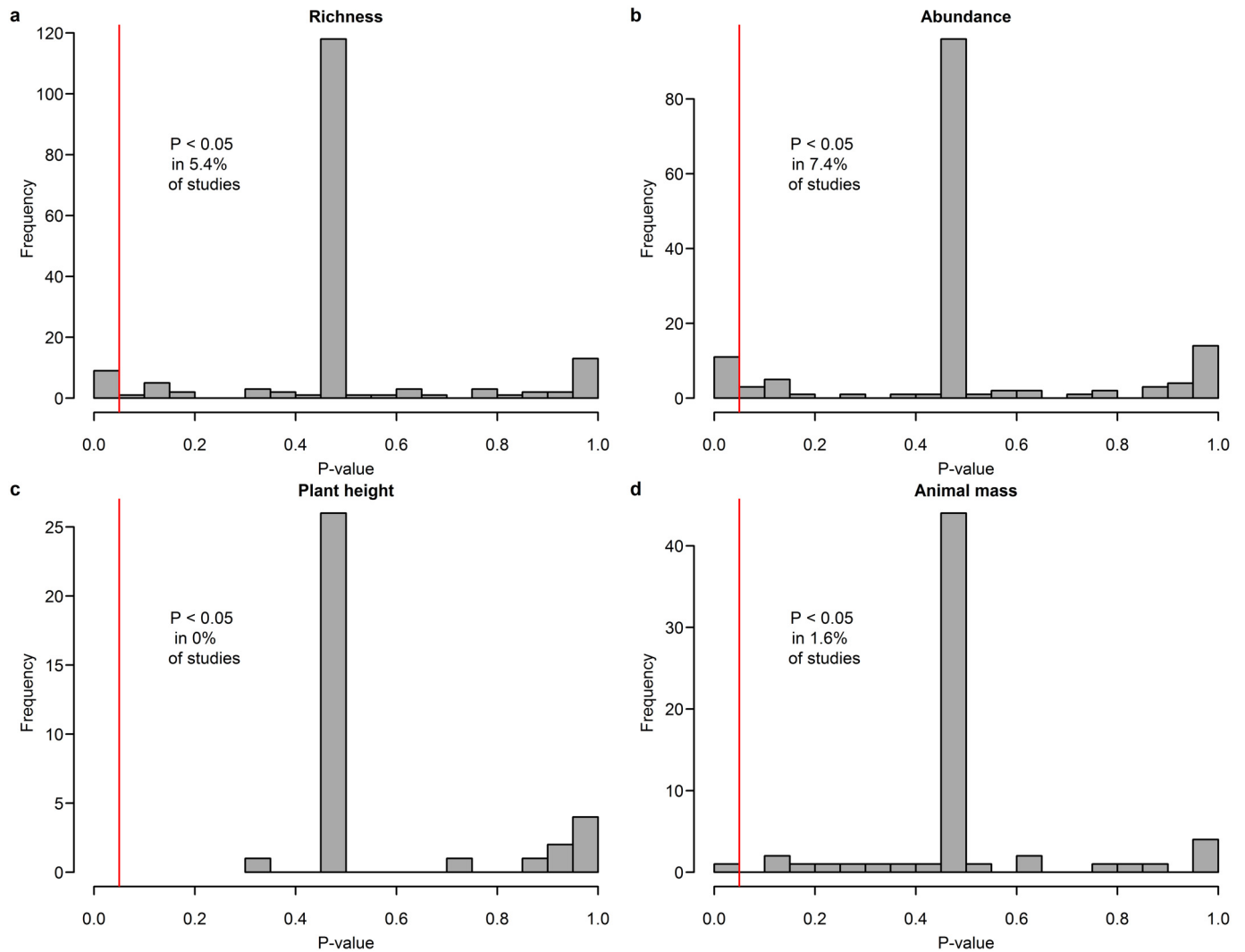
Extended Data Figure 3 | Robustness of modelled effects of human pressures. **a**, Effects of land use and land-use intensity on rarefaction-based species richness. **b**, To test that any differences between these results and the results for within-sample species richness presented in the main manuscript were not because rarefied species richness could only be calculated with a smaller data set, we also show modelled effects on within-sample species richness with the same reduced data set. **c**, **d**, Cross-validated robustness of

coefficient estimates for land use and land-use intensity. Crosses show 95% confidence intervals around the coefficient estimates under tenfold cross-validation, excluding data from approximately 10% of studies at a time (**c**), and under geographical cross-validation, excluding data from one biome at a time (**d**); colours, points, error bars and land-use labels are as in Fig. 1 in the main text. Sample sizes are given in full in the Methods.



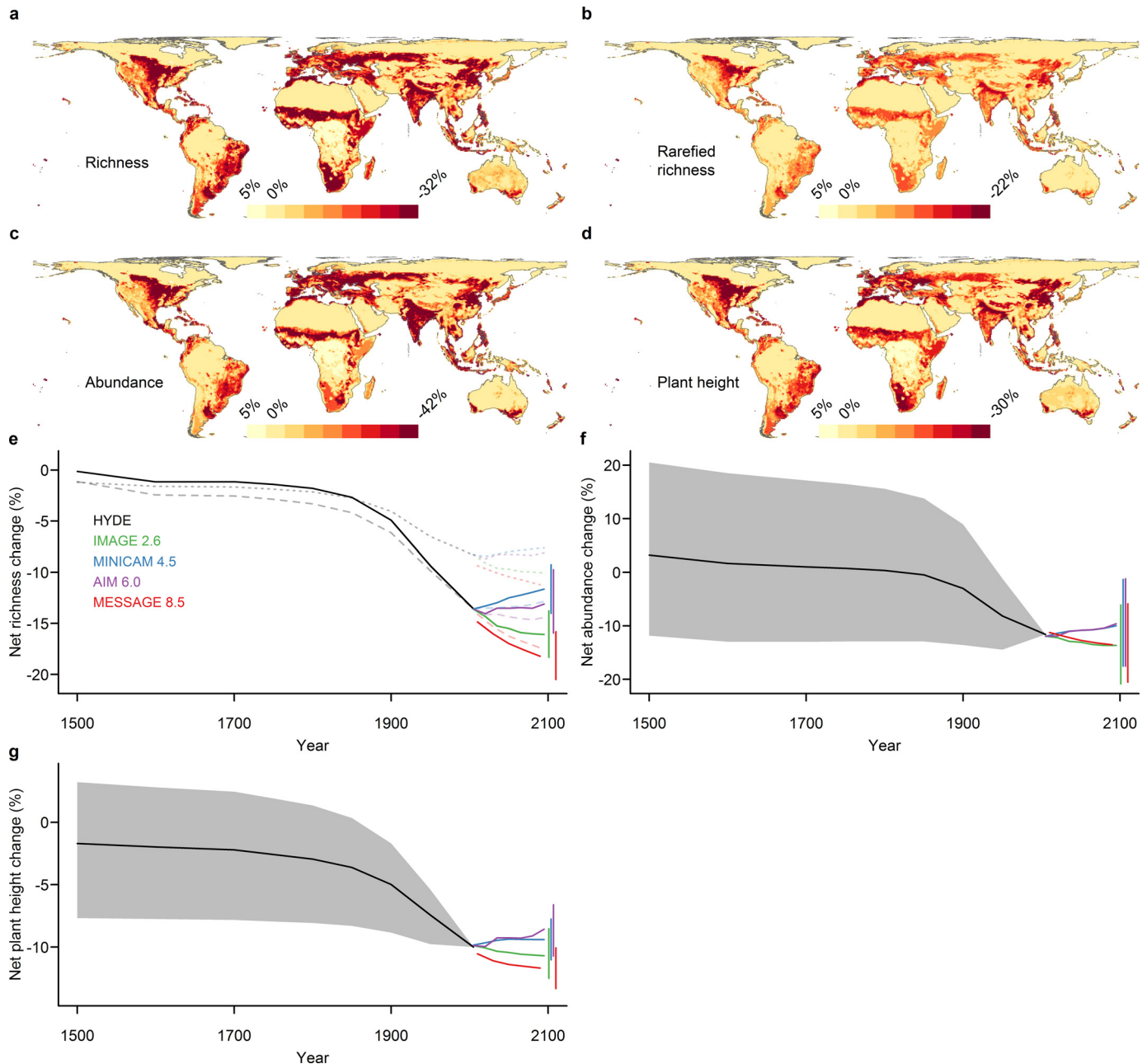
Extended Data Figure 4 | Tests of the potential for publication bias to influence the richness models and projections. Left-hand panels (a, d, g, j, m) show funnel plots of the relationship between the standard error around coefficient estimates (inversely related to the size of studies) and the coefficient estimates themselves for each coarse land-use type; there is evidence for publication bias with respect to some of the land-use types, as indicated by an absence of points on one or other side of zero for studies with large standard errors (but note that small studies are down-weighted in the model). Red points show studies with more than five sites in the land use in question (ten for secondary vegetation and plantation forest because there were more sites for these land uses and some studies with between five and ten sites showed variable responses); horizontal dashed lines show the modelled coefficients for each land use. Central panels (b, e, h, k, n) show the relationship between study

size (log-transformed total number of sites) and the random slope of the land use in question with respect to study identity, from a random-slopes-and-intercepts model. Where a significant relationship was detected using a linear model, fitted values and 95% confidence intervals are shown as a red dashed line and red dotted lines, respectively. Conversely to what would be expected if publication bias was present, where significant relationships between study size and random slopes were detected, these were negative (that is, larger studies detected more negative effects). Right-hand panels (c, f, i, l, o) show the robustness of modelled coefficients to removal of studies with few sites in a given land use (black points in the left-hand panels). Left-hand error bars show coefficient estimates for all studies and right-hand error bars show coefficient estimates for studies with more than five sites in that land use (ten for secondary vegetation and plantation forest).



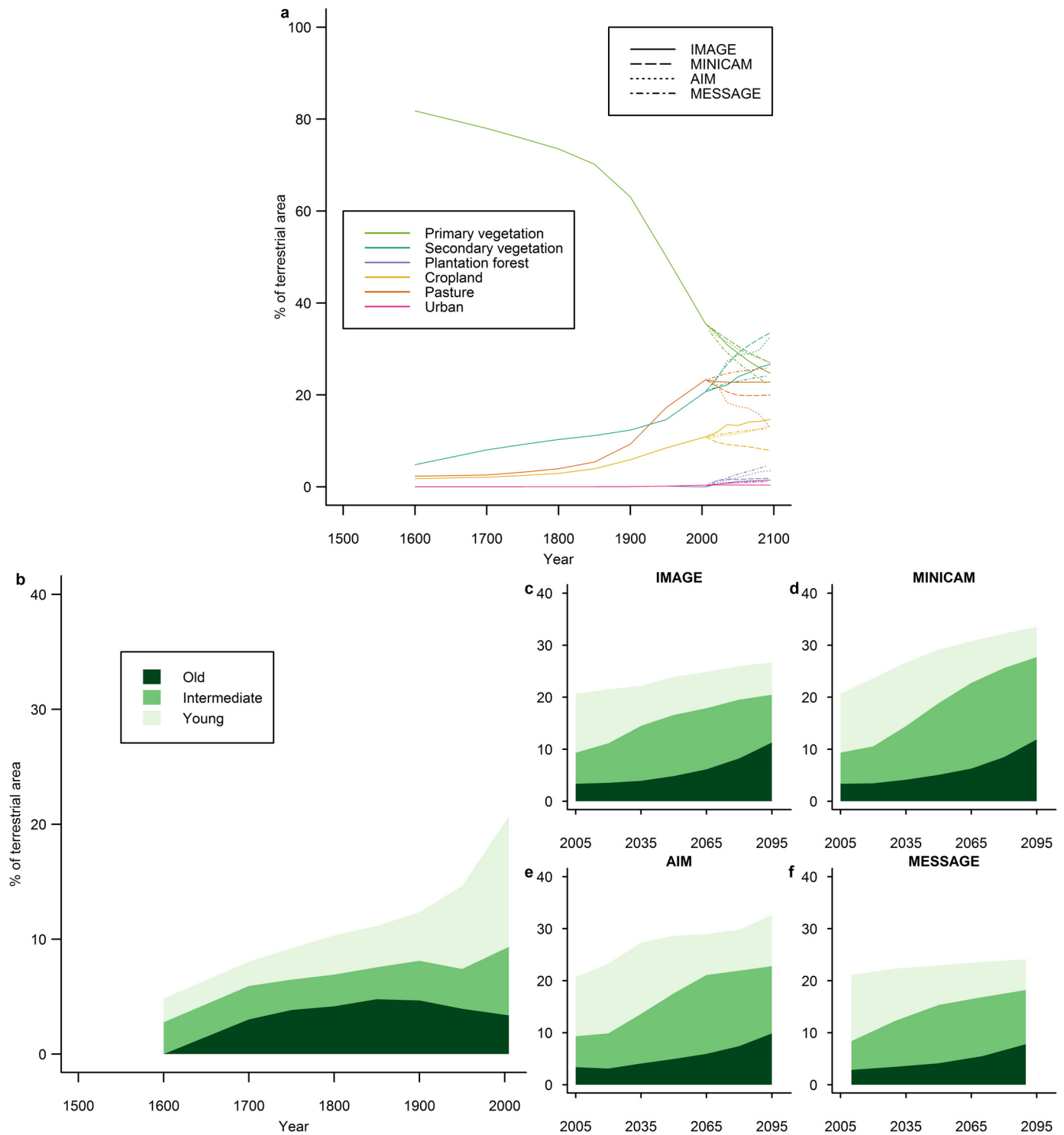
Extended Data Figure 5 | Tests for spatial autocorrelation in the model residuals. **a–d**, For the four main modelled metrics of site-level diversity—within-sample species richness (**a**), total abundance (**b**), community-weighted mean plant-height (**c**) and community-weighted mean animal mass

(**d**)—histograms of P values from sets of Moran's tests for spatial autocorrelation in the residuals of the best models for individual studies are shown. The percentage of studies with significant spatial autocorrelation ($P < 0.05$; indicated by a vertical red line) is shown.

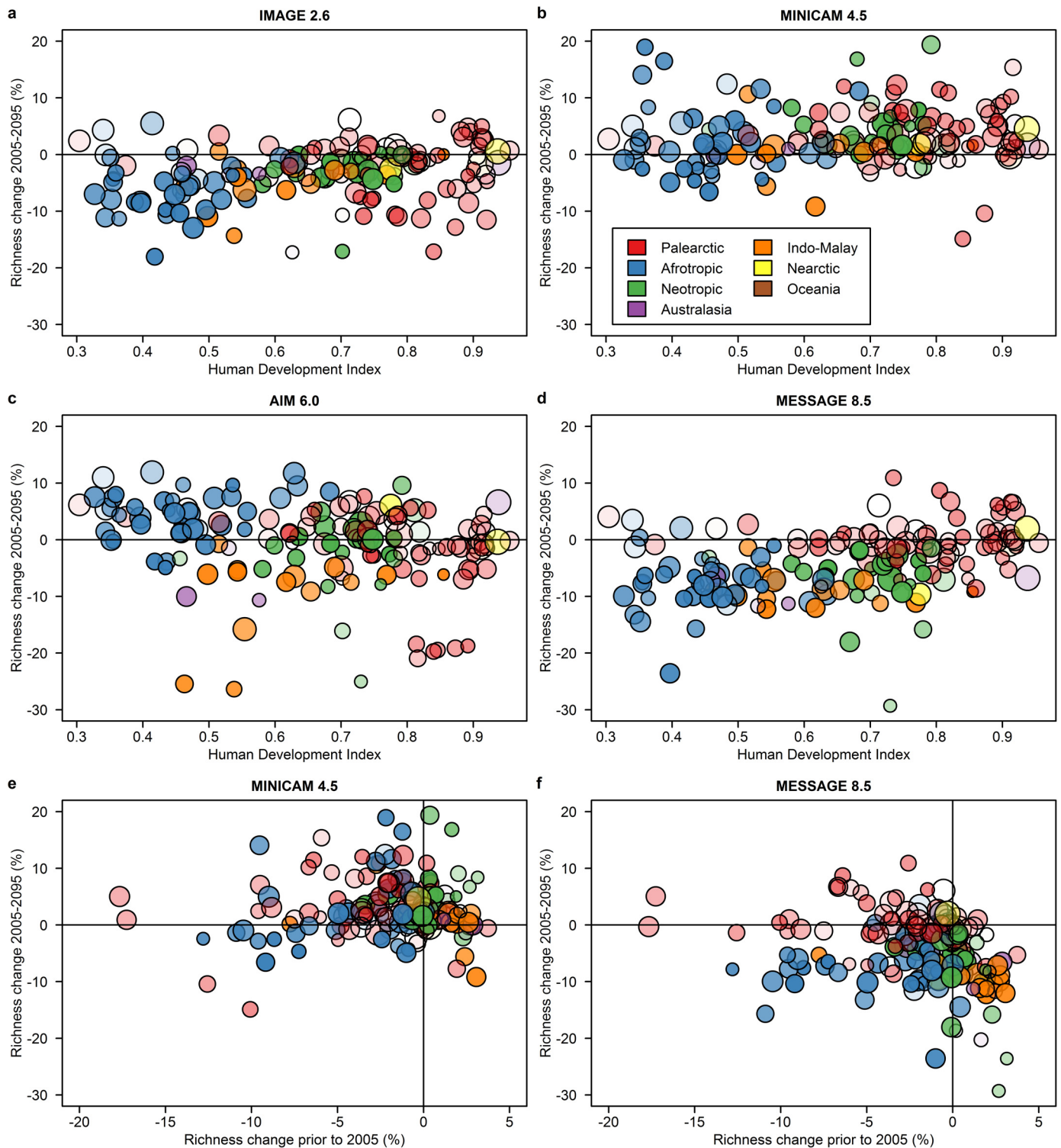


Extended Data Figure 6 | Current, past and future projections of all metrics of local biodiversity. **a–d**, Net change in local diversity caused by land use and related pressures by 2000 under an IMAGE reference scenario¹⁰. Changes in richness (**a**), rarefied richness (**b**), total abundance (**c**) and community-weighted mean plant height (**d**) are shown. Note that the values used to divide the colours are the same in all panels, but that the maximum and minimum values are different, as indicated in the legends. **e–g**, Historical and future estimates of net change in local diversity from 1500–2095, based on estimates of land-use, land-use intensity and human population density from the four RCP scenarios (Table 1). Net changes in richness (**e**), total abundance (**f**) and community-weighted mean plant height (**g**) are shown. Historical (shading)

and future (error bars) uncertainty shown as 95% confidence intervals, with uncertainty rescaled to be zero in 2005 to show uncertainty in past and future change separately. The global average projection for the MESSAGE scenario does not directly join the historical reconstruction because projections start in 2010 (human population estimates are available at 15-year intervals) and because human population (and thus land-use intensity) and plantation forest extent have not been harmonized among scenarios. In panel **e**, the dashed line shows projected diversity change under land-use change only (that is, without land-use intensity and human population density, the projections of which involved simplifying assumptions), and the dotted line shows projections of rarefaction-based species richness.



Extended Data Figure 7 | Reconstructed and projected total global land-use areas under the RCP scenarios. a, Estimated total area of the major land-use types. **b–f,** Estimated total area of secondary vegetation in different stages of recovery.



Extended Data Figure 8 | Biodiversity projections at the country level.

a–d, Country-level projections of net change in local richness between 2005 and 2095 under the four RCP scenarios (IMAGE 2.6 (**a**), MiniCAM 4.5 (**b**), AIM 6.0 (**c**) and MESSAGE 8.5 (**d**)), shown in relation to the Human Development Index (an indicator of education, life expectancy, wealth and standard of living) in the most recent year for which data are available. **e, f**, Country-level projections of net change in local richness between 2005 and 2095 under the

best- and worst-performing RCP scenarios in terms of biodiversity (MiniCAM 4.5 (**e**) and MESSAGE 8.5 (**f**), respectively), shown in relation to past change in biodiversity from a baseline with no human land-use effects to 2005 according to the HYDE land-use reconstruction. Colours indicate biogeographic realms (key in **b**); colour intensity reflects native vertebrate species richness (more intense colour represents higher species richness); point size is proportional to (log) country area.

Extended Data Table 1 | Land use and land-use intensity classification definitions (from ref. 16)

Level 1 Land Use	Predominant Land Use	Minimal use	Light use	Intense use
No evidence of prior destruction of the vegetation	Primary Vegetation	Any disturbances identified are very minor (e.g., a trail or path) or very limited in the scope of their effect (e.g., hunting of a particular species of limited ecological importance).	One or more disturbances of moderate intensity (e.g., selective logging) or breadth of impact (e.g., bushmeat extraction), which are not severe enough to markedly change the nature of the ecosystem. Primary sites in suburban settings are at least Light use.	One or more disturbances that are severe enough to markedly change the nature of the ecosystem; this includes clear-felling of part of the site too recently for much recovery to have occurred. Primary sites in fully urban settings should be classed as Intense use.
Recovering after destruction of the vegetation	Mature Secondary Vegetation			
	Intermediate Secondary Vegetation			
	Young Secondary Vegetation			
Human use (agricultural)	Secondary Vegetation (indeterminate age)	Extensively managed or mixed timber, fruit/coffee, oil-palm or rubber plantations in which native understorey and/or other native tree species are tolerated, which are not treated with pesticide or fertiliser, and which have not been recently (< 20 years) clear-felled.	Monoculture fruit/coffee/rubber plantations with limited pesticide input, or mixed species plantations with significant inputs. Monoculture timber plantations of mixed age with no recent (< 20 years) clear-felling. Monoculture oil-palm plantations with no recent (< 20 years) clear-felling.	Monoculture fruit/coffee/rubber plantations with significant pesticide input. Monoculture timber plantations with similarly aged trees or timber/oil-palm plantations with extensive recent (< 20 years) clear-felling.
	Plantation forest			
	Cropland			
	Pasture			
	Urban			
Human use (urban)	Urban	Extensive managed green spaces; villages.	Suburban (e.g. gardens), or small managed or unmanaged green spaces in cities.	Fully urban with no significant green spaces.

Extended Data Table 2 | Conversion between Global Land Systems data set and our intensity classification for each major land-use type

Global Land Systems classification	Primary	Secondary	Cropland	Pasture	Urban
Cropland, extensive with few livestock	NA	NA	minimal	light	NA
Cropland, extensive with bovines, goats & sheep	NA	NA	minimal	intense	NA
Cropland, extensive with pigs & poultry	NA	NA	minimal	intense	NA
Cropland, medium intensive with few livestock	NA	NA	light	light	NA
Cropland, medium intensive with bovines, goats & sheep	NA	NA	light	intense	NA
Cropland, medium intensive with pigs & poultry	NA	NA	light	intense	NA
Cropland, intensive with few livestock	NA	NA	intense	light	NA
Cropland, intensive with bovines, goats & sheep	NA	NA	intense	intense	NA
Cropland, intensive with pigs & poultry	NA	NA	intense	intense	NA
Mosaic cropland and grassland with bovines, goats and sheep	NA	NA	intense	intense	NA
Mosaic cropland and grassland with pigs & poultry	NA	NA	intense	intense	NA
Mosaic cropland (extensive) and grassland with few livestock	NA	NA	minimal	light	NA
Mosaic cropland (medium intensive) and grassland with few livestock	NA	NA	light	light	NA
Mosaic cropland (intensive) and grassland with few livestock	NA	NA	intense	light	NA
Mosaic cropland and forest with pigs & poultry	NA	NA	intense	intense	NA
Mosaic cropland (extensive) and forest with few livestock	NA	NA	minimal	light	NA
Mosaic cropland (medium intensive) and forest with few livestock	NA	NA	light	light	NA
Mosaic cropland (intensive) and forest with few livestock	NA	NA	intense	light	NA
Dense forest	minimal	minimal	NA	NA	NA
Open forest with few livestock	light	light	NA	light	NA
Open forest with pigs & poultry	intense	intense	NA	intense	NA
Mosaic grassland and forest	minimal	minimal	NA	NA	NA
Mosaic grassland and bare	minimal	minimal	NA	NA	NA
Natural grassland	minimal	minimal	NA	NA	NA
Grassland with few livestock	NA	NA	NA	light	NA
Grassland with bovines, goats and sheep	NA	NA	NA	intense	NA
Bare	NA	NA	NA	NA	NA
Bare with few livestock	NA	NA	NA	light	NA
Peri-urban and villages	NA	NA	NA	NA	minimal
Urban	NA	NA	NA	NA	intense

To estimate proportional coverage of each intensity class for each land-use type in the $0.5^{\circ} \times 0.5^{\circ}$ grid cells used for projection, we calculated the number of finer-resolution Global Land Systems³⁹⁷ cells with a matching intensity class for the land-use type in question, as a proportion of Global Land Systems cells matching any intensity class for the land-use type in question. For example, to calculate the proportion of urban land that is under intense use, we divided the number of cells with a Global Land Systems classification of 'urban' by the number of cells classified as 'urban' or 'peri-urban and villages'. None of the Global Land Systems classes could inform about the intensity of plantation forest, and so we assumed that any plantation forest was composed of equal proportions under minimal, light and intense use.

Loss of δ -catenin function in severe autism

Tychele N. Turner^{1,2,3}, Kamal Sharma⁴, Edwin C. Oh⁵, Yangfan P. Liu⁵, Ryan L. Collins⁶, Maria X. Sosa^{1,3}, Dallas R. Auer^{1,3}, Harrison Brand^{6,7}, Stephan J. Sanders^{3,8}, Daniel Moreno-De-Luca^{3,9}, Vasyi Pihur^{1,3}, Teri Plona¹⁰, Kristen Pike¹⁰, Daniel R. Soppet¹⁰, Michael W. Smith¹¹, Sau Wai Cheung¹², Christa Lese Martin^{3,13}, Matthew W. State^{3,8}, Michael E. Talkowski^{6,7}, Edwin Cook¹⁴, Richard Haganir⁴, Nicholas Katsanis⁵ & Aravinda Chakravarti^{1,3}

Autism is a multifactorial neurodevelopmental disorder affecting more males than females; consequently, under a multifactorial genetic hypothesis, females are affected only when they cross a higher biological threshold. We hypothesize that deleterious variants at conserved residues are enriched in severely affected patients arising from female-enriched multiplex families with severe disease, enhancing the detection of key autism genes in modest numbers of cases. Here we show the use of this strategy by identifying missense and dosage sequence variants in the gene encoding the adhesive junction-associated δ -catenin protein (*CTNND2*) in female-enriched multiplex families and demonstrating their loss-of-function effect by functional analyses in zebrafish embryos and cultured hippocampal neurons from wild-type and *Ctnnd2* null mouse embryos. Finally, through gene expression and network analyses, we highlight a critical role for *CTNND2* in neuronal development and an intimate connection to chromatin biology. Our data contribute to the understanding of the genetic architecture of autism and suggest that genetic analyses of phenotypic extremes, such as female-enriched multiplex families, are of innate value in multifactorial disorders.

Autism is a common neurodevelopmental disorder with a profound sex-bias: four times more males than females are affected¹ whereas disease recurrence risk to siblings of autistic females is larger than to siblings of affected males². Both features can be explained through autism's multifactorial inheritance where females are affected at higher biological thresholds of an underlying liability than males. Under this model, females escape the effect of deleterious mutations unless the alleles are severe and at key developmental steps. To accelerate discovery, we examine families with highest recurrence risk and, consequently, probably enriched for severe mutations in such genes. We hypothesize that one group of families that have this property, and yet are underrepresented in autism sequencing efforts, are those with two or more severely affected females (female-enriched multiplex families (FEMFs)).

The first genes discovered in autism were through syndromes (Supplementary Table 1), such as Rett and fragile X syndromes³. Today, genomic analyses have definitively identified 12 genes, from an estimated 500 (ref. 4), with an excess of *de novo* or segregating mutations in typical isolated cases that are overwhelmingly male (Supplementary Table 1). Given such heterogeneity, it may be crucial to identify those genes whose mutations impart the greatest autism risk. Increased recurrence risk is associated with lower incidence (the 'Carter' effect), since any rare class must arise from higher genetic liability (Fig. 1a)⁵. Consequently, gene discovery in epidemiologically rarer classes, namely female gender, high phenotypic severity and familial cases, may be fruitful; this is further enhanced if we increase the genetic load by considering individuals who have all three features.

These genetically loaded cases have either a greater number or frequency of deleterious alleles that are probably severe coding variants. This prediction arises from our studies of Hirschsprung disease, a neurodevelopmental disorder of enteric nervous system ganglionosis. Hirschsprung disease is a multifactorial disorder with a sex ratio of 4:1 in favour of males and whose risk factors are gender, phenotypic severity, and familiarity⁶. Although more than 15 genes for Hirschsprung disease have been identified, the major gene encodes the receptor tyrosine

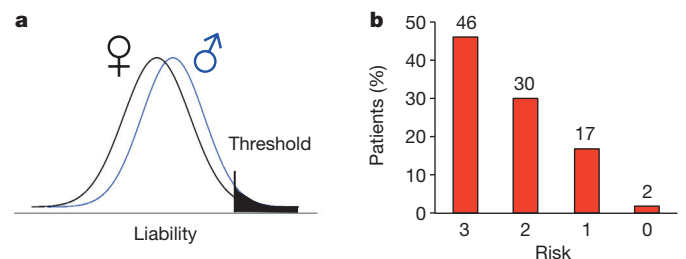


Figure 1 | Genetic features of a sex-dependent multifactorial model. **a**, Hypothetical sex-dependent liability distributions for autism under a multifactorial model of inheritance with a fixed biological threshold for affection. **b**, Percentage of patients having Hirschsprung disease with damaging coding mutations within different risk classes characterized by gender, segment length and familiarity. The risk class is labelled 3, 2, 1, 0 and is an additive score based on the number of factors with higher risk (female, long segment, multiplex); it comprises 13, 46, 60 and 55 patients, respectively (proportion trend test, $P = 3.1 \times 10^{-6}$).

¹Center for Complex Disease Genomics, Johns Hopkins University School of Medicine, Baltimore, Maryland 21205, USA. ²Predoctoral Training Program in Human Genetics and Molecular Biology, McKusick-Nathans Institute of Genetic Medicine, Johns Hopkins University School of Medicine, Baltimore, Maryland 21205, USA. ³National Institute of Mental Health (NIMH) Autism Centers of Excellence (ACE) Genetics Consortium at the University of California, Los Angeles, Los Angeles, California 90095, USA. ⁴Solomon H. Snyder Department of Neuroscience, Johns Hopkins University School of Medicine, Baltimore, Maryland 21205, USA. ⁵Center for Human Disease Modeling, Duke University, Durham, North Carolina 27710, USA. ⁶Center for Human Genetic Research, Massachusetts General Hospital and Harvard Medical School, Boston, Massachusetts 02114, USA. ⁷Department of Neurology, Massachusetts General Hospital and Harvard Medical School, Boston, Massachusetts 02114 USA. ⁸Department of Psychiatry, University of California, San Francisco, San Francisco, California 94158, USA. ⁹Department of Psychiatry, Yale University, New Haven, Connecticut 06511, USA. ¹⁰Leidos Biomedical Research, Inc., Frederick, Maryland 21702, USA. ¹¹National Human Genome Research Institute, Bethesda, Maryland 20892, USA. ¹²Baylor College of Medicine, Houston, Texas 77030, USA. ¹³Autism & Developmental Medicine Institute, Geisinger Health System, Lewisburg, Pennsylvania 17837, USA. ¹⁴University of Illinois at Chicago, Chicago, Illinois 60608, USA.

kinase RET, which harbours numerous rare loss-of-function coding and one common enhancer variant⁷. We estimated the proportion of 174 patients with Hirschsprung disease with damaging *RET* coding variants conditional on their having 3, 2, 1 or 0 risk factors, where higher risk categories were female gender, long segment aganglionosis and familiarity (Fig. 1b), to show that rare classes are significantly associated with a higher proportion of deleterious alleles, varying linearly between 46% and 2% from the highest to lowest risk class ($P = 3.1 \times 10^{-6}$); the non-coding variant had the reverse trend. Therefore, exome sequencing in autism can be similarly efficient in FEMFs. Since female incidence of autism is 0.0016, fewer than 10% of families are multiplex and fewer than 10% are severe, FEMFs have a crude incidence of less than 1.6×10^{-5} and represent a rare autism disorder enriched for deleterious coding variants⁷.

Here we demonstrate the utility of this strategy by exome sequence analyses of 13 unrelated females and identifying 18 candidate genes of which at least four, *CYFIPI1*, *DLG1*, *PLXNA3* and *CTNND2*, are of interest to autism aetiology. We have evaluated one of them, *CTNND2* (the δ -2-catenin gene encoding the δ -catenin protein), in depth using a combination of genetic, genomic and functional studies to show that (1) *CTNND2* harbours a significant excess of deleterious missense and copy number variants (CNVs) in autism; (2) these variants, by functional testing, are loss-of-function and affect Wnt signalling; (3) expression of *CTNND2* is highest in the fetal brain and is highly correlated with other autism genes; and (4) *CTNND2* correlated genes are enriched for chromatin and histone modification, as well as dendritic morphogenesis, functions. These results are consistent with the roles of *CTNND2* in the formation of dendritic spines⁸, and the regulation of beta (β)-catenin in neurons⁹. Given the recent finding of *de novo* autism mutations in pathways regulating β -catenin (Supplementary Table 1), loss-of-function of *CTNND2* is probably rate-limiting for dendritic morphogenesis and maintenance.

Exome sequencing of females with autism

We sampled 13 unrelated females, negative for deleterious variants in *MECP2*, from multiplex families who had severe autism (measured with the Autism Diagnostic Interview-Revised and the Autism Diagnostic Observation Schedule). Proband exomes were sequenced and analysed with sequence data from 71 European females (1000 Genomes Project; Extended Data Fig. 1). To identify pathogenic alleles, we focused on missense variants absent in public databases (dbSNP129, 1000 Genomes Project) and conserved to zebrafish, nonsense and canonical splice site variants. This led to 3,090 variants of interest in the combined 84 exomes within 2,516 genes, with 447 of these having two or more variants of interest; among them, the 13 autism cases harboured two or more variants of interest in 24 genes of which 18 reached significance ($P < 1 \times 10^{-4}$) (Supplementary Table 2). By searching their expression profiles (Supplementary Table 3), we identified four genes, with an excess of deleterious alleles, as candidates: *CYFIPI1*, *DLG1*, *PLXNA3* and *CTNND2*. On the basis of our previous genome-wide association study implicating chromosome 5p¹⁰, we followed up *CTNND2* at this locus.

CTNND2 as a novel autism gene

CTNND2 harboured two deleterious variants, G34S and R713C, both of which were absent in 3,889 European controls (1000 Genomes Project and Exome Variant Server); G34S was present at a frequency of 5.3×10^{-4} in 1,869 African ancestry samples (Exome Variant Server) and in one Luhyuan sample (NA19020) (Extended Data Fig. 2). To estimate their frequency, we genotyped 10,782 samples from the HapMap and autism collections: the only additional individuals with G34S were an affected female and her mother (SSC02696, SSC03276) from the Simons Simplex Collection (SSC). Principal component analysis on polymorphism data from individuals with G34S found that our autism cases were not of African ancestry, identifying a new ancestral origin for G34S (Extended Data Fig. 3). For R713C, only our FEMF samples were heterozygous.

Next-generation *CTNND2* sequencing in 362 additional females with autism (Extended Data Fig. 4) identified a total of seven variants (G34S, R713C and five new variants: P189L, P224L, G275C, R454H, T862M), of which four (G34S, G275C, R713C, T862M) were conserved to zebrafish (Fig. 2a and Supplementary Table 4). We also identified Q507P in an autistic male from 170 SSC probands. An identical analysis of 379 European ancestry control samples (1000 Genomes Project) yielded

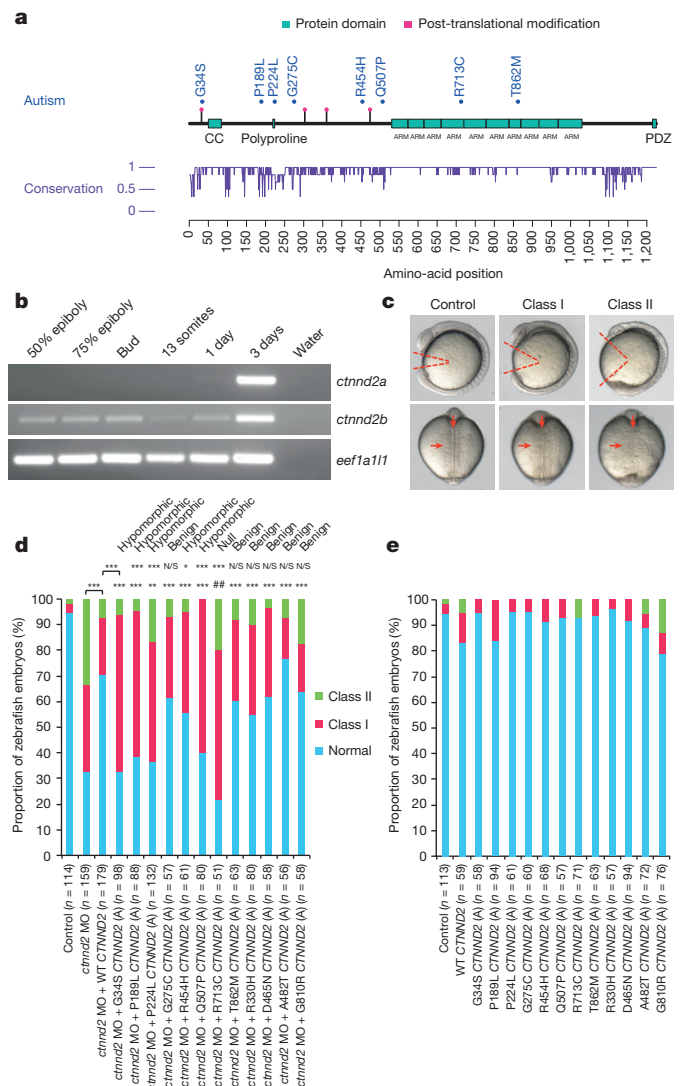


Figure 2 | Missense variants in human δ -catenin and their effect on protein function *in vivo*. **a**, *CTNND2* annotated with validated missense mutations in autism patients; G34S, G275C, Q507P, R713C, T862M variants are conserved to zebrafish. **b**, Expression of two *CTNND2* zebrafish orthologues (*ctnd2a*, *ctnd2b*) in development. Aberrant phenotypes are observed with *ctnd2b* (the only orthologue expressed at these gastrulation time points) morpholino knockdown only at key stages of gastrulation (50% epiboly, 75% epiboly, bud). Elongation factor alpha (*eef1a111*) is shown as a control for ubiquitous expression. **c**, Representative lateral and dorsal images of class I and class II *ctnd2b* morphants (2 ng morpholino) at the eight- to ten-somite stage reveal defective gastrulation movements. **d**, Quantification of gastrulation phenotype in control, morpholino and rescue constructs: wild type, autism variants (G34S, P189L, P224L, G275C, R454H, Q507P, R713C, T862M) and control variants (R330H, D465N, A482T, G810R) are indicated. **e**, Quantification of gastrulation phenotype in overexpression constructs: wild type, autism variants (G34S, P189L, P224L, G275C, R454H, Q507P, R713C, T862M) and control variants (R330H, D465N, A482T, G810R) are indicated. χ^2 tests were conducted: * $P < 0.05$, ** $P < 0.01$ and *** $P < 0.001$, respectively; ##, no rescue and worse than morpholino alone ($P < 0.01$). NS, not significant. Sample size (n) is marked for each condition.

three variants after validation (R330H, D465N, A482T), one conserved to zebrafish. On aggregate, variants at these conserved CTNND2 residues are significantly more frequent in autism than in controls ($P = 0.04$ versus 1000 Genomes Project; $P = 7.8 \times 10^{-4}$ versus Exome Variant Server).

We next assessed whether CNVs within *CTNND2* were enriched in autism. First, from the literature, we identified six deletions and one duplication. Second, we identified two deletions and one duplication from the Emory University and Baylor College of Medicine clinical cytogenetics laboratories. Third, from the Autism Genetic Resource Exchange (AGRE), we identified two previously unreported valid deletions (Extended Data Fig. 5). Therefore, we detected 12 CNVs (ten deletions, two duplications), seven overlapping one or more exons (Fig. 3 and Supplementary Table 5). As a control, we searched the Database of Genomic Variants to identify 33 variants, with only two overlapping exons (58.3% in our 12 CNVs versus 6.1% in the Database of Genomic Variants; $P = 5 \times 10^{-4}$). This significant excess of exon-disruptive deletions suggests *CTNND2* haploinsufficiency in autism. Most of our patients had an autism diagnosis; however, some probands were referred with a diagnosis of neurodevelopment disorder. To test whether *CTNND2* CNVs may be enriched in neurodevelopment disorders generally, we assessed CNVs from 19,556 independent cases referred for clinical diagnostic studies and 13,898 controls from population-based studies¹¹. Considering all dosage imbalances, we observed 25 instances in cases and three in controls, corresponding to an odds ratio of 5.9 ($P = 4.10 \times 10^{-4}$) (Extended Data Fig. 6 and Supplementary Table 6). The impact of loss-of-function (deletions, unbalanced translocations) mutations at this locus is significant, with an odds ratio of 14.7 ($P = 8.28 \times 10^{-5}$), with specificity for *CTNND2* since the effect size is comparable for intra-genic deletions (eight cases, one control; $P = 0.059$, odds ratio = 5.68) as for all CNVs.

The consequence of autism variants on function

To assess the *in vivo* functional consequences of autism *CTNND2* variants, we used a complementation assay in zebrafish embryos. Zebrafish have two genes for δ -catenin that are as divergent from each other (18.3%) as they are from humans (19.9%, 20.7%), at the protein level. We examined expression of both genes by PCR with reverse transcription (RT-PCR) at six developmental time points (Fig. 2b) and focused on *ctnnd2b* because it was expressed at all stages. Using a splice-blocking morpholino oligonucleotide targeting *ctnnd2b*, we injected

one- to eight-cell embryos and analysed them at the eight- to ten-somite stage. Morphant embryos had gastrulation phenotypes consistent with abnormal *Wnt* signalling (shortened body axes, longer somites, and broad and kinked notochords) (Fig. 2c). RT-PCR of *axin2* messenger RNA (mRNA), a direct target of canonical *Wnt* signalling¹², from ten-somite *ctnnd2b* morphants, showed significant decrease ($P < 0.01$), reinforcing the hypothesis of defective *Wnt* signalling (Extended Data Fig. 7a). Specificity of the morpholino was tested by co-injection of wild-type mRNA to observe significant ($P < 0.001$) rescue (Fig. 2d). To investigate the effect of each variant on protein function, injection cocktails containing morpholino and mutant variants were injected and compared with rescue with wild-type mRNA: five variants (G34S, P189L, P224L, R454H, Q507P) were better than morpholino alone ($P < 0.001$) but worse than wild-type rescue ($P < 0.001$), implicating these as hypomorphic (Fig. 2d). One variant (R713C) was functionally null while G275C and T862M were benign, and all four controls were benign, demonstrating specificity. To preclude the possibility of mRNA toxicity, we injected mutant mRNA corresponding to all alleles and observed no significant differences in the gastrulation phenotypes (Fig. 2e).

To replicate these findings with an *in vivo* assay querying *Wnt* signalling earlier in development, we assessed the consequences of *ctnnd2b* suppression on *chordin* expression during epiboly, whose ectopic expression is known in *Wnt* mutants¹³. Consistent with the role of *chordin* in *Wnt*-dependent dorsalization¹⁴, we observed shortening and widening of the *chordin* expression domain as well as loss of anterior-specific expression fields in *ctnnd2b* morphants (Extended Data Fig. 7b); this phenotype could be rescued by wild-type mRNA. Further, testing of two control alleles that scored benign in our mid-somatic assays (A482T, G810R) showed significant rescue ($P < 0.001$); the hypomorphic allele G34S rescued *chordin* expression to a level significantly worse than wild-type mRNA rescue ($P < 0.001$), while the null allele R713C did not rescue *chordin* expression (Extended Data Fig. 7c). Since *CTNND2* can bind *CTNNB1* (ref. 15), we tested this interaction with mutant *CTNND2*. Expression of green fluorescent protein (GFP)-tagged *CTNND2* and Flag-tagged *CTNNB1* revealed that wild-type *CTNND2* could immunoprecipitate *CTNNB1*; however, its interaction with *CTNNB1* was diminished upon expression of G34S or R713C (Extended Data Fig. 7d), suggesting *in vivo* *Wnt* phenotypes may result from attenuated *CTNNB1*–*CTNND2* interaction.

Finally, we asked if these major *CTNND2* sequence variants could affect neuronal circuitry by using a well-established *in vitro* model system. Dendritic spines are the primary sites for excitatory synapse formation, and their dysregulation underlies many neuropsychiatric disorders¹⁶. To test if *CTNND2* variants interfere with development and maintenance of spines, we prepared primary hippocampal neurons from embryonic day (E)18 rat embryos and introduced either GFP or GFP fusion to wild-type *CTNND2* or to its mutant variants at day *in vitro* (DIV)8. At DIV15, neurons were fixed and analysed to assess spine density. We found that wild-type *CTNND2* had a significantly higher spine density than GFP controls¹⁷. However, neurons expressing G34S had a significantly lower spine density than those expressing GFP or wild-type *CTNND2*. Neurons expressing R713C, on the other hand, had the same spine density as those expressing GFP but significantly less than the one that expressed wild-type *CTNND2*, suggesting a loss-of-function effect. In contrast, the A482T polymorphism had an effect similar to wild-type *CTNND2* (Extended Data Fig. 8). To test if observed changes in spine density reflected changes in excitatory synapse number in the networks, we analysed excitatory synapses: that is, overlapping region between postsynaptic marker PSD95 and presynaptic marker vGluT1 in mouse hippocampal neurons at DIV14 (Fig. 4A). As with spine density, we found an increase in excitatory synapse number in neurons that overexpressed wild-type but not mutant *CTNND2*. Further, loss-of-function of *CTNND2* led to a decrease in overall excitatory synapse density, as well as active synapses that expressed the GluA subunit of the AMPA (α -amino-3-hydroxy-5-methyl-4-isoxazole propionic acid)-type glutamate receptors (Fig. 4B, C). Taken together, these results

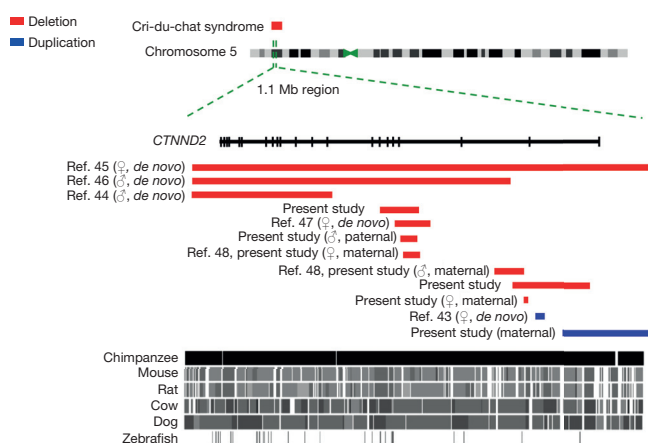


Figure 3 | CNV in human *CTNND2*. CNVs at the 1.1 megabase (Mb) *CTNND2* locus (chromosome 5: 10905332–12034584, hg19), the chromosomal location, the extent of each deletion and duplication, patient gender, parental origin and citation are shown for each variant identified in patients with autism and individuals with other neurodevelopmental disorders. Extensive genomic sequence conservation across the entire region in selected vertebrates is shown. References for CNV studies include refs 43–48.

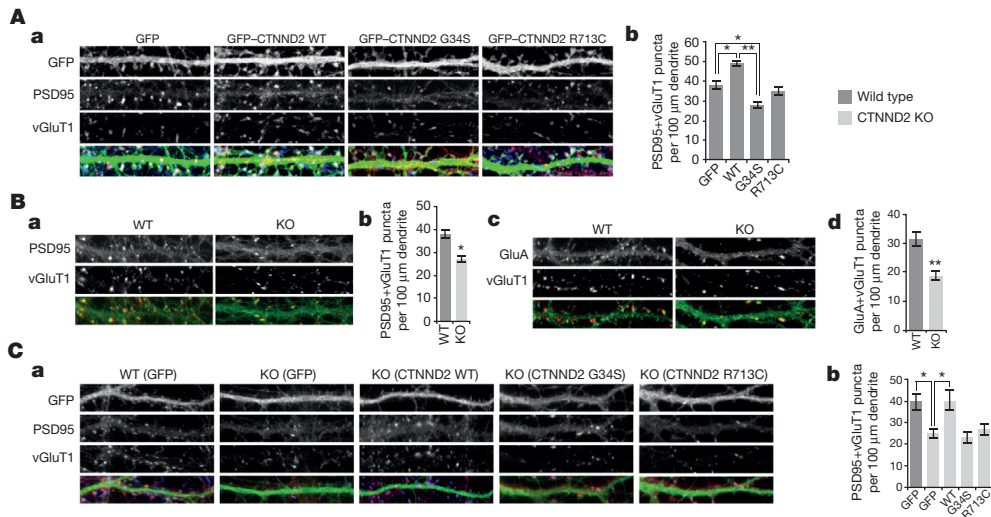


Figure 4 | δ-Catenin is critical for maintaining functional neuronal networks. **A**, Gain of function. **a**, Overexpression of *CTNND2* leads to an increase in the number of excitatory synapses. Primary dendrites from neurons transfected with GFP alone, GFP fusion with wild-type (WT) *CTNND2*, or mutant isoforms, and immunolabelled with vGluT1 and PSD95. **b**, Quantification of number of PSD95 + vGluT1-positive puncta per 100 μm of dendritic length ($N = 12$ each). **B**, Loss of function. **a**, Neurons from *Ctnnd2* null mutants have a significant reduction in synapse density. Synapses are identified as puncta with PSD95 and vGluT1 overlap. KO, knockout. **b**, Quantification of the number of PSD95 + vGluT1-positive puncta per 100 μm of dendritic length ($N = 13$ each). **c**, Alternatively, neurons were

immunolabelled with GluA and vGluT1 to identify active functional excitatory synapses. **d**, Quantification of the number of GluA + vGluT1-positive puncta per 100 μm of dendritic length ($N = 15$ each). **C**, Rescue of loss of function. **a**, WT *CTNND2* but not its mutant isoforms can rescue the loss of phenotype in neurons from *CTNND2* null mutants. Primary dendrites from neurons transfected with GFP alone, GFP fusion with wild-type *CTNND2*, or mutant isoforms, and immunolabelled with vGluT1 and PSD95. **b**, Quantification of the number of PSD95 + vGluT1-positive puncta per 100 μm of dendritic length ($N = 14$ each). Colour used for merged panels are GFP (green) PSD95 (red), GluA (Red) and vGluT1 (blue). Student's *t*-tests were conducted: * $P < 0.05$ and ** $P < 0.001$, respectively. Error bars, s.e.m.

suggest that *CTNND2* is critical to the formation and/or maintenance of synapses, in accord with other studies^{18,19}. Moreover, unlike wild-type *CTNND2*, the tested mutants failed to rescue the reduction in synapse density in *CTNND2* null background, demonstrating loss-of-function. Therefore, G34S and R713C impair development and/or the maintenance of mammalian neural circuitry.

Expression of *CTNND2* in the developing human brain

To understand *CTNND2* expression, we tested mRNA levels in 16 adult and eight fetal human tissues: *CTNND2* expression was highest in the fetal brain (20× the adult brain) (Extended Data Fig. 9). Therefore, we used the Allen Brain Atlas of the Developing Human Brain microarray data to identify other *CTNND2* co-expressed genes. We used the data normalized to 17,630 genes and linear regression on age and brain regions for estimating Pearsonian correlations between *CTNND2* and all other genes (absolute correlation > 0.3 , $P = 2.84 \times 10^{-6}$ given multiple comparisons). First, we performed pathway analysis on the 826 positively and 662 negatively correlated genes (Supplementary Table 7). The positive set was significantly enriched for genes encoding proteins localized to the cytoskeleton, cell junction, neuronal projection, with GTPase regulatory activity, and functioning in cell morphogenesis, chromatin modification, neuronal development and neuron projection formation. Of these, the role of *CTNND2* in dendritic development and spine morphogenesis is known¹⁷ as well as its involvement in actin dynamics and GTPase regulatory activity^{20,21}. However, its role in chromatin modification is novel. The closest known function of *CTNND2* to chromatin is based on *CTNND2* binding to ZBTB33 (ref. 22), a protein regulating transcription and *Wnt* pathway genes²³, and its possible nuclear localization and function²⁴. Second, we searched for transcription factors that may regulate *CTNND2*: among the correlated genes we identified 75 of which *PAX6* is the most biologically significant²⁵. A *Pax6* mutant rat show autism-related features²⁶ and genetic variation disrupting *PAX6* has been identified in individuals with autism²⁷. Also, *Pax6* can regulate *Ctnnd2* expression in cells, including the binding of *Pax6* to its promoter^{25,28}.

We searched the correlated genes for autism²⁹ (<https://gene.sfari.org/autdb/>) and intellectual disability candidates (Supplementary Table 7). Of 529 autism genes, 71 (61 positively, 10 negatively) were significantly correlated with *CTNND2*, representing significant enrichment ($P = 2.83 \times 10^{-6}$). Next, we examined the correlations between these 71 genes and *CTNND2* (Fig. 5a) to find an intimate relationship between *CTNND2* and autism genes. To interrogate the function of the 61 positively correlated genes, we again performed pathway analyses (Fig. 5b) to find significant enrichment of genes involved in dendrite morphogenesis ($P = 2.96 \times 10^{-3}$; *PDLIM5*, *MAP2*, *SHANK1*, *CDKL5*, *DLG4*) as well in chromatin modification ($P = 2.96 \times 10^{-3}$; *HDAC3*, *HUWE1*, *CREBBP*, *EP300*, *YEATS2*, *EP400*, *ATXN7*, *HCFC1*, *ARID1B*, *NSD1*).

Discussion

Our studies strongly implicate δ-2-catenin (*CTNND2*) as a critical gene in autism and an important neurodevelopmental protein given its role in FEMFs, functional association with other autism genes, cri-du-chat syndrome³⁰ and other diseases³¹. Clearly, *CTNND2* haploinsufficiency is common in autism and strongly associated with neurodevelopment disorder generally. Nevertheless, in the general population, the frequency of disease alleles we discovered is low (3.9×10^{-4} and 8.0×10^{-4} in individuals of European and African ancestry, respectively, in Exome Variant Server), consistent with their deleterious functional effects.

CTNND2 is a plakoglobin/armadillo family member with identity to PKP4, *CTNND1* and ARVCF. The armadillo domain is a key part of the protein that binds cadherins¹⁵, β-catenin¹⁵, presenilins 1 and 2 (ref. 32) and sphingosine kinase³³. It also harbours a coiled-coil domain, a polyproline tract at amino acids 219–224 where src receptor kinases bind³⁴, and a PDZ domain at the carboxy (C) terminus, which can bind Discs large homologue 4 (ref. 35) and erbin³⁶. These features suggest that *CTNND2* is important in neuronal actin dynamics and the cytoskeleton^{15,34}, as also supported by observations of induced branching of dendrite-like processes and enhanced dendrite morphogenesis by *CTNND2* overexpression³⁷. Importantly, *CTNND2* can directly bind to actin³⁷ and cortactin³⁴, and act on the Rho family to induce filopodia

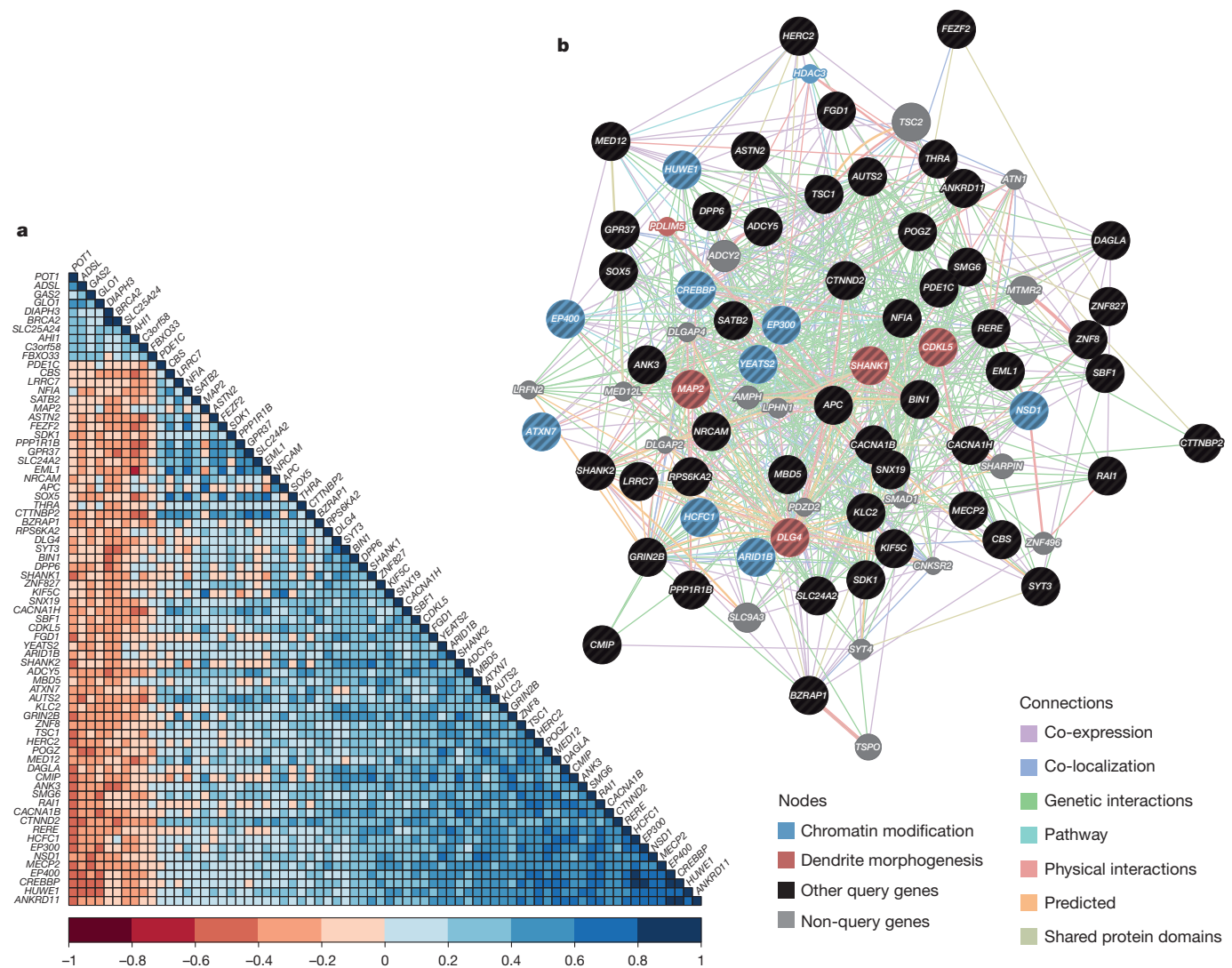


Figure 5 | Gene expression correlation between *CTNND2* and known autism genes. a, Plot of all autism genes significantly (positive and negative) correlated with *CTNND2* in the developing human brain (microarray data

from <http://www.brainspan.org>). **b**, Pathway analysis of the autism genes positively correlated with δ -catenin reveals significant enrichment of genes involved in chromatin modification and dendrite morphogenesis.

within neurons²⁰ and increase the number of dendritic spines¹⁷. Finally, we demonstrate a role of *CTNND2* in canonical *Wnt* signalling through zebrafish analyses: although the precise mechanism is not understood, it can bind to proteins (GSK-3 β , ZBTB33) that regulate *Wnt* signalling²³ and transcription²², in concert with *CTNNB1*. The other novel *CTNND2* function we implicate is its possible role in the nucleus, through its interaction with HDAC3 (Fig. 5). This is not unexpected, since *CTNND2* can affect gene expression after nuclear translocation²⁴. Furthermore, the armadillo family member p120ctn interacts with ZBTB33 (Kaiso) and the NCoR co-repressor complex containing HDAC3 (refs 22, 24, 38, 39). Thus, we hypothesize that *CTNND2* may be a nucleo-cytoplasmic protein whose autism effect may arise from its cytoplasmic or nuclear loss-of-function or both.

Published *Ctnnd2* knockout mice^{8,18,19}, and our analyses of their dendritic spines, give clues to the role of *CTNND2* in autism and in cognition. Homozygote mice exhibit structural and functional abnormalities at the synapse, as well as impaired spatial learning and fear conditioning^{18,19}, with reduced levels of PSD-95, β -catenin associated with cadherin, and N-cadherin. The interaction of PSD-95 with *CTNND2* was discovered as an important linkage to AMPA receptor binding protein and glutamate receptor interacting protein (GRIP)³⁵. Our results confirm that *CTNND2* is required for the maintenance of spine structures

*in vivo*¹⁹, and stability of some key components of the synaptogenic machinery such as N-cadherins and PSD95 (refs 8, 18). We show that loss of spines and reduction in total levels of synaptic proteins in null mice reflect reduction in the number of functional excitatory synapses at the subcellular level. Interestingly, acute loss of δ -catenin *in vitro* impairs activity-dependent formation of spines⁴⁰, reinforcing its importance in formation and maintenance of synaptic structures and cognitive functions.

Studying FEMFs is unconventional for a complex disease where most mutations have small effects. Nevertheless, our data suggest that modest numbers of samples of rare extreme phenotypes, in contrast to large numbers of typical cases, can be important. Note, we identified 18 candidate genes among which at least three others are worthy of follow-up: *CYFIP1* is in a 15q11-13 autism duplication, has altered expression in autism patients, interacts with FMRP and is involved in regulating dendritic spines through translational inhibition and actin dynamics⁴¹; *DLG1* is a multi-scaffolding postsynaptic density protein lying within a 3q29 autism and/or intellectual disability deletion; *PLXNA3* is known to alter dendritic spines and is a receptor for *SEMA5A*⁴², another autism gene¹⁰. The broader FEMFs hypothesis can thus be tested by sequencing larger numbers of cases for identifying genes critical to early brain development.

Online Content Methods, along with any additional Extended Data display items and Source Data, are available in the online version of the paper; references unique to these sections appear only in the online paper.

Received 29 January 2014; accepted 5 January 2015.

Published online 25 March 2015.

- Kogan, M. D. *et al.* Prevalence of parent-reported diagnosis of autism spectrum disorder among children in the US, 2007. *Pediatrics* **124**, 1395–1403 (2009).
- Jorde, L. B. *et al.* Complex segregation analysis of autism. *Am. J. Hum. Genet.* **49**, 932–938 (1991).
- Abrahams, B. S. & Geschwind, D. H. Advances in autism genetics: on the threshold of a new neurobiology. *Nature Rev. Genet.* **9**, 341–355 (2008).
- Ronemus, M., Iossifov, I., Levy, D. & Wigler, M. The role of *de novo* mutations in the genetics of autism spectrum disorders. *Nature Rev. Genet.* **15**, 133–141 (2014).
- Carter, C. O. Genetics of common disorders. *Br. Med. Bull.* **25**, 52–57 (1969).
- Chakravarti, A. 2013 William Allan Award: my multifactorial journey. *Am. J. Hum. Genet.* **94**, 326–333 (2014).
- Emison, E. S. *et al.* Differential contributions of rare and common, coding and noncoding Ret mutations to multifactorial Hirschsprung disease liability. *Am. J. Hum. Genet.* **87**, 60–74 (2010).
- Arikath, J. *et al.* δ -Catenin regulates spine and synapse morphogenesis and function in hippocampal neurons during development. *J. Neurosci.* **29**, 5435–5442 (2009).
- Bareiss, S., Kim, K. & Lu, Q. δ -Catenin/NPRAP: a new member of the glycogen synthase kinase-3 β signaling complex that promotes β -catenin turnover in neurons. *J. Neurosci.* **88**, 2350–2363 (2010).
- Weiss, L. A., Arking, D. E., Daly, M. J. & Chakravarti, A. A genome-wide linkage and association scan reveals novel loci for autism. *Nature* **461**, 802–808 (2009).
- Talkowski, M. E. *et al.* Sequencing chromosomal abnormalities reveals neurodevelopmental loci that confer risk across diagnostic boundaries. *Cell* **149**, 525–537 (2012).
- Jho, E. H. *et al.* Wnt/ β -catenin/Tcf signaling induces the transcription of Axin2, a negative regulator of the signaling pathway. *Mol. Cell. Biol.* **22**, 1172–1183 (2002).
- Itoh, K. & Sokol, S. Y. Graded amounts of *Xenopus* dishevelled specify discrete anteroposterior cell fates in prospective ectoderm. *Mech. Dev.* **61**, 113–125 (1997).
- Nojima, H. *et al.* Genetic evidence for involvement of maternally derived Wnt canonical signaling in dorsal determination in zebrafish. *Mech. Dev.* **121**, 371–386 (2004).
- Lu, Q. *et al.* δ -Catenin, an adhesive junction-associated protein which promotes cell scattering. *J. Cell Biol.* **144**, 519–532 (1999).
- Penzes, P., Cahill, M. E., Jones, K. A., VanLeeuwen, J. E. & Woolfrey, K. M. Dendritic spine pathology in neuropsychiatric disorders. *Nature Neurosci.* **14**, 285–293 (2011).
- Kim, H. *et al.* δ -Catenin-induced dendritic morphogenesis. An essential role of p190RhoGEF interaction through Akt1-mediated phosphorylation. *J. Biol. Chem.* **283**, 977–987 (2008).
- Isaely, I. *et al.* Deletion of the neuron-specific protein δ -catenin leads to severe cognitive and synaptic dysfunction. *Curr. Biol.* **14**, 1657–1663 (2004).
- Matter, C., Pribadi, M., Liu, X. & Trachtenberg, J. T. δ -Catenin is required for the maintenance of neural structure and function in mature cortex *in vivo*. *Neuron* **64**, 320–327 (2009).
- Abu-Elneel, K. *et al.* A δ -catenin signaling pathway leading to dendritic protrusions. *J. Biol. Chem.* **283**, 32781–32791 (2008).
- Wang, M., Dong, Q., Zhang, D. & Wang, Y. Expression of δ -catenin is associated with progression of human astrocytoma. *BMC Cancer* **11**, 514 (2011).
- Rodova, M., Kelly, K. F., VanSaun, M., Daniel, J. M. & Werle, M. J. Regulation of the rapsyn promoter by kaiso and δ -catenin. *Mol. Cell. Biol.* **24**, 7188–7196 (2004).
- Kim, S. W. *et al.* Non-canonical Wnt signals are modulated by the Kaiso transcriptional repressor and p120-catenin. *Nature Cell Biol.* **6**, 1212–1220 (2004).
- Koutras, C., Lessard, C. B. & Levesque, G. A nuclear function for the presenilin 1 neuronal partner NPRAP/ δ -catenin. *J. Alzheimer's Dis.* **27**, 307–316 (2011).
- Zhang, J. *et al.* Isoform- and dose-sensitive feedback interactions between paired box 6 gene and δ -catenin in cell differentiation and death. *Exp. Cell Res.* **316**, 1070–1081 (2010).
- Umeda, T. *et al.* Evaluation of Pax6 mutant rat as a model for autism. *PLoS ONE* **5**, e15500 (2010).
- Davis, L. K. *et al.* Pax6 3' deletion results in aniridia, autism and mental retardation. *Hum. Genet.* **123**, 371–378 (2008).
- Duparc, R. H., Boutemmine, D., Champagne, M. P., Tetreault, N. & Bernier, G. Pax6 is required for δ -catenin/neurojugin expression during retinal, cerebellar and cortical development in mice. *Dev. Biol.* **300**, 647–655 (2006).
- Pinto, D. *et al.* Functional impact of global rare copy number variation in autism spectrum disorders. *Nature* **466**, 368–372 (2010).
- Medina, M., Marinescu, R. C., Overhauser, J. & Kosik, K. S. Hemizygosity of δ -catenin (CTNND2) is associated with severe mental retardation in cri-du-chat syndrome. *Genomics* **63**, 157–164 (2000).
- Vrijenhoek, T. *et al.* Recurrent CNVs disrupt three candidate genes in schizophrenia patients. *Am. J. Hum. Genet.* **83**, 504–510 (2008).
- Zhou, J. *et al.* Presenilin 1 interaction in the brain with a novel member of the armadillo family. *Neuroreport* **8**, 2085–2090 (1997).
- Fujita, T. *et al.* δ -catenin/NPRAP (neural plakophilin-related armadillo repeat protein) interacts with and activates sphingosine kinase 1. *Biochem. J.* **382**, 717–723 (2004).
- Martinez, M. C., Ochiishi, T., Majewski, M. & Kosik, K. S. Dual regulation of neuronal morphogenesis by a δ -catenin-cortactin complex and Rho. *J. Cell Biol.* **162**, 99–111 (2003).
- Silverman, J. B. *et al.* Synaptic anchorage of AMPA receptors by cadherins through neural plakophilin-related arm protein AMPA receptor-binding protein complexes. *J. Neurosci.* **27**, 8505–8516 (2007).
- Laura, R. P. *et al.* The Erbin PDZ domain binds with high affinity and specificity to the carboxyl termini of δ -catenin and ARVCF. *J. Biol. Chem.* **277**, 12906–12914 (2002).
- Kim, K. *et al.* Dendrite-like process formation and cytoskeletal remodeling regulated by δ -catenin expression. *Exp. Cell Res.* **275**, 171–184 (2002).
- Daniel, J. M. & Reynolds, A. B. The catenin p120(ctn) interacts with Kaiso, a novel BTB/POZ domain zinc finger transcription factor. *Mol. Cell. Biol.* **19**, 3614–3623 (1999).
- Yoon, H. G., Chan, D. W., Reynolds, A. B., Qin, J. & Wong, J. N-CoR mediates DNA methylation-dependent repression through a methyl CpG binding protein Kaiso. *Mol. Cell* **12**, 723–734 (2003).
- Brigidi, G. S. *et al.* Palmitoylation of δ -catenin by DHHC5 mediates activity-induced synapse plasticity. *Nature Neurosci.* **17**, 522–532 (2014).
- De Rubeis, S. *et al.* CYFIP1 coordinates mRNA translation and cytoskeleton remodeling to ensure proper dendritic spine formation. *Neuron* **79**, 1169–1182 (2013).
- Matsuoka, R. L. *et al.* Class 5 transmembrane semaphorins control selective mammalian retinal lamination and function. *Neuron* **71**, 460–473 (2011).
- He, W. Z. *et al.* Analysis of *de novo* copy number variations in a family affected with autism spectrum disorders using high-resolution array-based comparative genomic hybridization. *Chin. J. Med. Genet.* **29**, 266–269 (2012).
- Harvard, C. *et al.* A variant Cri du Chat phenotype and autism spectrum disorder in a subject with *de novo* cryptic microdeletions involving 5p15.2 and 3p24.3-25 detected using whole genomic array CGH. *Clin. Genet.* **67**, 341–351 (2005).
- Marshall, C. R. *et al.* Structural variation of chromosomes in autism spectrum disorder. *Am. J. Hum. Genet.* **82**, 477–488 (2008).
- Qiao, Y. *et al.* Phenomic determinants of genomic variation in autism spectrum disorders. *J. Med. Genet.* **46**, 680–688 (2009).
- Sanders, S. J. *et al.* Multiple recurrent *de novo* CNVs, including duplications of the 7q11.23 Williams syndrome region, are strongly associated with autism. *Neuron* **70**, 863–885 (2011).
- Gai, X. *et al.* Rare structural variation of synapse and neurotransmission genes in autism. *Mol. Psychiatry* **17**, 402–411 (2012).

Supplementary Information is available in the online version of the paper.

Acknowledgements We acknowledge the participation of all of the families in the AGRE, NIMH and SSC studies that have been a model of public participatory research. The AGRE is a program of Autism Speaks and is supported, in part, by grant 1U24MH081810 from the National Institute of Mental Health. The SSC used here was developed by the following principal investigators: A. Beaudet, R. Bernier, J. Constantino, E. Cook, E. Fombonne, D. Geschwind, D. Grice, A. Klin, D. Ledbetter, C. Lord, C. Martin, D. Martin, R. Maxim, J. Miles, O. Ousley, B. Peterson, J. Piggot, C. Saulnier, M. State, W. Stone, J. Sutcliffe, C. Walsh, E. Wijsman. We thank the Allen Brain Atlas for use of their publicly available developing human brain expression data. Finally, we thank V. Kustanovich (AGRE) for helping with access to Autism Diagnostic Observation Schedule severity score data, D. Arking for sharing DNA from the SSC for Tagman genotyping, S. Maragh for zebrafish complementary DNA (cDNA) libraries and *eef1a11* primers, A. Kapoor for discussions, Q. Jiang for the translation of ref. 43, and J. A. Rosenfeld, L. G. Shaffer, Y. Shen and B.-L. Wu for sharing CNV data sets. Sequencing services were provided by the Johns Hopkins University Next Generation Sequencing Center, Sidney Kimmel Comprehensive Cancer Center, Illumina Sequencing Services and the Johns Hopkins University Genetic Resources Core Facility. E.C.O. is a National Alliance for Research on Schizophrenia and Depression young investigator. N.K. is a Distinguished George W. Brumley Professor. This work was funded by grants from the Simons Foundation to A.C. and to N.K., NIMH grant MH095867 to M.E.T., NIMH grants 5R25MH071584-07 and MH19961-14 to D.M.D.L. (Malison), National Institutes of Health grant RO1MH074090 to C.L.M., NIMH grant RO1MH081754 to A.C. and an Autism Speaks Dennis Weatherstone pre-doctoral fellowship (number 7863) to T.T.

Author Contributions Designed the study and wrote the manuscript (T.T., A.C.); edited the manuscript (all authors); examined phenotype data for the female autism patients (T.T., E.C.); *MECP2/CTNND2* sequencing and TagMan genotyping (T.T., M.X.S., T.P., K.P., D.S., M.W.S.); autism exome sequencing (T.T.); Simons exome sequencing analysis (S.S., M.S.); CNV analysis (S.W.C., C.L.M., D.M.D., S.S., R.C.C., H.B., M.E.T., M.S., T.T.); *CTNND2* molecular biology (T.T., M.X.S.); zebrafish gastrulation and protein-protein interaction studies (Y.P.L., E.O., N.K.); primary hippocampal neuron experiments and expression analysis (K.S., T.T., D.A.); bioinformatics analyses (T.T., V.P.).

Author Information All sequence data have been deposited in the National Database for Autism Research in NDAR Study 367 and are available at <http://dx.doi.org/10.15154/1171641>. Reprints and permissions information is available at www.nature.com/reprints. The authors declare no competing financial interests. Readers are welcome to comment on the online version of the paper. Correspondence and requests for materials should be addressed to A.C. (aravinda@jhmi.edu).

METHODS

Human subjects and animal experiment permissions. We studied 13 unrelated females, 12 from FEMFs and one from a family with an affected girl and boy, from the AGRE⁴⁹ and the NIMH collections (<https://www.nimhgenetics.org/>). Of these, 11 were of European, and one each of Hispanic and Native Hawaiian or Pacific Island ancestry. Studies of human subjects were approved by the Johns Hopkins Medicine Institutional Review Board (IRB NA_00015748). All protocols for animal care, use and euthanasia were reviewed and approved by the Institutional Animal Care and Use Committees of Johns Hopkins University (protocol MO12M412) and Duke University (protocol A229-12-08), and were in accordance with the Association for Assessment and Accreditation of Laboratory Animal Care guidelines. **DNA sequencing.** MECP2 sequencing. Each of the 13 individuals with autism was assessed for the four coding exons of MECP2 by PCR amplification of each exon and Sanger sequencing, performed at Beckman Coulter Genomics. The sequence traces were analysed in Sequencher version 4.7.

Exome sequencing and read mapping. We analysed ten female autism cases and one HapMap sample (NA18507) using the Agilent SureSelect Whole Exome capture (38 Mb) and SOLiD 3+ and 4 technologies. For three additional female individuals with autism, sequencing used the Illumina TruSeq Whole Exome capture (62 Mb) and Illumina technology; all Illumina exome experimental steps were performed at the Illumina sequencing centre. The SOLiD and Illumina data were mapped to the human genome build 37 using the BFAST⁵⁰ and BWA⁵¹ programs, respectively. Subsequently, the SAM output was converted to BAM output, duplicates were marked using Picard, and indel realignment and quality score recalibration were performed in GATK⁵². Variants were called across all exomes as well as 71 of the 1000 Genomes European female exomes. Each variant was annotated for genetic features using ANNOVAR⁵³. Additional annotations included presence in 1000 Genomes, conservation to zebrafish, and presence in autism, autism candidate, or intellectual disability genes based on the published literature (ref. 29 and <https://gene.sfsari.org/autdb/>). In total, we identified 37,424 non-synonymous, 486 stop gain, 32 stop loss, 35,549 synonymous and 273 splice variants.

CTNND2 sequencing and read mapping. Three hundred and sixty-two females with autism (300 unrelated, independent), ten HapMap samples and a pooled individual sample replicated eight times were sequenced for all of CTNND2 coding exons. To amplify the 22 RefSeq exons and seven Ensembl exons in CTNND2, 87 amplicons were designed on the Fluidigm Access Array Targeted Resequencing platform. Amplification and addition of barcodes were accomplished as described in the manual using the bidirectional sequencing primer strategy. Next, each sample was purified using Agencourt AMPure beads following the manufacturer's protocol. All samples were run on Agilent High Sensitivity DNA Chips on an Agilent 2100 Bioanalyzer to confirm size range and purity of the PCR product, followed by quantitative PCR for quantification before pooling all 384 samples for sequencing. The library was sequenced on a single lane of an Illumina HiSeq (100 base, single pass reads) instrument following the Illumina Sequencing Strategy as described in the Fluidigm Access Array manual. Each sample fastq read was assigned and partitioned to an amplicon based on its primer sequence using sabre (<https://github.com/najoshi/sabre>), then aligned only to that amplicon using BWA. All the resulting sam files for each individual were combined using Picard into one sample bam. Variants were called per individual using GATK and hard filters to get high-quality variants. To assess genotype quality of the HapMap samples, comparisons were made to HapMap genotype, OMNI genotype and 1000 Genomes data. The pooled individual replicate was also used for data quality control.

Variant validation. All CTNND2 missense changes identified were sequenced by Sanger chemistry for validation. Primers were designed to cover the exons in which the variants were found. A portion of each PCR product was run on a 1.8% agarose gel for 1.5 h to check for the expected product size. Upon confirmation, the rest of the product underwent PCR purification. The purified samples were quantified by nanodrop, diluted to 25 ng μl^{-1} and sent to Beckman Coulter Genomics for Sanger sequencing. Subsequently, the reads were analysed in Sequencher version 4.7.

Genotyping. CTNND2 TaqMan assay for the G34S and R713C variants. To test the frequency of the two CTNND2 variants we found in the autism exomes, we used TaqMan genotyping and created synthetic homozygous reference/mutant genotypes within a plasmid containing DNA from our patients, and used the patient DNA on each plate as a heterozygous control, to ensure that we would get three cluster plots in the SDS software. We ran a total of 11,788 reactions including 1,006 duplicates for which there was 100% genotype concordance. To genotype the G34S and R713C variants, custom TaqMan genotyping assays were designed for each variant.

Principal component analysis for ancestry. The five individuals (03C16092, 03C16094, SSC02696, SSC03276, NA19020) containing the G34S variant were assessed for ancestry by principal component analysis. A set of approximately 6,000 autosomal single nucleotide polymorphisms genotyped in common in all five samples (Affymetrix 5.0, Affymetrix 5.0, Illumina 1MDuo, Illumina 1MDuo,

Illumina OMNI 2.5) were analysed using the Eigenstrat program. Genotypes from reference populations came from the CEU, YRI and CHB/JPT populations.

Copy number validation. TaqMan Copy Number Assays were used for validation of CNVs in the AGRE samples (AU066818, AU075604, AU1178301, AU051503) and their family members. Three or four assays were run for each CNV region in each sample. NA10836 was used as a calibration sample in CopyCaller software version 2.0 for a copy number of 2 in each region.

Phylogenetic analysis. After alignment with ClustalW, Molecular Evolutionary Genetics Analysis (MEGA) software was used to generate a phylogenetic tree by the neighbour-joining method; a total of 1,163 and 678 positions were used to assess percentage identity for orthologues and paralogues, respectively.

Statistical analysis. Exome sequence. This study focused on variants of interest, defined as those that were absent in both dbSNP129 and 1000 Genomes low-pass sequencing data and were probably functionally deleterious (missense at residues conserved to zebrafish (human, chimp, dog, cow, mouse, rat and zebrafish from the University of California, Santa Cruz (UCSC) 46-way alignment), nonsense and canonical splice site changes). We compared each gene and its number of variants of interest with that expected on the basis of 10,000 replications of random sampling of 13 exomes from 71 female European controls. Genes having two or more variants of interest only in autism exomes were considered to be relevant candidates.

Allen Brain Atlas Data. The Allen Brain Atlas Microarray (Affymetrix Human Exon 1.0 ST data microarray summarized to genes ($n = 17,630$ genes)) data set for the Developing Human Brain (8 weeks after conception to 40 years) was downloaded from the Allen Brain Atlas website on 24 February 2012. Linear regression was performed on the data set for age and brain region (in R software). Pearsonian correlations were calculated for each gene (X) and CTNND2 (Y); genes with absolute values greater than 0.3 were retained, corresponding to an experiment-wise $P = 0.05$ (17,630 comparisons) significance level. Pathway analyses were performed using GeneMania (<http://www.genemania.org>). DAVID analysis was performed on all correlated genes using the following categories: GOTERMS (biological process, cellular compartment and molecular function) for function and UCSC TFBS.

Functional assays. Generation of human CTNND2 and mouse *Ctnnd2* constructs. Human CTNND2 was initially cloned into the pDONR221 Gateway vector. Subsequently, the human DNA was cloned into the pCS2 vector for zebrafish assays and pcDNA 6.2 N-EmGFP-DEST vector (Gateway) for the neuronal assays.

Zebrafish gastrulation assays. Using a splice-blocking morpholino targeting zebrafish *ctnnd2*, one- to eight-cell stage embryos were injected ($N = 50$ –180) and live embryos at the eight- to ten-somite stage were analysed for gastrulation phenotypes including shortened body axes, longer somites, and broad and kinked notochords in morphant embryos. Embryos with phenotypes were then classified as class I or II depending on their severity (features of the convergence/extension phenotype include a shortened body axis, wider somites and a kinked notochord, with class I having one or two and class II having all three of these components, respectively). Specificity of the morpholino reagent was tested by co-injection of wild-type human CTNND2 mRNA. To test CTNND2 variants, injection cocktails containing morpholino and mutant human CTNND2 variants were injected and compared with the rescue condition of wild-type human CTNND2.

Zebrafish chordin expression assay. Zebrafish embryos were harvested at 90% epiboly stage and fixed in 4% paraformaldehyde at 4 °C. Whole-mount RNA *in situ* hybridization was performed with a digoxigenin-labelled anti-chordin RNA probe synthesized by *in vitro* transcription (Roche). The chordin expression domain was measured in lateral view ('L' in Extended Data Fig. 7b). The middle point of the expression domain length and the centre of the embryo was linked with a dashed line (Extended Data Fig. 7b), along which the width of chordin expression domain ('W' in Extended Data Fig. 7b) was measured. Length:width ratio was calculated to quantify ectopic expression.

Immunoblotting. Cells were transfected with CTNND2 and CTNNB1 expression constructs and harvested 48 h later. Protein lysates were immunoprecipitated using an anti-GFP antibody (Roche 11814460001) and immunoblotted with an anti-Flag antibody (Sigma F7425).

Neuronal cultures and synapse analysis. Hippocampi from day E18 rats or E17 mouse embryos were prepared and maintained as described elsewhere⁵⁴. At DIV8, the cells were transfected with GFP constructs (pcDNA6.2/N-EmGFP-DEST: alone, fused to wild-type or variant allele containing CTNND2) and 500 ng of pCAG-DsRed2 using Lipofectamine 2000 (Life Technologies). On DIV16, cells were fixed with a 4% paraformaldehyde/4% sucrose solution, followed by immunolabelling with primary antibodies against the appropriate target as described and their respective secondary antibodies. Neurons were imaged either on a Zeiss 510 confocal for spine analysis or on Zeiss epifluorescence microscope for synapse analysis, and analysed using ImageJ. Synapses were defined as puncta with overlapping signal between vGluT1 (Millipore catalogue number AB5905) and PSD95 (K28/43 clone from Neuromab) or vGluT1 and GluA (polyclonal antibody raised in rabbit against the C terminus of GluA subunit). To assess the expression of transfected CTNND2

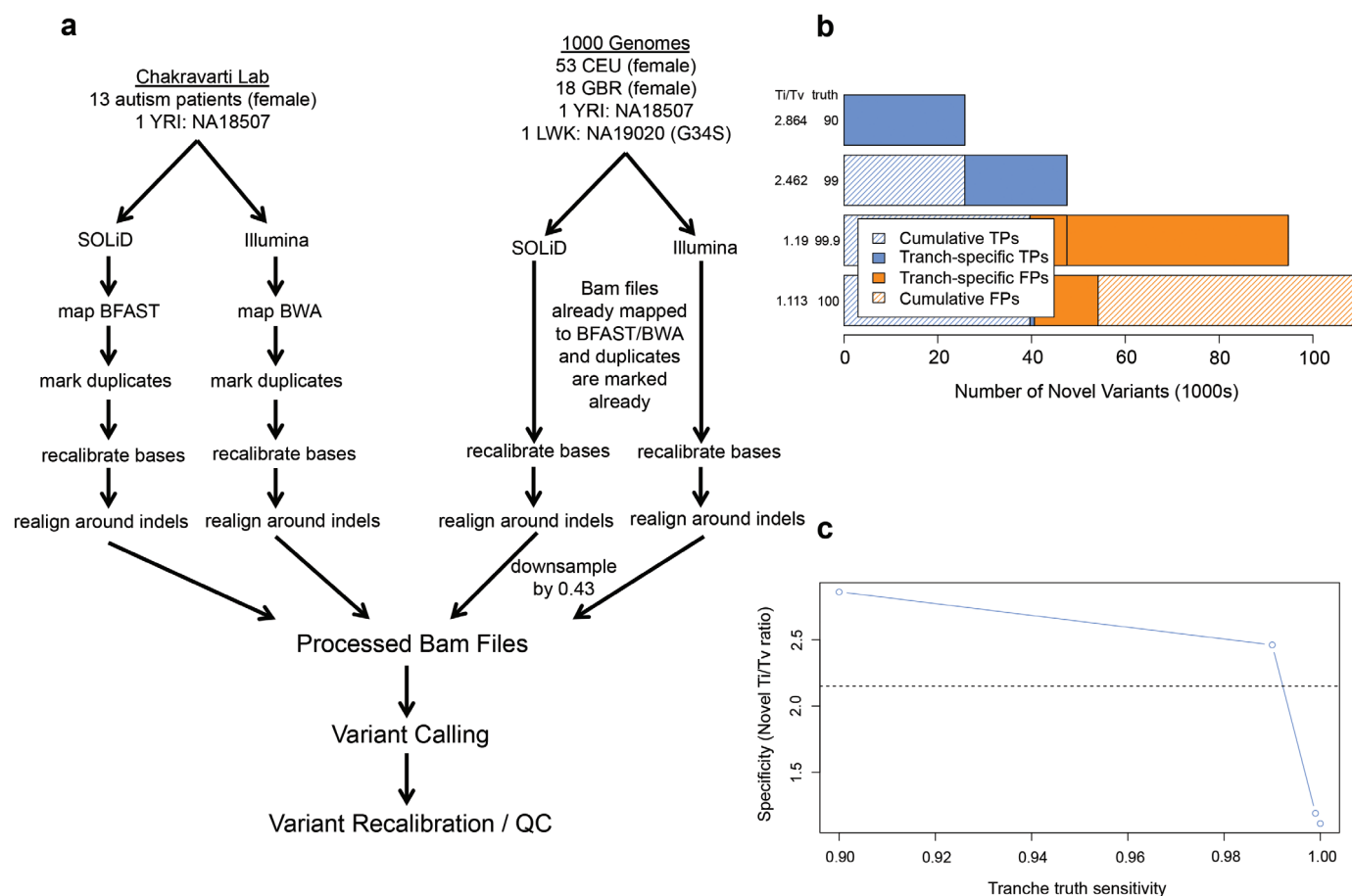
and its mutant alleles in the δ -catenin null background, we selected five pre-defined areas of interest with constant area in each dendrite (Extended Data Fig. 10).

Gene expression assays. Expression of *ctnnd2a* and *ctnnd2b* in zebrafish. To assess mRNA expression of the two zebrafish orthologues (*ctnnd2a*, *ctnnd2b*) of human δ -catenin, we performed PCR on normalized cDNA libraries (a gift of S. Maragh) from zebrafish at various developmental stages (50% epiboly, 75% epiboly, bud, 13 somite, 24 h after fertilization, and 3 days).

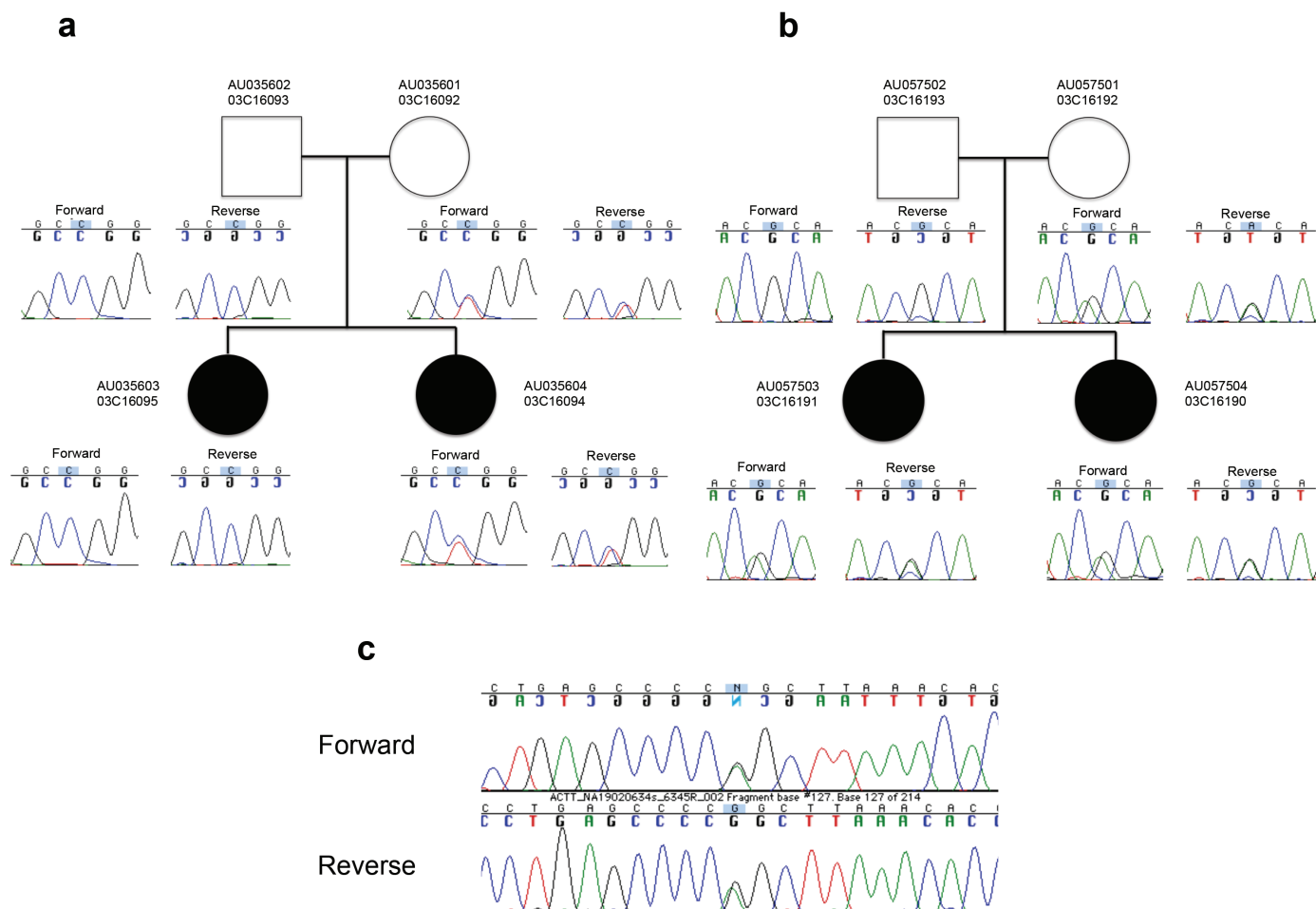
CTNND2 expression analysis in human and mouse tissues. To examine expression of *CTNND2* in different human tissues, the Human MTC cDNA Panel 1 (Clontech catalogue number 636742, lot number 7080213), Human MTC cDNA Panel II (Clontech catalogue number 636743, lot number 6040176) and the Human Fetal MTC cDNA Panel (catalogue number 636747, lot number 5090557) were analysed by a TaqMan gene expression assay (catalogue number Hs00181643_m1) for *CTNND2* and for a pipetting control (*GAPDH*, catalogue number 4333764T). Each tissue was tested in triplicate. Subsequently, the threshold cycle (C_t) values

were averaged and the ΔC_t values calculated between all of the tissues and the adult brain. The fold difference from brain was calculated as $(1/(2^{\Delta C_t}))$ for each tissue.

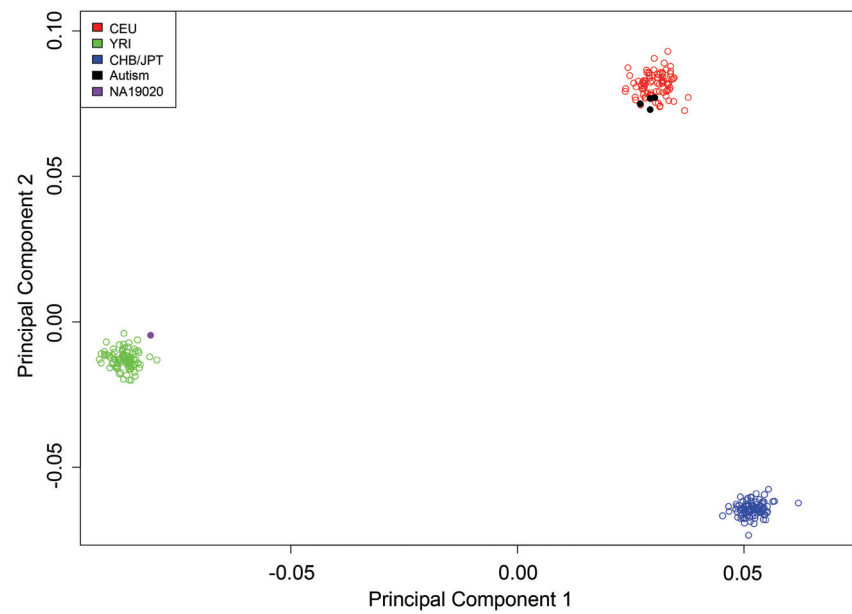
49. Geschwind, D. H. *et al.* The autism genetic resource exchange: a resource for the study of autism and related neuropsychiatric conditions. *Am. J. Hum. Genet.* **69**, 463–466 (2001).
50. Homer, N., Merriman, B. & Nelson, S. F. BFAST: an alignment tool for large scale genome resequencing. *PLoS ONE* **4**, e7767 (2009).
51. Li, H. & Durbin, R. Fast and accurate long-read alignment with Burrows–Wheeler transform. *Bioinformatics* **26**, 589–595 (2010).
52. McKenna, A. *et al.* The Genome Analysis Toolkit: a MapReduce framework for analyzing next-generation DNA sequencing data. *Genome Res.* **20**, 1297–1303 (2010).
53. Wang, K., Li, M. & Hakonarson, H. ANNOVAR: functional annotation of genetic variants from high-throughput sequencing data. *Nucleic Acids Res.* **38**, e164 (2010).
54. Brewer, G. J. Serum-free B27/neurobasal medium supports differentiated growth of neurons from the striatum, substantia nigra, septum, cerebral cortex, cerebellum, and dentate gyrus. *J. Neurosci. Res.* **42**, 674–683 (1995).



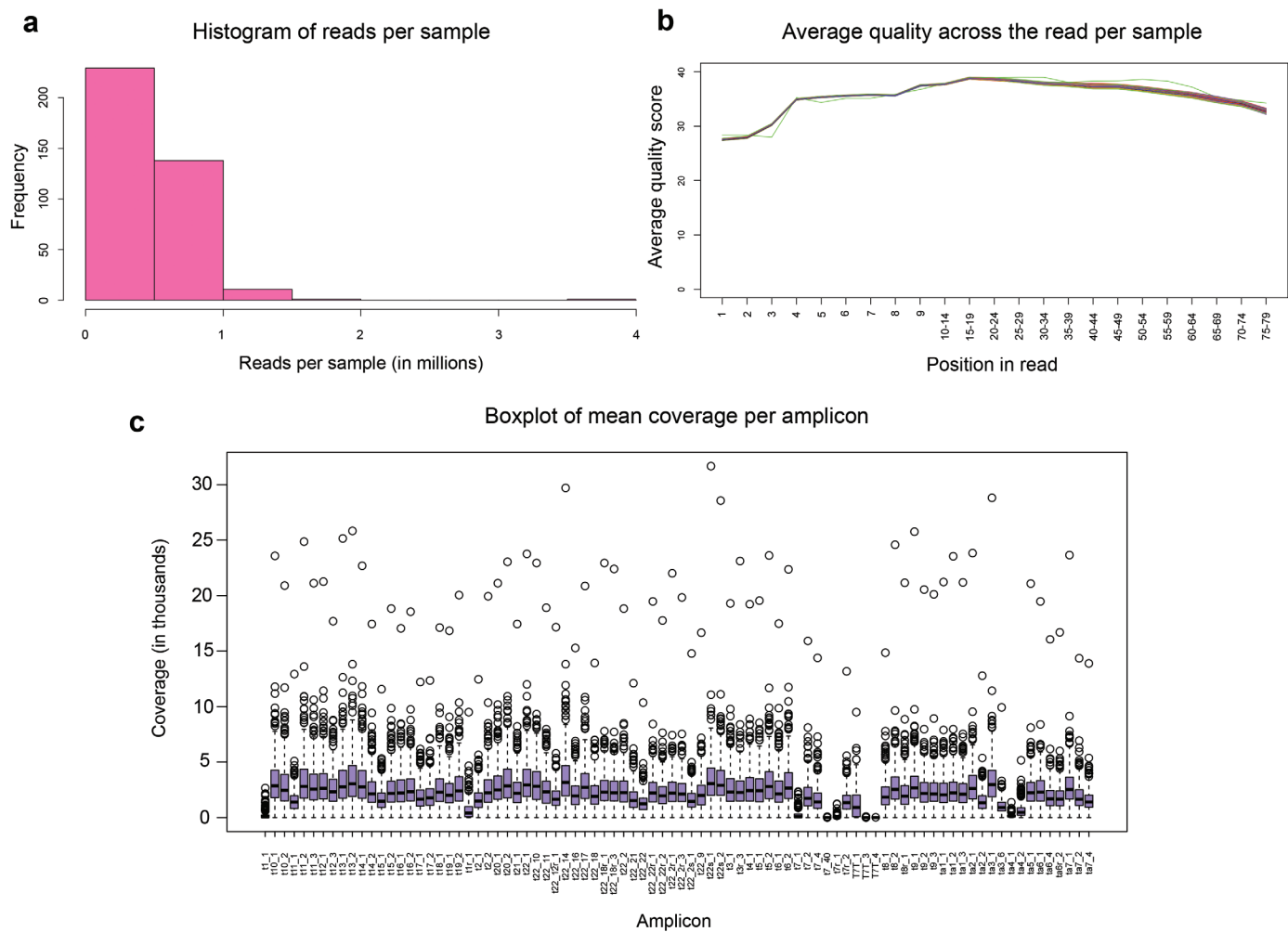
Extended Data Figure 1 | Exome sequencing workflow and quality control. **a**, Workflow of exome analysis in this study. **b**, Variant recalibration metrics exhibiting why a 99% cutoff was used for truth sensitivity. **c**, Variant recalibration specificity versus sensitivity.



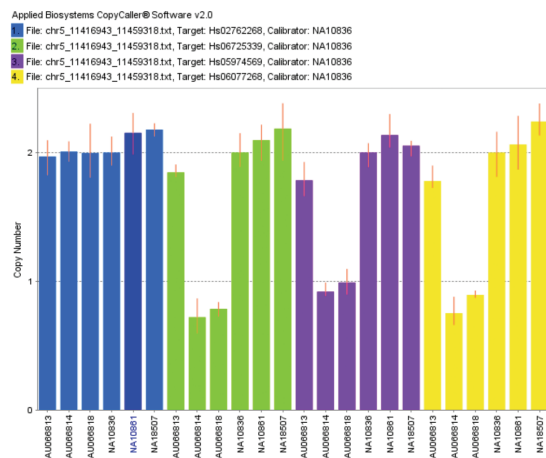
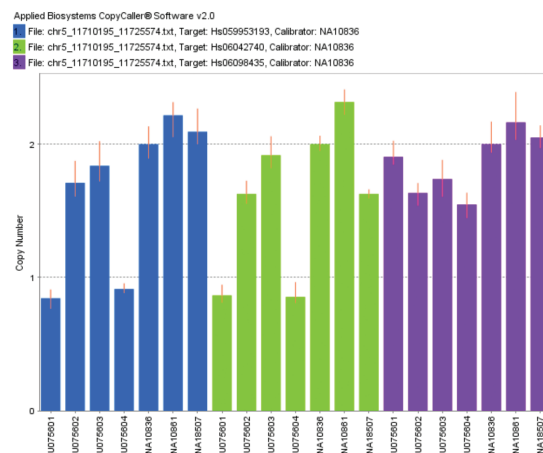
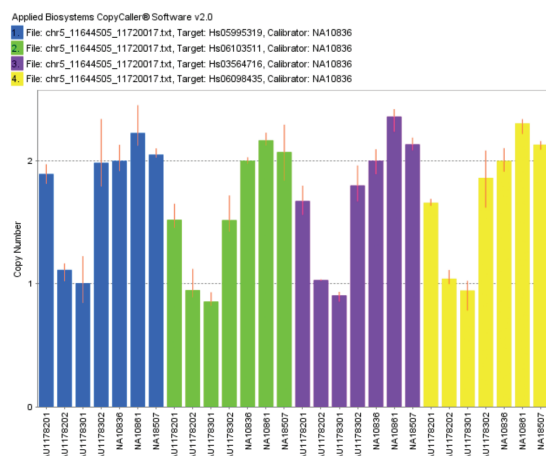
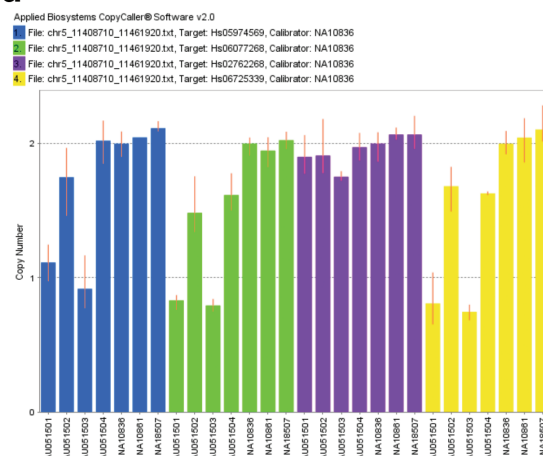
Extended Data Figure 2 | Sanger sequencing chromatograms. **a**, G34S variant in this study; **b**, R713C variants in this study; **c**, G34S in NA19020.



Extended Data Figure 3 | Principal component analysis of 6,211 shared autosomal single nucleotide polymorphisms in CEU, YRI, CHB/JPT, autism and NA19020 samples.

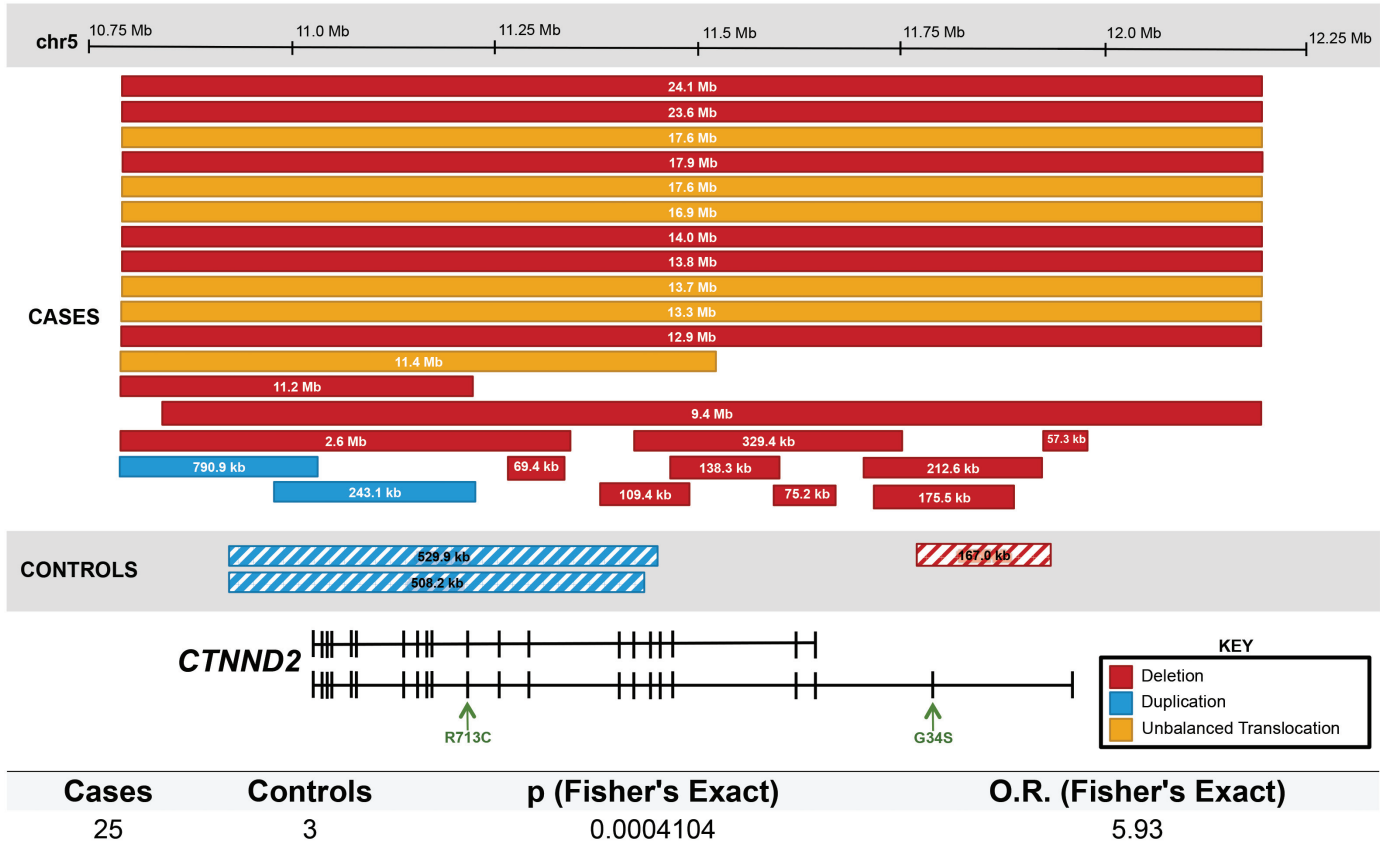


Extended Data Figure 4 | Read and amplicon metrics in *CTNND2* sequencing. **a**, Histogram of reads per sample. **b**, Average quality scores across the read across all samples with each sample represented by a separate line. **c**, Boxplot of coverage per amplicon.

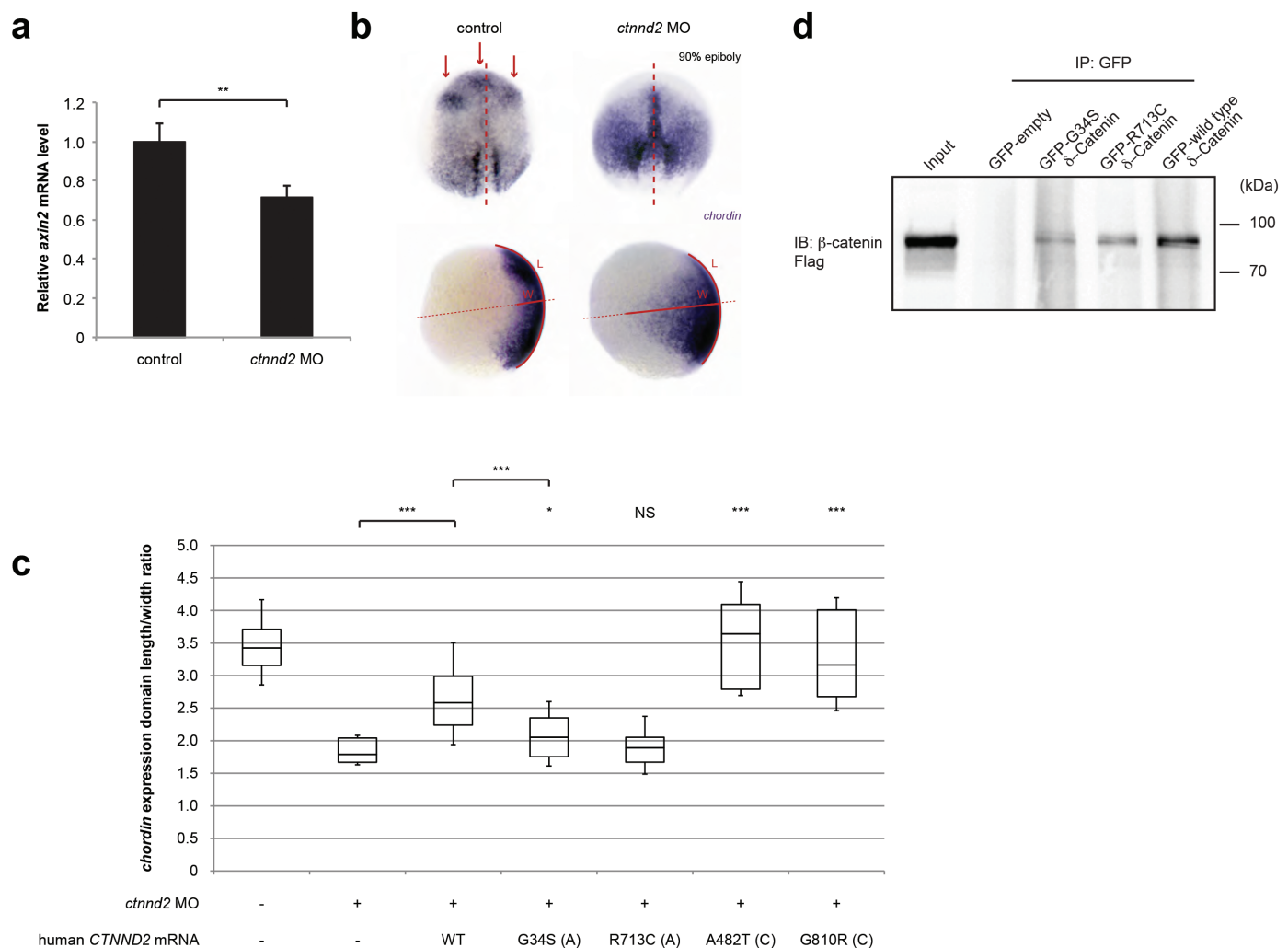
a**b****c****d**

Extended Data Figure 5 | Validation of deletions. a, In AU066818; b, in AU075604; c, in AU1178301 and AU1178202; d, in AU051503.

Neurodevelopmental Disease Phenotypes with Any Dosage Imbalance

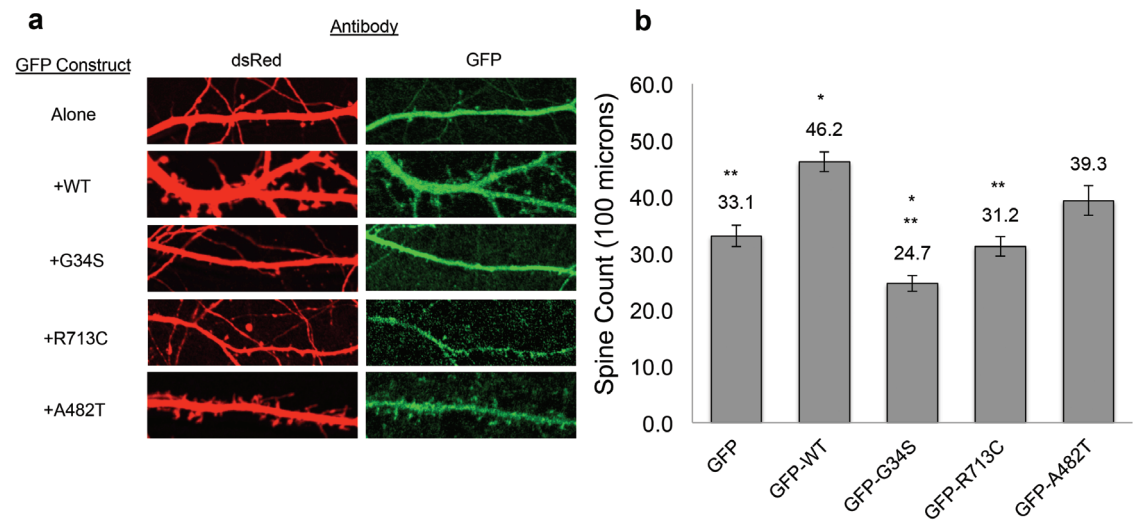


Extended Data Figure 6 | *CTNND2* CNVs from patients with neurodevelopment disorders studied using methods published in ref. 11.



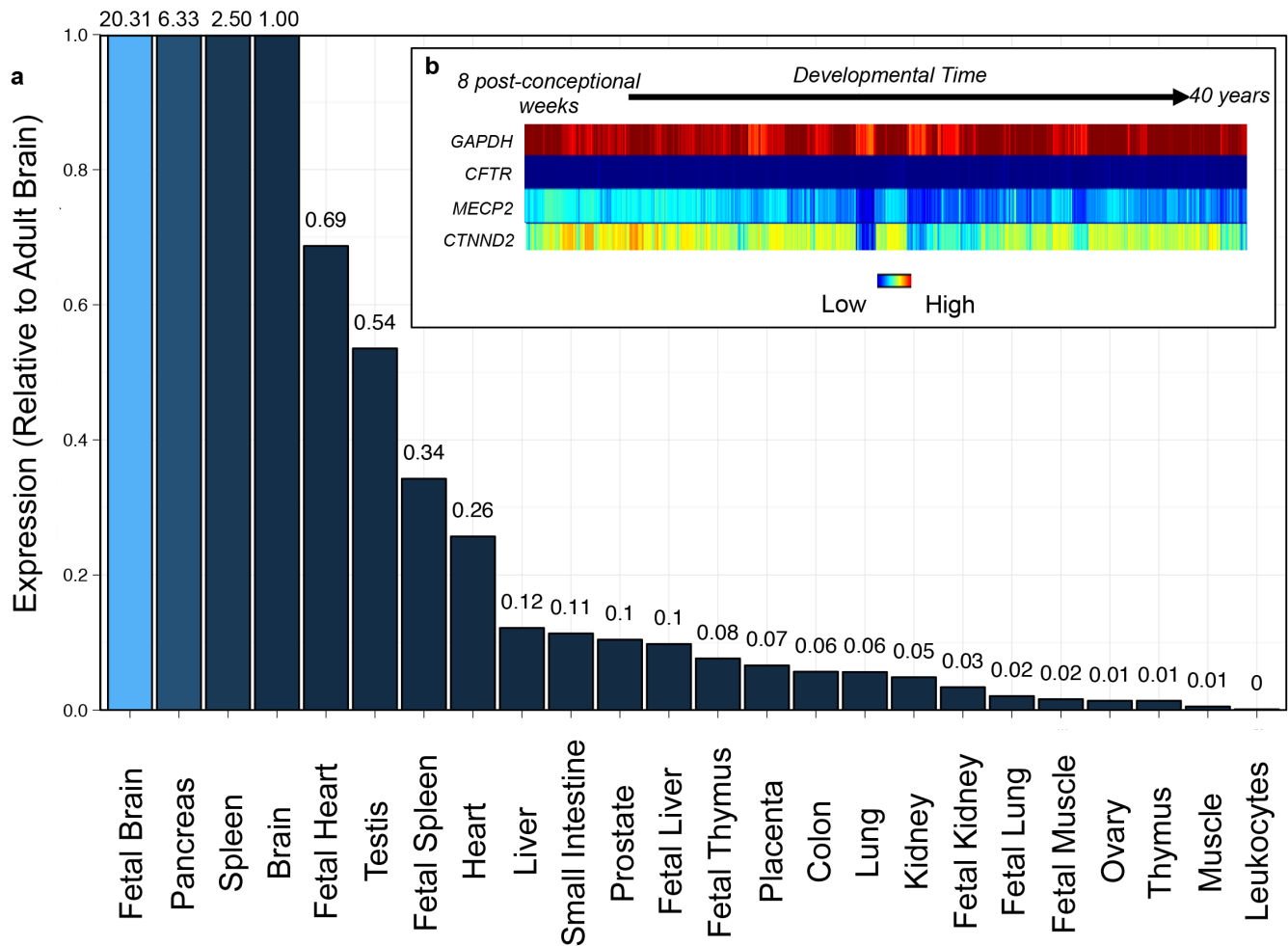
Extended Data Figure 7 | Wnt defects in *ctnd2b* zebrafish morphant embryos. **a**, Relative *axin2* mRNA level in the ten-somite stage in control versus morphant embryos. **b**, Wholemount RNA *in situ* hybridization of *chordin*. Dorsal view in upper panels with the anterior aspect at the apex. The dorsal axis is marked with a red dashed line, and regions with high expression are marked (arrows) in control embryos. Lateral view in lower panels,

length (*L*) and width (*W*) of *chordin* expression domains were measured. **c**, Quantification of *chordin* expression domains (length:width ratio) in injected embryos. **d**, Immunoblot showing a macromolecular interaction between Flag-tagged CTNNB1 and GFP-tagged CTNND2 with the corresponding variants. Two-sided *t*-tests were conducted: **P* < 0.05, ***P* < 0.01 and ****P* < 0.001, respectively. Sample size (*n*) is marked for each condition.



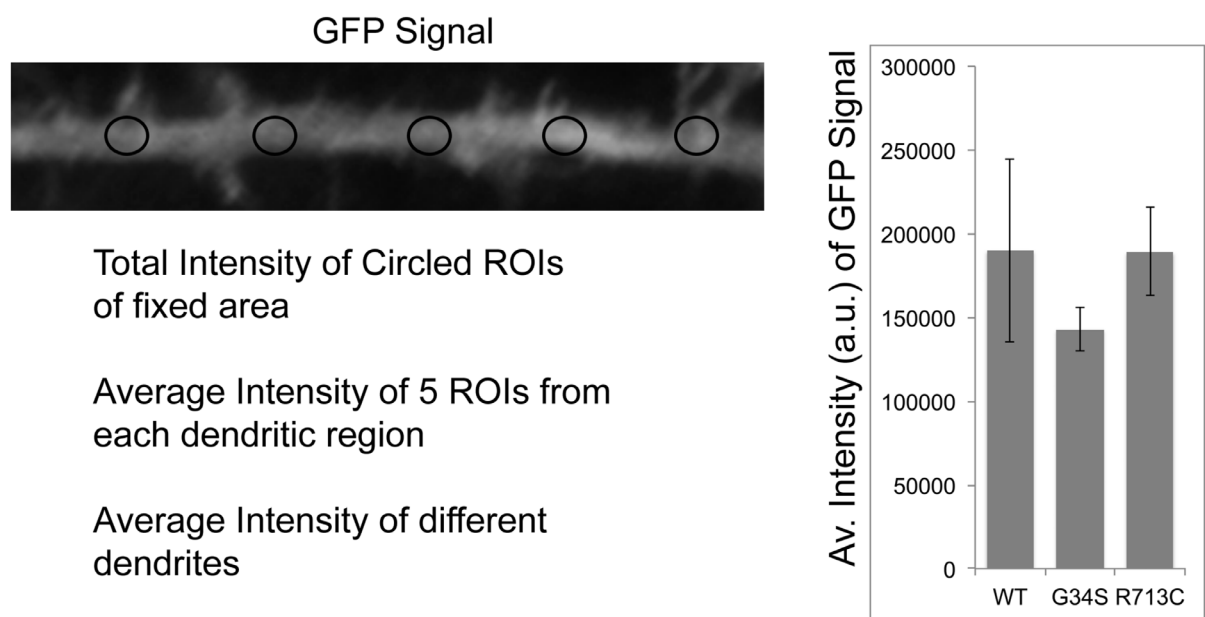
Extended Data Figure 8 | Functional *in vitro* modelling of δ -catenin missense variants in embryonic rat hippocampal neurons. a, Representation of spines along the dendrite in control and overexpression GFP vectors (empty or fused with wild-type or variant allele containing CTNND2 (G34S, R713C, A482T (control))). Cell counts for each construct were as follows: GFP

($N = 32$), GFP-WT ($N = 27$), GFP-G34S ($N = 29$), GFP-R713C ($N = 26$) and GFP-A482T ($N = 29$). **b,** Quantification of dendritic spine numbers and statistical comparisons by Tukey's honestly significant test following ANOVA. Both * and ** indicate $P < 0.05$ than GFP and significantly different from wild type, respectively.



Extended Data Figure 9 | Gene expression of *CTNND2* and co-expression with known autism genes. **a**, Expression of *CTNND2* in various human fetal and adult tissues, shown as fold difference relative to adult brain. **b**, RNA-Seq-based *CTNND2* gene expression in the developing human brain (<http://www.brainspan.org>); shown are \log_2 (RPKM expression) values at

time-points from 8 weeks after conception to 40 years of age, with the lowest to highest expression coloured from navy blue to red. Controls for high expression, low to no expression and known autism genes are *GAPDH*, *CFTR* and *MECP2*, respectively.



Extended Data Figure 10 | Analysis of overexpression of transiently transfected neurons. Representation of average intensity of five individual regions of interest from a selected dendritic region. Quantitative comparison

does not reveal a significant difference in expression levels of different variants of *CTNND2*.

Ferroptosis as a p53-mediated activity during tumour suppression

Le Jiang^{1*}, Ning Kon^{1*}, Tongyuan Li¹, Shang-Jui Wang¹, Tao Su^{2,3}, Hanina Hibshoosh^{2,3}, Richard Baer^{1,2,3} & Wei Gu^{1,2,3}

Although p53-mediated cell-cycle arrest, senescence and apoptosis serve as critical barriers to cancer development, emerging evidence suggests that the metabolic activities of p53 are also important. Here we show that p53 inhibits cystine uptake and sensitizes cells to ferroptosis, a non-apoptotic form of cell death, by repressing expression of *SLC7A11*, a key component of the cystine/glutamate antiporter. Notably, p53^{3KR}, an acetylation-defective mutant that fails to induce cell-cycle arrest, senescence and apoptosis, fully retains the ability to regulate *SLC7A11* expression and induce ferroptosis upon reactive oxygen species (ROS)-induced stress. Analysis of mutant mice shows that these non-canonical p53 activities contribute to embryonic development and the lethality associated with loss of *Mdm2*. Moreover, *SLC7A11* is highly expressed in human tumours, and its overexpression inhibits ROS-induced ferroptosis and abrogates p53^{3KR}-mediated tumour growth suppression in xenograft models. Our findings uncover a new mode of tumour suppression based on p53 regulation of cystine metabolism, ROS responses and ferroptosis.

Inactivation of the p53 tumour suppression pathway is a pivotal event in the formation of most human cancers^{1–5}. Traditionally, the tumour suppression activity of p53 was thought to reflect its ability to elicit cell-cycle arrest, apoptosis and/or senescence in response to cellular stress. However, recent studies suggest that other unconventional activities of p53 are also crucial for its tumour suppressor function^{4–8}. The p53 protein achieves its diverse cellular outcomes by serving as a DNA-binding transcription factor that selectively modulates the expression of certain p53 transcriptional target genes. Stress-induced activation of p53 protein is primarily achieved by post-translational modifications⁹, and our recent studies of mice expressing acetylation-defective p53 mutants revealed that acetylation differentially regulates p53-mediated cell-cycle arrest, apoptosis and senescence¹⁰. Notably, the mutant p53^{3KR} polypeptide, while defective for the three conventional p53 functions, still retains its tumour suppression function and the ability to modulate the expression of metabolic targets¹⁰, suggesting that p53-mediated metabolic regulation is critically involved in suppressing tumour formation *in vivo*.

Identification of *SLC7A11* as a p53 target

To elucidate the precise effects of p53-mediated metabolic regulation, we sought to identify novel p53 target genes by generating a tetracycline-controlled (tet-on) p53-inducible cell line for microarray analysis. Array data were examined with Partek software and genes that are differentially expressed between induced and non-induced cells were identified (Extended Data Table 1). *SLC7A11*, which encodes a component of the cystine/glutamate antiporter^{11–13}, was identified as a novel p53 target gene. While there was no obvious effect of tetracycline treatment on *SLC7A11* expression in the parental H1299 cells, progressive repression of *SLC7A11* mRNA expression was observed in the tet-on p53-inducible line (Extended Data Fig. 1a) and western blot analysis revealed that p53 activation severely reduced *SLC7A11* protein levels (Fig. 1a). The 5' flanking region of the human *SLC7A11* gene at chromosome 4q28–31 (ref. 13) contains one site that matches the consensus p53-binding sequence (Fig. 1b), and a p53–DNA complex was readily identified by

electrophoretic mobility shift analysis (EMSA) upon incubation of highly purified recombinant full-length human wild-type p53 with a radio-labelled oligonucleotide probe containing this site (Fig. 1c). Moreover, this p53–DNA complex was super-shifted in the presence of a p53-specific antibody and was markedly diminished by competition with the unlabelled probe. Furthermore, chromatin immunoprecipitation (ChIP) analysis of human osteosarcoma U2OS cells (which express wild-type p53) revealed that endogenous p53 polypeptides occupy the promoter region of the *SLC7A11* gene (Fig. 1d). Moreover, the protein levels of *SLC7A11* were markedly decreased when p53 is activated by nutlin-3 treatment¹⁴ or upon DNA damage (Fig. 1e and Extended Data Fig. 1b). In contrast, *SLC7A11* downregulation was completely abrogated under p53-knockdown conditions (Fig. 1e). Similar results were also observed in other human cancer cell lines expressing wild-type p53 (H460 and MCF-7), whereas no apparent effects were detected in p53-null cells (H1299 and SAOS-2) (Extended Data Fig. 1c–e). Together, these data indicate that the *SLC7A11* gene is a target of p53-mediated transcriptional repression.

Regulation of *SLC7A11* expression by p53^{3KR}

Our previous study showed that p53^{3KR} retains the ability to regulate metabolic targets¹⁰. To test the role of p53^{3KR} in modulating *SLC7A11* expression, we established a tet-on H1299 cell line in which p53^{3KR} expression can be induced by tetracycline. Consistent with our previous study¹⁰, p53^{3KR} was able to activate expression of TIGAR and MDM2, but not p21 (also known as CDKN1A) or PUMA (also known as BBC3). Notably, *SLC7A11* levels were drastically reduced at various time points after p53^{3KR} induction (Fig. 2a). Chromatin immunoprecipitation (ChIP) analysis showed that the p53^{3KR} protein is able to bind the promoter of the *SLC7A11* gene (Fig. 2b). To corroborate this finding under more physiological settings, we examined the levels of *SLC7A11* transcripts in mouse embryonic fibroblasts (MEFs) derived from p53^{+/+}, p53^{3KR/3KR} and p53^{−/−} mice. Quantitative reverse transcription polymerase chain reaction (RT–qPCR) analysis revealed that *SLC7A11* expression is markedly increased (~4 fold) in p53^{−/−} cells relative to wild-type MEFs (Fig. 2c

¹Institute for Cancer Genetics, College of Physicians & Surgeons, Columbia University 1130 St Nicholas Ave, New York, New York 10032, USA. ²Department of Pathology and Cell Biology, College of Physicians & Surgeons, Columbia University 630 West 168th Street, New York, New York 10032, USA. ³Herbert Irving Comprehensive Cancer Center, College of Physicians & Surgeons, Columbia University 1130 St Nicholas Ave, New York, New York 10032, USA.

*These authors contributed equally to this work.

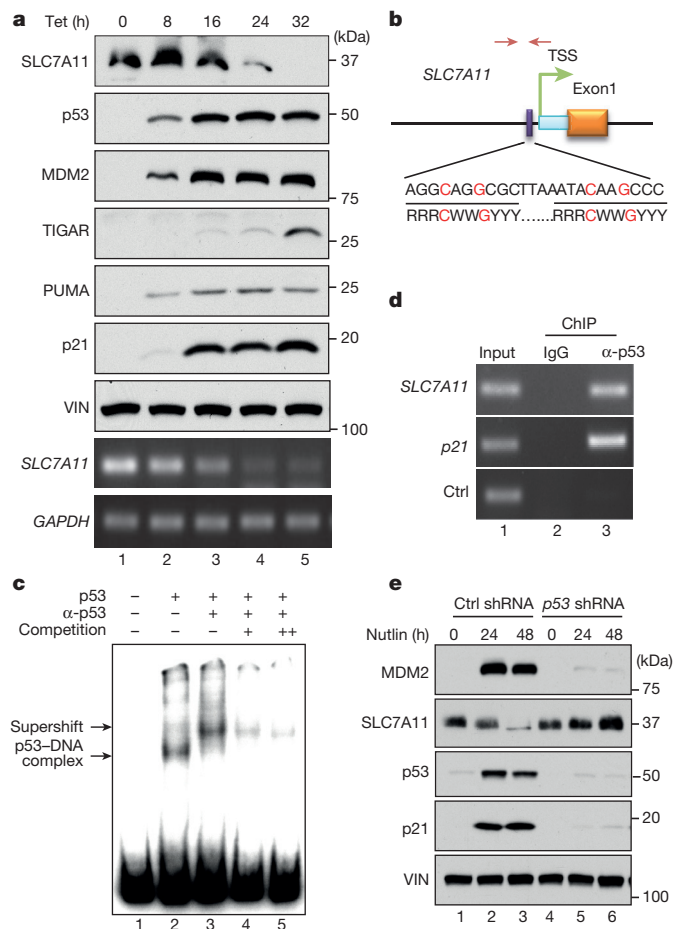


Figure 1 | Identification of *SLC7A11* as a target of p53. **a**, Western blot and RT-PCR for tet-on p53 stable line cells treated with doxycycline. VIN, vinculin. **b**, Schematic diagram of p53 binding location and sequence on human *SLC7A11* gene. Identified p53 binding sequence was compared with consensus sequence (R, A/G; W, A/T; Y, C/T; nucleotides C and G in red are essential for p53 binding). TSS, transcription start site. Facing arrows indicate primers for generating probes in **c** and PCR in **d**. **c**, EMSA was performed with indicated components. The double plus sign represents that more competition cold probes were added compared to the single plus sign (200-fold versus 100-fold to radioactive-labelled hot probes). **d**, ChIP assay was carried out in U2OS cells. **e**, U2OS cells with p53 knockdown were treated with nutlin and analysed by western blot. All data are representative of three independent experiments.

and Extended Data Fig. 1f). However, *SLC7A11* transcript levels remain low in *p53*^{3KR/3KR} cells, suggesting that *p53*^{3KR} can inhibit *SLC7A11* expression in a manner similar to wild-type p53. Moreover, ChIP analysis revealed that mouse p53 was recruited to the murine *Slc7a11* promoter region with the primers corresponding to the RE3 site in both wild-type and *p53*^{3KR} MEFs but not in p53-null MEFs (Extended Data Fig. 1g, h). These data demonstrate that the acetylation-defective mutant *p53*^{3KR} retains its ability to regulate *SLC7A11* expression *in vivo*.

Regulation of cystine uptake and ferroptosis

SLC7A11 is a key component of a plasma membrane transporter (the x_c^- system) that mediates Na^+ -independent cellular uptake of extracellular cystine in exchange for intracellular glutamate^{11–13}. To understand the functional consequences of p53-mediated repression of *SLC7A11* expression, we first examined the effect of p53 activation on cellular uptake of L-[¹⁴C]-cystine. Indeed, the cystine uptake levels of tet-on *p53*^{3KR}-inducible cells were reduced upon treatment with tetracycline (Fig. 2d). To investigate this effect in a more physiological setting, we also examined *p53*^{+/+}, *p53*^{3KR/3KR} and *p53*^{-/-} MEFs. As shown in Fig. 2e, cystine uptake was increased in *p53*^{-/-} MEFs to levels about

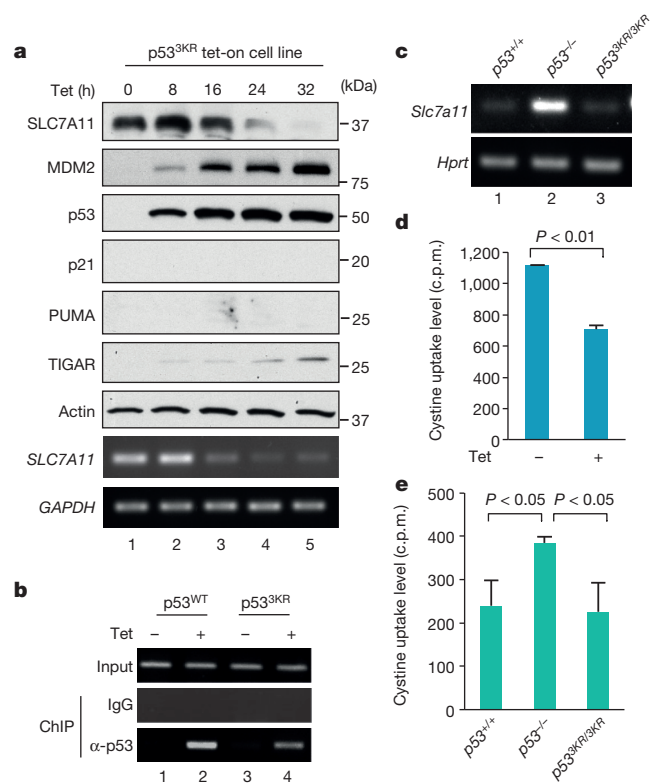


Figure 2 | *p53*^{3KR} in regulating *SLC7A11* and cystine uptake activity. **a**, Tet-on *p53*^{3KR} stable line cells were treated with doxycycline followed by western blots and RT-PCR. **b**, ChIP assay was performed in wild-type p53 (*p53*^{WT}) and *p53*^{3KR} tet-on stable line cells. **c**, Messenger RNA level of *Slc7a11* in MEFs with indicated genotype was determined by RT-PCR with *Hprt* as endogenous control. **d**, Cystine uptake activity (c.p.m., count per minute) was determined in *p53*^{3KR} stable line cells. Mean \pm s.d. from two technical replicates are shown. **e**, Cystine uptake levels (c.p.m.) were measured in MEFs derived from three individual embryos for each genotype (error bars, s.e.m.). All data were repeated independently three times with representatives shown.

60% higher than those of *p53*^{+/+} MEFs, validating that loss of p53 promotes cellular uptake of cystine. Nevertheless, we failed to detect any increase of cystine uptake in *p53*^{3KR/3KR} MEF cells, suggesting that *p53*^{3KR} retains the ability to suppress cystine uptake *in vivo*.

Notably, recent studies showed that *SLC7A11* expression is also critical for ferroptosis, an iron-dependent non-apoptotic cell death involving metabolic dysfunction¹⁵. To this end, we examined whether p53 influences cellular sensitivity to ferroptosis by treating early passage MEFs with erastin, a ferroptosis inducer. Although erastin induced high levels of cell death (>48%) in both *p53*^{+/+} and *p53*^{3KR/3KR} MEFs, only low levels (~20%) were observed in p53-null cells (Fig. 3a and Extended Data Fig. 2a). Moreover, upon kinetic analysis, cell death was readily detected in both *p53*^{+/+} and *p53*^{3KR/3KR} MEFs as early as 6 h after treatment (Fig. 3b). Although a small fraction of cell death was also detected in p53-null cells, differential effects on p53-null cells versus *p53*^{+/+} or *p53*^{3KR/3KR} MEFs are very obvious at different time points upon exposure to different concentrations of erastin (Fig. 3b and Extended Data Fig. 2b). By transmission electron microscopy of erastin-treated cells, we observed shrunken mitochondria with increased membrane density but no obvious DNA fragmentation (III and IV, Fig. 3c), a characteristic morphologic feature of apoptotic cells upon TNF- α treatment (Extended Data Fig. 2c). Western blot analysis revealed that erastin-induced cell death also failed to induce PARP1 cleavage and caspase 3 activation and the lack of DNA fragmentation in ferroptosis was confirmed using TUNEL assay (Extended Data Fig. 2d–f).

To confirm the mode of erastin-induced cell death, we treated cells with ferrostatin-1 (ferr-1), a specific inhibitor of ferroptosis¹⁵. Notably,

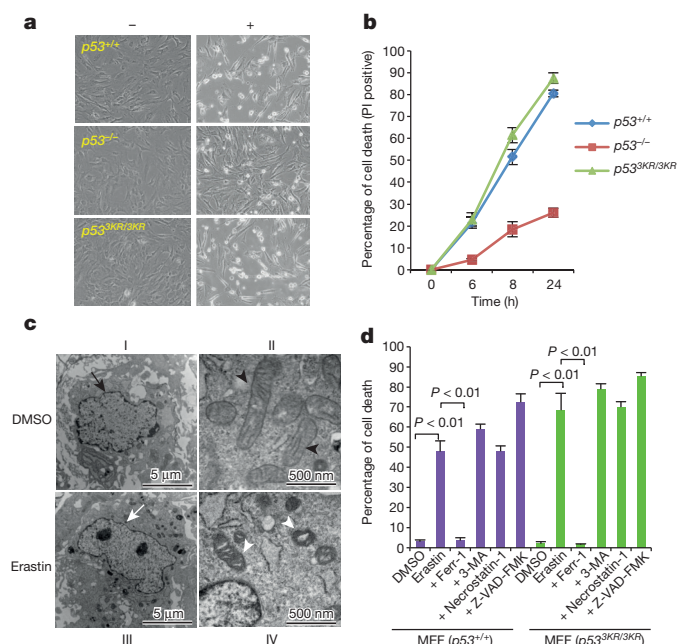


Figure 3 | Roles of p53 in ferroptosis. **a**, Representative phase-contrast images of MEFs treated with 4 μM erastin for 8 h (magnification, $\times 10$). **b**, Kinetics of cell death induced by 4 μM erastin over a 24-h period. Mean \pm s.d. from two replicate experiments are shown. PI, propidium iodide. **c**, Wild-type MEFs were treated with dimethyl sulfoxide (DMSO) or erastin and subjected to transmission electron microscopy. Arrows, nuclei; arrow heads, mitochondria. **d**, MEFs were treated with erastin and specific cell death inhibitors for 8 h and the percentage of cell death was determined (error bars, s.d. from two technical replicates). 3-MA, 3-methyladenine. All data are representative of three independent experiments.

ferr-1 completely rescued cell death in both $p53^{+/+}$ and $p53^{3KR/3KR}$ MEFs (Fig. 3d). In contrast, inhibitors of other forms of cell death, including autophagy (3-methyladenine), apoptosis (Z-VAD-FMK) and necroptosis (necrostatin-1), failed to suppress erastin-induced cell death (Fig. 3d and Extended Data Fig. 2g) despite their abilities to inhibit autophagy, necroptosis and apoptosis, respectively, in the same MEFs (Extended Data Fig. 3a–e). Moreover, several additional inhibitors of ferroptosis¹⁵ also proved to be effective in blocking p53-mediated ferroptosis of $p53^{3KR/3KR}$ MEFs (Extended Data Fig. 3f). Together, these data demonstrate that $p53^{3KR}$ retains the capacity to regulate cellular uptake of cystine and promote ferroptosis.

SLC7A11 in ferroptosis and tumour suppression

Previous studies have shown that *SLC7A11* overexpression is observed in several forms of human cancer^{16–18}. Upon analysis of 20 pairs of human tumours versus adjacent normal tissues, we observed *SLC7A11* overexpression in about 70% of human cancer specimens (8/10 colon tumour samples, 3/5 liver tumour samples, and 3/5 kidney tumour samples) (Extended Data Fig. 4a–c). To further evaluate its role in tumorigenesis, we performed immunofluorescence staining assays for *SLC7A11* on these tissue sections by using confocal microscopy. As shown in Fig. 4a, both the membrane marker (ATP1A1) (green) and *SLC7A11* (red) were localized predominantly on the plasma membrane. More importantly, although the levels of ATP1A1 (green) were similar in normal and cancerous tissues, the *SLC7A11* levels (red) were markedly higher in malignant cells compared to the adjacent normal cells (also see Extended Data Fig. 4d). Although *SLC7A11* levels are elevated in all p53-mutated tumours, *SLC7A11* upregulation also occurs in tumours expressing wild-type p53 (Extended Data Fig. 4e), suggesting that other factors may also influence *SLC7A11* expression in human cancers.

To explore the roles of p53-mediated *SLC7A11* and ferroptosis in human cancer cells, we first examined the effects of erastin on tet-on

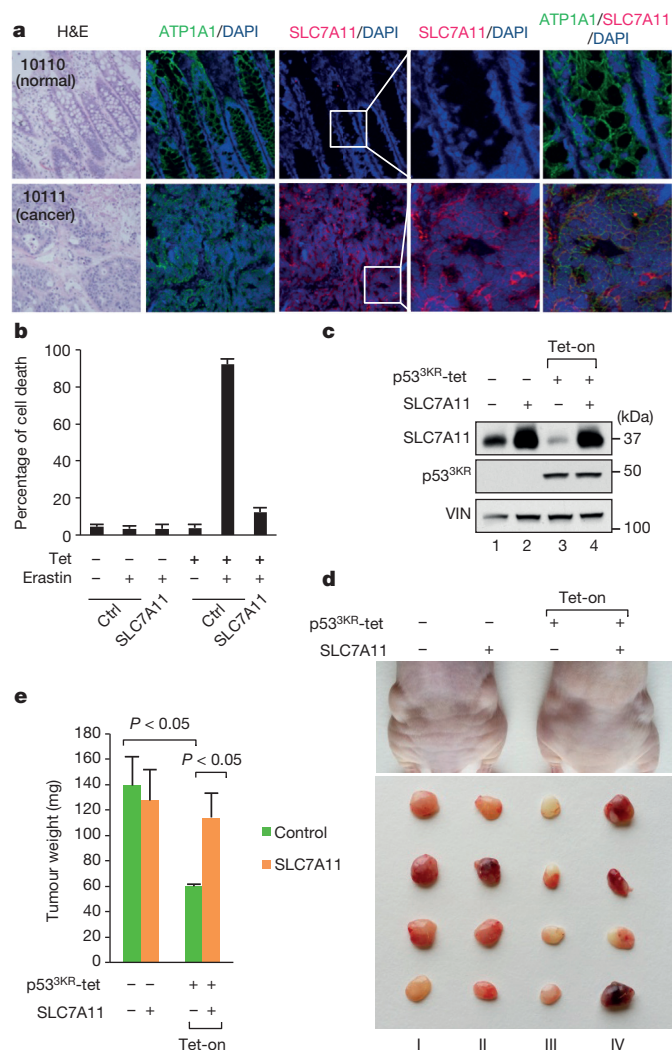


Figure 4 | Regulation of p53-mediated ferroptosis by *SLC7A11*.

a, Representative immunofluorescence staining of *SLC7A11* on paired colon normal tissues and adjacent cancer tissues. H&E, haematoxylin and eosin (magnification, $\times 20$). Numbers in the top left are specific tissue identification numbers of a normal/cancer tissue pair from one colon cancer patient. **b**, Tet-on $p53^{3KR}$ cells were transfected with either control or plasmid overexpressing *SLC7A11* followed by treatment as indicated. Quantification of cell death from two technical replicates is shown (mean \pm s.d.). **c**, Western blot analysis of tet-on $p53^{3KR}$ cells with or without *SLC7A11* overexpression. VIN, vinculin. **d**, Xenograft tumours from tet-on $p53^{3KR}$ cells shown in **c**. **e**, Tumour weight was determined (error bars, s.d. from four tumours). Independent experiments were repeated three times and representative data are shown.

$p53^{3KR}$ -inducible H1299 cells. As expected, these cells are very resistant to erastin-mediated ferroptosis in the absence of $p53^{3KR}$ induction (Fig. 4b and Extended Data Fig. 5a); conversely, high levels of cell death ($>80\%$) were observed upon tetracycline induction of $p53^{3KR}$ in the presence of erastin. Again, the ferroptosis activity induced by $p53^{3KR}$ was inhibited in the presence of ferr-1 (Extended Data Fig. 5b). Notably, *SLC7A11* overexpression rescued these cells from $p53^{3KR}$ -dependent ferroptosis (Fig. 4b) and also abrogated $p53^{3KR}$ -mediated reduction in colony formation (Extended Data Fig. 5c–e). These data indicate that *SLC7A11* is overexpressed in human tumour samples and that ectopic *SLC7A11* expression can suppress ferroptosis induced by $p53^{3KR}$ in human cancer cells.

To validate the role of p53-mediated effects on *SLC7A11* expression in modulating tumour suppression activity independent of cell growth arrest, apoptosis and senescence, we tested whether *SLC7A11* overexpression

affects tumour growth suppression induced by p53^{3KR} in xenograft tumour models. Upon p53^{3KR} expression induced by tetracycline (Fig. 4c), the growth of p53-null H1299 cells was dramatically reduced (Fig. 4d, III versus I) in xenograft tumour growth assays; however, the tumour suppression effects of p53^{3KR} were largely abrogated in the presence of SLC7A11 overexpression (Fig. 4d, IV versus III, also see Fig. 4e). These data demonstrate that SLC7A11 expression is crucial for the tumour growth suppression activity induced by p53^{3KR}.

Metabolic regulation by p53 in embryonic development

Several studies implicate that the canonical activities of p53 in apoptosis, cell growth arrest and senescence are the primary cause of the lethality observed in p53^{+/+}Mdm2^{-/-} mouse embryos, which die at days E3.5–E5.5 of development^{19–24}. To evaluate whether non-canonical activities of p53 contribute to this phenotype, p53^{3KR/3KR}Mdm2^{+/-} mice were intercrossed and their progenies genotyped. Given that the p53^{3KR} mutant fails to induce p53-mediated cell-cycle arrest, apoptosis or senescence¹⁰, we were surprised to find a complete absence of p53^{3KR/3KR}Mdm2^{-/-} pups in the progeny of these intercrosses (Extended Data Fig. 6a, b). Therefore, embryos obtained from timed intercrosses of p53^{3KR/3KR}Mdm2^{+/-} mice were examined. By day E7.5, p53^{3KR/3KR}Mdm2^{-/-} embryos displayed dramatically elevated p53 staining but largely normal developmental structures (Fig. 5a), indicating that the p53^{3KR} mutation elicits a substantial rescue of embryonic development. As expected, despite high p53^{3KR} expression, p53^{3KR/3KR}Mdm2^{-/-} embryos did not exhibit increasing levels of apoptosis as shown by absence of cleaved caspase-3 staining (Fig. 5a) and negative TUNEL signals (Extended Data Fig. 6c, d). The levels for Ki67 and BrdU staining also indicated that there is no cell growth inhibition in p53^{3KR/3KR}Mdm2^{-/-}

embryos (Fig. 5a and Extended Data Fig. 6d). Further analysis confirmed the high levels of p53^{3KR} protein, absence of cleaved caspase-3, and lack of induction of p21 or PUMA in p53^{3KR/3KR}Mdm2^{-/-} embryos (Extended Data Fig. 6e, f). Moreover, we failed to detect any cells staining positive for senescence-associated β -galactosidase activity in p53^{3KR/3KR}Mdm2^{-/-} embryos (Extended Data Fig. 6g–i), suggesting an absence of senescent cells in those embryos.

Nevertheless, *Slc7a11* mRNA expression was suppressed in p53^{3KR/3KR}Mdm2^{-/-} embryos (Fig. 5b), and by day E11.5 the developmental abnormalities of p53^{3KR/3KR}Mdm2^{-/-} embryos became very obvious (Extended Data Fig. 7a). To explore whether p53-mediated ferroptosis contributes to the developmental defects of p53^{3KR/3KR}Mdm2^{-/-} embryos, we injected the ferroptosis inhibitor ferr-1 into the peritoneal cavity at day E5.5 and collected embryos at day E14.5. As shown in Fig. 5c, ferr-1-treated p53^{3KR/3KR}Mdm2^{-/-} embryos showed clear organogenesis such as eye formation and limb differentiation at day E14.5 (II), at a time when untreated p53^{3KR/3KR}Mdm2^{-/-} embryos had been largely decimated (I, also see Extended Data Fig. 7b). The body sizes (from head to tail) of recovered p53^{3KR/3KR}Mdm2^{-/-} embryos were also significantly larger and the structure of the eyes was markedly improved upon ferr-1 treatment (Extended Data Fig. 7c, d). A recent study identified upregulation of *PTGS2* as a potential molecular marker of ferroptosis²⁵. As shown in Fig. 5d, *Ptgs2* was indeed significantly upregulated in p53^{3KR/3KR}Mdm2^{-/-} embryos; conversely, *Ptgs2* levels were not affected in p53^{-/-}Mdm2^{-/-} embryos, suggesting that *Ptgs2* upregulation in p53^{3KR/3KR}Mdm2^{-/-} embryos is p53-dependent. Taken together, these data indicate that p53-mediated effects on metabolic regulation and ferroptotic cell death contribute critically to the embryonic developmental defects observed in p53^{3KR/3KR}Mdm2^{-/-} embryos.

p53-mediated ferroptosis in ROS responses

To evaluate the regulation of ferroptosis in a more physiological setting, we examined whether p53^{3KR}-mediated ferroptotic cell death is involved in ROS stress responses. The method for ROS treatment has been described previously^{26,27}. As shown in Fig. 6a, no obvious cell death was observed upon either p53^{3KR} induction or ROS treatment alone. Notably, however, the combination of p53^{3KR} induction and ROS treatment induced massive cell death that was specifically inhibited by ferr-1 (Fig. 6a and Extended Data Fig. 8a) or by overexpression of SLC7A11 (Fig. 6b). These data indicate that activation of p53^{3KR} leads to ferroptotic cell death in the presence of ROS stress, independent of cell-cycle arrest, senescence and apoptosis.

Recent studies indicate that wild-type p53 proteins can be activated in human tumours by nutlin-3 (ref 14). In most human cancer cells, nutlin-3-mediated p53 activation induces reversible cell-cycle arrest but not cell death^{28,29}, which may limit its efficacy in cancer treatment. Therefore, we examined whether Mdm2 inhibition can modulate p53-mediated ferroptosis in human cancer cells. As expected, nutlin-3 treatment of U2OS cells induced high levels of p53 expression without eliciting cell death whereas the treatment of ROS alone, which did not induce strong p53 activation, also failed to elicit a cell death response (Fig. 6c and Extended Data Fig. 8b, c). However, massive cell death was observed upon combination treatment with both nutlin and ROS (Fig. 6c). The cell death response is p53-dependent since it was abrogated upon knockdown of endogenous p53 (Fig. 6c and Extended Data Fig. 8c), and the cell death was again rescued by the ferroptosis inhibitor ferr-1 (Extended Data Fig. 8d). Interestingly, although high levels of cell death were also induced in U2OS cells by DNA-damaging agents such as etoposide and doxorubicin, DNA-damage-induced cell death could not be suppressed by ferr-1 treatment (Extended Data Fig. 8e, f), suggesting that p53-mediated ferroptosis is specifically induced by ROS but not by DNA damage.

Finally, to evaluate SLC7A11 regulation of ferroptosis under more physiological conditions, we generated BAC transgenic mice overex-

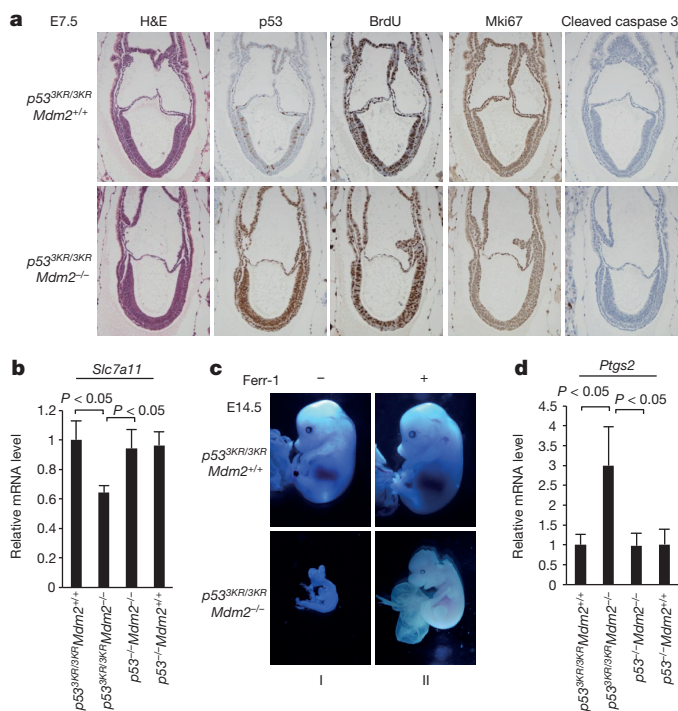


Figure 5 | p53-mediated metabolic regulation in embryonic development. **a**, Representative haematoxylin and eosin (H&E) and immunohistochemistry staining on E7.5 embryos with indicated genotype (magnification, $\times 20$). **b**, Messenger RNA expression levels of *Slc7a11* in E9.5 embryos with indicated genotype (error bars, s.d.; $n = 3$ for p53^{3KR/3KR}Mdm2^{+/+} and $n = 5$ for all other genotypes). **c**, Representative morphologies of E14.5 embryos treated with either dimethyl sulfoxide or ferr-1 (magnification, $\times 1.5$). **d**, Messenger RNA expression levels of *Ptgs2* determined similarly as in **b**. All data were repeated independently at least three times and representatives are shown.

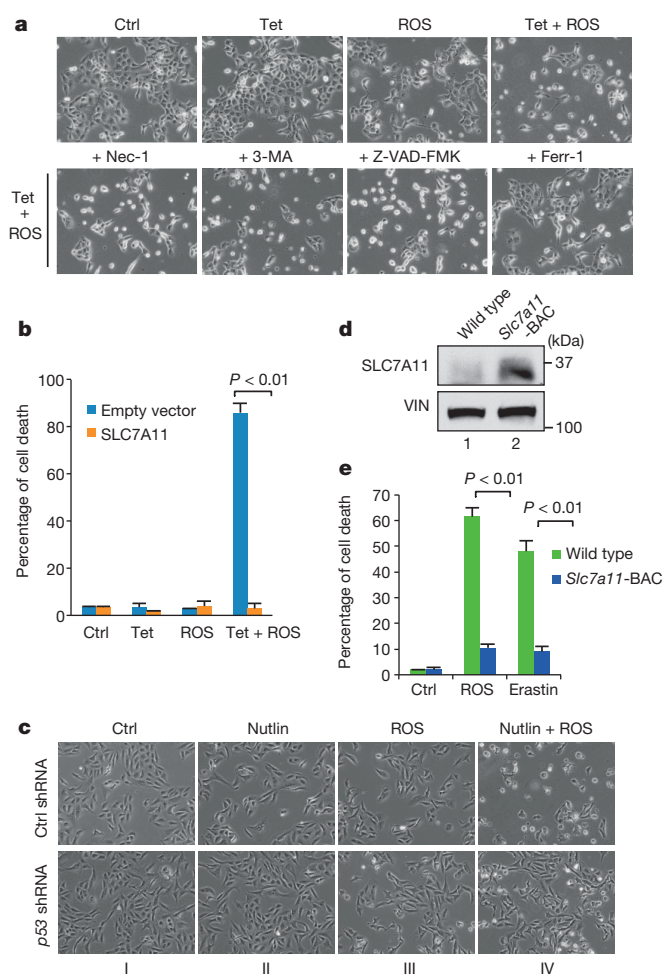


Figure 6 | p53-mediated ferroptosis in ROS responses. **a**, Tet-on p53^{3KR} cells were treated with doxycycline and ROS with specific cell death inhibitors for 24 h. Nec-1, necrostatin-1 (magnification, ×10). **b**, Tet-on p53^{3KR} cells were transfected with either control or plasmid overexpressing SLC7A11 followed by treatment of doxycycline and ROS for 16 h. Quantification of cell death from two technical replicates is shown (mean ± s.d.). **c**, U2OS cells with p53 knockdown were treated with nutlin and ROS for 24 h when images were taken. **d**, Western blots of MEFs generated from wild-type or *Slc7a11*-BAC transgenic mice. VIN, vinculin. **e**, MEFs from indicated genotype were treated with ROS or erastin for 8 h and quantification of cell death from two technical replicates (mean ± s.d.) is shown. All experiments were performed independently three times and representative data are shown.

pressing SLC7A11 (*Slc7a11* bacterial artificial chromosome, *Slc7a11*-BAC) (Extended Data Fig. 9). Although the phenotypes of *Slc7a11*-BAC mice need further analysis, we derived MEFs from both *Slc7a11*-BAC mice and their control littermates. As shown in Fig. 6d, SLC7A11 protein levels were elevated approximately fivefold higher in *Slc7a11*-BAC MEFs relative to the control MEFs. Notably, treatment with either ROS or erastin elicited high levels of ferroptosis in wild-type MEFs but ferroptotic cell death was largely abrogated in *Slc7a11*-BAC MEFs (Fig. 6e). Together, these data indicate that p53-mediated ferroptosis is specifically induced by ROS and that the levels of SLC7A11 are critical for p53-mediated ferroptotic responses.

Discussion

Although it is commonly accepted that p53-mediated cell-cycle arrest, apoptosis and senescence all serve as major mechanisms of tumour suppression, accumulating evidence indicates that other activities of p53, such as metabolic regulation, are also critical for tumour suppression¹⁰. While a number of metabolic targets of p53 such as TIGAR, GLS2 and SCO2 have been identified^{30–37}, it remains unclear how the metabolic

functions of p53 contribute to its tumour suppression activity. Here we show that, by transcriptional suppression of *SLC7A11*, a component of the cystine/glutamate antiporter, p53 inhibits cystine uptake and sensitizes cells to ferroptosis, a non-apoptotic form of cell death. Moreover, the p53^{3KR} mutant, which is defective for p53-dependent cell-cycle arrest, apoptosis and senescence, retains the ability to inhibit SLC7A11 expression and thereby regulate cystine metabolism and ferroptotic cell death. Using p53^{3KR/3KR} *Mdm2*^{−/−} mutant mice, we further show that this aspect of p53 function contributes critically to embryonic development and the lethality associated with loss of *Mdm2*. Ferroptosis is associated with metabolic dysfunction that results in production of both cytosolic and lipid ROS, independent of mitochondria^{15,25}. By repressing *SLC7A11* transcription, p53 activation reduces cystine uptake, which in turn limits production of intracellular glutathione (GSH), the primary cellular antioxidant. Thus, the sensitivity of ROS-induced ferroptosis is markedly increased in p53-activated cells. Notably, SLC7A11 is overexpressed in many types of human cancers and the levels of SLC7A11 are critical for the sensitivity of ferroptotic responses. By using the p53^{3KR} mutant in xenograft tumour models, we show that high levels of SLC7A11 expression lead to a significant abrogation of the tumour growth suppression activity induced by p53^{3KR}, which is independent of cell-cycle arrest, apoptosis and senescence.

Our data indicate that p53-mediated transcriptional repression of *SLC7A11* is critical for ROS-induced ferroptosis. Nonetheless, it is possible that additional p53 target genes may contribute to this novel p53 response. Future investigations are required to elucidate the roles of other metabolic targets of p53 in regulating ferroptosis. Interestingly, previous studies have shown that p53 ameliorates oxidative stress by upregulating metabolic targets, such as TIGAR (also known as C12orf5) and GLS2, that decrease cellular levels of ROS^{30–37}. Yet, we found that p53-mediated ferroptosis can be triggered by high levels of ROS (Fig. 6), consistent with the observation that ferroptosis is characterized by a lethal iron-dependent accumulation of lipid ROS^{15,25}. Although numerous studies implicate ROS in both metabolism and tumorigenesis, the mechanisms that underlie cellular responses to ROS are poorly understood. Nevertheless, the divergent effects of p53 on cellular ROS levels suggest an intriguing model. In response to low or basal ROS levels, p53 may prevent cells from accumulating lethal levels of ROS while also allowing survival and repair of moderate oxidative damage. However, in response to higher or inappropriate ROS levels (such as in cancer cells), p53 may instead promote the removal of unsalvageable cancer cells through ferroptosis. This model is reminiscent of the divergent effects of p53 on the cellular response to DNA damage^{1–6}. In that scenario, p53 activation promotes cell survival and repair of genotoxic damage (through target genes that facilitate cell cycle checkpoints and DNA repair) in response to low levels of DNA damage; however, upon severe DNA damage, high levels of p53-mediated apoptotic cell death eliminate damaged cells permanently. Taken together, our findings suggest that p53-mediated effects on cystine metabolism, ROS responses and ferroptotic cell-death represent a novel mechanism of tumour suppression.

Online Content Methods, along with any additional Extended Data display items and Source Data, are available in the online version of the paper; references unique to these sections appear only in the online paper.

Received 6 January 2014; accepted 18 February 2015.

Published online 18 March 2015.

- Berkers, C. R., Maddocks, O. D., Cheung, E. C., Mor, I. & Vousden, K. H. Metabolic regulation by p53 family members. *Cell Metab.* **18**, 617–633 (2013).
- Jackson, J. G. & Lozano, G. The mutant p53 mouse as a pre-clinical model. *Oncogene* **32**, 4325–4330 (2013).
- Aylon, Y. & Oren, M. New plays in the p53 theater. *Curr. Opin. Genet. Dev.* **21**, 86–92 (2011).
- Junttila, M. R. & Evan, G. I. p53—a Jack of all trades but master of none. *Nature Rev. Cancer* **9**, 821–829 (2009).
- Wang, S. J. & Gu, W. To be, or not to be: functional dilemma of p53 metabolic regulation. *Curr. Opin. Oncol.* **26**, 78–85 (2014).

6. Bieganski, K. T. & Attardi, L. D. Deconstructing p53 transcriptional networks in tumor suppression. *Trends Cell Biol.* **22**, 97–106 (2012).
7. Brady, C. A. *et al.* Distinct p53 transcriptional programs dictate acute DNA-damage responses and tumor suppression. *Cell* **145**, 571–583 (2011).
8. Valente, L. J. *et al.* p53 efficiently suppresses tumor development in the complete absence of its cell-cycle inhibitory and proapoptotic effectors p21, Puma, and Noxa. *Cell Rep.* **3**, 1339–1345 (2013).
9. Kruse, J. P. & Gu, W. Modes of p53 regulation. *Cell* **137**, 609–622 (2009).
10. Li, T. *et al.* Tumor suppression in the absence of p53-mediated cell-cycle arrest, apoptosis, and senescence. *Cell* **149**, 1269–1283 (2012).
11. Lo, M., Wang, Y. Z. & Gout, P. W. The xCT cystine/glutamate antiporter: a potential target for therapy of cancer and other diseases. *J. Cell. Physiol.* **215**, 593–602 (2008).
12. Conrad, M. & Sato, H. The oxidative stress-inducible cystine/glutamate antiporter, system xCT: cystine supplier and beyond. *Amino Acids* **42**, 231–246 (2012).
13. Sato, H., Tamba, M., Kuriyama-Matsumura, K., Okuno, S. & Bannai, S. Molecular cloning and expression of human xCT, the light chain of amino acid transport system xCT. *Antioxid. Redox Signal.* **2**, 665–671 (2000).
14. Vu, B. T. & Vassilev, L. Small-molecule inhibitors of the p53–MDM2 interaction. *Curr. Top. Microbiol. Immunol.* **348**, 151–172 (2011).
15. Dixon, S. J. *et al.* Ferroptosis: an iron-dependent form of nonapoptotic cell death. *Cell* **149**, 1060–1072 (2012).
16. Huang, Y., Dai, Z., Barbacioru, C. & Sadee, W. Cystine-glutamate transporter SLC7A11 in cancer chemosensitivity and chemoresistance. *Cancer Res.* **65**, 7446–7454 (2005).
17. Liu, X. X. *et al.* MicroRNA-26b is underexpressed in human breast cancer and induces cell apoptosis by targeting SLC7A11. *FEBS Lett.* **585**, 1363–1367 (2011).
18. Guo, W. *et al.* Disruption of xCT inhibits cell growth via the ROS/autophagy pathway in hepatocellular carcinoma. *Cancer Lett.* **312**, 55–61 (2011).
19. Montes de Oca Luna, R., Wagner, D. S. & Lozano, G. Rescue of early embryonic lethality in mdm2-deficient mice by deletion of p53. *Nature* **378**, 203–206 (1995).
20. Jones, S. N., Roe, A. E., Donehower, L. A. & Bradley, A. Rescue of embryonic lethality in Mdm2-deficient mice by absence of p53. *Nature* **378**, 206–208 (1995).
21. Gannon, H. S. & Jones, S. N. Using mouse models to explore MDM–p53 signaling in development, cell growth, and tumorigenesis. *Genes Cancer* **3**, 209–218 (2012).
22. Mendrysa, S. M. *et al.* Mdm2 is critical for inhibition of p53 during lymphopoiesis and the response to ionizing irradiation. *Mol. Cell. Biol.* **23**, 462–472 (2003).
23. Marine, J. C. & Lozano, G. Mdm2-mediated ubiquitylation: p53 and beyond. *Cell Death Differ.* **17**, 93–102 (2010).
24. Chavez-Reyes, A. *et al.* Switching mechanisms of cell death in mdm2- and mdm4-null mice by deletion of p53 downstream targets. *Cancer Res.* **63**, 8664–8669 (2003).
25. Yang, W. S. *et al.* Regulation of ferroptotic cancer cell death by GPX4. *Cell* **156**, 317–331 (2014).
26. Hughes, R. H., Silva, V. A., Ahmed, I., Shreiber, D. I. & Morrison, B. III. Neuroprotection by genipin against reactive oxygen and reactive nitrogen species-mediated injury in organotypic hippocampal slice cultures. *Brain Res.* **1543**, 308–314 (2014).
27. Wang, Z., Jiang, H., Chen, S., Du, F. & Wang, X. The mitochondrial phosphatase PGAM5 functions at the convergence point of multiple necrotic death pathways. *Cell* **148**, 228–243 (2012).
28. Lu, M. *et al.* Restoring p53 function in human melanoma cells by inhibiting MDM2 and cyclin B1/CDK1-phosphorylated nuclear iASPP. *Cancer Cell* **23**, 618–633 (2013).
29. Wade, M. & Wahl, G. M. Targeting Mdm2 and Mdmx in cancer therapy: better living through medicinal chemistry? *Mol. Cancer Res.* **7**, 1–11 (2009).
30. Wang, P. Y. *et al.* Increased oxidative metabolism in the Li-Fraumeni syndrome. *N. Engl. J. Med.* **368**, 1027–1032 (2013).
31. Liang, Y., Liu, J. & Feng, Z. The regulation of cellular metabolism by tumor suppressor p53. *Cell Biosci.* **3**, 9 (2013).
32. Bensaad, K. *et al.* TIGAR, a p53-inducible regulator of glycolysis and apoptosis. *Cell* **126**, 107–120 (2006).
33. Cairns, R. A., Harris, I. S. & Mak, T. W. Regulation of cancer cell metabolism. *Nature Rev. Cancer* **11**, 85–95 (2011).
34. Cheung, E. C., Ludwig, R. L. & Vousden, K. H. Mitochondrial localization of TIGAR under hypoxia stimulates HK2 and lowers ROS and cell death. *Proc. Natl Acad. Sci. USA* **109**, 20491–20496 (2012).
35. Cheung, E. C. *et al.* TIGAR is required for efficient intestinal regeneration and tumorigenesis. *Dev. Cell* **25**, 463–477 (2013).
36. Hu, W. *et al.* Glutaminase 2, a novel p53 target gene regulating energy metabolism and antioxidant function. *Proc. Natl Acad. Sci. USA* **107**, 7455–7460 (2010).
37. Suzuki, S. *et al.* Phosphate-activated glutaminase (GLS2), a p53-inducible regulator of glutamine metabolism and reactive oxygen species. *Proc. Natl Acad. Sci. USA* **107**, 7461–7466 (2010).

Acknowledgements This work was supported by the National Cancer Institute of the National Institutes of Health under awards 5R01CA172023, 5R01CA166294, 5R01CA169246, 5R01CA085533 and 2P01CA080058 to W.G. It was also supported by the National Cancer Institute under award 2P01CA097403 to R.B. and W.G. The content is solely the responsibility of the authors and does not necessarily represent the official views of the National Institutes of Health. L.J. and S.-J.W. were supported by NIH cancer biology training grant T32-CA09503. We thank S. Mendrysa for Mdm2 mutant mice.

Author Contributions The experiments were conceived and designed by L.J., N. K. and W.G. Experiments were performed mainly by L.J. and N.K. Some of the experiments were performed with help from T.L., S.-J.W., T.S., H.H. and R.B. The paper was written by J.L., N.K., R.B. and W.G.

Author Information Microarray data can be accessed through NCBI Gene Expression Omnibus (GEO) database with accession number GSE57841. Reprints and permissions information is available at www.nature.com/reprints. The authors declare no competing financial interests. Readers are welcome to comment on the online version of the paper. Correspondence and requests for materials should be addressed to W.G. (wg8@columbia.edu).

METHODS

Cell culture and stable lines. Cells were previously obtained from American Type Culture Collection (ATCC) and maintained in 37 °C incubator with 5% CO₂. All media used were supplemented with 10% FBS, 100 units per ml penicillin and 100 µg ml⁻¹ streptomycin. H1299, U2OS and MCF7 cells were maintained in DMEM medium; SOAS-2 cells in McCoy's 5A medium. MEFs were generated from day 13.5 embryos according to standard procedures. FBS used for MEFs was heat-inactivated and supplemented with 1% non-essential amino acids. To generate inducible stable lines, wild-type and 3KR (K117R, K161R and K162R) mouse p53 complementary DNA were cloned into tet-on pTRIPZ inducible expression vector (Thermo Open Biosystems). All sequences have been confirmed before transfection using Lipofectamine 2000 (Invitrogen), followed by selection and maintenance with puromycin (1 µg ml⁻¹) in DMEM medium containing 10% tetracycline-free FBS. To induce the expression of p53, 0.1 µg ml⁻¹ of doxycycline was added to the culture medium. To generate cells with stable knockdown of p53, U2OS cells were infected with GIPZ short hairpin RNA (shRNA) non-silencing control or shRNA against TP53 (Thermo Scientific) with the following target sequences: 3LHS_333919, TACACATGTAGTTGTAGTG and 3LHS_333920, TCTCTCTCTGTGCGCGG. Cells were then selected with puromycin (1 µg ml⁻¹) for 2 weeks.

Microarray and statistical analysis. Tet-on mouse wild-type p53 stable line cells were induced by doxycycline (0.1 µg ml⁻¹) for 0 or 24 h before total RNA was extracted. RNA was further purified by RNeasy column (Qiagen) and processed for expression microarray (Affymetrix human gene ST 1.0) following the manufacturer's instructions. Each condition was done in technical duplicates. Array data were analysed by Partek software (ver. 6.6) and selected genes that are differentially expressed (false-discovery-rate-corrected *P* value less than 0.05) between the induced and non-induced cells were listed in Extended Data Fig. 1. A two-tailed Student's *t*-test was used for comparisons between two groups and a *P* value of less than 0.05 was considered statistically significant. No statistical methods were used to predetermine sample size.

Plasmids and transfection. Full-length cDNA of *SLC7A11* was amplified by PCR from human HeLa Marathon-Ready cDNA (Clontech) and cloned into either TOPO (Invitrogen) or pCIN4-HA expression vector. Lipofectamine 2000 (Invitrogen) was used for plasmid transfection according to the manufacturer's protocols.

Chromatin immunoprecipitation assay. The procedure was performed essentially as described previously³⁸ with minor modifications. In brief, cells were crosslinked with 1% formaldehyde for 10 min at room temperature and neutralized by adding glycine to a final concentration of 0.125 M. After washing twice with cold PBS, cells were harvested and suspended in cold lysis buffer (10 mM Tris-Cl, pH 8.0, 85 mM KCl, 0.5% NP40, 5 mM EDTA, 0.25% Triton and 1× proteinase inhibitor). After 10 min incubation on ice, nuclei were harvested and re-suspended in LB3 buffer and sonicated to achieve DNA fragments of 200–500 base pairs. Magnetic beads coated with specific antibodies or IgG control were added to lysate and incubated overnight. Next day, beads were washed seven times with washing buffer (50 mM HEPES, pH 7.5, 500 mM LiCl, 1 mM EDTA, 1% NP-40 and 0.7% Na-deoxycholate) and once with TE buffer before the protein–DNA complex was eluted from the beads. After reverse crosslinking overnight at 55 °C, DNA was extracted and analysed by PCR followed by 2% agarose gel electrophoresis or by quantitative PCR.

RNA extraction, RT-PCR and sequencing of tumour samples. Total RNA was isolated using TRIzol (Invitrogen) according to the manufacturer's protocol. One microgram of total RNA was reverse transcribed by M-MuLV reverse transcriptase and Random Primer 9 (NEB) following manufacturer's protocol. Semi-quantitative RT-PCR was performed using Advantage 2 PCR kit (Clontech) within the linear range of PCR cycles for each primer pair. Quantitative PCR was done using a 7500 Fast Real-Time PCR System (Applied Biosystems) with standard protocol. To determine p53 mutational status, RNA was extracted and RT-PCR was performed for each patient tumour sample. Full length p53 PCR product was gel purified and sequenced using standard procedures.

PCR primers. For RT-PCR: human *SLC7A11* forward, TCATTGGAGCAGGAATCTTCA, reverse, TTCAGCATAAGACAAAGCTCCA; human *GAPDH* forward, ATCAATGGAAATCCCATCACCA, reverse, GACTCCACGACGTACTCAGCG; mouse *Slc7a11* forward, CCTCTGCCAGCTGTTATTGTT, reverse, CCTGGCAAACTGAGGAAAT; mouse *Hprt* forward, TCCTCCTCAGACCGCTTT, reverse, CCTGGTTCATCATCGCTAATC. For quantitative RT-PCR: human *SLC7A11* forward, ATGCAGTGGCAGTGACCTTT, reverse, GGCAACAAAGATCGGAAGT; human *GAPDH*, same as primers used for RT-PCR; mouse *Slc7a11* forward, TGGGTGGAAGTGTCTGTAAT, reverse, AGGATGTAGCGTCCAAATGC; mouse *Ptgs2* forward, GGGAGTCTGGAACATTGTGAA, reverse, GTGCACATTGTAAAGTGGTGAAT; mouse *Puma* forward, ACGACCTCAA CGCGCAGTACG, reverse, GAGGAGTCCCATG AAGAGATTG; mouse *Hprt*, same as primers used for RT-PCR. For ChIP-PCR: human *SLC7A11* forward, AGGCTTCTCATGTGGCTGAT, reverse, TGCATCGTGCTCTCAATTCT (same primers were used to generate probe for EMSA); human *p21* forward, CTTTCA

CCATTCCCCTACCC, reverse, AATAGCCACCAGCCTCTTCT; human ChIP control region forward, AGGAGAGGACTTCGACAACCC, reverse, CAGGTCC TTCCCATGCTTCC; mouse *Slc7a11* p53 RE1 forward, TGCCGAGACTGATAGCTGAG, reverse, AAAACTTCAAAGTGGGGTTAAAA; mouse *Slc7a11* p53 RE2 forward, GTTCTGGGAAATGCTTTTGA, reverse, CGTGGAAAGGTCCG TATTTA; mouse *Slc7a11* p53 RE3 forward, GTCATCGGATCAGGCATCTT, reverse, ACACACACTCACACCCCA.

Western blotting and antibodies. Proteins were lysed from cells using RIPA buffer containing 10 mM Tris-Cl, pH 8.0, 150 mM NaCl, 1% Triton X-100, 1% Na-deoxycholate, 1 mM EDTA, 0.05% SDS and fresh 1× proteinase inhibitor. Concentration was determined by the Bradford method using Bio-Rad protein assay before proteins were equally loaded and separated in polyacrylamide gels. Proteins were then transferred to Hybond ECL membrane (GE healthcare) and incubated overnight with primary antibodies against SLC7A11 (ab37185, abcam), p53 (human: Do-1, Santa Cruz; mouse: CM5, Leica biosystems), MDM2 (Ab5, Millipore), TIGAR (E-2, Santa Cruz), PUMA (H-136, Santa Cruz), p21 (SX118, Santa Cruz), cleaved caspase 3 (9664, Cell Signaling), LC3B (3868, Cell Signaling), PARP (9532, Cell Signaling), β-actin (A3853, Sigma-Aldrich), vinculin (V9264, Sigma-Aldrich) and haemagglutinin (11867431001, Roche). HRP-conjugated secondary antibodies were used and western blot signals were detected on autoradiographic films after incubating with ECL (GE healthcare) or SuperSignal West Dura reagents (Thermo scientific).

Colony formation assay. H1299 cells were transfected with either empty vector or Flag-tagged p53^{3KR}, haemagglutinin-tagged SLC7A11 expression plasmids. Cells were split 48 h post-transfection and seeded into 10-cm dishes at a density of 1,000 cells per dish and cultured in the presence of G418 (600 µg ml⁻¹) for 12 days. Cells were then fixed in ice-cold methanol and stained with crystal violet solution. Numbers of visible colonies were counted using ImageJ.

Electrophoretic mobility shift assay. Flag-tagged wild-type p53 protein was purified from transfected 293 cells. A DNA probe containing the p53 binding site for *SLC7A11* was PCR-amplified, labelled with γ-³²P-dATP by T4 kinase (NEB) and purified using Bio-Spin 30 columns (Bio-Rad). The protein–DNA binding reactions (total of 20 µl) contained 20 mM HEPES, pH 7.6, 80 mM NaCl, 0.1 mM EDTA, 12.5% glycerol, 2 mM MgCl₂, 2 mM spermidine, 0.7 mM DTT, 200 ng µl⁻¹ BSA, 20 ng µl⁻¹ sheared salmon sperm DNA, 10–20 fmol DNA probe and 200 ng Flag-p53. In supershift assays, 200 ng anti-p53 pAb421 antibody (Millipore) was added to the reaction. A non-radioactive labelled probe in excess of 100 or 200 fold was used to compete with the ³²P-labelled radioactive probe.

Drugs, cell death inhibitors and ROS treatment. All drugs were ordered from Sigma-Aldrich unless otherwise indicated. Ferrostatin-1 was from Xcess Biosciences. Drugs or cell death inhibitors are used at the following concentrations: nutlin-3a, 10 µM; ferr-1, 2 µM; 3-methyladenine, 2 mM; necrostatin-1, 10 µg ml⁻¹; Z-VAD-FMK, 10 µg ml⁻¹; DFO, 100 µM; U0126, 5 µM; β-ME, 50 µM and NAC, 1 mM. ROS were generated by tert-butyl hydroperoxide (TBH). Concentrations of TBH used in experiments shown in Fig. 6 are: 60 µM for Fig. 6a, 100 µM for Fig. 6b, 350 µM for Fig. 6c and 200 µM for Fig. 6e with erastin at 1 µM. Cells were about 50% confluent when medium containing TBH was added. Specific cell death inhibitors were added at the same time when erastin or TBH treatment was started.

Cell death assay. For cell death assays involving p53 activation, p53 was pre-activated for 24 h by either doxycycline (in tet-on stable line cells) or nutlin (in cancer cells) followed by treatment with either erastin or TBH. For quantification of cell death, cells were trypsinized and stained with trypan blue followed by counting with a haemocytometer using standard protocol. Cells stained blue were considered as dead cells. Quantification of cell death was further confirmed by propidium iodide staining followed by FACS analysis.

Cystine uptake assay. Cells cultured in six-well plates were washed twice in pre-warmed Na⁺-free uptake buffer containing 137 mM choline chloride, 3 mM KCl, 1 mM CaCl₂, 1 mM MgCl₂, 5 mM D-glucose, 0.7 mM K₂HPO₄ and 10 mM HEPES (pH 7.4). Cells were then incubated in 1 ml uptake buffer at 37 °C for 10 min. Buffer was replaced with 600 µl uptake buffer containing L-[3,3'-¹⁴C] cystine (0.2 µCi ml⁻¹) (PerkinElmer) and incubated at 37 °C for 3 min. Cells were then washed three times with ice-cold uptake buffer followed by addition of 600 µl of NaOH (0.1 M) to lyse the cells. Cell lysate (80 µl) was added into 1 ml scintillation fluid and radioactive ¹⁴C counts per minute (CPM) were obtained in a scintillation counter.

Immunofluorescence, immunohistochemistry, TUNEL, BrdU assay and transmission electron microscopy. Frozen human cancer tissues or fixed mouse deciduas from timed breeding were cut at 5 µm and immunostaining was performed according to standard procedures using antibodies against human SLC7A11 (no. 12691, Cell Signaling Technology), mouse p53 (CM5, Leica), BrdU (Ab6326, Abcam), Mki67 (Ab15580, Abcam) and cleaved caspase3 (9664, Cell Signaling). TUNEL assay was carried out using DeadEnd TUNEL system according to the manufacturer's instructions (Promega). Intraperitoneal injection of BrdU (BD Pharmagen) was given to pregnant mice at day E7.5 at 100 µg BrdU per g body weight. After 2 h,

the embryos were collected and fixed in 10% formalin at 4 °C overnight. The embryos were embedded in paraffin and serial sections were collected for BrdU staining. Transmission electron microscopy was performed using standard procedures by the Microscopy Core at NYU. At least 20 images were acquired for each structure of interest and representative images are shown.

Senescence-associated β -galactosidase activity assay. Senescence-associated β -galactosidase activity was examined according to published procedure³⁹. In brief, embryos were fixed with 0.2% glutaraldehyde in PBS, and washed in PBS supplemented with 2 mM MgCl₂. Embryos were then stained in X-gal solution (1 mg ml⁻¹ X-gal, 5 mM K₃Fe(CN)₆, 5 mM K₄Fe(CN)₆ and 2 mM MgCl₂ in PBS) overnight at 37 °C. The embryos were then post fixed in 10% formalin overnight.

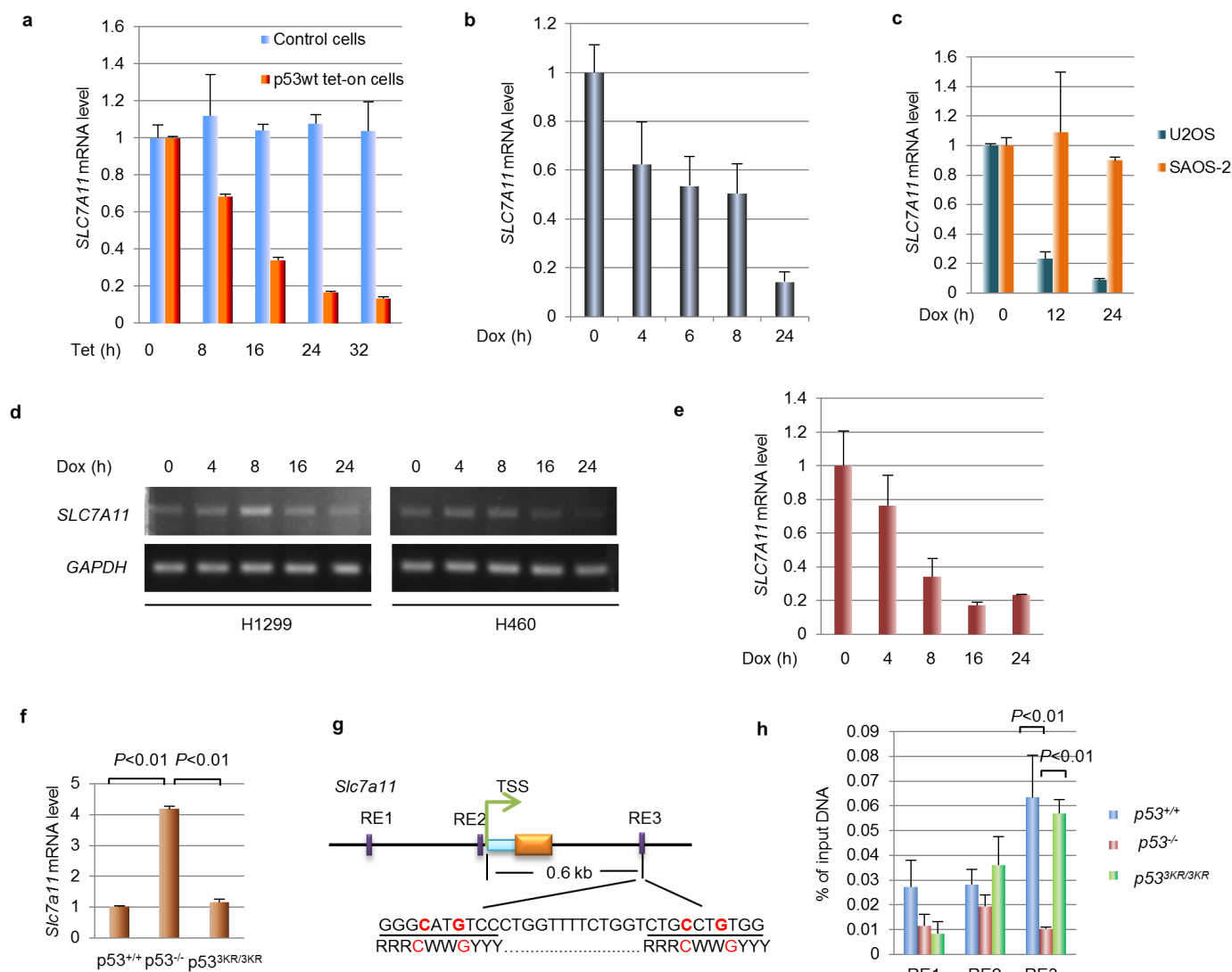
Slc7a11-BAC transgenic mice generation. *Slc7a11*-BAC transgenic mice were generated by pronuclear injection of mouse BAC (RP24-242E11 containing only the *Slc7a11* gene) at the Transgenic Mouse Shared Resource at Columbia University using standard procedures. A total of three founders were identified and germline transmission was confirmed.

Rescue of $p53^{3KR/3KR}$ *Mdm2*^{-/-} mice. Timed breeding was setup for $p53^{3KR/3KR}$ *Mdm2*^{+/-} intercross. Starting on day E5.5, dimethyl sulfoxide control or ferr-1 (100 μ l of 100 μ M solution per 20 g body weight) was injected into the peritoneal cavity of pregnant mice once a day. Embryos were collected at day E14.5 and imaged.

Genotype was determined using DNA extracted from the yolk sac. All mice used in this study are mixture of C57bl/6j and SV129 strain. All procedures performed in this study are approved by the Institutional Animal Care and Use Committee at Columbia University.

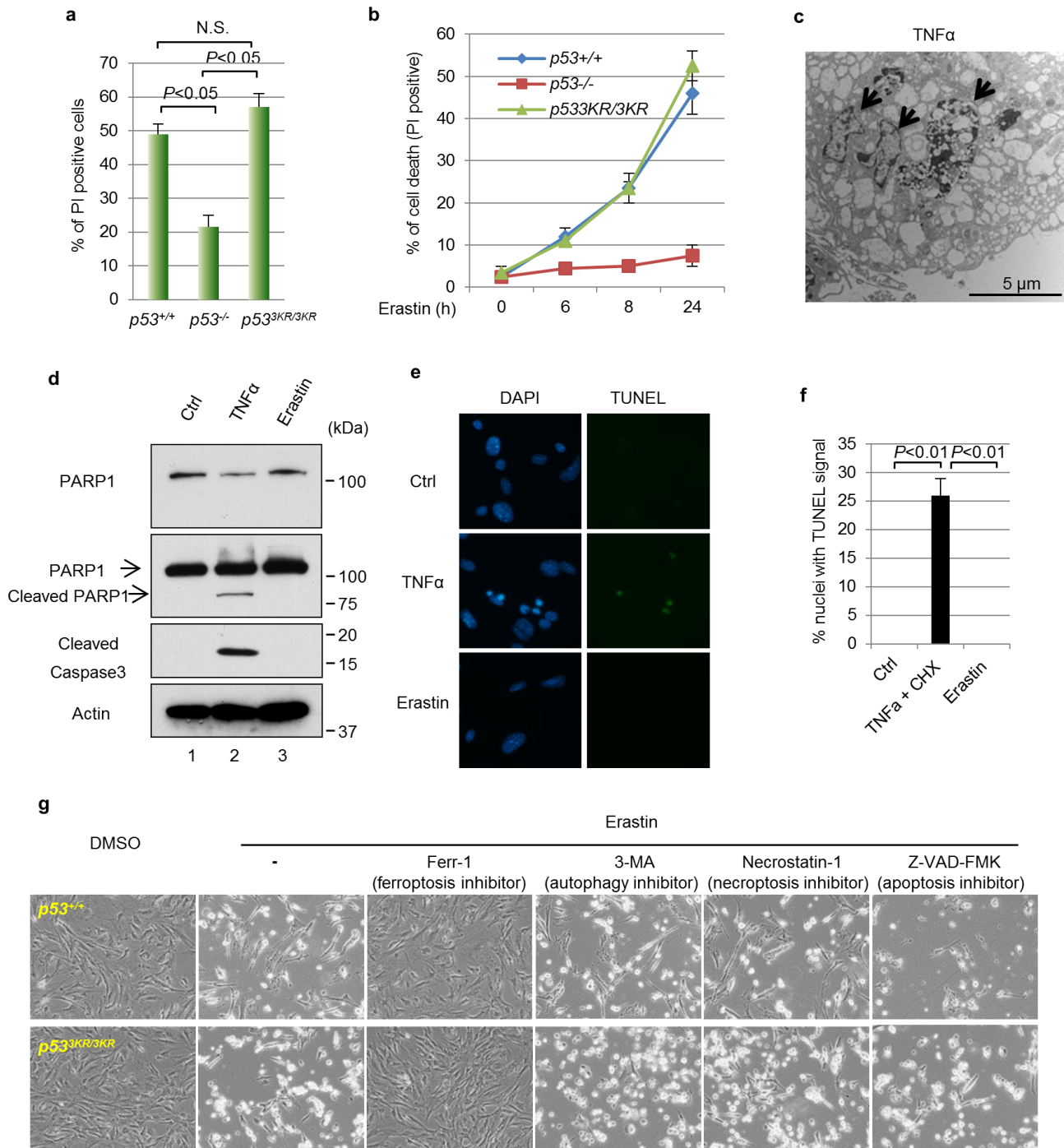
Mouse xenograft. Pooled stable cell lines were derived from H1299 tet-on $p53^{3KR}$ cells by transfecting either control vector or vector overexpressing *SLC7A11*. Cells were selected by G418 (1 mg ml⁻¹) for 2 weeks and then treated with or without doxycycline (0.5 μ g ml⁻¹) for 40 h. Cells (1.5×10^6) were then mixed with Matrigel (BD Biosciences) at 1:1 ratio (volume) and injected subcutaneously into nude mice (NU/NU, Charles River). Mice were fed either with control food or food containing doxycycline hyclate (Harlan, 625 mg kg⁻¹). Four weeks after injection, mice were euthanized and tumours were dissected from under the skin.

38. Schmidt, D. *et al.* ChIP-seq: using high-throughput sequencing to discover protein-DNA interactions. *Methods* **48**, 240–248 (2009).
39. Zheng, H. *et al.* A posttranslational modification cascade involving p38, Tip60, and PRAK mediates oncogene-induced senescence. *Mol. Cell* **50**, 699–710 (2013).
40. Kon, N. *et al.* Inactivation of HAUSP in vivo modulates p53 function. *Oncogene* **29**, 1270–1279 (2010).



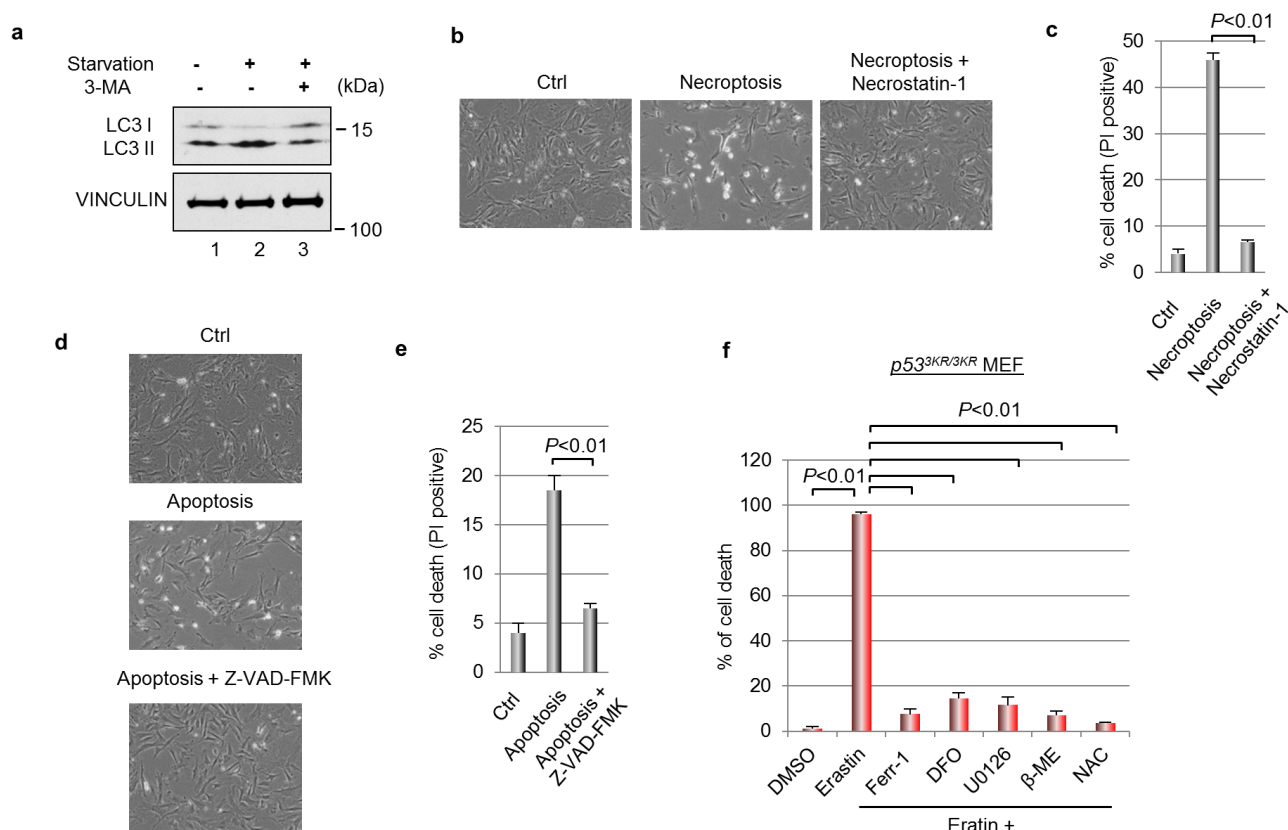
Extended Data Figure 1 | *SLC7A11* expression is downregulated by p53 and identification of p53 binding sites for mouse *Slc7a11* gene. **a**, Messenger RNA levels of *SLC7A11* in tet-on wild-type p53 stable line and parental H1299 cells treated with doxycycline ($0.1 \mu\text{g ml}^{-1}$). **b**, U2OS cells were treated with doxorubicin ($0.2 \mu\text{g ml}^{-1}$) and mRNA was quantified. **c**, Osteosarcoma cell lines, U2OS (p53 wild type) and SAOS-2 (p53 null) cells, were treated with doxorubicin ($0.2 \mu\text{g ml}^{-1}$) and mRNA levels were determined. **d**, Lung cancer cell lines, H1299 (p53 null) and H460 (p53 wild type) cells, were treated with doxorubicin ($0.2 \mu\text{g ml}^{-1}$) and RT-PCR was used to determine mRNA

expression. **e**, The breast cancer cell line MCF7 was treated with doxorubicin ($0.2 \mu\text{g ml}^{-1}$) for indicated duration and RT-qPCR was used to measure mRNA expression. **f**, RT-qPCR were used to determine the mRNA level of *Slc7a11* in MEFs with indicated genotype. **g**, Schematic diagram representing potential p53 binding locations and sequences on the mouse *Slc7a11* gene. TSS, transcription start site; light blue box, 5'-UTR. **h**, ChIP-qPCR was performed on MEFs that were treated with nutlin ($10 \mu\text{M}$) for 6 h. All qPCR was performed in two technical replicates and mean \pm s.d. are shown. All experiments were repeated independently three times.



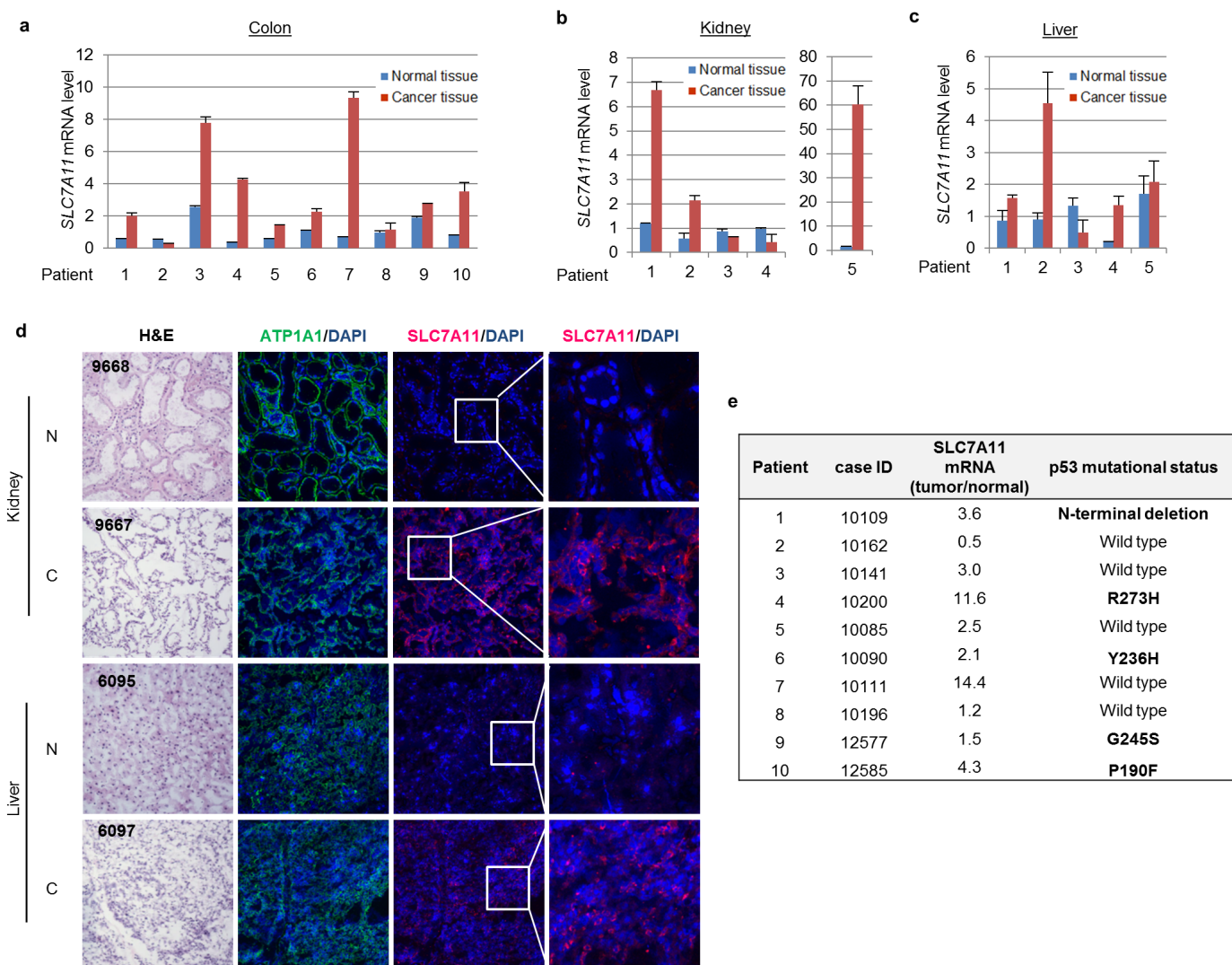
Extended Data Figure 2 | Characterization of erastin-induced cell death in MEFs. **a**, Quantification of cell death as shown in Fig. 3a. Error bars are s.d. from two technical replicates. **b**, Kinetics of cell death induced by erastin (1 μ M) over a 24-h period in MEFs with indicated genotypes. Technical replicates were performed and mean \pm s.d. are shown ($n = 2$). **c**, Transmission electron microscopy image of wild-type MEFs that were treated with TNF α (20 ng ml $^{-1}$) and CHX (5 μ g ml $^{-1}$) for 16 h with arrows pointing to fragmented nuclei. **d**, Wild-type MEFs were treated with mouse TNF α (20 ng ml $^{-1}$) and

CHX (5 μ g ml $^{-1}$) or erastin (1 μ M) for 8 h followed by western blots. **e**, TUNEL assay was carried out using wild-type MEFs treated as in **d**. **f**, Quantification of TUNEL signals for **e**. Mean \pm s.d. from ten random microscope views are shown (magnification, $\times 20$). **g**, MEFs with indicated p53 status were treated with erastin (4 μ M) and specific cell death inhibitors for 8 h before images were taken (magnification, $\times 10$). 3-MA, 3-methyladenine. All experiments were repeated at least three times and representative data are shown.



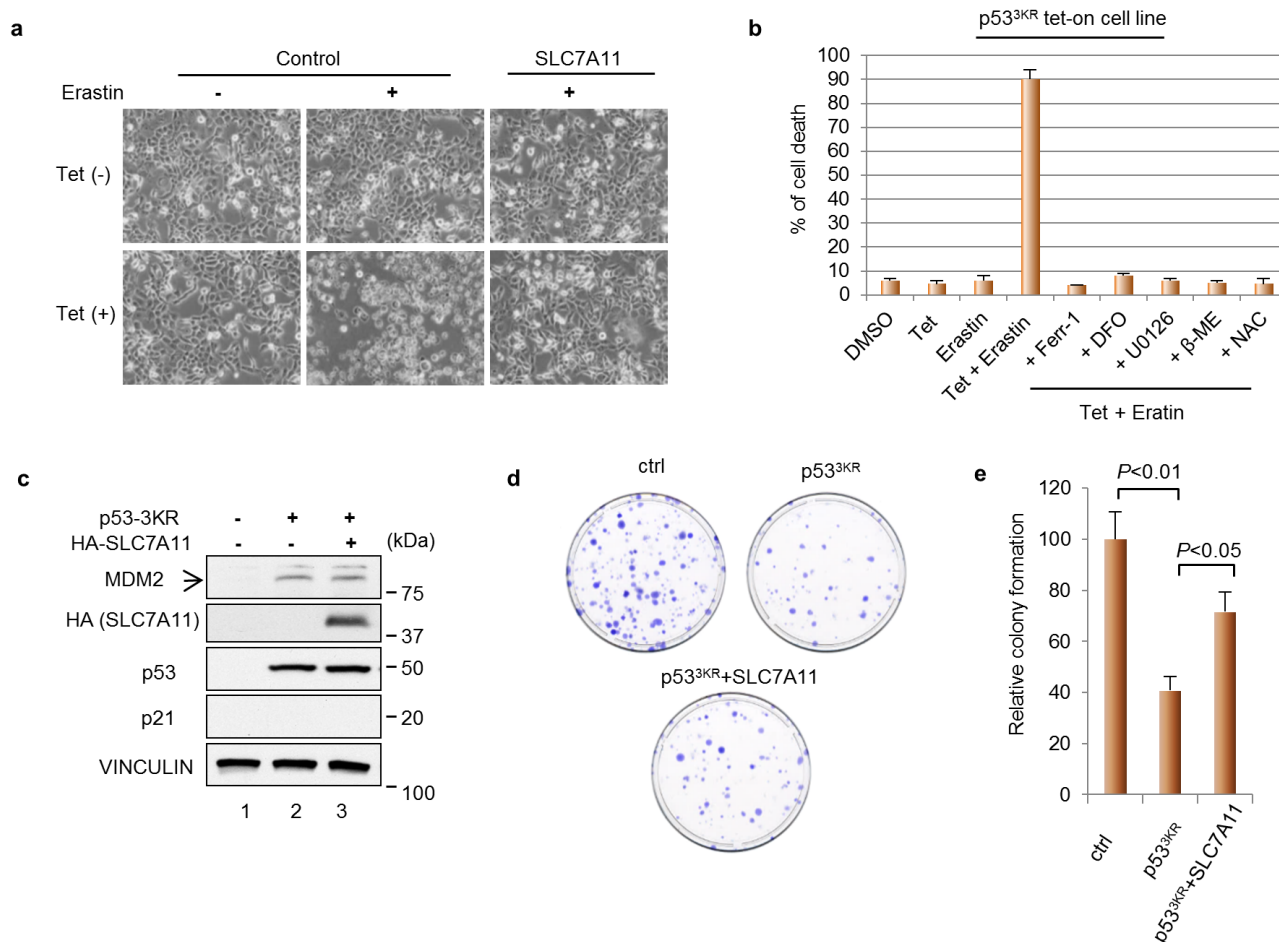
Extended Data Figure 3 | Effectiveness of cell death inhibitors. **a**, Wild-type MEF cells were starved in DMEM medium deprived of glucose, sodium pyruvate or L-glutamine for 2 h with or without 3-methyladenine (2 mM) followed by western blots. **b**, Wild-type MEFs were treated for 48 h with TNF α (20 ng ml⁻¹), SMAC mimetic (100 nM) and Z-VAD-FMK (10 μ g ml⁻¹) to induced necroptosis with or without the presence of necrostatin-1 (10 μ g ml⁻¹) (magnification, $\times 10$). **c**, Quantification of cell death as shown in **b**. PI, propidium iodide. Mean \pm s.d. from two technical replicates are shown. **d**, Wild-type MEFs were treated for 48 h with TNF α (20 ng ml⁻¹), SMAC mimetic (100 nM) and necrostatin-1 (10 μ g ml⁻¹) to induce apoptosis with or

without the presence of Z-VAD-FMK (10 μ g ml⁻¹) (magnification, $\times 10$). **e**, Quantification of cell death as shown in **d**. Mean \pm s.d. from two technical replicates are shown. **f**, *p53^{3KR/3KR}* MEFs were treated with erastin (4 μ M) and various chemicals that block ferroptosis for 24 h before the percentage of cell death was determined; error bars, s.d. from two technical replicates. DMSO, dimethyl sulfoxide; DFO, deferoxamine; U0126, 1,4-diamino-2,3-dicyano-1,4-bis[2-aminophenylthio] butadiene; β -ME, β -mercaptoethanol; NAC, N-acetyl-L-cysteine. All experiments were independently repeated three times.



Extended Data Figure 4 | SLC7A11 is overexpressed in tumours of human cancer patients. **a–c**, Quantitative RT–PCR was used to determine the expression levels of *SLC7A11* in paired normal and cancer tissues from colon (**a**), kidney (**b**) and liver (**c**); average expression levels from normal tissues were normalized to 1 in each type of cancer. Mean \pm s.d. from two technical replicates are shown. **d**, Representative heamatoxylin and eosin (H&E) and

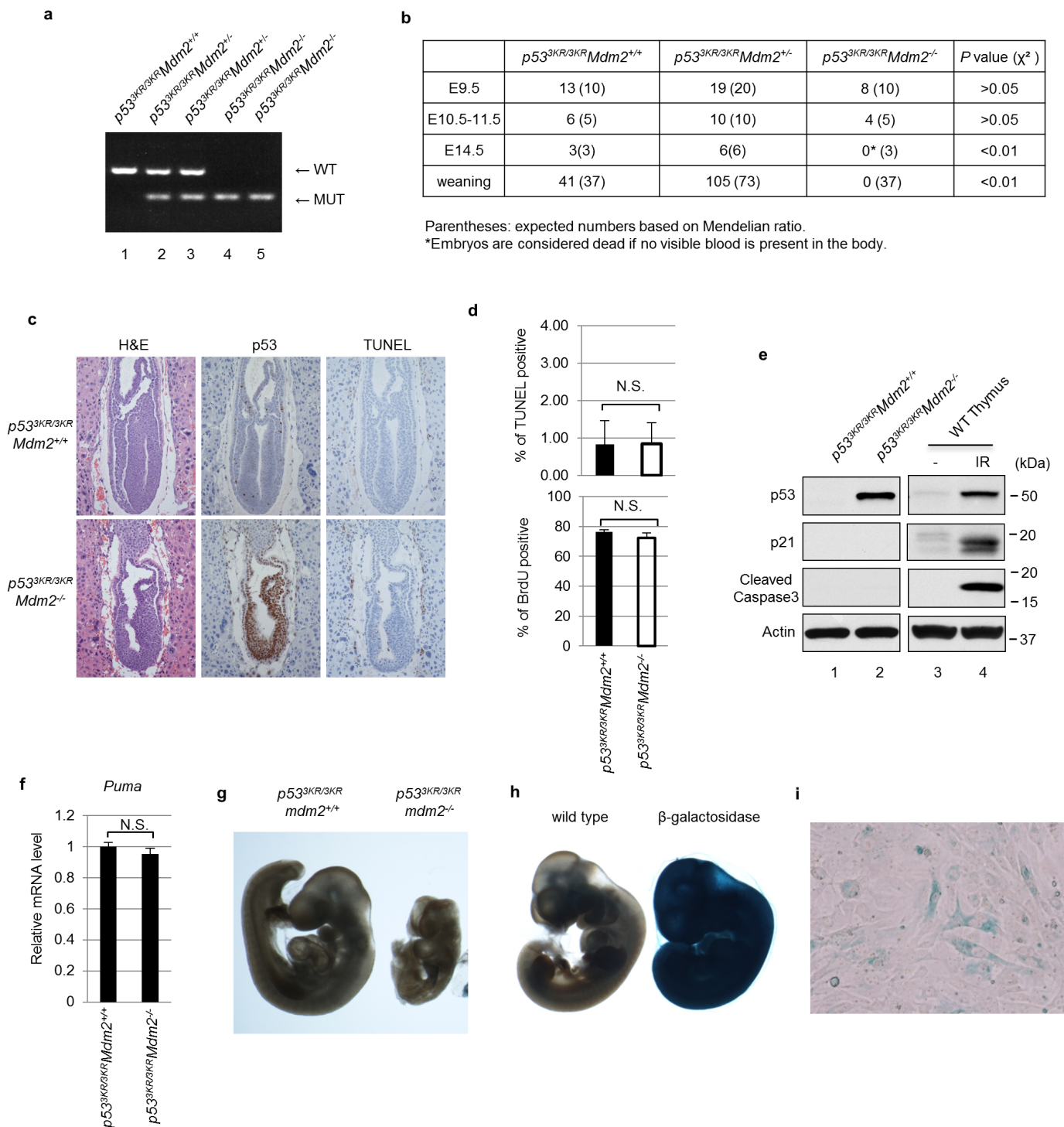
immunofluorescence staining of SLC7A11 on frozen sections of paired patient cancer and adjacent normal tissues. Magnification, $\times 20$. N, normal tissue; C, cancer tissue. Blue, DAPI; green, anti-ATP1A1; red, anti-SLC7A11. **e**, DNA sequencing was performed on colon cancer samples and specific mutations were identified. Independent experiments were repeated three times and representative data are shown.



Extended Data Figure 5 | Cell death induced by p53^{3KR} and erastin is ferroptosis and effect of SLC7A11 overexpression on colony formation.

a, Representative phase-contrast images of cell cultures as treated in Fig. 4b (magnification, $\times 10$). **b**, p53^{3KR} tet-on stable line cells were treated as indicated and the percentage of cell death was quantified (DFO, deferoxamine; U0126, 1,4-diamino-2,3-dicyano-1,4-bis[2-aminophenylthio] butadiene; β -ME, beta-mercaptoethanol; NAC, N-acetyl-L-cysteine). Mean \pm s.d. from

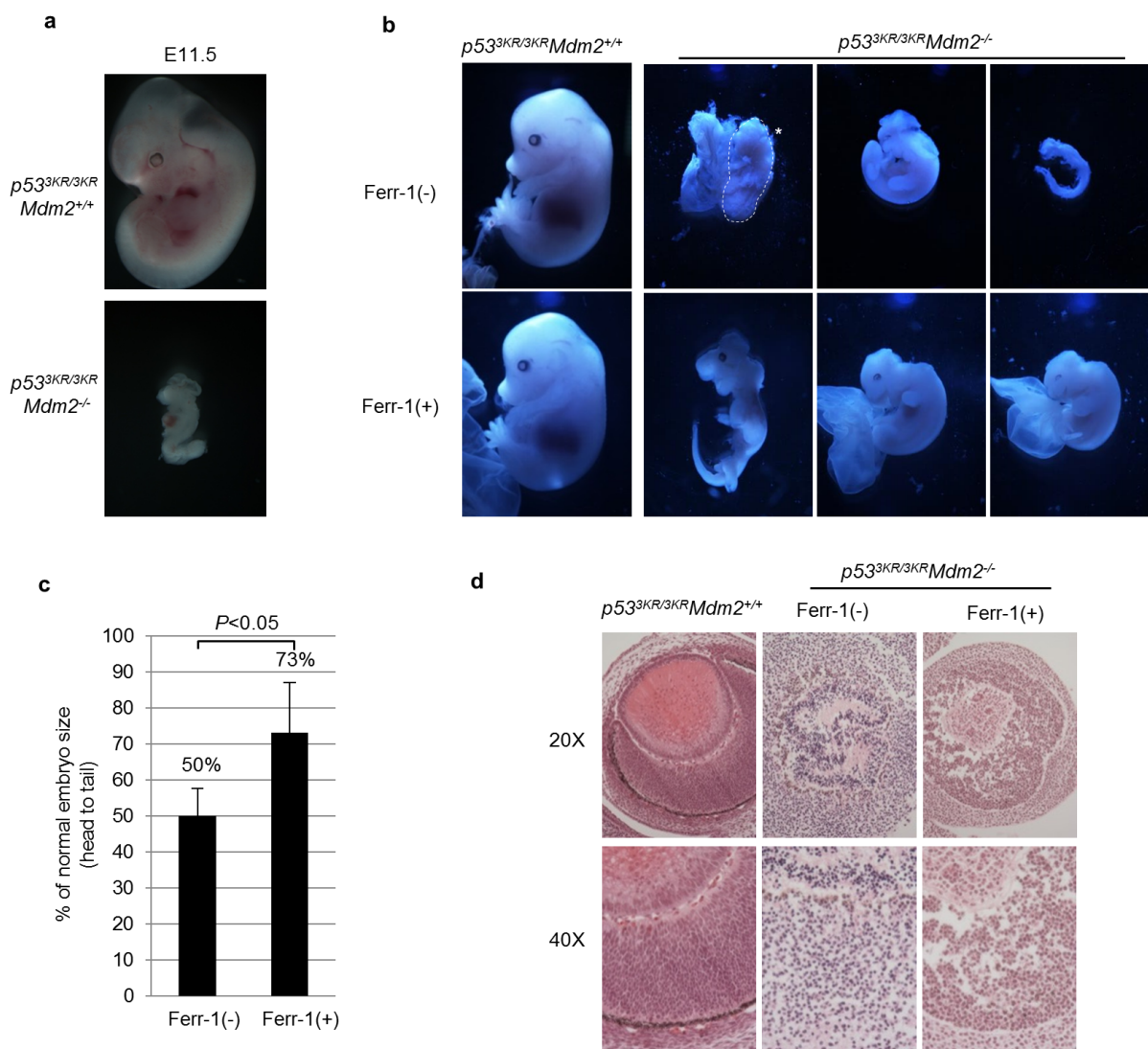
two technical replicates are shown. **c**, H1299 cells were transfected with indicated plasmids followed by western blot 24 h later. HA, haemagglutinin **d**, Representative images of colony formation assay in 10-cm plates as transfected in **c**. **e**, Quantification of colony formation assay as shown in **d**. Numbers of colonies formed in control plates were normalized to 100 and mean \pm s.d. from two technical replicates are shown. All experiments were repeated three times with representative data shown.



Extended Data Figure 6 | *p53^{3KR/3KR}Mdm2^{-/-}* mice are embryonic lethal.

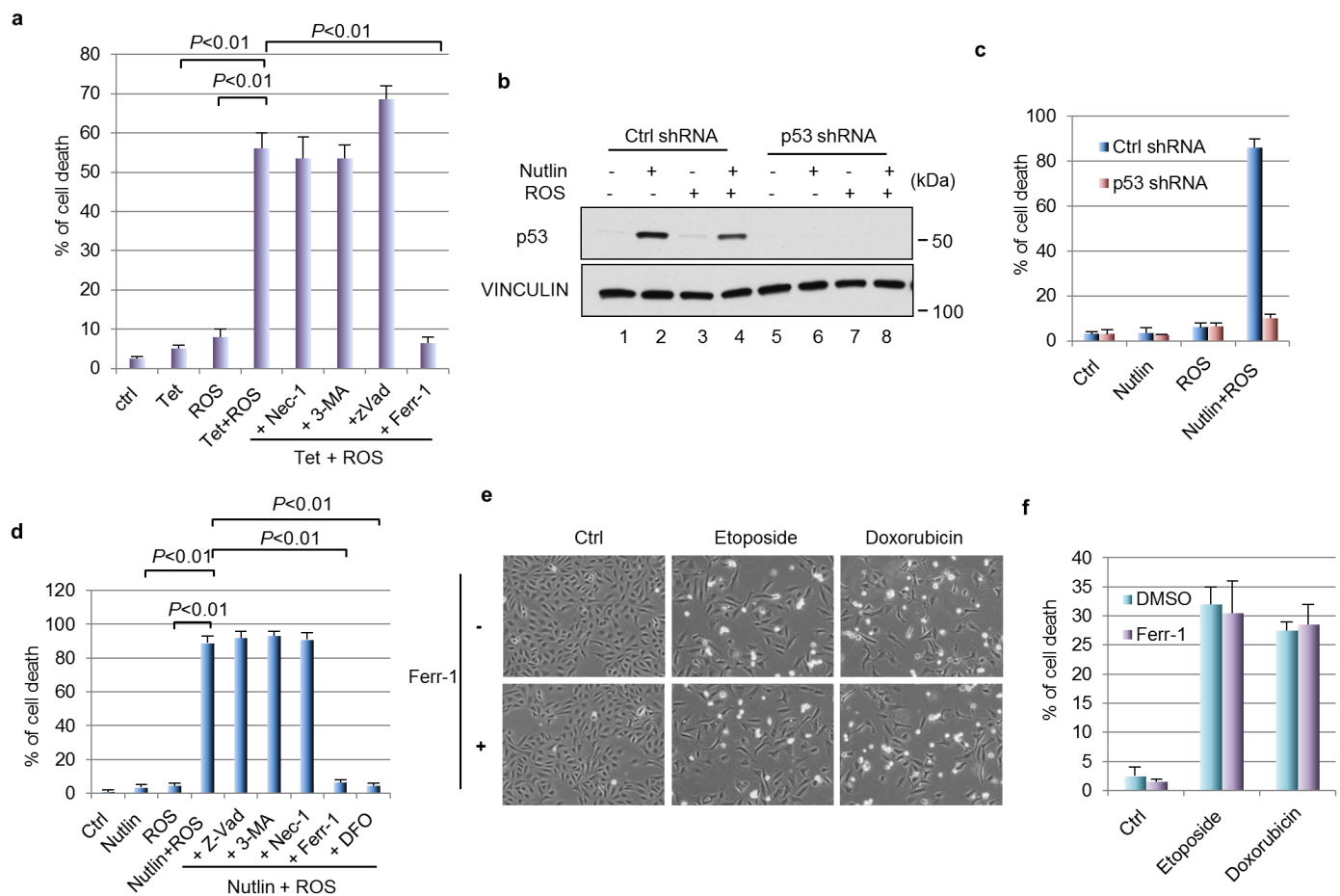
a, Representative gel images for genotyping of *Mdm2* status in *p53^{3KR/3KR}* background mice. **b**, Summary of numbers of live embryos and pups recovered from *p53^{3KR/3KR}Mdm2^{+/-}* intercross breeding. **c**, Haematoxylin and eosin (H&E) and immunohistochemistry staining of p53 and TUNEL assay on E7.5 embryos of indicated genotype (magnification, $\times 20$). **d**, Percentage of cells with positive TUNEL or BrdU were determined by counting 100 cells in each section from three different embryos. Error bars, s.d.; N.S., not significant. **e**, Whole-embryo extracts from E9.5 embryos were used for western blot. As positive controls, thymus protein lysate from irradiated (IR) wild-type mouse

(8 Gy) was used. **f**, Messenger RNA expression levels of *Puma* were determined by RT-qPCR using E9.5 embryos with indicated genotype ($n = 3$ for *p53^{3KR/3KR}Mdm2^{+/+}* and $n = 5$ for *p53^{3KR/3KR}Mdm2^{-/-}*; error bars, s.d.; N.S., not significant). **g**, Representative images of whole-mount senescence-associated β -galactosidase staining using E9.5 mouse embryos with indicated genotype (magnification, $\times 2$). **h**, Same protocol as in **g** was used to stain control wild-type embryos and embryos of HAUSP heterozygous knockouts, which express β -galactosidase⁴⁰ (magnification, $\times 2$). **i**, Late passage senescent wild-type MEFs were stained for senescence-associated β -galactosidase activity using the same protocol as in **g** (magnification, $\times 10$).



Extended Data Figure 7 | Ferrostatin-1 partially rescues $p53^{3KR/3KR} Mdm2^{-/-}$ mice. **a**, Representative morphologies of E11.5 mouse embryos of indicated genotype (magnification, $\times 3$). **b**, Representative embryos recovered from $p53^{3KR/3KR} Mdm2^{+/+}$ intercross with or without ferritin-1 injection. The dashed line marked by an asterisk highlights the body of a dead $p53^{3KR/3KR} Mdm2^{-/-}$ embryo, which disintegrated upon further dissection

(magnification, $\times 1.5$). **c**, Head-to-tail lengths of $p53^{3KR/3KR} Mdm2^{-/-}$ embryos were measured and compared to $p53^{3KR/3KR} Mdm2^{+/+}$ controls ($n = 4$ for each group of $p53^{3KR/3KR} Mdm2^{-/-}$ embryos with or without ferritin-1 treatment; error bars, s.d.). **d**, Representative haematoxylin and eosin (H&E) staining of eye structures of $p53^{3KR/3KR} Mdm2^{+/+}$ and $p53^{3KR/3KR} Mdm2^{-/-}$ mouse embryos (magnification, $\times 20$ and $\times 40$ as indicated).



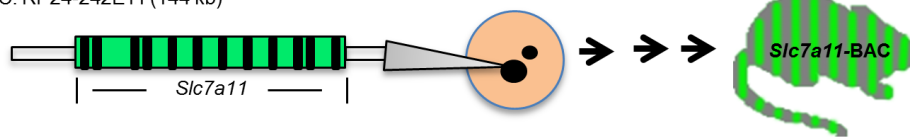
Extended Data Figure 8 | Synergized ferroptosis by nutlin/ROS.

a, Percentage of cell death as shown in Fig. 6a was quantified. Mean \pm s.d. from two technical replicates are shown. **b**, U2OS cells with stable knockdown of p53 were treated by nutlin (10 μ M) for 24 h followed by addition of ROS (tert-butyl hydroperoxide, 350 μ M) for 4 h. Western blots were performed. **c**, Quantification of cell death as shown in Fig. 6c. Mean \pm s.d. from two technical replicates are shown. **d**, U2OS cells were treated with nutlin (10 μ M)

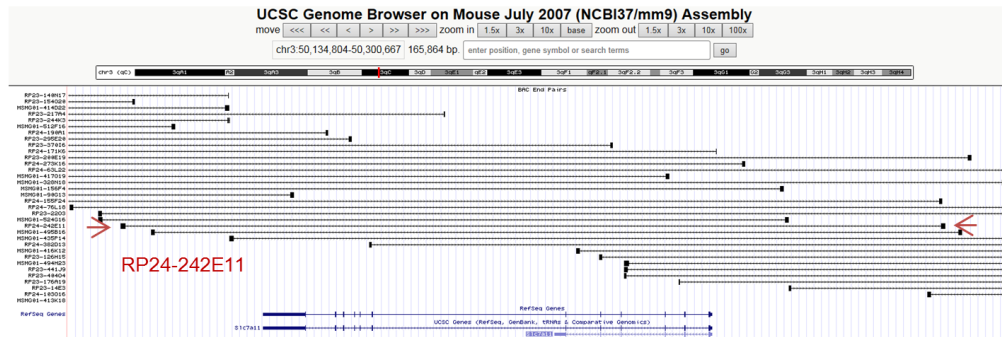
for 24 h first, followed by ROS (tert-butyl hydroperoxide, 350 μ M) along with indicated cell death inhibitors; cell death were quantified 24 h later. Error bars, s.d. from two technical replicates. **e**, U2OS cells were treated with DNA-damaging agents (etoposide, 20 μ M; doxorubicin, 0.2 μ g ml⁻¹) for 48 h with or without the presence of ferr-1 (2 μ M) (magnification, $\times 10$); cell death was quantified in **f** with mean \pm s.d. shown ($n = 2$ technical replicates). All data were repeated three times independently.

a

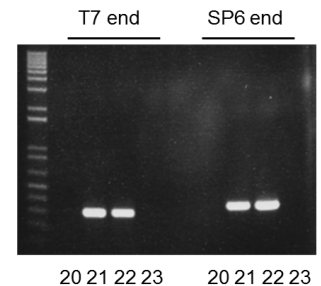
BAC: RP24-242E11 (144 kb)



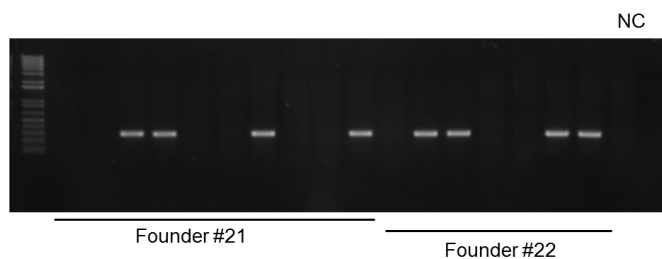
b



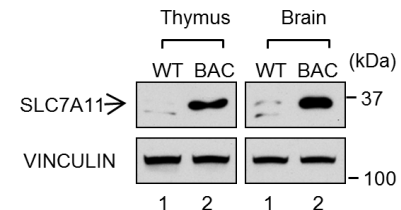
c



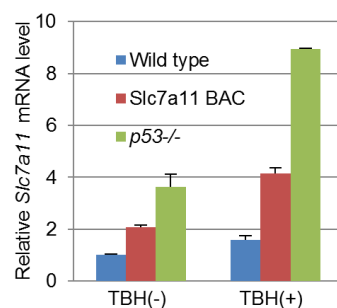
d



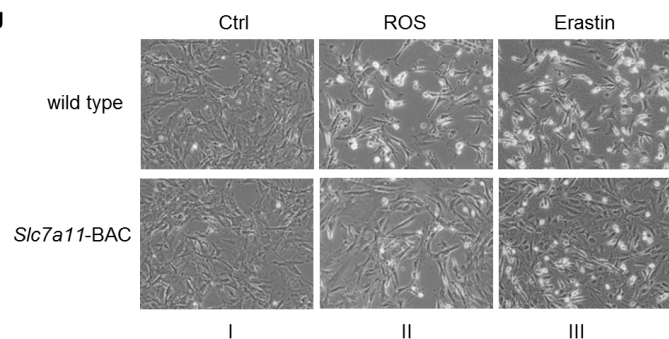
e



f



g



Extended Data Figure 9 | Generation of BAC transgenic mice for *Slc7a11* overexpression. **a**, Schematic diagram showing the procedure for generation of *Slc7a11*-BAC transgenic mice. **b**, Snap shot of BACs surrounding mouse *Slc7a11* genes. BAC (RP24-242E11) that contains only the *Slc7a11* gene was selected for injection. **c**, PCR at both ends of the BAC construct identified founders (no. 21 and no. 22) as positive BAC transgenic mice. **d**, Germline transmission was confirmed from both founders identified in **c**. NC, no

template control. **e**, Thymus and brain tissues from 3-week-old litter mates of control and *Slc7a11*-BAC transgenic mice were lysed and examined by western blots. **f**, MEF cells with indicated genotypes were treated as in Fig. 6e for 2 h and mRNA levels were determined by RT-qPCR. Mean \pm s.d. from two technical replicates are shown. **g**, Representative images of cells treated as in Fig. 6e (magnification, $\times 10$).

Extended Data Table 1 | p53-regulated genes identified in the wild-type p53 inducible stable line through microarray analysis

Functional group	Gene symbol	Gene name	RefSeq	Fold Change	p-value
Transport & Metabolism	TIGAR	TP53-induced glycolysis and apoptosis regulator	AY425618	4.55812	2.3798E-07
	<i>SLC7A11</i>	solute carrier family 7, (cationic amino acid transporter, y ⁺ system) member 11	AB026891	-2.66607	7.0681E-05
	<i>GLS2</i>	glutaminase 2 (liver, mitochondrial)	AF110330	17.0011	4.8505E-09
	<i>SESN1</i>	sestrin 1	AF033122	9.78117	8.93E-09
	<i>TAP1</i>	transporter 1, ATP-binding cassette, sub-family B (MDR/TAP)	AB012644	2.95728	7.1604E-08
	<i>PANK1</i>	pantothenate kinase 1	AY027661	5.72688	1.456E-06
	<i>ACER2</i>	similar to alkaline ceramidase 2; alkaline ceramidase 2	ENST00000340967	5.34687	1.1182E-05
	<i>SESN2</i>	sestrin 2	BC013304	2.59232	7.8217E-06
	<i>CHAC1</i>	ChaC, cation transport regulator homolog 1 (E. coli)	BC001683	4.81706	4.0584E-08
	<i>ORAI3</i>	ORAI calcium release-activated calcium modulator 3	BC015555	3.23129	7.6884E-06
	<i>ABHD4</i>	abhydrolase domain containing 4	AK293198	10.3618	1.1017E-09
	<i>ALDH1L2</i>	aldehyde dehydrogenase 1 family, member L2	AK300373	13.0247	6.7912E-08
	<i>ANK1</i>	ankyrin 1, erythrocytic	M28880	2.72917	3.7932E-06
	<i>BCAT1</i>	branched chain aminotransferase 1, cytosolic	ENST00000261192	-2.64027	3.6497E-07
	<i>CMBL</i>	carboxymethylenebutenolidase homolog (Pseudomonas)	ENST00000510532	5.0088	4.8907E-07
	<i>DGKA</i>	diacylglycerol kinase, alpha 80kDa	BC023523	5.92523	5.4931E-07
	<i>FDXR</i>	ferredoxin reductase	AK298908	7.05275	1.1567E-09
	<i>PHGDH</i>	phosphoglycerate dehydrogenase	AF171237	-1.31044	5.8696E-05
	<i>GPT2</i>	glutamic pyruvate transaminase (alanine aminotransferase) 2	AL833351	2.78579	9.8714E-07
	<i>KLHL24</i>	kelch-like 24 (Drosophila)	AK000066	2.50394	1.6715E-06
	<i>LRP1</i>	low density lipoprotein-related protein 1 (alpha-2-macroglobulin receptor)	AK122840	3.52784	1.1368E-08
	<i>TM7SF2</i>	transmembrane 7 superfamily member 2	AF096304	6.93921	2.5897E-08
Cell cycle & Proliferation	<i>CDKN1A/p21</i>	cyclin-dependent kinase inhibitor 1A (p21, Cip1)	AK298901	10.9225	3.0979E-09
	<i>BTG2</i>	BTG family, member 2	BC105948	14.9562	6.8143E-09
	<i>GADD45A</i>	growth arrest and DNA-damage-inducible, alpha	BC011757	2.93357	1.0756E-07
	<i>CAV1</i>	caveolin 1, caveolae protein, 22kDa	AK290871	2.65042	3.2047E-07
	<i>CCNK</i>	cyclin K	BT006950	2.90074	9.9132E-07
	<i>DUSP1</i>	dual specificity phosphatase 1	AK298047	3.06448	6.6673E-10
	<i>PLK2</i>	polo-like kinase 2 (Drosophila)	AK297298	5.30746	2.2421E-08
	<i>PLK3</i>	polo-like kinase 3 (Drosophila)	AJ293866	18.2063	9.4625E-10
	<i>RB1</i>	retinoblastoma 1	AK299179	2.69757	1.4404E-07
	<i>SFN</i>	stratfin	AF029082	3.45591	7.6309E-06
	<i>TRIM22</i>	tripartite motif-containing 22	AK298934	2.81865	5.2447E-05
	<i>FBXW7</i>	F-box and WD repeat domain containing 7	AF411971	3.23697	9.4834E-06
	<i>ZMAT3</i>	zinc finger, matrix type 3	AF355465	5.73607	6.5446E-08
	<i>CCNE2</i>	cyclin E2	AF102778	-10.5563	9.6454E-09
	<i>MNS1</i>	meiosis-specific nuclear structural 1	ENST00000260453	-2.97374	0.00015946
Apoptosis	<i>BAX</i>	BCL2-associated X protein	L22474	1.88726	3.7902E-06
	<i>TP53INP1</i>	tumor protein p53 inducible nuclear protein 1	AF409115	12.3711	6.2069E-09
	<i>TP53I3</i>	tumor protein p53 inducible protein 3	ENST00000407482	15.126	2.3803E-09
	<i>TNFRSF10D</i>	death domain	AF021233	2.82197	4.2642E-07
	<i>AIFM2</i>	apoptosis-inducing factor, mitochondrion-associated, 2	AF337957	2.9952	5.8401E-07
	<i>APAF1</i>	apoptotic peptidase activating factor 1	AF013263	10.2862	4.0106E-10
	<i>CASP6</i>	caspase 6, apoptosis-related cysteine peptidase	BC000305	9.60075	2.8464E-08
	<i>GDF15</i>	growth differentiation factor 15	AB000584	13.1249	1.1527E-08
	<i>PCBP4</i>	poly(rC) binding protein 4	AF176330	4.50693	9.552E-09
	<i>PERP</i>	PERP, TP53 apoptosis effector	BC010163	3.02863	1.9567E-08
	<i>RPS27L</i>	ribosomal protein S27-like	BC003667	3.53852	1.0771E-05
	<i>SCN3B</i>	sodium channel, voltage-gated, type III, beta	BC117282	8.94659	4.3472E-08
	<i>DDIT3</i>	DNA-damage-inducible transcript 3	BC003637	2.63317	0.0001017
Others	<i>DRAM1</i>	DNA-damage regulated autophagy modulator 1	BC018435	3.67323	7.8723E-08
	<i>MDM2</i>	MDM2 oncogene, E3 ubiquitin protein ligase	AF092845	7.44673	5.4175E-08
	<i>RRM2B</i>	ribonucleotide reductase M2 B (TP53 inducible)	ENST00000395910	4.53617	4.0021E-07
	<i>XPC</i>	xeroderma pigmentosum, complementation group C	ENST00000285021	2.72401	4.349E-05
	<i>PRKAB1</i>	protein kinase, AMP-activated, beta 1 non-catalytic subunit	AK301165	3.35515	1.2744E-07
	<i>ANKRA2</i>	ankyrin repeat, family A (RFXANK-like), 2	AF251051	12.5615	2.8927E-06
	<i>APOBEC3C</i>	apolipoprotein B mRNA editing enzyme, catalytic polypeptide-like 3C	AF165520	4.85886	3.1852E-08
	<i>ARID5B</i>	AT rich interactive domain 5B (MRF1-like)	AK296921	3.56829	3.3834E-07
	<i>BMP6</i>	bone morphogenetic protein 6	AK300628	-3.88207	7.2324E-07
	<i>C4ORF21</i>	chromosome 4 open reading frame 21	AK090556	-3.97572	1.401E-06
	<i>C5ORF28</i>	chromosome 5 open reading frame 28	BC013351	-3.03553	5.0792E-05
	<i>CALCOCO1</i>	calcium binding and coiled-coil domain 1	AB040969	5.94756	3.9553E-08
	<i>FERMT1</i>	fermitin family homolog 1 (Drosophila)	AB105105	4.28817	6.2732E-07
	<i>GATS</i>	GATS, stromal antigen 3 opposite strand	AK124689	4.13525	1.1626E-07
	<i>MR1</i>	major histocompatibility complex, class I-related	AF010446	4.56814	2.5677E-07
	<i>PCDHB11</i>	protocadherin beta 11	BC112132	4.26781	3.3776E-05
	<i>PCDHB14</i>	protocadherin beta 14	AF152493	2.76533	9.4183E-05
	<i>PLXNB2</i>	plexin B2	AK056543	2.79781	1.2076E-08
	<i>PROCR</i>	protein C receptor, endothelial (EPCR)	BC014451	3.27997	6.7976E-08
	<i>VCAN</i>	versican	ENST00000343200	15.2705	2.7969E-07
	<i>WDR63</i>	WD repeat domain 63	ENST00000294664	19.3466	1.204E-08
	<i>ZNF702P</i>	zinc finger protein 702 pseudogene	NR_003578	3.99824	3.3623E-05

Previously known direct p53 targets are in upright font and potentially novel targets are in italic. Fold changes are induced versus non-induced.

Planet heating prevents inward migration of planetary cores

Pablo Benítez-Llambay¹, Frédéric Masset², Gloria Koenigsberger² & Judit Szulágyi³

Planetary systems are born in the disks of gas, dust and rocky fragments that surround newly formed stars. Solid content assembles into ever-larger rocky fragments that eventually become planetary embryos. These then continue their growth by accreting leftover material in the disk. Concurrently, tidal effects in the disk cause a radial drift in the embryo orbits, a process known as migration^{1–4}. Fast inward migration is predicted by theory for embryos smaller than three to five Earth masses^{5–7}. With only inward migration, these embryos can only rarely become giant planets located at Earth's distance from the Sun and beyond^{8,9}, in contrast with observations¹⁰. Here we report that asymmetries in the temperature rise associated with accreting infalling material^{11,12} produce a force (which gives rise to an effect that we call 'heating torque') that counteracts inward migration. This provides a channel for the formation of giant planets⁸ and also explains the strong planet–metallicity correlation found between the incidence of giant planets and the heavy-element abundance of the host stars^{13,14}.

We solve the equations governing the disk hydrodynamics in combination with the equations of radiative transfer. Planets have an angular momentum that increases with their orbital radius. In the case of a nearly circular orbit, the rate of change of angular momentum, or torque, gives the migration rate. Our calculations are performed in three dimensions, yielding a reliable value for the net torque, from which the direction and rate of migration are inferred.

Our fiducial computation is one in which a rocky core of three Earth masses ($3M_{\oplus}$) is located at a distance comparable to that of Jupiter from the Sun and is being bombarded by solid material at a rate that doubles its mass in 100,000 years. We assume that the gravitational energy of the infalling solid material is transformed entirely into heat and ultimately radiated by the planet¹¹. A second computation is performed with the same setup, but without the planet's radiation, to distinguish the effects of the heating torque from other torques. We find that the heating torque (defined as the torque difference between cases with accretion turned respectively on and off) has a positive sign (Fig. 1), which enables it to counteract the effect of the standard, negative torque. The latter includes all torque components of the non-heating case, and is always negative for small mass embryos (typically smaller than $5M_{\oplus}$). Thus, the effect of the heating torque is to slow down the inward migration, cancel it, or reverse its direction.

The most important factors governing the strength of the heating torque and thus, the direction of migration, are the accretion rate of the embryo, its mass and the opacity of the disk. For our fiducial values of opacity, disk structure and embryo mass, we find that outward migration occurs for accretion rates corresponding to a mass-doubling time of less than approximately 60,000 years. For larger mass-doubling times (that is, smaller accretion rates), the heating torque may slow down the inward migration but not reverse it (Fig. 2). The heating torque has a large efficiency over the mass interval $0.5M_{\oplus}$ to $3M_{\oplus}$, which is precisely the range of masses for which counteracting inward migration is required in order to allow further embryo growth at distances where giant planets are expected to form⁹. Masses smaller than $0.5M_{\oplus}$, for which

the heating torque has a lower efficiency, migrate inward only a negligible fraction of their orbital radius by the time they double their mass.

Some insight into the physics of our new torque component can be gained by examination of a mass-density map in the planet's vicinity. The energy released by the planet heats the optically thick disk in its vicinity. As the latter maintains its pressure equilibrium, hotter regions are less dense than the surrounding ambient material. As a consequence of the flow pattern around the planet, two under-dense lobes appear, one leading and one following the planet, when the heating is included in the calculation (Fig. 3). Protoplanetary disks rotate in general at a speed slightly smaller than the Keplerian speed, and the corotation (the location at which the material orbits the star at same pace as the planet) lies slightly towards its star from the planet. This situation favours the lobe that appears behind the planet: its material approaches closer to the planet, receives more heat and is consequently less dense than the other lobe, leading to a positive torque on the planet. We explored the dependence of the heating torque on the gradient of surface density (which leads to the shift between the planet and its corotation), and we found that the heating torque does indeed scale with the distance to corotation. Only in the non-realistic cases in which the corotation is further out than the planet (when the gas pressure increases outward) do we find a negative heating torque. The heating torque therefore constitutes a robust trap against inward migration in any realistic disk, when accretion rates are large enough.

In the limit of a very large accretion rate, the heating torque largely dominates other torque components, and the net torque is directly proportional to the accretion rate. Since the migration rate is proportional to the torque, it follows that the final distance over which a planetary embryo migrates is a function of the mass it accretes. We find that an

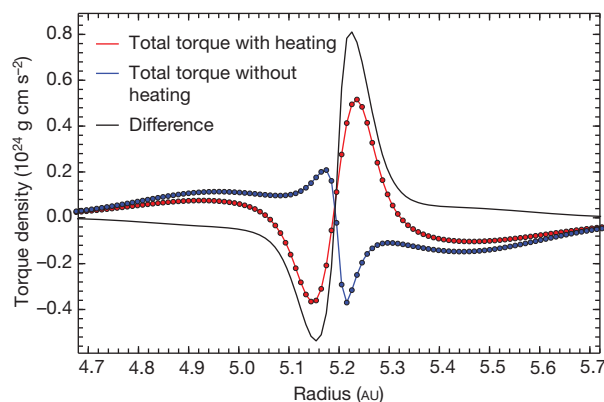


Figure 1 | Comparison of the torques in the cases with and without heating. The blue curve shows the torque radial density (that is, torque exerted by rings of unitary radial width upon the planet) in the non-heating case and the red curve when the heating is included. Their difference shows the heating torque density (black). This calculation corresponds to an embryo planet of $3M_{\oplus}$ that is located at 5.2 AU from its central star.

¹IATE, Observatorio Astronómico, Universidad Nacional de Córdoba, Laprida 854, Córdoba, X5000BGR, Argentina. ²Instituto de Ciencias Físicas, Universidad Nacional Autónoma de México, Avenida Universidad s/n, 62210 Cuernavaca, Morelos, Mexico. ³University of Nice-Sophia Antipolis, CNRS, Observatoire de la Côte d'Azur, Laboratoire Lagrange, F-06304 Nice, France.

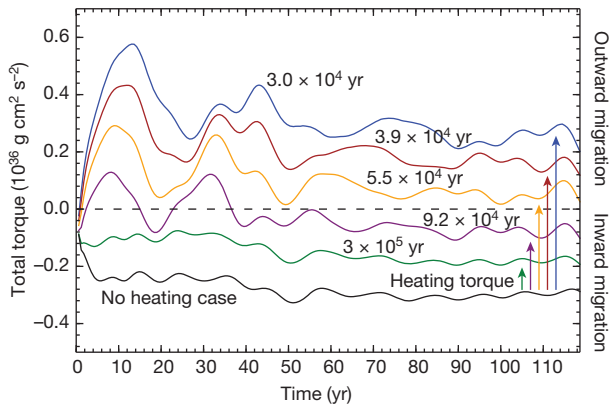


Figure 2 | Heating torque for different growth timescales. The curves are labelled with the planetary mass-doubling time (that is, the time it takes the accreting planet to double its mass) and show the torque exerted on an embryo planet of $3M_{\oplus}$ over the first 118 years of our calculation (ten orbits). With low or no heating, the planet migrates inward while for larger rates (mass doubling time shorter than 92,000 years) it migrates outward. The dashed line corresponds to no migration. The vertical arrows show the magnitude of the heating torque.

embryo initially smaller than the Earth would at most double its semi-major axis by the time it reaches $5M_{\oplus}$.

The finding that the heating torque can produce outward migration for accreting embryos in their earliest stage of development has implications for the formation of planetary systems in general, and the Solar System in particular. It opens a new route for the formation of gas giant planets and alleviates the problem encountered by current models of planetary population synthesis that predict too many super-Earths⁹ and a low yield of giant planets. The general picture that now emerges is

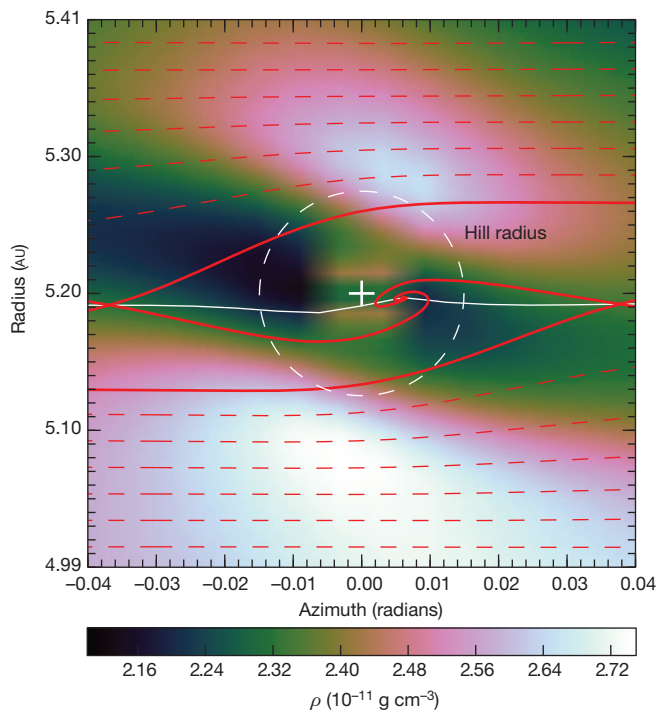


Figure 3 | Density in the vicinity of an irradiating embryo. This equatorial slice of the mass density shows two low-density lobes on each side of the planet (marked with a cross). The more apparent one (left) gives rise to the positive torque. Such lobes are absent for a non-radiating embryo. The dashed circle shows the planetary Hill radius. Streamlines are in red showing the outer limits of the co-orbital region (bold) and paths of material further from the planet (dashed). The white nearly horizontal curve shows corotation, that is, the place where the material is at rest in the planetary frame.

that embryos with masses in the range $0.3M_{\oplus}$ – $5M_{\oplus}$ are able to avoid inward migration when accretion rates are large. By the time the heating torque efficiency drops, they have entered a regime in which other mechanisms driving outward migration come into play^{5,9,15}. Embryos that are formed when accretion rates are low will still undergo inward migration but at a slower rate. The overall migration behaviour therefore displays a bifurcation depending on the accretion rate of solids.

This bifurcation provides a simple and natural explanation for the very strong correlation found between the incidence of giant planets and the heavy-element content (that is, metallicity) of the host star^{13,14}. That is, since the heating torque scales with the accretion rate and the accretion rate, in turn, scales with the amount of solid content (a proxy of which is the metallicity), protoplanetary disks with larger metallicity will engender planets that can avoid inward migration and grow to become giant planets. In contrast, embryos born in lower-metallicity environments cannot avoid inward migration, leading to results as hitherto found in models of planetary population synthesis, with low yields of giant planets and ubiquitous super-Earths. These might therefore be more abundant in metal-poor systems, as suggested by a recent planet search with accurate stellar metallicities¹⁶. The incidence of super-Earths with the metallicity of the host star is however debated¹⁴.

Recent models have contemplated the *in situ* formation of super-Earths at small orbital distances from the star^{17,18} ($\lesssim 1$ AU, where one astronomical unit (AU) is the average distance from the Earth to the Sun). We have not performed calculations for embryos so close to the star, where the disk parameters are still poorly constrained, but we note that the very short mass-doubling times inferred for some planets very close to their star¹⁸ would probably yield an extremely large heating torque, the magnitude of which remains to be properly calculated before the likelihood of *in situ* formation scenarios can be assessed.

The implications for the formation of our own Solar System are somewhat more speculative, but are important to highlight. The parameters of our fiducial run are typical of those found beyond the snow line (the distance at which water-ice condenses). On the warm side of the snow line we expect the heating torque to have a much reduced efficiency, because the bombardment rate and the disk opacity drop substantially. With a heating torque producing outward migration, we expect all embryos having formed beyond the ultimate location of the snow line to have experienced a sizeable outward migration, thus causing a large depletion of solid material in this region. Hence, a prediction of our torque mechanism is that a depleted region should be present inside the orbit of the first giant planet in many planetary systems. In our Solar System, such a region may correspond to the asteroid belt, which contains only approximately $0.001M_{\oplus}$ of solid material¹⁹. Within our framework, Jupiter's rocky core could have been assembled from embryos originating from this region.

A priori, the heating torque would not have been expected to have the same order of magnitude as the tidal torque. It depends primarily on the planet's physical radius, dust opacity and mass accretion rate, whereas the tidal torque depends on the gaseous disk's surface density and temperature. The serendipitous coincidence of both torques is remarkable and allows the bifurcation between inward and outward migration to occur for accretion rates that lie within the range of the largest and smallest accretion rates believed to prevail in protoplanetary systems.

Although further implications of this new torque component can be derived only from a fine-tuned analysis of all parameters of the disk and the embryo, it is clear that the heating torque provides a unifying mechanism for gaining a deeper understanding of giant planet formation in general and the specifics which gave rise to our own system.

Online Content Methods, along with any additional Extended Data display items and Source Data, are available in the online version of the paper; references unique to these sections appear only in the online paper.

Received 3 December 2014; accepted 29 January 2015.

1. Goldreich, P. & Tremaine, S. Disk-satellite interactions. *Astrophys. J.* **241**, 425–441 (1980).

2. Ward, W. R. Protoplanet migration by nebula tides. *Icarus* **126**, 261–281 (1997).
3. Kley, W. & Nelson, R. P. Planet-disk interaction and orbital evolution. *Annu. Rev. Astron. Astrophys.* **50**, 211–249 (2012).
4. Baruteau, C. *et al.* Planet-disc interactions and early evolution of planetary systems. Preprint at <http://arxiv.org/abs/1312.4293> (2013).
5. Paardekooper, S.-J., Baruteau, C. & Kley, W. A torque formula for nonisothermal type I planetary migration—II. Effects of diffusion. *Mon. Not. R. Astron. Soc.* **410**, 293–303 (2011).
6. Masset, F. S. & Casoli, J. Saturated torque formula for planetary migration in viscous disks with thermal diffusion: recipe for protoplanet population synthesis. *Astrophys. J.* **723**, 1393–1417 (2010).
7. Tanaka, H., Takeuchi, T. & Ward, W. R. Three-dimensional interaction between a planet and an isothermal gaseous disk. I. Corotation and Lindblad torques and planet migration. *Astrophys. J.* **565**, 1257–1274 (2002).
8. Levison, H. F., Thommes, E. & Duncan, M. J. Modeling the formation of giant planet cores. I. Evaluating key processes. *Astron. J.* **139**, 1297–1314 (2010).
9. Cossou, C., Raymond, S. N., Hersant, F. & Pierens, A. Hot super-Earths and giant planet cores from different migration histories. *Astron. Astrophys.* **569**, A56 (2014).
10. Howard, A. W. Observed properties of extrasolar planets. *Science* **340**, 572–576 (2013).
11. Pollack, J. B. *et al.* Formation of the giant planets by concurrent accretion of solids and gas. *Icarus* **124**, 62–85 (1996).
12. Mordasini, C., Mollière, P., Dittkrist, K.-M., Jin, S. & Alibert, Y. Global models of planet formation and evolution. Preprint at <http://arxiv.org/abs/1406.5604> (2014).
13. Fischer, D. A. & Valenti, J. The planet-metallicity correlation. *Astrophys. J.* **622**, 1102–1117 (2005).
14. Wang, J. & Fischer, D. A. Revealing a universal planet-metallicity correlation for planets of different solar-type stars. *Astron. J.* **149**, 14 (2015).
15. Bitsch, B., Crida, A., Morbidelli, A., Kley, W. & Dobbs-Dixon, I. Stellar irradiated discs and implications on migration of embedded planets. I. Equilibrium discs. *Astron. Astrophys.* **549**, A124 (2013).
16. Jenkins, J. S. *et al.* in *European Physical Journal Web of Conferences* Vol. 47, 5001 (2013); <http://dx.doi.org/10.1051/epjconf/20134705001>.
17. Hansen, B. M. S. & Murray, N. Testing in situ assembly with the Kepler Planet Candidate Sample. *Astrophys. J.* **775**, 53 (2013).
18. Chiang, E. & Laughlin, G. The minimum-mass extrasolar nebula: in situ formation of close-in super-Earths. *Mon. Not. R. Astron. Soc.* **431**, 3444–3455 (2013).
19. Walsh, K. J., Morbidelli, A., Raymond, S. N., O'Brien, D. P. & Mandell, A. M. A low mass for Mars from Jupiter's early gas-driven migration. *Nature* **475**, 206–209 (2011).

Acknowledgements We thank A. Morbidelli for a critical reading of a first version of this manuscript. P.B.-L.I. thanks CONICET for financial support. This research was supported by UNAM grants PAPIIT IA101113 and IN105313 and by CONACyT grants 178377 and 129343. J.Sz. acknowledges support from the Capital Fund Management's J. P. Aguilar Grant. We also thank U. Amaya Olvera, R. García Carreón and J. Verleyen for their assistance in setting up the GPU cluster on which the calculations presented here have been run.

Author Contributions P.B.-L.I. performed the numerical simulations and their subsequent reduction. F.M. designed the project and wrote the Methods. G.K. wrote the main paper. J.Sz. provided assistance with the radiative transfer module. All authors contributed to the discussion presented in this manuscript.

Author Information Reprints and permissions information is available at www.nature.com/reprints. The authors declare no competing financial interests. Readers are welcome to comment on the online version of the paper. Correspondence and requests for materials should be addressed to F.M. (fmasset@cea.fr).

METHODS

Code and numerical method. We use the publicly available hydrocode FARGO3D (<http://fargo.in2p3.fr>) to solve the hydrodynamics and radiative transfer equations on a spherical mesh, spanning in azimuth the whole range $[-\pi, \pi]$, in radius the range $[a/2, (3/2)a]$ (where a is the planet's semi-major axis), and in colatitude the range $[\pi/2 - 3h, \pi/2]$ (where $h = H/r$ is the aspect ratio of the disk). The governing equations of the hydrodynamics module are the continuity equation, the Navier–Stokes equations including all components of the viscous stress tensor, and the energy equation. The equation of state of ideal gases is used. At each hydrodynamical time step, in addition, we solve the radiative energy on the mesh, using flux-limited diffusion and a two-temperature approach in the grey approximation, and we solve the coupling between thermal and radiative energies¹⁵. These techniques are standard in the context of protoplanetary disks, in which they allow a simultaneous description of hydrodynamical and radiative effects at reasonable computational cost²⁰.

Fiducial calculation. The parameters of our fiducial run are a constant opacity of $\kappa = 1 \text{ cm}^2 \text{ g}^{-1}$, a kinematic viscosity of $\nu = 10^{15} \text{ cm}^2 \text{ s}^{-1}$, a planetary mass of $M_p = 3M_\oplus$, a planetary orbital radius of $a = 5.2 \text{ AU}$, the ratio of the specific heat at constant pressure to the specific heat at constant volume $\gamma = 1.4$, the mean molecular weight of the gas $\mu = 2.3 \text{ g mol}^{-1}$ and a surface density law given by:

$$\Sigma(r) = 200 \left(\frac{r}{a}\right)^{-\sigma} \text{ g cm}^{-2} \quad (1)$$

with $\sigma = 1/2$. This results in a value at 5.2 AU that is roughly 30% above the value quoted for the ‘minimum mass solar nebula’ (the protoplanetary disk of minimum mass needed to form the Solar System) (ref. 21). The planetary potential is given by:

$$\phi_p = -\frac{GM_p}{(r^2 + \epsilon^2)^{1/2}} \quad (2)$$

where G is the gravitational constant, r is the distance to the planet, and $\epsilon = 2.5 \times 10^{-3} a$ is a softening length used to avoid a divergence of the force in the planet's vicinity.

Comparison with a second hydrocode. The numerical scheme of the FARGO3D code is in many aspects similar to that of the ZEUS code²². There are, however, two notable differences: FARGO3D conserves (angular) momentum to machine accuracy, and it features orbital advection (which gives its name to the code through the acronym Fast Advection in Rotating Gaseous Objects²³). We have checked our results on the fiducial run using a version of the nested mesh code JUPITER²⁴ that features a MUSCL–Hancock predictor step together with an exact adiabatic Riemann solver. As in FARGO3D, at each hydrodynamical time step, a radiative diffusion module based on flux-limited diffusion in a two-temperature approach is used to update the radiative and thermal energies. Solving for the radiative energy across the different mesh levels is done as in ref. 25. The heating torque that we find with this alternative code is within 25% of the heating torque found with FARGO3D on the same setup.

Numerical setup. Our mesh has resolution $1,024 \times 512 \times 64$ in, respectively, azimuth, radius, and colatitude, with cell interfaces evenly spaced along each dimension. Since the energy is released in the immediate vicinity of the planet, the effect on the torque appears on a short timescale (typically the dynamical timescale), so that meaningful results can be obtained with short-term simulations. We therefore run all our simulations over only ten orbits. We have checked nevertheless with one setup (not presented here) that the heating torque is constant over a duration of 100 orbits, longer than the horseshoe libration timescale of our planets, from which we can discard the possibility that the heating torque could be a transient effect that would appear upon the insertion of the planet in the disk. For each given setup, we run in succession: (1) a meridian (r, θ) two-dimensional simulation to allow the disk to relax towards hydrostatic and radiative equilibrium. (2) a first three-dimensional calculation in which a planet is inserted without releasing energy in the ambient disk, which takes as initial condition the outcome of the previous run. (3) a second three-dimensional calculation, which also takes as initial condition the outcome of the first run, in which we insert a planet of the same mass as introduced in the previous run but which this time is allowed to release energy.

Our mesh is designed so that the planet is at the intersection between cell interfaces in azimuth, radius and colatitude. The planet therefore lies at the centre of an eight-cell cube. The energy it releases is added evenly to these eight cells at each time step. When integrating the torque exerted by the disk on the planet, we cut off

the contribution of the cells that lie within half a Hill radius of the planet²⁶. We find this cutoff to have only a mild effect on the torque value.

The amount of energy released by the planet per unit time is:

$$\dot{E} = \frac{GM\dot{M}}{R_p} = \frac{GM^2}{\tau R_p} \quad (3)$$

where $\tau = M/\dot{M}$ is the planetary mass-doubling time, and R_p is the physical radius of the planet, calculated assuming a density $\rho = 3 \text{ g cm}^{-3}$. The mass-doubling time in our fiducial run is $\tau = 10^5 \text{ yr}$. This equation applies to embryos that are not surrounded by a dense envelope, and it neglects the latent heat for vaporization of the material (which is at most of order $10^{11} \text{ erg g}^{-1}$, whereas $GM_p/R_p \approx 10^{12} \text{ erg g}^{-1}$ for the fiducial run). We make no assumptions regarding the size of the solids that are impinging onto the core. Although we might expect a vigorous heating torque when an embryo is subjected to the potentially extremely effective ‘pebble accretion’ mechanism, further progress is needed to assess the altitude at which pebbles deposit their energy and the ultimate core luminosity. However, regardless of the core luminosity that might arise from pebble accretion, a minimal value for the luminosity is set by the accretion of planetesimals, which leads to mass-doubling times typical of those considered in our analysis.

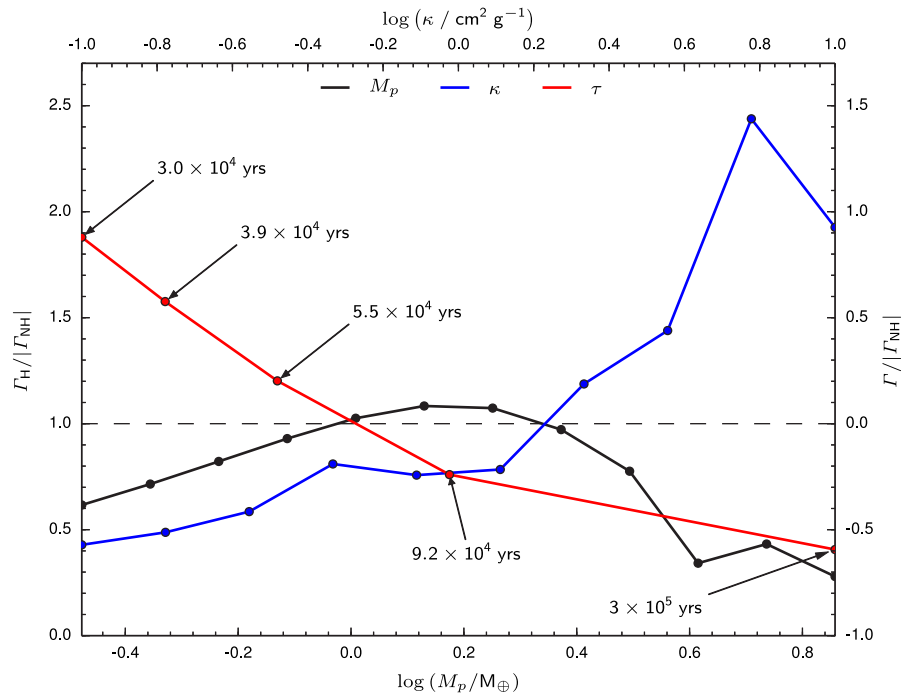
Exploration of parameter space. We have performed systematic explorations of the magnitude of the heating torque by varying one parameter at a time of our fiducial setup. Namely, we have varied the viscosity between $4 \times 10^{14} \text{ cm}^2 \text{ s}^{-1}$ and $4 \times 10^{15} \text{ cm}^2 \text{ s}^{-1}$, the surface density between 100 g cm^{-2} and $1,000 \text{ g cm}^{-2}$, the mass doubling time between $3 \times 10^4 \text{ yr}$ and $3 \times 10^5 \text{ yr}$, the opacity between $0.1 \text{ cm}^2 \text{ g}^{-1}$ and $10 \text{ cm}^2 \text{ g}^{-1}$, the planetary mass from $1/3M_\oplus$ to $7M_\oplus$, and the exponent σ of the power law of the surface density from -2 to 1.5 . These explorations show that the heating torque, normalized to the torque of the non-accreting case, depends only weakly on the surface density and viscosity. The dependency on σ as mentioned in the main text: the heating torque is found to scale with the distance between the planet and corotation. For the other parameters, we find the dependencies given in Extended Data Fig. 1. The torque values reported in this figure are time-averages of the torque measured over orbits 5 to 10 of each calculation.

The heating torque depends strongly on the opacity and on the mass-doubling time. At larger opacity, the energy radiated by the planet is trapped nearby it, so the under-dense lobes are more pronounced and the net effect is stronger than for smaller opacity. When the mass-doubling time decreases, the heating torque increases since \dot{E} increases. We also find that the heating torque has a large efficiency over the mass interval $0.5M_\oplus$ to $3M_\oplus$. Its decline past this mass is compatible with the fact that the distance of the planet to corotation becomes an ever smaller fraction of the Hill sphere, so that the flow in the vicinity of the planet (and therefore the under-dense lobes) become more symmetric.

A final comment is warranted regarding the torque resulting from the angular momentum that is transferred to the planet by the material being accreted. We find it to be several orders of magnitude smaller than the heating torque, so it can safely be neglected.

Code availability. The FARGO3D code is publicly available at the address <http://fargo.in2p3.fr>. This public version does not yet include the radiative transfer module, which will be made available once it has been fully documented. The JUPITER code is not publicly available at present.

20. Ramsey, J. P. & Dullemond, C. P. Radiation hydrodynamics including irradiation and adaptive mesh refinement with AZEUS. I. Methods. Preprint at <http://arxiv.org/abs/1409.3011> (2014).
21. Hayashi, C., Nakazawa, K. & Nakagawa, Y. in *Protostars and Planets II* (eds Black, D. C. & Matthews, M. S.) 1100–1153, 1985.
22. Stone, J. M. & Norman, M. L. ZEUS-2D: A radiation magnetohydrodynamics code for astrophysical flows in two space dimensions. I.—The hydrodynamic algorithms and tests. *Astrophys. J. Suppl. Ser.* **80**, 753–790 (1992).
23. Masset, F. FARGO: A fast eulerian transport algorithm for differentially rotating disks. *Astron. Astrophys. Suppl.* **141**, 165–173 (2000).
24. Szulágyi, J., Morbidelli, A., Crida, A. & Masset, F. Accretion of Jupiter-mass planets in the limit of vanishing viscosity. *Astrophys. J.* **782**, 65 (2014).
25. Commerçon, B., Debout, V. & Teyssier, R. A fast, robust, and simple implicit method for adaptive time-stepping on adaptive mesh-refinement grids. *Astron. Astrophys.* **563**, A11 (2014).
26. Crida, A., Baruteau, C., Kley, W. & Masset, F. The dynamical role of the circumplanetary disc in planetary migration. *Astron. Astrophys.* **502**, 679–693 (2009).



Extended Data Figure 1 | Exploration of the parameter space. Heating torque Γ_H normalized to the absolute value of the torque of the non-accreting case $|\Gamma_{\text{NH}}|$, as a function of embryo mass M_p , opacity κ and mass doubling time τ . Whenever one parameter is varying, others have the value of the fiducial

run. Mass-doubling times are given in units of years and show that a positive torque results for $\tau \lesssim 60,000$ years. The right axis shows the total torque $\Gamma = \Gamma_H + \Gamma_{\text{NH}}$, also normalized to $|\Gamma_{\text{NH}}|$. The horizontal dashed line corresponds to no migration. Source data for this figure are available online.

Atomic Hong–Ou–Mandel experiment

R. Lopes¹, A. Imanaliev¹, A. Aspect¹, M. Cheneau¹, D. Boiron¹ & C. I. Westbrook¹

Two-particle interference is a fundamental feature of quantum mechanics, and is even less intuitive than wave–particle duality for a single particle. In this duality, classical concepts—wave or particle—are still referred to, and interference happens in ordinary space-time. On the other hand, two-particle interference takes place in a mathematical space that has no classical counterpart. Entanglement lies at the heart of this interference, as it does in the fundamental tests of quantum mechanics involving the violation of Bell's inequalities^{1–4}. The Hong, Ou and Mandel experiment⁵ is a conceptually simpler situation, in which the interference between two-photon amplitudes also leads to behaviour impossible to describe using a simple classical model. Here we report the realization of the Hong, Ou and Mandel experiment using atoms instead of photons. We create a source that emits pairs of atoms, and cause one atom of each pair to enter one of the two input channels of a beam-splitter, and the other atom to enter the other input channel. When the atoms are spatially overlapped so that the two inputs are indistinguishable, the atoms always emerge together in one of the output channels. This result opens the way to testing Bell's inequalities involving mechanical observables of massive particles, such as momentum, using methods inspired by quantum optics^{6,7}, and to testing theories of the quantum-to-classical transition^{8–11}. Our work also demonstrates a new way to benchmark non-classical atom sources^{12,13} that may be of interest for quantum information processing¹⁴ and quantum simulation¹⁵.

A pair of entangled particles is described by a state vector that cannot be factored as a product of two state vectors associated with each particle. Although entanglement does not require that the two particles be identical², it arises naturally in systems of indistinguishable particles owing to the symmetrization of the state, which leads to non-trivial, multiparticle interference. A remarkable illustration is the Hong, Ou and Mandel (HOM) experiment, in which two photons enter the two input channels of a 50:50 beam-splitter (one photon in each channel) and the correlation is measured between detectors at the two outputs.

A joint detection at these detectors arises from two possible processes: either both photons are transmitted by the beam-splitter or both are reflected (Fig. 1c). For two indistinguishable photons, both processes lead to the same final quantum state and the probability of joint detection results from the addition of their amplitudes. Because the beam-splitter corresponds to a unitary operation, these amplitudes have same modulus but opposite signs, thus their sum vanishes and so also the probability of joint detection^{16,17} (see also Methods). To be truly indistinguishable, not only must the photons have the same energy distribution and polarization, but their final spatio-temporal modes must be identical. Thus, the two photons must enter the beam-splitter in modes that are the exact images of each other. As a result, when measured as a function of the delay between the arrival times of the photons on the beam-splitter, the correlation exhibits the 'HOM dip', ideally going to zero at zero delay.

Our experiment is equivalent in all important respects to the HOM experiment, but is performed with bosonic atoms instead of photons. We produce freely propagating twin beams of metastable ⁴He atoms¹⁸, which we then reflect and overlap on a beam-splitter using Bragg scattering on an optical lattice (ref. 19 and Fig. 1). The photon counters

after the beam-splitter are replaced by a time-resolved, multi-pixel atom-counting detector²⁰, which enables the measurement of intensity correlations between the atom beams in well defined spatial and spectral regions. The temporal overlap between the atoms can be continuously tuned by changing the moment when the atomic beam-splitter is applied. We observe the HOM dip when the atoms simultaneously pass through the beam-splitter. The key technical advance that has enabled

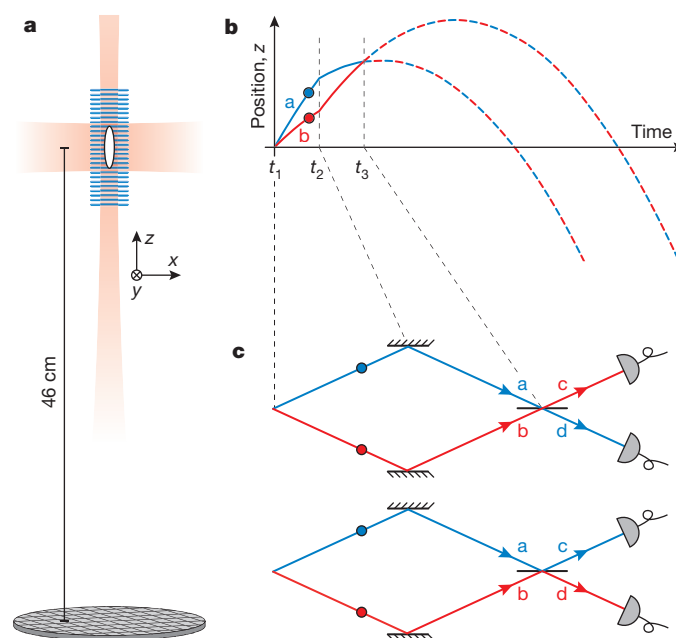


Figure 1 | Schematic of the experiment. **a**, A Bose–Einstein condensate (BEC, white oval) of metastable ⁴He atoms is trapped in an elongated optical trap (red shaded area). A moving optical lattice, here depicted in blue, is superimposed on the BEC and triggers the scattering of atom pairs along the *z* axis. When this lattice and the trap are switched off, the atoms fall towards a microchannel plate detector located 46 cm below the initial position of the BEC (drawing not to scale). **b**, The time diagram shows the evolution of the twin atoms' vertical coordinates (blue line for beam *a* and red line for beam *b*). Between *t*₁ and *t*₂, *t*₂ and *t*₃, and after *t*₃, the atoms move under the sole influence of gravity (drawing not to scale). At *t*₂, the twin atom velocities are swapped using Bragg diffraction on an optical lattice. At time *t*₃, when the atomic trajectories cross again, the same lattice is applied for half the amount of time in order to realize a beam-splitter. The lines alternately dashed in red and blue symbolize the indiscernibility of the atoms' trajectories after the beam-splitter. The filled red and blue circles indicate the position of the atoms at a given time before the beam-splitter is applied. **c**, In the centre-of-mass frame of reference, the trajectories of the atoms resemble those of the photons in the Hong–Ou–Mandel experiment. A joint detection arises either when both atoms are transmitted through the beam-splitter (upper panel) or when both are reflected (lower panel). If the two particles are indistinguishable, these processes end in the same final quantum state and the probability of joint detection results from the addition of their amplitudes. For bosons these amplitudes have same modulus but opposite signs, thus their sum vanishes and so also does the probability of joint detection.

¹Laboratoire Charles Fabry, Institut d'Optique Graduate School – CNRS – Université Paris Sud, 2 avenue Augustin Fresnel, 91127 Palaiseau, France.

this work was the improvement of the atom pair production so as to permit optimal adjustment of the mode populations¹⁸.

We begin by producing a Bose–Einstein condensate (BEC) of metastable ^4He atoms in the $1s2s\ ^3S_1$ internal state (here we represent this by $2\ ^3S_1$), with the projection of the total electronic angular momentum $m = 1$. The BEC contains $(5\text{--}6) \times 10^4$ atoms and is confined in an elliptical optical trap with its long axis along the vertical (z) direction (Fig. 1a). The atomic cloud has radii of 58 and $5\ \mu\text{m}$ along the longitudinal (z) and transverse (\perp) directions, respectively. A moving optical lattice, superimposed on the BEC for $300\ \mu\text{s}$, induces the scattering of atom pairs (hereafter referred to as twin atoms) in the longitudinal direction through a process analogous to spontaneous four-wave mixing^{18,21,22} (see also Methods). This mixing process resembles that used in refs 23–25 to generate entangled states in the spin sector, but it involves the motional degrees of freedom. One beam, labelled a, has a free-space velocity $v_z \approx 12.1\ \text{cm s}^{-1}$ in the laboratory frame of reference and the other beam, labelled b, has a velocity $v_z \approx 7.0\ \text{cm s}^{-1}$ (Fig. 1b, c). The twin atom beams clearly appear in the velocity distribution of the atoms, which is displayed in Fig. 2. The visible difference in population between the beams is attributed to secondary scattering processes in the optical lattice, leading to the decay over time of the quasi-momentum states¹⁸. After the optical lattice has been switched off (at time t_1), the twin atoms propagate in the optical trap for $200\ \mu\text{s}$. At this moment, the trap itself is switched off and the atoms are transferred to the magnetically insensitive $m = 0$ internal state by a two-photon Raman transition (Methods).

From here on, the atoms evolve under the influence of gravity and continue to move apart (Fig. 1b). At time $t_2 = t_1 + 500\ \mu\text{s}$, we deflect the beams using Bragg diffraction on a second optical lattice, so as to make them converge. In the centre-of-mass frame of reference, this deflection reduces to a simple specular reflection (Fig. 1c and Methods). At time $t_3 \approx 2t_2 - t_1$, we apply the same diffraction lattice for half the amount of time in order to realize a beam-splitting operation on the

crossing atom beams. Changing the time t_3 allows us to tune the degree of temporal overlap between the twin atoms. Figure 1c shows the atomic trajectories in the centre-of-mass frame of reference and reveals the close analogy with a photonic HOM experiment.

The atoms end their fall on a microchannel plate detector located 46 cm below the position of the initial BEC, and we record the time and transverse position of each atomic impact with a detection efficiency $\eta \approx 25\%$ (Methods). The time of flight to the detector is approximately 300 ms, long enough for the recorded signal to yield the three components of the atomic velocity. By collecting data from several hundred repetitions of the experiment under the same conditions, we are able to reconstruct all desired atom number correlations within variable integration volumes of extent $\Delta v_z \times \Delta v_\perp^2$. These volumes play a similar role to that of the spatial and spectral filters in the HOM experiment and can be adjusted to erase the information that could allow tracing back the origin of a detected particle to one of the input channels.

The HOM dip should appear in the cross-correlation between the detection signals in the output channels of the beam-splitter¹⁶ (see also Methods), $G_{cd}^{(2)}$:

$$G_{cd}^{(2)} = \left(\frac{\eta}{\Delta v_z \Delta v_\perp^2} \right)^2 \iint \mathcal{V}_c \times \mathcal{V}_d \langle \hat{a}_{v_c}^\dagger \hat{a}_{v_d}^\dagger \hat{a}_{v_d} \hat{a}_{v_c} \rangle d^3 v_c d^3 v_d \quad (1)$$

Here, \hat{a}_v and \hat{a}_v^\dagger denote the annihilation and creation operators of an atom with three-dimensional velocity \mathbf{v} , respectively, $\langle \cdot \rangle$ stands for the quantum and statistical average and $\mathcal{V}_{c,d}$ designates the integration volumes centred on the output atom beams c and d (Fig. 1c). We have measured this correlation as a function of the duration of propagation $\tau = t_3 - t_2$ between the mirror and the beam-splitter (Fig. 3) and for various integration volumes (see Methods and Extended Data Fig. 1). We observe a marked reduction of the correlation when τ is equal to the duration of propagation from the source to the mirror ($t_3 - t_2 \approx t_2 - t_1$) and for small enough integration volumes, corresponding to a

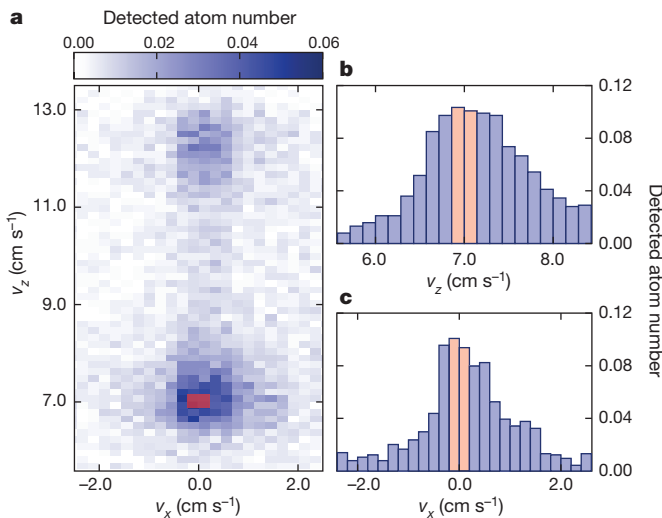


Figure 2 | Velocity distribution of the twin atoms. **a**, Two-dimensional velocity distribution of the twin atom beams emitted by the source. The red shaded area, drawn here only for the lower beam, labelled b in Fig. 1b and c, shows the integration volume \mathcal{V}_b used for computing the correlation function displayed in Fig. 3. The distribution corresponds to an average over about 1,100 measurements and is not corrected for the limited detection efficiency. The velocities are given relative to the laboratory frame of reference. The size of each pixel is $0.24\ \text{cm s}^{-1}$ in the transverse directions (x and y) and $0.14\ \text{cm s}^{-1}$ in the longitudinal (z) direction and an integration over 2 pixels is performed along the y direction. **b**, **c**, Cuts of the two-dimensional velocity distribution through the centre of the lower beam along the longitudinal (**b**) and transverse (**c**) directions. The data points result from the average over 2 pixels along the direction perpendicular to the cut. The red shaded area again shows the integration volume.

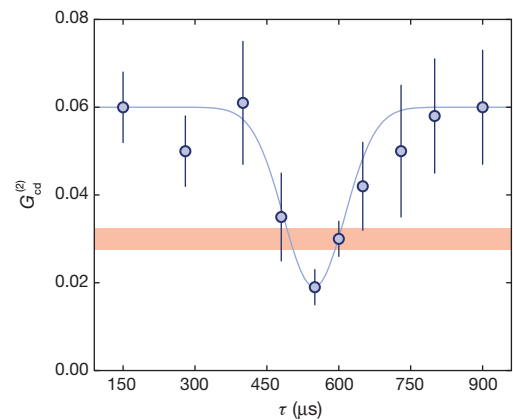


Figure 3 | HOM dip in the cross-correlation function. The correlation $G_{cd}^{(2)}$ between the output channels of the beam-splitter, defined in equation (1), was measured as a function of the duration of propagation $\tau = t_3 - t_2$ between the mirror and the beam splitter. The HOM dip is directly visible as a marked reduction of the correlation when τ approximately equals the duration of propagation between the source and the mirror, $t_2 - t_1 \approx 500\ \mu\text{s}$. This situation corresponds to symmetric paths between the source and the beam-splitter, that is, when one cannot distinguish between the two diagrams of Fig. 1c. A Gaussian fit (blue line) precisely locates the dip at $\tau = 550(50)\ \mu\text{s}$, with a full-width at half-maximum of $150(40)\ \mu\text{s}$, where the uncertainty corresponds to the 68% confidence interval. The fitted value of the background correlation is $0.060(5)$ and the measured visibility is $V = 0.65(7)$. It is two standard deviations beyond the classical-to-quantum threshold represented by the red shaded area, at half the background correlation value. Each data point was obtained from an average over about 500 to 1,400 repetitions of the experiment. Error bars denote the standard deviation of the statistical ensemble. The mean detected atom number was constant over the range of values of τ displayed here (see Methods and Extended Data Fig. 2).

full overlap of the atomic wave-packets on the beam-splitter. Fitting the data with an empirical Gaussian profile yields a visibility:

$$V = \frac{\max_{\tau} G_{cd}^{(2)}(\tau) - \min_{\tau} G_{cd}^{(2)}(\tau)}{\max_{\tau} G_{cd}^{(2)}(\tau)} = 0.65(7) \quad (2)$$

where the number in parenthesis stands for the 68% confidence interval. As we shrink the integration volumes, we observe that the dip visibility first increases and then reaches a saturation value, as is expected when the integration volumes become smaller than the elementary atomic modes. The data displayed in Fig. 3 were obtained for $\Delta v_z = 0.28 \text{ cm s}^{-1}$ and $\Delta v_{\perp} = 0.48 \text{ cm s}^{-1}$, which maximizes the reduction of the correlation while preserving a statistically significant number of detection events (see Methods and Extended Data Fig. 1).

The dip in the cross-correlation function cannot be explained in terms of classical particles, for which we would have no correlation at all between the detections in the output channels (Methods). But when the atoms are viewed as waves, demonstrating the quantum origin of the dip necessitates a deeper analysis. The reason is that two waves can interfere at a beam-splitter and give rise to an intensity imbalance between the output channels. If, in addition, the coherence time of the waves is finite, the cross-correlation can display a dip similar to the one observed in our experiment. But once averaged over the phase difference between the beams, the classical visibility is bounded from above and cannot exceed 0.5 (ref. 26 and Methods). In our experiment, this phase difference is randomized by the shot-to-shot fluctuations of the relative phase between the laser beams used for Bragg diffraction (Methods). Since our measured visibility exceeds the limit for waves by two standard deviations, we can safely rule out any interpretation of our observation in terms of interference between two ‘classical’ matter waves or, in other words, between two ordinary wave functions describing each of the two particles separately.

Two contributions may be responsible for the non-zero value of the correlation function at the centre of the dip: the detected particles may not be fully indistinguishable and the number of particles contained in the integration volume may exceed unity for each beam (see Methods). The effect of the atom number distribution can be quantified by measuring the intensity correlations of the twin atom beams upstream of the beam-splitter (Fig. 1c), which bound the visibility of the dip through the relation:

$$V_{\max} = 1 - \frac{G_{aa}^{(2)} + G_{bb}^{(2)}}{G_{aa}^{(2)} + G_{bb}^{(2)} + 2G_{ab}^{(2)}} \quad (3)$$

where $G_{aa}^{(2)}$, $G_{bb}^{(2)}$ and $G_{ab}^{(2)}$ are defined by analogy to equation (1) (ref. 26 and Methods) and the integration volumes $\mathcal{V}_{a,b}$ have the same extent as $\mathcal{V}_{c,d}$. Here, one immediately sees that the finite probability of having more than one atom per input channel, which translates to finite values of the auto-correlations $G_{aa}^{(2)}$, $G_{bb}^{(2)}$, leads to a reduced visibility. We have performed the measurement of these correlations following the same experimental procedure as before, except that we did not apply the mirror and beam-splitter. We find non-zero values $G_{aa}^{(2)} = 0.016(5)$, $G_{bb}^{(2)} = 0.047(9)$, and $G_{ab}^{(2)} = 0.048(7)$, yielding $V_{\max} = 0.60(10)$, where the uncertainty is the standard deviation of the statistical ensemble. Because of the good agreement with the measured value of the visibility, we conclude that the atom number distribution in the input channels entirely accounts for the visibility of the HOM dip. For the present experiment, we estimate the average number of incident atoms to be 0.5(1) in \mathcal{V}_a and 0.8(2) in \mathcal{V}_b , corresponding to a ratio of the probability for having two atoms to that for having one atom of 0.25(5) and 0.40(10), respectively (Methods). Achieving much smaller values is possible, for instance by reducing the pair production rate, but at the cost of lower counting statistics.

Although multiparticle interference can be observed with independently prepared photons^{27,28}, atoms¹³ and electrons^{29,30}, twin particle sources are at the heart of many protocols for quantum information

processing¹⁴ and quantum simulation¹⁵. The good visibility of the HOM dip in our experiment demonstrates that our twin atom source produces beams that have highly correlated populations and are well mode matched. This is an important achievement in itself, which may have the same impact on quantum atom optics as the development of twin photon sources using nonlinear crystals had for quantum optics.

Online Content Methods, along with any additional Extended Data display items and Source Data, are available in the online version of the paper; references unique to these sections appear only in the online paper.

Received 9 November 2014; accepted 6 February 2015.

- Bell, J. S. On the Einstein-Podolsky-Rosen paradox. *Physics* **1**, 195–200 (1964).
- Aspect, A. Bell’s inequality test: more ideal than ever. *Nature* **398**, 189–190 (1999).
- Giustina, M. *et al.* Bell violation using entangled photons without the fair-sampling assumption. *Nature* **497**, 227–230 (2013).
- Christensen, B. G. *et al.* Detection-loophole-free test of quantum nonlocality, and applications. *Phys. Rev. Lett.* **111**, 130406 (2013).
- Hong, C. K., Ou, Z. Y. & Mandel, L. Measurement of subpicosecond time intervals between two photons by interference. *Phys. Rev. Lett.* **59**, 2044–2046 (1987).
- Rarity, J. G. & Tapster, P. R. Experimental violation of Bell’s inequality based on phase and momentum. *Phys. Rev. Lett.* **64**, 2495–2498 (1990).
- Lewis-Swan, R. J. & Kheruntsyan, K. V. Motional-state Bell inequality test with ultracold atoms. Preprint at <http://arxiv.org/abs/1411.0191> (2014).
- Penrose, R. Quantum computation, entanglement and state reduction. *Phil. Trans. R. Soc. Lond. A* **356**, 1927–1939 (1998).
- Zurek, W. H. Decoherence, einselection, and the quantum origins of the classical. *Rev. Mod. Phys.* **75**, 715–775 (2003).
- Schlosshauer, M. Decoherence, the measurement problem, and interpretations of quantum mechanics. *Rev. Mod. Phys.* **76**, 1267–1305 (2005).
- Leggett, A. J. How far do EPR-Bell experiments constrain physical collapse theories? *J. Phys. A* **40**, 3141–3149 (2007).
- Bücker, R. *et al.* Twin-atom beams. *Nature Phys.* **7**, 608–611 (2011).
- Kaufman, A. M. *et al.* Two-particle quantum interference in tunnel-coupled optical tweezers. *Science* **345**, 306–309 (2014).
- Nielsen, M. A. & Chuang, I. L. *Quantum Computation and Quantum Information* (Cambridge Univ. Press, 2000).
- Kitagawa, T., Aspect, A., Greiner, M. & Demler, E. Phase-sensitive measurements of order parameters for ultracold atoms through two-particle interferometry. *Phys. Rev. Lett.* **106**, 115302 (2011).
- Ou, Z. Y. *Multi-Photon Quantum Interference* (Springer, 2007).
- Grynberg, G., Aspect, A. & Fabre, C. *Introduction to Quantum Optics: From the Semiclassical Approach to Quantized Light* (Cambridge Univ. Press, 2010).
- Bonneau, M. *et al.* Tunable source of correlated atom beams. *Phys. Rev. A* **87**, 061603 (2013).
- Cronin, A. D., Schmiedmayer, J. & Pritchard, D. E. Optics and interferometry with atoms and molecules. *Rev. Mod. Phys.* **81**, 1051–1129 (2009).
- Schellekens, M. *et al.* Hanbury Brown Twiss effect for ultracold quantum gases. *Science* **310**, 648–651 (2005).
- Hilligsøe, K. M. & Mølmer, K. Phase-matched four-wave mixing and quantum beam splitting of matter waves in a periodic potential. *Phys. Rev. A* **71**, 041602 (2005).
- Campbell, G. K. *et al.* Parametric amplification of scattered atom pairs. *Phys. Rev. Lett.* **96**, 020406 (2006).
- Gross, C. *et al.* Atomic homodyne detection of continuous-variable entangled twin-atom states. *Nature* **480**, 219–223 (2011).
- Lücke, B. *et al.* Twin matter waves for interferometry beyond the classical limit. *Science* **334**, 773–776 (2011).
- Bookjans, E., Hamley, C. & Chapman, M. Strong quantum spin correlations observed in atomic spin mixing. *Phys. Rev. Lett.* **107**, 210406 (2011).
- Lewis-Swan, R. J. & Kheruntsyan, K. V. Proposal for demonstrating the Hong–Ou–Mandel effect with matter waves. *Nature Commun.* **5**, 3752 (2014).
- Beugnon, J. *et al.* Quantum interference between two single photons emitted by independently trapped atoms. *Nature* **440**, 779–782 (2006).
- Lang, C. *et al.* Correlations, indistinguishability and entanglement in Hong–Ou–Mandel experiments at microwave frequencies. *Nature Phys.* **9**, 345–348 (2013).
- Bocquillon, E. *et al.* Coherence and indistinguishability of single electrons emitted by independent sources. *Science* **339**, 1054–1057 (2013).
- Dubois, J. *et al.* Minimal-excitation states for electron quantum optics using levitons. *Nature* **502**, 659–663 (2013).

Acknowledgements We thank J. Ruau and M. Bonneau for contributions to the early steps of the experiment. We also thank K. Kheruntsyan, J. Chwedenczuk and P. Deuar for discussions. We acknowledge funding by IFRAP, Triangle de la Physique, Labex PALM, ANR (PROQU, QEAGE), FCT (scholarship SFRH/BD/74352/2010 co-financed by ESF, POPH/QREN and EU to R.L.) and EU (ERC grant 267775, QUANTATOP, and Marie Curie CIG 618760, CORENT).

Author Contributions All authors contributed extensively to this work.

Author Information Reprints and permissions information is available at www.nature.com/reprints. The authors declare no competing financial interests. Readers are welcome to comment on the online version of the paper. Correspondence and requests for materials should be addressed to R.L. (raphael.lopez@institutoptique.fr) or M.C. (marc.cheneau@institutoptique.fr).

METHODS

Twin atom source. The twin atom beams result from a scattering process between pairs of atoms from the BEC occurring when the gas is placed in a moving one-dimensional optical lattice. The use of a BEC is dictated primarily by the need to maximize the atomic density to assure a sufficiently high scattering rate. The experimental set-up has been described in ref. 18. The lattice is formed by two laser beams derived from the same source emitting at the wavelength $\lambda = 1,064$ nm. In contrast to our previous work, the axis of the optical lattice was now precisely aligned with the long axis of the optical trap confining the atoms. The laser beams intersect with an angle of $\theta = 166^\circ$, their frequency difference is set to 100.5 kHz and the lattice depth to $0.8 E_{\text{rec}}$ (see below). This constrains the longitudinal wave vector of the twin atoms to the values $k_{z,a} = 0.75 k_{\text{rec}}$ and $k_{z,b} = 1.30 k_{\text{rec}}$ in order to fulfil the conservation of quasi-momentum and energy in the frame co-propagating with the lattice. Here, $k_{\text{rec}} = 2\pi \sin(\theta/2)/\lambda$ is the recoil wave vector along the longitudinal axis gained upon absorption of a photon from a lattice laser and $E_{\text{rec}} = \hbar^2 k_{\text{rec}}^2 / 2m$ is the associated kinetic energy, with \hbar the reduced Planck constant and $m = 6.64 \times 10^{-27}$ kg the mass of a ^4He atom. The observed velocities of the twin atom beams coincide with the expected values above, using the relation $v = \hbar k / m$. The optical lattice is turned on and off adiabatically so as to avoid diffraction of the atoms during this phase of the experiment. The relative velocities of the pair is such that during the interferometer sequence, the maximum separation of the beams is only 25 μm , smaller than the size of the clouds. This separation, however, plays no role in the experiment; we need only ensure that the atoms in a pair are distinguishable by some observable, in our case the momentum. Thus a second reason to use a BEC in the experiment is to benefit from its narrow momentum distribution, which results in well separated pairs in momentum space.

Transfer to the magnetically insensitive internal state. Transfer to the $m = 0$ state after the optical trap has been switched off is made necessary by the presence of stray magnetic fields in the vacuum chamber that otherwise would lead to a severe deformation of the atomic distribution during the long free fall. The transfer is achieved by introducing a two-photon coupling between the $m = 1$ state, in which the atoms are initially, and the $m = 0$ state using two laser beams derived from a single source emitting at 1,083 nm and detuned by 600 MHz from the 2^3S_1 to 2^3P_0 transition. The frequency difference of the laser beams is chirped across the two-photon resonance so as to realize an adiabatic fast passage transition (the frequency change is 300 kHz in 300 μs). We have measured the fraction of transferred atoms to be 94%. The remaining 6% stay in the $m = 1$ state and are pushed away from the integration volumes by stray magnetic field gradients.

Atomic mirror and beam-splitter. The mirror and beam-splitter are both implemented using Bragg scattering on a second optical lattice. This effect can be seen as a momentum exchange between the atoms and the laser beams forming the lattice, a photon being coherently absorbed from one beam and emitted into the other. In our experiment, the laser beams forming the lattice have a waist of 1 mm and are detuned by 600 MHz from the 2^3S_1 to 2^3P_0 transition (they are derived from the same source as the beams used for the Raman transfer). In order to fulfil the Bragg resonance condition for the atom beams, the laser beams are made to intersect at an angle of 32° and the frequency of one of the beams is shifted by 57 kHz. In addition to this fixed frequency difference, a frequency chirp is performed to compensate for the acceleration of the atoms during their free fall. The interaction time between the atoms and the optical lattice was 100 μs for the mirror operation (π -pulse) and 50 μs for the beam-splitter operation ($\pi/2$ -pulse). The resonance condition for the momentum state transfer is satisfied by all atoms in the twin beams but only pairs of states with a well defined momentum difference are coupled with each other. We measured the reflectivity of the mirror and the transmittance of the beam-splitter to be 0.95(2) and 0.49(2), respectively. Spontaneous scattering of photons by the atoms was negligible.

Interactions between atoms can alter the effect of the beam-splitter³¹. In our experiment, however, the atomic density at the beam-splitter is so low that the frequency associated with the typical interparticle interaction energy is more than 3 orders of magnitude smaller than the inverse of the time it takes for Bragg scattering to take place. Thus particle interactions are negligible during the beam splitting process.

Detection efficiency. Our experiment relies on the ability to detect the atoms individually. The detection efficiency is an essential parameter for achieving good signal to noise ratios, although it does not directly influence the visibility of the HOM dip. Our most recent estimate of the detection efficiency relies on the measurement of the variance of the atom number difference between the twin beams. For this we use the same procedure as described in ref. 18, but with an integration volume that includes the entire velocity distribution of each beam. We find a normalized variance of 0.75(5), well below the Poissonian floor. Since for perfectly correlated twin beams the measured variance would be $1 - \eta$, we attribute the lower limit of 25(5)% to our detection efficiency. This value for η is a factor of about 2 larger than the lower bound quoted in ref. 32. The difference is due to the change of method employed for

transferring the atoms from the $m = 1$ to the $m = 0$ state after the optical trap has been switched off. We previously used a radio-frequency transfer with roughly 50% efficiency whereas the current optical Raman transfer has close to 100% efficiency.

Distribution of the number of incident atoms. We have estimated the average number of incident atoms in each input channel of the beam-splitter, n_a and n_b , by analysing the distribution of detected atoms in the integration volumes \mathcal{V}_a and \mathcal{V}_b . We fitted these distributions by assuming an empirical Poissonian law for the distribution of incident atoms and taking into account the independently calibrated detection efficiency. The values of n_a and n_b given in the main text are the mean values of the Poissonian distributions that best fit the data. The probabilities for having one or two atoms in each of the input channels of the beam-splitter was obtained from the same analysis. The uncertainty on these numbers mostly stems from the uncertainty on the detection efficiency.

The HOM effect. The HOM effect appears in the correlator $\langle \hat{a}_{v_c}^\dagger \hat{a}_{v_d}^\dagger \hat{a}_{v_a} \hat{a}_{v_b} \rangle$ of equation (1). The simplest way to calculate such a correlator is to transform the operators and the state vector back in the input space before the beam-splitter and to use the Heisenberg picture. The transformation matrix between the operators $\hat{a}_{v_c}(t_3)$, $\hat{a}_{v_d}(t_3)$ and $\hat{a}_{v_a}(t_3)$, $\hat{a}_{v_b}(t_3)$ can be worked out from first principles. For the Bragg beam-splitter, and using a Rabi two-state formalism, we find:

$$\begin{cases} \hat{a}_{v_c} = \frac{1}{\sqrt{2}} (i e^{i\phi} \hat{a}_{v_a} + \hat{a}_{v_b}) \\ \hat{a}_{v_d} = \frac{1}{\sqrt{2}} (\hat{a}_{v_a} + i e^{-i\phi} \hat{a}_{v_b}) \end{cases}$$

where ϕ is the relative phase between the laser beams forming the optical lattice. In the ideal case of an input state with exactly one atom in each channel, $|1_{v_a}, 1_{v_b}\rangle$, we therefore obtain:

$$\begin{aligned} \|\hat{a}_{v_d} \hat{a}_{v_c} |1_{v_a}, 1_{v_b}\rangle\|^2 &= \frac{1}{4} \left\| \left(i e^{i\phi} \hat{a}_{v_a}^2 + i e^{-i\phi} \hat{a}_{v_b}^2 + \hat{a}_{v_a} \hat{a}_{v_b} + i^2 \hat{a}_{v_b} \hat{a}_{v_a} \right) |1_{v_a}, 1_{v_b}\rangle \right\|^2 \\ &= \frac{1}{4} \|0 + (1 + i^2) |0_{v_a}, 0_{v_b}\rangle\|^2 \\ &= 0 \end{aligned}$$

meaning that the probability of joint detection is strictly zero. (Here we use $\|...\|$ to indicate vector norm.) The detailed calculation above makes clear that the perfect destructive interference between the two-particle state amplitudes associated with the two diagrams of Fig. 1c is at the heart of the HOM effect. By contrast, input states containing more than one atom per channel are transformed into a sum of orthogonal states and the interference can only be partial. Taking $|2_{v_a}, 2_{v_b}\rangle$, for instance, yields:

$$\begin{aligned} \|\hat{a}_{v_d} \hat{a}_{v_c} |2_{v_a}, 2_{v_b}\rangle\|^2 &= \frac{1}{4} \left\| \left(i e^{i\phi} \hat{a}_{v_a}^2 + i e^{-i\phi} \hat{a}_{v_b}^2 + \hat{a}_{v_a} \hat{a}_{v_b} + i^2 \hat{a}_{v_b} \hat{a}_{v_a} \right) |2_{v_a}, 2_{v_b}\rangle \right\|^2 \\ &= \frac{1}{2} \left\| i e^{i\phi} |0_{v_a}, 2_{v_b}\rangle + i e^{-i\phi} |2_{v_a}, 0_{v_b}\rangle + \sqrt{2} (1 + i^2) |1_{v_a}, 1_{v_b}\rangle \right\|^2 \\ &= \frac{1}{2} \|e^{i\phi} |0_{v_a}, 2_{v_b}\rangle + e^{-i\phi} |2_{v_a}, 0_{v_b}\rangle\|^2 \\ &= 1 \end{aligned}$$

Finally, we note that losses in one of the incident beams, for instance beam a, can be modelled by a fictitious beam-splitter with a transmission coefficient T . In the above calculation, these losses would therefore only manifest by an additional factor \sqrt{T} in front of every operator \hat{a}_{v_a} , leaving unaffected the destructive interference that gives rise to the HOM effect.

Stability of the atom number in the output ports. The mean detected atom number in the output ports c and d is plotted as a function of τ in Extended Data Fig. 2a and b. It remains constant within the statistical uncertainty, which confirms the interpretation of the dip as a destructive two-particle interference. To easily compare the atom number fluctuations with the variation of the cross-correlation across the HOM dip, the product of the averaged populations $\langle n_c \rangle \cdot \langle n_d \rangle$ and the cross-correlation $G_{cd}^{(2)}$ are displayed together as a function of τ in Extended Data Fig. 2c. In contrast to the cross-correlation, it is impossible to identify a marked reduction of $\langle n_c \rangle \cdot \langle n_d \rangle$ around $\tau = 550 \mu\text{s}$.

Influence of the integration volume on the dip visibility. The visibility of the HOM dip is plotted in Extended Data Fig. 1 as a function of the longitudinal (Extended Data Fig. 1a) and transverse (Extended Data Fig. 1b) integration volumes. The red dots identify the integration volume used in Fig. 3 of the main text and correspond to a compromise between signal-to-noise ratio and visibility amplitude. As we shrink the integration volumes, the dip visibility first increases and then reaches a saturation value, meaning that the integration volume becomes smaller than the elementary atomic modes^{33–35}. Reducing further the integration volume only leads to an increase of the statistical uncertainty.

The visibility V is obtained by fitting the cross-correlation function $G_{\text{cd}}^{(2)}(\tau)$ measured in the experiment with the empirical function:

$$f(\tau) = G_{\text{bg}}^{(2)} (1 - V \exp(-(\tau - \tau_0)^2 / 2\sigma^2))$$

where the background correlation $G_{\text{bg}}^{(2)}$, the centre of the dip τ_0 and the width of the dip σ are all left as free parameters.

Visibility of the HOM dip. A slightly less general form of equation (3) has been derived in ref. 26 assuming a two-mode squeezed state as an input state. The same calculation can be performed for an arbitrary input state. Leaving aside the integration over the velocity distribution, we find that the cross-correlation for indistinguishable particles can be expressed as:

$$G_{\text{cd}}^{(2)} \Big|_{\text{indisc.}} = \frac{1}{4} (G_{\text{aa}}^{(2)} + G_{\text{bb}}^{(2)} + \mathcal{A}) \quad , \quad \mathcal{A} = 2\eta^2 \text{Re} \left[e^{2i\phi} \left\langle \hat{a}_{\nu_a}^\dagger \hat{a}_{\nu_a}^\dagger \hat{a}_{\nu_b} \hat{a}_{\nu_b} \right\rangle \right]$$

whereas that of distinguishable particles reads:

$$G_{\text{cd}}^{(2)} \Big|_{\text{disc.}} = \frac{1}{4} (G_{\text{aa}}^{(2)} + G_{\text{bb}}^{(2)} + 2G_{\text{ab}}^{(2)})$$

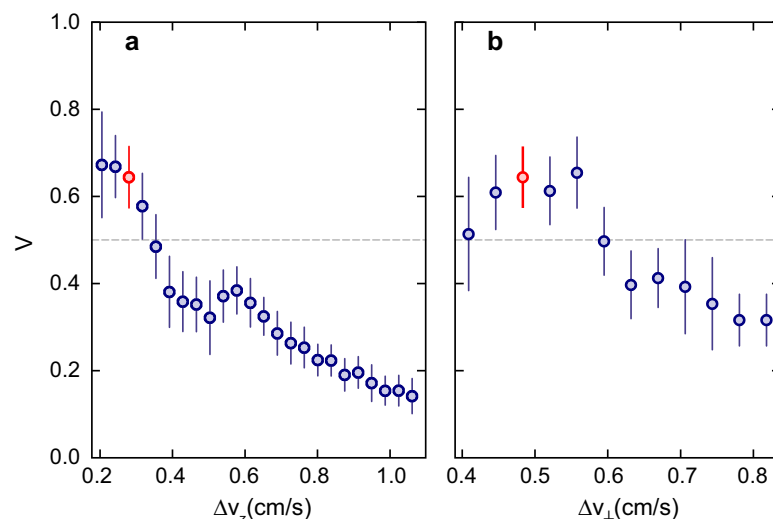
Here, the correlators appearing in the right-hand side are taken at time t_1 , that is, immediately after the atom beams have been produced. The term \mathcal{A} corresponds to an interference between single-particle matter waves. It depends on both the relative phase between the atom beams and the relative phase between the laser beams used for Bragg diffraction. The latter is counted once for the atomic mirror and once for the atomic beam-splitter. Twin beams with perfect correlations in their population would have a fully random relative phase. In our experiment however, the population imbalance between the atom beams could entail a residual phase coherence. Instead, the relative phase between the laser beams was left uncontrolled and

its value was randomly distributed between two repetitions of the experiment. As a result, the term \mathcal{A} must average to zero and the visibility of the HOM dip be given by equation (3), as observed in the experiment. Following ref. 26, we also note that equation (3) yields the ultimate bound for waves interfering on the beam-splitter:

because waves must fulfil the Cauchy–Schwarz inequality, $G_{\text{ab}}^{(2)} < \sqrt{G_{\text{aa}}^{(2)} G_{\text{bb}}^{(2)}}$, the visibility of the classical dip cannot exceed 0.5 (ref. 36).

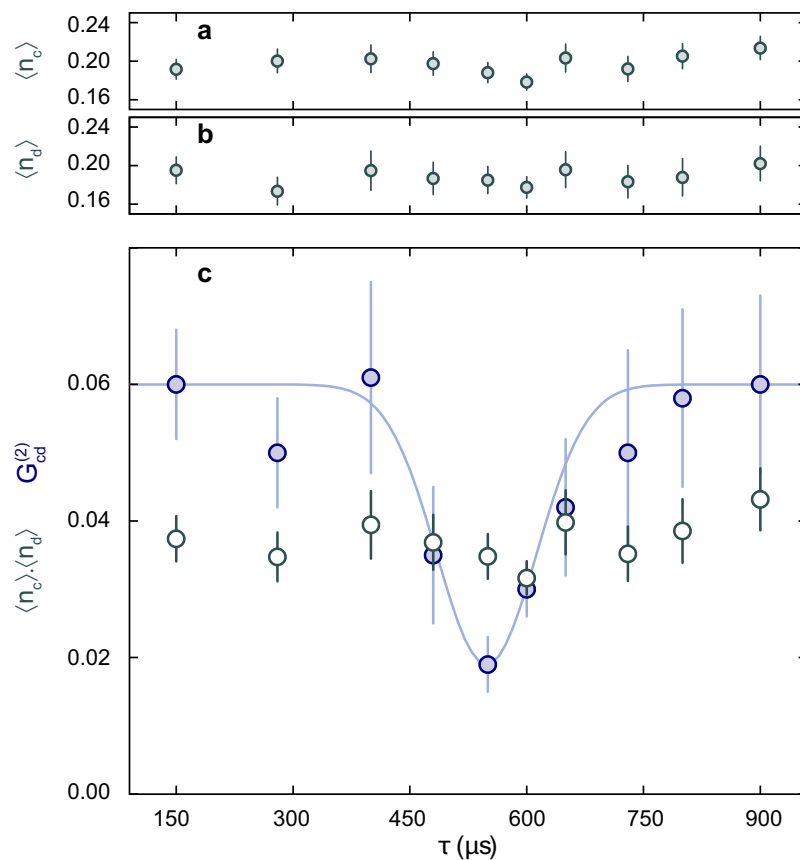
The above results hold true for a finite integration over the atomic velocity distribution provided that two conditions are met: (1) it must remain impossible to distinguish the atoms entering the beam-splitter through channel a from the atoms entering through channel b once they have exited the beam-splitter; (2) the transformation matrix of the beam-splitter must keep the same form after integration. In our experiment, the second condition is naturally satisfied because the Bragg diffraction only couples atomic states with a well defined momentum difference and we fulfil the first condition by reducing the integration volume as much as it is necessary.

31. Andersson, E., Fontenelle, M. & Stenholm, S. Quantum statistics of atoms in microstructures. *Phys. Rev. A* **59**, 3841–3850 (1999).
32. Jaskula, J.-C. *et al.* Sub-Poissonian number differences in four-wave mixing of matter waves. *Phys. Rev. Lett.* **105**, 190402 (2010).
33. Rarity, J. G. & Tapster, P. R. Fourth-order interference in parametric downconversion. *J. Opt. Soc. Am. B* **6**, 1221–1226 (1989).
34. Treps, N., Delaubert, V., Maître, A., Courty, J. M. & Fabre, C. Quantum noise in multipixel image processing. *Phys. Rev. A* **71**, 013820 (2005).
35. Morizur, J.-F., Armstrong, S., Treps, N., Janousek, J. & Bachor, H.-A. Spatial reshaping of a squeezed state of light. *Eur. Phys. J. D* **61**, 237–239 (2011).
36. Ou, Z. Y. Quantum theory of fourth-order interference. *Phys. Rev. A* **37**, 1607–1619 (1988).



Extended Data Figure 1 | HOM dip visibility as a function of the integration volumes. **a**, Visibility V as a function of the longitudinal integration interval Δv_z . The transverse integration interval is kept constant at $\Delta v_\perp = 0.48 \text{ cm s}^{-1}$. **b**, Visibility as a function of the transverse integration

interval Δv_\perp . The longitudinal integration interval is kept constant at $\Delta v_z = 0.28 \text{ cm s}^{-1}$. The red points mark the values discussed in the main text. Error bars denote the standard deviation of the statistical ensemble.



Extended Data Figure 2 | Averaged number of incident atoms over the HOM dip. **a**, Averaged atom number detected in \mathcal{V}_c , n_c , as a function of the propagation time τ . The mean value of $n_c(\tau)$ is 0.20 with a standard deviation of 0.01. **b**, Averaged atom number detected in \mathcal{V}_d , n_d , as a function of the

propagation time τ . The mean value of $n_d(\tau)$ is 0.19 with a standard deviation of 0.01. **c**, The cross-correlation between the output ports c and d (solid blue circles), displaying the HOM dip, is compared to $\langle n_c \rangle \cdot \langle n_d \rangle$ (open grey circles). Error bars denote the standard deviation of the statistical ensemble.

Monolayer semiconductor nanocavity lasers with ultralow thresholds

Sanfeng Wu¹, Sonia Buckley², John R. Schaibley¹, Liefeng Feng^{1,3}, Jiaqiang Yan^{4,5}, David G. Mandrus^{4,5,6}, Fariba Hatami⁷, Wang Yao⁸, Jelena Vučković², Arka Majumdar⁹ & Xiaodong Xu^{1,10}

Engineering the electromagnetic environment of a nanometre-scale light emitter by use of a photonic cavity can significantly enhance its spontaneous emission rate, through cavity quantum electrodynamics in the Purcell regime. This effect can greatly reduce the lasing threshold of the emitter^{1–5}, providing a low-threshold laser system with small footprint, low power consumption and ultrafast modulation. An ultralow-threshold nanoscale laser has been successfully developed by embedding quantum dots into a photonic crystal cavity (PCC)^{6–8}. However, several challenges impede the practical application of this architecture, including the random positions and compositional fluctuations of the dots⁷, extreme difficulty in current injection⁸, and lack of compatibility with electronic circuits^{7,8}. Here we report a new lasing strategy: an atomically thin crystalline semiconductor—that is, a tungsten diselenide monolayer—is non-destructively and deterministically introduced as a gain medium at the surface of a pre-fabricated PCC. A continuous-wave nanolaser operating in the visible regime is thereby

achieved with an optical pumping threshold as low as 27 nanowatts at 130 kelvin, similar to the value achieved in quantum-dot PCC lasers⁷. The key to the lasing action lies in the monolayer nature of the gain medium, which confines direct-gap excitons to within one nanometre of the PCC surface. The surface-gain geometry gives unprecedented accessibility and hence the ability to tailor gain properties via external controls such as electrostatic gating and current injection, enabling electrically pumped operation. Our scheme is scalable and compatible with integrated photonics for on-chip optical communication technologies.

Monolayer transition-metal dichalcogenides (TMDCs) with chemical formula MX_2 ($\text{M} = \text{W}, \text{Mo}; \text{X} = \text{S}, \text{Se}, \text{Te}$; see Fig. 1a for the crystal structure) are the first class of two-dimensional (2D) semiconductors to be discovered that have a direct bandgap in the visible frequency range^{9,10}; tightly bound excitons with novel properties are being found in these systems at such frequencies^{11–13}. These structurally stable, mechanically strong, electrically

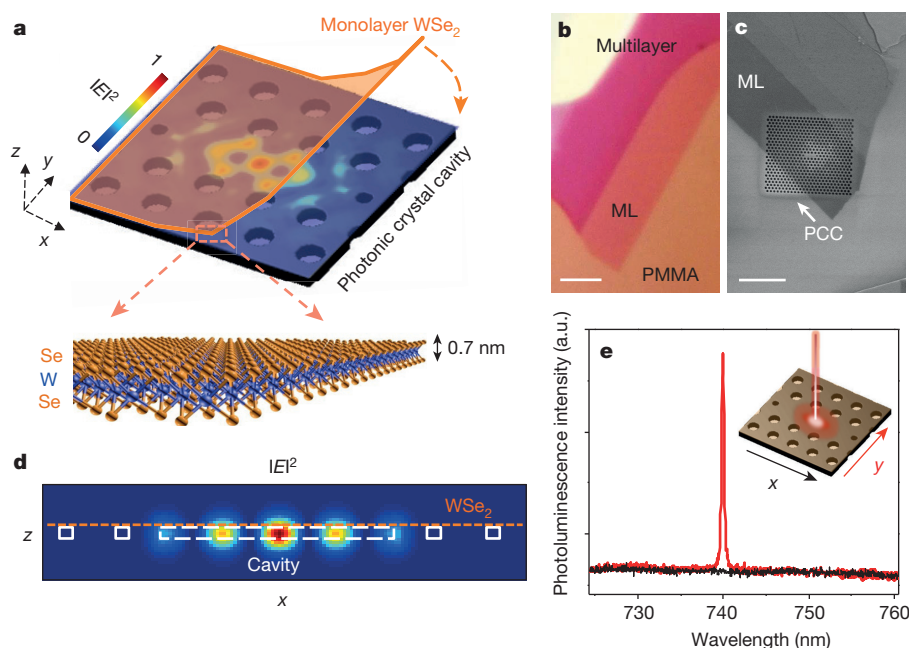


Figure 1 | Hybrid monolayer WSe_2 -PCC nanolasers. **a**, Cartoon depiction of our device architecture, where the electric-field profile (in-plane, x - y) of the fundamental cavity mode (pristine cavity before WSe_2 transfer) is embedded as the colour plot. Inset, cartoon of the atomic structure of monolayer WSe_2 . **b**, Optical image of monolayer (ML) WSe_2 on PMMA before transfer. **c**, SEM image of the hybrid device. Q-factor is $\sim 8,000$ in this cavity before WSe_2 transfer. Scale bars: $3 \mu\text{m}$. **d**, Cross-section electric-field intensity ($|E|^2$) profile

(x - z) of the fundamental mode; the dashed orange line indicates the ideal position for monolayer WSe_2 , the solid white rectangles for air holes, and dashed white lines for the cavity region. **e**, Polarization-resolved photoluminescence spectrum of our device taken at 80 K, showing a completely polarized narrow emission at $\sim 740 \text{ nm}$. Black (red) line corresponds to detected linear polarization in the x (y) direction.

¹Department of Physics, University of Washington, Seattle, Washington 98195, USA. ²Ginzton Laboratory, Stanford University, Stanford, California 94305, USA. ³Department of Applied Physics, Tianjin University, Tianjin 300072, China. ⁴Materials Science and Technology Division, Oak Ridge National Laboratory, Oak Ridge, Tennessee 37831, USA. ⁵Department of Materials Science and Engineering, University of Tennessee, Knoxville, Tennessee 37996, USA. ⁶Department of Physics and Astronomy, University of Tennessee, Knoxville, Tennessee 37996, USA. ⁷Department of Physics, Humboldt University, D-12489 Berlin, Germany. ⁸Department of Physics and Center of Theoretical and Computational Physics, University of Hong Kong, Hong Kong, China. ⁹Department of Electrical Engineering, University of Washington, Seattle, Washington 98195, USA. ¹⁰Department of Material Science and Engineering, University of Washington, Seattle, Washington 98195, USA.

tunable and optically active materials have generated substantial interest in the scientific community owing to their potential for use in 'spin-valleytronics'^{14,15}, field effect transistors¹⁶, light emitting diodes^{17–19}, solar cells²⁰ and photodetectors²¹, thereby possibly expanding the science and device applications of 2D crystals.

Here we demonstrate the first nanoscale laser system based on 2D quantum materials, harnessing the unique advantages of atomically thin crystals for coherent light generation. In our architecture, monolayer tungsten diselenide (WSe₂), as seen in the optical image in Fig. 1b, is selected as the gain medium owing to its desirable bandwidth and relatively high photoluminescence quantum yield compared to other TMDC monolayers. The monolayer is coupled to a prefabricated PCC on a gallium phosphide (GaP) thin membrane²² that is transparent to WSe₂ emission (see Fig. 1a and Methods). An L3 type of PCC is employed²³, in which three neighbouring holes in a linear arrangement are missing, as shown in the scanning electron microscopy (SEM) image in Fig. 1c. The PCC is carefully designed; the mode with the highest quality factor (*Q*-factor) is resonant around 740 nm, which is in the band of the monolayer photoluminescence.

Controlled spontaneous emission was recently demonstrated in monolayer semiconductors, where low *Q*-factor (~ 300) PCCs^{24,25} or distributed Bragg reflectors²⁶ were used. In our devices, the as-fabricated PCCs have *Q*-factors of about 10^4 (Extended Data Fig. 1), representing an improvement of ~ 30 times. This results in a significant improvement of the Purcell factor^{24,25} (see Methods), which is crucial for lasing. To achieve such a high *Q*-factor in the visible region, we use a 125-nm-thick membrane (see Methods), which is 55 nm thinner than our previously reported low-*Q* cavity where no lasing behaviour was observed²⁵. This design significantly improves the cavity *Q*-factors, owing to an optimal thickness-to-lattice-constant ratio, and more importantly, an improved sidewall verticality due to the lower aspect ratio of the etched holes. Conical (non-vertical) etching of the holes leads to coupling to leaky TM modes of the slab²⁷, which eventually decreases the *Q*.

Gain-cavity coupling is achieved through directly transferring the WSe₂ monolayer onto the top of the PCC, using methods that are well established for 2D materials. In the cartoon plot of Fig. 1a, we show the electric-field intensity profile (*x*–*y* plane) of the fundamental mode defined by our cavity, simulated by the finite-difference time-domain (FDTD) method²³. Figure 1d illustrates the cross-section (*x*–*z* plane) profile of the mode, where the orange dashed line indicates the ideal position of WSe₂ monolayer. The corresponding electric-field intensity at the monolayer is about 40% of the possible maximum (which is located at the centre), allowing for efficient overlap between the cavity mode and the monolayer WSe₂ on the surface. In our geometry, even though the gain medium is placed outside the cavity, the miniaturization of the monolayer (with a thickness of ~ 0.7 nm) allows minimal degradation of gain-cavity coupling.

Lasing at a reduced threshold power is achieved by enhancing spontaneous emission into a resonant cavity mode. Figure 1e shows a typical emission spectrum of the hybrid structure, taken under optical pumping by a 632 nm continuous-wave (CW) laser at 80 K. The laser emission is the sharp feature located at 739.7 nm; we measure a line width of 0.3 nm at the half-maximum of this spectrum. The peak is polarized in the *y* direction, consistent with the fundamental mode of the cavity.

One hallmark feature of a laser is the nonlinear 'kink' that occurs around the lasing threshold in the log scale plot of the output light intensity (detected power obtained by integrating over the spectrum) as a function of incident pump power (the 'light-light', or L–L, curve). In Fig. 2a, b, we present the L–L curves (red filled squares) for the monolayer laser at temperatures of 130 K and 80 K, respectively; both curves show the nonlinear 'kink' at the laser threshold region. We estimate typical emission power levels (after the objective lens) of our lasing devices in this region to be ~ 10 fW with 100 nW incident pump power. A set of power-dependent data for spontaneous emission off cavity resonance is also shown in Fig. 2a for contrast (violet half-filled squares); no 'kink' signature is observed. The photoluminescence spectra corresponding to the denoted data

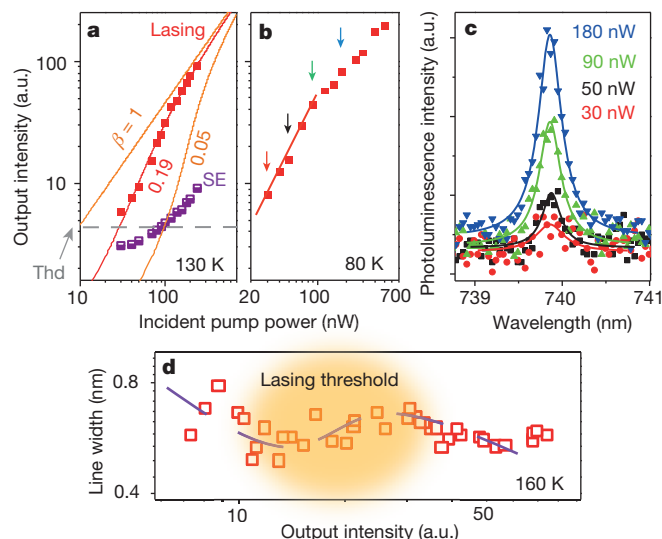


Figure 2 | Lasing characteristics. **a**, Light output intensity (detected power after spectrometer) as a function of the optical pump power (L–L curve) at 130 K. Red filled squares correspond to the cavity emission. Violet half-filled squares correspond to the spontaneous emission (SE) off cavity resonance. Solid lines are the simulated curves using the laser rate equation with different β -factors. $\beta = 0.19$ is the best fit to the lasing data. Dark grey dashed line corresponds to the defined laser threshold, labelled by 'Thd'. **b**, L–L curve for the same lasing device at 80 K (red squares), where the solid line is a guide for the eye to the transition region. **c**, The photoluminescence spectra corresponding to the data points in **b** indicated by the coloured arrows. The solid lines are Lorentzian fits to the photoluminescence spectra. **d**, Cavity line width as a function of the detected output power at 160 K (open red squares). See Extended Data Fig. 3 for the line width at 80 K. Dashed line is a guide to the eye to the nonlinear line width re-broadening area, which corresponds to the lasing threshold region. a.u., arbitrary units.

points (arrows in Fig. 2b) are shown in Fig. 2c. The L–L curve in Fig. 2a is fitted by the cavity laser rate equation (see Methods), as shown by the solid lines.

In a nanocavity laser, the β -factor is the figure of merit that characterizes the laser threshold, and is defined as the fraction of spontaneous emission into the cavity mode (see Methods). A large β -factor reduces the lasing threshold power. We find that $\beta = 0.19$ is the best fit to our observed data, while $\beta = 0.05$ and $\beta = 1$ are also plotted in Fig. 2a for reference. This indicates that in our WSe₂-cavity system, about 19% of the total spontaneous emission is coupled to the cavity mode, comparable to the performance achieved in quantum-dot photonic crystal cavity lasers. We calculate the lasing threshold of our device to be 27 nW (~ 1 W cm^{−2}), as measured by the incident power. Such ultralow-threshold lasing behaviour demonstrates that the cavity-gain coupling in the surface-gain geometry is as efficient as that in the embedded quantum-dot structure^{6,7}.

The observed ultralow lasing threshold relies on the high-*Q* cavity mode. This assertion can be further supported by the data taken from the same device with a lowered *Q*-factor, achieved by covering the device with a poly(methyl methacrylate) (PMMA) layer on top. In this situation, the lasing threshold increases up to around 100 μ W (Extended Data Fig. 2).

We also study the line width evolution around the lasing threshold region. Figure 2d shows the line width as a function of output intensity at 160 K. A pronounced 'kink' appears around the threshold, similar to that in the L–L curve. Below the threshold, the observed line width narrows from ~ 0.75 nm to ~ 0.50 nm as output power increases. At the threshold regime, it broadens to ~ 0.65 nm, and then continues to narrow to 0.55 nm. This line width-dependence is a well-known feature that has been observed in semiconductor nanocavity lasers, such as quantum-well²⁸ and quantum-dot nanolasers⁷. The 'kink' arises during the phase transition from spontaneous emission into stimulated emission, where the coupling between intensity and phase noise (gain–refractive index coupling) significantly

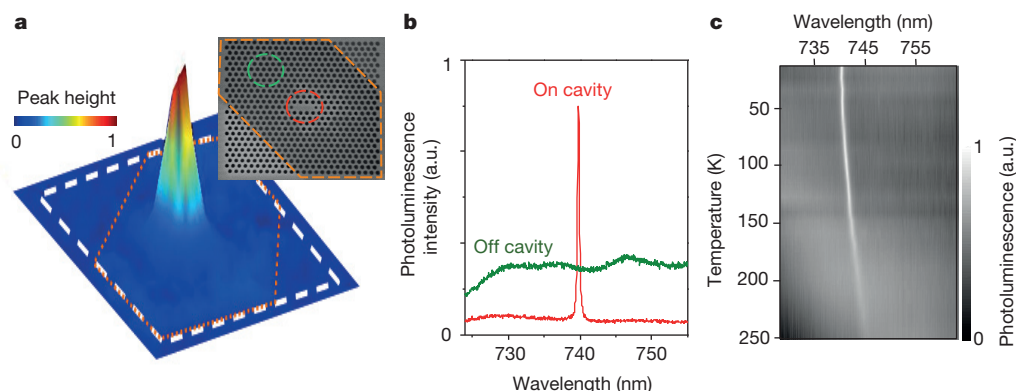


Figure 3 | Spatially resolved emission and temperature-dependent device behaviour. **a**, Peak distinguishing spatial map of our device, where peak height—that is, normalized intensity difference between peak summit (739.7 nm) and bottom (738 nm), is mapped out at 80 K. Dashed white line indicates the photonic crystal area and the dashed orange line shows the area

that is covered by monolayer WSe₂. Inset, corresponding device image in SEM. **b**, Photoluminescence spectra taken on (red) and off (green) the cavity region, indicated by the dashed colour circles in **a** inset. **c**, Temperature dependence of the device emission spectra in a grey-scale map.

influences the line width, and leads to a broadened emission spectrum^{7,28,29}. Such an observed line width plateau, together with the L–L curve, clearly reveals the lasing behaviour in our monolayer semiconductor nanocavity system.

It is essential to lasing that the cavity mode dominates the emission. To illustrate this, we present a contrast experiment between on- and off-cavity regions, by performing a scanning micro-photoluminescence measurement on our device. In Fig. 3a, we plot a peak distinguishing map, in which the normalized peak height of the lasing spectrum (at 739.7 nm) is mapped out over the entire photonic crystal region, indicated by the dashed white line. The dashed orange line indicates the position of the monolayer WSe₂, as also shown in the inset SEM device image. The laser emission only comes from the cavity. A set of typical spectra taken on and off cavity (indicated by dashed circles in Fig. 3a) is shown in Fig. 3b. The on-cavity emission is dominated by the lasing mode while the non-lasing spontaneous emission is largely suppressed, compared to the off-cavity emission. This is strikingly different from observations of the same type in the low-*Q* device, in which the on-cavity measurement shows a level of broad emission similar to that found in off-cavity measurements^{24,25}.

Temperature-dependent emission behaviour of our high-*Q* device is presented in Fig. 3c. A redshift of the emission wavelength with increasing temperature is consistent with the energy shift of the cavity mode²². We have examined lasing characteristics at temperatures below 160 K. As the temperature is increased up to about 250 K, the cavity peak diminishes into the recovered background spontaneous emission. A possible explanation of this could be degradation of the cavity resonance induced by differential thermal expansion between the GaP membrane and the WSe₂ monolayer. Nevertheless, in principle there should be no limitation on increasing the lasing temperature. Further improvement of the *Q* factor by optimizing cavity design and fabrication procedures would be one way to achieve room-temperature lasing. An alternative way would be to find other monolayers or monolayer heterostructures that emit photons at energies compatible with silicon photonics. We could then use silicon PCCs, which have much higher *Q*-values than that of GaP.

We finally discuss the reproducibility of our new lasing architecture, based on a monolayer semiconductor and a PCC. It is routine to fabricate multiple PCCs on a single chip, while deterministic multiple-transfer of monolayer semiconductors onto different PCCs can be achieved to make monolayer hybrid devices (Fig. 4a). In Fig. 4b, we present the lasing spectrum taken from three different devices on the same chip under similar conditions. The lasing devices can be robustly reproduced, which suggests that mass production could be achieved, especially if large-area monolayers grown from chemical or physical vapour deposition are used.

Our design demonstrates the possibility of achieving scalable nanolasers using monolayer gain for integrated chip systems. The advantage of such a surface geometry is that the construction of the optical nanocavity and that of the gain material is naturally separated, allowing fabrication of both parts individually at high quality, before their non-destructive and deterministic combination as hybrids. This enables their realistic application in a scalable and designable way, compatible with integrated electronic circuits. Electrically pumped operation and electrostatic tuning of the carrier concentration could also be achieved directly, in contrast to conventional designs. Our monolayer surface-gain geometry presents a versatile lasing technology and an advance relative to quantum-dot nanocavity lasers, with gain material being incorporated after the laser cavity fabrication, which eliminates the degradation of the gain medium during the fabrication process and enables its replacement if needed.

The exotic properties of 2D semiconductors may also lead to other novel devices using our device architecture, such as valley-selective lasers. Moving beyond nanolasers, other on-chip photonic implementations, such as the study of strongly coupled cavity quantum electrodynamics³⁰,

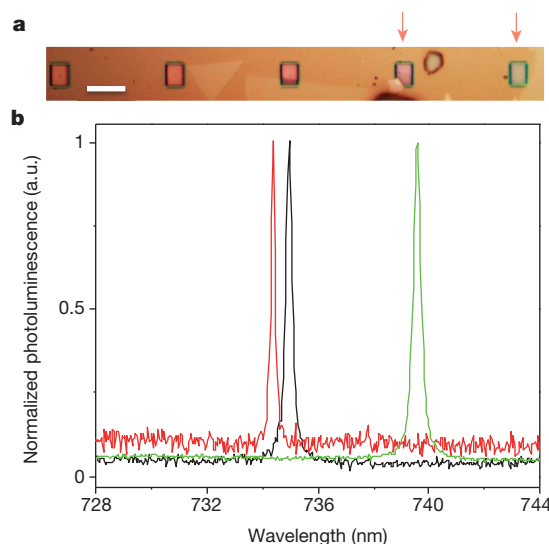


Figure 4 | Reproducibility and scalability of the 2D nanolasers. **a**, An example of deterministic fabrication of multiple devices on one chip. Here we show an optical image of a typical area with 5 PCC devices in a row; the last two devices (indicated by the arrows) are covered with monolayer WSe₂. Scale bar: 10 μm. **b**, Lasing spectra (three) can be reproducibly taken from different devices on the same chip under similar conditions.

nonlinear optics, and photonic quantum control, could open new horizons owing to the use of 2D quantum materials and their heterostructures.

Online Content Methods, along with any additional Extended Data display items and Source Data, are available in the online version of the paper; references unique to these sections appear only in the online paper.

Received 12 October 2014; accepted 3 February 2015.

Published online 16 March 2015.

- Oulton, R. F. *et al.* Plasmon lasers at deep subwavelength scale. *Nature* **461**, 629–632 (2009).
- Lu, Y.-J. *et al.* Plasmonic nanolaser using epitaxially grown silver film. *Science* **337**, 450–453 (2012).
- Painter, O. *et al.* Two-dimensional photonic band-gap defect mode laser. *Science* **284**, 1819–1821 (1999).
- Khajavikhan, M. *et al.* Thresholdless nanoscale coaxial lasers. *Nature* **482**, 204–207 (2012).
- Hill, M. T. *et al.* Lasing in metallic-coated nanocavities. *Nature Photon.* **1**, 589–594 (2007).
- Strauf, S. *et al.* Self-tuned quantum dot gain in photonic crystal lasers. *Phys. Rev. Lett.* **96**, 127404 (2006).
- Strauf, S. & Jahnke, F. Single quantum dot nanolaser. *Laser Photon. Rev.* **5**, 607–633 (2011).
- Ellis, B. *et al.* Ultralow-threshold electrically pumped quantum-dot photonic-crystal nanocavity laser. *Nature Photon.* **5**, 297–300 (2011).
- Mak, K. F., Lee, C., Hone, J., Shan, J. & Heinz, T. F. Atomically thin MoS₂: a new direct-gap semiconductor. *Phys. Rev. Lett.* **105**, 136805 (2010).
- Splendiani, A. *et al.* Emerging photoluminescence in monolayer MoS₂. *Nano Lett.* **10**, 1271–1275 (2010).
- Mak, K. F. *et al.* Tightly bound trions in monolayer MoS₂. *Nature Mater.* **12**, 207–211 (2013).
- Ross, J. S. *et al.* Electrical control of neutral and charged excitons in a monolayer semiconductor. *Nature Commun.* **4**, 1474 (2013).
- Jones, A. M. *et al.* Optical generation of excitonic valley coherence in monolayer WSe₂. *Nature Nanotechnol.* **8**, 634–638 (2013).
- Xiao, D., Liu, G.-B., Feng, W., Xu, X. & Yao, W. Coupled spin and valley physics in monolayers of MoS₂ and other group-VI dichalcogenides. *Phys. Rev. Lett.* **108**, 196802 (2012).
- Xu, X., Yao, W., Xiao, D. & Heinz, T. F. Spin and pseudospins in layered transition metal dichalcogenides. *Nature Phys.* **10**, 343–350 (2014).
- Radisavljevic, B. & Kis, A. Mobility engineering and a metal-insulator transition in monolayer MoS₂. *Nature Mater.* **12**, 815–820 (2013).
- Sundaram, R. S. *et al.* Electroluminescence in single layer MoS₂. *Nano Lett.* **13**, 1416–1421 (2013).
- Baughner, B. W. H., Churchill, H. O. H., Yang, Y. & Jarillo-Herrero, P. Optoelectronic devices based on electrically tunable p-n diodes in a monolayer dichalcogenide. *Nature Nanotechnol.* **9**, 262–267 (2014).
- Ross, J. S. *et al.* Electrically tunable excitonic light-emitting diodes based on monolayer WSe₂ p-n junctions. *Nature Nanotechnol.* **9**, 268–272 (2014).
- Pospischil, A., Furchi, M. M. & Mueller, T. Solar-energy conversion and light emission in an atomic monolayer p-n diode. *Nature Nanotechnol.* **9**, 257–261 (2014).
- Lopez-Sanchez, O., Lembke, D., Kayci, M., Radenovic, A. & Kis, A. Ultrasensitive photodetectors based on monolayer MoS₂. *Nature Nanotechnol.* **8**, 497–501 (2013).
- Rivoire, K., Faraon, A. & Vuckovic, J. Gallium phosphide photonic crystal nanocavities in the visible. *Appl. Phys. Lett.* **93**, 063103 (2008).
- Chalcraft, A. R. A. *et al.* Mode structure of the L3 photonic crystal cavity. *Appl. Phys. Lett.* **90**, 241117 (2007).
- Gan, X. *et al.* Controlling the spontaneous emission rate of monolayer MoS₂ in a photonic crystal nanocavity. *Appl. Phys. Lett.* **103**, 181119 (2013).
- Wu, S. *et al.* Control of two-dimensional excitonic light emission via photonic crystal. *2D Mater.* **1**, 011001 (2014).
- Schwarz, S. *et al.* Two-dimensional metal-chalcogenide films in tunable optical microcavities. *Nano Lett.* **14**, 7003–7008 (2014).
- Tanaka, Y., Asano, T., Akahane, Y., Song, B.-S. & Noda, S. Theoretical investigation of a two-dimensional photonic crystal slab with truncated cone air holes. *Appl. Phys. Lett.* **82**, 1661–1663 (2003).
- Henry, C. Theory of the linewidth of semiconductor lasers. *Quantum Electron. IEEE J.* **18**, 259–264 (1982).
- Björk, G., Karlsson, A. & Yamamoto, Y. On the linewidth of microcavity lasers. *Appl. Phys. Lett.* **60**, 304–306 (1992).
- Liu, X., Galfsky, T., Sun, Z., Xia, F. & Lin, E. Strong light-matter coupling in two-dimensional atomic crystals. Preprint at <http://arxiv.org/abs/1406.4826> (2014).

Acknowledgements We thank C. Dodson for helping with reflection measurements of nanocavities. This work was mainly supported by AFOSR (FA9550-14-1-0277). A.M. is supported by NSF-EFRI-1433496. Photonic crystal fabrication was performed in part at the Stanford Nanofabrication Facility of NNIN supported by the NSF under grant no. ECS-9731293, and at the Stanford Nano Center. S.W. was partially supported by the State of Washington through the University of Washington Clean Energy Institute. S.B. and J.V. were supported by the Presidential Early Award for Scientists and Engineers (PECASE) administered through the Office of Naval Research, under grant number N00014-08-1-0561. S.B. was also supported by a Stanford Graduate Fellowship. J.Y. and D.G.M. were supported by US DoE, BES, Materials Sciences and Engineering Division. F.H. acknowledges support from the European Commission (FP7-ICT-2013-613024-GRASP).

Author Contributions X.X. and A.M. conceived the experiments. S.B. and A.M. fabricated and characterized PCCs under the supervision of J.V. S.W. fabricated the hybrid devices and performed the measurements with assistance from J.R.S. and L.F., under the supervision of X.X. S.W., X.X., A.M. and S.B. analysed the data, and acknowledge discussions with W.Y. and J.V. J.Y. and D.G.M. provided the bulk WSe₂. F.H. grew the GaP membrane. S.W. wrote the paper with input from all authors.

Author Information Reprints and permissions information is available at www.nature.com/reprints. The authors declare no competing financial interests. Readers are welcome to comment on the online version of the paper. Correspondence and requests for materials should be addressed to X.X. (xuxd@uw.edu) or A.M. (arka@uw.edu).

METHODS

Purcell factor estimation. We estimate the maximum achievable Purcell factor of the cavity, that is, the peak enhancement of the emission rate, through:

$$F_{\max} = \frac{3}{4\pi^2} \frac{Q}{V} \left(\frac{\lambda_c}{n} \right)^3$$

Here F_{\max} is the maximum Purcell factor, Q is the cavity quality factor, $V \approx \left(\frac{\lambda_c}{n} \right)^3$ is the mode volume, $n \approx 3.1$ is the GaP refractive index and $\lambda_c \approx 740$ nm is the cavity emission wavelength. We obtain $F_{\max} \approx 607$ for the as-fabricated cavity $Q = 8,000$.

The Q -factor can be smaller after the monolayer transfer. At room temperature, the Q -factor measured after monolayer transfer reduces to $\sim 1,300$, consistent with the photoluminescence emission at high temperatures. When cooled down to low temperatures, the Q -factor recovers to $\sim 2,500$. The spatial displacement (z direction), due to the surface-gain geometry, and the random dipole directions of the emitter could also affect the enhancement of the spontaneous emission rate. Considering these effects, the Purcell factor should be written as:

$$F = F_{\max} |\psi(s)|^2 \langle \cos^2 \xi \rangle$$

Here $|\psi(s)|^2 = \left| \frac{E(s)}{E_{\max}} \right|^2 \approx 0.4$ is the field intensity ratio (Fig. 1d) between the surface and the central maximum of the cavity, describing the effect of spatial detuning. ξ is the angle between the emitter dipole direction (random in the x - y plane) and the

electric field polarization (the y direction); $\langle \cos^2 \xi \rangle = \frac{1}{2\pi} \int_0^{2\pi} \cos^2 \xi d\xi = \frac{1}{2}$. Therefore

we estimate the Purcell factor as $F \approx 37$ for $Q \approx 2,500$, where we consider the monolayer exciton that is spectrally tuned on the cavity resonance and located right above the centre of the cavity.

In a real situation, this value could be further reduced. For example, we may also need to consider the spatial displacement of the exciton in lateral directions, which would require knowledge of the in-plane exciton distribution that is as yet unknown. Moreover, spectral fluctuations of the excitonic line width would lead to variation in the Purcell factor over time described by the Lorentzian of the cavity spectrum. However, the spontaneous emission coupling factor β is estimated to be ~ 0.19 from our measurements (see next section and Fig. 2a), reflecting an efficient Purcell enhancement in this geometry.

Laser rate equation. The spontaneous emission coupling factor β is an essential figure of merit for a nanocavity laser. To extract its value, we use a rate equation⁶ model to describe the evolution of carrier (exciton) number N and the cavity photon number P in the monolayer-PCC system:

$$\dot{N} = R_{\text{ex}} - \frac{N}{\tau_{\text{SE}}} - \frac{aNP}{\tau_{\text{cav}}}, \dot{P} = -\frac{P}{t_c} + \Gamma \frac{N}{\tau_{\text{cav}}} + \Gamma \frac{aNP}{\tau_{\text{cav}}}, \beta = \frac{\tau_{\text{SE}}}{\tau_{\text{cav}}}$$

Here, R_{ex} is the optical pumping rate, τ_{SE}^{-1} is the total spontaneous emission rate, τ_{cav}^{-1} is the emission rate into the cavity mode, t_c^{-1} is the cavity photon decay rate, aNP is the stimulated emission, which is proportional to $N \cdot P$ with coefficient a , and Γ is the cavity confinement factor. We have ignored non-radiative relaxation processes. The rate of non-radiative decay in monolayer semiconductors is currently not known. Any non-radiative decay would induce additional loss, which would result in a larger β factor³¹. The transparent carrier number is set to be zero, since it does not affect the fitting result significantly.

We set $\dot{N} = 0$ and $\dot{P} = 0$ to obtain the steady state solution of the above coupled equations. The solution is: $R_{\text{ex}} = \frac{P}{\Gamma t_c (1 + aP)} \left(\frac{1}{\beta} + aP \right)$. The lasing threshold is defined as the condition when the stimulated emission is equal to the spontaneous emission in the cavity, that is, $aP = 1$. When $aP > 1$, stimulated emission dominates in the hybrid system and lasing behaviour occurs.

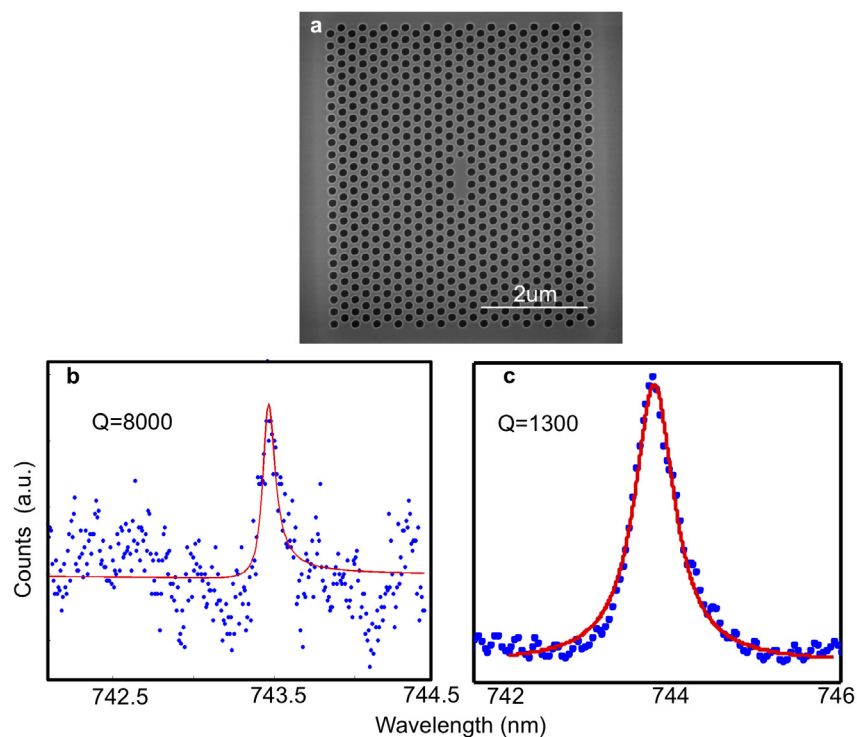
We fit our experimental L-L curve with above equation, as plotted in Fig. 2a. $\beta = 0.19$ is found to be the best fit to the data taken at 130 K.

PCC fabrication. To fabricate the photonic crystal structures, a 125-nm-thick GaP membrane was grown on top of a 1- μm -thick sacrificial $\text{Al}_{0.8}\text{Ga}_{0.2}\text{P}$ layer on a GaP wafer via gas-source molecular beam epitaxy (GSMBE). The patterns were first defined in ZEP520 resist by electron-beam lithography (JEOL JBX 6300, 100 keV) and then transferred to the GaP membrane by a chlorine-based reactive ion etch. Excess resist was removed with Microposit remover 1165 followed by oxygen plasma. The sacrificial layer was finally undercut with hydrofluoric acid to yield suspended membrane structures with high index contrast, followed by cleaning in dilute KOH to remove any by-products of the undercut.

Hybrid device fabrication. The PCC-WSe₂ hybrid structure was fabricated through a standard polymer microtransfer process. A monolayer WSe₂ was first mechanically exfoliated onto a polymer-coated silicon substrate where water-soluble polyvinyl alcohol (PVA, 1%) followed by poly(methyl methacrylate) (PMMA, 950, 6%) was spin-coated on the chip. The stacked monolayer WSe₂/PMMA/PVA/Si substrate was then placed on water, dissolving the PVA layer to separate the silicon substrate. The floating WSe₂/PMMA membrane was transferred using a 'perfect loop' (Ted Pella, Inc.), placing the monolayer onto the pre-fabricated PCC under a microscope followed by heating. The PMMA cover layer was dissolved by a 2-h acetone bath and a 2-min isopropyl alcohol bath.

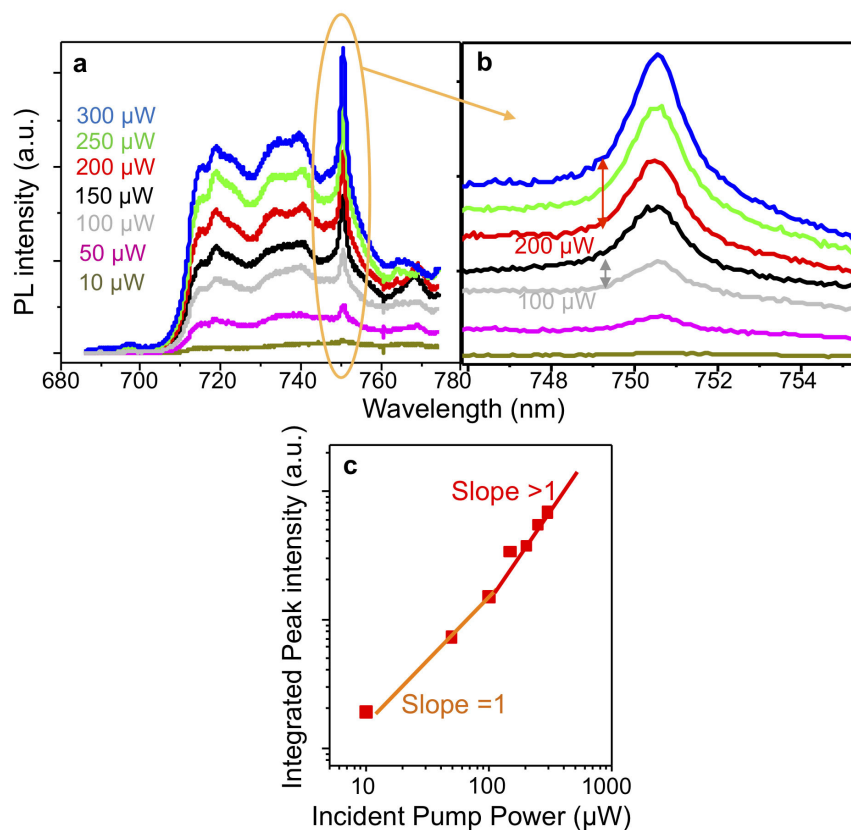
Sample size. In the above analyses, no statistical methods were used to predetermine sample size.

31. Björk, G., Karlsson, A. & Yamamoto, Y. Definition of a laser threshold. *Phys. Rev. A* **50**, 1675–1680 (1994).



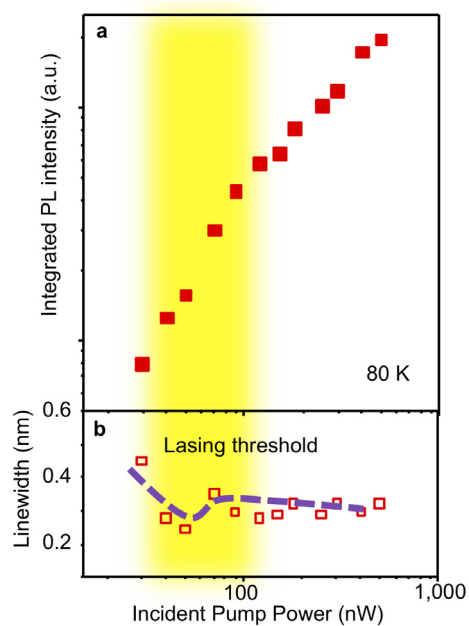
Extended Data Figure 1 | Cavity Q -factor determination. **a**, SEM image of a typical PCC. **b**, **c**, Room-temperature cross-polarized reflection taken from this cavity, before (**b**) and after (**c**) monolayer WSe₂ transfer. As-fabricated cavities (before transfer) of our lasing devices typically have Q -factors ranging

from 5,000 to 14,000. After monolayer transfer, the Q -factor is reduced from 8,000 to 1,300 in this device. After cooling down to cryogenic temperatures, the Q -factor recovers to $\sim 2,500$.



Extended Data Figure 2 | Behaviour of device with Q -factor reduced by poly(methyl methacrylate). **a**, Photoluminescence spectra taken from the PMMA covered device at different pumping powers (30 K), showing pronounced cavity peaks. **b**, Magnified view of cavity peaks ringed in **a**. **c**, Power dependence of the integrated peak intensity. A nonlinear ‘kink’ appears around

100 μW . The PMMA layer reduces the Q -factor to ~ 500 , and also shifts the resonance to lower energy (750.7 nm). This supports the conclusion that the ultralow lasing threshold in our device results from the high Q -factor, by significantly enhancing the spontaneous emission rate into the lasing mode.



Extended Data Figure 3 | Nonlinear 'kinks' in plots of device properties at 80 K. **a, b,** Plots show pump power dependence of integrated emission intensity (**a**) and line width (**b**). The same set of data are shown here as in Fig. 2b.

Shape-changing magnetic assemblies as high-sensitivity NMR-readable nanoprobe

G. Zabow^{1,2}, S. J. Dodd¹ & A. P. Koretsky¹

Fluorescent and plasmonic labels and sensors have revolutionized molecular biology, helping visualize cellular and biomolecular processes^{1–3}. Increasingly, such probes are now being designed to respond to wavelengths in the near-infrared region, where reduced tissue autofluorescence and photon attenuation enable subsurface *in vivo* sensing⁴. But even in the near-infrared region, optical resolution and sensitivity decrease rapidly with increasing depth. Here we present a sensor design that obviates the need for optical addressability by operating in the nuclear magnetic resonance (NMR) radio-frequency spectrum, where signal attenuation and distortion by tissue and biological media are negligible, where background interferences vanish, and where sensors can be spatially located using standard magnetic resonance imaging (MRI) equipment. The radio-frequency-addressable sensor assemblies presented here comprise pairs of magnetic disks spaced by swellable hydrogel material; they reversibly reconfigure in rapid response to chosen stimuli, to give geometry-dependent, dynamic NMR spectral signatures. The sensors can be made from biocompatible materials, are themselves detectable down to low concentrations, and offer potential responsive NMR spectral shifts that are close to a million times greater than those of traditional magnetic resonance spectroscopies. Inherent adaptability should allow such shape-changing systems to measure numerous different environmental and physiological indicators, thus providing broadly generalizable, MRI-compatible, radio-frequency analogues to optically based probes for use in basic chemical, biological, medical and engineering research.

Despite growing interest, MRI-based biosensing remains comparatively limited. Magnetic resonance spectroscopy can detect certain commonly occurring biomolecules but low sensitivity precludes high-resolution imaging of these and of many other potential biomarkers. Responsive MRI contrast agents⁵ offer alternatives but their reliance on changes in image contrast, or relaxivity, complicates quantification. Signal intensities vary for many reasons, including variation in contrast agent concentrations rather than in the biomarkers themselves. Using multiple agents enables ratiometric correction, but requires identical agent pharmacokinetics to avoid artefacts⁶. Potentially quantitative hyperpolarized agents⁷ and (paramagnetic) chemical exchange saturation transfer ((PARA)CEST) agents⁸ that provide inherently ratiometric signals⁹ have also been demonstrated, but they typically require continual agent replenishment and high (millimolar) concentrations, respectively. In comparison, many potential biomarkers, including many proteins, occur at micro- to femtomolar levels. With rare exceptions, existing agents also lack multiplexing capabilities that could allow multi-variable measurements to better differentiate environmental conditions or medical pathologies and hasten early disease detection.

A first step towards multiplexable, high-sensitivity radio-frequency (RF) sensors can be made using recently developed microengineered multispectral MRI contrast agents^{10–14}. Whereas conventional T_1 and T_2 contrast agents modify NMR relaxivities, microengineered multispectral agents employ specially shaped magnetizable micro- or nanostructures to controllably shift NMR frequencies. Different structure

shapes generate different local magnetic fields and associated NMR frequency shifts, enabling differently ‘coloured’ RF tags to be used for multiplexed labelling, analogous to optical tags. With their NMR frequencies geometrically determined, such multispectral tags can be transformed into RF ‘colorimetric’ sensors by incorporating flexible sensor elements that modify tag geometries in response to the environment. Stimuli-responsive hydrogels are one possibility¹⁵. They offer reversible, tunable swelling that can be specifically sensitized to numerous biomolecules and environmental conditions. Redesigned around such gels, the dynamically reconfiguring magnetic elements of the resulting tags can transduce responsive hydrogel swellings into quantitative, NMR-readable, spectral shifts.

Here we introduce these geometrically encoded magnetic (GEM) sensors by demonstrating: (1) pH measurement, (2) spatiotemporal mapping of ion concentration gradients, (3) real-time tracking of cell metabolism, and (4) co-localized sensing through spectrally separable sensors that would otherwise be unresolvable. Although this reflects a limited set of examples, the ability to tailor gel responsiveness to different targets suggests that the same sensor modality could support RF monitoring of many different biomarkers and physiological or environmental processes.

Localized pH sensing, in particular, can help indicate various pathologies including inflammation, ischaemia and cancer. Although not yet realized for clinical MRI, the biomedical importance of pH monitoring already motivates considerable research, including MRI spectroscopies (^1H , ^{19}F , and ^{31}P)^{16–18} and CEST agents^{9,19}, hyperpolarized substrates^{20,21}, and pH-dependent relaxation⁶. All show promise, but can suffer from limited sensitivity, short agent lifetimes, or a need for multi-agent ratiometric concentration normalization, respectively. Shape-changing GEM sensors, on the other hand, are not fundamentally lifetime-limited, offer high sensitivities (detailed below) and, unlike many MRI agents, do not rely on signal amplitude variations, providing instead concentration-independent frequency readouts for more precise, unambiguous quantitation.

The sensor design builds on a multispectral MRI agent geometry comprising spaced, magnetizable disk pairs that, owing to their magnetic shape anisotropy, automatically align themselves with applied magnetic fields¹⁰ (see Fig. 1a and b). When magnetically saturated in the field of an NMR/MRI, such self-aligning assemblies generate tailorable, homogeneous, offset magnetic fields between the disks. The NMR frequencies of water self-diffusing through these homogeneous field regions are then shifted proportionally to the offset field magnitude. Examples of such field-shifted, or spectrally offset, NMR signals are shown in Fig. 1c through histograms of calculated magnetic fields, which closely mimic NMR spectra, in the vicinity of such magnetic structures. The spectral offsets, ω_{offset} , define the structures’ NMR frequencies, or effective RF colours, and are tunable by changing structure shapes and materials according to¹⁰:

$$\omega_{\text{offset}} \approx -4\gamma J_s \left[\frac{hr^2}{(4r^2 + d^2)^{3/2}} \right] \quad (1)$$

¹Laboratory of Functional and Molecular Imaging, National Institute of Neurological Disorders and Stroke, National Institutes of Health, Bethesda, Maryland 20892, USA. ²Electromagnetics Division, Physical Measurements Laboratory, National Institute of Standards and Technology, Boulder, Colorado 80305, USA.

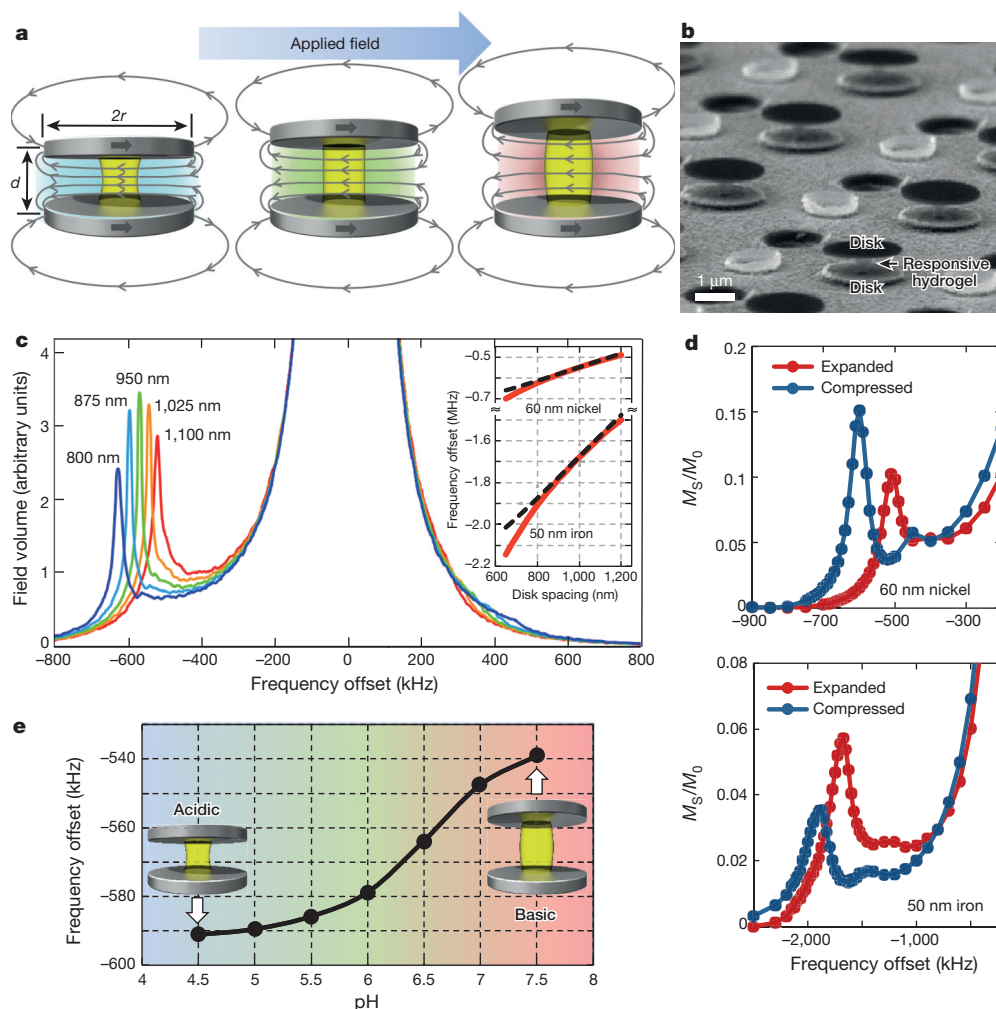


Figure 1 | Principles of shape-changing RF colorimetric sensors.

a, Schematic of sensor assemblies comprising two parallel disks magnetized by applied MRI field (blue arrow) and separated by stimuli-responsive hydrogel spacers (yellow). Resulting magnetic fields (grey curves) are uniform between the disks and locally shift NMR frequencies of water passing through proportionally to the field magnitude, which depends on disk spacing d . Different frequency shifts represent different effective RF ‘colours’. **b**, Scanning electron micrograph of sensors. (Interspersed features are non-magnetic residual topography from the microfabrication process.) **c**, Theoretical precession frequency (or equivalently, field) histograms, mimicking NMR spectra, for 60-nm-thick, 1- μm -radius nickel disk pairs with disk spacings

indicated. Background water appears at zero offset; shifted peaks result from uniform field regions between the disks. Inset: frequency offset versus disk spacing for nickel and iron disks with thicknesses shown. Dashed black curves are analytic approximations (see equation (1)); red curves result from numerical field simulations. **d**, Experimental NMR z-spectra for nickel (top) and iron (bottom) sensors with hydrogel spacers in compressed and expanded states. Magnetization saturated out M_S is normalized to the initial water magnetization M_0 . **e**, Experimental pH-dependent NMR shifts for nickel-based sensors containing pH-sensitive hydrogel spacers designed to shrink (expand) at low (high) pH with peak sensitivity in the physiological pH range.

Here h , r , and d are disk thickness, radii, and separation, respectively, γ is the proton gyromagnetic ratio, and J_S is the saturation magnetic polarization density of the disk material, which may reach 2 T (for iron), enabling large spectral offsets. These offsets are scale invariant, permitting a broad range of sensor sizes. Offsets do vary, however, if aspect ratios change. For disks separated by a responsive hydrogel spacer, differentiation predicts the additional NMR frequency shift, $\Delta\omega_{\text{offset}}$, as the gel changes size:

$$\frac{\Delta\omega_{\text{offset}}}{\omega_{\text{offset}}} \approx - \left(\frac{3d^2}{4r^2 + d^2} \right) \frac{\Delta d}{d} \approx - \frac{1}{2} \frac{\Delta d}{d} \quad (2)$$

That is, the fractional change in NMR frequency shift scales roughly linearly with the fractional length change of the spacer (see also the inset to Fig. 1c).

Sensors described here are microfabricated (see Methods). They comprise 800–1,000-nm-tall, 300–400-nm-wide posts of biocompatible, antifouling, poly(ethylene glycol)-based hydrogel sandwiched between

two 10–60-nm-thick, 900–1,000-nm-radius disks of nickel, or for biocompatibility, iron. Gel pH sensitivity arises from deprotonation of incorporated methacrylic acid side groups in relatively basic conditions. The resulting charged gel swells, increasing the disk separation, d , and thereby reducing the internal field magnitude and the resulting ω_{offset} value. Conversely, in relatively acidic conditions, protonation allows elastic recovery, decreasing d and increasing the magnitude of ω_{offset} . As examples, the resonance shifts of nickel and of iron sensors with compressed and expanded hydrogel spacers are compared in Fig. 1d through NMR z-spectra (Methods), which show the frequency-dependent water magnetization saturated out, M_S , as a fraction of initial water magnetization M_0 . In Fig. 1e, a pH curve records resonance shifts from sensors submerged in a series of different pH buffers across the physiological pH range. Sensor response times are limited by gel shrinking and swelling times, but with submicrometre-scale to nanometre-scale hydrogel elements these times are easily sub-second (see Methods and Supplementary Video 1), allowing for real-time reporting and spatio-temporally well-localized measurements.

In buffered pH conditions, ionic concentrations can also be measured. Local ion concentrations influence much cellular activity, guiding intracellular function, intercellular communication, and, through chemotactic gradients, extracellular migration. In sensor terms, higher ion concentrations increase electrostatic shielding of the gel, reducing swelling and increasing ω_{offset} . Spatially arrayed sensors therefore enable MRI visualization of ion gradients. To demonstrate, we record the diffusive mixing between a phosphate buffer and an adjacent water-based agarose gel, which acts as a local water source and ion sink (Fig. 2). Sensor readings spatially and temporally match diffusion simulations of expected ion concentration profiles (see Fig. 2b and c, Methods, and Supplementary Video 2).

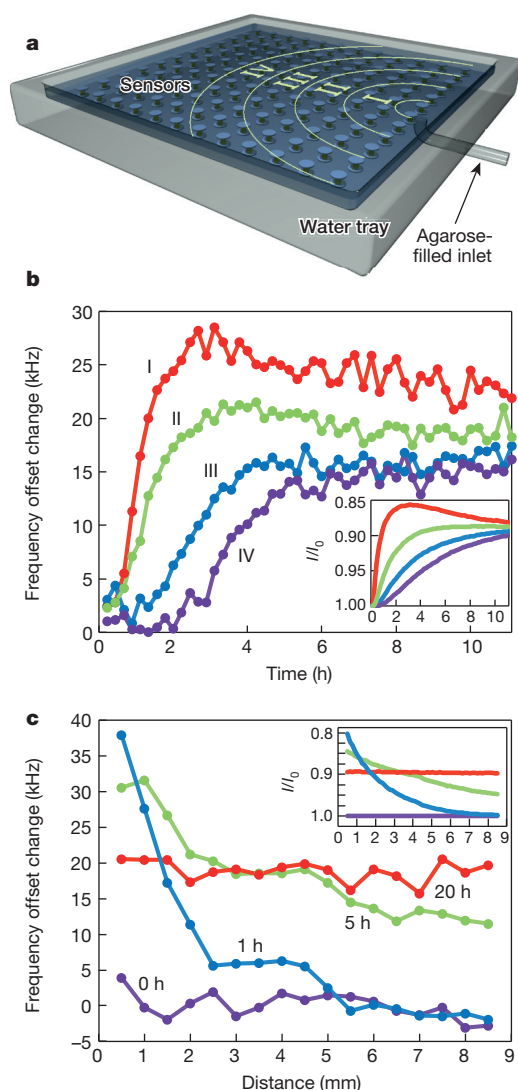


Figure 2 | Spatiotemporal mapping of ion concentrations. **a**, Schematic of array of sensors (not to scale) submerged in a water tray filled with a 0.1 M, pH 7.5 buffer that contacts one end of a short tube filled with water-based agarose gel. As ions diffuse from the buffer solution into the agarose, locally depleted ion concentrations within the buffer are detected through induced shifts in sensor resonances. With an agarose volume one-tenth that of the buffer, complete mixing corresponds to a 10 mM ion reduction, but smaller transient dilutions are also resolvable. **b**, Time evolution of sensor readings in zones I, II, III, and IV, corresponding to distances from the agar inlet of approximately 1–3 mm, 3–5 mm, 5–7 mm, and 7–9 mm, respectively. **c**, Spatial variation in sensor readings as a function of distance from agarose at various time points. Insets in **b** and **c** show numerical simulations of expected spatiotemporal variations in ionic strength, I , normalized to initial ionic strength, I_0 . Inset x axes are in the same units as the main graph axes.

To verify extended operation in biological fluids, we also tracked the metabolic rates of Madin-Darby canine kidney (MDCK) cells placed with GEM sensors in an enclosed volume of Dulbecco's modified Eagle's medium (DMEM) with 10% fetal bovine serum. With no circulating air, the sensors measure the cell growth medium's acidification due to metabolic CO_2 production and cell necrosis in the increasingly hypoxic surroundings. Experiments were performed at 37 °C and at 32 °C with half the cell density used at 37 °C (Methods). Total oxygen consumption rates should decrease at lower cell numbers and at lower temperatures, which slow cell metabolism. As expected, recorded acidification and time to cell death (inferred by cessation of acidification) were faster at 37 °C than at 32 °C (Fig. 3). Comparing Figs 3b and 1e, spectral shifts also indicate decreases of roughly 1 and 0.7 (or $\log(10)$ and $\log(5)$) pH units, confirming that at half the cell density the sensors register half the acidification.

While spacer gel expansions determine sensor frequency shifts, $\Delta\omega_{\text{offset}}$, initial ω_{offset} values are independently tunable over large frequency ranges by changing disk shapes and materials (see equation (1)). Thus different sensors can be spectrally isolated from one another, providing selective addressing and spatially co-localized, multiplexed sensing. As an example, we interleave two hierarchically patterned arrays of sensors of different geometries. Selective detection is demonstrated by decoupling the overlaid sensor images (Fig. 4).

Any biomarker detection is ultimately limited by reporter sensitivity, including absolute probe detectability and the relative biomarker-induced changes therein. Several factors combine to amplify GEM reporter sensitivity. First, the sensors' spatially extended homogeneous field regions allow sensor states to be simultaneously sampled by many water molecules. Second, because water continually diffuses in and out of these regions, magnetization transfer imaging can greatly multiply the effective water signal volume (Methods). Third, large ω_{offset} values shift sensor signals far from any natural background and satisfy slow-exchange limitations⁸ even while facilitating more rapid water transfer, which further boosts signal. As an example, Extended Data Fig. 5 shows nearly 2.5% saturation transfer arising from approximately 75,000 GEM sensors submerged in a 15 mm × 15 mm × 0.1 mm water volume. This extrapolates to 5% signal change (the standard for reliable detection) at

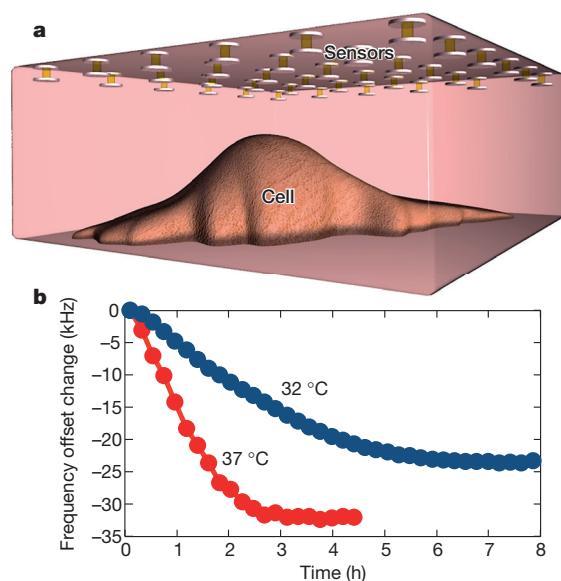


Figure 3 | Tracking cell metabolism. **a**, Schematic of experiment showing sensors suspended above MDCK cells in sealed volume of cell growth medium. **b**, Shifts in sensor resonance frequencies over time as cells acidify the surrounding medium through metabolic CO_2 production and cell necrosis. Different curve slopes and amplitudes confirm different metabolic rates and levels of acidification for experiments run at 37 °C and at 32 °C, with higher and lower cell densities, respectively.

a sensor concentration of approximately 10 femtomoles per litre, a promising level for targeted molecular imaging and potential monitoring of biomarkers that occur at concentrations undetectable with any other responsive MRI agent.

Converted to metal ion concentrations, the above example, which used iron-based sensors with 10-nm-thick, 900-nm-radius disks, corresponds to about 50 μM iron, below clinical Gd^{3+} and conventional PARACEST lanthanide ion concentrations, and comparable to those of specialized high-sensitivity polymeric and supramolecular PARACEST^{22,23}. However, while GEM agents may consist predominantly of iron, Gd or PARACEST macromolecules are commonly tenfold more massive than their lanthanide ions alone. That is, despite each sensor being far larger than each lanthanide agent, for equivalent signal contrast the total mass of exogenous material required may be an order of magnitude less for GEM agents. At less than a picogram per sensor, this total mass amounts to a few micrograms per gram, or millilitre, of water. Notably, the above numbers derive from unoptimized first-generation sensors. Detection limits should improve with more accurate microfabrication²⁴, and with optimized pulse sequence and sensor size and shape design.

Being ferromagnetic, GEM sensor disks are magnetically saturated in most MRI fields. This yields large, field-independent frequency offsets and, according to equation (2), proportionally large, responsive frequency shifts that further augment sensitivity by magnifying biomarker changes. Large frequency shifts are also particularly advantageous at lower, clinical MRI field strengths, where natural background can overwhelm the smaller shifts of traditional spectroscopic and chemical-exchange-based approaches. At clinical fields of 1.5 T, for example, the sensors' 32-kHz spectral splitting per pH unit (Fig. 1e) represents approximately 500 parts per million (p.p.m.) separation. However, this results from thin nickel disks and a full-range hydrogel expansion of just 20% (see Methods). Switching to iron more than triples this splitting. Thicker disks can also increase spectral shifting several-fold, as can smaller disk diameters (see equation (1)). And hydrogel expansions can be increased substantially. Many responsive gels readily double in size; some hydrogels can even reversibly lengthen 20-fold²⁵. Over narrow pH ranges, such expansions could improve sensitivity another one to two orders of magnitude. Combined, these modifications suggest potential spectral shifts approaching a million times those of conventional ^1H , ^{19}F , or ^{31}P NMR, which yield of the order of 1 p.p.m. per pH unit^{16–18}.

The inherent adaptability of the GEM reporter platform should also allow measurement of many variables besides pH. Different hydrogels, responsive to other environmental parameters, such as temperature, can be substituted. Additionally, through molecular imprinting²⁶, or by incorporating catalytic enzymes²⁷, enzyme cleavable substrates²⁸, or specific receptor-ligand type bondings²⁹ into the hydrogel, sensors can be reconfigured to measure (in a continuously reversible or irreversible manner) a broad array of analytes including numerous metabolites, antigens, and proteins. Specific protein recognition may in turn also enable sensitive RF mapping of reporter gene expression. Moreover, hydrogel responses can be tuned for optimal sensor range and linearity. For example, for pH sensing, expansions can be tailored through gel composition, crosslink density, and fractional acid content, with active ranges independently selected through acid pK_a values.

While GEM sensors are already far smaller than biological cells, at present they still suffer from biological delivery issues associated with nano- to microscale materials. There is, however, growing interest in biomedical applications of materials in these size ranges³⁰. Nor should current sizes limit many *in vitro* or environmental sensing applications. Still, further sensor miniaturization should be possible, further boosting speed and biological utility. (See Methods for preliminary results in this direction with 250-nm-radius disks.) Faster water exchange does start broadening linewidths at nanoscale sizes, but hydrogel-based spacers can also help slow water diffusion, pushing ultimate achievable sensor sizes below 50 nm. Ultimate spectral resolutions depend on sensor resonance linewidths, which depend on sensor field inhomogeneities and are at present limited by imperfect microfabrication²⁴. Even with current

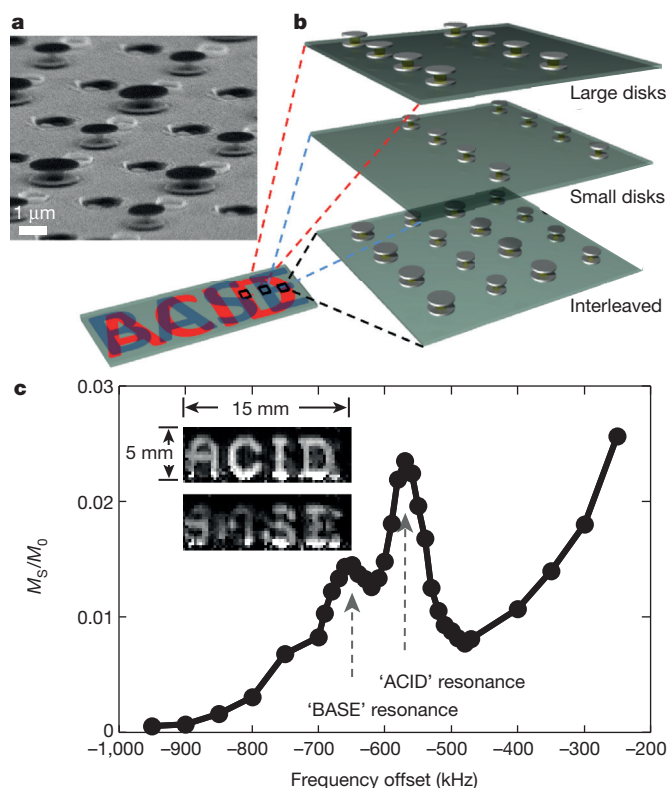


Figure 4 | Sensor multiplexing. **a**, Scanning electron micrograph showing array of interleaved sensors with alternately larger and smaller disk sizes. (Interspersed features are non-magnetic residual topography from the microfabrication process.) **b**, Schematic of hierarchical, interleaved sensor patterning. The words 'ACID' and 'BASE' are patterned out of two interleaved arrays of sensors. 'ACID' characters are spatially patterned from sensors with larger disks; 'BASE' characters are from sensors with smaller disks. At locations where characters overlap, both sensor variants are present. **c**, NMR z-spectrum showing two spectrally separated resonances from sensors comprising larger ('ACID') and smaller ('BASE') disks. The inset shows two MRI difference images of the same sample region acquired at different offset frequencies, showing selective addressing of different sensor populations. With alternate sensors interleaved every 6.4 μm , but an image resolution of 250 μm , images also show that different sensor signals can be simultaneously resolved even if coincident in the same MRI voxel, allowing co-localized multiplexed sensing. Images are created from signal intensity differences between magnetization transfer images acquired at an offset of -1 MHz (at which water is unaffected by sensors) and at frequencies corresponding to the two different sensor resonances seen in the z-spectrum.

sensors, however, a nanometre change in disk separation can provide resolvable kilohertz shifts, raising the prospects of subnanometre displacement detection and potential NMR-accessible RF analogues to optical plasmonic and fluorescent molecular rulers.

Online Content Methods, along with any additional Extended Data display items and Source Data, are available in the online version of the paper; references unique to these sections appear only in the online paper.

Received 12 November 2014; accepted 3 February 2015.

Published online 16 March 2015.

1. Zhang, J., Campbell, R. E., Ting, A. Y. & Tsien, R. Y. Creating new fluorescent probes for cell biology. *Nature Rev. Mol. Cell Biol.* **3**, 906–918 (2002); erratum **4**, 80 (2003).
2. Michalet, X. *et al.* Quantum dots for live cells, *in vivo* imaging, and diagnostics. *Science* **307**, 538–554 (2005).
3. Anker, J. N. *et al.* Biosensing with plasmonic nanosensors. *Nature Mater.* **7**, 442–453 (2008).
4. Hilderbrand, S. A. & Weissleder, R. Near-infrared fluorescence: application to *in vivo* molecular imaging. *Curr. Opin. Chem. Biol.* **14**, 71–79 (2010).
5. Yoo, B. & Pagel, M. D. An overview of responsive MRI contrast agents for molecular imaging. *Front. Biosci.* **13**, 1733–1752 (2008).

6. Martinez, G. V. *et al.* Imaging the extracellular pH of tumors by MRI after injection of a single cocktail of T₁ and T₂ contrast agents. *NMR Biomed.* **24**, 1380–1391 (2011).
7. Schröder, L., Lowery, T. J., Hilty, C., Wemmer, D. E. & Pines, A. Molecular imaging using a targeted magnetic resonance hyperpolarized biosensor. *Science* **314**, 446–449 (2006).
8. Woods, M., Woessner, D. E. & Sherry, A. D. Paramagnetic lanthanide complexes as PARACEST agents for medical imaging. *Chem. Soc. Rev.* **35**, 500–511 (2006).
9. Ward, K. M. & Balaban, R. S. Determination of pH using water protons and chemical exchange dependent saturation transfer (CEST). *Magn. Reson. Med.* **44**, 799–802 (2000).
10. Zabow, G., Dodd, S., Moreland, J. & Koretsky, A. Micro-engineered local field control for high-sensitivity multispectral MRI. *Nature* **453**, 1058–1063 (2008).
11. Zabow, G., Dodd, S. J., Moreland, J. & Koretsky, A. P. The fabrication of uniform cylindrical shells and their use as spectrally tunable MRI contrast agents. *Nanotechnology* **20**, 385301 (2009).
12. Zabow, G., Dodd, S. J. & Koretsky, A. P. Ellipsoidal microcavities: electromagnetic properties, fabrication, and use as multispectral MRI agents. *Small* **10**, 1902–1907 (2014).
13. Wang, X., Wang, C., Anderson, S. & Zhang, X. Microfabricated iron oxide particles for tunable, multispectral magnetic resonance imaging. *Mater. Lett.* **110**, 122–126 (2013).
14. Wang, C., Wang, X., Anderson, S. W. & Zhang, X. Biocompatible, micro- and nano-fabricated magnetic cylinders for potential use as contrast agents for magnetic resonance imaging. *Sens. Actuators B Chem.* **196**, 670–675 (2014).
15. Peppas, N. A., Hilt, J. Z., Khademhosseini, A. & Langer, R. Hydrogels in biology and medicine: from molecular principles to bionanotechnology. *Adv. Mater.* **18**, 1345–1360 (2006).
16. Pan, J. W., Hamm, J. R., Rothman, D. L. & Shulman, R. G. Intracellular pH in human skeletal muscle by ¹H NMR. *Proc. Natl Acad. Sci. USA* **85**, 7836–7839 (1988).
17. Taylor, J. S. & Deutsch, C. Fluorinated α -methylamino acids as ¹⁹F NMR indicators of intracellular pH. *Biophys. J.* **43**, 261–267 (1983).
18. Moon, R. B. & Richards, J. H. Determination of intracellular pH by ³¹P magnetic resonance. *J. Biol. Chem.* **248**, 7276–7278 (1973).
19. Wu, Y., Soesbe, T. C., Kiefer, G. E., Zhao, P. & Sherry, A. D. A responsive europium(III) chelate that provides a direct readout of pH by MRI. *J. Am. Chem. Soc.* **132**, 14002–14003 (2010).
20. Gallagher, F. A. *et al.* Magnetic resonance imaging of pH *in vivo* using hyperpolarized ¹³C-labelled bicarbonate. *Nature* **453**, 940–943 (2008).
21. Jindal, A. K. *et al.* Hyperpolarized ⁸⁹Y complexes as pH sensitive NMR probes. *J. Am. Chem. Soc.* **132**, 1784–1785 (2010).
22. Wu, Y. *et al.* Polymeric PARACEST agents for enhancing MRI contrast sensitivity. *J. Am. Chem. Soc.* **130**, 13854–13855 (2008).
23. Aime, S., Delli Castelli, D. & Terreno, E. Supramolecular adducts between poly-L-arginine and [Tm^{III}dotp]: a route to sensitivity-enhanced magnetic resonance imaging-chemical exchange saturation transfer agents. *Angew. Chem. Int. Ed.* **42**, 4527–4529 (2003).
24. Zabow, G., Koretsky, A. P. & Moreland, J. Design and fabrication of a micromachined multispectral magnetic resonance imaging agent. *J. Micromech. Microeng.* **19**, 025020 (2009).
25. Sun, J.-Y. *et al.* Highly stretchable and tough hydrogels. *Nature* **489**, 133–136 (2012).
26. Byrne, M. E., Park, K. & Peppas, N. A. Molecular imprinting within hydrogels. *Adv. Drug Deliv. Rev.* **54**, 149–161 (2002).
27. Fischel-Ghodsian, F., Brown, L., Mathiowitz, E., Brandendurg, D. & Langer, R. Enzymatically controlled drug delivery. *Proc. Natl Acad. Sci. USA* **85**, 2403–2406 (1988).
28. Plunkett, K. N., Berkowski, K. L. & Moore, J. S. Chymotrypsin responsive hydrogel: application of a disulfide exchange protocol for the preparation of methacrylamide containing peptides. *Biomacromolecules* **6**, 632–637 (2005).
29. Miyata, T., Asami, N. & Urugami, T. A reversibly antigen-responsive hydrogel. *Nature* **399**, 766–769 (1999).
30. Shapiro, E. M., Skrtic, S. & Koretsky, A. P. Sizing it up: cellular MRI using micron-sized iron oxide particles. *Magn. Reson. Med.* **53**, 329–338 (2005).

Supplementary Information is available in the online version of the paper.

Acknowledgements This work was supported in part by the NIH NINDS Intramural Research Program. We thank the NIH Mouse Imaging Facility for use of their 14 T MRI, Y. Chen for providing the MDCK cells, and J. Moreland for discussion and NIST Boulder cleanroom access.

Author Contributions G.Z. conceived of the project, designed the experiments, fabricated the sensors, analysed the data, and wrote the manuscript. S.J.D. designed all NMR/MRI pulse sequences used, helped acquire all NMR/MRI data, and helped write the manuscript. A.P.K. oversaw the work, provided critical feedback, and helped write the manuscript.

Author Information Reprints and permissions information is available at www.nature.com/reprints. The authors declare no competing financial interests. Readers are welcome to comment on the online version of the paper. Correspondence and requests for materials should be addressed to G.Z. (gary.zabow@nist.gov).

METHODS

Sensor microfabrication. To minimize hydrogel exposure to microfabrication processes³¹ that might unpredictably affect the gel spacers' subsequent operation, hydrogels are introduced as late as possible in the fabrication process. This requires fabricating the sensor disks before adding the hydrogel spacer between, which requires a temporary support to suspend the top disks above the base. This more complex fabrication does, however, offer advantages: (1) hydrogels need not be exposed to processing solvents that might contaminate the gel or cause delamination from the processing substrate; (2) hydrogels need not be exposed to high processing temperatures that may affect expansion behaviour³²; (3) having top and bottom disk surfaces exposed before the gel is inserted allows for chemical pretreatment of these surfaces to improve bonding to hydrogels, if desired; (4) since the gel needs only to fill the gap between the disks, fabrication does not depend strongly on differing gel properties, simplifying future sensor fabrication by easing the interchange of different gels designed to respond to different targets³³.

Fabrication begins by evaporating a layer of magnetic material—typically, nickel or iron—with thickness equal to that of the sensor disks (Extended Data Fig. 1a) onto a glass substrate. (Transparent substrates are used to allow for exposure through the backside for ultraviolet crosslinking of hydrogel precursor solutions (detailed below)). Photoresist spun over this magnetic layer is photolithographically patterned to leave disk-shaped resist islands after development (Extended Data Fig. 1b). These islands function as protective masks during a subsequent ion milling that removes the exposed magnetic material and leaves, after photoresist removal, disk-shaped regions of magnetic material (Extended Data Fig. 1c). A second layer of photoresist (which we call the 'spacer layer') is then spun up to a thickness equal to the desired spacing between top and bottom sensor disks, and patterned with an array of holes interstitial to the base disk array (Extended Data Fig. 1d). Next, a second layer of magnetic material (equal in thickness to the base magnetic layer) is evaporated on top (Extended Data Fig. 1e), and covered with a third layer of resist (Extended Data Fig. 1f) patterned similarly to that in Extended Data Fig. 1b. A second ion milling defines the top array of disks directly above the base disks similarly to that in Extended Data Fig. 1c except that now the remaining photoresist islands are temporarily retained (Extended Data Fig. 1g). Copper is then evaporated on top at a 45° angle while the substrate is simultaneously rotated (Extended Data Fig. 1h). The copper therefore coats both the upward-facing surfaces and the sidewalls of the holes in the spacer resist layer. A fourth layer of photoresist spun over the copper is then patterned with small holes offset from both the disk array and the hole array in the spacer layer (Extended Data Fig. 1i) and used as a mask for ion milling replicas of the small holes into the copper layer beneath, leaving the copper structure shown (Extended Data Fig. 1j). These small holes access the underlying resist spacer layer, which is then dissolved away with acetone, exposing the top side of the base disks and the bottom side of the top disks suspended above (Extended Data Fig. 1k). Precursor hydrogel solution poured over then flows through the ion-milled holes in the copper, filling the region between the substrate and the copper support structure. A second substrate placed on top of the hydrogel solution then protects it from atmospheric oxygen, which would otherwise interfere with the cross-linking process³⁴ (Extended Data Fig. 1l), and the gel is crosslinked by ultraviolet exposure through the back side of the original transparent substrate. Removing the top substrate then strips off the solidified hydrogel above the copper support structure (Extended Data Fig. 1m) and the re-exposed copper is then ion-milled away, with the top sensor disks being protected by the photoresist islands that were not removed previously (Extended Data Fig. 1n). To improve copper removal from the photoresist sidewalls and the edges of the top disks, the ion milling is performed at 45° while the substrate rotates about its surface normal. This does lead to cyclical shadowing by the photoresist islands, requiring a longer ion milling duration than normal. On permanently unshadowed surfaces this therefore results in excess milling, which is responsible for the substrate surface depressions seen in the scanning electron micrographs in Figs 1 and 4. (Because of residual hydrogel material, some copper does sometimes remain from the surroundings of the access holes in the copper support, which is also evident as residual ring-like structures in the same scanning electron micrograph images). Finally, an oxygen plasma is timed such that it etches away the remaining photoresist islands and crosslinked hydrogel to leave narrow central hydrogel spacer posts connecting top and bottom disks (Extended Data Fig. 1o).

Although the schematic shows just four sensors, many millions are fabricated simultaneously on each substrate in square arrays with lattice spacings of 51.2 μm for the detection sensitivity experiments, 12.8 μm for the interleaved multiplexed 'acid-base' experiments, and 6.4- μm or 1.6- μm spacings for all other 1,000-nm-radius and 250-nm-radius sensors, respectively. Note that the above represents just one possible fabrication protocol; other protocols (including, for example, lift-off patterning) should also be feasible. Note also that the disk geometry represents only one possible sensor design; just as multispectral MRI contrast agents can have different geometries, GEM sensors can also be envisioned with different magnetic assemblies.

Hydrogel composition. Hydrogel precursor solutions were mixed as a 1:1 ratio (w/w) of poly(ethylene glycol)(n) dimethacrylate (with a poly(ethylene glycol) block molecular weight of approximately 200, Polysciences) and methacrylic acid (Sigma-Aldrich). (Chemical supplier names are included solely to specify experimental details; they do not indicate National Institute of Standards and Technology (NIST) or National Institutes of Health (NIH) endorsement of any particular company.) To this was added 5% (w/w) of 2,2-dimethoxy-2-phenylacetophenone (also from Sigma-Aldrich), used as a photoinitiator. Cross-linking was performed using an i-line ultraviolet source with 5 J cm⁻² flood exposure through half-millimetre-thick borosilicate glass substrates. Before sensors were used, they were soaked in water or pH buffer (typically in pH 7 to pH 7.5) to wash out unreacted initiator and/or monomer, which might otherwise impede water access and hydrogel swelling or shrinking.

Hydrogel expansion. The 20% expansion quoted in the main text can be derived from equation (2), which shows that the frequency shift (about 10% between compressed and expanded gel spacer) is approximately half that of the gel expansion percentage. As a cross-check, however, we also tested a macroscopic sample of the hydrogel, formulated similarly to that used in the nanoscopic hydrogel spacers. The test sample was polymerized against a substrate with surface relief patterns pre-etched at two different length scales: a series of etched lines (1 μm wide with 2- μm centre-to-centre spacing), which formed an optical diffraction grating, together with wider grid lines that divide up the diffraction grating into millimetre-scale squares. This pattern is transferred into the polymerized hydrogel surface and is visible when the hydrogel is removed from the substrate, simplifying measurement of gel expansion or contraction. Extended Data Fig. 2 shows such a hydrogel sample in the compressed and expanded state (immediately after being removed and lightly wiped dry after submerging in a pH 8 buffer). Images agree with an isotropic linear expansion of about 20%. Admittedly, in the sensor configuration, expansion may not be completely isotropic. The cylindrical gel spacers are laterally constrained at their top and bottom end surfaces through contact to the magnetic disks. During expansion this manifests as radial (transverse) compressive strain near the two ends of the spacer that may slightly increase the axial expansion³⁵ (by an amount that depends on the Poisson's ratio of the gel and on the extent of the radial strain towards the cylinder ends). Such additional expansion is likely to be small, however, because the transverse squeezing exists over only a fraction of the gel cylinder. Total expansion therefore seems in good agreement with sensor NMR field shift measurements.

pH buffers. All buffers were 0.1 M phosphate buffers mixed from monosodium phosphate and its conjugate base, disodium phosphate.

Curve fitting. To avoid any bias in extracting sensor resonant frequencies, each z-spectrum was automatically curve fitted to a linear background-subtracted Gaussian curve with the central frequency of the fitting Gaussian being taken as the sensor's resonant spectral offset. (In the case of the agarose-buffer ion mapping experiments, where separate z-spectra were collected for each imaging voxel, signal-to-noise levels were sometimes insufficient to guarantee convergence of the curve-fitting algorithm. Therefore, to ensure consistency, those z-spectra were first averaged over several voxels in space and/or time).

Agarose-buffer interdiffusion experiment, simulation, and animation. Diffusion mapping was based on a 0.1 M, 7.5 pH phosphate buffer solution filling an approximately 15 mm \times 15 mm \times 0.1 mm water tray with one surface covered in a 14 mm \times 14 mm array of 1,000-nm-radius sensors (lattice spacing 6.4 μm). A hole drilled into the tray material from underneath provided access to the water in the tray at a position 1–2 mm from one edge of the square water tray. A 1-mm-inner-diameter tube, filled with an \sim 3-mm length of agarose, was inserted into this hole such that one end of the agarose contacted the water in the tray.

To confirm that shifts in sensor resonant frequencies were due to changes in ionic strength, and not inadvertent changes in pH as the buffer strength was diluted by the water in the agarose gel, a separate experiment was performed with pH 7.5 buffer solution poured directly over a volume of agarose gel twice as large as the buffer volume (to amplify any effect). After sitting for a day, the pH, as measured by conventional pH meter, had shifted by no more than 0.1 pH units, and did not shift any further thereafter. Since the ratio of agarose to pH buffer volume in the actual diffusion experiment was 20 times smaller than this, any pH changes in the actual experiment were assumed to be negligible.

Because of the finite dimensions of the agarose source/sink and the water tray, diffusion dynamics are not easily analytically approximated. Therefore, a numerical simulation of the ion diffusion between buffer and agarose was performed. Extended Data Fig. 3 shows sample simulation-derived in-plane ion concentration variations at various times. Theory insets to Fig. 2b and c were derived from these simulations.

The animation (Supplementary Video 2) derived from the sensor-recorded ion concentration data was generated by automatically curve-fitting all z-spectra collected,

in space and time. The animation comprises a sequential time series of spatial maps of the measured sensor resonant frequencies.

Hierarchically patterned 'ACID'/'BASE' sample. The 'ACID'/'BASE' sample was microfabricated using the protocol described above except that the patterning steps represented in Extended Data Fig. 1b and f were modified. Arrays with interleaved rows of large and small disks were first optically exposed and then, before photoresist development, re-exposed with a pattern that removed disks everywhere except for locations corresponding to the 'ACID'/'BASE' patterns. Since both sensor sizes were processed simultaneously, remaining hydrogel posts are wider for larger disk sensors than for smaller ones.

Z-spectra and magnetization transfer imaging. Sensor signals come predominantly from water whose NMR precession frequency is shifted by the homogeneous field between the sensor's disks. Because self-diffusion continually replenishes the water within this homogeneous field region, however, the volume of water from which signal is acquired can be orders of magnitude larger than the volume between the disks. We exploit this diffusion-driven signal amplification by using a magnetization transfer imaging³⁶ method. As shown schematically in Extended Data Fig. 4, trains of preparatory RF-pulses (generally $\pi/2$ pulses) are applied at an off-resonant frequency to 'saturate out' the magnetization of any water that is shifted to that particular frequency as it diffuses through the magnetic fields surrounding the sensor structure. This is followed by an on-resonance pulse and free-induction-decay acquisition that measures the remaining bulk water magnetization not yet saturated out. Noting the saturation as a function of the offset frequency of the applied RF-pulse train builds up the z-spectra³⁷ used to measure sensor spectral shifts. Since the fields external to the sensor structures are inhomogeneous and decay rapidly in space, relatively little saturation occurs at most offset frequencies; conversely, when the frequency of the off-resonant preparatory pulses matches the frequency shift due to the extended internal homogeneous field regions of the sensors, a substantial saturation signal can accrue from water as it diffuses in and out between the sensor disks. Exact signal amplification depends on how often water between the sensor disks is replenished before the accumulated magnetization deficit decays appreciably due to longitudinal relaxation. Since the time to diffuse a given distance scales quadratically with that distance, refresh rates are higher for smaller sensor structures allowing higher signal gains. A caveat is that the water exchange should not be so fast that it frequency-broadens the shifted sensor lines to such a degree that they overlap the unshifted background water line. Sensors with larger spectral shifts therefore allow faster water exchange rates and, accordingly, greater signal amplifications.

Sensor detection concentration limit. Detection concentration limit experiments (see Extended Data Fig. 5) were performed using an array of sensors made from 900-nm radius, 10-nm-thick iron disks. The sensor array was approximately 14 mm \times 14 mm with square lattice spacing of 51.2 μ m, equalling about 75,000 sensors, and was submerged in a 15 mm \times 15 mm \times 0.1 mm volume of water. Imperfect microfabrication did unnecessarily broaden sensor linewidths somewhat and lead to some fraction of these sensors being malformed, implying a true count of operable sensors less than 75,000. For calculations, however, we have assumed 75,000; that is, real sensor detection limits are probably better than those quoted here.

Cell metabolism experiments. All cells were incubated in DMEM cell growth medium with 10% fetal bovine serum at 37 °C in a custom-designed 15 mm \times 15 mm \times 0.1 mm sample holder, with initial cell number and incubation time selected to give, for the high-density experiment, a monolayer coverage of cells adherent to the sample holder base. Before MRI scanning, the medium was replaced with fresh growth medium and the sample holder sealed with a flat lid containing the array of sensors on its underside. To allow immediate recording, the MRI bore was prewarmed to 37 °C or 32 °C (to slow cell metabolism³⁸) by setting the gradient coil chiller instead to heat appropriately. Following experiments, it was noted that the phenol red pH indicator dye present in the DMEM cell medium had turned from an initially pinkish colour to a yellowish one, indicating that the medium pH had fallen at least below 6.8. Also, pipetting the cell medium liquid from a separate control experiment onto a pH test paper revealed a final pH of 6.5 ± 0.3 , in agreement with the GEM sensor readings.

250-nm-radius double-disk structures. Paper results are based on 900–1,000-nm-radius sensors, but we are currently exploring how to shrink the sensors further. A sample z-spectrum is shown in Extended Data Fig. 6 from preliminary 250-nm-radius, 20-nm-thick, double-disk structures. As yet, our microfabrication is not optimized for these smaller structures. Signals are therefore lower than possible but still easily resolvable, suggesting the feasibility of considerably smaller structures.

Sensor response rates. GEM sensor response times are limited by the response rates of their hydrogel spacers. Macroscopic hydrogels often respond slowly because they are limited by the time taken for solute (or solvent) to penetrate through the gel. Being a primarily diffusive process, this is slow for large gels but speeds up roughly quadratically as gel sizes shrink. For sensors with nanoscale spacing posts, diffusion times through the gels are predicted to be in the millisecond range or below, enabling sensor responses that are fast on NMR timescales. This aids real-time

tracking of local changes in the environment but can complicate measurement of the exact sensor response speed itself, since sensor transient dynamics may be too fast even to be recorded by NMR.

In control experiments, however, we find that it is also possible to optically observe sensor action. We find that light reflecting off an array of the top disks of sensor structures can interfere with light reflecting off the sensor's bottom disks or substrate, producing different interference colours that depend on the top-to-bottom disk separation in a manner akin to 'thin-film interference' phenomena more commonly seen in soap bubbles, thin oil films, and so on. For appropriate viewing angles, as the hydrogels change size the reflected light oscillates between being biased towards the red or blue end of the spectrum. Specifically, for close to normal incidence, the 20% length change in the hydrogel spacers used in the paper translates into a total optical path length change of 400 nm to 500 nm (assuming a water refraction index of ~ 1.33). This corresponds to almost a full oscillation through the reflected colours, implying that as the hydrogel spacers shrink, an initially reddish reflection, say, would be expected to turn green/blue and then partially return to red again (and vice versa). An example of this is shown in Supplementary Video 1, which shows an array of sensors covering a 15 mm \times 15 mm substrate submerged in phosphate-buffered saline and subjected to a short pulse of a few drops of dilute hydrochloric acid, which lowers the local pH as it sweeps through the solution. The video (in real-time at 30 frames per second) shows rapid colour change, which implies rapid sensor response, following the acid front. (Note that owing to surface dirt and resulting microfabrication errors, sensors at different points on the substrate have slightly different initial hydrogel spacer lengths, which impart different initial reflected colours at various points across the substrate).

To better quantify the rate of change, Extended Data Fig. 7 shows the colour change observed as a function of time at different points on the substrate as the acid front moves over. Also shown is a sample sequence of still frames from the same video. Once the acid front reaches any given point on the substrate, the reflected colour can be seen to change rapidly, with virtually all the colour change occurring within 100–200 ms. Unfortunately, we currently cannot discern what fraction of this time period is actually consumed by sensor response versus simply the time it takes for the acid first to locally mix with and acidify the solution surrounding the sensors. The data do, however, establish a ceiling for sensor response time of 0.2 s or less.

MRI pulse sequence parameters. All data were acquired on either a 14 T scanner with commercial birdcage transmit/receive coil or on an 11.7 T scanner with home-built solenoid transmit/receive coil. Field strength and coil type were chosen based on scanner and coil availability and are not necessarily optimal. Similarly, pulse sequence parameters are not necessarily optimized.

Compressed and expanded Ni and Fe sensor z-spectra. For each frequency point in each of the z-spectra shown (Fig. 1d), a series of 15,000 off-resonant $\pi/2$ gaussian-shaped pulses of length 0.1 ms with centre-to-centre spacings of 0.35 ms were first applied. Following these preparatory off-resonance pulses, a single on-resonance $\pi/2$ hard pulse was applied followed by free-induction-decay acquisition of the on-resonance water (see pulse schematic in Extended Data Fig. 4). A 6-s delay was added after the acquisition before the next series of off-resonance pulses were applied. Data presented are based on two averages.

pH curve. Each point in Fig. 1e records the sensors' resonance frequency determined from a z-spectrum acquired from sensors submerged in the relevant pH buffer. Each z-spectrum was acquired similarly to those for the compressed and expanded Ni and Fe sensor examples above, except that the preparatory pulse series consisted of 12,000 pulses.

Agarose-buffer ion diffusion. The same preparatory off-resonance pulse sequences were used in Fig. 2b and c as for the pH-curve z-spectra above. However, each train of off-resonance pulses was followed by a gradient-echo imaging sequence with repeat/echo times (TR/TE) = 20/2.2 ms, matrix size = 32×32 , 30° flip angle, total field of view (FOV) = 19.2 mm \times 19.2 mm, and with centre-out phase encoding (total acquisition time for each image at each offset frequency = 640 ms).

Cell metabolism. The same pulse sequence as for the pH-curve z-spectra was used for Fig. 3b with the experiment repeated continually until no further frequency change was observed.

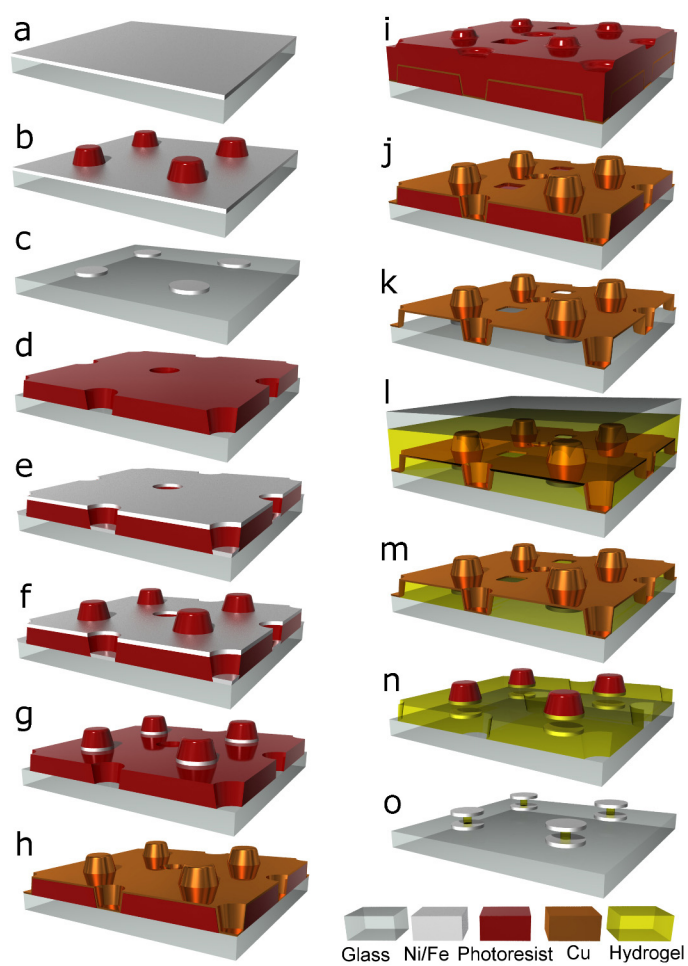
Multiplexed 'ACID'/'BASE' z-spectra. The same pulse sequence as for the pH-curve z-spectra was used in Fig. 4c.

Multiplexed 'ACID'/'BASE' image. The same pulse sequence as for the pH-curve z-spectra was used for the inset to Fig. 4c. However, each train of off-resonance pulses was followed by a gradient-echo imaging sequence with TR/TE = 25/2.3 ms, matrix size = 64×32 , 30° flip angle, total FOV = 15 mm \times 7.5 mm, and with centre-out phase encoding (total acquisition time for each image at each offset frequency = 800 ms). This acquisition was repeated 100 times allowing for signal averaging.

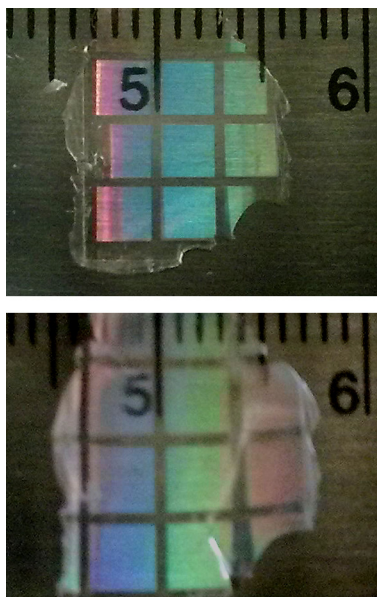
Detection concentration limit z-spectrum. A similar acquisition sequence as to the pH-curve z-spectra was used in Extended Data Fig. 5 except this time applying 25,000 off-resonance π pulses.

250-nm-radius double-disk spectrum. A similar acquisition sequence as to the pH-curve z-spectra was used in Extended Data Fig. 6 except this time applying 15,000 pulses and an 8-s delay between acquisition of each point in the spectrum.

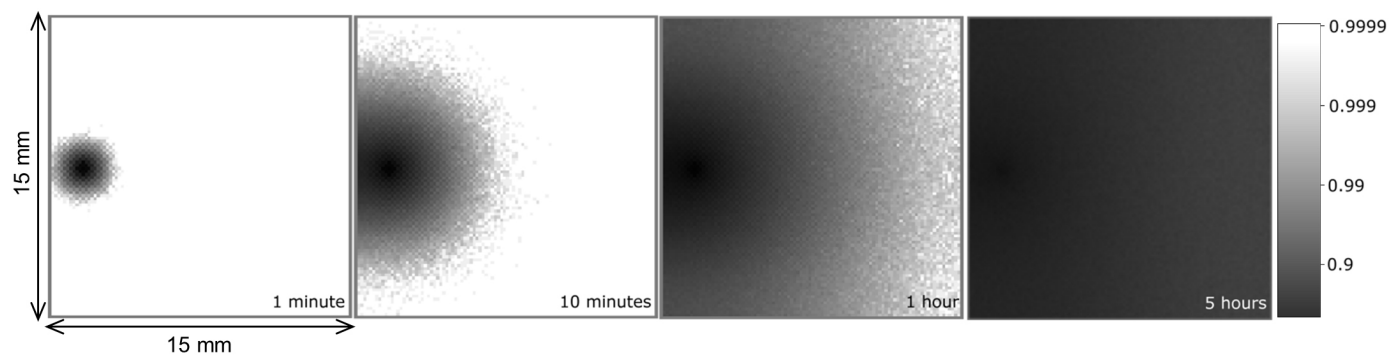
31. Madou, M. J. *Fundamentals of Microfabrication: the Science of Miniaturization* (CRC Press, 2002).
32. Kabiri, K., Mirzadeh, H. & Zohuriaan-Mehr, M. J. Undesirable effects of heating on hydrogels. *J. Appl. Polym. Sci.* **110**, 3420–3430 (2008).
33. Ulijn, R. V. *et al.* Bioresponsive hydrogels. *Mater. Today* **10**, 40–48 (2007).
34. Decker, C. & Jenkins, A. D. Kinetic approach of O₂ inhibition in ultraviolet- and laser-induced polymerizations. *Macromolecules* **18**, 1241–1244 (1985).
35. Yoon, J., Cai, S., Suo, Z. & Hayward, R. C. Poroelastic swelling kinetics of thin hydrogel layers: comparison of theory and experiment. *Soft Matter* **6**, 6004–6012 (2010).
36. Henkelman, R. M., Stanisz, G. J. & Graham, S. J. Magnetization transfer in MRI: a review. *NMR Biomed.* **14**, 57–64 (2001).
37. Grad, J. & Bryant, R. G. Nuclear magnetic cross-relaxation spectroscopy. *J. Magn. Reson.* **90**, 1–8 (1990).
38. Jorjani, P. & Ozturk, S. S. Effects of cell density and temperature on oxygen consumption rate for different mammalian cell lines. *Biotechnol. Bioeng.* **64**, 349–356 (1999).



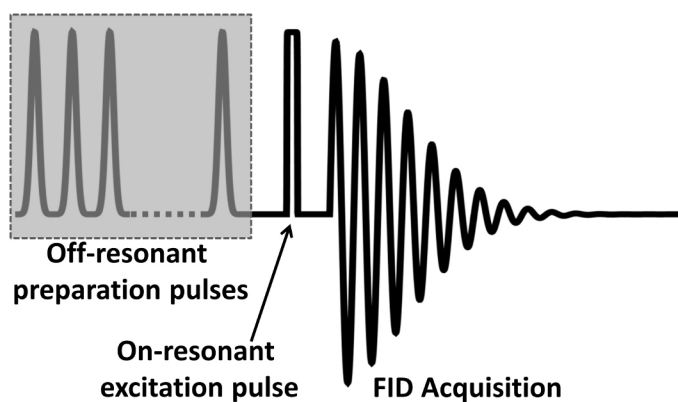
Extended Data Figure 1 | Schematic of microfabrication protocol. See Methods for explanation of panels a–o.



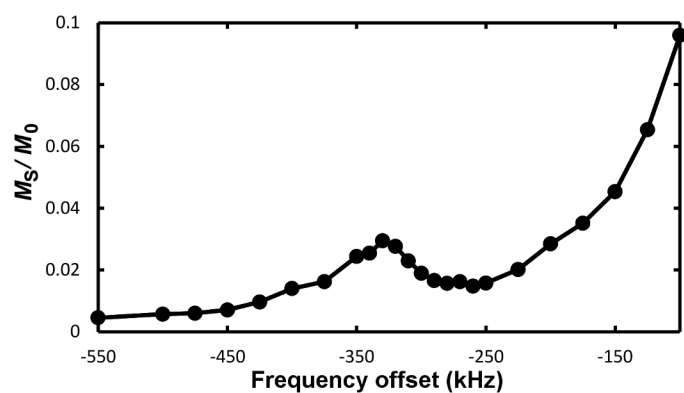
Extended Data Figure 2 | Hydrogel expansion. Hydrogel sample in compressed (top) and expanded (bottom) state, showing $\sim 20\%$ linear expansion.



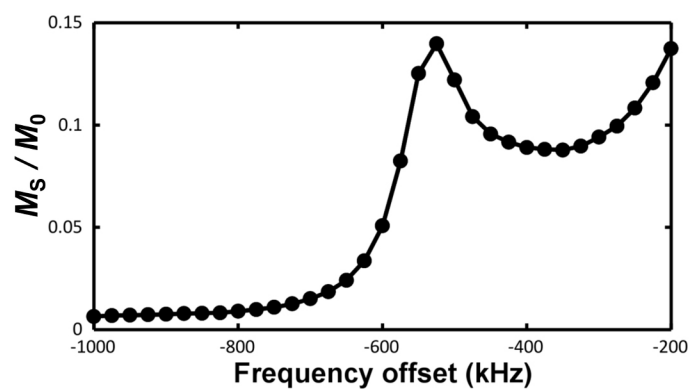
Extended Data Figure 3 | Diffusion simulations. Logarithmically shaded (greyscale bar) plots of numerically simulated ion-concentrations (normalized to initial concentration of unity) due to diffusion between pH buffer solution and water-based agarose gel.



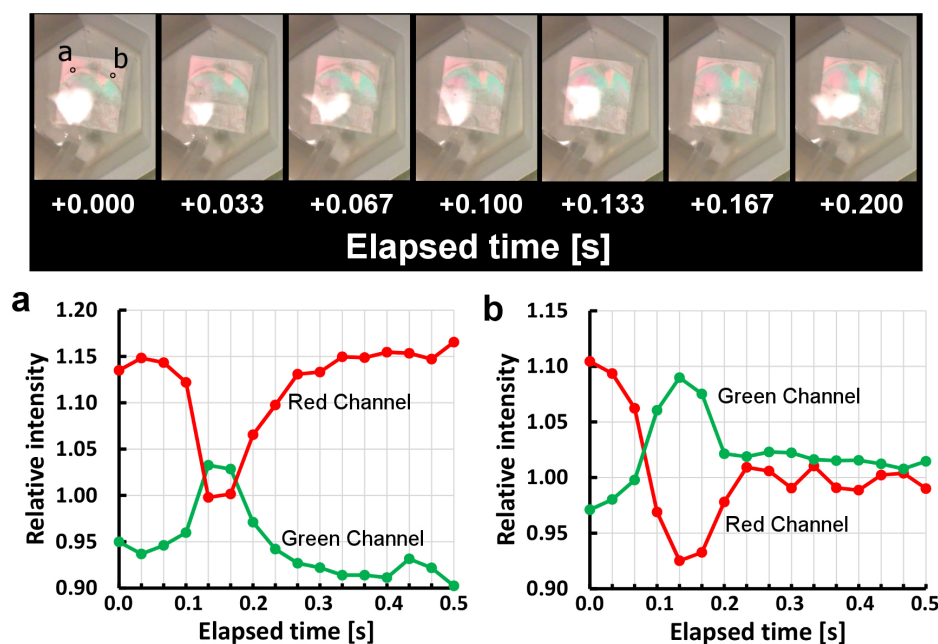
Extended Data Figure 4 | Pulse protocol. Schematic showing off-resonant preparatory pulse train, followed by on-resonant excitation pulse and free-induction-decay (FID) acquisition. The sequence is repeated, each time with different offset frequency, to acquire each point in the z-spectrum.



Extended Data Figure 5 | Sensor sensitivity. z-spectrum, showing magnetization saturated out M_S , normalized to the initial water magnetization M_0 , from sensors with Fe disks of radii 900 nm and thickness 10 nm with resonance around -325 kHz.



Extended Data Figure 6 | Sensor miniaturization. z-spectrum, showing magnetization saturated out M_S , normalized to the initial water magnetization M_0 , for double-disk structures of radii 250 nm with resonance around -525 kHz.



Extended Data Figure 7 | Optically probed sensor response rates. Top panel, a series of consecutive still frames from Supplementary Video 1, showing the propagation of an acid front over an array of sensors. The resulting changes in reflected colours are due to changes in spacing between the top and bottom disks of the sensor, indicating rapid sensor response to introduced acid. Bottom

panels, reflected light intensity in green and red channels (normalized to average light intensity across all colour channels) recorded frame-by-frame at the substrate points a and b indicated in leftmost top panel. Slightly different starting and end points within colour oscillation are due to unintentional sensor microfabrication variation across the substrate.

Orbital-specific mapping of the ligand exchange dynamics of $\text{Fe}(\text{CO})_5$ in solution

Ph. Wernet¹, K. Kunnus^{1,2}, I. Josefsson³, I. Rajkovic^{4†}, W. Quevedo^{4†}, M. Beye¹, S. Schreck^{1,2}, S. Grübel^{4†}, M. Scholz⁴, D. Nordlund⁵, W. Zhang^{6†}, R. W. Hartsock⁶, W. F. Schlottner⁷, J. J. Turner⁷, B. Kennedy^{8†}, F. Hennies⁸, F. M. F. de Groot⁹, K. J. Gaffney⁶, S. Techert^{4,10,11}, M. Odelius³ & A. Föhlisch^{1,2}

Transition-metal complexes have long attracted interest for fundamental chemical reactivity studies and possible use in solar energy conversion^{1,2}. Electronic excitation, ligand loss from the metal centre, or a combination of both, creates changes in charge and spin density at the metal site^{3–11} that need to be controlled to optimize complexes for photocatalytic hydrogen production⁸ and selective carbon–hydrogen bond activation^{9–11}. An understanding at the molecular level of how transition-metal complexes catalyse reactions, and in particular of the role of the short-lived and reactive intermediate states involved, will be critical for such optimization. However, suitable methods for detailed characterization of electronic excited states have been lacking. Here we show, with the use of X-ray laser-based femtosecond-resolution spectroscopy and advanced quantum chemical theory to probe the reaction dynamics of the benchmark transition-metal complex $\text{Fe}(\text{CO})_5$ in solution, that the photo-induced removal of CO generates the 16-electron $\text{Fe}(\text{CO})_4$ species, a homogeneous catalyst^{12,13} with an electron deficiency at the Fe centre^{14,15}, in a hitherto unreported excited singlet state that either converts to the triplet ground state or combines with a CO or solvent molecule to regenerate a penta-coordinated Fe species on a sub-picosecond timescale. This finding, which resolves the debate about the relative importance of different spin channels in the photochemistry of $\text{Fe}(\text{CO})_5$ (refs 4, 16–20), was made possible by the ability of femtosecond X-ray spectroscopy to probe frontier-orbital interactions with atom specificity. We expect the method to be broadly applicable in the chemical sciences, and to complement approaches that probe structural dynamics in ultrafast processes.

In our experimental setup (Fig. 1a), the valence electronic structure of $\text{Fe}(\text{CO})_5$ is probed with femtosecond-resolution resonant inelastic X-ray scattering (RIXS) at the Fe L_3 -edge (Fe L_3 -RIXS, illustrated in Fig. 1b). The frontier orbitals of ironpentacarbonyl, $\text{Fe}(\text{CO})_5$, and its photofragments are the Fe-centred d_π and d_{σ^*} orbitals. With an incident photon energy of 710 eV to select the lowest-energy X-ray resonance corresponding to $2p \rightarrow \text{LUMO}(d_{\sigma^*})$ (where LUMO is the lowest unoccupied molecular orbital) excitations and scattering inelastically to the valence-excited ligand-field states with $d_\pi^7 d_{\sigma^*}^1$ configuration, we effectively probe $d_\pi \rightarrow d_{\sigma^*}$ transitions (note that the single-electron orbital-based assignments can be applied at the level that the system is studied here; see Supplementary Information). The energies of these transitions equal the measured energy transfers (that is, the difference between incident and scattered photon energies indicated by ‘in’ and ‘out’ in Fig. 1b), and directly reflect the changes in chemical bonding and ligand coordination. The intensities of the transitions in $\text{Fe}(\text{CO})_5$ are marked

in Fig. 1c (top). The main intensity maximum involves $2p \rightarrow 2\pi^*$ excitations at 711.5 eV with excitation to the ligand-centred $2\pi^*$ orbitals and inelastic scattering to $d_\pi^7 d_{\sigma^*}^1$ charge-transfer states (Fig. 1c) and is not further analysed.

The unsaturated carbonyl $\text{Fe}(\text{CO})_4$ was generated in ethanol (EtOH) solution by the photodissociation of $\text{Fe}(\text{CO})_5$ with optical (266 nm)

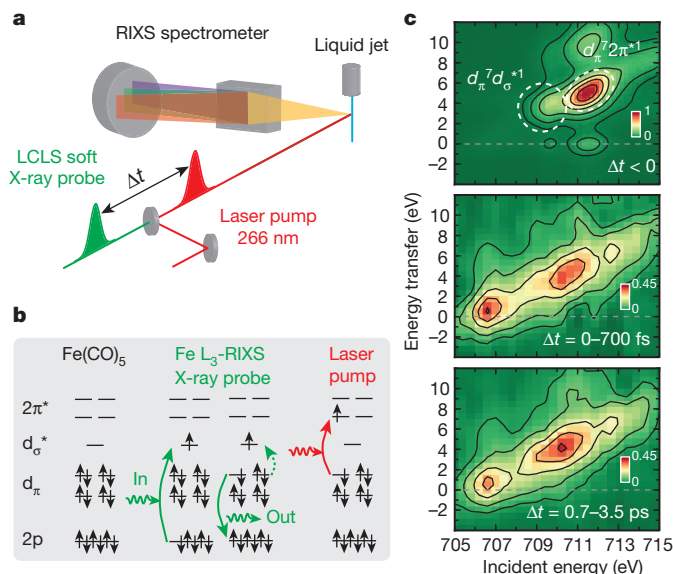


Figure 1 | Scheme and results of the experiment. **a**, Scheme with optical-laser pump and soft X-ray probe after the pump–probe time delay Δt . The intensity of RIXS is measured at the Fe L_3 -absorption edge with a dispersive grating spectrometer. **b**, Electron configuration of ground-state $\text{Fe}(\text{CO})_5$ with single-electron transitions of X-ray probe and laser-pump processes (orbital assignments according to Fe $2p$ and $3d$ or ligand 2π character and according to symmetry along the Fe–CO bonds; the asterisk marks antibonding orbitals). RIXS at the Fe L_3 -absorption edge with $2p \rightarrow d_{\sigma^*}$ excitation involves scattering to final $d_\pi^7 d_{\sigma^*}^1$ ligand-field excited states. Optical $d_\pi \rightarrow 2\pi^*$ excitation triggers dissociation. **c**, Measured Fe L_3 -RIXS intensities (encoded in colour) versus energy transfer and incident photon energy. Top: ground-state $\text{Fe}(\text{CO})_5$ (negative delays, probe before pump). Middle and bottom: difference intensities for delay intervals of 0–700 fs and 0.7–3.5 ps, respectively, isolating transients by subtracting scaled intensities of unpumped $\text{Fe}(\text{CO})_5$ from the measured intensities (scaling factor 0.9). For details of the experiment and a deduction of the scaling factor see Supplementary Information.

¹Institute for Methods and Instrumentation for Synchrotron Radiation Research, Helmholtz-Zentrum Berlin für Materialien und Energie GmbH, Albert-Einstein-Strasse 15, 12489 Berlin, Germany. ²Institut für Physik und Astronomie, Universität Potsdam, Karl-Liebknecht-Strasse 24/25, 14476 Potsdam, Germany. ³Department of Physics, Stockholm University, AlbaNova University Center, 106 91 Stockholm, Sweden. ⁴FG Structural Dynamics of (bio)chemical Systems, Max Planck Institute for Biophysical Chemistry, Am Fassberg 11, 37077 Göttingen, Germany. ⁵Stanford Synchrotron Radiation Lightsource, SLAC National Accelerator Laboratory, 2575 Sand Hill Road, Menlo Park, California 94025, USA. ⁶PULSE Institute, SLAC National Accelerator Laboratory, Stanford University, Stanford, California 94305, USA. ⁷Linac Coherent Light Source, SLAC National Accelerator Laboratory, Menlo Park, California 94025, USA. ⁸MAX-lab, PO Box 118, 221 00 Lund, Sweden. ⁹Department of Chemistry, Utrecht University, Universiteitsweg 99, 3584 CG Utrecht, Netherlands. ¹⁰Institute for X-ray Physics, Göttingen University, Friedrich Hund Platz 1, 37077 Göttingen, Germany. ¹¹Structural Dynamics of (Bio)chemical Systems, DESY, Notkestrasse 85, 22607 Hamburg, Germany. †Present addresses: Paul Scherrer Institut, 5232 Villigen PSI, Switzerland (I.R.); Institute for Methods and Instrumentation for Synchrotron Radiation Research, Helmholtz-Zentrum Berlin für Materialien und Energie GmbH, 12489 Berlin, Germany (W.Q., B.K.); Swiss Light Source, Paul Scherrer Institut, 5232 Villigen PSI, Switzerland (S.G.); Ultrafast Optical Processes Laboratory, Department of Chemistry, University of Pennsylvania, Philadelphia, Pennsylvania 19104, USA (W.Z.).

femtosecond laser pulses in less than 100 fs. Our experiment consisted of recording Fe L_3 -RIXS intensities versus energy transfer while scanning incident photon energy and pump-probe time delay with a time resolution of 300 fs. The observed bimodal spectral distribution shows different intensities for different delays (Fig. 1c, middle and bottom), reflecting changes in $2p \rightarrow$ LUMO resonance energies within the range 706.5–710 eV and changes in $d_\pi \rightarrow d_\sigma^*$ transition energies within the

range –1 to 6 eV. These changes quantify the changes in the frontier-orbital interactions caused by changes in ligand coordination when going from $\text{Fe}(\text{CO})_5$ to $\text{Fe}(\text{CO})_4$ and during the subsequent excited-state dynamics. Ligand dissociation is expected to create a ‘localized hole on the metal’¹⁵ with a concomitant decrease in the d_π – d_σ^* splitting (see the molecular-orbital diagram in Supplementary Information). This manifests itself in the Fe L_3 -RIXS spectra at time delays of 0–700 fs (Fig. 1c, middle) as a new $2p \rightarrow$ LUMO resonance at 706.5 eV and as the maximum of the $d_\pi \rightarrow d_\sigma^*$ transitions shifted to lower energies by –4 eV relative to $\text{Fe}(\text{CO})_5$. Coordinative saturation through ligation with CO or EtOH restores the d_π – d_σ^* splitting, mostly as a result of σ -bonding between $\text{Fe}(\text{CO})_4$ and CO or EtOH. This could explain the occurrence of $2p \rightarrow$ LUMO and $d_\pi \rightarrow d_\sigma^*$ transition energies comparable to $\text{Fe}(\text{CO})_5$ at late delays of 0.7–3.5 ps (at 709.5 and 3 eV; Fig. 1c, bottom).

To substantiate this and to quantitatively analyse the time-resolved data in Fig. 2a, we performed *ab initio* Fe L_3 -RIXS calculations for selected structures. The calculated spectra of the three lowest electronic states of $\text{Fe}(\text{CO})_4$, of the lowest states of $\text{Fe}(\text{CO})_4$ –EtOH complexes and of $\text{Fe}(\text{CO})_5$ in optimized and distorted geometries account for all experimental features. Figure 2b shows the spectra and electronic configurations corresponding to excited singlet-state $\text{Fe}(\text{CO})_4$ ($d_\pi^7 d_\sigma^{*1}$, 1B_2), triplet-state $\text{Fe}(\text{CO})_4$ ($d_\pi^7 d_\sigma^{*1}$, 3B_2), singlet-state $\text{Fe}(\text{CO})_4$ ($d_\pi^8 d_\sigma^{*0}$, 1A_1), ‘hot’ singlet $\text{Fe}(\text{CO})_5$ ($d_\pi^8 d_\sigma^{*0}$, $^1A_1'$), as represented by structures with distorted geometries compared to the optimized one) and singlet complexes with the solvent $\text{Fe}(\text{CO})_4$ –EtOH ($d_\pi^8 d_\sigma^{*0}$, $^1A_1'$).

The most informative spectral regions in our data, labelled 1–4 in Fig. 2a, overlap maximally with the calculated spectral features best able to identify and distinguish the respective intermediate species. The intensities at negative transfers in region 1 result from outgoing X-rays with higher energy than the incoming X-rays and can only result when the X-rays scatter inelastically off $\text{Fe}(\text{CO})_4$ fragments in d_π and d_σ^* electronic excited states. Region 2 is dominated by contributions of excited and triplet $\text{Fe}(\text{CO})_4$. We emphasize that RIXS gives unique chemical resolution, because integrating over the energy transfer and measuring only time-dependent changes in X-ray absorption would prevent us from distinguishing the dynamics of the species assigned to regions 1 and 2. Region 3 identifies the dynamics of ligated $\text{Fe}(\text{CO})_4$ species; that is, $\text{Fe}(\text{CO})_5$ and $\text{Fe}(\text{CO})_4$ –EtOH. Region 4 corresponds to the $2p \rightarrow 2\pi^*$ X-ray resonances with $d_\pi \rightarrow 2\pi^*$ RIXS transitions in most of the calculated species, and seems dominated by the depletion of $\text{Fe}(\text{CO})_5$.

The temporal evolution of the Fe L_3 -RIXS intensities measured in regions 1–4 is plotted in Fig. 2c, together with the result of a kinetic model that simultaneously fits the sum of the calculated excited-state singlet, triplet and ligated $\text{Fe}(\text{CO})_4$ spectra in each region to the measured data (see Supplementary Information for details of the kinetic model and the contribution of singlet $\text{Fe}(\text{CO})_4$). This fitting procedure indicates the appearance of the excited singlet state of $\text{Fe}(\text{CO})_4$ (1B_2) within the time resolution of our experiment (which is insufficient to resolve the initial, ultraviolet-generated excited state of $\text{Fe}(\text{CO})_5$). This allows us to assign unambiguously, within the single-electron orbital picture, the related RIXS intensities at negative energy transfers to $2p \rightarrow d_\pi$ excitations in excited $\text{Fe}(\text{CO})_4$ ($d_\pi^7 d_\sigma^{*1}$, 1B_2) with predominant inelastic scattering to states with $d_\pi^8 d_\sigma^{*0}$ configuration. As is apparent from the molecular orbital diagram of excited $\text{Fe}(\text{CO})_4$ in Fig. 2b, these transitions entail negative energy transfer because the incident photon energy is smaller than the scattered photon energy. The detection and characterization of electronic excited states free from background by non-excited states, enabled by RIXS at negative energy transfers, provides a powerful approach to studying the electronic excited states of chemically active molecules.

The decay of excited singlet-state $\text{Fe}(\text{CO})_4$ (1B_2) coincides with the rise of the triplet $\text{Fe}(\text{CO})_4$ ground state in solution (3B_2), for which our model gives a time constant of 300 ± 100 fs. Within the experimental uncertainty, our data indicate the simultaneous rise of coordinatively saturated ‘hot’ $\text{Fe}(\text{CO})_5$ arising from geminate recombination with CO and of $\text{Fe}(\text{CO})_4$ –EtOH arising from complexation with solvent molecules

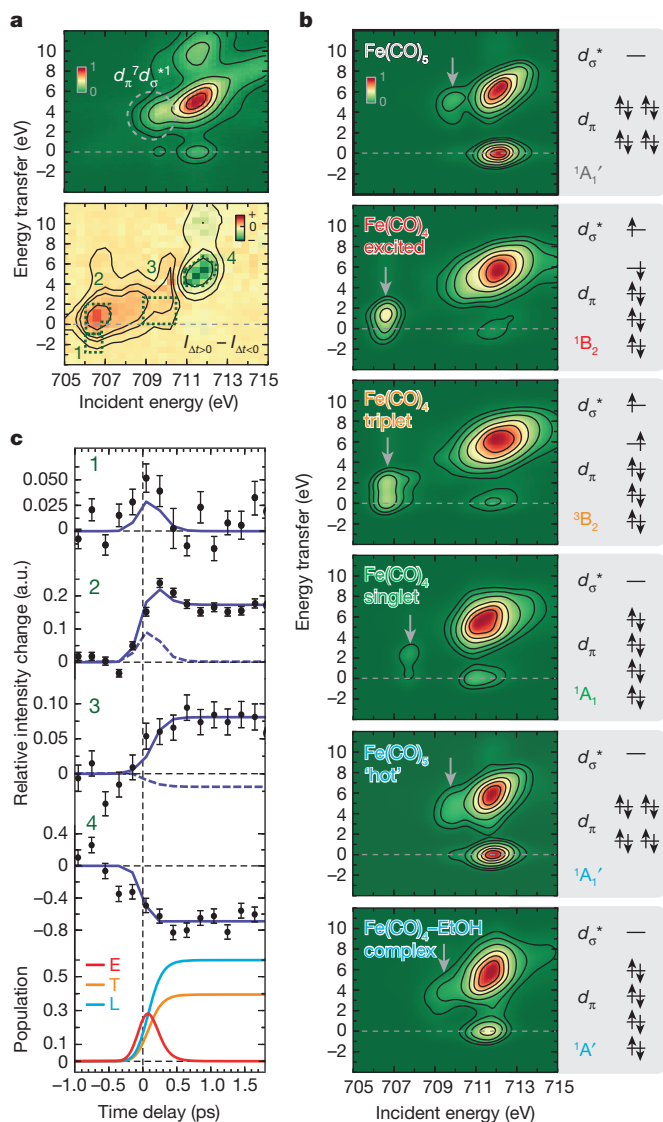


Figure 2 | Fe-specific changes in the electronic structure of $\text{Fe}(\text{CO})_4$ after femtosecond spin crossover and ligation. **a**, Measured Fe L_3 -RIXS of $\text{Fe}(\text{CO})_5$ (top, as in Fig. 1c) and measured difference intensities (bottom, integrated intensities of all positive pump-probe delays minus integrated intensities of all negative delays). The numbers 1–4 mark energy-transfer/incident-photon energy regions for which the temporal evolutions of intensities are plotted in **c**. **b**, Calculated Fe L_3 -RIXS intensities and electronic configurations of the given species ($2p \rightarrow$ LUMO and $d_\pi \rightarrow d_\sigma^*$ transitions marked by arrows; the LUMO can be d_σ^* or d_π , depending on the electron configuration). **c**, Plot of measured intensities in regions 1–4 against pump-probe delay (means \pm s.d.) with the best global fit of a kinetic model (solid lines) with extracted populations of excited (E), triplet (T) and ligated (L) $\text{Fe}(\text{CO})_4$ (L is a sum of ‘hot’ $\text{Fe}(\text{CO})_5$ and $\text{Fe}(\text{CO})_4$ –EtOH). The dashed lines in regions 2 and 3 represent alternative models without triplet and ligated $\text{Fe}(\text{CO})_4$, respectively. The measured signals stayed constant up to 3 ps. For details of the calculations, structures and energies of the species and how ligation in $\text{Fe}(\text{CO})_4$ –EtOH can occur through the alkyl or hydroxyl group see Supplementary Information.

(fitted time constant 200 ± 100 fs). The failure of kinetic models without triplet $\text{Fe}(\text{CO})_4$ ($^3\text{B}_2$) (dashed curve in Fig. 2c, region 2) or without ligated $\text{Fe}(\text{CO})_4$ (dashed curve in Fig. 2c, region 3) justifies the use of three distinct photoproducts in the kinetic modelling and underlines the robustness of our detection of triplet $\text{Fe}(\text{CO})_4$ ($^3\text{B}_2$) in parallel with 'hot' $\text{Fe}(\text{CO})_5$ and $\text{Fe}(\text{CO})_4\text{-EtOH}$. Because we cannot spectroscopically distinguish geminately recombined 'hot' $\text{Fe}(\text{CO})_5$ from solvent-complexed $\text{Fe}(\text{CO})_4\text{-EtOH}$, their ratio in the kinetic model is fixed at 1:1, consistent with the measured quantum yield of 0.8 for solvent-separated $\text{Fe}(\text{CO})_4$ and CO (ref. 21).

Figure 3 sketches the reaction pathways established in this study, with detection of the excited singlet-state $\text{Fe}(\text{CO})_4$ ($^1\text{B}_2$) confirming the suggestion¹⁶ that the primary reaction steps in solution also involve the singlet pathway as seen in the gas phase^{17,18}. The proposed relaxation of excited singlet $\text{Fe}(\text{CO})_4$ ($^1\text{B}_2$) to singlet $\text{Fe}(\text{CO})_4$ ($^1\text{A}_1$) through internal conversion¹⁷ is consistent with our data (see Supplementary Information), but we also observe triplet $\text{Fe}(\text{CO})_4$ ($^3\text{B}_2$) that was previously seen in solution^{4,19} and in rare-gas matrix¹⁶ experiments. This triplet arises from a singlet state with a time constant of 300 fs, consolidating the notion⁶ that sub-picosecond intersystem crossing seems to be common in the excited-state dynamics of transition-metal complexes^{7,22–24}. The persistence of the triplet $\text{Fe}(\text{CO})_4$ ($^3\text{B}_2$) up to our maximum time delay of 3 ps is consistent with its undergoing a slow, spin-forbidden reaction with intersystem crossing to a solvent-complexed singlet state on a 50–100 ps timescale^{4,5,25}. However, the observed branching on a sub-picosecond timescale into the competing and simultaneous reaction channels of spin crossover and ligation to form coordinatively saturated species introduces an efficient pathway circumventing this spin barrier. It also supports the idea that the high density of electronic excited states and the relatively large amount of excess energy available in the system determine the course of the excited-state dynamics, rather than spin selection rules alone^{5,6}. Fast ligation could be facilitated along the singlet pathway, confirming the general notion that solvent-stabilized metal centres form fast^{3,4,11}; this is also consistent with the observation of the unsaturated carbonyl $\text{Cr}(\text{CO})_5$ forming a solvent complex in alcohol solution within 1.6 ps (ref. 26). An alternative proposal²⁰ for $\text{Fe}(\text{CO})_5$ involves a concerted exchange of CO and EtOH on the timescale of ligand dissociation of 100–150 fs. This would also proceed along a singlet pathway and would be in agreement with our results,

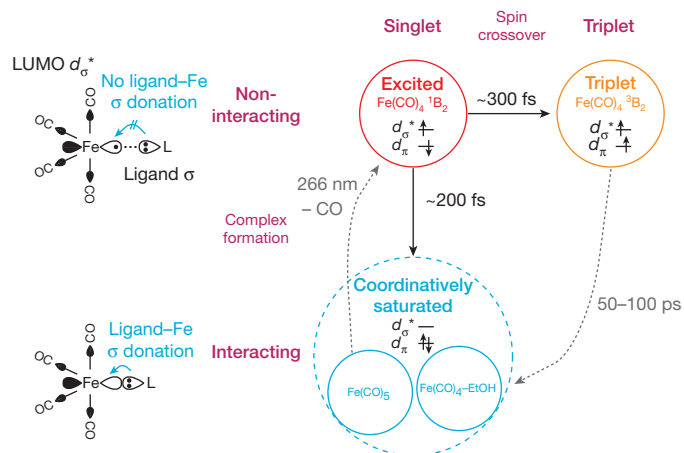


Figure 3 | Schematic reaction pathways of $\text{Fe}(\text{CO})_4$ in EtOH. Parallel evolution from excited singlet-state $\text{Fe}(\text{CO})_4$ to triplet-state $\text{Fe}(\text{CO})_4$ through spin crossover (rise of triplet with a time constant of 300 ± 100 fs) and to coordinatively saturated 'hot' singlet $\text{Fe}(\text{CO})_5$ through geminate recombination and $\text{Fe}(\text{CO})_4\text{-EtOH}$ by means of solvent-complex formation (increase in ligated $\text{Fe}(\text{CO})_4$ with time constant 200 ± 100 fs). A triplet pathway to $\text{Fe}(\text{CO})_4\text{-EtOH}$ complex formation within 50–100 ps is indicated in grey. Interaction of the d_{σ}^* LUMO of $\text{Fe}(\text{CO})_4$ with a ligand σ orbital (different phases are shown in black and white) is shown in the sketches with ligand–Fe σ donation in the coordinatively saturated species.

because the temporal resolution of our measurements is not sufficient to distinguish between this concerted process and the alternative sequential process. Revealing in detail the influence of solvent–solute interactions remains the subject of future studies, which could also explore whether the structure of the solute before dissociation²⁰ influences the excited-state branching ratio between the different pathways.

We find that the ligation capability of $\text{Fe}(\text{CO})_4$ is determined mostly by its d_{σ}^* LUMO, which receives σ donation from occupied CO or EtOH ligand orbitals. Population of the antibonding d_{σ}^* orbital in excited singlet ($^1\text{B}_2$) and triplet ($^3\text{B}_2$) $\text{Fe}(\text{CO})_4$ impedes σ donation from ligands (see the sketches in Fig. 3), explaining the inertness of these species against ligation; this problem is absent in the ligation channel that produces coordinatively saturated species. Establishment of this correlation of orbital symmetry with spin multiplicity and reactivity²⁷ is enabled by the atom specificity with which X-ray laser-based femtosecond-resolution spectroscopy can explore frontier-orbital interactions. This ability gives unique access to the reaction mechanisms of metal complexes in a way that extends and complements methods that probe structural dynamics in ultrafast chemical processes in solution^{28–30}.

Received 3 July 2014; accepted 5 February 2015.

- Parshall, G. W. Organometallic chemistry in homogeneous catalysis. *Science* **208**, 1221–1224 (1980).
- Gray, H. B. & Maverick, A. W. Solar chemistry of metal complexes. *Science* **214**, 1201–1205 (1981).
- Bengali, A. A., Bergman, R. G. & Moore, C. B. Evidence for the formation of free 16-electron species rather than solvate complexes in the ultraviolet irradiation of $\text{CpCo}(\text{CO})_2$ in liquefied noble gas solvents. *J. Am. Chem. Soc.* **117**, 3879–3880 (1995).
- Snee, P. T., Payne, C. K., Mebane, S. D., Kotz, K. T. & Harris, C. B. Dynamics of photosubstitution reactions of $\text{Fe}(\text{CO})_5$: an ultrafast infrared study of high spin reactivity. *J. Am. Chem. Soc.* **123**, 6909–6915 (2001).
- Besora, M. *et al.* A combined theoretical and experimental study on the role of spin states in the chemistry of $\text{Fe}(\text{CO})_5$ photoproducts. *J. Am. Chem. Soc.* **131**, 3583–3592 (2009).
- Juban, E. A., Smeigh, A. L., Monat, J. E. & McCusker, J. K. Ultrafast dynamics of ligand-field excited states. *Coord. Chem. Rev.* **250**, 1783–1791 (2006).
- Chergui, M. On the interplay between charge, spin and structural dynamics in transition metal complexes. *Dalton Trans.* **41**, 13022–13029 (2012).
- Heyduk, A. F. & Nocera, D. G. Hydrogen produced from hydrohalic acid solutions by a two-electron mixed-valence photocatalyst. *Science* **293**, 1639–1641 (2001).
- Arndtsen, B. A., Bergman, R. G., Mobley, T. A. & Peterson, T. H. Selective intermolecular carbon–hydrogen bond activation by synthetic metal complexes in homogeneous solution. *Acc. Chem. Res.* **28**, 154–162 (1995).
- Labinger, J. A. & Bercaw, J. E. Understanding and exploiting C–H bond activation. *Nature* **417**, 507–514 (2002).
- Bromberg, S. E. *et al.* The mechanism of a C–H bond activation reaction in room-temperature alkane solution. *Science* **278**, 260–263 (1997).
- Wrighton, M. S., Ginley, D. S., Schroeder, M. A. & Morse, D. L. Generation of catalysts by photolysis of transition metal complexes. *Pure Appl. Chem.* **41**, 671–687 (1975).
- Whetten, R. L., Fu, K.-J. & Grant, E. R. Pulsed-laser photocatalytic isomerization and hydrogenation of olefins. *J. Am. Chem. Soc.* **104**, 4270–4272 (1982).
- Langmuir, T. Types of valence. *Science* **54**, 59–67 (1921).
- Hoffmann, R. Building bridges between inorganic and organic chemistry. *Angew. Chem. Int. Edn Engl.* **21**, 711–724 (1982).
- Poliakoff, M. & Turner, J. J. The structure of $[\text{Fe}(\text{CO})_4]$ —an important new chapter in a long-running story. *Angew. Chem. Int. Edn Engl.* **40**, 2809–2812 (2001).
- Trushin, S. A., Fuss, W., Kompa, K. L. & Schmid, W. E. Femtosecond dynamics of $\text{Fe}(\text{CO})_5$ photodissociation at 267 nm studied by transient ionization. *J. Phys. Chem. A* **104**, 1997–2006 (2000).
- Ihee, H., Cao, J. & Zewail, A. H. Ultrafast electron diffraction of transient $[\text{Fe}(\text{CO})_4]$: determination of molecular structure and reaction pathway. *Angew. Chem. Int. Edn Engl.* **40**, 1532–1536 (2001).
- Snee, P. T., Payne, C. K., Kotz, K. T., Yang, H. & Harris, C. B. Triplet organometallic reactivity under ambient conditions: an ultrafast UV pump/IR probe study. *J. Am. Chem. Soc.* **123**, 2255–2264 (2001).
- Ahr, B. *et al.* Picosecond X-ray absorption measurements of the ligand substitution dynamics of $\text{Fe}(\text{CO})_5$ in ethanol. *Phys. Chem. Chem. Phys.* **13**, 5590–5599 (2011).
- Nayak, S. K., Farrell, G. J. & Burkey, T. J. Photosubstitution of two iron pentacarbonyl CO's in solution via a single-photon process: dependence on dispersed ligands and role of triplet intermediates. *Inorg. Chem.* **33**, 2236–2242 (1994).
- Zhang, W. *et al.* Tracking excited-state charge and spin dynamics in iron coordination complexes. *Nature* **509**, 345–348 (2014).
- Bressler, C. *et al.* Femtosecond XANES study of the light-induced spin crossover dynamics in an iron(II) complex. *Science* **323**, 489–492 (2009).
- Huse, N. *et al.* Femtosecond soft X-ray spectroscopy of solvated transition-metal complexes: deciphering the interplay of electronic and structural dynamics. *J. Phys. Chem. Lett.* **2**, 880–884 (2011).

25. Portius, P. *et al.* Unraveling the photochemistry of $\text{Fe}(\text{CO})_5$ in solution: observation of $\text{Fe}(\text{CO})_3$ and the conversion between $^3\text{Fe}(\text{CO})_4$ and $^1\text{Fe}(\text{CO})_4$ (solvent). *J. Am. Chem. Soc.* **126**, 10713–10720 (2004).
26. Joly, A. G. & Nelson, K. A. Metal carbonyl photochemistry in organic solvents: femtosecond transient absorption and preliminary resonance Raman spectroscopy. *Chem. Phys.* **152**, 69–82 (1991).
27. Fukui, K. The role of frontier orbitals in chemical reactions. *Angew. Chem. Int. Edn Engl.* **21**, 801–809 (1982).
28. Lim, M., Jackson, T. A. & Anfinsen, P. A. Binding of CO to myoglobin from a heme pocket docking site to form nearly linear Fe–C–O. *Science* **269**, 962–966 (1995).
29. Nibbering, E. T. J., Fidler, H. & Pines, E. Ultrafast chemistry: using time-resolved vibrational spectroscopy for interrogation of structural dynamics. *Annu. Rev. Phys. Chem.* **56**, 338–367 (2005).
30. Greaves, S. J. *et al.* Vibrationally quantum-state-specific reaction dynamics of H atom abstraction by CN radical in solution. *Science* **331**, 1423–1426 (2011).

Supplementary Information is available in the online version of the paper.

Acknowledgements This work was supported by the Volkswagen Stiftung (M.B.) the Swedish Research Council (M.O.), the Carl Tryggers Foundation (M.O.), the Magnus Bergvall Foundation (M.O.), the Collaborative Research Centers SFB 755 and SFB 1073 (I.R., S.G., W.Q., M.S. and S.T.) and the Helmholtz Virtual Institute ‘Dynamic Pathways in

Multidimensional Landscapes’. W.Z., R.W.H. and K.J.G. acknowledge support through the AMOS program within the Chemical Sciences, Geosciences, and Biosciences Division of the Office of Basic Energy Sciences, Office of Science, US Department of Energy. Portions of this research were performed on the Soft X-ray Materials Science (SXR) Instrument at the Linac Coherent Light Source (LCLS), a division of SLAC National Accelerator Laboratory and an Office of Science user facility operated by Stanford University for the US Department of Energy. The SXR Instrument is funded by a consortium whose membership includes the LCLS, Stanford University through the Stanford Institute for Materials Energy Sciences (SIMES), Lawrence Berkeley National Laboratory (LBNL), the University of Hamburg through the BMBF priority program FSP 301, and the Center for Free Electron Laser Science (CFEL).

Author Contributions Ph.W., K.K., I.R., W.Q., M.B., S.S., D.N., W.F.S., J.J.T., F.H., S.T. and A.F. designed the experiment. Ph.W., K.K., I.R., W.Q., M.B., S.S., S.G., M.S., D.N., W.Z., R.W.H., W.F.S., J.J.T., B.K., F.H., K.J.G., S.T. and A.F. did the experiment. K.K., Ph.W., M.B. and A.F. analysed the experimental data. I.J., K.K. and M.O. performed the calculations. Ph.W., K.K. and K.J.G. wrote the manuscript with input from all authors.

Author Information Reprints and permissions information is available at www.nature.com/reprints. The authors declare no competing financial interests. Readers are welcome to comment on the online version of the paper. Correspondence and requests for materials should be addressed to Ph.W. (wernet@helmholtz-berlin.de), M.O. (odelius@fysik.su.se) or A.F. (alexander.foehlich@helmholtz-berlin.de).

Osteichthyan-like cranial conditions in an Early Devonian stem gnathostome

Sam Giles¹, Matt Friedman¹ & Martin D. Brazeau^{2,3}

The phylogeny of Silurian and Devonian (443–358 million years (Myr) ago) fishes remains the foremost problem in the study of the origin of modern gnathostomes (jawed vertebrates). A central question concerns the morphology of the last common ancestor of living jawed vertebrates, with competing hypotheses advancing either a chondrichthyan^{1–3} or osteichthyan-like^{4,5} model. Here we present *Janusiscus schultzei* gen. et sp. nov., an Early Devonian (approximately 415 Myr ago) gnathostome from Siberia previously interpreted as a ray-finned fish⁶, which provides important new information about cranial anatomy near the last common ancestor of chondrichthyans and osteichthyans. The skull roof of *Janusiscus* resembles that of early osteichthyans, with large plates bearing vermiform ridges and partially enclosed sensory canals. High-resolution computed tomography (CT) reveals a braincase bearing characters typically associated with either chondrichthyans (large hypophyseal opening accommodating the internal carotid arteries) or osteichthyans (facial nerve exiting through jugular canal, endolymphatic ducts exiting posterior to the skull roof) but lacking a ventral cranial fissure, the presence of which is considered a derived feature of crown gnathostomes^{7,8}. A conjunction of well-developed cranial processes in *Janusiscus* helps unify the comparative anatomy of early jawed vertebrate neurocrania, clarifying primary homologies in ‘placoderms’, osteichthyans and chondrichthyans. Phylogenetic analysis further supports the chondrichthyan affinities of ‘acanthodians’, and places *Janusiscus* and the enigmatic *Ramiroisuaresia*⁹ in a polytomy with crown gnathostomes. The close correspondence between the skull roof of *Janusiscus* and that of osteichthyans suggests that an extensive dermal skeleton was present in the last common ancestor of jawed vertebrates⁴, but ambiguities arise from uncertainties in the anatomy of *Ramiroisuaresia*. The unexpected contrast between endoskeletal structure in *Janusiscus* and its superficially osteichthyan-like dermal skeleton highlights the potential importance of other incompletely known Siluro-Devonian ‘bony fishes’ for reconstructing patterns of trait evolution near the origin of modern gnathostomes.

Gnathostomata Gegenbaur, 1874

Janusiscus schultzei gen. et sp. nov.

Etymology. Generic name refers to double-sided nature of the specimen, with an osteichthyan-like dorsal skull roof, but a braincase that displays an array of plesiomorphic gnathostome characters (Latin *Ianus*, the god of doorways and transitions, often depicted as having two faces; [*p*] *iscis*, fish). Specific name in honour of Hans-Peter Schultze (University of Kansas), who first described these specimens⁶.

Holotype. GIT (Institute of Geology, Tallinn, Estonia) 496-6 (Pi.1384), skull roof and braincase, both missing anterior region (Fig. 1 and Extended Data Figs 1a, 3).

Referred material. We refer a second, more complete skull roof (GIT 496-7 (Pi. 1383); Extended Data Fig. 1c) from the type locality to *Janusiscus*. Rhombic scales lacking clear dorsal pegs are also known from this deposit (GIT 496-8–496-16; Extended Data Fig. 2a–c), but cannot be definitively associated with cranial material. All of these remains were previously

attributed⁶ to *Dialipina markae*, the type of which is an isolated scale bearing a modest peg from the Lower Devonian of Kotelnny Island, New Siberian Islands¹⁰ (approximately 1,500 km from the Sida River site).

Locality and horizon. Lower member, Kureika Formation, Sida River, Kotui Basin, Siberia. The presence of the zone fossil *Rhinopteraspis crouchi* in a lateral equivalent of the Kureika Formation¹¹ restricts the age of this deposit to middle Lochkovian (approximately 415 Myr ago)¹². This is consistent with evidence drawn from other biostratigraphic markers (Supplementary Notes).

Diagnosis. A jawed vertebrate characterized by a rectilinear pattern of skull roof bones bearing vermiform ridges but lacking endochondral bone, a ventral cranial fissure and vestibular fontanelles. Skull roof differs from those attributed to the type species of *Dialipina* (*Dialipina salgueiroensis*)¹³ in having postparietals longer than parietals, and parietals lacking anterolateral extensions. Principal autapomorphy of *Janusiscus* is a boundary between parietals and postparietals that slopes posteriorly towards the midline, with the postparietals forming distinct anterolateral processes (as per the original description⁶). Braincase with broad otic region, and narrow sphenoid pierced by large hypophyseal opening and bearing pronounced ventrolateral ridges.

Description. The skull roof comprises paired parietals and postparietals, and a median pineal plate (Fig. 1a and Extended Data Fig. 1). The anterior part of the skull roof, including the pineal, is not preserved in the holotype. All bones are ornamented with vermiform ridges, although the histological structure of these ridges is not preserved (Extended Data Fig. 2h–j). The supraorbital sensory canals extend across the parietals and postparietals in open grooves but are enclosed in bony tubes posteriorly (Extended Data Fig. 3). The postparietal bears a middle pit-line behind the termination of the supraorbital canal. The pattern of dermal ornament in the posterior part of the skull suggests the presence of posteriorly placed pitlines (as in ‘*Ligulalepis*’¹⁴).

High-resolution CT scanning of GIT 496-6 reveals a nearly complete perichondrally ossified neurocranium, lacking evidence of endochondral mineralization (Fig. 1 and Extended Data Figs 4, 5). The incompletely preserved ethmoid is co-mineralized with the remainder of the braincase. The basisphenoid is elongate and mediolaterally narrow, resembling conditions in *Acanthodes*³ and osteichthyans^{15,16}. The basisphenoid bears a large, diamond-shaped hypophyseal opening but no evidence of a parasphenoid. Subcranial ridges like those of *Doliodus*¹⁷ define the lateral margins of the basisphenoid and extend posteriorly to the otic region (Extended Data Fig. 5). The modest basiptyergoid processes emerge as slight flanges posterior to the level of the hypophysis. Like ‘placoderms’^{18,19} and many chondrichthyans^{20,21}, *Janusiscus* lacks a ventral cranial fissure. The gently concave parachordal region tapers towards the occiput, where its edges form ventral cristae that border grooves for the lateral dorsal aortae. The occipital margin bears a notch that is aligned with a midline thickening of the parachordal surface.

Two prominent transverse processes are present (Fig. 1a, b). The postorbital process defines the rear margin of the orbit. The passage of the jugular vein through the postorbital process is unclear. It bears a ventral notch and a posterodorsal opening, either of which may have

¹Department of Earth Sciences, University of Oxford, South Parks Road, Oxford, OX1 3AN, UK. ²Naturalis Biodiversity Center, P.O. Box 9517, 2300 RA Leiden, the Netherlands. ³Department of Life Sciences, Imperial College London, Silwood Park Campus, Buckhurst Road, Ascot SL5 7PY, UK.

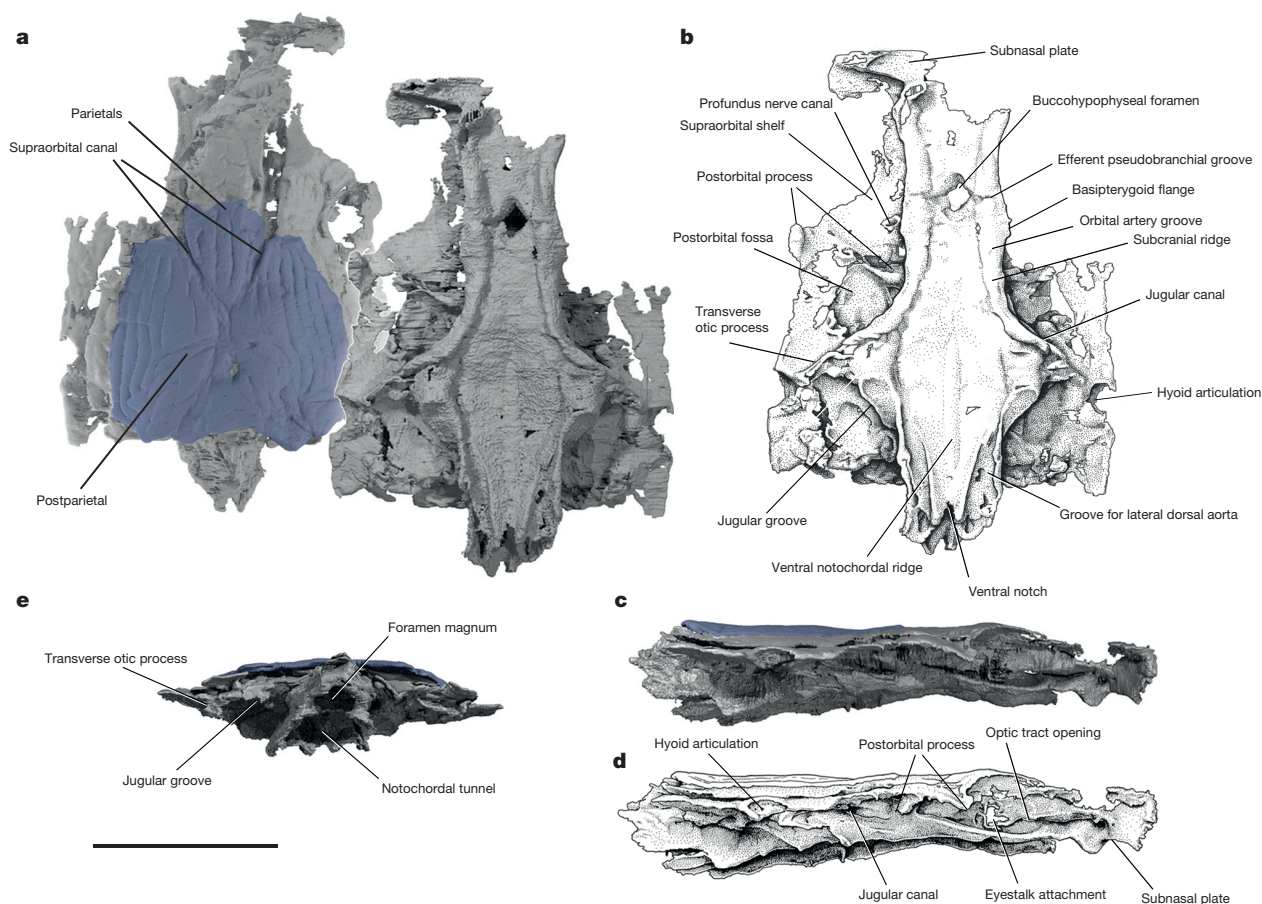


Figure 1 | The skull of *Janusiscus schultzei* gen. et sp. nov. based on high-resolution CT of GIT 496-6 (Pi.1384). **a**, Dorsal (left) and ventral views. **b**, Interpretive drawing of ventral view. **c**, Right lateral view. **d**, Interpretive drawing of right lateral view. **e**, Posterior view. Scale bar, 5 mm.

accommodated the jugular vein. The transverse otic process is separated from the postorbital process by a wide postorbital fossa. This process terminates distally in a single hyomandibular facet, and is pierced by the jugular canal. An enclosed canal for the hyomandibular branch of the facial nerve intersects that of the jugular (Extended Data Fig. 3).

The suborbital and supraorbital shelves are well developed. The orbital wall is interrupted by a large eyestalk attachment with a raised posteroventral rim (Fig. 1c, d and Extended Data Fig. 6c–e). The optic nerve exited through a foramen anterior to the eyestalk area. Foramina for the oculomotor, profundus and abducens nerves, along with associated myodomes, are present along an arc in the rear of the orbit (Extended Data Fig. 6).

The otic capsules are broad, protruding well beyond the lateral margins of the basicranium (Extended Data Fig. 3). Paired endolymphatic ducts emerge from the roof of the braincase immediately posterior to the skull roof (Extended Data Figs 2j and 3). Vestibular fontanelles are absent, but the condition of the metotic fissure is unclear. The narrow occipital region extends well behind the otic capsules. A mineralized shelf separates the cavum cranii from the notochordal canal (Fig. 1e).

Janusiscus presents an unexpected suite of osteichthyan, chondrichthyan and generalized gnathostome traits. A rectilinear pattern of skull roof bones bearing vermiform ornament, partially buried sensory canals, endolymphatic ducts opening posterior to the dermal skull roof, and the exit of the hyomandibular branch of the facial nerve into the jugular canal are features typically associated with osteichthyans^{22,23}. However, the combination of a flat-based braincase, weakly developed basipterygoid processes, the absence of vestibular fontanelles, and the absence of a ventral cranial fissure are inconsistent with *Janusiscus* as a crown-group osteichthyan and therefore also with the original actinopterygian

diagnosis⁶ and its current use as a fossil calibration in ray-finned fish molecular clocks²⁴.

Janusiscus possesses some chondrichthyan-like features, including the absence of paired openings for the internal carotids, a condition also shared with *Acanthodes*. Instead, the internal carotids entered the braincase through the large hypophyseal opening. The subcranial ridges flanking the ventrolateral angle of the braincase in *Janusiscus* strongly resemble those in the early chondrichthyan *Doliodus*¹⁷.

At least four pairs of transverse cranial processes are present on the braincases of some early gnathostomes (Supplementary Notes, Fig. 2 and Extended Data Fig. 7). The prominent transverse walls in *Janusiscus* allow us to address the primary homology of the anterior two processes. Comparison with crown-group osteichthyans and placoderms reveals that the so-called ‘supraorbital process’ of arthrodires corresponds to the postorbital process of crown-group gnathostomes (including the postorbital pila of sarcopterygians²⁵) and the postorbital pila of *Entelognathus*⁴. The ‘anterior postorbital process’ of placoderms can be homologized with the transverse otic process of osteichthyans. The transverse otic process appears to be substantially reduced or lost in *Acanthodes*³ and the earliest chondrichthyans^{7,8,17}, although it may correspond to the prominent lateral otic process of later chondrichthyans such as *Orthacanthus* and *Tamiodontis* (Extended Data Fig. 7). This further corroborates recent anatomical reinterpretations of *Acanthodes*³ and its placement in the chondrichthyan total group^{4,5}.

Phylogenetic analysis recovers *Janusiscus* in a polytomy with *Ramirosoarezia* and the gnathostome crown. This corroborates our removal of the Siberian material from the genus *Dialipina*, which we recover as a stem osteichthyan^{2–5}. Our result provides the first analytical placement for the enigmatic *Ramirosoarezia*, which has previously been

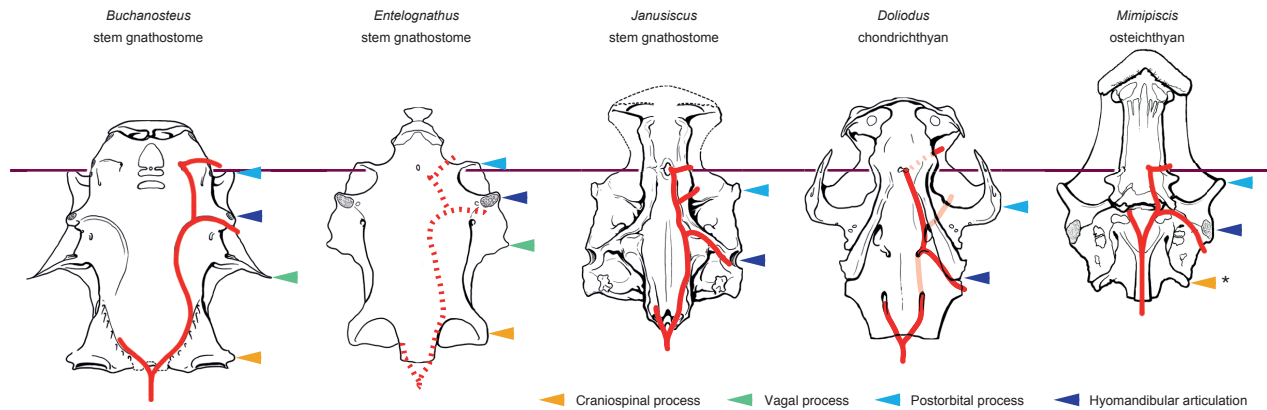


Figure 2 | Comparative braincase morphology of selected Palaeozoic gnathostomes. Braincases are aligned on the hypophyseal opening, the position of which is indicated by the horizontal purple line. The path of the major cranial blood vessels is shown in red, with inferred paths represented by

compared with ‘placoderm’-grade stem gnathostomes^{9,26} and holocephalan chondrichthyans⁹.

Although our analysis favours the stem gnathostome hypothesis for *Janusiscus*, we consider stem chondrichthyan and stem osteichthyan placements to be reasonable alternatives: both require only one additional step. Placement of *Janusiscus* on the chondrichthyan stem may seem provocative, but the hypothesis of micromery as a derived chondrichthyan trait predicts macromeric stem chondrichthyans. While there is ambiguity in the position of *Janusiscus* relative to the three branches incident to the gnathostome crown node, we reject an actinopterygian interpretation⁶, which requires seven additional steps.

The new anatomical details of *Janusiscus* and our phylogenetic result corroborate the recently revived hypothesis that ‘acanthodians’ are, in fact, total-group chondrichthyans. The osteichthyan-like skull roof of *Janusiscus* strongly implies that the continuous dermal armour common to ‘placoderms’ and bony fishes is a gnathostome symplesiomorphy^{4,5}. However, uncertainty about conditions of the exoskeleton in *Ramiro-suarezia* precludes more definitive statements about the nature of the

dotted lines. Character distributions reject the homology of craniospinal processes in ‘placoderms’ and actinopterygians. Illustrations are redrawn with permission from refs 4, 16, 17 (Wiley), 29 (Wiley).

dermal skeleton in the earliest crown gnathostomes. We find that chondrichthyans (including all ‘acanthodians’) and osteichthyans are united to the exclusion of *Janusiscus* by the presence of a ventral cranial fissure separating the otic and sphenoid regions of the braincase (Fig. 3). The revised comparative framework for gnathostome braincases provided by *Janusiscus* highlights substantial neurocranial modifications uniting total-group chondrichthyans (for example, loss of the jugular vein canal in the otic region, hyomandibular articulation at the level of the posterior semicircular canal; Fig. 3)²³, while casting doubt on the validity of some supposed osteichthyan synapomorphies (for example, exit of the hyomandibular branch of the facial nerve through the jugular canal; Extended Data Fig. 3).

This work reinforces an emerging consensus for osteichthyan-like anatomical conditions in stem gnathostomes and also in the last common ancestor of crown-group gnathostomes^{4,5}. The recognition that many features of the bony fish dermal skeleton might be general traits of modern jawed vertebrates highlights the need to revisit the roughly half-dozen supposed stem osteichthyans known only from isolated

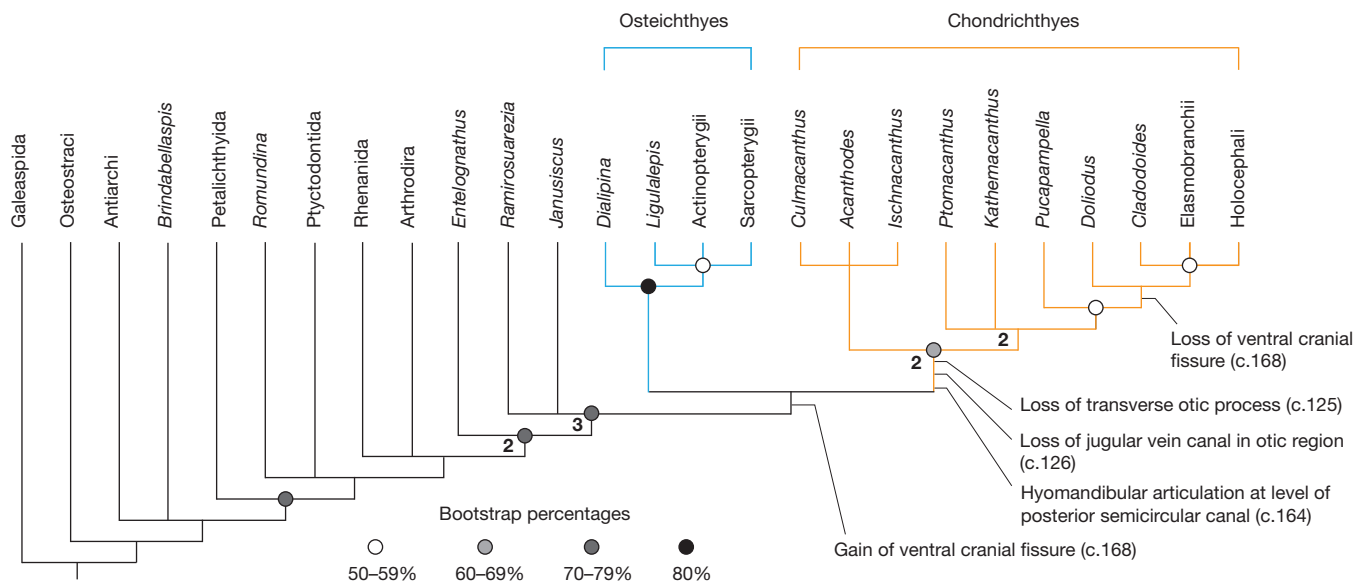


Figure 3 | Summary result of phylogenetic analyses. Some clades are collapsed or omitted for simplicity. Shaded disks represent ranges of bootstrap support, numbers at nodes are decay indices. Numbers refer to characters in

character list (Supplementary Notes). Full cladograms are provided in Extended Data Figs 8, 9 and Supplementary Fig. 1.

dermal fragments^{22,27,28}. Notably, our results suggest the plausibility of alternative placements for some of these taxa as either stem gnathostomes or even stem chondrichthyans.

Online Content Methods, along with any additional Extended Data display items and Source Data, are available in the online version of the paper; references unique to these sections appear only in the online paper.

Received 10 March; accepted 11 November 2014.

Published online 12 January 2015.

- Miles, R. S. in *Interrelationships of Fishes* (eds Greenwood, P. H., Miles, R. S. & Patterson, C.) 63–103 (Academic, 1973).
- Brazeau, M. D. The braincase and jaws of a Devonian ‘acanthodian’ and modern gnathostome origins. *Nature* **457**, 305–308 (2009).
- Davis, S. P., Finarelli, J. A. & Coates, M. I. Acanthodes and shark-like conditions in the last common ancestor of modern gnathostomes. *Nature* **486**, 247–250 (2012).
- Zhu, M. *et al.* A Silurian placoderm with osteichthyan-like marginal jaw bones. *Nature* **502**, 188–193 (2013).
- Dupret, V., Sanchez, S., Goujet, D., Tafforeau, P. & Ahlberg, P. E. A primitive placoderm sheds light on the origin of the jawed vertebrate face. *Nature* **507**, 500–503 (2014).
- Schultze, H.-P. in *Fossil Fishes as Living Animals* (ed. Mark-Kurik, E.) 233–242 (Academy of Sciences of Estonia, 1992).
- Maisey, J. G. in *Major Events in Early Vertebrate Evolution* (ed. Ahlberg, P. E.) 263–288 (Taylor & Francis, 2001).
- Maisey, J. G. & Anderson, M. E. A primitive chondrichthyan braincase from the Early Devonian of South Africa. *J. Vertebr. Paleontol.* **21**, 702–713 (2001).
- Pradel, A., Maisey, J. G., Tafforeau, P. & Janvier, P. An enigmatic gnathostome vertebrate skull from the Middle Devonian of Bolivia. *Acta Zoologica* **90**, 123–133 (2009).
- Schultze, H.-P. Ausgangsform und Entwicklung der rhombischen Schuppen der Osteichthyes (Pisces). *Paläontol. Z.* **51**, 152–168 (1977).
- Blieck, A. & Janvier, P. in *Palaeozoic Vertebrate Biostratigraphy and Biogeography* (ed. Long, J. A.) 87–103 (Belhaven, 1993).
- Gradstein, F. M., Ogg, J. G., Schmitz, M. & Ogg, G. *The Geologic Time Scale 2012* (Elsevier, 2012).
- Schultze, H.-P. & Cumbaa, S. L. in *Major Events in Early Vertebrate Evolution* (ed. Ahlberg, P. E.) 315–332 (Taylor & Francis, 2001).
- Basden, A. M. & Young, G. C. A primitive actinopterygian neurocranium from the Early Devonian of Southeastern Australia. *J. Vertebr. Paleontol.* **21**, 754–766 (2001).
- Jarvik, E. *Basic Structure and Evolution of Vertebrates* (Academic, 1980).
- Gardiner, B. G. The relationships of the palaeoniscid fishes, a review based on new specimens of *Mimia* and *Moythomasia* from the Upper Devonian of Western Australia. *Bull. Br. Mus. Nat. Hist.* **37**, 173–428 (1984).
- Maisey, J. G., Miller, R. & Turner, S. The braincase of the chondrichthyan *Doliodus* from the Lower Devonian Campbellton Formation of New Brunswick, Canada. *Acta Zoologica* **90** (suppl. 1), 109–122 (2009).
- Stensiö, E. Anatomical studies on the arthrodiran head, part I. *Kungl. Svensk. Vetensk. Handl.* **9**, 1–419 (1963).
- Goujet, D. *Les Poissons Placodermes du Spitsberg* (Centre National de la Recherche Scientifique, 1984).
- Schaeffer, B. The xenacanth shark neurocranium, with comments on elasmobranch monophyly. *Bull. Am. Mus. Nat. Hist.* **169**, 1–66 (1981).
- Maisey, J. G. Braincase of the Upper Devonian shark *Cladodoides wildungensis* (Chondrichthyes, Elasmobranchii), with observations on the braincase in early chondrichthyans. *Bull. Am. Mus. Nat. Hist.* **288**, 1–103 (2005).
- Friedman, M. & Brazeau, M. D. A reappraisal of the origin and basal radiation of the Osteichthyes. *J. Vertebr. Paleontol.* **30**, 36–56 (2010).
- Brazeau, M. D. & Friedman, M. The characters of Palaeozoic jawed vertebrates. *Zool. J. Linn. Soc.* **170**, 779–821 (2014).
- Broughton, R. B.-R., Li, C., Arratia, G., Orti, G. & Richard, E. Multi-locus phylogenetic analysis reveals the pattern and tempo of bony fish evolution. *PLoS Curr.* <http://dx.doi.org/10.1371/currents.tol.2ca8041495ffafdc92756e75247483e> (2013).
- Yu, X.-B. A new porolepiform-like fish, *Psarolepis romeri*, gen. et sp. nov. (Sarcopterygii, Osteichthyes) from the Lower Devonian of Yunnan, China. *J. Vertebr. Paleontol.* **18**, 261–274 (1998).
- Anderson, P. S. L., Friedman, M., Brazeau, M. D. & Rayfield, E. J. Initial radiation of jaws demonstrated stability despite faunal and environmental change. *Nature* **476**, 206–209 (2011).
- Botella, H., Blom, H., Dorka, M., Ahlberg, P. E. & Janvier, P. Jaws and teeth of the earliest bony fishes. *Nature* **448**, 583–586 (2007).
- Cunningham, J. A., Rucklin, M., Blom, H., Botella, H. & Donoghue, P. C. J. Testing models of dental development in the earliest bony vertebrates, *Andreolepis* and *Lophosteus*. *Biol. Lett.* **8**, 833–837 (2012).
- Young, G. C. New information on the structure and relationships of *Buchanosteus* (Placodermi: Euarthrodira) from the Early Devonian of New South Wales. *Zool. J. Linn. Soc.* **66**, 309–352 (1979).

Supplementary Information is available in the online version of the paper.

Acknowledgements We thank U. Toom for access to material, E. Mark-Kurik for discussions on stratigraphy and specimen provenance, W. Renema and R. Garwood for assistance with scanning. This work was supported by a Natural Environment Research Council Cohort NE/J500045/1 grant to S.G., the Philip Leverhulme Prize and John Fell Fund, both to M.F., and the European Research Council (ERC) under the European Union's Seventh Framework Programme (FP/2007-2013)/ERC Grant Agreement number 311092 to M.D.B.

Author Contributions The project was conceived by M.D.B. and M.F. CT scanning was conducted by M.F. and M.D.B. S.G. generated the CT renderings. Figs 1–3 were produced by M.D.B. and S.G. with input from M.F. All authors participated in the generation of phylogenetic data. M.D.B. conducted the phylogenetic analyses. All authors participated in the interpretation of the specimen data and writing the manuscript, and generating Extended Data Figs 1–9, Supplementary Fig. 1 and Supplementary Notes.

Author Information The Life Science Identifiers (LSIDs) [urn:lsid:zoobank.org:pub:CFD16449-8A34-4401-9E01-289EA91C2C77](http://zoobank.org/pub:CFD16449-8A34-4401-9E01-289EA91C2C77) (article), [urn:lsid:zoobank.org:act:652A7405-164B-4D58-B5AF-F21EDF552303](http://zoobank.org/act:652A7405-164B-4D58-B5AF-F21EDF552303) (genus), and [urn:lsid:zoobank.org:act:3BD31DC4-11E1-4510-A185-B295CC626C07](http://zoobank.org/act:3BD31DC4-11E1-4510-A185-B295CC626C07) (species) have been deposited in ZooBank. Reprints and permissions information is available at www.nature.com/reprints. The authors declare no competing financial interests. Readers are welcome to comment on the online version of the paper. Correspondence and requests for materials should be addressed to M.D.B. (m.brazeau@imperial.ac.uk).

METHODS

X-ray computed microtomography. GIT 496-6 was scanned using a SkyScan 1172, combining two vertically overlapping scan series of 7,200 projections with an energy of 100 kV and 100 μ A and 4.75 s exposure. Scan data were analysed using Mimics (<http://biomedical.materialise.com/mimics>; Materialise). After segmenting, surface meshes were exported into and imaged in Blender (<http://blender.org>; Stitching Blender Foundation).

Phylogenetic analysis. Phylogenetic analysis was performed in PAUP* v.4.0b10 (ref. 30) using a data set with 236 characters (three of which were ordered: 64, 126 and 166) and 78 taxa. The data set is based on ref. 3. In addition to a number of coding changes, one highly incomplete taxon (*Rhadinacanthus*) and four characters were deleted from the matrix of ref. 3; full justification for excluded characters is given in the character list. Additional characters were taken from a variety of sources, and are referenced in the character list. In addition to *Janusiscus* and taxa carried forward from the data set of ref. 3, we added 18 taxa spanning most taxonomic assemblages of Palaeozoic gnathostomes. In the case of *Janusiscus*, we coded as unknown any characters relating to scale morphology and histology; the Siberian scales originally referred to *D. markae* were not directly associated with the braincase, and their affinity is thus uncertain (for further details, see Supplementary Notes). We follow a similar convention with the braincase attributed to '*Ligulalepis*', and hence scale and histology characters are coded as uncertain. We assessed taxonomic equivalence³¹ using the software package TAXEQ3 (ref. 32). No taxa showed non-unique combinations of character states that would permit safe taxonomic reduction, so analyses were executed with a complete taxon set. Although several taxa are highly incomplete, we followed previous recommendations^{33,34} by maximizing the absolute number of characters instead of deleting incomplete or fragmentary taxa.

We conducted a heuristic search using 1,000 random addition sequence replicates, holding 5 trees at each step, and the tree bisection and reconnection (TBR) strategy. Maxtrees was set to automatically increase by 100. To prevent outgroup taxa from moving to the ingroup or collapsing of the ingroup node, we employed a rooted constraint tree, keeping only trees consistent with the following general topology: (Galeaspida(Osteostraci(Ingroup))).

Bootstrap values were calculated using 15,000 replicates of a heuristic search using random addition sequence, 10 replicates, holding 5 trees at each step, using the TBR strategy. To speed up the search, we set a limit of 20 million rearrangements per addition sequence replicate (options: rearrlimit = 20000000 limitperrep = yes in the hsearch command in PAUP*).

Node decay values (that is, Bremer support) were calculated manually using 20 random addition sequence replicates of a heuristic search, rearrlimit = 20000000, limitperrep = yes, and by incrementing the KEEP score by 1 over the length of the shortest tree found. Nodes retained in the strict consensus tree had their decay index incremented by one.

We conducted a set of further searches using the protocols outlined earlier with the following modifications. First, we conducted an equally weighted analysis minus *Janusiscus* to assess whether inferred patterns of relationships among early gnathostomes were robust to exclusion of the genus. To test whether the tree topology was sensitive to the removal of random taxa, we conducted an additional five searches each following the removal of a randomly selected terminal. Random selection was conducted using Microsoft Excel's RANDBETWEEN function with parameters set to 3 and 78 (we excepted the outgroup from random pruning) and used the first five results obtained to draw taxa from the list following their order in the Nexus

file. To speed up these searches, we used rearrlimit = 10000000 and limitperrep = yes. Finally, we reweighted all characters by their retention indices in the shortest trees recovered by our initial analysis that applied equal character weights.

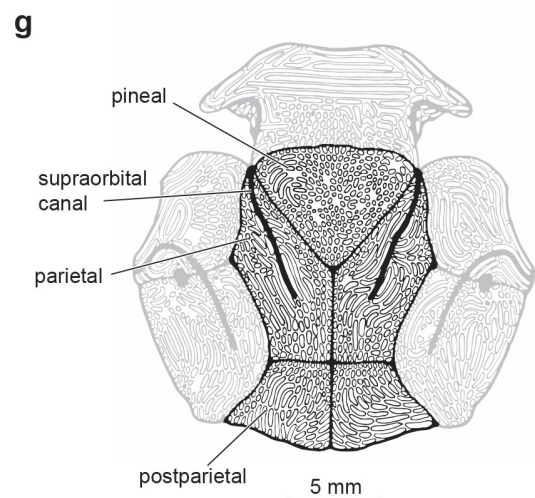
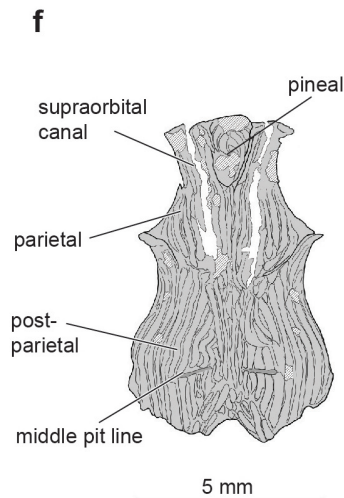
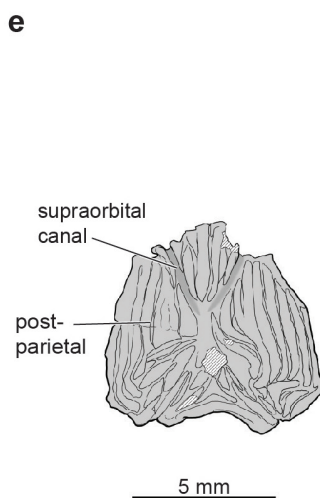
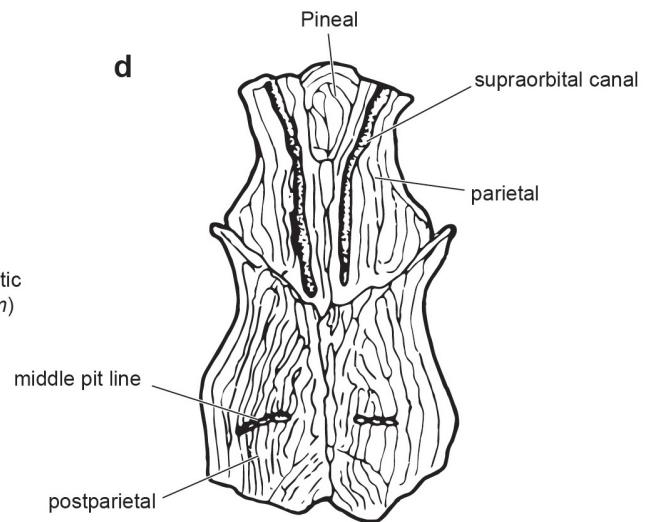
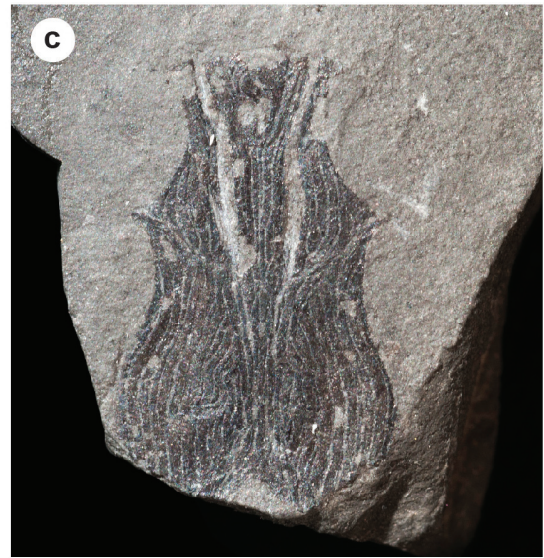
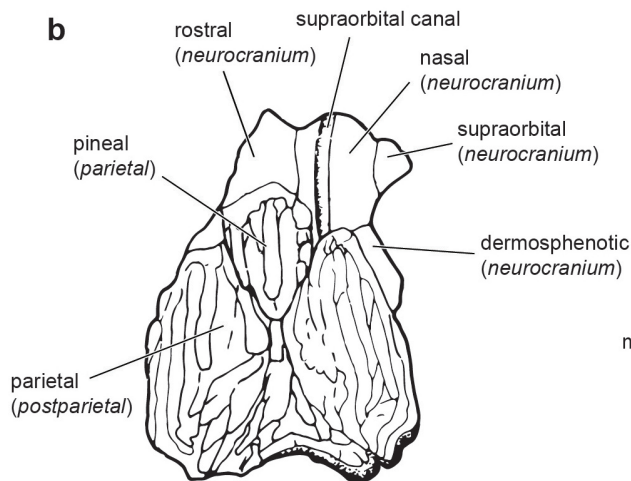
Phylogenetic results. The phylogenetic search resulted in 522,936 trees of 639 steps. A summary strict consensus tree with some clades omitted or collapsed is shown in Fig. 3. The complete result is shown in Extended Data Fig. 8a. The Adams consensus tree is shown in Extended Data Fig. 8b. All unambiguous character state transformations are shown in Supplementary Fig. 1. A summary strict consensus tree of an analysis of the data set with characters reweighted by retention index is shown in Extended Data Fig. 9a. It preserves all major branching patterns found in the analysis of equally weighted characters, but shows greater resolution within some clades.

Inferred interrelationships are not changed when *Janusiscus* is removed from the analysis (Extended Data Fig. 9b), as its influence on how cranial processes are recognized and coded pervades large parts of the data set. The removal of an additional five taxa at random (*Cladoselache*, *Tristychius*, *Acanthodes*, *Kentuckia*, *Lupopsyrus*) each had no considerable impact on the overall tree topology, excepting differences in the degree of resolution.

The overall large number of trees results in polychotomous branchings primarily concentrated in the chondrichthyan stem compounded with a smaller number of polychotomous branchings in the gnathostome and osteichthyan stems. The Adams consensus shows two principal branching patterns that are consistent within the results. One is a clade of stem chondrichthyans comprising acanthodiforms, ischnacanthids, some diplacanthids, as well as *Latviacanthus* and *Euthacanthus*. The other branching consisted of most *Climatius*-like taxa and conventionally defined chondrichthyans (including the crown group).

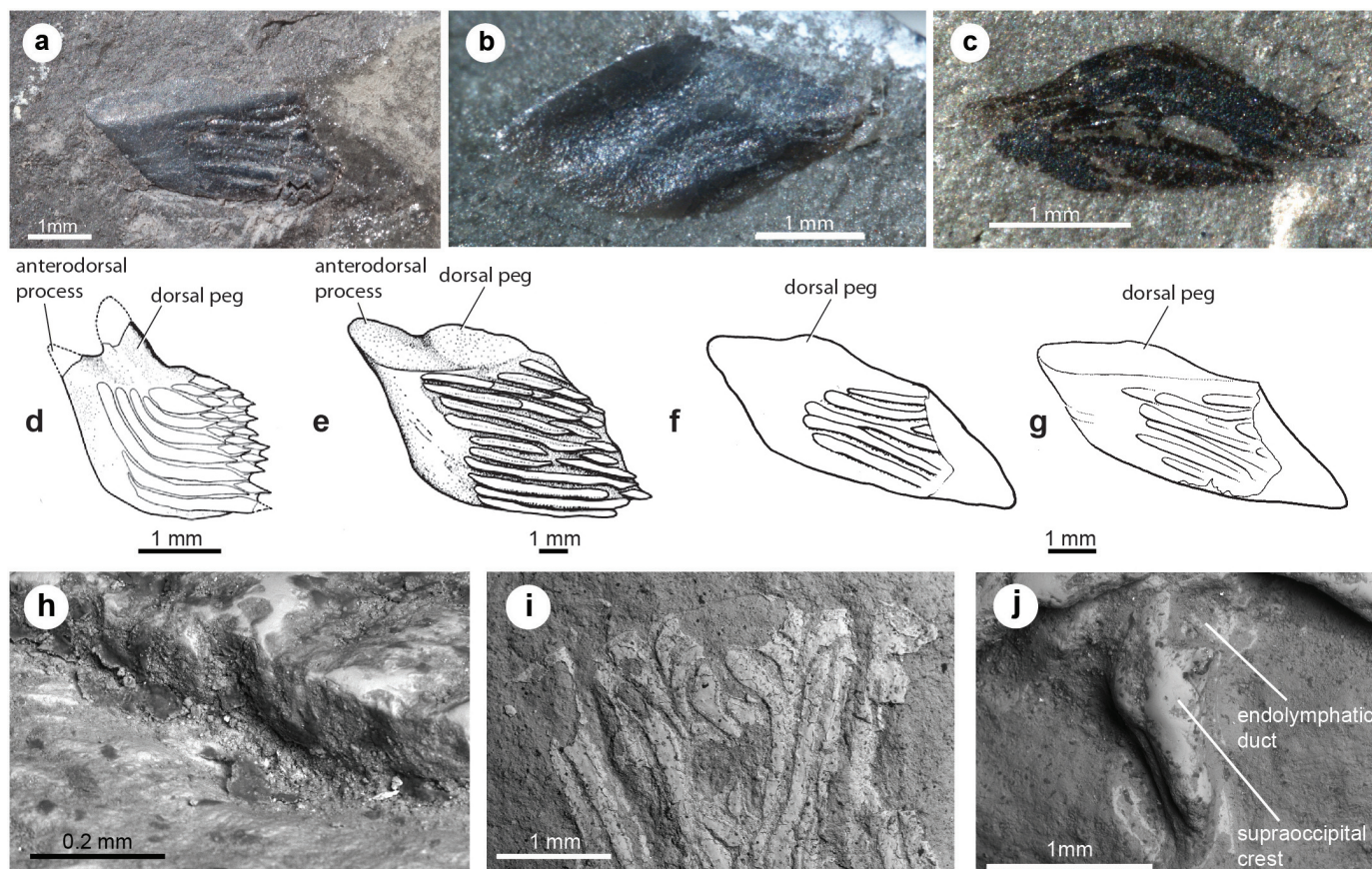
Support for key nodes is summarized in Fig. 3, with full details given Extended Data Fig. 8a. Unsurprisingly, most are quite low. The highest values are found within well-studied groups (for example, sarcopterygians and actinopterygians) or associated with clades with numerous specializations (for example, holocephalans, bothriolepidid antiarchs). A decay index of 2 and a bootstrap support of 68% are recovered for the clade comprising all chondrichthyans and acanthodians. A decay index greater than 1 is consistent with the very long branch subtending this clade (Supplementary Fig. 1). The low bootstrap value might be explained by the fact that more than half of the transformations along this branch are homoplasious and have a consistency index of 0.5 or less. In spite of this, the branch is supported by five invariant, unambiguous synapomorphies (see Supplementary Fig. 1).

30. Swofford, D. L. *PAUP*: Phylogenetic Analysis Using Parsimony (*And Other Methods)* v.4.0b 10 (Sinauer Associates, 2003).
31. Wilkinson, M. Coping with missing entries in phylogenetic inference using parsimony. *Syst. Biol.* **44**, 501–514 (1995).
32. Wilkinson, M. *TAXEQ3: Software and Documentation* (Department of Zoology, Natural History Museum, 2001).
33. Wiens, J. J. Missing data, incomplete taxa, and phylogenetic accuracy. *Syst. Biol.* **52**, 528–538 (2003).
34. Wiens, J. J. Incomplete taxa, incomplete characters, and phylogenetic accuracy: is there a missing data problem? *J. Vertebr. Paleontol.* **23**, 297–310 (2003).
35. Long, J. A., Barwick, R. E. & Campbell, K. S. W. Osteology and functional morphology of the osteolepiform fish *Gogonasus andrewsae* Long, 1985, from the Upper Devonian Gogo Formation, Western Australia. *Rec. West. Austral. Mus.* **53**, 1–89 (1997).



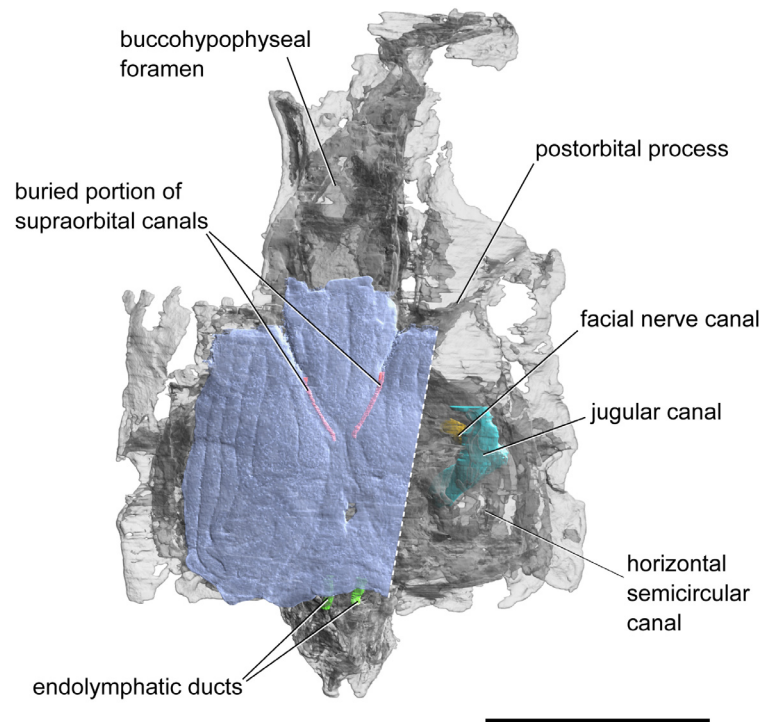
Extended Data Figure 1 | Dermal skull roofing bones of *Janusiscus* and *Dialipina salgueiroensis*. **a**, Photograph of the holotype (GIT 496-6 (Pi.1384)). **b**, Original interpretation modified with permission from ref. 6. Reinterpretation of bones italicized in brackets (where applicable). **c**, Photograph of the referred skull roof (GIT 496-7 (Pi.1383)). **d**, Original

interpretation modified with permission from ref. 6. **e**, New interpretive drawing of the holotype (GIT 496-6 (Pi.1384)). **f**, New interpretive drawing of the referred skull roof (GIT 496-7 (Pi.1383)). **g**, *Dialipina salgueiroensis*, modified with permission from ref. 13.

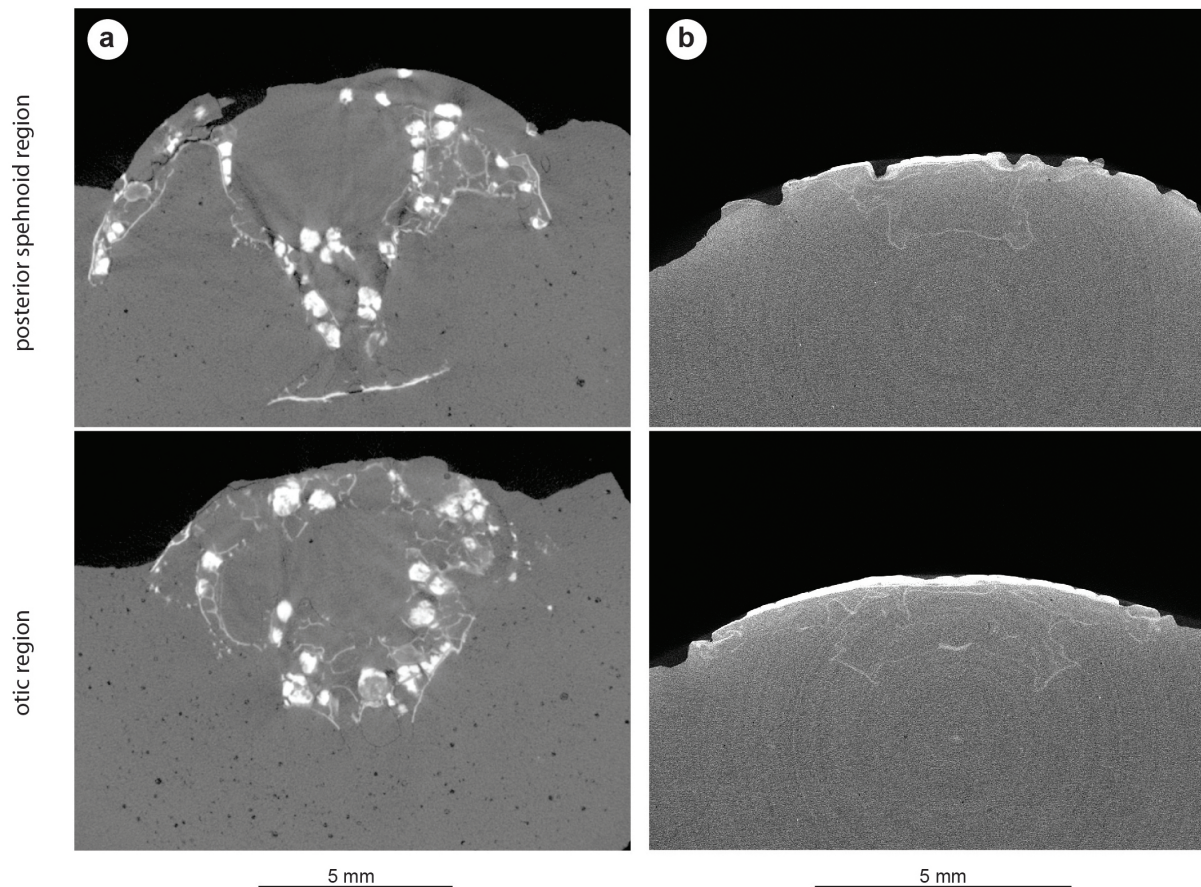


Extended Data Figure 2 | Scales attributed to *Dialipina* and scanning electron micrograph images of *Janusiscus schultzei* gen. et sp. nov. Scales from the localities of the Kureika Formation along the Sida River, Kotui Basin, Siberia, previously referred to *D. markae*, in: **a**, external view (GIT 496-8 (Pi.1384a)), previously figured by Schultze⁶ (plate 1, figure 3); **b**, internal view (GIT 496-10 (Pi.1385b)); **c**, external view (GIT 496-16 (Pi.1387)), ventral margin at upper right. **d**, **e**, Gross-scale morphology of *D. salgueiroensis* and referred species of *Dialipina*. **d**, Holotype of *D. salgueiroensis*, from the Emsian of Canada. Reproduced from ref. 10 (Fig. 3h) (with kind permission from Springer Science and Business Media). **e**, Holotype of *D. markae*, from the Lochkovian of the New Siberian Islands. Reproduced from ref. 10 (Fig. 3a) (with kind permission from Springer Science and Business Media). **f**, Scale from the Kureika Formation, Siberia, referred to *D. markae* and figured previously

(reproduced with permission from figure 4 in ref. 6). This scale is the same specimen as in **a**⁶. **g**, New interpretive drawing of scale in **a**. **h**, Broken edge of the skull roof in the holotype (GIT 496-6 (Pi.1384)). The histological structure is not preserved. **i**, The anterior part of the referred skull roof (GIT 496-7). The dermal bone is poorly preserved, with the bone in the centre of each ridge missing. The histological structure is not preserved. **j**, The holotype (GIT 496-6 (Pi.1384)) in dorsal view, showing the endoskeletal supraoccipital crest and openings of the endolymphatic ducts. Images in **a**, **b**, and **c** are modified slightly with permission from those by the Institute of Geology at Talinn University of Technology and licensed by CC 3.0 (http://geokogud.info/git/specimen_image/496/496-8.jpg; http://geokogud.info/git/specimen_image/496/496-10.jpg; http://geokogud.info/git/specimen_image/496/496-16.jpg).

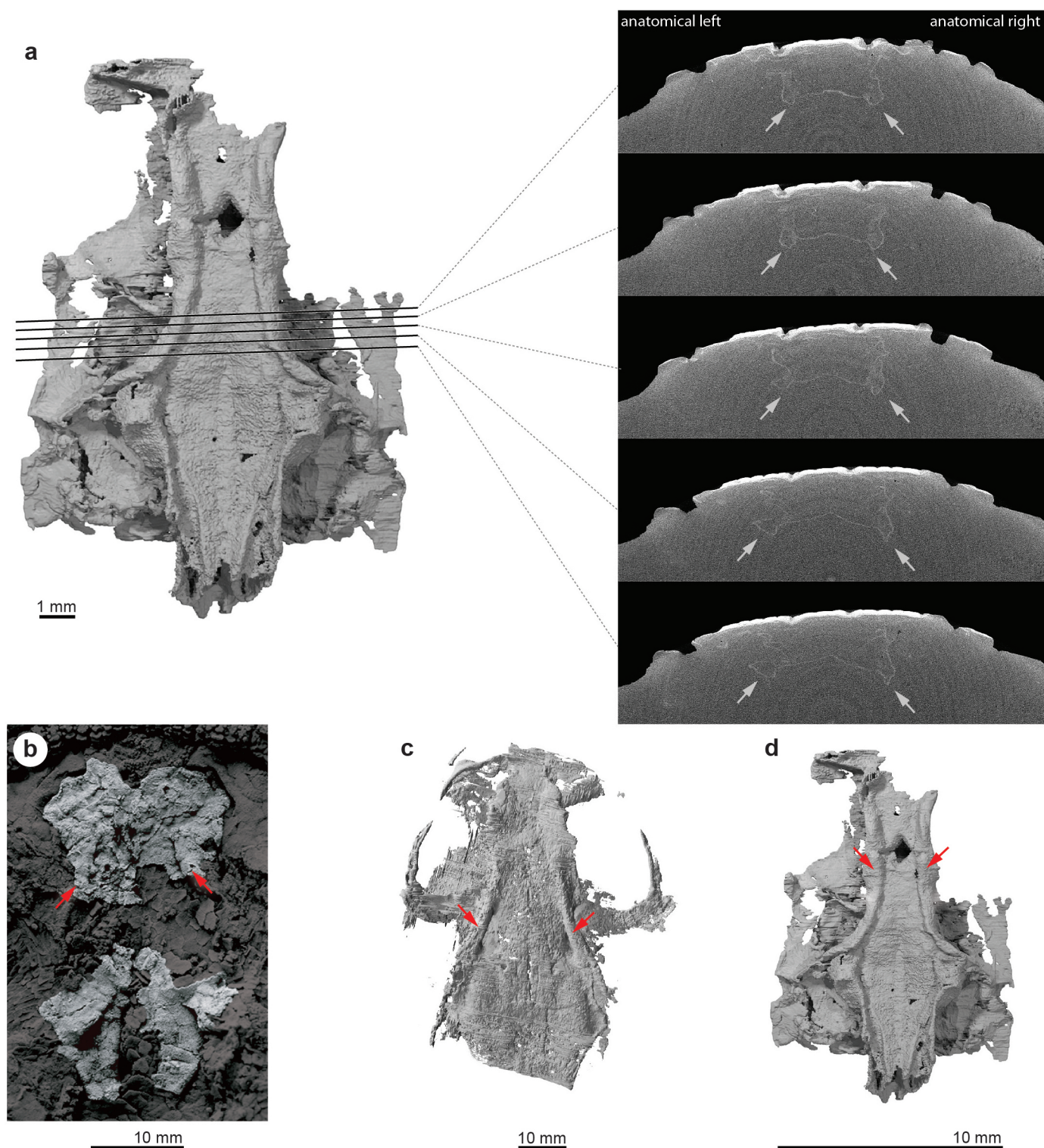


Extended Data Figure 3 | Semi-transparent rendering of the skull of *Janusiscus schultzei* gen. et sp. nov. showing osteichthyan-like traits not visible externally. Scale bar, 5 mm.



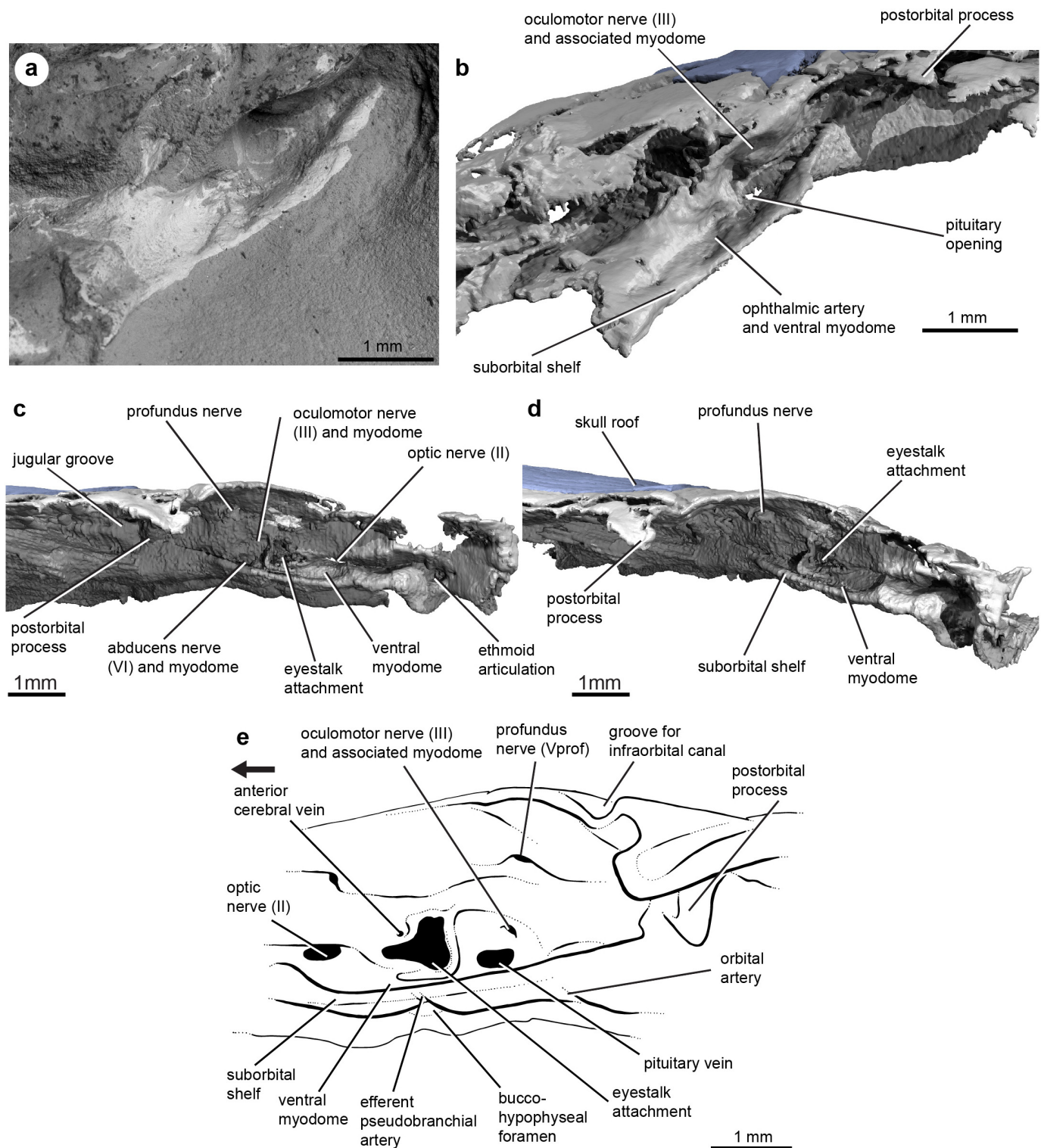
Extended Data Figure 4 | *Janusiscus* lacks endochondral ossification. **a**, The actinopterygian *Kentuckia deani* MCZ 5226; tomographs showing extensive and well-developed endochondral ossification in both the sphenoid (top) and otic (bottom) regions. Bright white objects are voids within spongy endochondral bone that have been diagenetically infilled with dense (probably

iron) minerals. **b**, *Janusiscus schultzei* gen. et sp. nov. GIT 496-6 (Pi.1384); tomographs showing lack of obvious endochondral ossification in either the sphenoid (top) or otic (bottom) regions. There is also no visual indication of endochondral bone in a break across the ethmoid region of this same specimen.



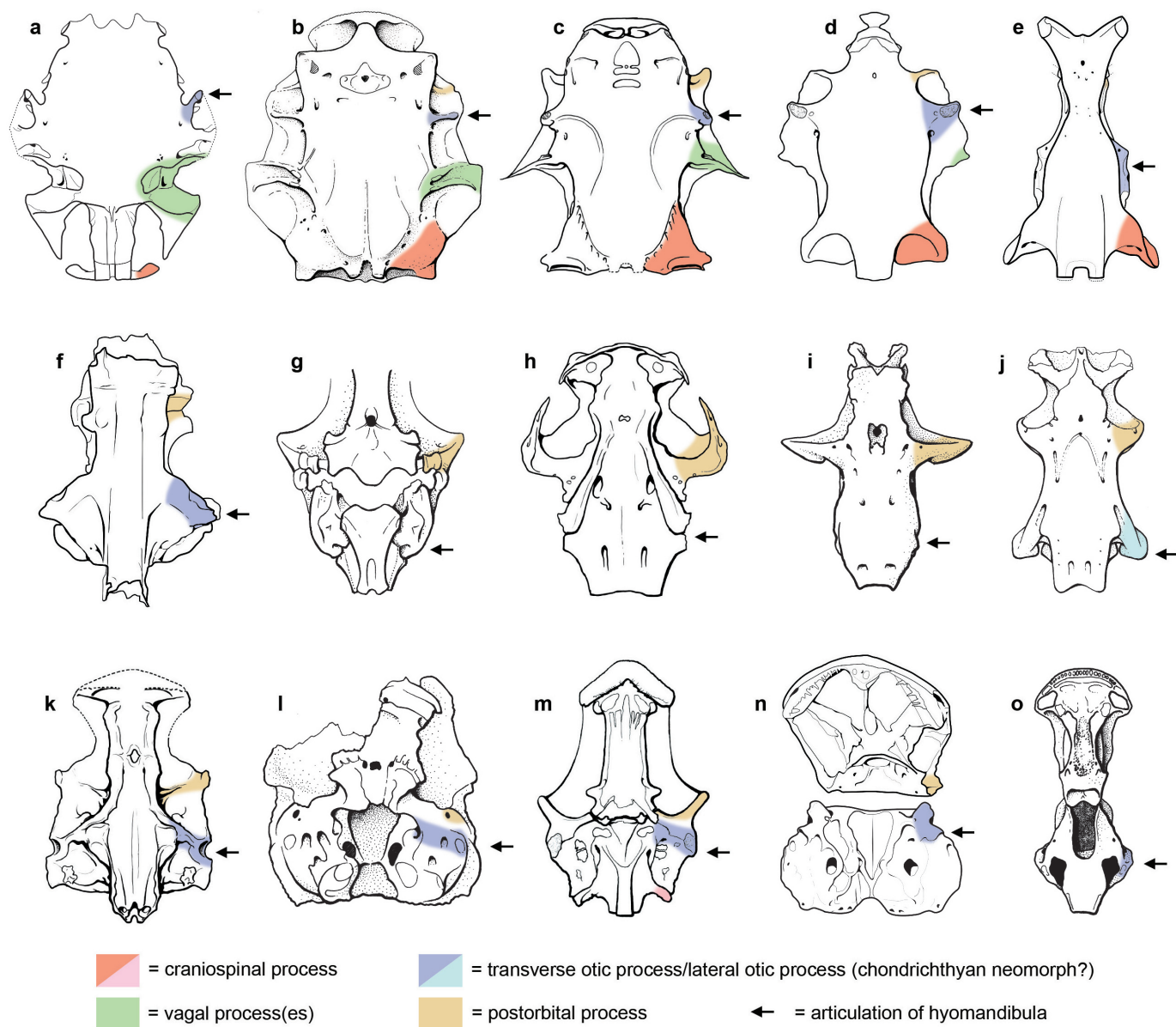
Extended Data Figure 5 | Subcranial ridges in *Janusiscus* and early crown gnathostomes. **a**, Reconstructed tomographs showing that the thickenings along the lateral margins of the sphenoid region of *Janusiscus* do not represent artefacts of post-mortem compression. **b**, The ‘acanthodian’ *Ptomacanthus anglicus* NHMUK PV P 24919a; a silicone peel of the specimen preserved in negative, dusted with ammonium chloride. Portions of the skull other than the

neurocranium are partially masked for clarity. **c**, The chondrichthyan *Doliodus problematicus* NBMG 10127/1a; a reconstruction of the neurocranium based on CT data. **d**, *Janusiscus schultzei* gen. et sp. nov. GIT 496-6 (Pi.1384); a reconstruction of the neurocranium based on CT data. Red arrows in each panel indicate subcranial ridges.



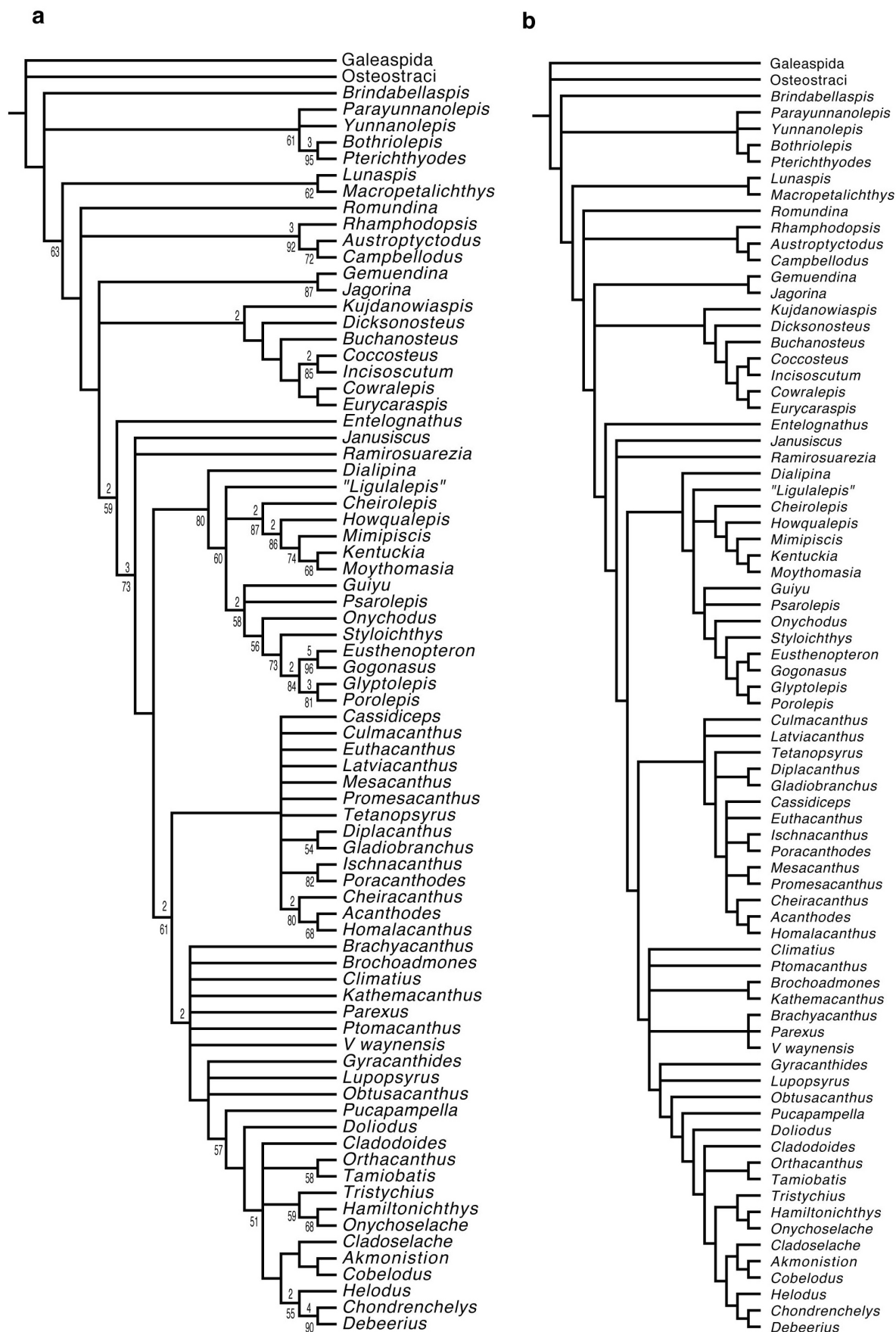
Extended Data Figure 6 | Orbit anatomy of *Janusiscus schultzei* gen. et sp. nov. **a**, Scanning electron micrograph image into left orbit showing endoskeletal bone and surrounding matrix. **b**, Image based on X-ray computed microtomography scan with matrix digitally removed. **c**, Lateral view into right

orbit, with matrix digitally removed. **d**, Anterolateral view into right orbit, with matrix digitally removed. **e**, Interpretive drawing of the orbit, based on a composite of the left and right orbits of the holotype (GIT 496-6 (Pi.1384)). Arrow points to anterior.



Extended Data Figure 7 | Comparison of transverse processes in the braincases of early gnathostomes. **a**, *Macropetalichthys* (redrawn from ref. 18). **b**, *Dicksonosteus* (redrawn from ref. 19). **c**, *Buchanosteus* (redrawn from ref. 29). **d**, *Entelognathus* (redrawn from ref. 4). **e**, *Jagorina* (redrawn from ref. 19). **f**, *Ramirosuarezia* (redrawn from ref. 9). **g**, *Acanthodes* (redrawn from

ref. 3). **h**, *Doliodus* (redrawn from ref. 17). **i**, *Cladodoides* (redrawn from ref. 21). **j**, *Orthacanthus* (redrawn from ref. 20). **k**, *Janusiscus*. **l**, *Ligulalepis* (redrawn from ref. 14). **m**, *Mimipiscis* (redrawn from ref. 16). **n**, *Psarolepis* (redrawn from ref. 25). **o**, *Gogonassus* (redrawn from ref. 35).



Extended Data Figure 8 | Results of phylogenetic analysis. **a**, Strict consensus of the 522,936 shortest trees (639 steps) for 78 taxa and 236 equally weighted characters. Digits above nodes indicate Bremer decay indices above 1.

Digits below nodes indicate percentage bootstrap support. **b**, Adams consensus tree of the 522,936 shortest trees for 78 taxa and 236 equally weighted characters.



Extended Data Figure 9 | Results of modified phylogenetic analyses. **a**, Strict consensus tree of 216 trees with a score of 452.52565 resulting from analysis of characters reweighted according to retention index. **b**, Strict consensus of the

128,395 shortest trees for 77 taxa and 236 equally weighted characters, with *Janusiscus* removed from the data set.

Evolution of the snake body form reveals homoplasy in amniote *Hox* gene function

Jason J. Head¹ & P. David Polly²

Hox genes regulate regionalization of the axial skeleton in vertebrates^{1–7}, and changes in their expression have been proposed to be a fundamental mechanism driving the evolution of new body forms^{8–14}. The origin of the snake-like body form, with its deregionalized pre-cloacal axial skeleton, has been explained as either homogenization of *Hox* gene expression domains⁹, or retention of standard vertebrate *Hox* domains with alteration of downstream expression that suppresses development of distinct regions^{10–13}. Both models assume a highly regionalized ancestor, but the extent of deregionalization of the primaxial domain (vertebrae, dorsal ribs) of the skeleton in snake-like body forms has never been analysed. Here we combine geometric morphometrics and maximum-likelihood analysis to show that the pre-cloacal primaxial domain of elongate, limb-reduced lizards and snakes is not deregionalized compared with limbed taxa, and that the phylogenetic structure of primaxial morphology in reptiles does not support a loss of regionalization in the evolution of snakes. We demonstrate that morphometric regional boundaries correspond to mapped gene expression domains in snakes, suggesting that their primaxial domain is patterned by a normally functional *Hox* code. Comparison of primaxial osteology in fossil and modern amniotes with *Hox* gene distributions within Amniota indicates that a functional, sequentially expressed *Hox* code patterned a subtle morphological gradient along the anterior–posterior axis in stem members of amniote clades and extant lizards, including snakes. The highly regionalized skeletons of extant archosaurs and mammals result from independent evolution in the *Hox* code and do not represent ancestral conditions for clades with snake-like body forms. The developmental origin of snakes is best explained by decoupling of the primaxial and abaxial domains and by increases in somite number¹⁵, not by changes in the function of primaxial *Hox* genes^{9,10}.

In Amniota (Mammalia + Reptilia), *Hox* genes are expressed sequentially in the somitic mesoderm, resulting in a series of distinct anatomical regions along the anterior–posterior axis of the vertebral column. Anatomical boundaries coincide with anterior borders of *Hox* gene expression or areas where expression of two genes overlaps^{4,5}. In Squamata (lizards, including snakes), the pre-cloacal vertebral column is less differentiated than in highly regionalized mammals and extant archosaurs. Vertebrae possessing synapophyses that articulate with dorsal ribs extend from the first post-atlanto-axial vertebra to the sacrum in many squamates¹⁶ (Fig. 1 and Extended Data Fig. 1a). In limbed lizards, two regional boundaries, cervical–thoracic and thoracic–lumbar, are known to correspond to *Hox* gene expression patterns^{10,12}. These boundaries are not recognized in snakes and snake-like squamates, which are considered to possess ‘deregionalized’¹¹ axial skeletons with increased numbers of vertebrae and ribs and reduction or loss of limbs and sternum¹⁶.

Two conflicting hypotheses have been proposed for the role of *Hox* genes in the evolution of the snake-like axial skeleton on the basis of domain mapping and transgenic expression^{9–13}. In the first hypothesis, loss of regionalization is caused by upstream modification of *Hox* expression and (or resulting in) a shift of *HoxC6* and *HoxC8* domains, which are associated with the thoracic region in mammals and archosaurs, forward

to the first post-atlanto-axial vertebral position⁹. In the second, loss of regionalization in snakes is caused not by shifts in the boundaries of *Hox* expression, but by downstream changes in *cis*-regulation^{10–13}. Both hypotheses invoke modifications to *Hox* activity in the paraxial mesoderm, which forms the primaxial skeleton (vertebrae, dorsal ribs¹⁷), but axial regionalization is at least partially dependent upon spatial relationships with the abaxial skeleton (limbs, sternum^{17,18}), which is derived from lateral plate mesoderm and has independent *Hox* regulation^{4,5}. The extent to which the primaxial domain has become homogenized in clades with snake-like body forms has, to our knowledge, never been examined in a comparative phylogenetic context.

To test the hypothesis that the primaxial skeleton of snakes and snake-like squamates is deregionalized relative to limbed amniotes, we performed geometric morphometric analysis on vertebral morphology to measure quantitatively intracolumnar shape variance and combined it with a maximum-likelihood estimation of the number of regions and positions of regional boundaries in the pre-cloacal skeleton of representative taxa based on segmented linear regression (Methods, Extended Data Fig. 2 and Extended Data Table 1). To capture the axial gradient in shape, we placed 12 homologous landmarks on vertebrae along the pre-cloacal skeleton¹⁹ (Fig. 1, Methods and Extended Data Table 2). We included comparisons with *Alligator mississippiensis* and *Mus musculus* because *Hox* expression boundaries in their regionalized axial skeletons are well documented^{2–6,20} (Methods and Extended Data Fig. 3).

We found that total intracolumnar shape variance in the primaxial domain was substantially less in all squamates than in *Alligator* (Fig. 2a). Mean variance was significantly lower in snake-like squamates than in

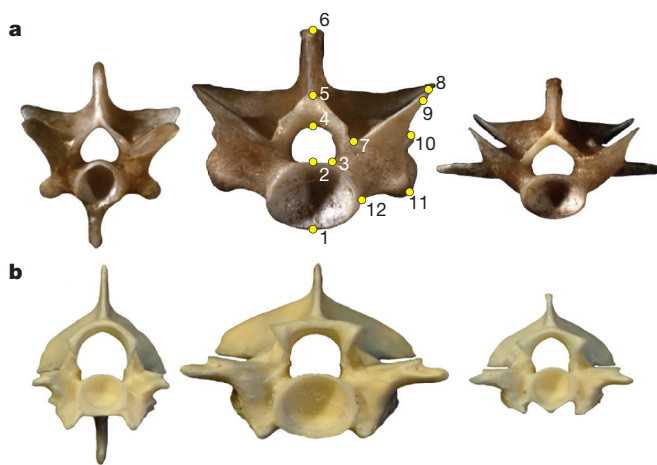


Figure 1 | Morphological variation in the pre-cloacal vertebral column of limbed lizards and snakes. **a, b**, *Pogona vitticeps* (**a**) and *Pantherophis guttatus* (**b**) pre-cloacal vertebrae in anterior view, from left: first post-atlanto-axial, mid-trunk and posterior-most pre-cloacal vertebrae. Numbered landmarks shown on mid-trunk vertebra of *Pogona* were used to characterize vertebral shape (Extended Data Table 2).

¹Department of Earth and Atmospheric Sciences and Nebraska State Museum of Natural History, University of Nebraska–Lincoln, Lincoln, Nebraska 68588-0340, USA. ²Departments of Geological Sciences, Biology and Anthropology, Indiana University, Bloomington, Indiana 47405-1405, USA.

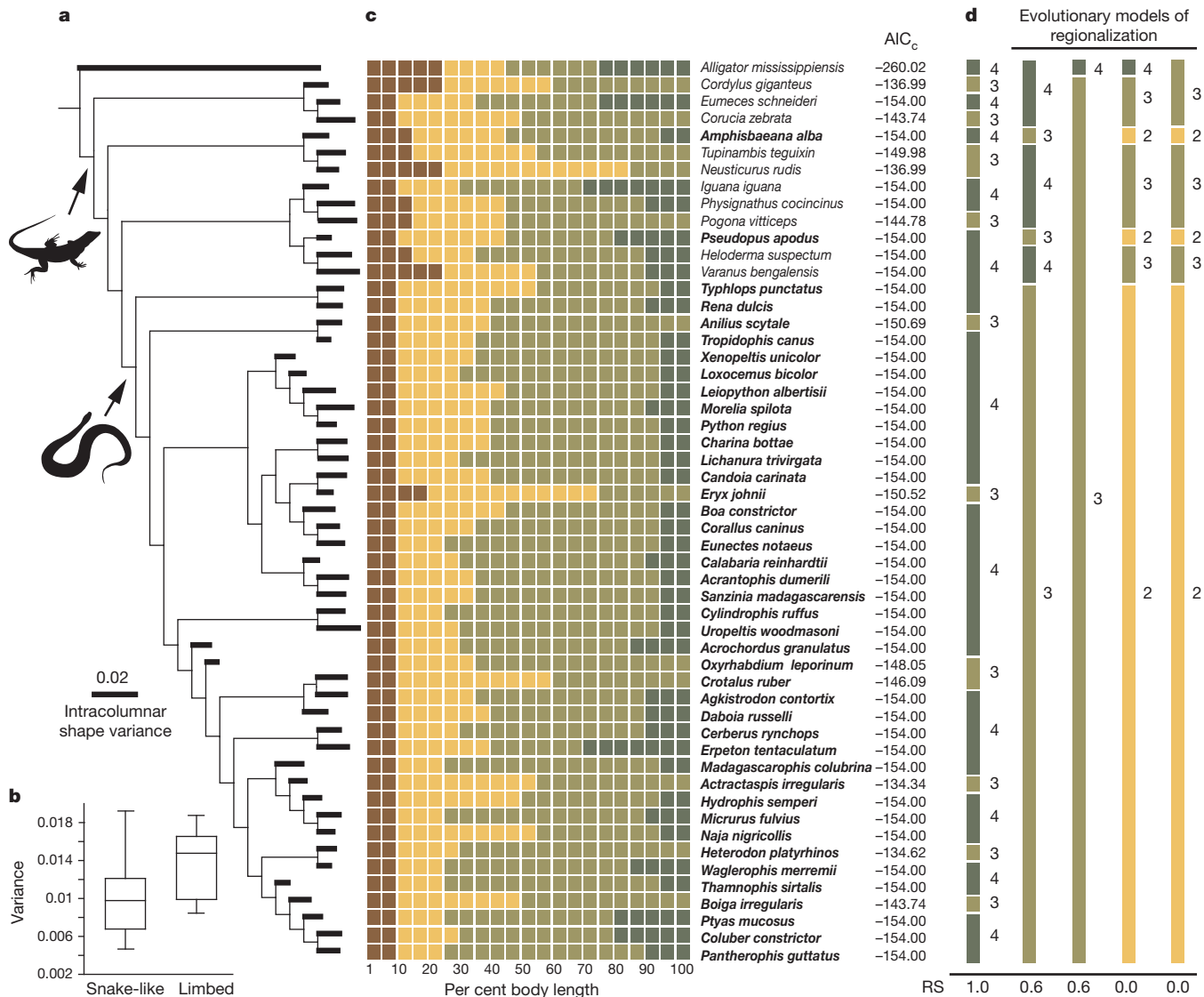


Figure 2 | Regional boundaries, evolutionary models of regional changes, and intracolumnar variance. **a**, Consensus phylogeny of selected taxa. Terminal branch lengths are scaled to intracolumnar shape variance. **b**, Box plot of intracolumnar variances in limbed ($n = 10$ specimens) and snake-like ($n = 42$ specimens) squamates. **c**, Regional boundaries in primaxial domains for each taxon subsampled at 5% intervals. Coloured cells represent vertebrae in

limbed taxa (see Methods). Nevertheless, there was no consistent difference in shape variance between limbed and snake-like squamates, and the range of variances in snake-like squamates exceeds the range in limbed taxa (Fig. 2b). Several snake taxa have greater intracolumnar shape variance than any of the sampled limbed squamates, even after standardizing for differences in the number of vertebrae.

The number of primaxial regions in snakes and snake-like lizards does not systematically differ from limbed squamates and *Alligator* (Fig. 2c, d). Three or four regions were found in all taxa, irrespective of the presence or absence of limbs or the total number of vertebrae. The origin of snake-like body forms was not associated with a reduction in the number of regions when we tested four competing evolutionary models of deregionalization (Fig. 2d, Methods and Extended Data Table 3). The model in which limbed squamates and *Alligator* have four regions and this is reduced to three in snake-like taxa was no better supported than the hypothesis that all squamates share three regions and *Alligator* has four (relative support = 0.6 for both hypotheses). Models in which snake-like taxa have two regions and limbed taxa have either three or four regions

different regions of the best-fit model, for which corrected Akaike information criterion (AIC_c) scores are given. Taxa in bold are snakes and snake-like squamates. **d**, Best-fit distribution of regions (left) compared with four models for evolutionary changes in regionalization. Each is depicted by the number of regions (2 to 4) expected in limbed and snake-like taxa. RS, relative support (Methods).

had virtually no support (relative support = 0). These results indicate that, although average shape variance within and between individual primaxial regions of snake-like taxa is less than in their limbed relatives, there was no reduction in the number of regions or changes in the relative location of regional boundaries associated with the origin of snakes or snake-like taxa.

To determine if morphometric regional boundaries are associated with *Hox* expression, we fit regional models to entire pre-cloacal primaxial skeletons of representative taxa and compared best-fit results to mapped *Hox* expression boundaries^{3,4,20}. Four regions were found in most taxa (Extended Data Fig. 4 and Extended Data Table 4). In *Mus* and *Alligator*, four-region models recovered morphometric boundaries that either exactly matched *Hox* expression boundaries for regional transitions or were within one vertebral position of boundaries (Fig. 3 and Supplementary Information).

In the snake *Pantherophis guttatus*, the best-fit regional boundaries correspond to *Hox* expression domains that govern the cervical–thoracic transition and the thoracic region in limbed amniotes (Fig. 3). The

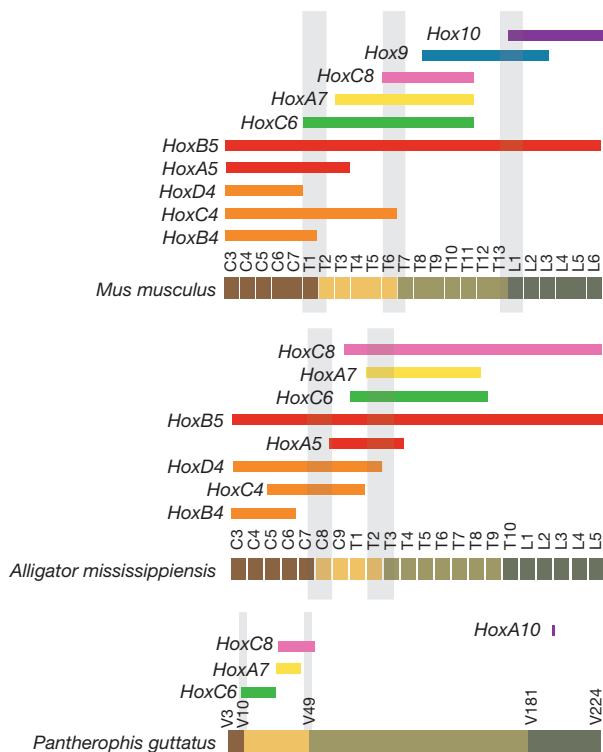


Figure 3 | Correspondence between *Hox* expression domains and morphometric boundaries for four-region models of primaxial regionalization. Coloured bars represent expression domains for *Mus*^{4,20} and *Alligator*²⁰, and the range of anterior expression boundaries for *Pantherophis*^{10–12}. *Hox* expression domains for the thoracic–lumbar transition in *Alligator* have not yet been mapped²⁰. Cells represent individual vertebrae in each region for the entire pre-cloacal/pre-sacral vertebral column in each taxon. Cell colours represent morphometric regions. Grey bars indicate regions of overlap between genes and morphometric regions. C, cervical; L, lumbar; T, thoracic; V, vertebra.

boundary between the first and second regions occurs between post-atlanto-axial vertebrae 10–11, which corresponds to the diffuse anterior expression boundary of *HoxC6* (ref. 10). This correspondence was also recovered in limbed squamates (Supplementary Information). The boundary between the second and third morphological regions occurs between post-axial vertebrae 49–50, which falls within the diffuse anterior expression boundary of *HoxC8* (ref. 10) and is only five vertebrae posterior to the anterior expression region for *HoxA7* (ref. 10). The boundary between the third and fourth morphological regions in *Pantherophis* occurs between post-axial vertebrae 180–181, which is anterior to expression of *HoxA10* and *C10* near somites 195 to 210 (refs 10, 12). This apparent discrepancy may arise from individual, possibly sex-linked²¹, differences in vertebral number between our sample and *Hox*-mapped specimens (Supplementary Information). Regardless, the fit of the fourth morphometric regional boundary to *Hox10* expression boundaries was statistically indistinguishable from the best-fit model (Methods and Extended Data Fig. 5).

Regional transitions in *Pantherophis* and the other squamates in our study are gradational, unlike the more abrupt boundaries of *Mus* or *Alligator*, in which differences in the presence, articulation or fusion of vertebral processes and ribs add to regional differentiation (Extended Data Fig. 1 and Fig. 4). Both boundary types emerge from *Hox* gene expression. *HoxC8* expression is associated with relative sizes of the neural arch and apophyses²⁰, and the expression of this gene is graded over a series of segments in snakes rather than having a sharply defined boundary as in limbed taxa¹⁰. Topographic correlation between *Hox* expression boundaries and morphometric regions in *Pantherophis* (Fig. 3) is evidence that *Hox* domains in the snake primaxial skeleton are functional, even though regional boundaries lack discrete structural changes in processes and ribs.

Paleozoic amniotes, including stem members of Reptilia and Mammalia, possessed a comparatively homogeneous vertebral column and dorsal rib cage that lacked the distinct regional boundaries found in mammals and extant archosaurs, even though mapped domains for extant reptiles, mammals and anamniotes^{4,10,20,22,23} indicate that a fully regionalized and functional set of *Hox* genes along the anterior–posterior axis was ancestral for Amniota (Fig. 4). Our evidence indicates that the specific functions of *Hox* genes in patterning the regionalized primaxial domain of mammals and extant archosaurs are probably homoplastic

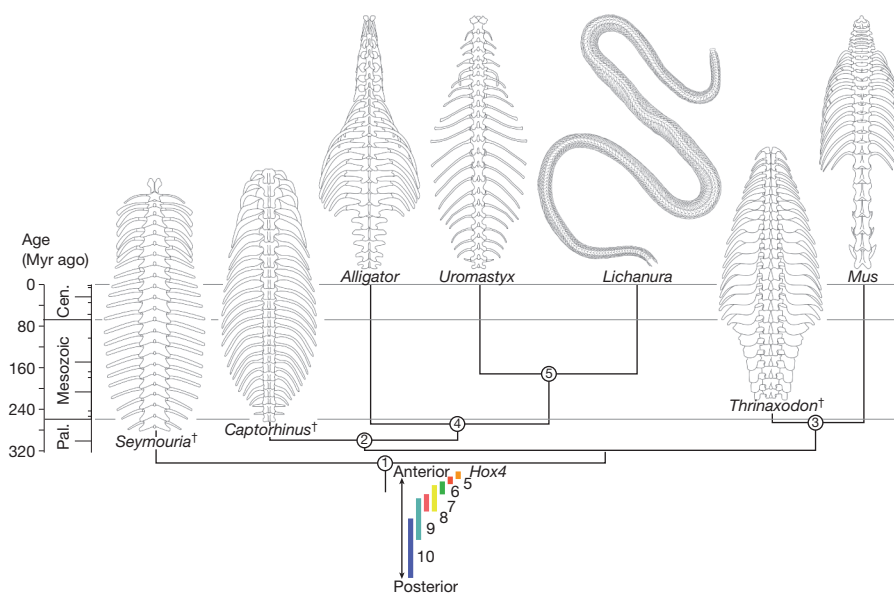


Figure 4 | Time-calibrated phylogeny of selected extant and fossil amniotes, illustrating pre-cloacal and pre-sacral primaxial skeletal regionalization and the generalized ancestral amniote pattern of *Hox* expression. Node numbers label the total clades for Amniota (1), Reptilia (2) and Mammalia (3), and the crown clades for Reptilia (4) and Squamata (5). Archosauria is

represented by *Alligator*, crown Mammalia is represented by *Mus*. Coloured bars represent relative positions of anterior expression domain boundaries for *Hox4–10* paralogues along the anterior–posterior axis in Amniota. See Supplementary Information for data sources. Cen., Cenozoic; Pal., Palaeozoic. Daggers indicate fossil taxa.

exaptations of an ancestral *Hox* code whose original function in amniotes was regulation of subtle gradations in primaxial morphology. This pattern is conserved in snakes and most other squamates (Fig. 4).

We conclude that the origin of snakes was not associated with deregionalization of the primaxial domain, but rather with loss of the abaxial skeleton and increases in vertebral numbers independent of primaxial *Hox* domain boundaries. We recommend that future studies of the origin of the snake-like body form concentrate on elucidating the developmental mechanisms by which the primaxial and abaxial skeletons become dissociated^{18,24}. The lateral somitic frontier is recognized as the boundary between the two developmental systems²⁵, and we hypothesize that future mapping of that frontier will demonstrate that major innovations in squamate body form are the result of abaxial modification whereas primaxial regionalization is conserved across amniotes, and potentially across vertebrates.

Online Content Methods, along with any additional Extended Data display items and Source Data, are available in the online version of the paper; references unique to these sections appear only in the online paper.

Received 30 July; accepted 4 November 2014.

Published online 5 January 2015.

- Favier, B. & Dollé, P. Developmental functions of mammalian *Hox* genes. *Mol. Hum. Reprod.* **3**, 115–131 (1997).
- Burke, A. C., Nelson, C. E., Morgan, B. A. & Tabin, C. *Hox* genes and the evolution of vertebrate axial morphology. *Development* **121**, 333–346 (1995).
- Wellik, D. M. & Capecchi, M. R. *Hox10* and *Hox11* genes are required to globally pattern the mammalian skeleton. *Science* **301**, 363–367 (2003).
- Wellik, D. M. *Hox* patterning of the vertebrate skeleton. *Dev. Dyn.* **236**, 2454–2463 (2007).
- McIntyre, D. C. *et al.* *Hox* patterning of the vertebrate rib cage. *Development* **134**, 2981–2989 (2007).
- Carapuço, M., Novoa, A., Bobola, N. & Mallo, M. *Hox* genes specify vertebral types in the presomitic mesoderm. *Genes Dev.* **19**, 2116–2121 (2005).
- Vinagre, T. *et al.* Evidence for a myotomal *Hox/Myf* cascade governing nonautonomous control of rib specification with global vertebral domains. *Dev. Cell* **18**, 655–661 (2010).
- Gaunt, S. J. Conservation in the *Hox* code during morphological evolution. *Int. J. Dev. Biol.* **38**, 549–552 (1994).
- Cohn, M. J. & Tickle, C. Developmental basis of limblessness and axial patterning in snakes. *Nature* **399**, 474–479 (1999).
- Woltering, J. M. *et al.* Axial patterning in snakes and caecilians: evidence for an alternative interpretation of the *Hox* code. *Dev. Biol.* **332**, 82–89 (2009).
- Woltering, J. M. From lizard to snake; behind the evolution of an extreme body plan. *Curr. Genomics* **13**, 289–299 (2012).
- Di-Poi, N. *et al.* Changes in *Hox* genes' structure and function during the evolution of the squamate body plan. *Nature* **464**, 99–103 (2010).
- Guerreiro, I. *et al.* Role of a polymorphism in a *Hox/Pax*-responsive enhancer in the evolution of the vertebrate spine. *Proc. Natl Acad. Sci. USA* **110**, 10682–10686 (2013).
- Müller, J. *et al.* Homeotic effects, somitogenesis and the evolution of vertebral numbers in recent and fossil amniotes. *Proc. Natl Acad. Sci. USA* **107**, 2118–2123 (2010).
- Gomez, C. *et al.* Control of segment number in vertebrate embryos. *Nature* **454**, 335–339 (2008).
- Hoffstetter, R. & Gasc, J. P. in *Biology of the Reptilia* (eds Gans, C., Bellair, A. d'A. & Parsons, T. S.) Vol. 1, 201–310 (Academic, 1969).
- Burke, A. C. & Nowicki, J. L. A new view of patterning domains in the vertebrate mesoderm. *Dev. Cell* **4**, 159–165 (2003).
- Buchholtz, E. A. & Stepien, C. C. Anatomical transformation in mammals: developmental origin of aberrant cervical anatomy in tree sloths. *Evol. Dev.* **11**, 69–79 (2009).
- Polly, P. D. & Head, J. J. in *Morphometrics—Applications in Biology and Paleontology* (ed. Elewa, A. M. T.) 197–222 (Springer, 2004).
- Mansfield, J. H. & Abzhanov, A. *Hox* expression in the American Alligator and evolution of archosaurian axial patterning. *J. Exper. Zool. B Mol. Dev. Evol.* **314**, 629–644 (2010).
- Shine, R. Vertebral numbers in male and female snakes: the roles of natural, sexual, and fecundity selection. *J. Evol. Biol.* **13**, 455–465 (2000).
- Prince, V. E., Joly, L., Ekker, M. & Ho, R. K. Zebrafish *hox* genes: genomic organization and modified colinear expression patterns in the trunk. *Development* **125**, 407–420 (1998).
- Mallo, M., Wellik, D. M. & Deschamps, J. *Hox* genes and regional patterning of the vertebrate body plan. *Dev. Biol.* **344**, 7–15 (2010).
- Shearman, R. M. & Burke, A. C. The lateral somatic frontier in ontogeny and phylogeny. *J. Exp. Zool. B Mol. Dev. Evol.* **312**, 603–612 (2009).
- Nowicki, J. L., Takimoto, R. & Burke, A. C. The lateral somitic frontier: dorso-ventral aspects of antero-posterior regionalization in avian embryos. *Mech. Dev.* **120**, 227–240 (2003).

Supplementary Information is available in the online version of the paper.

Acknowledgements We thank K. DeQueiroz, G. Zug, R. McDiarmid, K. Seymour, D. Gower, C. McCarthy, C. Bell, H. Voris, C. J. Cole, P. Holroyd and T. Labedz for specimen access, A. K. Behrensmeyer for access to microscopy facilities, and A. Goswami, K. Johnson, P. Mitteroecker, R. Raff, R. Reisz and M. Rowe for useful comments and discussion. This work was supported in part by a US National Science Foundation Postdoctoral Fellowship in Biological Informatics (DBI-0204082) to J.J.H., a Natural Sciences and Engineering Research Council of Canada Discovery Grant to J.J.H., and a US National Science Foundation Grant (EAR-0843935) to P.D.P.

Author Contributions J.J.H. and P.D.P. designed the study. J.J.H. and P.D.P. collected morphometric data. J.J.H. and P.D.P. conducted morphometric analysis. P.D.P. designed and conducted segmented linear regression and maximum-likelihood analyses. J.J.H. and P.D.P. prepared figures and wrote the manuscript.

Author Information Morphometric data have been deposited in Dryad (<http://dx.doi.org/10.5061/dryad.jq285>). Reprints and permissions information is available at www.nature.com/reprints. The authors declare no competing financial interests. Readers are welcome to comment on the online version of the paper. Correspondence and requests for materials should be addressed to J.J.H. (jhead2@unl.edu) or P.D.P. (pdpolly@indiana.edu).

METHODS

Morphometric analysis. We quantified morphological regionalization using principal component shape variables derived from Procrustes superimposition²⁶ of two-dimensional landmarks on vertebrae in anterior view¹⁹. We chose a taxonomic sample that covers all major squamate body forms and major clades ($n = 54$ specimens; Extended Data Table 1). We selected anterior view because the centrum, neural arch and apophyses could all be identified by homologous landmarks. The landmarks we selected (Fig. 1 and Extended Data Table 2) define the aforementioned structures, and are homologous among sampled squamates. For anatomical regions where distinct dorsal ribs are fused with vertebral apophyses (the ultimate pre-sacral vertebra in *Pogona*, *Physignathus* and *Cordylus*; Fig. 1), landmarks for the diapophysis and parapophysis were placed at the dorsal and ventral edges of points of fusion. In *Alligator* and *Mus*, we modified the landmarks for their taxon-specific vertebral morphologies (Extended Data Fig. 3 and Extended Data Table 2; see Supplementary Information for discussion and references). Because vertebrae are approximately bilaterally symmetrical, we digitized only the left side and midline of each specimen¹⁹. We omitted the atlas-axis complex from all analyses because it is a distinct anatomical system common to all amniotes. We used two-dimensional landmarks to make our data set more applicable for future analyses of fossil specimens whose breakage and flattening frequently prohibits accurate three-dimensional analysis. Scores from the first five components, which represent more than 90% of shape differences along the anterior-posterior axis for all taxa, were used as shape variables for maximum-likelihood analyses of regionalization. To minimize the effects of ontogenetic variation, we only sampled somatically mature specimens for each taxon.

Sampling along the anterior-posterior axis. For most analyses we used a standardized sampling strategy in which we collected shape data at 5% intervals along the anterior-posterior axis beginning with the first post-atlanto-axial vertebra. If a vertebra at a sampling point was pathologically or teratologically malformed, we sampled the next normally shaped element. This strategy facilitates comparisons of regional models between taxa with radically different numbers of vertebrae, but does not allow the correspondence between morphological regions and *Hox* expression boundaries to be assessed at the level of individual segments. To make direct comparisons between morphometric regions and *Hox* expression boundaries, we sampled the complete pre-clacal column for key taxa.

Intracolumnar shape variance. We measured intracolumnar shape variation for each individual specimen as the total variance of Procrustes coordinates among the pre-clacal vertebrae. Total variance is expected to be higher in taxa with more regional differentiation. We used a permutation test to determine whether intracolumnar variance in squamate vertebral shape was significantly different in limbed versus snake-like taxa and in taxa identified as having four versus three regions. To adjust for biases related to imbalance in the number of taxa in each category and non-normal distribution of variances, we used a non-parametric permutation test in which the observed difference in the average variance in each group was compared to a distribution of the same statistic calculated from 10,000 random permutations of taxa between groups. Limbed taxa had significantly greater intervertebral variance (limbed = 0.0133, snake-like = 0.0095, $P = 0.0037$), but taxa with four regions were not significantly more variable than taxa with three regions (four region = 0.0103, three region = 0.0100, $P = 0.8245$).

Likelihood models of regionalization. Our analysis treats vertebral column regions as a series of morphological gradients. Vertebrae within a region are not expected to be identical: adjoining vertebrae spanning the boundary of two regions may be more similar than each is to its opposite regional end member. Standard cluster analysis is therefore inappropriate because it recovers hierarchical patterns of variation, not gradients of similarity. Our approach uses segmented linear regression (SLR)^{27,28} on the first five PC scores to recover gradients of morphology and the breaks between them (Extended Data Fig. 2). In SLR, a series of contiguous regression lines are fit to the data such that each segment has its own slopes and intercepts. Boundaries are estimated by finding the break points that minimize the residual sum of squares, adding an additional parameter to the model for each pair of segments. In our models, each segment of the regression therefore corresponds to a morphological region, its slope(s) describe its shape gradient, and the break points correspond to the regional boundaries.

To estimate the number of regions and the positions of regional boundaries, we iteratively fit four classes of model with one, two, three and four segments, respectively, to each vertebral column. The classes correspond to a morphological spectrum from complete derelocalization (one segment) to hyper-regionalized (four segments: cervical, anterior thoracic, posterior thoracic, lumbar). Each class of model has many specific instances that differ in the slope of the regression segments and the position of the boundaries between them (Extended Data Fig. 2). The likelihood of each instance of each model was assessed using a likelihood ratio, which in its general form is:

$$\lambda(x) = \frac{L(\theta_0|x)}{L(\theta_1|x)} \quad (1)$$

where $\lambda(x)$ is the likelihood of hypothesis H_0 relative to hypothesis H_1 (the hypotheses in our case are different models of regionalization), $L(\theta_0|x)$ is the likelihood of θ_0 , which are the parameters of the H_0 model given the data (which in our case are the vertebral shape scores), and $L(\theta_1|x)$ is the likelihood of the H_1 model parameters. Specifically, we calculated the log-likelihood ratio test statistic, D , for our segmented regressions using the residual sum of squares (RSS) as follows:

$$D = -2\ln(\lambda) = n\ln(S_0/S_1) \quad (2)$$

where λ is the likelihood ratio, n is the number of data points (five times the number of vertebrae since we used scores from the first five dimensions of our vertebral shape spaces), and S_0 and S_1 are the RSS for H_0 and H_1 , respectively²⁹. The regression slopes and intercepts were found by exact calculation (the parameters that maximize the likelihood function are the same as those found by least-squares fitting). We used a grid search to calculate the likelihood of every possible set of regional breaks, thus providing us with a complete statistical distribution for testing alternative regional models²⁹.

Model selection using AIC_c. The likelihoods of models with different numbers of regions are not directly comparable because the number of parameters differ. Our models have $10k + k - 1$ parameters for each of their k regions: one slope and intercept for each of the five dimensions in each region plus one boundary between each region (Extended Data Fig. 2). Our one-region model class has 10 parameters, the two-region class has 21 parameters, the three-region class has 62, and the four-region class has 83. The more parameters a model has, the better it fits the data (when the number of regions increases to equal the number of vertebrae it will always fit the data perfectly). Model comparisons thus require an adjustment for the number of parameters, especially when comparing taxa with different numbers of vertebrae (a 20-region model will fit a 20-vertebrae lizard column perfectly, but it will not fit a 200-vertebrae snake column as well). We used the corrected AIC_c to adjust the likelihood ratios by the number of model parameters and data points so that they could be compared between model classes to objectively select the best model of regionalization:

$$AIC_c = D - 2(p+1) \frac{n}{n-p-2} \quad (3)$$

where D is the log-likelihood ratio from equation (2), p is the number of parameters ($10k + k - 1$ for our study, where k is the number of regions), and n is the number of data points (five times the number of vertebrae in our study). This correction penalizes the log likelihood for each additional parameter and makes the penalty proportionally heavier for smaller data sets. This value is scaled so that the best model is the one with the highest AIC_c value.

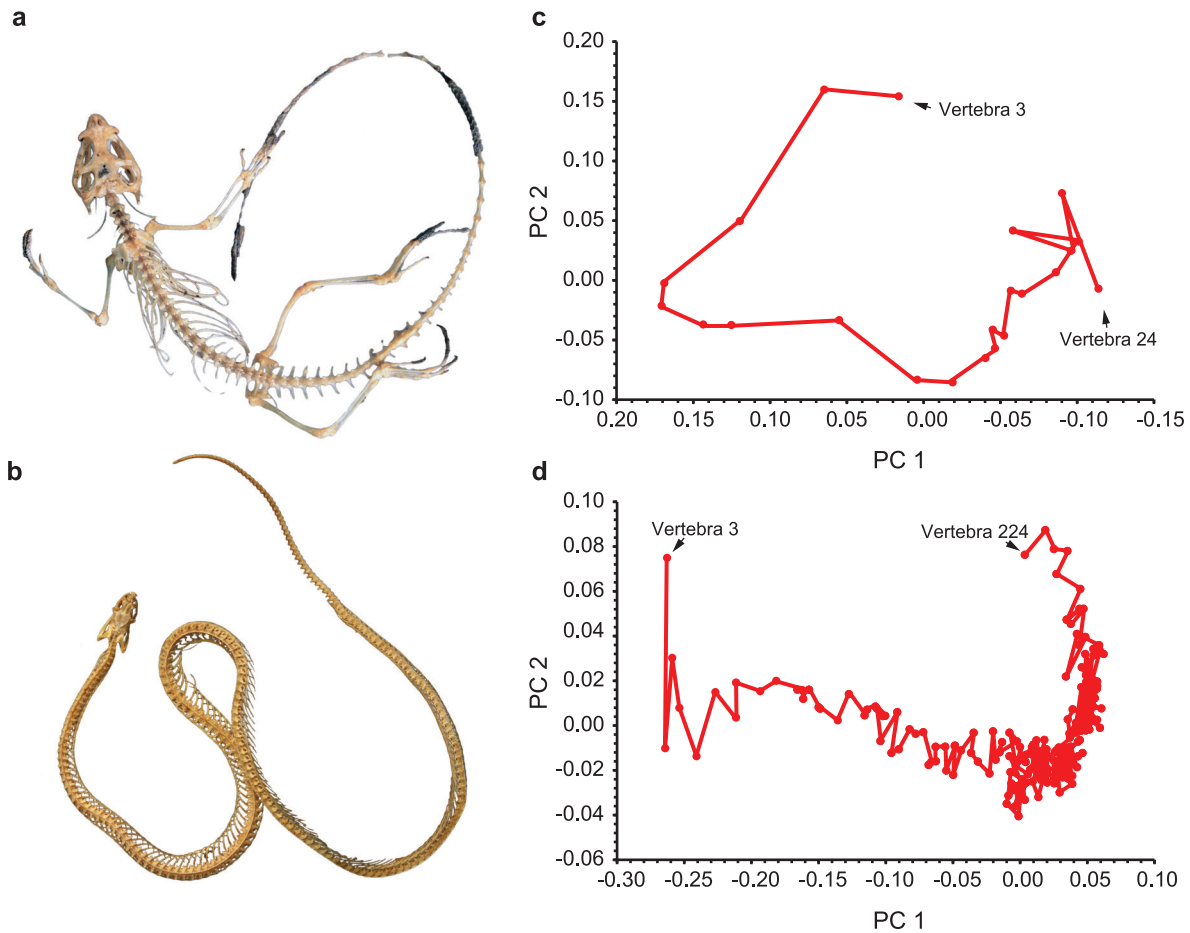
Testing hypotheses of evolutionary changes in regionalization. We assessed the relative support for four competing hypotheses of evolutionary changes in regionalization in squamates and the ancestral state of regionalization in snake-like forms. For each hypothesis, the expected number of regions was mapped onto phylogeny (Fig. 2d). Total support for each hypothesis was estimated as the sum of the AIC_c support values for the best corresponding regional model for each taxon (Extended Data Table 3). For example, support for the hypothesis that all reptiles have two vertebral regions can be calculated by summing the AIC_c values for the best two-region model of all of species in the analysis. The highest possible support for any such hypothesis occurs when each taxon is assigned the number of regions that is best supported by its own data (Fig. 2d, left bar). The sum of the AIC_c values is not meaningful when taxa vary in the number of vertebrae, so we used the data sampled at 5% intervals, which have a maximum summed AIC_c support of $-8,140.6$. Note that, although this measure of total support varies with the number of taxa included in an analysis, the number of taxa is constant across the four hypotheses; relative support for the competing evolutionary hypotheses can therefore be measured as the fractional difference of the summed AIC_c values of each model relative to the total AIC_c of the best- and worst-supported hypothesis ($1.0 = \text{best}$, $0.0 = \text{worst}$)³⁰.

Comparison of morphometric boundaries to boundaries of *Hox* expression. Because one of our aims is to determine whether morphological regionalization corresponds to *Hox* gene expression domains, it is necessary to test statistically whether the morphometric regional boundaries differ from expression boundaries. Our likelihood framework allows the relative support of the best morphometric regional model to be compared to other models. The probability that an alternative set of boundaries differs from the best morphometric model was assessed by counting values in which the fit was better than or equal to the alternative model and normalizing by the number of possible regional models. The resulting P value is the

probability that expression boundaries differ from the best regional model (Extended Data Fig. 5).

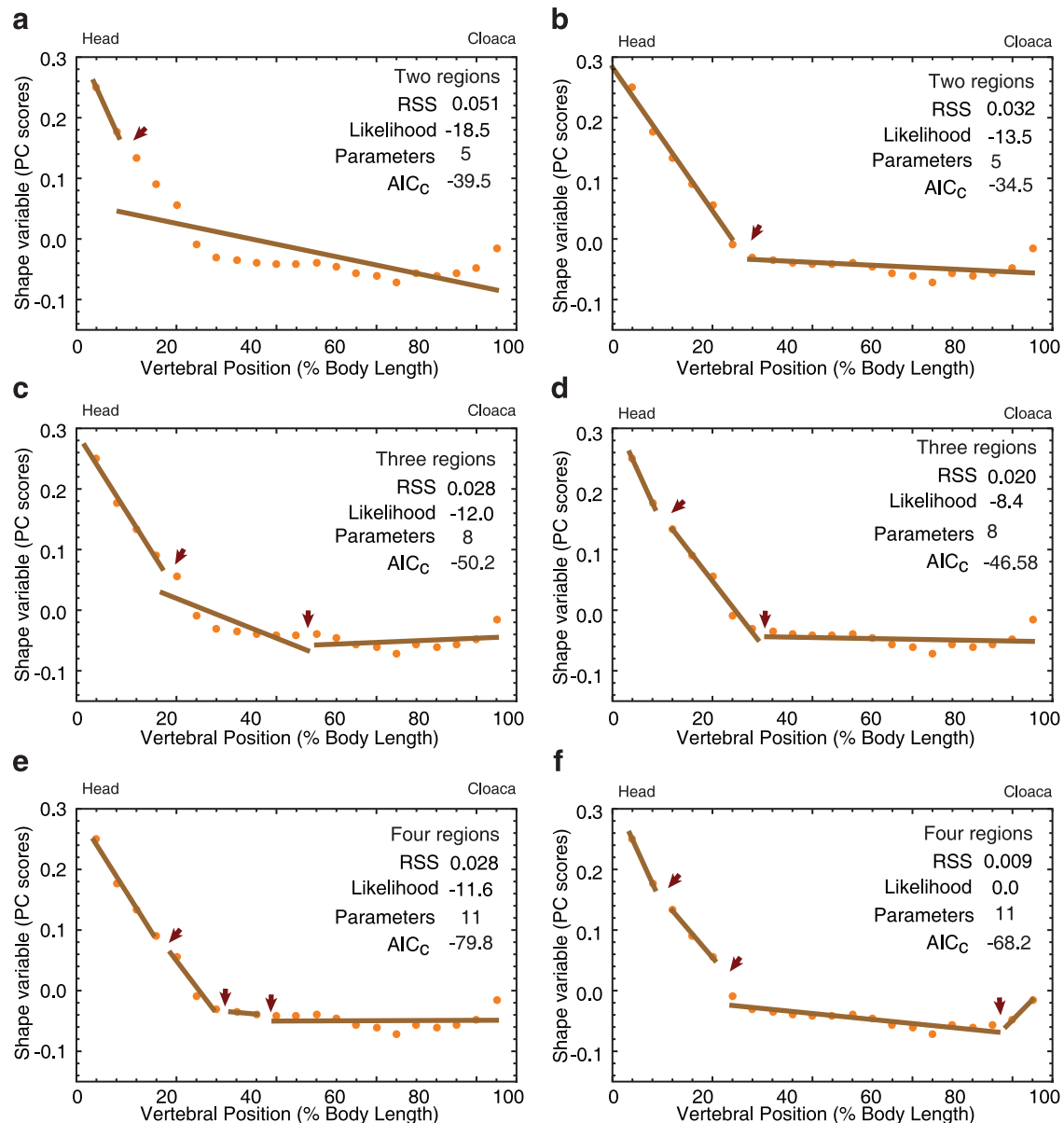
All calculations were performed using Mathematica v.9.0.

26. Rohlf, F. J. & Slice, D. Extensions of the Procrustes method for the optimal superimposition of landmarks. *Syst. Biol.* **39**, 40–59 (1990).
27. Hudson, D. Fitting segmented curves whose join points have to be estimated. *J. Am. Stat. Assoc.* **61**, 1097–1129 (1966).
28. Feder, P. The log likelihood ratio in segmented regression. *Ann. Stat.* **3**, 84–97 (1975).
29. Lerman, P. Fitting segmented regression models by grid search. *Appl. Stat.* **29**, 77–84 (1980).
30. Claeskens, G. & Hjort, N. *Model Selection and Model Averaging* (Cambridge Univ. Press, 2008).



Extended Data Figure 1 | Skeletal morphology and intracolumnar shape variation in the pre-cloacal vertebral column of limbed lizards and snakes. **a**, Skeleton of limbed lizard (*Pogona minor*) in dorsal view. **b**, Skeleton of snake (*Hypsiglena torquata*) in dorsal view. **c**, Principal component analysis (PCA) ordination of pre-cloacal vertebral shape variables derived from geometric morphometric analysis in a limbed lizard (*Pogona vitticeps*) based on

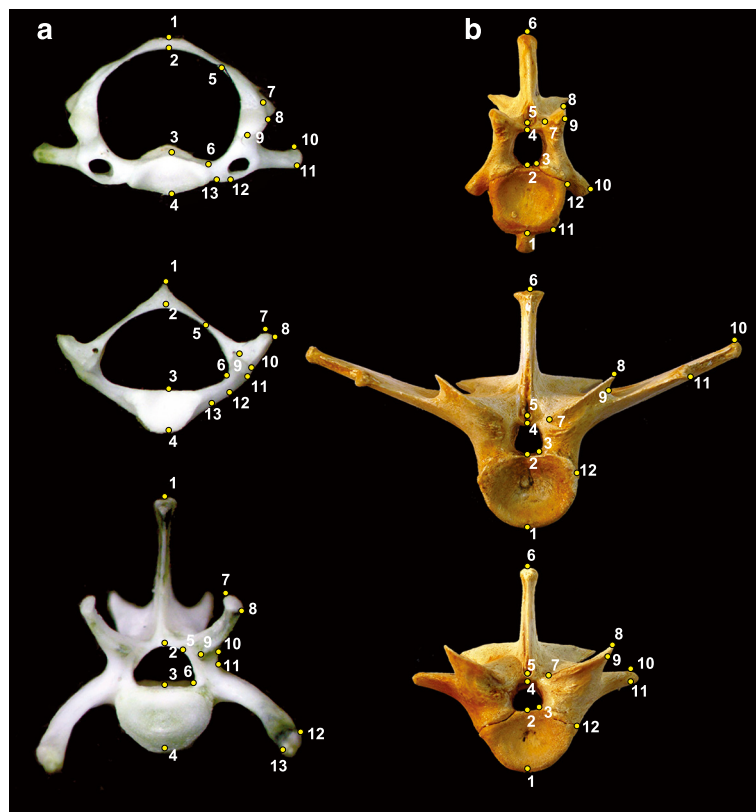
first two principal components (PC 1 and PC 2). **d**, PCA ordination of pre-cloacal vertebral shape variables in a snake (*Pantherophis guttatus*). Ordination using the first two components describes intracolumnar shape change along the anterior-posterior axis of the pre-cloacal vertebral column and explains >90% of overall shape variation.



Extended Data Figure 2 | Model fitting with segmented linear regression.

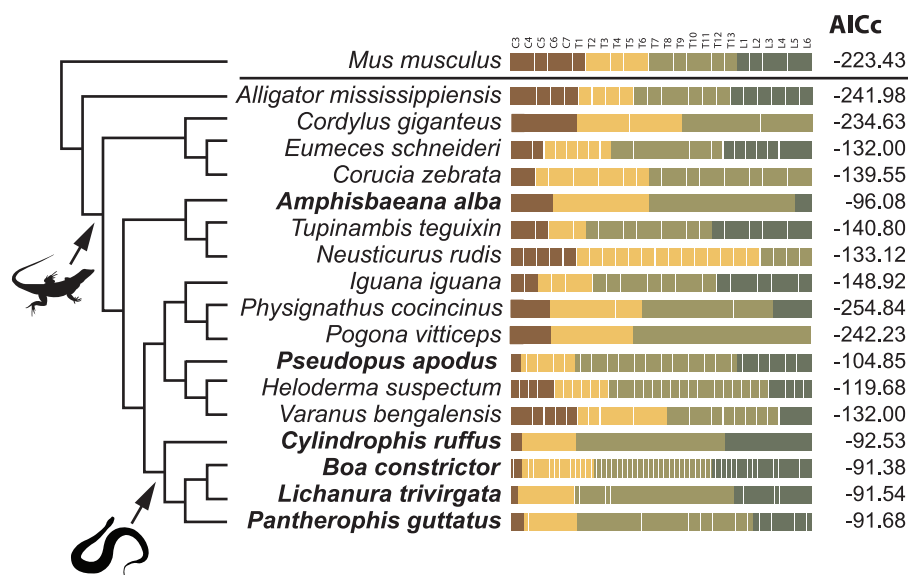
a–f, A series of regional models were fit to each taxon using a series of segmented linear regressions. In each case vertebral shape variables (orange dots) were regressed onto position in the vertebral column (brown lines). Models differ in both the number of regions and the position of regional boundaries. **a–f**, Two examples are shown for each of two, three and four regions, where the right column shows the best fitting example for each. Red arrows mark the regional boundaries in each example. The slope of each segment (heavy dark line) represents the shape gradient each region and the

residual sum of squares (RSS) represents the lack of fit of the model to the data. **f**, The model with the highest likelihood. The log likelihood of each model is proportional to this model. However, the number of parameters increases with the number of regions, as does the likelihood of the model; therefore corrected Akaike adjustment (AIC_c) is required to select the best model. **b**, The best model using AIC_c . It is the two-region model with the breakpoint 25% along the pre-cloacal vertebral column. This example is based on the first principal component of *Eunectes notaeus*.

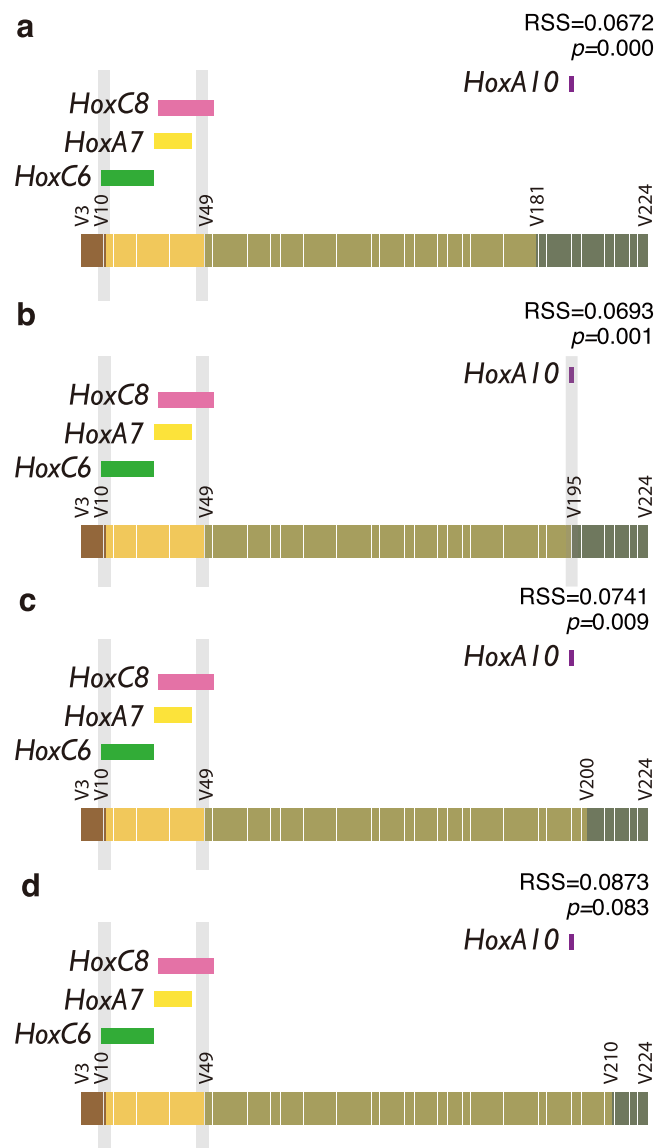


Extended Data Figure 3 | Morphometric landmarks used to quantify primaxial shape variance and regionalization in pre-cloacal vertebrae of *Mus* and *Alligator*. a, b, Elements for both *Mus* (a) and *Alligator* (b) are, from top to bottom: first post-atlanto-axial vertebrae, third thoracic (*Mus*) and

sixth dorsal vertebrae (*Alligator*), last lumbar vertebrae. See Extended Data Table 2 and Supplementary Information for description of landmarks and discussion of landmark selection.



Extended Data Figure 4 | Best-fit regionalization models for complete pre-cloacal skeletons of *Mus*, *Alligator* and select squamates. AIC_c scores are reported for the best regional model from each taxon. Taxa in bold are snakes or have snake-like body forms. Cells represent individual vertebrae in each region for the complete pre-cloacal/pre-sacral vertebral column in each taxon. Cell colours represent morphometric regions. C, cervical; L, lumbar; T, thoracic.



Extended Data Figure 5 | Comparison of best-fit four-region model with models fitting morphometric regional boundaries to expression boundaries for *Hox10* genes. **a**, Best-fit model. **b**, Fit to anterior expression boundaries of *HoxA10* and *HoxC10* from ref. 12. **c**, Fit to anterior expression boundary for *HoxC10* from ref. 10. **d**, Fit to posterior expression boundaries of *HoxA10* and *HoxC10* from ref. 12. Abbreviations are the same as for Fig. 3. Only the posterior boundaries of *Hox10* expression are significantly worse fits than the best-fit model. RSS, residual sum of squares for segmented linear regression. *P* values are probability that the *Hox* boundaries differ from the best regional model.

Extended Data Table 1 | Examined specimens

Taxon	Specimen
<i>Acrantophis dumerilli</i>	USNM 497683
<i>Acrochordus granulatus</i>	USNM 497610
<i>Actractuspsis irregularis</i>	USNM 297313
<i>Agkistrodon contortix</i>	USNM 330134
<i>Alligator mississippiensis</i>	ROMV-R 0395
<i>Amphisbaena alba</i>	ROMV-R 0357
<i>Anilius scytale</i>	USNM 204080
<i>Boa constrictor</i>	USNM 220299
<i>Boiga irregularis</i>	USNM 331387
<i>Calabaria reinhardtii</i>	USNM 523576
<i>Candoia carinata</i>	USNM 348502
<i>Cerberus rynchops</i>	USNM 497588
<i>Charina bottae</i>	USNM 009255
<i>Coluber constrictor</i>	USNM 297523
<i>Corallus caninus</i>	ROMV-R 7498
<i>Cordylus giganteus</i>	ROMV-R 0462
<i>Corucia zebrata</i>	ROMV-R 3812
<i>Crotalus ruber</i>	USNM 311091
<i>Cylindrophis ruffus</i>	USNM 52365
<i>Daboia russelli</i>	USNM 297365
<i>Erpeton tentaculatum</i>	TMM M-8282
<i>Eryx johni</i>	FMNH 31319
<i>Eumeces schneideri</i>	ROMV-R 8271
<i>Eunectes notaeus</i>	ROMV-R 7286
<i>Heloderma suspectum</i>	ROMV-R 0279
<i>Heterodon platyrhinos</i>	USNM 310959
<i>Hydrophis semperi</i>	USNM 499890
<i>Hypsiglena torquata</i>	ROMV-R 1520*
<i>Iguana iguana</i>	ROMV-R 5821
<i>Leiopython albertisi</i>	USNM 523581
<i>Lichanura trivirgata</i>	AMNH 73360, UCMP 440374*
<i>Loxocemus bicolor</i>	USNM 348509
<i>Madagascarophis colubrina</i>	USNM 345553
<i>Micrurus fulvius</i>	USNM 292571
<i>Morelia spilota</i>	USNM 523583
<i>Mus musculus</i>	UNL ZM 30667, UNL ZM 30048*, IU 8410148*, IU 210040*
<i>Naja nigricolis</i>	USNM 348606
<i>Neusticurus rudis</i>	ROMV-R 0410
<i>Oxyrhabdium leporinum</i>	USNM 497051
<i>Pantherophis guttatus</i>	ROMV-R 8176, UNL ZM 6909*
<i>Physignathus cocincinus</i>	ROMV-R 0412
<i>Pogona minor</i>	TMM R15688*
<i>Pogona vitticeps</i>	ROMV-R 8105
<i>Pseudopus apodus</i>	ROMV-R 8197
<i>Ptyas mucosus</i>	USNM 297339
<i>Python regius</i>	USNM 523587
<i>Rena dulcis</i>	USNM 161288
<i>Sanzinia madagascariensis</i>	USNM 220313
<i>Thamnophis sirtalis</i>	USNM 326566
<i>Tropidophis canus</i>	USNM 345562
<i>Tupinambis teguixin</i>	ROMV-R 0340
<i>Typhlops punctatus</i>	BMNH-R 1911.6.9.2
<i>Uromastyx maliensis</i>	ROMV-R 8031
<i>Uropeltis woodmasoni</i>	TMM M-8663
<i>Varanus benegalensis</i>	USNM 149140
<i>Waglerophis merremii</i>	USNM 523656
<i>Xenopeltis unicolor</i>	USNM 523682

AMNH, American Museum of Natural History, New York; BMNH-R, The Natural History Museum, London; FMNH, Field Museum of Natural History; IU, Indiana University; ROMV-R, Royal Ontario Museum Recent Vertebrate Collection; TMM, Texas Memorial Museum, University of Texas at Austin; UCMP, University of California Museum of Paleontology; UNL ZM, University of Nebraska—Lincoln, Museum of Zoology; USNM, United States National Museum, Smithsonian Institution.

* Specimens not used in morphometric analysis.

Extended Data Table 2 | Landmarks and corresponding morphology used in morphometric analysis

Landmark	Described morphology
Squamata	
1	Midline ventral margin of centrum
2	Midline dorsal margin of centrum
3	Medial contact between centrum and neural arch
4	Midline ventral margin of neural arch
5	Midline dorsal margin of neural arch
6	Dorsal margin of neural spine
7	Ventromedial margin of prezygapophyseal articular facet
8	Dorsolateral margin of prezygapophyseal articular facet
9	Lateral edge of prezygapophyseal body
10	Dorsomedial edge of diapophysis
11	Ventromedial edge of parapophysis
12	Ventrolateral contact between apophyses and centrum
Alligator	
1	Midline ventral margin of centrum
2	Midline dorsal margin of centrum
3	Medial contact between centrum and neural arch
4	Midline ventral margin of neural arch
5	Midline dorsal margin of neural arch
6	Dorsal margin of neural spine
7	Ventromedial margin of prezygapophyseal articular facet
8	Dorsolateral margin of prezygapophyseal articular facet
9	Lateral edge of prezygapophyseal body
10	Dorsomedial edge of diapophysis/ dorsolateral edge of lumbar transverse process
11	Ventromedial edge of parapophysis/ ventrolateral edge of lumbar transverse process
12	Ventrolateral contact between neural arch and centrum
Mus	
1	Dorsal midline of neural arch/spine
2	Ventral midline of neural arch
3	Dorsal midline of centrum
4	Ventral midline of centrum
5	Dorsolateral point of curvature of neural arch
6	Ventrolateral point of curvature of neural arch
7	Dorsomedial corner of mammillary / transverse process
8	Ventrolateral corner of mammillary / transverse process
9	Medial edge of prezygapophysis
10	Dorsal corner of tip of fused cervical rib/ ventrolateral margin of neural arch
11	Ventral corner of tip of fused cervical rib/ ventrolateral margin of neural arch
12	Ventral margin of neural arch/ dorsolateral corner of lumbar transverse process
13	Ventral margin of neural arch/ ventromedial corner of lumbar transverse process

Landmarks document intracolumnar variation in vertebral shape for squamates, *Alligator* and *Mus*. For discussion and references, see Supplementary Information.

Extended Data Table 4 | AIC_c values for regionalization models

Number of regions	1	2	3	4
Taxon				
<i>Mus musculus</i>	-311.5	-256.8	-240	-223.4
<i>Alligator mississippiensis</i>	-506.6	-353.4	-283.7	-242.0
<i>Cordylus giganteus</i>	-328.9	-277.8	-234.6	-246.9
<i>Eumeces schneideri</i>	-305.7	-224.4	-145.9	-132.0
<i>Corucia zebrata</i>	-215.1	-153.7	-139.6	-140.8
<i>Amphisbaena alba</i>	-922.6	-379.2	-195.8	-96.1
<i>Tupinambis teguixin</i>	-353.6	-249.1	-183.9	-140.8
<i>Neusticurus rudis</i>	-239.2	-161.9	-133.1	-144.6
<i>Iguana iguana</i>	-324.0	-221.0	-182.8	-148.9
<i>Physignathus cocincinus</i>	-486.7	-384.8	-295.7	-254.8
<i>Pogona vitticeps</i>	-375.8	-290.9	-242.2	-244.8
<i>Pseudopus apodus</i>	-559.8	-319.3	-204.3	-104.9
<i>Heloderma suspectum</i>	-405.8	-247.8	-181.2	-119.7
<i>Varanus bengalensis</i>	-375.1	-259.3	-174.0	-132.0
<i>Cylindrophis ruffus</i>	-1857.1	-737.2	-290.7	-92.5
<i>Boa constrictor</i>	-2881.6	-922.8	-454.6	-91.4
<i>Lichanura trivirgata</i>	-2949.5	-1167.7	-511.2	-91.5
<i>Pantherophis guttatus</i>	-2512.8	-1073.7	-424.1	-91.7

Values are for models from one to four morphological regions through the complete pre-sacral/pre-cloacal vertebral columns of select amniotes.

Primary transcripts of microRNAs encode regulatory peptides

Dominique Lauressergues^{1,2}, Jean-Malo Couzigou^{1,2}, Hélène San Clemente^{1,2}, Yves Martinez³, Christophe Dunand^{1,2},
Guillaume Bécard^{1,2} & Jean-Philippe Combier^{1,2}

MicroRNAs (miRNAs) are small regulatory RNA molecules that inhibit the expression of specific target genes by binding to and cleaving their messenger RNAs or otherwise inhibiting their translation into proteins¹. miRNAs are transcribed as much larger primary transcripts (pri-miRNAs), the function of which is not fully understood. Here we show that plant pri-miRNAs contain short open reading frame sequences that encode regulatory peptides. The pri-miR171b of *Medicago truncatula* and the pri-miR165a of *Arabidopsis thaliana* produce peptides, which we term miPEP171b and miPEP165a, respectively, that enhance the accumulation of their corresponding mature miRNAs, resulting in downregulation of target genes involved in root development. The mechanism of miRNA-encoded peptide (miPEP) action involves increasing transcription of the pri-miRNA. Five other pri-miRNAs of *A. thaliana* and *M. truncatula* encode active miPEPs, suggesting that miPEPs are widespread throughout the plant kingdom. Synthetic miPEP171b and miPEP165a peptides applied to plants specifically trigger the accumulation of miR171b and miR165a, leading to reduction of lateral root development and stimulation of main root growth, respectively, suggesting that miPEPs might have agronomical applications.

The biogenesis of miRNAs involves two maturation steps: processing of large pri-miRNAs to shorter pre-miRNAs, and their subsequent maturation to produce active, mature miRNAs¹. Whether the pri-miRNAs themselves have a regulatory function is not known. Like protein-encoding mRNAs, pri-miRNAs are synthesized by RNA polymerase II¹; therefore, we hypothesized that they might also encode proteins or peptides. To test this hypothesis, we studied the miR171 family in the model plant *Medicago truncatula*, because we have previously documented the role of one of its members (miR171h) in mycorrhization². Here we selected miR171b for further analysis because it regulates the formation of lateral roots, a more easily monitored developmental step. We first identified the primary transcript of miR171b by performing a rapid amplification of cDNA ends (RACE)-PCR analysis (Extended Data Fig. 1). The DNA sequence surrounding the miR171b of 284 ecotypes of *M. truncatula*, (<http://www.medicago-hapmap.org>) were compared for single-nucleotide polymorphism (SNP). As expected, the regions corresponding to the pre-miRNA, the miRNA and its partially complementary sequence miRNA* were highly conserved, with only 0.85% of SNPs in the pre-miRNA sequence, and none in the miRNA and in the miRNA* sequences (Extended Data Table 1). By contrast, the promoter and 3' region of the pri-miRNA were much more divergent (8.07% and 15.06% of SNPs, respectively; Extended Data Table 1), whereas the sequence of the 5' part of the pri-miRNA was more conserved (3.1% of SNPs), suggesting a functional constraint for coding regions. In support of our hypothesis, we identified two putative open reading frames (ORFs) potentially encoding peptides of 20 and 5 residues in this region of the pri-miR171b (Extended Data Fig. 1).

To investigate whether the start codons of the two putative ORFs are active, we fused the β -glucuronidase reporter gene *GUS* to the promoter region of the pri-miR171b. This region was sufficient to confer expression

specifically at lateral root initiations (Fig. 1a and Extended Data Fig. 2a–c). We next fused the *GUS* and the promoter region before either one of the two ATG and observed that only the first ATG drove the translation of the reporter gene at these sites (Fig. 1b); no translation was detected when *GUS* was placed downstream of the second ATG (Fig. 1c). Finally, we fused the promoter region and the first ORF (ORF1) to *GUS* and observed translation of this small ORF where lateral roots initiated (Fig. 1d and Extended Data Fig. 2d–f), demonstrating that ORF1 is translated in the plant.

To detect the endogenously produced peptide encoded by ORF1 in *M. truncatula*, we produced an antibody against this peptide. Immunofluorescence microscopy using this antibody indicated the presence of the peptide in lateral root initiations (Fig. 1e, f and Extended Data Fig. 2g-r), suggesting co-expression of the pri-miRNA. Immunoblotting showed that this antibody is highly specific for the peptide and that the peptide is produced naturally in *M. truncatula* roots (Fig. 1g). We call this miRNA-encoded peptide miPEP171b.

To investigate the possible regulatory role of miPEP171b in miR171b production, we used transformation of tobacco leaves³ to express native and mutant forms of *M. truncatula* pri-miR171b. In contrast to the large amount of miR171b produced by expression of the native pri-miR171b (Fig. 2a), expression of a mutant in which ORF1 was deleted produced smaller amounts of miR171b (Fig. 2a). Likewise, expression of a pri-miR171b in which the ATG start codon of ORF1 was mutated to ATT also produced smaller amounts of miR171b than did expression of the native pri-miR171b (Fig. 2a). This suggests that miPEP171b enhances the accumulation of its corresponding miRNA. To test this hypothesis further, we expressed the pri-miR171b together with the miPEP171b or with a control. The miR171b was more abundant when co-expressed with miPEP171b than with the control (Fig. 2b). Mutation of the start codon of the miPEP171b ORF from ATG to ATT abolished this enhanced accumulation of miR171b (Fig. 2b). Finally, a mutated miPEP171b ORF in which most nucleotides were changed without modifying the amino acid sequence of the peptide retained its positive effect on the accumulation of miR171b, reinforcing the conclusion that the ORF sequence acts as a peptide, not as an RNA (Fig. 2b).

To test whether miPEP171b enhances accumulation of miR171b in *M. truncatula*, we overexpressed miPEP171b in *M. truncatula* roots. This led to increased accumulation of endogenous miR171b (Fig. 2c). Also, overexpression of miPEP171b reduced lateral root density to a similar extent as did overexpression of pri-miR171b (Extended Data Fig. 3). Finally, overexpression of miPEP171b had no effect on the expression of other miRNAs we analysed, suggesting that miPEPs are active specifically on their respective miRNAs (Extended Data Fig. 4a).

We next investigated whether a synthetic miPEP171b applied exogenously would modify the expression of miR171b, and consequently modify plant development. The addition of miPEP171b to *M. truncatula* seedlings increased the abundance of miR171b (Fig. 2d), with consequent reduction of lateral root formation (Extended Data Fig. 3c). Treatment with a control peptide, with the same amino acid composition

¹Université de Toulouse, UPS, UMR5546, Laboratoire de Recherche en Sciences Végétales, 31326 Castanet-Tolosan, France. ²Centre National de la Recherche Scientifique, CNRS, UMR5546, 31326 Castanet-Tolosan, France. ³Fédération de Recherches FR3450 CNRS, 31326 Castanet-Tolosan, France.

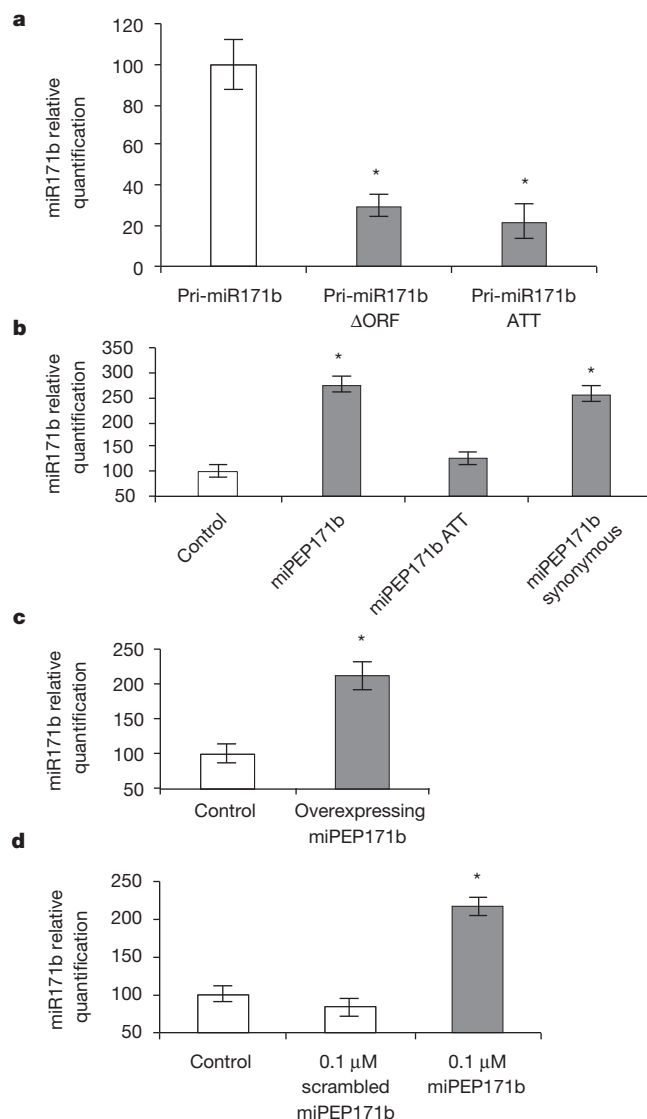
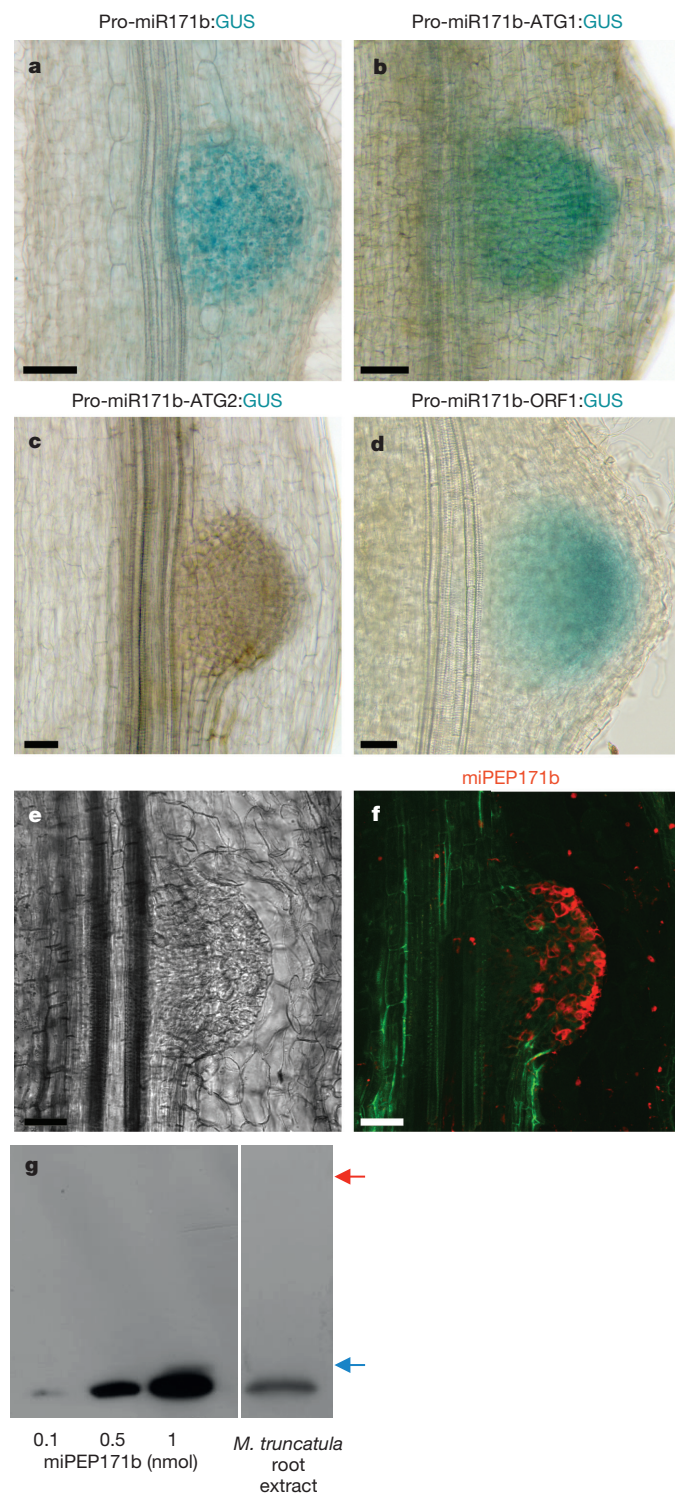


Figure 2 | Effect of miPEP171b on accumulation of miR171b.

a, Quantification of miR171b in tobacco leaves expressing the pri-miR171b, or the pri-miR171b in which the ORF1 was deleted (Δ ORF), or in which the ORF1 start codon was mutated to ATT. **b**, Quantification of miR171b in tobacco leaves expressing the pri-miR171b and a control, or the native miPEP171b, or a miPEP171b in which the ORF1 start codon was mutated to ATT, or in which the ORF1 nucleotide sequence was mutated without modifying the amino acid sequence (synonymous). **c**, Quantification of miR171b in control and miPEP171b-overexpressing *M. truncatula* roots. **d**, Quantification of miR171b in *M. truncatula* roots treated with solvent (control), synthetic scrambled or miPEP171b peptides. (Error bars, s.e.m.; asterisks, significant difference according to Student's *t*-test (**a, b**) or a Kruskal–Wallis test (**c, d**); $n = 30$ leaves or $n = 10$ roots, $P < 0.05$.)

as the miPEP171b but a scrambled sequence, had no effect (Fig. 2d). Finally, exogenous application of miPEP171b had no effect on other *M. truncatula* miRNAs (Extended Data Fig. 4b).

To see whether plant pri-miRNAs generally encode miPEPs, we analysed the data from ref. 4, which contain the sequences of the 5' ends of 50 pri-miRNAs in *Arabidopsis thaliana*. All of these pri-miRNAs contained at least one putative ORF, the 5'-most ORFs encoding peptides of 3–59 amino acid residues, without any indication of biological evidence (Extended Data Table 2). We found no common signature among them, suggesting each of these putative miPEPs is likely specific for its miRNA (Extended Data Table 2).

We next examined whether the miPEP encoded by pri-miR165a of *A. thaliana* might have similar regulatory functions in this plant as

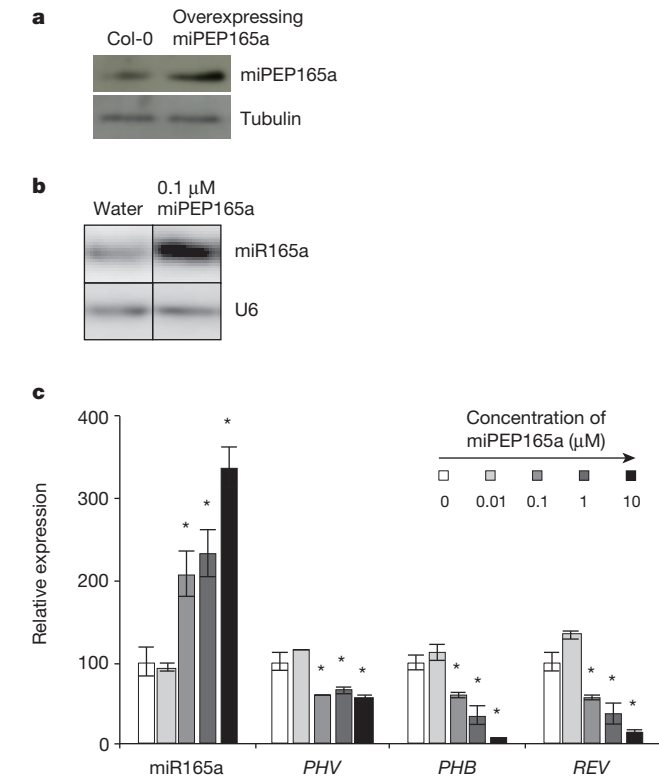


Figure 3 | Expression and effect of *A. thaliana* miPEP165a.

a, Immunoblotting of miPEP165a in wild-type (Col-0) and in miPEP165a overexpressing seedlings. **b**, Northern blot analysis of miR165a in seedlings treated with water or with synthetic miPEP165a. (**a**, **b**, see full scan blots in Supplementary Information.) **c**, Quantification of miR165a and of its target genes (*PHAVOLUTA* (*PHV*), *PHABOLUSA* (*PHB*) and *REVOLUTA* (*REV*))⁵ in seedlings treated with water or with synthetic miPEP165a. Darker bars represent increasing concentration of miPEP165a. One representative experiment of three (**a**) or four (**b**) performed is shown. Error bars, s.e.m.; asterisks, significant difference according to a Kruskal–Wallis test; $n = 10$ seedlings, $P < 0.05$.

those of the miPEP171b in *M. truncatula*. This miRNA is normally expressed in the root endodermis cells⁵. Notably, the miPEP165a amino acid sequence is well conserved in Brassicales (Extended Data Fig. 5). We first expressed fusions between the *GUS*-*GFP* and the promoter region before the first ATG or before putative alternative start codons CTG and GTG of pri-miR165a in *A. thaliana* (Extended Data Fig. 6a). The first ATG was active in endodermis cells, whereas the CTG and GTG codons were not active, indicating that the ATG is the functional start codon of this peptide (Extended Data Fig. 6b–f). Notably, the ribosome footprint data of ref. 6 revealed that the sequence encoding miPEP165a in pri-miR165a is occupied by ribosomes in *A. thaliana* seedlings, strongly suggesting that this sequence is translated (data not shown). Indeed, immunoblotting with an antibody recognizing the miPEP165a showed the presence of this peptide in wild-type (Col-0) seedlings, and the amount of the peptide increased when overexpressing the miPEP165a (Fig. 3a).

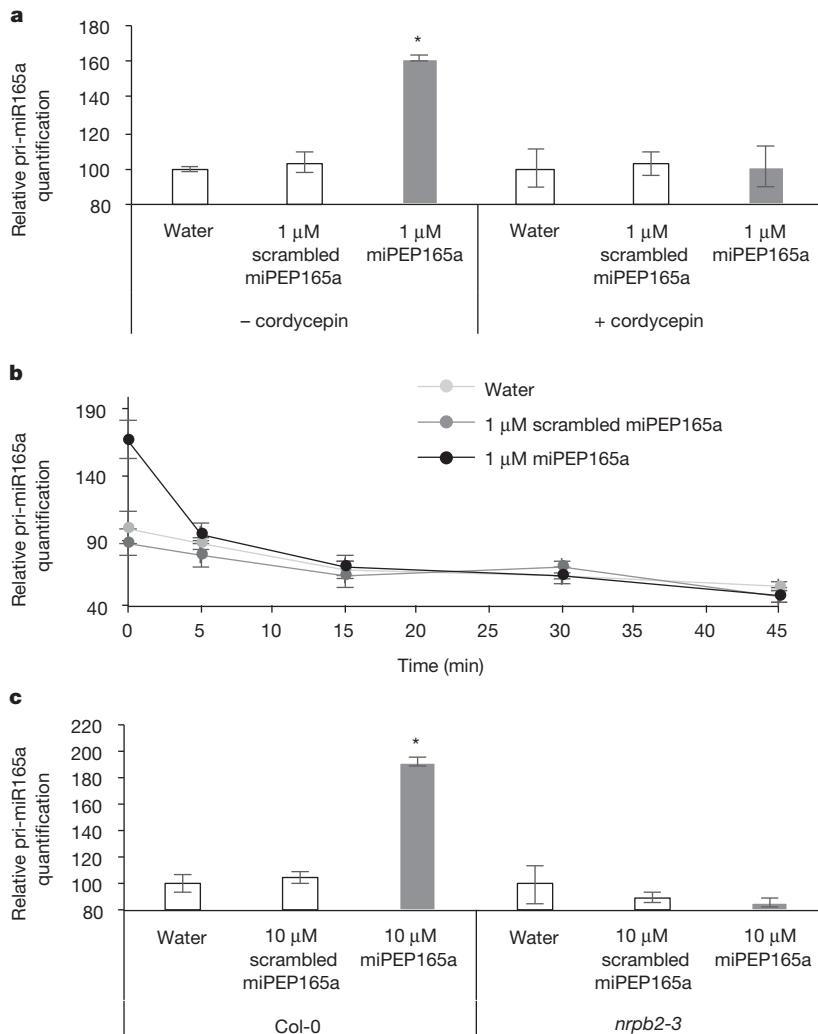


Figure 4 | Mode of action of miPEP165a.

a, Quantification of pri-miR165a in seedlings treated for 2 h with water or synthetic scrambled or miPEP165a peptides, simultaneously with or without cordycepin. **b**, Quantification of pri-miR165a in seedlings treated for 12 h with water or synthetic scrambled or miPEP165a peptides and then with cordycepin for up to 45 min. **c**, Quantification of pri-miR165a in wild-type (Col-0) or *nrpb2-3* mutant seedlings treated with water or scrambled or miPEP165a peptides. Error bars, s.e.m.; asterisks, significant difference according to a Kruskal–Wallis test, $n = 10$ seedlings, $P < 0.05$.

Treatment of *A. thaliana* seedlings with synthetic miPEP165a increased the accumulation of miR165a (Fig. 3b). Moreover, the effect of miPEP165a on accumulation of miR165a, downregulation of its target genes, and increase of root length was proportional to the dose of peptide (Fig. 3c and Extended Data Fig. 6g).

To know whether this activation of miRNAs by miPEPs is a general phenomenon, we tested five additional miPEPs and miRNAs from different miRNA families in *M. truncatula* and *A. thaliana*. In each case, application of the synthetic peptide or overexpression of the miPEP increased accumulation of the corresponding miRNA (Extended Data Fig. 7).

To understand better how miPEPs result in accumulation of their corresponding miRNAs, we analysed the expression of pri-miR165a in seedlings treated with miPEP165a for 2 h. This treatment increased the amount of pri-miR165a, unlike the treatments with water or with scrambled miPEP165a (Fig. 4a), suggesting that the miPEP either stabilized the pri-miRNA or increased its transcription. To distinguish between these two hypotheses, we treated the seedlings with miPEP165a, water or scrambled peptide for 2 h but in the presence of cordycepin, an inhibitor of RNA synthesis⁷. Cordycepin treatment completely abolished the positive effect of miPEP165a on pri-miR165a accumulation, suggesting that miPEPs activate the transcription of miRNAs (Fig. 4a). We also treated plants with miPEP165a, water or scrambled peptide, and 12 h later with cordycepin. Then we quantified the pri-miR165a at various times (Fig. 4b). As expected, the miPEP165a treatment increased the amount of pri-miR165a at time 0 (before treatment with cordycepin) compared to control roots. Upon inhibition of RNA synthesis, however, the loss of pri-miR165a was similar over time in the treated and control roots (except during the first 5 minutes), showing that the peptide does not increase the stability of pri-miR165a. Finally, we analysed the effect of miPEP165a in *nrbp2-3* mutant plants. These mutants carry a weak allele of a subunit of RNA polymerase II, which transcribes pri-miRNAs^{8,9}. We treated wild-type (Col-0) and *nrbp2-3* plants with miPEP165a, water or scrambled peptide and found no increase in the accumulation of miR165a in the mutant plants in response to the miPEP165a (Fig. 4c), further supporting the hypothesis that miPEPs are transcriptional activators of their corresponding pri-miRNAs.

The discovery of miPEPs encoded by pri-miRNAs and their effect on pri-miRNA transcription raises several questions (see Supplementary Information). Not least, how is pri-miRNA translation in the cytoplasm co-ordinated with the maturation of pri-miRNAs in the nucleus? How do miPEPs interact with the transcriptional machinery and what is the molecular basis of their specificity for their corresponding pri-miRNAs? From a practical perspective, the fact that exogenous application

of miPEPs can specifically modify plant development may have important agronomical applications.

Online Content Methods, along with any additional Extended Data display items and Source Data, are available in the online version of the paper; references unique to these sections appear only in the online paper.

Received 30 June 2014; accepted 16 February 2015.

Published online 25 March 2015.

1. Voinnet, O. Origin, biogenesis, and activity of plant microRNAs. *Cell* **136**, 669–687 (2009).
2. Lauressergues, D. *et al.* The microRNA miR171h modulates arbuscular mycorrhizal colonization of *Medicago truncatula* by targeting NSP2. *Plant J.* **72**, 512–522 (2012).
3. Combier, J. P., de Billy, F., Gamas, P., Niebel, A. & Rivas, S. Trans-regulation of the expression of the transcription factor MthAP2–1 by a uORF controls root nodule development. *Genes Dev.* **22**, 1549–1559 (2008).
4. Xie, Z. *et al.* Expression of *Arabidopsis* MIRNA genes. *Plant Physiol.* **138**, 2145–2154 (2005).
5. Carlsbecker, A. *et al.* Cell signalling by microRNA165/6 directs gene dose-dependent root cell fate. *Nature* **465**, 316–321 (2010).
6. Juntawong, P., Girke, T., Bazin, J. & Bailey-Serres, J. Translational dynamics revealed by genome-wide profiling of ribosome footprints in *Arabidopsis*. *Proc. Natl Acad. Sci. USA* **111**, E203–E212 (2014).
7. Han, M. H., Goud, S., Song, L. & Fedoroff, N. The *Arabidopsis* double-stranded RNA-binding protein HYL1 plays a role in microRNA-mediated gene regulation. *Proc. Natl Acad. Sci. USA* **101**, 1093–1098 (2004).
8. Kim, Y. J. *et al.* The role of Mediator in small and long noncoding RNA production in *Arabidopsis thaliana*. *EMBO J.* **30**, 814–822 (2011).
9. Zheng, B. *et al.* Intergenic transcription by RNA polymerase II coordinates Pol IV and Pol V in siRNA-directed transcriptional gene silencing in *Arabidopsis*. *Genes Dev.* **23**, 2850–2860 (2009).

Supplementary Information is available in the online version of the paper.

Acknowledgements This work was funded by the French ANR project miRcorrhiza (ANR-12-JSV7-0002-01), the CNRS, Paul Sabatier University Toulouse. This work is also supported by Toulouse Tech Transfer (<http://www.toulouse-tech-transfer.com>) for valorization and transfer. It was carried out in the LRSV which belongs to the Laboratoire d'Excellence intitulé TULIP (ANR-10-LABX-41). We thank the GenoToul bioinformatics facility for providing computing and storage resources. We also thank J.-M. Prospéri (UMR AGAP 1334, Montpellier, France) for *M. truncatula* seeds, X. Chen (University of California, USA) for *nrbp2-3* seeds, V. Cotelle (LRSV) for help with protein analyses, C. Rosenberg (LIPM, Castanet Tolosan, France) for providing modified pCAMBIA 2200, and F. Payre and S. Plaza (CBD CNRS, Toulouse), J. Cavaillé (LBME CNRS, Toulouse) and C. Featherstone for critical reading of the manuscript.

Author Contributions J.-P.C. designed the research; J.-P.C., D.L. and G.B. designed the experiments and discussed the results; J.-P.C., D.L., J.-M.C. and Y.M. performed the experiments; J.-P.C., H.S.C. and C.D. performed bioinformatics analyses; J.-P.C. and G.B. wrote the paper.

Author Information Reprints and permissions information is available at www.nature.com/reprints. The authors declare no competing financial interests. Readers are welcome to comment on the online version of the paper. Correspondence and requests for materials should be addressed to J.-P.C. (combier@lrsv.ups-tlse.fr).

METHODS

Biological materials. *Medicago truncatula* Gaertn cv. Jemalong genotype A17 plants were cultivated on Fahraeus medium as described previously³. *Arabidopsis thaliana* Col-0 plants were cultivated on Murashige and Skoog (MS)-based medium containing 4.4 g l⁻¹ MS base (Sigma), 10% sucrose (Sigma), 6 g l⁻¹ agarose (Sigma), pH 5.8.

Plasmid constructs. Plasmids were obtained by using pPEX or pBIN³ vectors or Golden Gate cloning strategy¹⁰. Expressions in tobacco leaves were performed using 35S promoter. pPEX and pBIN plasmids were used for overexpression studies, by cloning the fragment of interest with XhoI-NotI and ClaI-BamHI, respectively (see Extended Data Table 3 for primers used). A modified pCambia2200 binary vector¹¹ was used with the Golden Gate strategy for other cloning. The fragments to be cloned were flanked by *BsaI* restriction sites during the PCR amplification step. One-step digestion–ligation reactions were carried out with 100 ng modified pCambia, 100 ng of each PCR fragment, 1 µl 10× ligase buffer (Promega), 2.5 U T4 DNA ligase (Promega), 2.5 U *BsaI* (NEB), in a final volume of 10 µl and incubated at 37 °C for 30 min and 16 °C for 30 min and repeated once. A final incubation step at 50 °C for 20 min was used to cleave any remaining undigested cloning vector. In studies of miPEP171b and miPEP165a, 2.3 kilobase (kb) and 4 kb of promoter sequences were used for GUS analyses, respectively.

Plant transformation. Composite plants of *M. truncatula* A17 with *Agrobacterium rhizogenes*-transformed roots were obtained by the procedure described previously³. Tobacco leaf transformation was performed as described previously³. *A. thaliana* were transformed according to ref. 12. Transformants were selected on MS medium (4.4 g l⁻¹ MS base (Sigma), 10% sucrose (Sigma), 6 g l⁻¹ agarose (Sigma), pH 5.8) supplemented with 25 mg l⁻¹ kanamycin.

Histochemical staining. GUS staining was performed as described previously³. The samples were observed with an Axiozoom V16 microscope (Zeiss).

Expression analyses. miRNA quantification was performed by northern blot analyses², or by stem-loop quantitative reverse transcription (qRT)–PCR¹³. In brief, RNAs were extracted by using the TRI Reagent (Molecular Research Center, Inc.) following the manufacturer's instructions, except that the RNAs were precipitated with three volumes of ethanol. RNAs were reverse-transcribed using a specific reverse-transcription-primer stem-loop in combination with hexamers, adapted from ref. 13. One microgram of RNAs was added to stem loop primer (0.2 µM), hexamers (500 ng), reverse transcription buffer (1×), SSIII (Invitrogen) (1 U), dNTPs (0.2 mM each), and dithiothreitol (0.8 mM) in a total volume of 25 µl. Gene expression was measured by qRT–PCR (see Extended Data Table 3 for primers used) and performed as described previously³. Actin was used as housekeeping gene to normalize qRT–PCR analyses on *A. thaliana* (See Extended Data Table 3). For northern blotting analyses, U6, which is a non-coding small nuclear RNA was used as a control for equal loading. Levels of expression in Fig. 4a, c for the controls were set at 100. For all the qPCR, each biological sample has two technical replicates.

Statistical analyses. The mean values of relative gene expression, lateral root production or root length were compared by using Student's *t*-test (when *n* > 30) or the Kruskal–Wallis test (when *n* < 30). In each case, *n* represents independent biological replicates. Error bars represent the standard error of the mean (s.e.m.). Asterisks indicate significant differences (*P* < 0.05). No statistical methods were used to predetermine sample size.

Peptide assays. Peptides were synthesized by Smartox (<http://www.smartox-biotech.com>) and dissolved at 10 mM in water (miPEP164a, miPEP65a), in 10% acetic acid (v/v) (miPEP169d), or in 40% water, 50% acetonitrile and 10% acetic

acid (v/v/v) (miPEP171b). Plants were treated with concentrations from 0.01 to 10 µM peptide diluted in the agar growth medium or in solution in water (for Fig. 4a, b).

Sequences. miPEP164a: MPSWHGMVLLPYVKHSTHSTHTHTHNYGCACE LVFH; miPEP165a: MRVKLFQLRGMLSGSRL; scrambled miPEP165a: SMKQ RVLLGRLSIFGLMR; miPEP169d: MVKESFMERLKVR; miPEP171b: MLLHRLS KFCKIERDIVYIS; scrambled miPEP171b: LIVSHLYSEKFDCMRKILRI.

Antibodies. Polyclonal antibodies against full-length miPEP165a and miPEP171b were obtained by inoculating rabbits (<http://www.agrobio.com>). Antibodies were purified by affinity chromatography on columns containing the appropriate peptide.

Immunoblots. Total protein extracts were obtained as described previously³, and 50 µg were loaded and separated by SDS PAGE. Transfer was performed in phosphate buffer overnight at 4 °C and at 15 V, and the membrane was incubated for 45 min at room temperature in 0.2% (v/v) glutaraldehyde. Primary antibodies were used at 1:1,000 (v/v) dilution and HRP-conjugated goat anti-rabbit IgG (<http://www.agrobio.com>) was used as secondary antibody at 1:40,000 (v/v) dilution. Immunoblotting of tubulin was performed as a control for equal loading (Fig. 3a).

Immunohistochemistry. Hairy roots and plantlets of *M. truncatula* were fixed for two hours in 4% (v/v) formalin in 50 mM cacodylate buffer (pH 7.2). Then they were embedded in 5% low melting-point agarose dissolved in water. Semi-thin sections (100 µm) were prepared and placed on Teflon-coated well slides in phosphate buffer for immunology (PBi: 0.1 M potassium phosphate buffer pH 7.5). The sections were blocked by incubating in PBi containing 2% Tween (PBiT) and 1% bovine serum albumin for 2 h (PBiT–BSA), then incubated overnight (12 h) at 4 °C with primary antibody diluted 1:50 (v/v) in PBiT–BSA. They were then washed five times with PBiT over the course of 3 hours and incubated at room temperature for 2 hours with a goat anti-rabbit IgG coupled to Alexa Fluor 633 (Molecular Probes) diluted 1:1,000 (v/v) in PBiT–BSA. Finally, the slides were washed in PBi for 1 hour, mounted in Citifluor (antifading mounting medium) and observed by confocal microscopy on a LeicaTCS SP2 laser scanning confocal microscope. The signal obtained from controls with pre-immune serum instead of primary antibody, or in the absence of primary antibody, were subtracted from the signal obtained with the specific antibody.

RNA stability. Two-week-old plants grown vertically on solid MS medium were transferred into wells of six-well plates containing 1 ml liquid MS medium. Simultaneously or after 16 h incubation with 1 µM miPEP165a, the plants were treated with 100 µg ml⁻¹ cordycepin (Sigma) and harvested after various times for RNA extraction and quantification. Experiments were repeated three times.

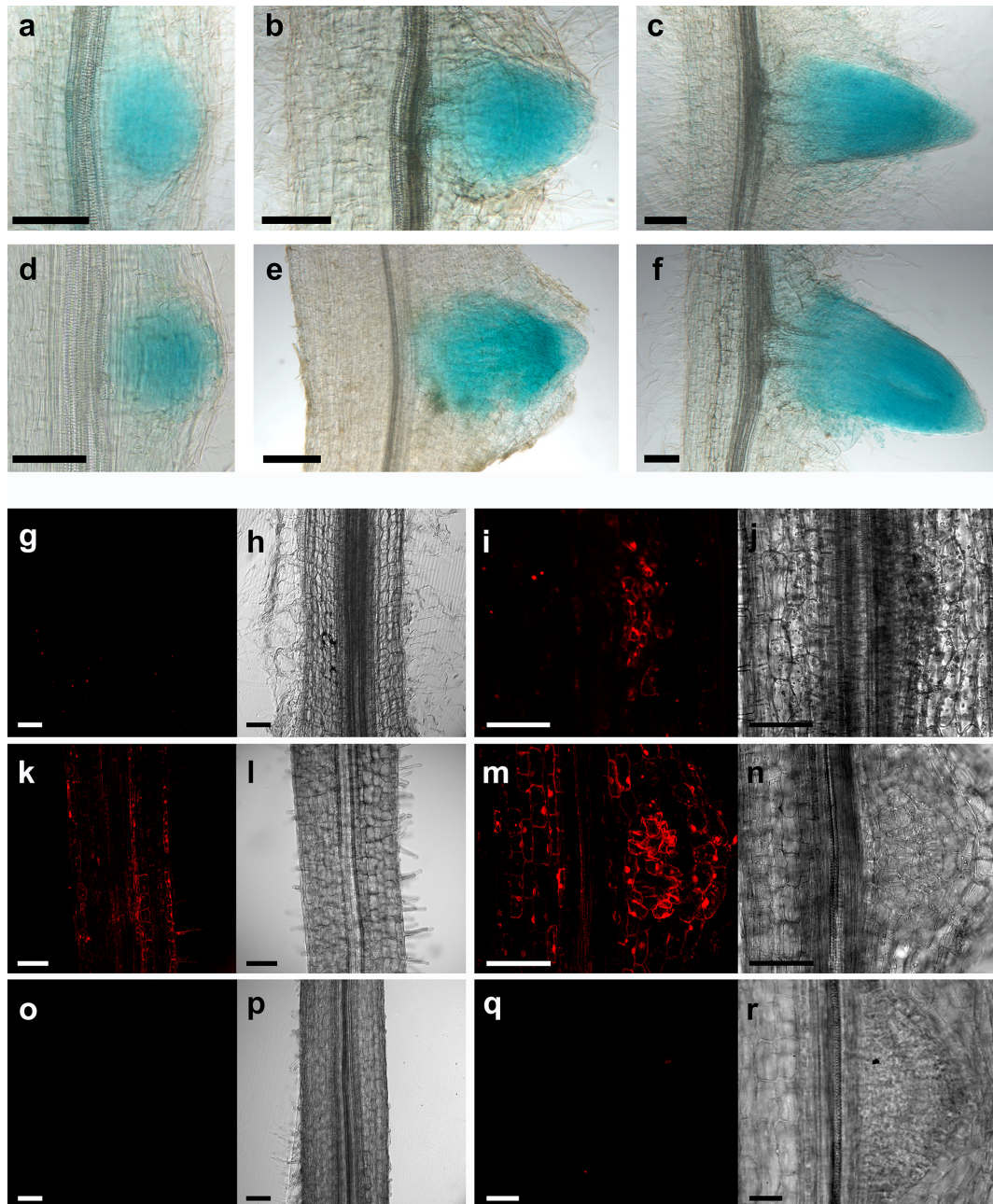
RACE–PCR. For pri-miRNA 5' end identification, RACE–PCR was carried out following the manufacturer's instructions (FirstChoiceRLM–RACE kit, Ambion). For pre-miRNA 5' end identification, the Calf Intestinal Phosphatase treatment was omitted.

- Engler, C., Kandzia, R. & Marillonnet, S. A one pot, one step, precision cloning method with high throughput capability. *PLoS ONE* **3**, e3647 (2008).
- Fliegmann, J. et al. Lipo-chitooligosaccharidic symbiotic signals are recognized by LysM receptor-like kinase LYR3 in the legume *Medicago truncatula*. *ACS Chem. Biol.* **8**, 1900–1906 (2013).
- Clough, S. J. & Bent, A. F. Floral dip: a simplified method for *Agrobacterium*-mediated transformation of *Arabidopsis thaliana*. *Plant J.* **16**, 735–743 (1998).
- Mestdagh, P. et al. High-throughput stem-loop RT-qPCR miRNA expression profiling using minute amounts of input RNA. *Nucleic Acids Res.* **36**, e143 (2008).

ATTGGTCAAACATACATACAGTAGCACTAGCTGGTTTCATTATCCACTATG¹CTTCTTCATAGGCTCTCC
M L L H R L S
AAATTTTGCAAAATTGAAAGAGACATAGTATATATATCTTAGCAAGGAGAAATTCAGGATATTGAGGATG²
K F C K I E R D I V Y I S M
AAGATTGAAGAGTAA TCAGTGATGAAGAAAGCAAGCAAGGTA TTGGCGCGCCTCAATTTGAATACATGGCT
K I E E
ATAAAAAATGCATCATATCAGCCATGTAGTTTGATTGAGCCGCGTCAATATCTTGGTTTCCATCTCCAA//

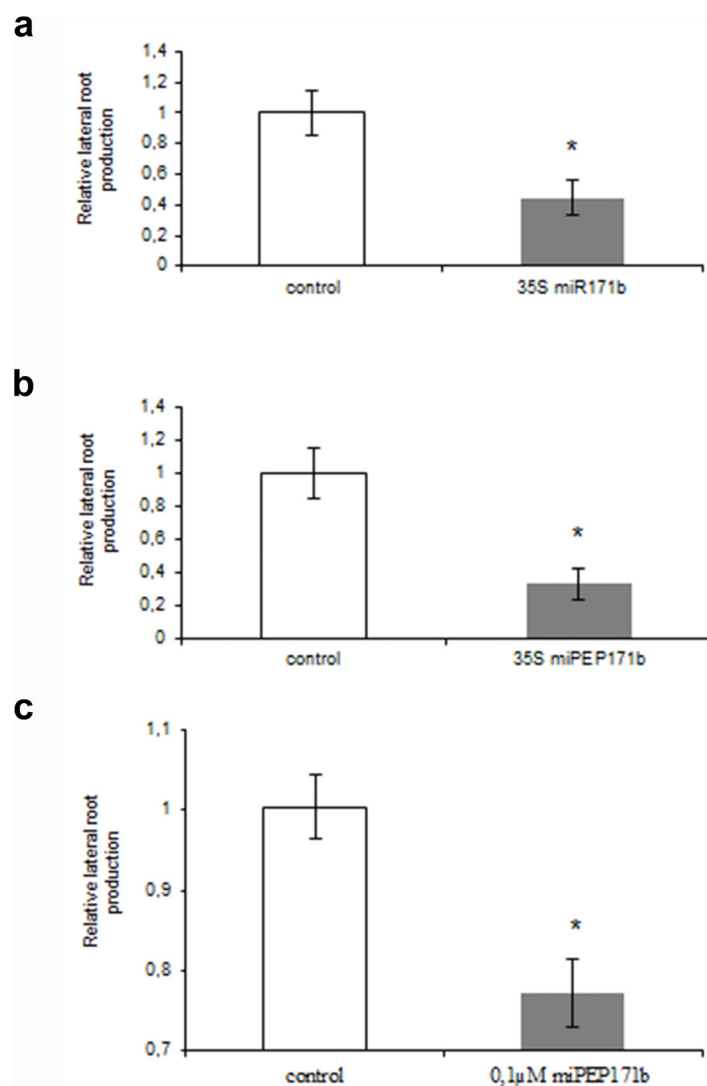
Extended Data Figure 1 | Characterization of the *M. truncatula* miPEP171b. The 5' part of the pri-miR171b, as identified by 5' RACE-PCR analysis. The short putative ORFs are in blue, the miR171b* in green, and the mature miR171b in red. The two first ATG start codons of the pri-miR171b

are underlined, and the sequences of their corresponding peptides are shown below. The black vertical line indicates the 5' end of the pre-miR171b precursor, identified by 5' RACE-PCR.



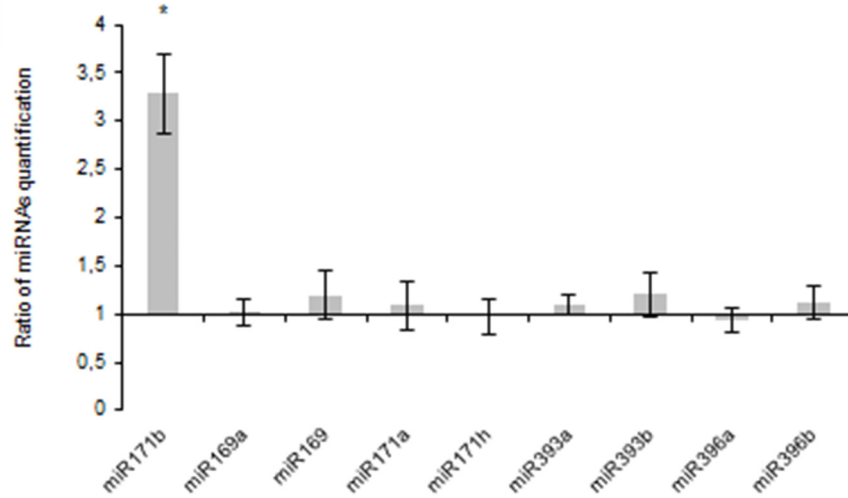
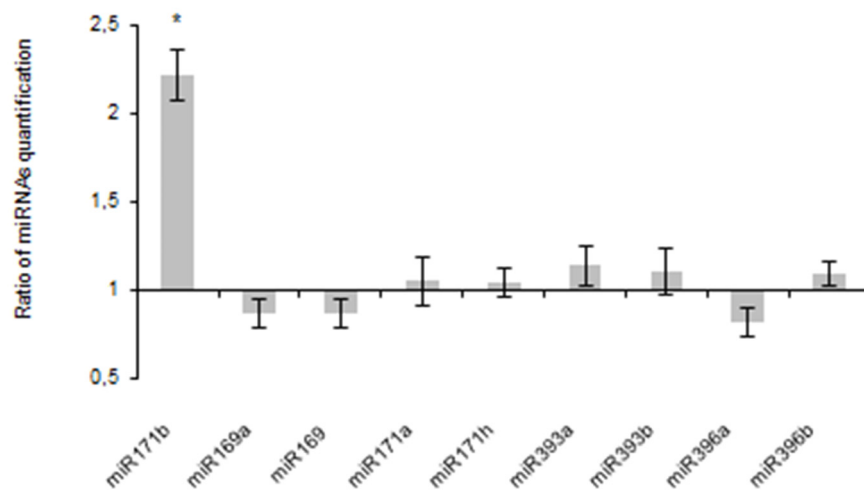
Extended Data Figure 2 | Expression of miPEP171b in *M. truncatula* roots. **a–c**, Staining for GUS activity (blue) showing expression of the miR171b at different stages of lateral root development. **d–f**, Staining for GUS activity (blue) showing expression of the miPEP171b at different stages of lateral root development. **g–r**, Immunolocalization of miPEP171b. Confocal immunofluorescence microscopy of endogenous miPEP171b (red) in the main roots (**g**) and lateral root primordia (**i**) of wild-type plants, and their corresponding bright-field images (**h**, **j**). Confocal immunofluorescence

microscopy of miPEP171b (red) in main roots (**k**) and lateral root primordia (**m**) in roots overexpressing miPEP171b, and their corresponding bright-field images (**l**, **n**). Controls for immunofluorescence staining of main roots (**o**) and lateral root primordia (**q**) of wild-type plants, and their corresponding bright-field images (**p**, **r**), in which the primary antibody was omitted (scale bars, 100 μ m). One representative experiment of nine (**g–j**), four (**k–n**) or seventeen (**o–r**) performed is shown.



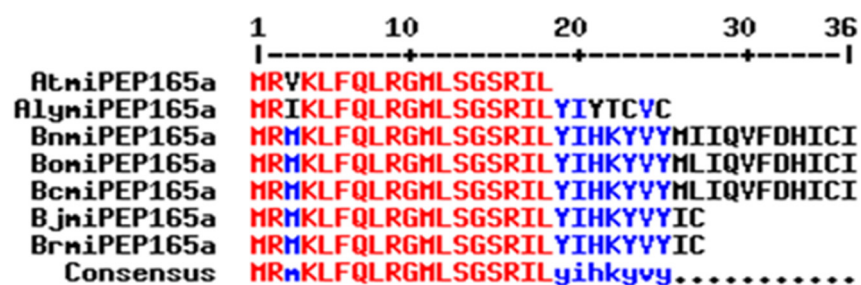
Extended Data Figure 3 | Effect of an upregulation of the miR171b on root development in *M. truncatula*. **a**, Relative production of lateral roots in roots overexpressing the pri-miR171b compared to the production in control roots. **b**, Relative production of lateral roots in roots overexpressing the miPEP171b compared to the production in control roots. **c**, Relative

production of lateral roots in plants treated with 0.1 μ M miPEP171b synthetic peptide (0.1 μ M miPEP171b) compared to the production in roots treated with control solvent (control). Error bars represent s.e.m., asterisks indicate a significant difference between the overexpressing roots and the control according to Student's *t*-test ($n = 100$ independent plants, $P < 0.05$).

a**b**

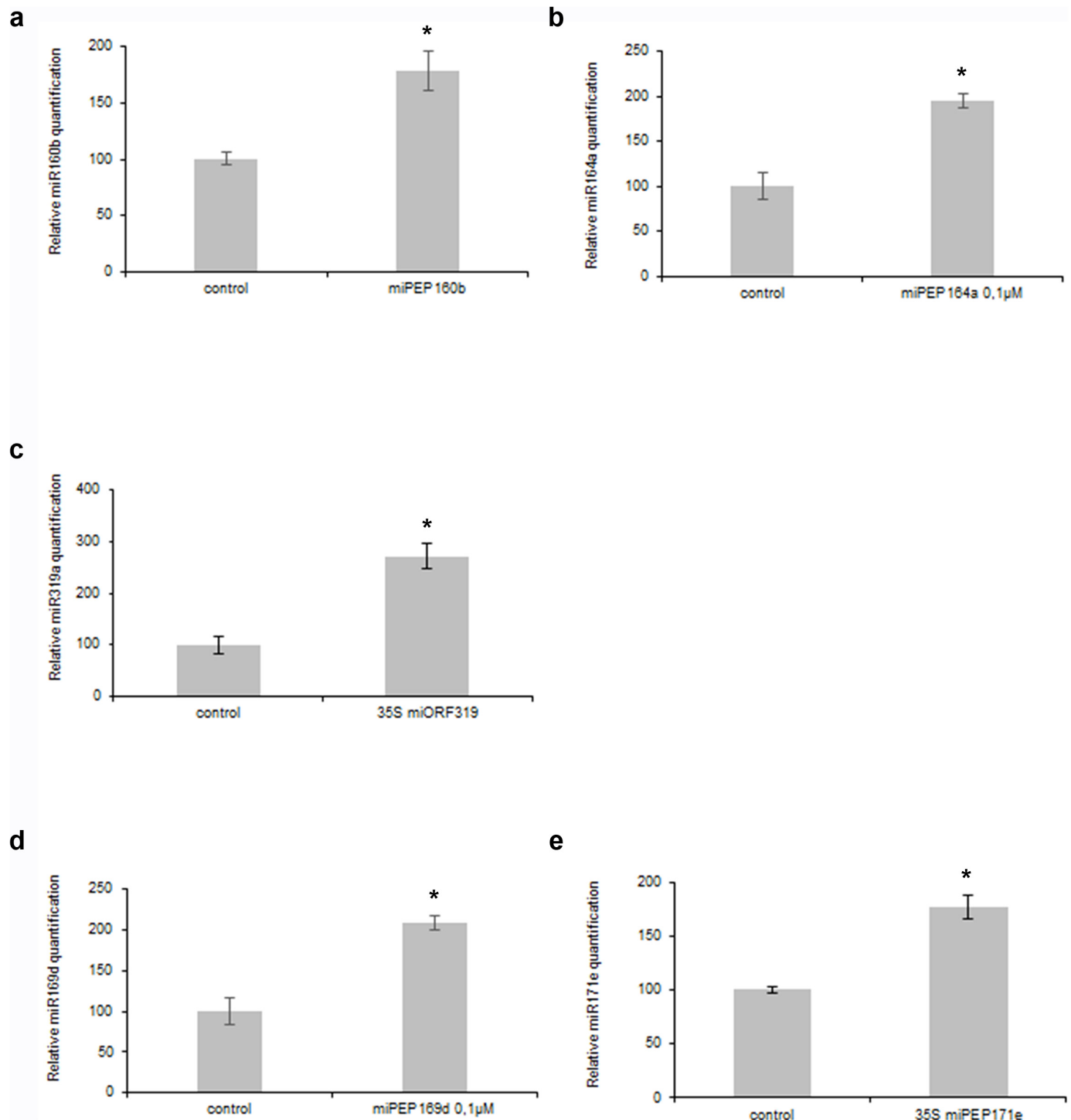
Extended Data Figure 4 | Effect of miPEP171b on the expression of various miRNAs in *M. truncatula*. **a**, Effect of overexpression of miPEP171b. **b**, Effect of exogenous treatment with 0.1 μ M of the synthetic miPEP171b. Histograms represent the relative expression of each miRNA in roots overexpressing

miPEP171b compared to wild-type roots (**a**) or in roots treated with the peptide compared to the roots treated with solvent (**b**). Error bars represent s.e.m., asterisks indicate a significant difference between the treatment and the control according to a Kruskal–Wallis test ($n = 10$ independent roots, $P < 0.05$).



Extended Data Figure 5 | Alignment of miPEP165a amino acid sequences of seven species of Brassicales using MultAlin. MultAlin available at <http://multalin.toulouse.inra.fr/multalin/multalin.html>. At, *Arabidopsis thaliana*; Aly, *Arabidopsis lyrata*; Bn, *Brassica napus*; Bo, *Brassica oleracea*;

Bc, *Brassica carinata*; Bj, *Brassica juncea*; Br, *Brassica rapa*. Red represents homology in all seven species; blue represents homology in most of the species. Upper-case letters denote high-consensus sequence; lower-case letters denote low-consensus sequence.



Extended Data Figure 7 | Effect of various miPEPs from *Arabidopsis thaliana* and *Medicago truncatula* on the expression of their corresponding miRNA. a–c, miPEPs from *A. thaliana*. a, Expression of miR160b in response to overexpression of miPEP160b. b, Expression of miR164a in response to treatment with 0.1 μM of miPEP164a. c, Expression of miR319a in response to overexpression of miPEP319a. d–e, miPEPs from *M. truncatula*. d, Expression

of miR169d in response to treatment with 0.1 μM of miPEP169d. e, Expression of miR171e in response to overexpression of miPEP171e. Error bars represent s.e.m., asterisks indicate a significant difference between the treatment and the control according to a Kruskal–Wallis test ($n = 10$ independent roots or tobacco leaves, $P < 0.05$).

Extended Data Table 1 | DNA polymorphism analysis of various regions of the pri-miR171b in 284 ecotypes of *M. truncatula*

	size	# SNPs	# mutations	% SNP	# haplotypes
Promoter pri-mir171b	1127	91	100	8.07	161
5' pri-miR171b	129	4	4	3.1	5
miPEP171b	62	2	2	3.22	3
Pre-miR171b	118	1	1	0.85	2
miR171b+miR171b*	42	0	0	0	1
3' pri-miR171b	259	39	42	15.06	89

A haplotype is defined as a sequence that differs by at least one SNP from the other haplotypes.

Extended Data Table 2 | List of putative miPEPs identified in *A. thaliana* (in which the putative start codon is ATG)

name	sequence	size (aa)	size (MW)
miPEP156a	MFCSIQCVAHFLPLHVREIKKATRAIKKGKTL	33	3824
miPEP156c	MKDNFPLLLRL	11	1359
miPEP156e	MIYINKYGSISAVEDD	16	1818
miPEP156f	MSQR	4	520
miPEP157c	MMLHITHRFESDVGC	15	1776
miPEP157d	MLYV	4	524
miPEP159a	MTWPLLSLSFLLSKYV	16	1898
miPEP159b	MFYLS	5	659
miPEP160a	MFCLLIPIFS FVFSNRLRLQEQ	24	2936
miPEP160b	MFSPQ	5	608
miPEP160c	MEMRRGLVYNNIYI	14	1790
miPEP161	MKIPLELPKL	10	1199
miPEP162a	MVSGQEDSWLKLSLCLFLSLDLSLI	27	3045
miPEP162b	MFLILFLRLIMICVCSSTDFLRSVNYFCLFIYDL	34	4114
miPEP163	MSTTQEHRS	9	1076
miPEP164a	MPSWHGMVLLPYVKHTHASTHTHTHNIYGCACELVFH	37	4256
miPEP164b	MMKVCDEQDGEAGHVHY	17	1949
miPEP165a	MRVKLFQLRGMLSGSRIL	18	2105
miPEP166a	MILDLFNSNNRIEPSDFRFD	19	2372
miPEP166b	MRDR	4	576
miPEP166c	MKKRITRINLEEQIKKTLDDSRTRLHSP	28	3407
miPEP166d	MKKIGSIDSF	10	1125
miPEP167a	MNRKISLSLS	10	1148
miPEP167b	MMGCFVGF	8	891
miPEP169a	MTCRFK	6	784
miPEP169c	MPHTNLKDLFIFS PNVFFSFAIYLHNSWNKNYIHKRENFHNTS FALIFFSSIMS INYG	59	7110
miPEP169h	MVT	3	349
miPEP169l	MRHES	6	786
miPEP169n	MKCMKKRGLTWRKASCLVAKDDLPLDLRLHDSISNSCILDYYTF	45	5315
miPEP170	MFPRESL	7	879
miPEP171a	MNLLKKEQRQRQSRIGSHCIASLVLDGVMKKI	34	4057
miPEP171b	MVLSGKLT	9	995
miPEP171c	MLSLSHFHC	10	1187
miPEP172a	MASKIW	6	734
miPEP172b	MCTYYLILNKYF	12	1621
miPEP172c	MFPKWCRLES	11	1367
miPEP172e	MGSLSLFKSQLEIIMLLLSLSK	22	2452
miPEP319a	MNIHTYHLLFPLSVFHQSSEVPNALS LHIHTYEYIIIVVIDPFRITLAFR	50	5917
miPEP319b	MVPQINLWSSRVILKIRIDSSTHREEDHCIONHKHGLSFI FFF	43	5120
miPEP394a	MSLQFYERVSFKNTVK	16	1977
miPEP395c	MTEQEEESQMST	12	1429
miPEP395e	MYLQYIDNVI SIYSNNRRVGRMFSRVPLSTSLEIQFFIK	39	4700
miPEP396a	MTLSVFFHSFLELQNFRRFFFSFDISYA	29	3636
miPEP397b	MSKEIFFSPGFE	12	1418
miPEP399b	MKRNM	5	678
miPEP399c	MSLAKGELPCHCFRINTVYNRFC	23	2703
miPEP399d	MQCEI	5	622
miPEP403	MFCA	4	470
miPEP447a	MVMAHH	6	724
miPEP447b	MLLIIVELVL	10	1155

aa, amino acids; MW, molecular weight.

Extended Data Table 3 | List of primers used

name	sequence
promiR171b 5'	GGGCTCTCCATGGGCTGTTAGATCCAACTTCGG
promiR171b 3'	GGGCTCTCCATGGGCTGTTAGATCCAACTTCGG
promiR171b 3' ATG1	22GGTCTCgACACAAGCATAGTGGAAATGAAACC
promiR171b 3' ATG2	2222GGTCTCgCCATCTTCATCCTCAATATCCTAATTC
promiR171b 3' fusionORF1	22GGTCTCgACACAGATATATATATATGCTCTCTTCA
miR171b5'	222GGTCTC C TAGC TTGGTCAAAACATACATACAGTAGCACTAG
miR171b 3'	222GGTCTCgCGTAAATTTGTACTGATTGAATGAAATGGTACAC
miORF171b5'	TCAGTCCGCTCGAGATGCTTCTTCATAGGCTCTCC
miORF171b3'	AAGGAAAAAAGCGGCGCGCTAAGATATATATATGCTCTCTTCAA
miORF171b5'ATT	TCAGTCCGCTCGAGATTCTTCTTCATAGGCTCTCC
miORF171b5'delta orf	CAAGGAGAAATTCAGGATATTGAGGATGA
miORF171b3'delta orf	TCATCTCAATATCTGAATTTCTCTTGAAGTGAATAATGAAACCAGCTAG
miORF5' synonymous	AAGTTCTGTAAGATAGAGCGGATATTGTTTACATTAGCTAGCAAGGAGAAATTCAGGATATTGAGGATGA
miORF3' synonymous	CAATATCGCGCTCTATCTTACAGAACTTACTTAAGCGGTGTAATAACATAGTGGAAATAATGAAACCAGCTAG
miR160b5'	222GGTCTCgTAGCACTCATAACTCTCCCCAAATTC
miR160b3'	222GGTCTCgCGTAGAAAGAATGTTGCGAAAAAC AATG
miORF160b5'	TAGCATGTTTTCCCTCAATGA
miORF160b3'	cgt2TCATTGAGGGGAAACAT
miR319a5'	tcacgAGAGAGAGCTTCTTGAGTC
miR319a3'	tcgggatccAGAGGGAGCTCCCTTCAGT
miORF319a5'	tcacgATGAATATACATACATACCATCAT
miORF319a3'	tcgggatccTCTAAAAGCTAAAGTGATTCTAAA
miR171e5'	TCAGTCCGCTCGAGGAATAAGTGAATATTATCGATATTT
miR171e3'	AAGGAAAAAAGCGGCGCAAGTGATATTGGCGCGGCT
miORF171e5'	tcacgATGATGGTGTGTTGGGAAGCC
miORF171e3'	tcgggatccTACATGTAATCCGCTTCCGG
promiR165aBsal5	aGGTCTCCAAATttaaactgtca gtgc atg gat gt
miORF165a fusion GTG Bsal 3	aGGTCTCgACACattcacaatttt ttgtt gta ga gag
miORF165a fusion CTG Bsal 3	aGGTCTCgACACtagcagattcac aa atttt ttgtt g
miORF165a fusion ATG Bsal 3	aGGTCTCgACACcctcatgataatcg atctt agc a
miORF165aBsal5	tcacgATGAGGGTTAAGCTATTTAGT
miORF165aBam3	tcgggatccTAATATCTCGATCCAGACAAC
MtubiQ5	GCAGATAGACACGCTGGGA
MtubiQ3	AACTCTTGGGCAGGCAATAA
miR171bQ5	GTCGTATCCAGTGCAGGGTCCGAGGTATTGCACTGGATACG ACGATATT
miR171bQ3	TGCGTTGATTGAGCGCGTGC
LOM1Q5	AATGATGGATGCTTCGGTTC
LOM1Q3	TGTTTCTGCTGCTGATGTC
LOM2Q5	CTGAAACTGATGAGCCGACA
LOM2Q3	TGGATATTTGCATGGCTCAA
pri-miR165aQ5	CTTGGGCAAAATACAAAAGC
pri-miR165aQ3	GCCATGCAAGAAAGATTCAA
AtPHVQ5	GCAACTGCAGTGGAAATAGCA
AtPHVQ3	GCGACCTTCATGGGTCTAA
AtPHBQ5	CTCAGCATCAGCAACGTGAT
AtPHBQ3	AACTCTGCTAGGGCTCTCTC
AtREVQ5	TCACAACCTCTCAGCATTCG
AtREVQ3	ACCCAATCAACAGCAGTTCC
Atactine2F	GGTAACATTGTGCTCAGTGG
Atactine2R	CTCGGCTTGAGATCCACA

G-protein-independent coupling of MC4R to Kir7.1 in hypothalamic neurons

Masoud Ghamari-Langroudi¹, Gregory J. Digby¹, Julien A. Sebag¹, Glenn L. Millhauser², Rafael Palomino², Robert Matthews¹, Taneisha Gillyard^{1,3}, Brandon L. Panaro¹, Iain R. Tough⁴, Helen M. Cox⁴, Jerod S. Denton^{5,6} & Roger D. Cone¹

The regulated release of anorexigenic α -melanocyte stimulating hormone (α -MSH) and orexigenic Agouti-related protein (AgRP) from discrete hypothalamic arcuate neurons onto common target sites in the central nervous system has a fundamental role in the regulation of energy homeostasis. Both peptides bind with high affinity to the melanocortin-4 receptor (MC4R); existing data show that α -MSH is an agonist that couples the receptor to the G_{α_s} signalling pathway¹, while AgRP binds competitively to block α -MSH binding² and blocks the constitutive activity mediated by the ligand-mimetic amino-terminal domain of the receptor³. Here we show that, in mice, regulation of firing activity of neurons from the paraventricular nucleus of the hypothalamus (PVN) by α -MSH and AgRP can be mediated independently of G_{α_s} signalling by ligand-induced coupling of MC4R to closure of inwardly rectifying potassium channel, Kir7.1. Furthermore, AgRP is a biased agonist that hyperpolarizes neurons by binding to MC4R and opening Kir7.1, independently of its inhibition of α -MSH binding. Consequently, Kir7.1 signalling appears to be central to melanocortin-mediated regulation of energy homeostasis within the PVN. Coupling of MC4R to Kir7.1 may explain unusual aspects of the control of energy homeostasis by melanocortin signalling, including the gene dosage effect of MC4R⁴ and the sustained effects of AgRP on food intake⁵.

To better understand the diametrically opposed regulation of food intake by α -MSH and AgRP, we sought to identify mechanism(s) by which these peptides control firing activity of MC4R neurons in the paraventricular nucleus of the hypothalamus (PVN), a brain nucleus in which MC4R is known to control food intake⁶. Using electrophysiology with murine hypothalamic slice preparations in which MC4R PVN neurons are labelled with green fluorescent protein (GFP), α -MSH increases the frequency of action potential firing in PVN MC4R neurons recorded from loose patches (Fig. 1a), depolarizing these cells on average by ~ 8 mV through action on postsynaptic MC4R (Fig. 1b). α -MSH had no effect on neighbouring non-GFP-labelled neurons (Fig. 1c). AgRP hyperpolarized PVN MC4R neurons (Fig. 1d), inhibiting their firing activity.

We next examined if α -MSH depolarized neurons through activation of the G_{α_s} -adenylyl cyclase-cAMP-PKA pathway. PKAi (20 μ M intrapipette), a peptide inhibitor of PKA, failed to abolish the α -MSH-induced increase in firing frequency in PVN neurons during whole cell recording, (not shown) or to block α -MSH-induced depolarization of membrane potential (Fig. 1e). Inhibition of adenylyl cyclase with SQ22536 (25 μ M) similarly failed to block α -MSH-induced depolarization of membrane potential (Fig. 1f). Finally, we examined whether blocking G protein signalling can inhibit MC4R-mediated depolarization by loading cells with the inhibitory GDP analogue, GDP β S. To verify that GDP β S blocked G-protein function, we examined effects of activation of D1 dopamine receptor, known to depolarize neurons via activation of G_{α_s} . Activation of D1 dopamine receptor by the D1 agonist SKF83822 (5 μ M) depolarized PVN neurons (Fig. 1g). GDP β S (5 mM) blocked D1-mediated

depolarization, but failed to block α -MSH-induced depolarization of PVN MC4R neurons (Fig. 1g). Several other inhibitors of components of G protein signalling were also ineffective in blocking neuronal firing

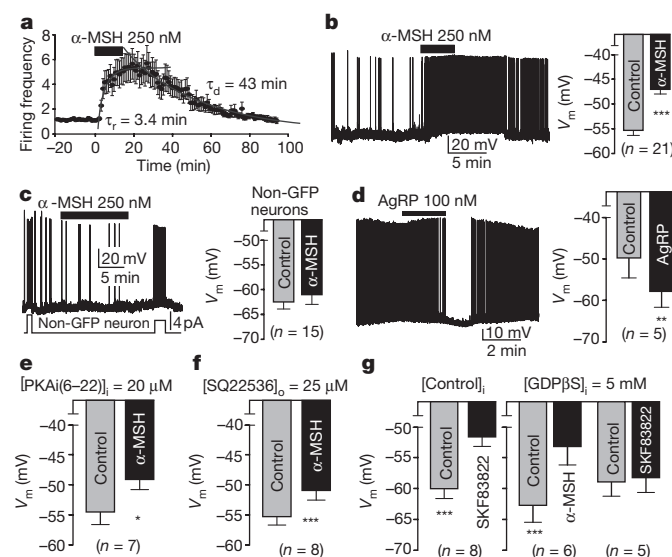


Figure 1 | Depolarization of hypothalamic PVN MC4R neurons by α -MSH is G-protein independent. **a**, Normalized mean amplitude (\pm s.e.m.) and time-course of α -MSH action on firing frequencies of PVN MC4R neurons ($n = 14$) recorded in loose-patch configuration using hypothalamic slice preparations from MC4R-GFP mice before and after the addition of 250 nM α -MSH and washout. **b**, A representative depolarizing response of a PVN MC4R neuron recorded in current clamp to bath application of 250 nM α -MSH. The bar graph represents mean \pm s.e.m. ($***P < 0.001$). V_m , membrane potential in millivolts (mV). **c**, A representative response of a non-GFP-expressing PVN neuron recorded in current clamp to bath application of 250 nM α -MSH. Application of brief current pulses (lower trace) caused depolarization and burst firing (upper trace), while α -MSH failed to depolarize this neuron. The bar graph represents mean \pm s.e.m. ($P > 0.1$). **d**, A representative hyperpolarizing response of a PVN MC4R neuron recorded in current clamp to bath application of 100 nM AgRP. The bar graph represents mean \pm s.e.m. ($**P < 0.01$). **e**, Intracellular PKA inhibitor, PKAi (6–22 amide) at 20 μ M, fails to block the α -MSH-induced depolarization of membrane potential in PVN MC4R neurons. **f**, Inhibition of adenylyl cyclase by SQ22536 fails to block depolarizing effects of α -MSH. **g**, Application of 5 μ M SKF83822, a selective D1 receptor agonist, causes depolarization of PVN neurons (left panel). Intrapipette addition of 5 mM GDP β S, a blocker of G-protein signalling (right panel), fails to block the α -MSH-induced depolarization in PVN MC4R neurons, but blocks the depolarization and firing activity induced by SKF83822. Data in panels **e**, **g** show mean \pm s.e.m., $*P < 0.05$, $***P < 0.001$, paired t -test. In all electrophysiological studies, each n represents an independent neuron and slice, and no more than two slices were used per animal.

¹Department of Molecular Physiology & Biophysics, Vanderbilt University Medical Center, Nashville, Tennessee 37232, USA. ²Department of Chemistry & Biochemistry, University of California, Santa Cruz, California 95064, USA. ³Department of Pharmacology, Meharry Medical College, Nashville, Tennessee 37208, USA. ⁴King's College London, Wolfson Centre for Age-Related Diseases, Guy's Campus, London SE1 1UL, UK. ⁵Department of Anesthesiology, Vanderbilt University Medical Center, Nashville, Tennessee 37232, USA. ⁶Department of Pharmacology, Vanderbilt University Medical Center, Nashville, Tennessee 37232, USA.

or depolarization of PVN MC4R neurons by α -MSH (Extended Data Fig. 1a–d), including GTP γ S (a non-hydrolysable GTP analogue, 1.5 mM), gallein (a G $\beta\gamma$ blocker, 25 μ M), or U0126 (a MAPK inhibitor, 1 μ M). Together, these findings support a novel hypothesis: a G-protein-independent pathway for MC4R-mediated depolarization of PVN neurons.

The currents underlying MC4R mediated depolarization of PVN neurons were then characterized with current–voltage (I–V) analysis in external 20 mM K⁺. Using whole-cell recording from voltage clamped neurons pre-treated with 0.5 μ M tetrodotoxin (TTX), 200 μ M picrotoxin (PTX) and 1 mM kynurenic acid (KYN), current responses of PVN MC4R neurons to voltage ramps (–120 to –20 mV for 2 s) were used to generate the I–V relationships of the α -MSH-induced response (Fig. 2a–c). α -MSH significantly (33%) decreased cell membrane conductance from 5.7 ± 1.0 nS in control to 3.8 ± 0.8 nS (Fig. 2g), with current generated by α -MSH being linear from –120 to –60 mV that rectified inwardly at membrane potentials negative to its reversal of polarity. Its reversal potential was near -48.1 ± 3.4 mV in the presence of 20 mM external K⁺, with an estimated reversal potential of K⁺ near –53.5 mV (Nernst equation). These results, in addition to those performed in 3.1 mM external [K⁺] (estimated ErevK⁺ \approx –98 mV, not shown), suggest that α -MSH generates an inward current by closure of a steady-state K⁺-mediated inward rectifier current, as in hypothalamic arcuate (ARC) neurons⁸.

We next tested the hypothesis that AgRP hyperpolarizes cells by activating K⁺-mediated currents. Current responses of PVN neurons to voltage ramps (–110 to –50 mV for 2 s) were used to generate I–V relationships of the AgRP-induced response in 20 mM external [K⁺] (Fig. 2d–f). Application of AgRP (50 nM) significantly increased membrane conductance (75%, Fig. 2g), and the AgRP-activated current displayed a reversal of polarity (-46.7 ± 3.0 mV) and rectification properties similar to α -MSH, suggesting that AgRP increases the density of an inward rectifying K⁺ current.

A hallmark of Kir channel-mediated current is the relative blockade of K⁺ outward current by intracellular polyamines and Mg²⁺ at membrane potentials positive to the ErevK⁺ (ref. 9). To further characterize the MC4R-regulated current, we examined whether the amplitude of K⁺ outward current affected by α -MSH is greater in Mg²⁺ depleted intracellular solution. Recordings from PVN neurons voltage clamped around –55 mV indicated that the amplitude of the α -MSH regulated current was approximately ten times greater when intracellular Mg²⁺ was depleted compared to control (Fig. 2h–j). Another characteristic of Kir channels is sensitivity to phosphatidylinositol 4,5-bisphosphate (PtdIns(4,5)P₂)¹⁰. While this response is attenuated in zero ATP internal solution in which phospholipid synthesis is blocked (Fig. 2k), addition of 100 μ M PtdIns(4,5)P₂ diC8 (1,2-dioctanoyl) to the internal solution potentiated the α -MSH-induced response. (Fig. 2k).

To identify the subtype(s) of Kir channels involved in the α -MSH-induced depolarization, we used a panel of Kir channel blockers (Fig. 2l and Supplementary Table 1) with previously characterized channel subtype specificity¹¹. Additionally, we used the bee venom tertiapin Q, a blocker of Kir3.x and Kir1.1 and glibenclamide, a blocker of Kir6.x/SURx. The depolarizing effect of α -MSH was inhibited \sim 80% by 15 μ M VU573, a selective blocker of Kir2.3, Kir3.x and Kir7.1, and blocked by the Kir7.1 blocker VU590, but not VUR5C, an inactive VU573 analogue, tertiapin Q, glibenclamide, or VU591. These data suggest that Kir7.1 generates the current underlying the α -MSH-induced depolarization in mouse PVN neurons. Kir7.1 is reported to be resistant to external BaCl₂ or CsCl, at concentrations that block other Kir channels¹², and the α -MSH-induced depolarization persisted in the presence of BaCl₂ or CsCl. The increased amplitude of this response in higher concentrations of BaCl₂ (>1 mM) and CsCl (>2.5 mM), may result from non-selective blockade of other voltage-sensitive outward currents (Fig. 2m–o). Additionally, Kir7.1 is more permeable to rubidium than other Kir(s)¹³, and when potassium gluconate in the patch pipette was replaced with RbCl (RbCl 130 mM and KCl 4 mM), α -MSH-induced, Rb-mediated depolarization was observed and its magnitude was significantly greater than physiological K⁺-mediated depolarization (Extended Data Fig. 2). Using dual fluorescence

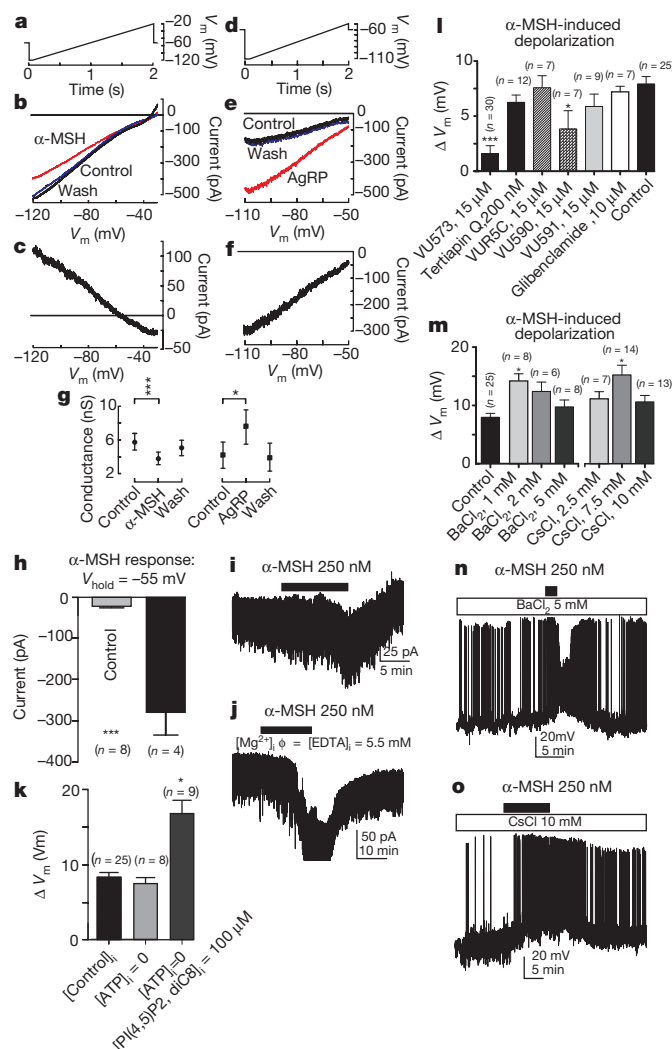


Figure 2 | α -MSH depolarizes and AgRP hyperpolarizes hypothalamic PVN MC4R neurons by regulating Kir7.1. **a–c, g,** Current–voltage (I–V) analysis of MC4R PVN neurons indicates that 250 nM α -MSH generates depolarizing current by closure of inward rectifying K⁺ channels. **d–g,** I–V analysis of PVN MC4R neurons indicates that 50 nM AgRP generates hyperpolarizing current by opening of inward rectifying K⁺ channels. Current responses of voltage clamped PVN neurons to voltage ramps (**a, d**) were used to generate the I–V relationship of the α -MSH- and AgRP-induced response in the presence of 20 mM external K⁺. The resultant I–V relationships (**b, e**) indicate that application of α -MSH and AgRP decrease and increase the cell membrane conductance, respectively, which rectifies inwardly at membrane potentials negative to its reversal of polarity that are near the estimated reversal potential of K⁺ (α -MSH, $n = 14$, **b, c, g**, AgRP, $n = 6$, **e–g**). **h–j,** Depletion of intracellular Mg²⁺ significantly increases K⁺ efflux through MC4R regulated channels at membrane potentials positive to the ErevK⁺. **h–j,** Averaged groups (**h**) and their representative current responses to α -MSH (**i, j**) from PVN MC4R neurons voltage clamped at –55 mV in normal control (**i**) and in Mg²⁺-depleted (**j**) internal solutions. **k,** While zero ATP pipette solution slightly attenuated depolarization amplitude, the addition of 100 μ M PtdIns(4,5)P₂ diC8 to zero ATP solution significantly increased the amplitude of the α -MSH-induced depolarization recorded from PVN MC4R neurons. **l,** Effects of blockers of inward rectifying K⁺ channels on α -MSH (250 nM)-induced depolarization of PVN MC4R neurons compared to α -MSH alone (control). **m–o,** Effects of various concentrations of BaCl₂ or CsCl on the α -MSH-induced depolarization measured in current clamp using similar protocol as in **l**. The α -MSH-induced depolarization was not blocked in higher concentrations of BaCl₂ (**m, n**) or CsCl (**m, o**), exhibiting a greater amplitude in the presence of these non-selective Kir blockers. Bars indicate mean \pm s.e.m., * $P < 0.05$, *** $P < 0.001$, unpaired t -test.

in situ hybridization in sections of mouse PVN, we also determined that approximately 90% of PVN neurons expressing MC4R messenger RNA co-expressed Kir7.1 mRNA (Extended Data Figs 3 and 4).

To confirm that MC4R signalling is capable of modulating Kir7.1 function, we transfected MC4R and Kir7.1 channels into HEK293 cells, using an M125R variant of Kir7.1 that exhibits higher unitary conductance than the native channel, previously demonstrated to allow detection of the channel in cell lines¹⁴. Whole-cell recordings were performed 24–48 h after co-transfecting cells with MC4R, Kir7.1(M125R) and GFP expression plasmids to examine effects of α -MSH on membrane current by examining the I–V analysis of α -MSH response. α -MSH significantly decreased the amplitude (>50%) and slope of current responses, indicating closure of Kir7.1 channels (Fig. 3a–c). This effect was reversible, and the current amplitude was reduced to less than 25% of its own control by 2 mM Ba^{2+} , consistent with the increased sensitivity of the Kir7.1(M125R) variant to Ba^{2+} (ref. 14). Use of HEK293 cells allowed

for a more direct assessment of kinetics of the α -MSH-induced current, indicating a rapid activation time course with an average τ_{rise} of 32 s. Co-transfection of tagged MC4R and Kir7.1 (also known as *KCNJ13*) genes, followed by immunoprecipitation and western blot analysis showed a quantitative association of the two proteins in this system (Extended Data Fig. 5).

By loading HEK293 cells with a Ti^{+} -sensitive fluorescent dye, Thallo, the flux of Ti^{+} ions through open K^{+} channels can be measured¹⁵. The effect of receptor modulation on channel conductance can then be studied by subtracting flux intensity after experimental treatments from levels after vehicle. Using this system, dose–response analysis indicated that α -MSH mediates a MC4R-dependent closure of Kir7.1 channels with an half-maximal inhibitory concentration (IC_{50}) of $10^{-7.5}$ M (Fig. 3d, e). Conversely, AgRP mediated a MC4R-dependent increase in Ti^{+} flux through Kir7.1, with an EC_{50} of $10^{-8.6}$ M (Fig. 3f, g). AgRP did not appear to couple the MC4R to the cAMP inhibitory G protein, $\text{G}\alpha_i$ ¹⁶, or to

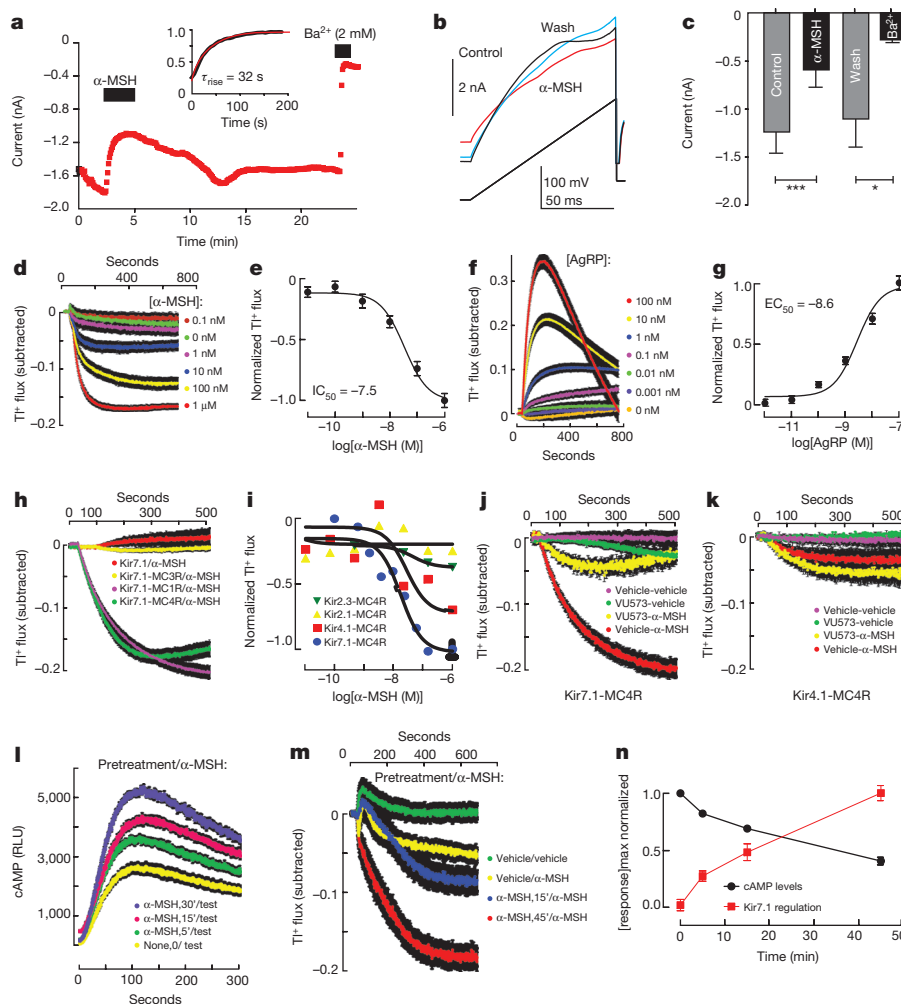


Figure 3 | α -MSH and AgRP couple MC4R to Kir7.1 in HEK293 cells. **a–c**, Current responses of transfected HEK293 cells to voltage steps (**a**) and ramps (**b**) in control, 300 nM α -MSH, and washout. Bath application of α -MSH significantly reduced the amplitude (**c**) and slope of responses to voltage steps and ramps in a reversible manner (bar graph indicates mean \pm s.e.m.; $*P < 0.05$, $***P < 0.01$, $n = 6$, paired t -test). **d–g**, α -MSH reduces flux (IC_{50} near $10^{-7.5}$ M, **d** and **e**) and AgRP increases flux (EC_{50} near $10^{-8.6}$ M, **f** and **g**) through Kir7.1 channels in a concentration-dependent manner. Concentration–response curves in **e** and **g** are plotted using the maxima from data in **d** and **f**. **h–k**, Specificity of melanocortin receptor–Kir subunit coupling. **h**, α -MSH-induced decrease in Ti^{+} flux in MC4R and MC1R expressing cells containing Kir7.1, but not in cells co-expressing Kir7.1 and the MC3R, or expressing Kir7.1 alone. **i**, α -MSH-induced decrease in Ti^{+} flux via the MC4R is observed in cells transfected with Kir7.1, more weakly in cells

expressing Kir4.1, and is not in cells expressing Kir2.1 or Kir2.3. **j**, VU573 (10 μM) blocks Ti^{+} flux in MC4R+Kir7.1 transfected cells. **k**, VU573 does not block MC4R–Kir4.1-mediated Ti^{+} flux in the transfected cell assay. **l, m**, Pre-incubation with 100 nM α -MSH of MC4R-glo expressing HEK293 cells directly depresses a cAMP test response to a second exposure to 100 nM α -MSH (**l**). RLU, relative light units. Pre-incubation MC4R–Kir7.1 HEK293 cells with 100 nM α -MSH directly increases the amplitude of the response of Kir7.1 to a second 100 nM α -MSH exposure (**m**). **n**, Kinetics of the normalized maximal cAMP (black) and Kir7.1 (red) response to a single dose of 100 nM α -MSH, calculated from **l** and **m**. In all Ti^{+} flux and cAMP accumulation assays, coloured traces indicate mean and bars (black) indicate s.e.m. **d–n**, Panels show combined data from three or four (**d** and **e** only) independent experiments; points are means from the following number of wells. **d, e**, $n = 111$; **f, g**, $n = 96$; **h, i**, $n = 40$ –48; **j, k**, $n = 27$ –28; **l, m**, $n = 12$; **n**, $n = 48$.

recruit β -arrestin to the receptor (Extended Data Fig. 6a–c). These data support a G-protein-independent mechanism for the MC4R-mediated regulation of Kir7.1 by AgRP as well. To examine the selectivity of coupling between melanocortin receptors and Kir7.1, we created stable HEK293 cells expressing Kir7.1(M125R) alone, or Kir7.1(M125R) plus MC1R, MC3R, or MC4R. α -MSH (100 nM) significantly decreased Ti^+ flux in Kir7.1 HEK293 cells expressing MC1R or MC4R, but not MC3R (Fig. 3h). α -MSH (100 nM) significantly decreased Ti^+ flux in HEK293 cells transfected with MC4R plus Kir7.1 or Kir4.1, but not cells expressing Kir2.1 or Kir2.3 (Fig. 3i). The Kir7.1-specific channel blocker VU573 blocked the α -MSH effects on Kir7.1 function in the HEK293 cells (Fig. 3j), as in the slice (Fig. 2l). However, VU573 had no effect on α -MSH inhibition of Kir4.1 in HEK293 cells (Fig. 3k), suggesting the conductance regulated by α -MSH in MC4R PVN neurons primarily involves Kir7.1. PKA activity was also not required for α -MSH-induced closure of Kir7.1 in HEK293 cells (Extended Data Fig. 7a, b), and we also observed a synergistic effect of α -MSH and cAMP on Kir7.1 closure, in this system (Extended Data Fig. 7a–d).

G-protein-coupled signalling of the MC4R exhibits β -arrestin-mediated desensitization. Pre-treatment of MC4R + Kir7.1 expressing HEK293 cells with α -MSH reduced the subsequent magnitude of the G-protein-mediated cAMP response of these cells to α -MSH (Fig. 3l). Supporting the argument that coupling of the MC4R to Kir7.1 is non-G-protein-mediated, the MC4R-dependent inhibition of Ti^+ flux through Kir7.1 was hypersensitized by prior treatment with α -MSH (Fig. 3m). Thus, while the time course of acute effects of MC4R activation on Kir7.1 was rapid (Fig. 3a), the long term effects on the cAMP and Kir7.1 signalling pathways were highly divergent (Fig. 3n). While cAMP levels peak between 1–2 min after α -MSH treatment, inhibition of Ti^+ flux by α -MSH treatment continues to increase up to 45 min post-treatment. Low-dose AgRP treatment (1 nM) increased Ti^+ flux for up to 24 h (data not shown); the apparent reduction in Ti^+ flux after high-dose AgRP treatment (for example, Fig. 3f) is probably owing to saturation of the fluorescent dye binding substrate.

Additional data support a role for Kir7.1 in regulation of food intake by MC4R *in vivo*. The AgRP analogue miniAgRP (AgRP_{87–120}, C105A) retains normal affinity for MC4R, and potency in inhibition of MC4R coupling to G_{α_s} (Fig. 4a), yet exhibits 70% reduction in its ability to stimulate food intake in rats⁵. In parallel with loss of orexigenic activity, this peptide has lost its ability to couple MC4R to Kir7.1 (Fig. 4b). Conversely, we have also identified an α -MSH analogue, MC4-NN2-0453¹⁷ (Novo), that preferentially couples MC4R to Kir7.1 over G_{α_s} in cell culture, and potently depolarizes PVN MC4R neurons (Fig. 4c–f). MC4-NN2-0453 also exhibited biased actions at MC4R *in vivo*. In a cAMP-mediated response, the peptide was unable to induce intestinal peptide YY (PYY) release *in vivo*¹⁸ (Fig. 4g), and is a partial agonist *ex vivo* (Extended Data Fig. 8). In contrast, the peptide potently inhibited food intake at doses equimolar to other α -MSH analogues (Fig. 4h). Knock-down of Kir7.1 gene expression in wild-type and MC4R mutant larval zebrafish, but not Kir7.1 mutant *jaguar* zebrafish, produced a reduction in linear growth and upregulation of *GHRH* gene expression, responses reported previously for activation of the MC4R¹⁹, (Extended Data Fig. 9a–e), further supporting the argument that Kir7.1 acts downstream of MC4R.

These data show the MC4R can depolarize or hyperpolarize hypothalamic PVN neurons in response to α -MSH or AgRP, respectively, through a novel G protein independent signalling pathway involving regulation of the activity of Kir7.1. While MC4R also is likely to couple to G_{α_s} in most cells, cAMP/PKA-dependent activation of K_{ATP} channels, producing α -MSH-induced hyperpolarization, has been demonstrated in MC4R neurons in the brainstem²⁰. Thus, while Kir7.1 signalling appears to be essential for depolarization of PVN MC4R neurons by α -MSH, G_{α_s} signalling and elevation of cAMP may be depolarizing or hyperpolarizing, depending on the cellular context (Extended Data Fig. 10).

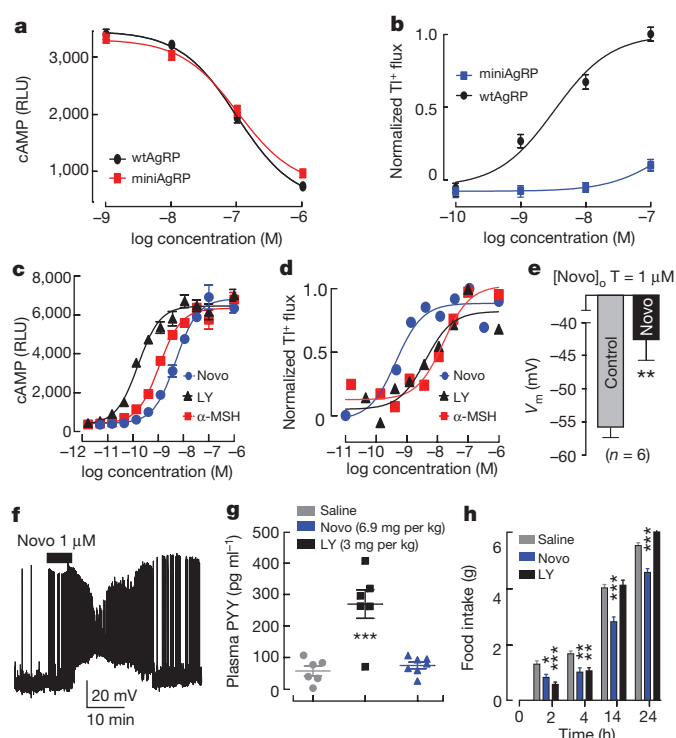


Figure 4 | Biased agonists of the MC4R support a role for Kir7.1 in melanocortin signalling *in vivo*. **a**, The potencies of wtAgRP (amino acids 83–132, $\text{IC}_{50} = 9.9 \times 10^{-8}$) and miniAgRP (amino acids 87–120, C105A $\text{IC}_{50} = 1.0 \times 10^{-7}$) for inhibition of MC4R constitutive activity, measured by applying AgRPs indicated are not significantly different ($P > 0.1$). **b**, Potencies of wtAgRP (3.6×10^{-9}) and miniAgRP (1.7×10^{-7}) are significantly different for stimulation of Kir7.1 activity. **c**, **d**, The α -MSH analogue MC4-NN2-0453 (Novo) is a biased agonist for coupling of the MC4R to Kir7.1. Coupling to intracellular cAMP: (Novo $\text{EC}_{50} = 4.9 \times 10^{-9}$ M; α -MSH agonist LY2112688 (LY) $\text{EC}_{50} = 41.6 \times 10^{-10}$ M); Coupling to inhibition of thallium flux through Kir7.1 (Novo $\text{EC}_{50} = 4.5 \times 10^{-10}$ M; LY $\text{EC}_{50} = 4.1 \times 10^{-9}$ M; α -MSH $\text{EC}_{50} = 1.6 \times 10^{-8}$ M). **e**, **f**, Application of Novo induced significant depolarization of membrane potential in PVN neurons. **g**, Intraperitoneal administration of LY stimulated PYY release from L cells *in vivo* via an MC4R-dependent pathway, while NOVO did not. Data show mean and s.e.m., *** $P < 0.001$. **h**, Novo is a potent inhibitor of cumulative food intake, following an overnight fast and administration of equimolar doses of compounds indicated (6.9 mg Novo or 3 mg LY per kg of mouse) Data show mean \pm s.e.m., * $P < 0.05$; ** $P < 0.01$, *** $P < 0.001$, by paired *t*-test (**e**), or one-way ANOVA with Bonferroni post-test (**g**, **h**). $n = 24$ (**a**, **b**), 12 (**c**, **d**) or 6 (**e**, **g**, **h**). Data are representative of two (**g**, **h**), three (**a**–**d**) or six (**e**) independent experiments.

Direct interactions between GPCRs and K^+ channels, such as binding and regulation of Kv4.3 by the type 1 angiotensin receptor²¹, or of Kir4.1 and Kir4.2 by the Ca^{2+} -sensing receptor²² have been previously reported. Kir7.1 is a widely expressed inwardly rectifying potassium channel, suggesting the possibility of regulation by other GPCRs. Mutations in Kir7.1 cause pigmentary defects in the *jaguar* zebrafish²³. Interestingly, we also find that the MC1R couples to Kir7.1, suggesting that the induction of pheomelanin (yellow-red pigments) synthesis in mammals, may involve MC1R–Kir7.1 regulation by agouti²⁴.

The discovery of independent agonist activity for AgRP through opening of Kir7.1 also necessitates revision (Extended Data Fig. 10) of the current neuroanatomical model of hypothalamic melanocortin signalling, in which AgRP acts primarily by antagonism of α -MSH²⁵. Preliminary data from a limited electron micrographic reconstruction of the PVN, showing dendrites specifically targeted by POMC synapses and cell soma specifically targeted by AgRP synapses, suggests a potential neuroanatomical basis as well for independent action of AgRP and α -MSH²⁶. The non-G protein signalling mechanism reported here may

also provide a basis for understanding the persistent action of AgRP on food intake⁵, and the gene dosage effect of MC4R mutations⁴, not typically seen for GPCRs. Furthermore, the pronounced bias for coupling the MC4R to Kir7.1 of α -MSH analogue MC4-NN2-0453, shown to potentially inhibit food intake in the absence of a pressor response, suggests that biased agonists of the MC4R may exhibit useful therapeutic properties.

Online Content Methods, along with any additional Extended Data display items and Source Data, are available in the online version of the paper; references unique to these sections appear only in the online paper.

Received 4 November 2013; accepted 10 November 2014.

Published online 19 January 2015.

- Mountjoy, K. G., Mortrud, M. T., Low, M. J., Simerly, R. B. & Cone, R. D. Localization of the melanocortin-4 receptor (MC4-R) in neuroendocrine and autonomic control circuits in the brain. *Mol. Endocrinol.* **8**, 1298–1308 (1994).
- Ollmann, M. M. *et al.* Antagonism of central melanocortin receptors *in vitro* and *in vivo* by agouti-related protein. *Science* **278**, 135–138 (1997).
- Srinivasan, S. *et al.* Constitutive activity of the melanocortin-4 receptor is maintained by its N-terminal domain and plays a role in energy homeostasis in humans. *J. Clin. Invest.* **114**, 1158–1164 (2004).
- Huszar, D. *et al.* Targeted disruption of the melanocortin-4 receptor results in obesity in mice. *Cell* **88**, 131–141 (1997).
- Madonna, M. E., Schurdak, J., Yang, Y. K., Benoit, S. & Millhauser, G. L. Agouti-related protein segments outside of the receptor binding core are required for enhanced short- and long-term feeding stimulation. *ACS Chem. Biol.* **7**, 395–402 (2012).
- Balthasar, N. *et al.* Divergence of melanocortin pathways in the control of food intake and energy expenditure. *Cell* **123**, 493–505 (2005).
- Ghamari-Langroudi, M., Srisai, D. & Cone, R. D. Multinodal regulation of the arcuate/paraventricular nucleus circuit by leptin. *Proc. Natl Acad. Sci. USA* **108**, 355–360 (2011).
- Smith, M. A. *et al.* Melanocortins and agouti-related protein modulate the excitability of two arcuate nucleus neuron populations by alteration of resting potassium conductances. *J. Physiol. (Lond.)* **578**, 425–438 (2007).
- Matsuda, H., Saigusa, A. & Irisawa, H. Ohmic conductance through the inwardly rectifying K channel and blocking by internal Mg^{2+} . *Nature* **325**, 156–159 (1987).
- Huang, C. L., Feng, S. & Hilgemann, D. W. Direct activation of inward rectifier potassium channels by PIP_2 and its stabilization by $G\beta\gamma$. *Nature* **391**, 803–806 (1998).
- Swale, D. R., Kharade, S. V. & Denton, J. S. Cardiac and renal inward rectifier potassium channel pharmacology: emerging tools for integrative physiology and therapeutics. *Curr. Opin. Pharmacol.* **15**, 7–15 (2014).
- Krapivinsky, G. *et al.* A novel inward rectifier K^+ channel with unique pore properties. *Neuron* **20**, 995–1005 (1998).
- Shimura, M. *et al.* Expression and permeation properties of the K^+ channel Kir7.1 in the retinal pigment epithelium. *J. Physiol. (Lond.)* **531**, 329–346 (2001).
- Döring, F. *et al.* The epithelial inward rectifier channel Kir7.1 displays unusual K^+ permeation properties. *J. Neurosci.* **18**, 8625–8636 (1998).
- Weaver, C. D., Harden, D., Dworetzky, S. I., Robertson, B. & Knox, R. J. A thallium-sensitive, fluorescence-based assay for detecting and characterizing potassium channel modulators in mammalian cells. *J. Biomol. Screen.* **9**, 671–677 (2004).
- Büch, T. R., Heling, D., Damm, E., Gudermann, T. & Breit, A. Pertussis toxin-sensitive signaling of melanocortin-4 receptors in hypothalamic GT1-7 cells defines agouti-related protein as a biased agonist. *J. Biol. Chem.* **284**, 26411–26420 (2009).
- Conde-Frieboes, K. *et al.* Identification and *in vivo* and *in vitro* characterization of long acting and melanocortin 4 receptor (MC4-R) selective α -melanocyte-stimulating hormone (α -MSH) analogues. *J. Med. Chem.* **55**, 1969–1977 (2012).
- Panaro, B. L. *et al.* The melanocortin-4 receptor is expressed in enteroendocrine L cells and regulates the release of peptide YY and glucagon-like peptide 1 *in vivo*. *Cell Metab.* **20**, 1018–1029 (2014).
- Zhang, C., Forlano, P. M. & Cone, R. D. AgRP and POMC neurons are hypophysiotropic and coordinately regulate multiple endocrine axes in a larval teleost. *Cell Metab.* **15**, 256–264 (2012).
- Sohn, J. W. *et al.* Melanocortin 4 receptors reciprocally regulate sympathetic and parasympathetic preganglionic neurons. *Cell* **152**, 612–619 (2013).
- Doronin, S. V., Potapova, I. A., Lu, Z. & Cohen, I. S. Angiotensin receptor type 1 forms a complex with the transient outward potassium channel Kv4.3 and regulates its gating properties and intracellular localization. *J. Biol. Chem.* **279**, 48231–48237 (2004).
- Huang, C. *et al.* Interaction of the Ca^{2+} -sensing receptor with the inwardly rectifying potassium channels Kir4.1 and Kir4.2 results in inhibition of channel function. *Am. J. Physiol. Renal Physiol.* **292**, F1073–F1081 (2007).
- Iwashita, M. *et al.* Pigment pattern in *jaguar/obelix* zebrafish is caused by a Kir7.1 mutation: implications for the regulation of melanosome movement. *PLoS Genet.* **2**, e197 (2006).
- Hida, T. *et al.* Agouti protein, mahogunin, and attractin in pheomelanogenesis and melanoblast-like alteration of melanocytes: a cAMP-independent pathway. *Pigment Cell Melanoma Res.* **22**, 623–634 (2009).
- Cone, R. D. Anatomy and regulation of the central melanocortin system. *Nature Neurosci.* **8**, 571–578 (2005).
- Atasoy, D. *et al.* A genetically specified connectomics approach applied to long-range feeding regulatory circuits. *Nature Neurosci.* **17**, 1830–1839 (2014).

Supplementary Information is available in the online version of the paper.

Acknowledgements We thank C. Zhang and A. M. Bradshaw for advice and technical assistance in performance of experiments in the zebrafish. We thank D. M. Parichy for providing the *jaguar* zebrafish strain. We thank B. S. Wulff and K. W. Conde-Frieboes and Novo Nordisk A/S for the contribution of MC4-NN2-0543. This work was supported by NIH R01DK070332 (R.D.C.), NIH 5R01 DK082884-03 (J.S.D.), and NIH R01DK064265 (G.L.M.). R.D.C. is also supported by the Vanderbilt Diabetes Research and Training Center grant DK020593.

Author Contributions M.G.-L., G.J.D., J.A.S., G.L.M., R.M., H.M.C., J.S.D. and R.D.C. designed experiments, M.G.-L., G.J.D., J.A.S., R.M., B.L.P., T.G. and I.R.T. performed experiments, G.L.M. and R.P. synthesized, purified and folded the AgRP mini peptide, and M.G.-L. and R.D.C. analysed the data and wrote the manuscript. All authors reviewed and commented on the manuscript.

Author Information Reprints and permissions information is available at www.nature.com/reprints. The authors declare no competing financial interests. Readers are welcome to comment on the online version of the paper. Correspondence and requests for materials should be addressed to either M.G.-L. (masoud.ghamari-langroudi@vanderbilt.edu) or R.D.C. (roger.cone@vanderbilt.edu).

METHODS

Hypothalamic slice electrophysiology. MC4R-GFP mice, backcrossed onto the C57BL/6J background, were previously characterized by dual immunohistochemistry and *in situ* hybridization to validate that GFP-positive neurons in the PVN expressed MC4R RNA²⁷. Randomly selected MC4R-GFP male and female mice, 8–12 weeks of age, were deeply anaesthetized with isoflurane before decapitation. The brain was entirely removed and immediately submerged in ice-cold, gassed (95% O₂, 5% CO₂) artificial cerebrospinal fluid (aCSF), containing (in mM): 126.2 NaCl, 3.1 KCl, 2 CaCl₂, 1 MgCl₂, 1 NaH₂PO₄, 26.2 NaHCO₃, 10 glucose and 11 sucrose (320 mosm per kg, pH 7.39 when gassed with 95% O₂, 5% CO₂ at room temperature). Brain blocks of containing hypothalamus were made by trimming the whole brains while immersed in oxygenated, near-freezing aCSF and glued to a dental-cement cast customized to the size of the block mounted on a plate with adjustable angle. Brain slices of 200- μ m thicknesses were then cut at angle range between 44° and 49° in reference to horizontal plane and transferred to a glass beaker containing oxygenated ACSF at 31 °C. After an incubation period lasting at least one hour, a slice was transferred to a recording chamber (~2.0 ml in volume), then submerged and immobilized with nylon strands drawn taut across a C-shaped platinum wire (1 mm outer diameter), and perfused with warmed (31–32 °C) oxygenated ACSF at a rate of 2–3 ml min⁻¹.

EGFP-fluorescent neurons were unambiguously identified and patched using combined epifluorescence and IR-DIC optics. Fluorescent neurons of healthy IR-DIC appearance but of every level of fluorescence brightness were chosen for electrophysiological recordings.

Drugs were either added to aCSF and bath applied to the slice via the perfusion system (for extracellular applications) or to the pipette solution to perform whole cell recordings (for intracellular applications). The small volume of the recording chamber relative to the flow rate assured a complete exchange of solution occurring in less than 1 min. The persisting effects of a peptide were therefore due to prolonged effects rather than a slow wash out.

In this study, whole-cell patch-clamp recordings were used to obtain information about action potential firing activity, and membrane potentials and currents. Unless stated otherwise, whole cell recordings were performed using patch pipettes of 3.4 M Ω to 5 M Ω resistance when filled with a solution containing (in mM): 125 K gluconate, 8 KCl, 4 MgCl₂, 10 HEPES, 5 NaOH, 4 Na₂ATP, 0.4 Na₃GTP, 5 Na₂-creatine phosphate, 7 sucrose and 7 KOH which resulted in a pH ~7.23 and osmolality of 295–300 mosmol per kg. The permeability of the α -MSH regulated channels were investigated by replacing K gluconate and KCl with 130 RbCl and 4 KCl, but otherwise similar condition. The examination of effects of Mg²⁺-free internal solution on the α -MSH-induced current was conducted in voltage clamp mode from PVN neurons held at -55 mV. The Mg²⁺-free internal solution contained 103 K-gluconate, 30 KCl, 10 HEPES-KOH, 0.5 CaCl₂, 5.5 EDTA-KOH, pH 7.23, with osmolality 304 mosmol per kg. The ATP free solution contained 83 K-gluconate, 30 KCl, 10 HEPES-KOH, 0.5 CaCl₂, 4 MgCl₂, 5.5 EGTA-KOH, pH 7.2 and osmolality 298 mosmol per kg.

Neuronal integrity was assessed by all of the following: small holding current (\leq 30 pA at -70 mV) when voltage-clamped, large amplitude rebound spikes, the ability to fire and lack of obvious morphological deterioration (that is, lack of blebbing and nucleus not visually present).

In order to quantify the action potential firing and amplitude of depolarization induced by α -MSH, current clamp recordings were performed in continuous mode while the membrane potential of neurons were held between -55 and -60 mV to prevent continuous spontaneous action potential firing. Effects of AgRP were measured while cells were held around -50 mV to allow neurons to fire action potentials spontaneously. The firing frequency and membrane potential of neurons was measured during a 3-min period before the application of the peptides, and for another 3-min period 7–11 min after administration of peptide, and results compared.

Voltage-clamp recordings in episodic mode were used to study I–V relationships of the α -MSH and AgRP responses. The series resistance was not compensated but was monitored during voltage clamp experiments. Trials were excluded if the series resistance changed more than 10–15 M Ω during episodic voltage-clamp recordings. To characterize the currents generated by peptides, we compared the I–V relationships of the TTX pre-treated PVN neurons obtained in control with that in the presence of bath-applied peptide and wash. Individual I–V relationships were established by analysing the current responses of each cell to a depolarizing voltage ramps of 2 s duration applied from hyperpolarized potentials. This protocol was repeated at regular intervals in control media, in the presence of a peptide, and after 10–15 min of washout of the peptide. Current and voltage traces from between 3–4 successive trials in control conditions were then digitally averaged offline and were compared with similarly averaged traces from an identical number of trials obtained after wash out. The values of the averaged current responses elicited under each condition were then plotted as a function of the corresponding values during voltage ramps to obtain individual I–V relationships.

Data were acquired at 10 kHz using a MultiClamp 700A amplifier (2,000 \times gain, -3 dB filter frequency 5 kHz) and Clampex 10.0.1 software (Axon Instruments, Union City, CA). GraphPad Prism 5.0 (Graphpad Software, Inc., San Diego, CA) and Excel 2010 (Microsoft) were used for data analysis. Statistical tests used included the paired *t*-test, when examining response of the same neurons before and after treatment with a compound, and the unpaired *t*-test when comparing the responses of different sets of neurons. All studies were approved by the animal care and use committee of Vanderbilt University.

Thallium assay. HEK293 cells (ATCC, tested mycoplasma negative) stably expressing human MC4R and Kir7.1(M125R), or other human receptors (MC1R, MC3R) or channels (Kir2.1, Kir2.3, Kir4.1) as indicated, were grown in MEM medium with 10% FBS without antibiotics, suspended in 20 μ l of medium plus 1 μ g ml⁻¹ tetracycline, used to induce expression of the transfected tet-sensitive Kir7.1 gene, and plated in 384-well poly-D-lysine coated optical bottom plates (BD Biosciences) at 20,000 cells per well. Plates were incubated overnight for 22–24 h in the cell incubator at 37 °C, 5% CO₂. The following day, each individual cell plate was washed and replaced with 20 μ l assay buffer (Hank's balanced salt solution with HEPES). A thallium-sensitive dye, ThalloS (TEFLabs), was diluted with assay buffer to 0.9 ng ml⁻¹, and 20 μ l was loaded into each well. Cell plates were kept in the dark for 1 h at room temperature and then washed again with assay buffer to remove residual extracellular dye. Cell plates were then incubated with peptides, drugs and/or controls as indicated for 25 min (unless indicated otherwise). Thallium (10 μ l of a 0.48 mM stock in assay buffer) was then loaded and fluorescence generated by thallium influx was recorded for up to 15 min, as indicated, using a Hammamatsu FDSS plate reader.

Zebrafish. Wild-type Tab 14 or AB strain zebrafish were raised and bred at 26–28 °C, with 14 h light/10 h dark cycle. All zebrafish studies were conducted in larvae unselected with regard to gender. Larval stage was determined according to ref. 28. The *mc4r*^{-/-} mutant strain was obtained from the Sanger Institute Zebrafish Mutation Project; the *jaguar* (G157E) mutant was kindly provided by D. M. Parichy. All studies were approved by the animal care and use committee of Vanderbilt University.

β -arrestin recruitment assays. β -arrestin recruitment was measured using PathHunter hMC4R cells (DiscoverX; Fremont, CA) stably expressing pro-link attached β -arrestin proteins according to the manufacturer's protocol. Cells were plated in 384-well plates at 5,000 cells per well. The following day, cells were treated with drug and incubated at 37 °C for 90 min. Substrate was added to each well and luminescence values were obtained after 60 min at room temperature using a Spectromax plate reader (Molecular Devices; Sunnydale, CA).

Morpholino oligonucleotide injection, and body length measurement. Morpholino oligonucleotides, described below, were dissolved in nuclease-free water and stored in -20 °C as 1 mM stock. Serial dilutions were made using nuclease-free water to 0.01, 0.05, 0.1, 0.2, 0.3, and 0.4 mM working solution with 20% Phenol Red (Sigma; 0.5% in DPBS, sterile filtered, endotoxin tested). Before the injection, Morpholino oligonucleotides were denatured at 65 °C for 5 min and quickly spun to avoid the formation of aggregates. Three to five microlitres was loaded in a microinjection machine, and embryos at one or two cell stages were injected with 1–2 nl of a solution containing antisense targeting morpholino or standard control oligo. Each MO oligo injection was repeated at least three times, and doses were adjusted to optimize the phenotype-to-toxicity ratio. Following morpholino injections, embryos were raised in egg water, changed daily, under standard light/dark cycle up to 6 days post-fertilization (dpf). Dead embryos were excluded at 1 dpf. Embryos were assayed for quantitative RT-PCR of GHRH at 5 dpf. Linear body length (forehead to tail fin) was determined using a micrometre at 5 dpf. Embryos were mounted in 2.5% methyl cellulose, and images were taken by AxionVision (Ver3.1) software with a Lumar V12 Stereo Microscope (Carl Zeiss).

Quantitative PCR. Embryos were homogenized in lysis buffer with a sonic dismembrator (model 100, Fisher Scientific, Pittsburgh, PA). Total RNA was extracted using an RNeasy Mini Kit (Qiagen, Valencia, CA) according to the manufacturer's instructions. To remove genomic DNA, On-Column DNase Digestion was performed using an RNase-Free DNase Set (Qiagen). One microgram of purified total RNA was reverse transcribed with iScript cDNA Synthesis Kit (Bio-Rad, Hercules, CA). qPCR primers were designed by Beacon Designer 7.0 (Premier Biosoft International, Palo Alto, CA) to minimize primer self-dimerization, and primer sequences are indicated below. qPCRs were performed using 2 μ l cDNA (20 ng) as template, 5 pmol of each of forward and reverse primers, and 2 \times Power SYBR PCR mix (Applied Biosystems, Carlsbad, CA) with nuclease free water (Promega, Madison, WI) to make the final volume to 20 μ l in a 96-well plate (Bioexpress, Kaysville, UT). qPCRs were performed using an Mx3000PTM (Stratagene, Santa Clara, CA). The PCR cycle was performed according to manufacturer's instructions with initial denaturation at 95 °C for 10 min, followed by 45 cycles of 95 °C 20 s, 60 °C, 60 s. At the end of the cycles, melting curves of the products were verified for the specificity of PCR products. A standard curve with serial dilutions of cDNA sample was performed

on each plate. All measurements were performed in duplicate, and Graph Pad Prism 5.0 was used for the interpretation and analysis of data.

Morpholino and qPCR oligonucleotides. Antisense morpholino oligonucleotide (MO) against the ATG translation initiation site of *agrp*, *kcj13* and standard control MO were designed and synthesized by GeneTools, LLC (Philomath, OR USA). For morpholino injection *agrp* ATG MO: 5'-TTTCAGCACCGCCGTCGTCATT TTC-3'

Zebrafish Standard Control MO: 5'-CCTCTTACCTCAGTTACAATTATA-3' *kcj13* MO targeting intron-exon boundary: 5'-CAATGCACCTGATGGGCAG AGAAA-3'

For qPCR: *ghrh* (growth hormone releasing hormone), forward primer 5'-GTGC TTATGCTGCTTGTACTATC-3', reverse primer 5'-ATACTTGACTGACGCT TTACATTG-3'.

ef1a (Elongation Factor 1 alpha), with forward primer 5'-CTGGAGGCCAGCTCA AACAT-3', reverse primer 5'-ATCAAGAAGAGTAGTACCGCTAGCATTAC-3'.

MC4R-mediated PYY release assay. Male C57BL/6J mice were ordered from The Jackson Laboratory (Bar Harbour, ME). Experiments were run when the mice reached 12 weeks of age. On the day of study, the mice were fasted during the daytime for 4 h to reduce plasma PYY levels to baseline. Following the fast, mice were randomly selected to receive an intraperitoneal injection of saline (vehicle), 3 mg per kg of the α -MSH agonist LY2112688 (LY), or an equimolar dose of 6.9 mg per kg of MC4-NN2-0453 (NOVO). MC4-NN2-0453 corresponds to the previously reported peptide 19¹⁷. Numbers for each test were chosen based on prior experience suggesting significance could be achieved with as few as 6 animals per condition. At 10 min post-injection, the mice were quickly bled via the submandibular vein to obtain approximately 200 μ l of whole blood. The blood was collected into vials containing EDTA and protease inhibitor cocktail for mammalian tissues (Sigma-Aldrich P8340) to prevent degradation of PYY. The vials containing whole blood were spun for 15 min at 1,500g at 4 °C to isolate the plasma. The plasma was stored at -80 °C until PYY levels were assayed. PYY was assayed in duplicate using the Milliplex magnetic bead based mouse metabolic hormone panel (Millipore MMHMAG-44K, 1-plex kit for total PYY). Results were analysed against a standard curve and concentrations were determined using Milliplex Analyst 5.1 software. Results were plotted and analysed using Graphpad Prism. All animal care and experimental procedures were approved by Vanderbilt University Medical Center Institutional Animal Care and Use Committee.

Food intake analysis. 18 wild-type male C57BL6 were obtained from Jackson Laboratory. Upon arrival, mice were single-housed and allowed to acclimatize at 22 °C–24 °C with a 12-h light/12-h dark cycle with standard chow and water provided ad libitum for one week. For 5 days after the environment acclimation, mice were handled during the light cycle and given subcutaneous injections of 100 μ l of saline to get them accustomed to being handled. During this time, daily food intake was also measured to establish a baseline. Mice were food deprived for 16 h before drug treatment, starting shortly before the beginning of the dark cycle on the fifth day. Experiments were blinded; drug compounds were prepared and coded the morning of the injections by an individual who would not be conducting the experiment. The randomly selected experimental groups were as follows: 6 animals were given vehicle (100 μ l of saline), 6 animals were given 100 μ l of 3.0 mg per kg LY2112688 (LY), and 6 animals were given an equimolar dose of MC4-NN2-0453 (NOVO; 100 μ l of 6.9 mg per kg) subcutaneously. Numbers needed to achieve significant inhibition of food intake by a melanocortin compound versus saline were based on prior experience. Food intake was measured at 2 h, 4 h, 14 h, and 24 h after injection. The data was collected and analysed using GraphPad Prism. Statistical significance was established using one-way ANOVA and Bonferroni post-hoc with a $P < 0.05$ significance value. All animal care and experimental procedures were approved by Vanderbilt University Medical Center Institutional Animal Care and Use Committee.

Coimmunoprecipitation and western blotting. HEK293T cells were plated in six-well plates and transfected with indicated plasmids 24 h before the experiment. Cells were rinsed once with PBS and proteins were crosslinked with 0.5 mM dithiobismaleimidoethane (DTME) in PBS for 30 min at room temperature. Cross-linking solution was removed and remaining crosslinker was quenched using a quenching solution (20 mM Tris-HCl pH 7.4, 5 mM L-cysteine) for 10 min at room temperature. Cells were lysed in 0.1% N-dodecyl- β -maltoside in PBS with protease inhibitors for 20 min, lysates were spun at 10,000 r.p.m. for 10 min and supernatants were transferred to new tubes. Lysates were incubated with indicated antibody (M2 anti-flag, Sigma F3165; anti-HA monoclonal antibody, Vanderbilt Antibody and Protein Resource, 12CA5) at 1:5,000 with rotation for 1 h at room temperature. Antibodies were pulled down using protein-G coated magnetic beads (Dynabeads, Life Technologies). Beads were washed 3 times with lysis buffer and proteins were eluted and crosslinking reversed with sample buffer containing 100 mM DTT. Samples were separated by SDS-PAGE and membranes blotted using M2 anti-Flag

1:5,000. Blots were revealed by ECL and film scanned. Densitometry analysis was done using Adobe Photoshop. $n = 2$.

Mucosal electrophysiology. Male C57BL/6J mouse descending colon mucosa devoid of overlying muscle was cut into 6 adjacent pieces and each placed between the two halves of an Ussing chamber (aperture 0.14 cm²) and bathed in oxygenated Krebs-Henseleit (KH) buffer (in mM: 117 NaCl, 24.8 NaHCO₃, 4.7 KCl, 1.2 MgSO₄, 1.2 KH₂PO₄, 2.5 CaCl₂ and 11.1 D-glucose), 5 ml on both sides. Mucosae were voltage-clamped at 0 mV and the resultant vectorial ion transport measured as short-circuit current (I_{sc}) as described previously²⁹. After a 15 min equilibration period, vasoactive intestinal peptide (VIP, 10 nM) was added to stimulate epithelial anion secretion and 5–10 min later (once the VIP maximum had been achieved) a single concentration of either MC4-NN2-0453 (3 nM–3 μ M) or α -MSH (300 nM) was administered. Consequent MC4R mediated reductions in I_{sc} were measured for 20 min before a control concentration of PYY (10 nM) was added to reduce I_{sc} levels via epithelial Y₁ receptors²⁹. All additions were basolateral and changes in I_{sc} were converted to μ A cm². MC4R activity and individual peptide responses were pooled and analysed using Graphpad Prism (version 5). All animal care and experimental procedures were approved by the King's College London Ethical Review Process Committee.

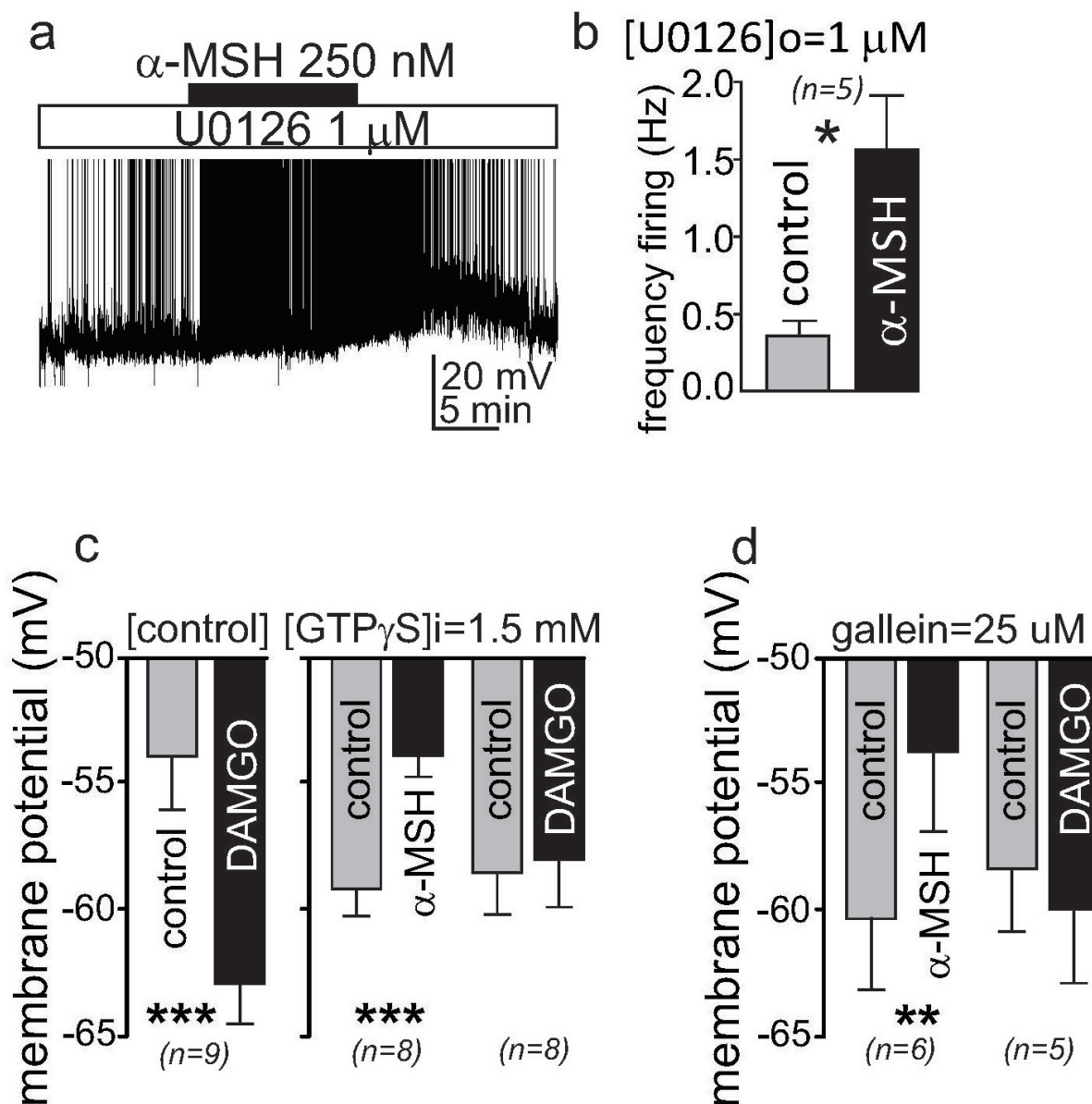
Fluorescent *in situ* hybridization for MC4R and Kir7.1 mRNA. Various mRNA species expressed by PVN neurons were visualized with a variation of FISH (fluorescent *in situ* hybridization) called RNAscope (ACD; Advanced Cell Diagnostics, Inc., Hayward, CA). RNAscope cDNA probes and detection kits were purchased from ACD and used according to the company's online protocols. The probe sets directed against MC4R and Kir7.1 mRNA were designed from sequence information from the mouse RefSeq mRNA IDs NM_016977 and NM_001110277, respectively.

Four wild type male MC4-GFP littermates were euthanized with an overdose of Nembutal (100 mg per kg, intraperitoneally) and brains were quickly removed and frozen in powdered dry ice. Brains from three MC4R knockout mice⁴ were prepared the same way. All brains were stored at -80 °C until cut on a cryostat (Leica CM3000). 16- μ m sections were adhered to warm Fisher plus slides (Fisher Scientific) and immediately refrozen. Slides were stored at -80 °C until fixed with ice-cold 4% paraformaldehyde according to the ACD protocol for fresh frozen tissue. After fixation for 15 min, slides were dehydrated in an ethanol dilution series (50%, 70%, 100% \times 2). Slides were then air-dried for 5 min and a hydrophobic barrier was drawn around each section with an Immedge barrier pen. Sections were then incubated with ACD's pretreatment 4 solution for 30 min at room temperature in a humidified chamber. After pretreatment, sections were incubated with RNAscope probes and a series of signal amplification steps according to the ACD protocol for the Fluorescent Multiplex Kit. In brief, incubation steps included: probe mixtures at kit recommended dilutions for the C1 channel (blank or probes for ubiquitin C mRNA), the C2 channel (MC4R mRNA) and the C3 channel (Kir7.1 mRNA) for 2 h at 40 °C, wash twice, AMP-1 FL reagent for 30 min at 40 °C, wash twice, AMP-2 FL reagent for 15 min at 40 °C, wash twice, AMP-3 FL reagent for 30 min at 40 °C, wash twice, AMP-4 FL alt A or B reagent for 15 min at 40 °C, wash twice, DAPI reagent for 1–2 min at room temperature, remove standing liquid and immediately cover slip with either SlowFade Gold (Molecular Probes) or Aqua-Polymount (Polysciences, Inc.). 40 °C incubations were carried out in a HyBeZ oven (ACD). Each run of 5 to 10 slides included one positive control (3 probe sets to house-keeping gene mRNA, ACD) and one negative control (3 probe sets for bacterial mRNA, ACD). 3–6 sections of the PVN from each animal, representative of rostral (AP = -0.58 to -0.80 relative to bregma), middle (AP = -0.80 to -1.0) and caudal (AP = -1.0 to -1.2; ref. 30) levels, were processed for imaging.

Sections were imaged with a Zeiss 710 scanning confocal microscope using either a LD C-Apochromat \times 40/1.1 water lens or a Plan-Apochromat \times 63/1.40 oil lens. Z stacks were done on all sections using pin hole settings that resulted in 1.0- μ m thick optical sections. Images were opened in Imapar (version 7.6), background subtracted and then contrast enhanced by increasing gamma to 1.5 to 2.3, then exported in tiff format for counting mRNA signals and labelled cells. Numbers of round, fraction delimited spots over and surrounding DAPI-labelled nuclei were manually counted with the aid of Metamorph software. Borders between cells were resolved with the help of grey scale DIC images overlaid on maximum intensity projections of the Z stacks. Negative control sections were used to count fluorescent dots that represented auto-fluorescent signals plus non-specific labelling by the multiplex kit. Sections of WT PVN hybridized with probes against bacterial mRNA were used to count background dots in the KIR7.1 channel and sections from MC4R knockout mice hybridized with the probes against MC4R mRNA were used to count background dots in the MC4R channel. The average number of dots per cell for the MC4R and Kir7.1 negative controls were 1.60 ± 0.87 standard deviations and 1.31 ± 0.70 , respectively (354 cells from 6 sections for MC4R and 54 cells from 2 sections for Kir7.1; see supplementary figure). For cell counts in PVN sections from wild-type mice, cells were counted as positively labelled for MC4R and/or Kir7.1 mRNA if the number of dots per cell exceeded the mean plus

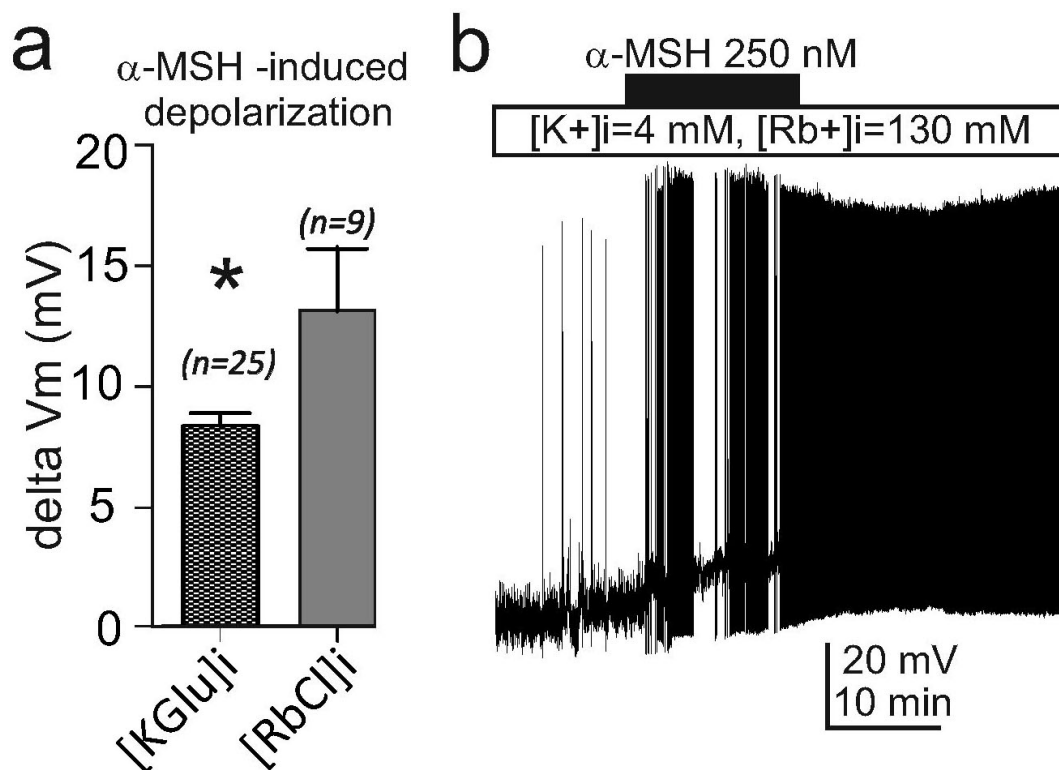
3× standard deviations of their respective negative controls (5 or more dots for MC4R and 4 or more dots for Kir7.1). Two of the images from wild-type mice were also analysed by an automated cell counting multiplex FISH module from Indica Labs, Inc. (Ahmedabad, India). The automated cell counts agreed with our manual count data with >90% of all MC4R mRNA positive cells also positive for Kir7.1 mRNA in the PVN. All animal care and experimental procedures were approved by Vanderbilt University Medical Center Institutional Animal Care and Use Committee.

27. Liu, H. *et al.* Transgenic mice expressing green fluorescent protein under the control of the melanocortin-4 receptor promoter. *J. Neurosci.* **23**, 7143–7154 (2003).
28. Kimmel, C. B., Ballard, W. W., Kimmel, S. R., Ullmann, B. & Schilling, T. F. Stages of embryonic development of the zebrafish. *Dev. Dyn.* **203**, 253–310 (1995).
29. Cox, H. M. *et al.* Peptide YY is critical for acylethanolamine receptor Gpr119-induced activation of gastrointestinal mucosal responses. *Cell Metab.* **11**, 532–542 (2010).
30. Franklin, K. B. J. & Paxinos, G. *The Mouse Brain in Stereotaxic Coordinates* (Academic Press, 1997).



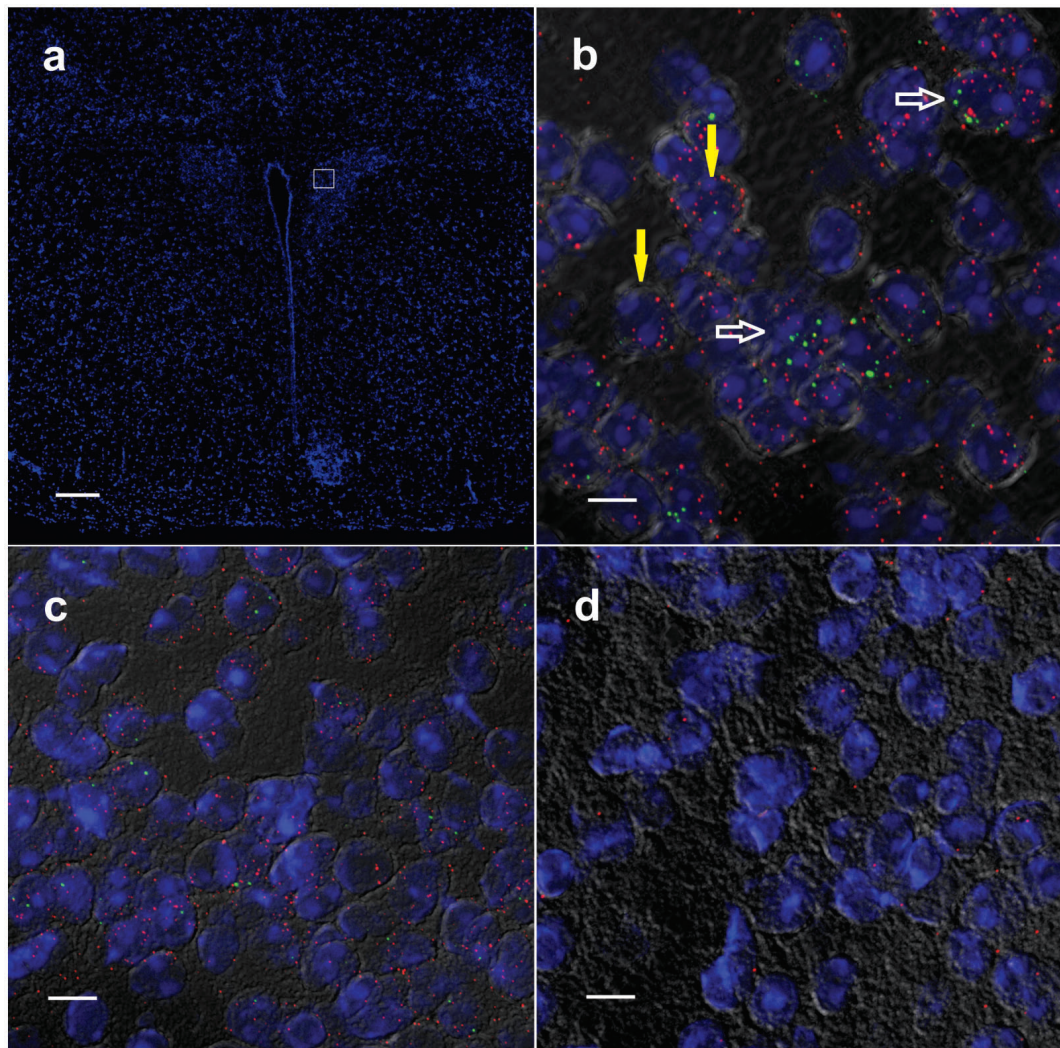
Extended Data Figure 1 | G protein signalling is not required for α -MSH-induced depolarization of PVN MC4R neurons. **a**, A MAP kinase kinase inhibitor, 1 μ M U0126, fails to block α -MSH-induced increase in firing frequency of PVN MC4R neurons recorded in whole cell configuration, (**a**, left panel shows a representative trace from one neuron, **b**, right panel shows mean \pm s.e.m. of firing frequency, $*P < 0.05$, paired t -test). **c**, GTP γ S, a non-hydrolysable GTP analogue, fails to block the depolarization induced by α -MSH, measured in whole-cell configuration. This drug however does block

the hyperpolarization induced by μ -opioid agonist, DAMGO (10 μ M), (mean \pm s.e.m., $***P < 0.001$, paired t -test). **d**, The G $\beta\gamma$ inhibitor gallein fails to inhibit α -MSH-induced depolarization of PVN MC4R neurons (mean \pm s.e.m., $**P < 0.01$, paired t -test), although it blocks the effects of DAMGO (10 μ M) on membrane potential. In all electrophysiological studies, each n represents an independent neuron and slice, and no more than two slices were used per animal.



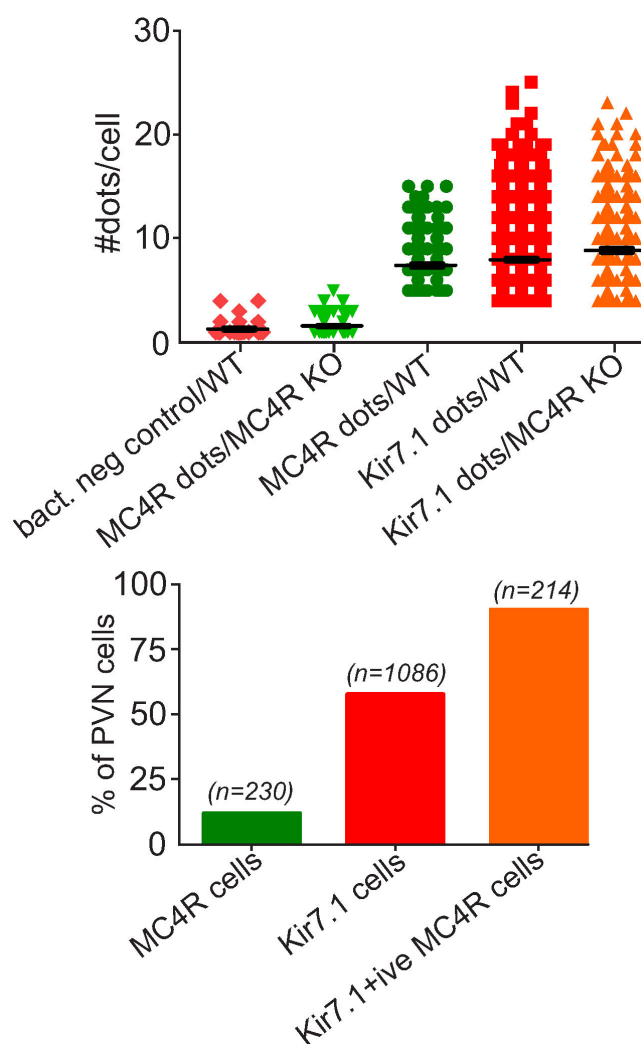
Extended Data Figure 2 | The charge generated by rubidium permeation through MC4R-regulated channels depolarizes PVN MC4 neurons.
a, b, Rb⁺ efflux through MC4R-gated Kir channels can generate greater

α -MSH-induced depolarization of PVN MC4R neurons loaded with 130 mM RbCl and 4 mM K⁺ through the recording pipette. Data show the mean and s.e.m. (**a**, * $P < 0.05$, unpaired t -test), and a representative trace (**b**).

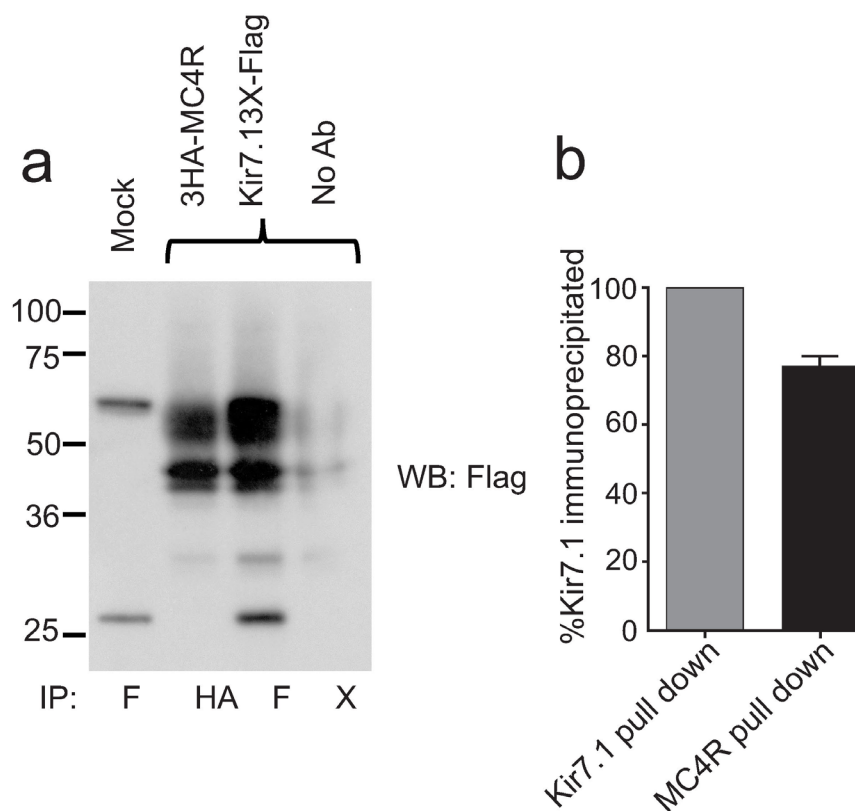


Extended Data Figure 3 | Co-expression of MC4R and Kir7.1 in the PVN. **a–d**, Detection of MC4R and Kir7.1 mRNA in PVN slices using fluorescent *in situ* hybridization (RNAscope). Images demonstrate the region of the hypothalamus under study (**a**; scale bar, 200 μ m), colocalization of MC4R (green) and Kir7.1 (red) mRNAs (**b**, white open arrows, double labelled cells;

yellow arrows, Kir7.1 expression only; scale bar, 10 μ m), and negative controls (**c**, MC4R probe with tissue from MC4R knockout mice; scale bar, 10 μ m; **d**, bacterial probe with tissue from wild-type mice; scale bar, 10 μ m). Data is representative of four male mice.

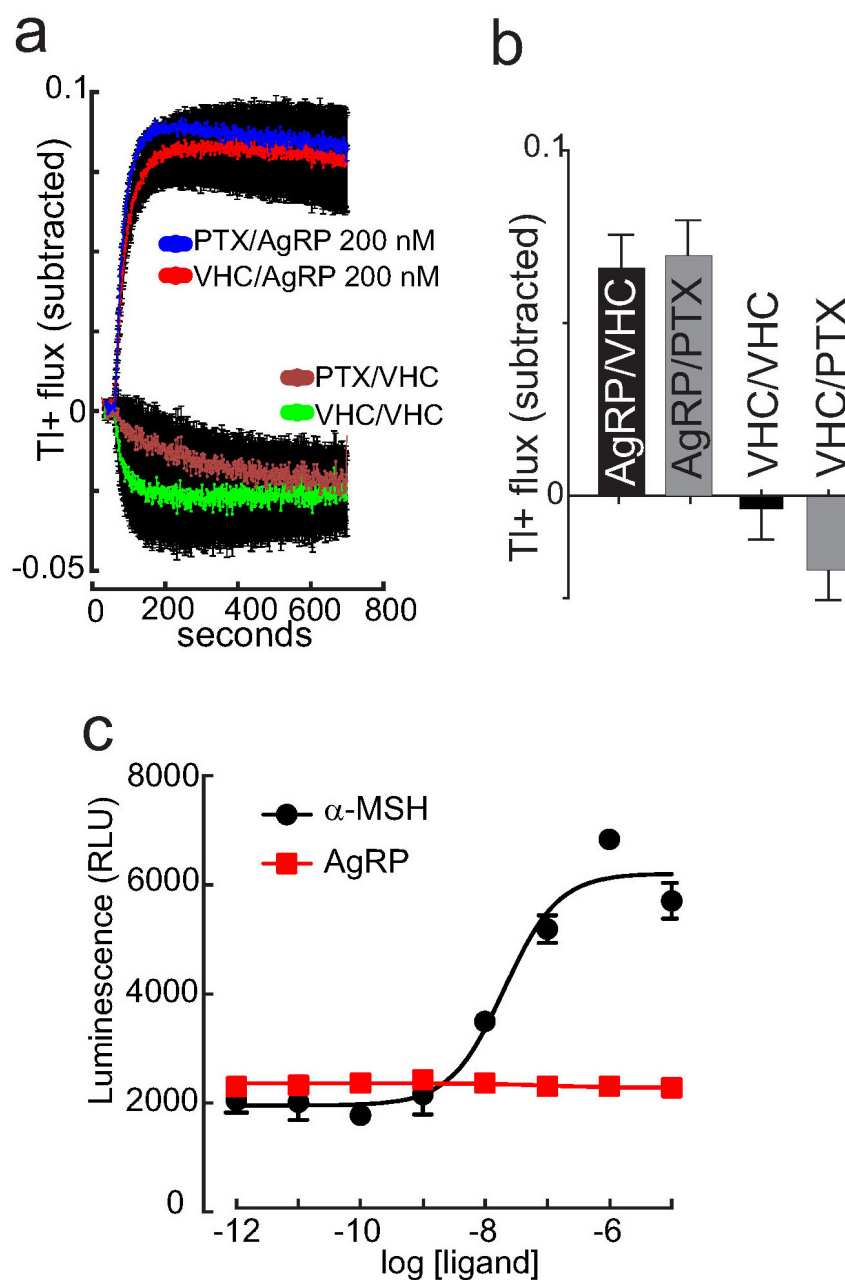


Extended Data Figure 4 | Quantitation of MC4R and Kir7.1 RNA in PVN cells. Single-molecule RNA detection in sections was quantitated by counting fluorescent dots associated with individual cells (Extended Data Fig. 3). Background threshold was determined from the number of dots per cell in sections resulting from hybridization using a negative bacterial DNA control, or from hybridization of the MC4R probe to sections from the MC4R knockout mouse (top panel, columns 1 and 2). Threshold-subtracted dot numbers were then used to determine the per cent of PVN cells expressing MC4R or Kir7.1, and the per cent of MC4R cells expressing Kir7.1; cells were considered positive if the number of dots exceeded the mean of the negative controls by $3\times$ standard deviations (bottom panel). Data from the number of cells indicated was collected from multiple PVN sections derived from four male mice.



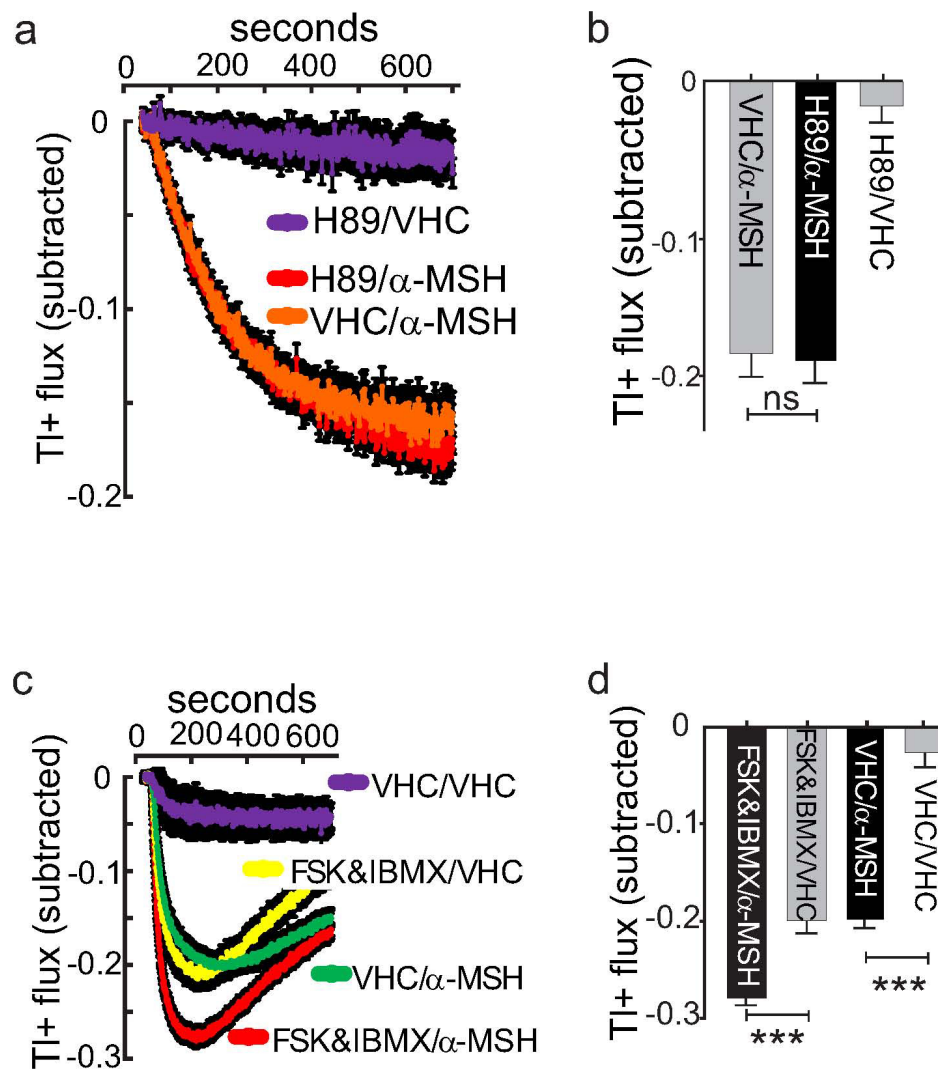
Extended Data Figure 5 | MC4R and Kir7.1 coimmunoprecipitate from transfected HEK293 cells. **a**, Cells transfected with the indicated genetically flagged proteins were incubated with the reversible crosslinker dithiobismaleimidoethane (DTME) before lysis. Lysates were immunoprecipitated using the indicated antibody (F, Flag; HA, haemagglutinin; X, no antibody), crosslinking was reversed with 100 mM DL-dithiothreitol (DTT), and samples separated by SDS-PAGE. The membrane was blotted with the M2 anti-Flag antibody to detect Kir7.1. **b**, Relative quantitation of protein immunoprecipitation. Densitometry analysis to measure the amount of immunoreactive Kir7.1

material was performed using Adobe Photoshop. Amount of material immunoprecipitated with the Kir7.1-3X-Flag was set at 100%. Data shows relative amount of Kir7.1 immunoprecipitated using an antibody against the 3HA-MC4R protein; bars indicate range of data from 2 independent lanes. The protein molecular weight of Kir7.1 is calculated at 40 kDa, and the two larger bands represent glycosylated forms of the protein that are absent when the *N*-linked glycosylation site at position 93 is mutated (data not shown). Data are representative of three independent experiments.



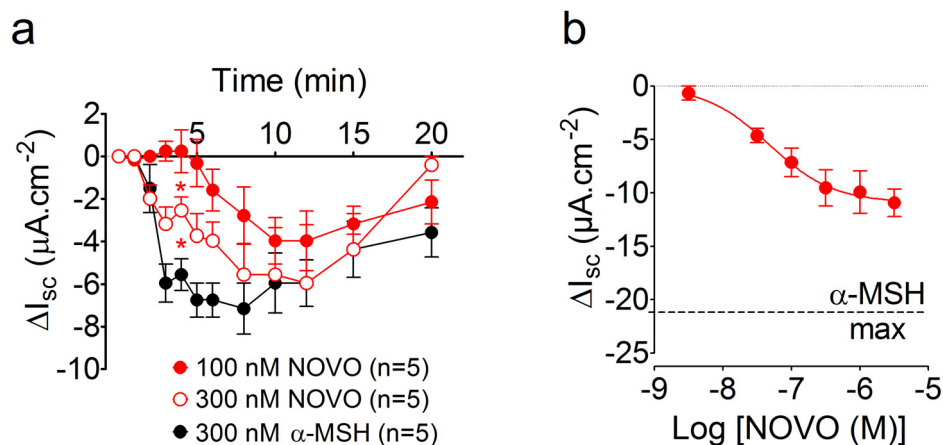
Extended Data Figure 6 | AgRP-induced increase in thallium flux does not involve G_i signalling or β -arrestin recruitment. **a, b,** Subtracted Tl^+ flux examining effects of 200 nM AgRP indicates that 8 h pre incubation with pertussis toxin of MC4R- and Kir7.1-expressing HEK293 cells fails to block AgRP-induced Kir7.1 regulation (mean \pm s.e.m., $n = 110$, combined data from three independent experiments). **c,** Addition of α -MSH stimulates β -arrestin

recruitment to the MC4R in HEK cells stably expressing MC4R and β -arrestin fused to complementary fragments of β -galactosidase (DiscoverRx PathHunter assay, black line, $\log EC_{50} = -7.69$). In contrast, increasing concentrations of AgRP are without any effect using the same assay (red line). Individual points show mean \pm s.e.m. $n = 12$, representative of 3 independent experiments.



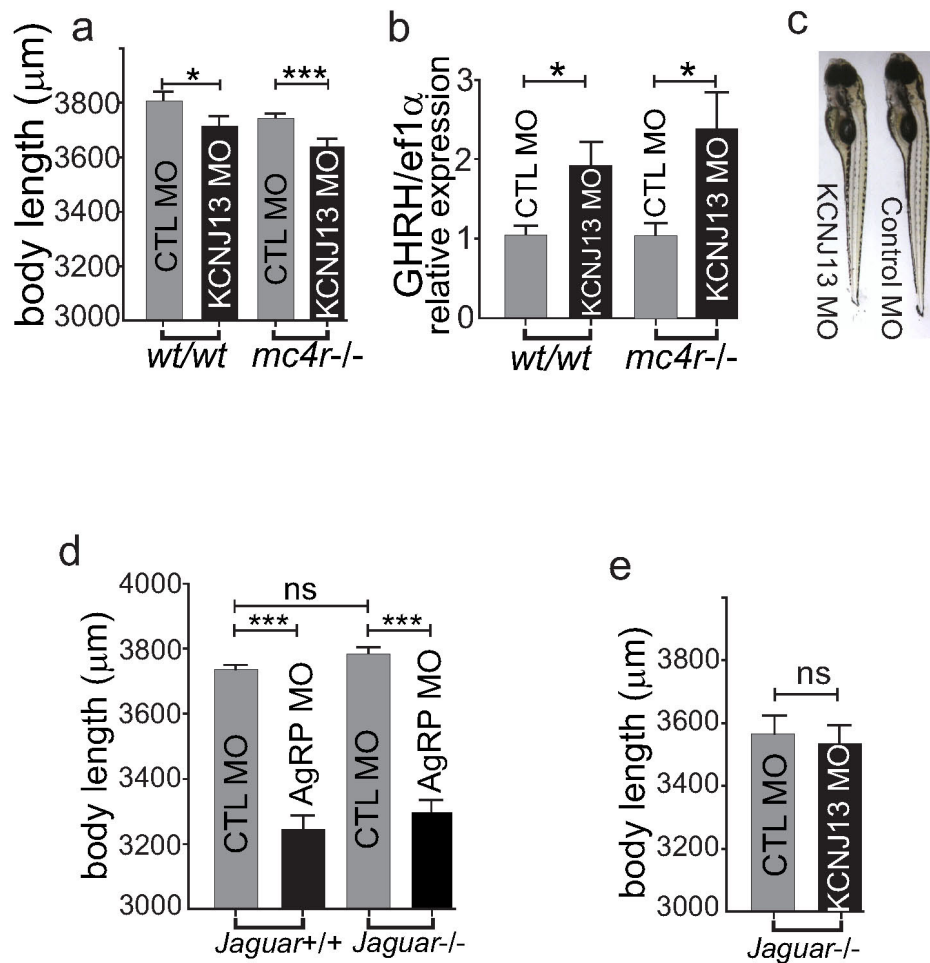
Extended Data Figure 7 | Role of PKA and cAMP in the α -MSH-induced closure of Kir7.1. **a, b,** Subtracted Tl⁺ flux assay examining effects of 100 nM α -MSH indicate that pre-incubation with 1 μ M H89, a PKA inhibitor, fails to block α -MSH-induced regulation of Kir7.1. Data ($n = 16$) show mean \pm s.e.m. of kinetic traces (**a**) and maxima (**b**). VHC = vehicle. **c, d,** Subtracted Tl⁺

flux assay examining effects of raising intracellular cAMP by forskolin (FSK, 20 μ M) and IBMX treatment, with and without 100 nM α -MSH. Data show kinetic traces (**c**) and maxima (**d**). IBMX, 100 μ M 3-isobutyl-1-methylxanthine; VHC, vehicle, mean \pm s.e.m., $n = 64$, *** $P < 0.01$, unpaired t -test. Data representative of 3 independent replicates.



Extended Data Figure 8 | The α -MSH analogue MC4-NN2-0453 (NOVO) is a partial agonist of the MC4R in a murine colon mucosal assay of MC4R activity. The activation of the MC4R inhibits vectorial ion transport across colonic epithelium, measured as reductions in the short circuit current (I_{sc}). **a**, Kinetic response to a sub-maximal basolateral concentration of α -MSH or NOVO, showing more rapid achievement of maximal activity with α -MSH, * $P < 0.05$, one-way ANOVA with Bonferroni's post-test. **b**, Full

concentration-response to MC4-NN2-0453 (NOVO), showing that the compound does not achieve the efficacy reached by a maximal dose of α -MSH (denoted by the dashed line. Full characterization of the MC4R mediated α -MSH response in colonic epithelium is presented elsewhere¹⁸. Each data point represents the mean of five measurements from independent colon samples, with approximately six samples per animal obtained from 15 mice.

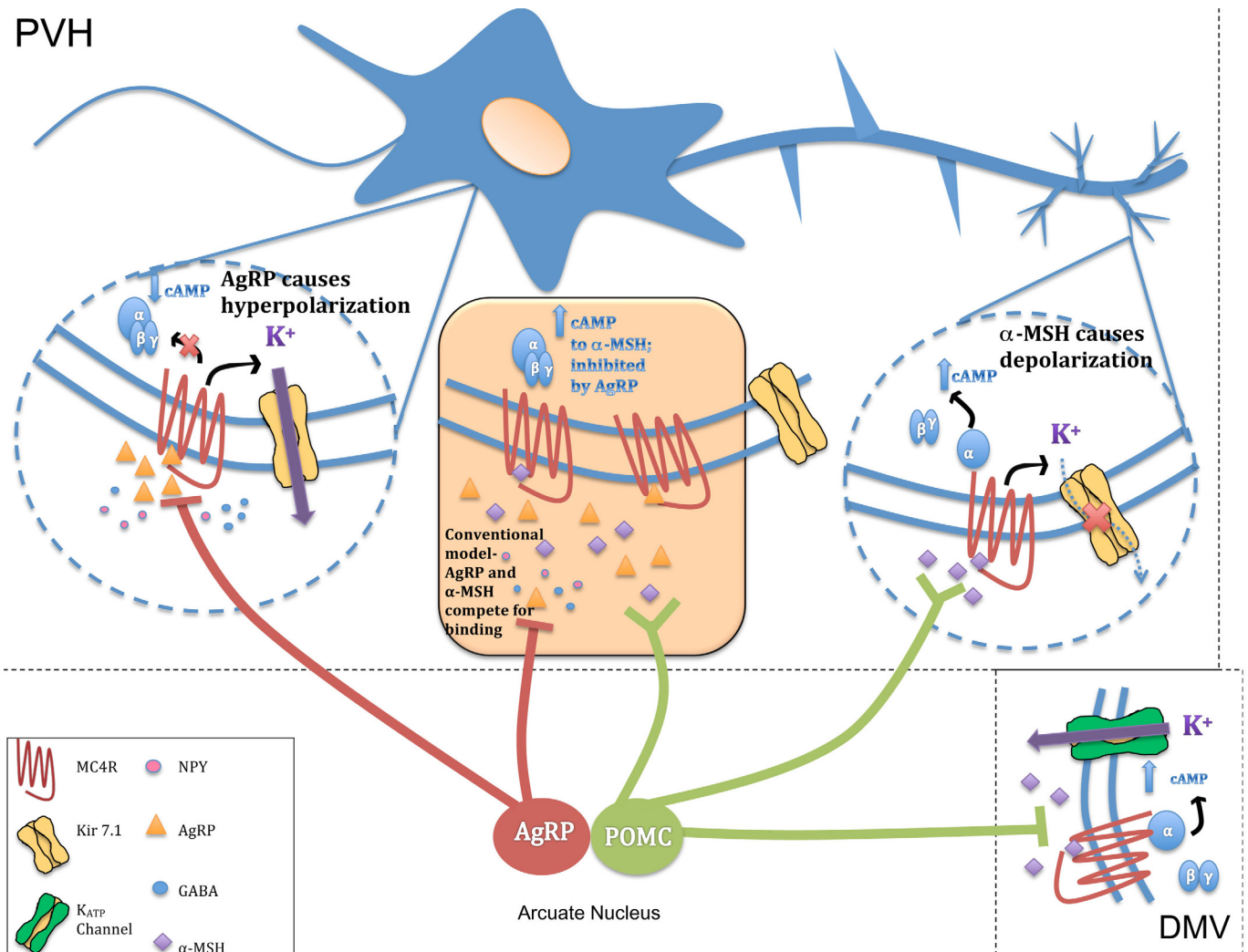


Extended Data Figure 9 | Effects of Kir7.1 and MC4R signalling in larval zebrafish. **a–c**, Knock-down of the *Kir7.1* gene by *kcnj13* morpholino oligonucleotide (MO) suppresses the axial growth of larvae in wild-type and *mc4r* null zebrafish. Sibling wild-type or *mc4r*-null zygotes were bred and injected with antisense *kcnj13* morpholino oligonucleotide at day 0. **a**, The axial body length was measured at 5 dpf. Each group of 30 fish was harvested for RNA extraction and cDNA synthesis. **b**, Relative expression of *ghrh* mRNA was measured and normalized to the house keeping gene *ef1a* with qRT-PCR. The wild type fish that were injected with MO against *kcnj13* expressed significantly higher copies of *ghrh* mRNA than those that were injected with control MO. (control MO, $n = 9$, 1.056 ± 0.116 vs *kcnj13* MO, $n = 9$, 1.935 ± 0.294 , unpaired *t*-test, $*P < 0.05$). MC4R-null fish that were injected

with *kcnj13* MO have significantly higher GHRH expression than MC4R-null fish that were injected with control MO (control MO, $n = 9$, 1.040 ± 0.164 vs KCNJ MO, $n = 8$, 2.395 ± 0.461 , one-way ANOVA, $P < 0.05$).

c, Representative WT fish injected with *kcnj13* MO vs control MO. **d**, **e**, *jaguar* wild-type and null mutant siblings were bred and injected with 7.5 ng non-targeting standard control or 7.5 ng antisense morpholino oligonucleotide targeting *agrp* or *kcnj13*. **d**, Knockdown of AgRP with *agrp* MO in the absence of Kir7.1 also reduces larval growth (mean \pm s.e.m., $n = 43$, $***P < 0.001$, unpaired *t*-test). **e**, The deletion of Kir7.1 in *jaguar* null blocks effects of KCNJ13 MO on MC4R-mediated inhibition of growth (mean \pm s.e.m., $n = 58$, unpaired *t*-test). Data are representative of three independent experiments.

PVH



Extended Data Figure 10 | A model for α -MSH and AgRP signalling at PVN MC4R neurons. Data presented here supports a model in which MC4R may couple to both G_{α_s} signalling and regulation of Kir7.1 activity in PVN MC4R neurons. α -MSH results in elevation of intracellular cAMP through activation of G_{α_s} , and inhibition of K^+ efflux through Kir7.1, both of which are depolarizing. AgRP lowers the constitutive activity of the MC4R and blocks α -MSH binding, but data here show that AgRP also acts as an agonist to increase K^+ efflux through Kir7.1, producing a strong hyperpolarizing signal. The relative distribution and composition of the MC4R signalling complex in different subcellular compartments of PVN MC4R neurons has not been directly determined. Earlier models of α -MSH and AgRP action suggested competitive binding of these peptides to individual MC4R sites (orange box). Existing neuroanatomical data characterizing POMC and AgRP neuronal projections show that α -MSH may act independently of AgRP at many sites in the central nervous system, since AgRP immunoreactive fibres are only observed in a subset of MC4R-expressing nuclei containing POMC-immunoreactive fibres (right circle, for review see ref. 25). The ability of AgRP to act independently of α -MSH as a potent hyperpolarizing agonist, via regulation of Kir7.1, suggests the likely existence of independent AgRP sites of

action (left circle). Recent reconstruction of electron microscopy images of the PVN in which POMC- and AgRP-containing synaptic vesicles have been specifically labelled with a genetically encoded marker provides preliminary anatomical support for this new model²⁶. This study demonstrates that 52% of AgRP boutons in the PVN are not found in synapses, potentially supporting volume transmission of AgRP that may lead to competition with α -MSH at synaptic and/or non-synaptic sites. Additionally, the study found the vast majority of AgRP and POMC synaptic sites localized to different subcellular compartments of PVN neurons, supporting the independent action of both peptides. Synaptic release sites on soma were almost exclusively AgRP-containing, while POMC release sites were concentrated on distal dendrites. Another MC4R signalling pathway, involving cAMP/PKA-dependent activation of K_{ATP} channels and α -MSH-induced hyperpolarization, has been demonstrated in MC4R neurons in the dorsal motor nucleus of the vagus in the brainstem (bottom right)²¹. Thus, while Kir7.1 signalling appears to be essential for depolarization of PVN MC4R neurons by α -MSH, G_{α_s} signalling and elevation of cAMP may be depolarizing or hyperpolarizing, depending on the cellular context.

Growth and host interaction of mouse segmented filamentous bacteria *in vitro*

Pamela Schnupf^{1,2}, Valérie Gaboriau-Routhiau^{2,3,4}, Marine Gros^{4,5}, Robin Friedman¹, Maryse Moya-Nilges⁶, Giulia Nigro¹, Nadine Cerf-Bensussan^{2,4*} & Philippe J. Sansonetti^{1,7*}

The gut microbiota plays a crucial role in the maturation of the intestinal mucosal immune system of its host^{1,2}. Within the thousand bacterial species present in the intestine, the symbiont segmented filamentous bacterium (SFB) is unique in its ability to potently stimulate the post-natal maturation of the B- and T-cell compartments and induce a striking increase in the small-intestinal Th17 responses^{3–5}. Unlike other commensals, SFB intimately attaches to absorptive epithelial cells in the ileum and cells overlying Peyer's patches^{6,7}. This colonization does not result in pathology; rather, it protects the host from pathogens⁴. Yet, little is known about the SFB–host interaction that underlies the important immunostimulatory properties of SFB, because SFB have resisted *in vitro* culturing for more than 50 years. Here we grow mouse SFB outside their host in an SFB–host cell co-culturing system. Single-celled SFB isolated from mono-colonized mice undergo filamentation, segmentation, and differentiation to release viable infectious particles, the intracellular offspring, which can colonize mice to induce signature immune responses. *In vitro*, intracellular offspring can attach to mouse and human host cells and recruit actin. In addition, SFB can potently stimulate the upregulation of host innate defence genes, inflammatory cytokines, and chemokines. *In vitro* culturing thereby mimics the *in vivo* niche, provides new insights into SFB growth requirements and their immunostimulatory potential, and makes possible the investigation of the complex developmental stages of SFB and the detailed dissection of the unique SFB–host interaction at the cellular and molecular levels.

SFB or 'Candidatus Arthromitus' are anaerobic, clostridia-related, spore-forming commensals found in the gut of many vertebrate species, including mice and probably humans^{8,9}. SFB have garnered much interest because of their unique ability to educate the gut immune system and to induce a healthy state of physiological inflammation^{3,4}. SFB colonization leads to the maturation of the gut mucosal lymphoid tissue, induces a strong and broad IgA response, stimulates the T-cell compartment, and upregulates intestinal innate defence mediators^{4,5,10}. In addition, SFB colonization exerts an adjuvant effect on systemic responses and can thus exacerbate pathologies in mouse models of encephalitis and arthritis, while protecting genetically predisposed mice against the development of type I diabetes^{11–15}. Recent sequencing of the rat and mouse SFB genomes revealed the highly auxotrophic needs of SFB and placed SFB between obligate and facultative symbionts. These findings suggest that SFB obtain at least some of their nutritional requirements from their interaction with the host^{16–19}.

To culture SFB, we aimed to mimic their replicative niche. We therefore designed an SFB–host cell co-culturing system whereby SFB²⁰ isolated from monoassociated mice were cultured with eukaryotic cells grown in low but physiological oxygen conditions²¹ in a rich tissue culture medium containing bacterial medium components and additional supplements.

SFB from monoassociated mice were collected, filtered through a 100- μ m mesh, separated from most other faecal matter using a Nycodenz column and passed through a 5- μ m filter to obtain a pure culture of unicellular intracellular offspring (average 0.7 μ m) (Fig. 1a). Eukaryotic cells grown on tissue culture wells or transwells were placed in a humidified anaerobic cabinet, challenged with intracellular offspring, and kept at either strict anaerobic conditions within a sealed box or left in the anaerobic cabinet where the oxygen concentration was maintained at low levels (0.5–1.4% O₂). After 4 days, bacterial growth in the culture supernatant was quantified by quantitative PCR (qPCR) using SFB-specific 16S rDNA primers (Fig. 1b) and confirmed using scanning electron microscopy (SEM) (Fig. 1c). SFB growth was observed in all conditions for most cell lines assayed but growth was usually enhanced on transwells compared with tissue culture wells and growth was significantly better in the presence of oxygen, revealing SFB to be a relatively aerotolerant anaerobe. Both human (TC7/HeLa) and mouse (mICd2/CMT93) cell lines supported growth but the TC7 was the most resilient cell line generally supporting SFB growth most robustly. On the basis of temporal analysis, the highest exponential growth phase occurred between days 1 and 3, with an average maximum doubling time of 5.0 h (Fig. 1d).

Next we dissected the growth requirements for SFB. SFB growth had a striking dependence on host cell number, decreasing in number with decreasing cell density (Fig. 1e). In addition, negligible growth occurred in medium alone, medium supplemented with cell lysate, or when cells were fixed before SFB challenge (Fig. 1f), indicating that live host cells are required for SFB proliferation. SFB also required close contact for efficient growth as only little growth (0–6%) occurred when intracellular offspring were added to the bottom chamber of transwells or when bacteria were placed in transwells above cells in tissue culture wells (Fig. 1f, g). Yet, as host cell contact was not an absolute requirement, it suggests that host cells may release a soluble factor that promotes SFB growth. To address the requirement for medium supplementation, SFB were grown on TC7 cells in complete medium or medium missing individual additives. Brain–heart infusion, a yeast/peptone/casein amino acid mixture, and particularly iron supplementation were critical for SFB growth (Fig. 1h, i).

In the 1970s, transmission electron microscopy studies of SFB present in the murine gut led to a proposed life cycle: attachment to epithelial cells via the holdfast at the intracellular offspring tip leads to filamentous growth and is followed by a complex developmental progression that starts at the distal tip and ultimately leads to intracellular offspring formation and release (Fig. 2A)^{7,22}. According to this model, when filaments grow beyond 50 μ m in length, the large primary filament segments start to undergo a symmetrical division to form smaller secondary segments. These differentiate by dividing asymmetrically to form a mother/daughter cell. The daughter cell becomes engulfed and subsequently divides to form two intracellular offspring within the surrounding

¹Unité de Pathogénie Microbienne Moléculaire and Institut national de la santé et de la recherche médicale (INSERM) unit U786, Institut Pasteur, 25–28 Rue du Dr Roux, 75724 Paris Cedex 15, France.

²INSERM, UMR1163, Laboratory of Intestinal Immunity, Institut Imagine, 24, Boulevard du Montparnasse, 75015 Paris, France. ³Institut national de la recherche agronomique (INRA) Micalis UMR1319, 78350 Jouy-en-Josas, France. ⁴Université Paris Descartes-Sorbonne Paris Cité and Institut Imagine, 75015 Paris, France. ⁵Ecole Normale Supérieure de Lyon, Department of Biology, 69007 Lyon, France.

⁶Imagopole, Ultrastructural Microscopy Platform, Institut Pasteur, 25–28 Rue du Dr Roux, 75724 Paris Cedex 15, France. ⁷Microbiologie et Maladies Infectieuses, Collège de France, 11 Marcelin Berthelot Square, 75005 Paris, France.

*These authors contributed equally to this work.

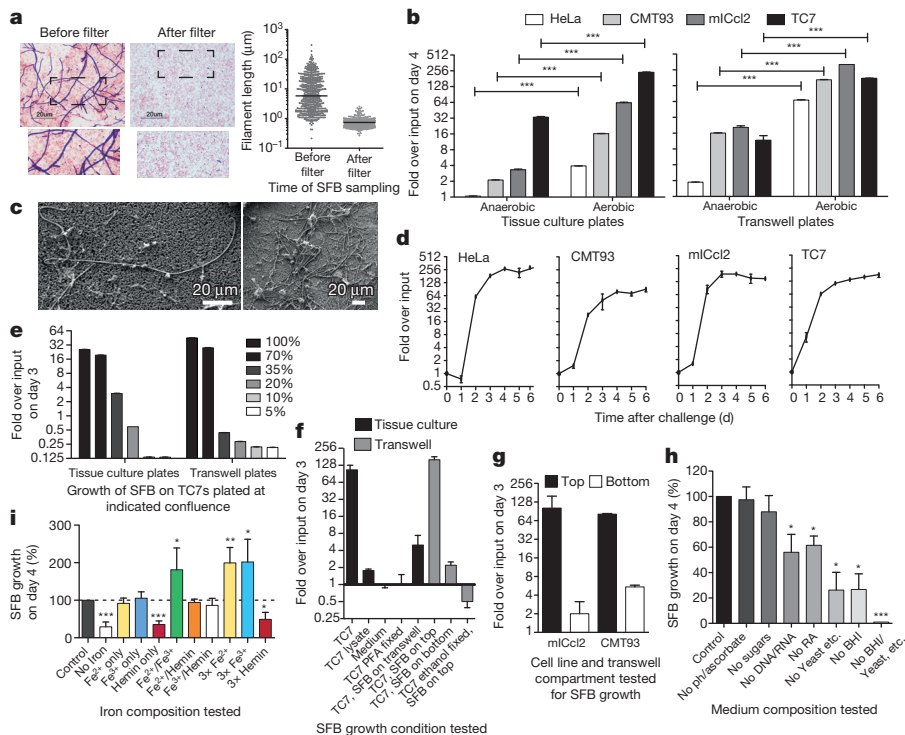


Figure 1 | Growth and growth requirements of SFB *in vitro*. **a**, Gram stain and length of SFB before and after 5-μm filtration. **b**, qPCR of SFB growth on host cells at the indicated conditions. **c**, SEM images of 4-day-old SFB filaments grown anaerobically on TC7 cells on transwells. **d–i**, SFB growth at low oxygen concentrations on the indicated cell line seeded on transwells (**d**); on TC7 cells at indicated cell confluence (**e**); under various conditions and with different cell lines (**f, g**); and on TC7 cells on transwells with indicated medium composition (**h, i**). **a–e**, Representative images and values from one of three experiments performed in triplicate with means \pm s.d. **f, h**, Cumulative values with means \pm s.e.m. from three experiments performed in duplicate. **b, i, h**, Statistical analysis using the two-tailed *t*-test (* P < 0.05, ** P < 0.01, *** P < 0.001).

mother cell segment. Intracellular offspring are then released from the filament by breakdown of the filament septa and cell wall and reattach to the host.

In vitro, growth of SFB on TC7 cells often yielded considerable quantities of long filaments that could be clumped together in a hairball-like

phenotype easily seen with the naked eye (Fig. 2B). Most of these filaments were undifferentiated after 4 days, with only some filaments showing a characteristic heterogeneous staining of differentiating filaments (Fig. 2B, left-hand column, bottom two panels). Intracellular offspring could be seen located at the filament tip or occasionally in the central

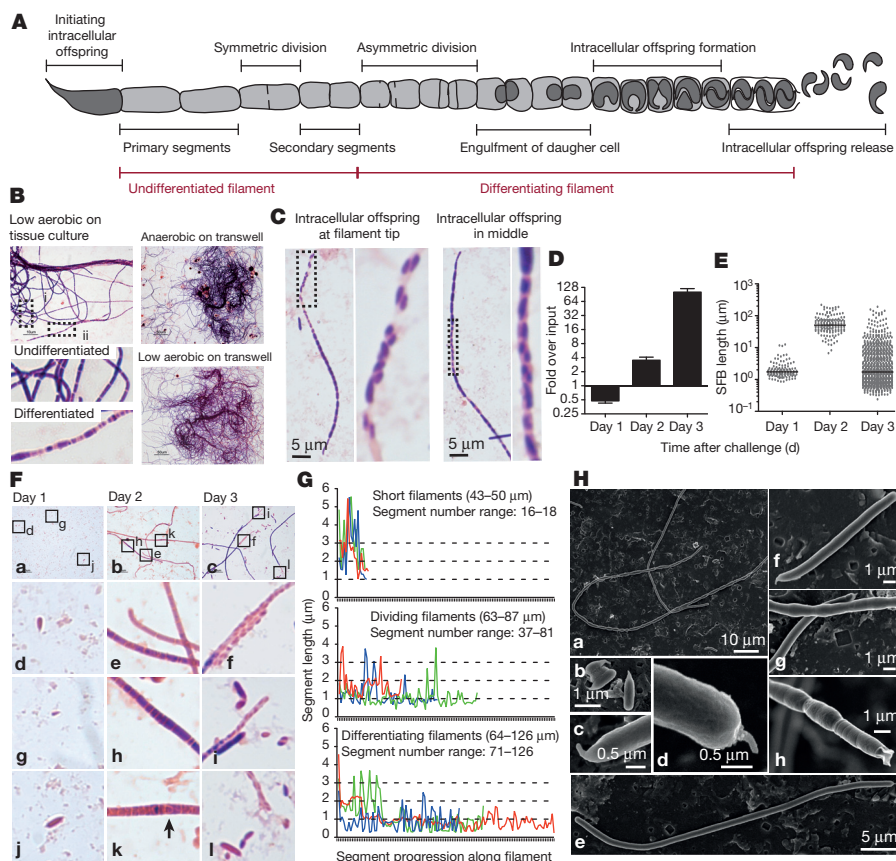


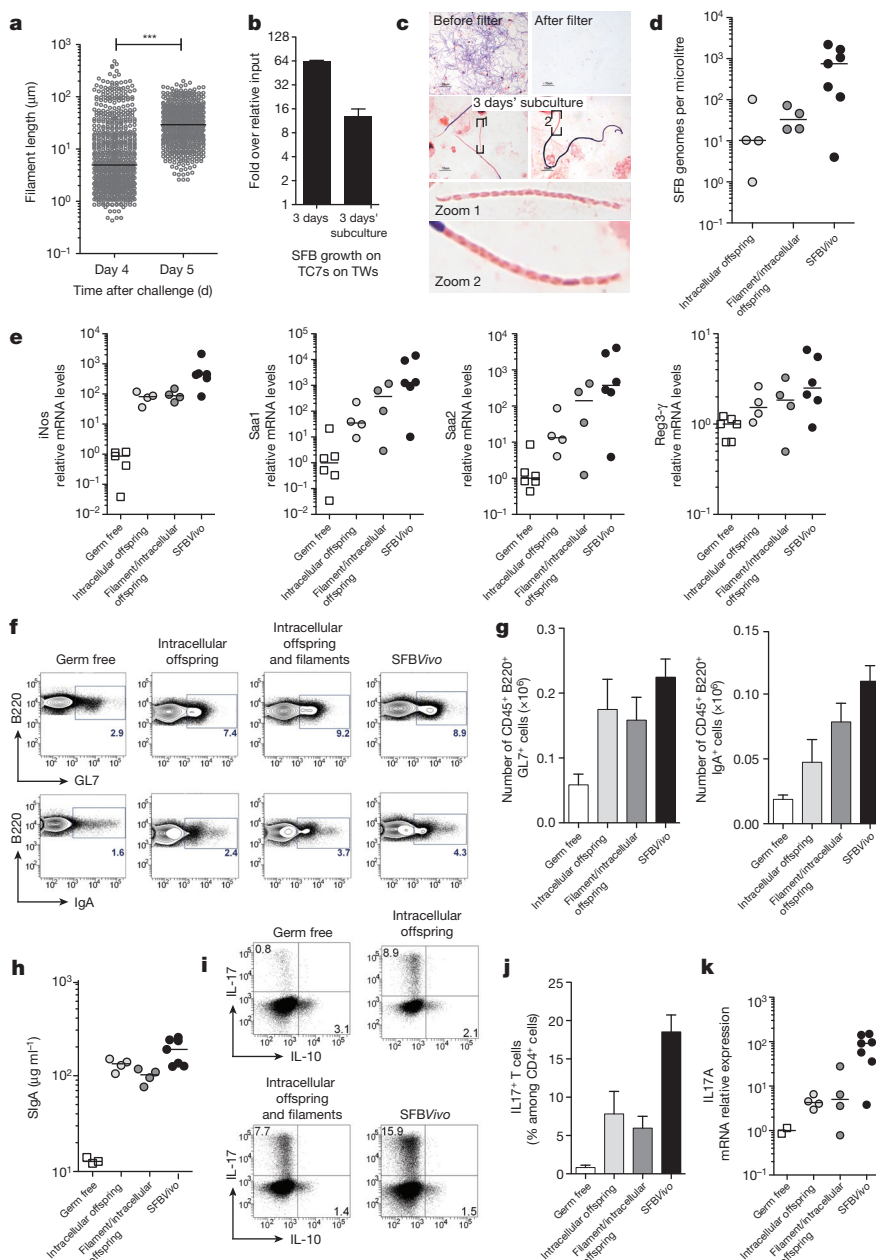
Figure 2 | Differentiation of SFB from filaments to intracellular offspring during *in vitro* growth. **A**, Schematic representation of an SFB filament highlighting stages of its growth and differentiation. Gram stain of SFB after 4 days of growth on TC7 cells incubated at the indicated condition (**B**); and TC7 cells grown on transwells in low oxygen (**C**). (**D–H**) Analysis of SFB grown on mCcl2 cells (**D–G**) and TC7 cells (**H**) on transwells at 1–2.5% O₂. **D**, qPCR quantification (mean \pm s.d. of triplicates); **E**, length of individual SFBs; **F**, Gram stain; and **G**, segment length analysis of representative 2-day-old SFB filaments. **H**, SEM of SFB after 4 days of growth. **B–H**, Representative images and values from one of three experiments performed in triplicate.

part of a filament (Fig. 2C), similar to filaments recovered from SFB-monoassociated mice (data not shown). Differentiation of SFB occurred on all four cell lines tested, but we noticed that differentiation was more pronounced when higher oxygen concentrations (1–2.5%) were used. In time-course analysis at this higher oxygen concentration (Fig. 2D), only short bacteria were detected 1 day after challenge (Fig. 2E, F). After 2 days, only long filaments were present (Fig. 2E, F) and the bacterial septa could be identified quite clearly using the Gram stain (Fig. 2F). Three types of filament were found (Fig. 2F, G): short filaments with long intracellular segments of $\sim 2.6 \mu\text{m}$; medium-sized filaments with smaller intracellular segments of $\sim 1.2 \mu\text{m}$; and medium to long filaments that had a more heterogeneous distribution of segment lengths including very small segments (Fig. 2F, G) and rare segments with half-circular structures (Fig. 2F, day 2, arrow) that resembled the engulfment of a daughter cell by a mother cell. After 3 days of growth, most filaments had differentiated, at least in part, to the final intracellular offspring stage and intracellular offspring could be seen in a characteristic doublet orientation at the filament tip where the filament cell wall appeared to have lost its structure (Fig. 2F, right-hand column). Many

intracellular offspring of varying lengths were also no longer associated with filaments. SEM confirmed the presence of the needle-like holdfast structure on intracellular offspring and at the tip of filaments (Fig. 2H, b–g), and could clearly distinguish between undifferentiated thin and smooth filaments (Fig. 2H, a, e–g) and those that were broader with a heterogeneous and bulbous morphology that corresponded to differentiating filaments (Fig. 2H, a, g, h)^{7,22}. In addition, cell-wall remnants could be detected at the distal tip of differentiating filaments where intracellular offspring had been released (Fig. 2H, h and Extended Data Fig. 1b)⁷. Together, these data demonstrate that *in vitro* culturing of SFB supports the full differentiation of *in vitro*-grown SFB filaments to the intracellular offspring stage and confirms the SFB life cycle inferred from *in vivo* observations.

The viability and infectivity of *in vitro*-formed intracellular offspring was then tested. SFB were first grown on TC7 cells under aerobic conditions (Fig. 3a) until many intracellular offspring appeared. After one additional day, intracellular offspring were no longer present and the average bacterial length was significantly longer, indicating intracellular offspring outgrowth into filaments. Similarly, when intracellular

Figure 3 | Viability, colonization, and immunostimulatory potential of *in vitro*-grown SFB. **a**, SFB length after growth on TC7 cells on transwells. **b**, **c**, Quantification (**b**) and Gram stain (**c**) of SFB growth on TC7 cells on transwells before and after a 3-day sub-culturing of the 5- μm filtrate. **d–k**, Analysis of germ-free C57BL/6 mice gavaged with either filament/intracellular offspring mix, intracellular offspring, or faeces of SFB-monoassociated mice (SFBVivo). **d**, Quantification of ileum-associated SFB. **e**, **k**, Host gene expression in the ileal lamina propria. **f**, **g**, **i**, **j**, Representative flow cytometry plots and quantification of B220⁺ B cell (**f**, **g**) and CD45⁺CD3⁺CD4⁺ T cell (**i**, **j**) frequencies of the indicated markers. **h**, Faecal secretory IgA quantification by ELISA. **a–k**, Images and values are representatives from one of two experiments performed in duplicate with means \pm s.d. (**a–c**) or performed with four to seven mice per group (**d–k**). Statistical analysis using the two-tailed *t*-test (***P* < 0.001).

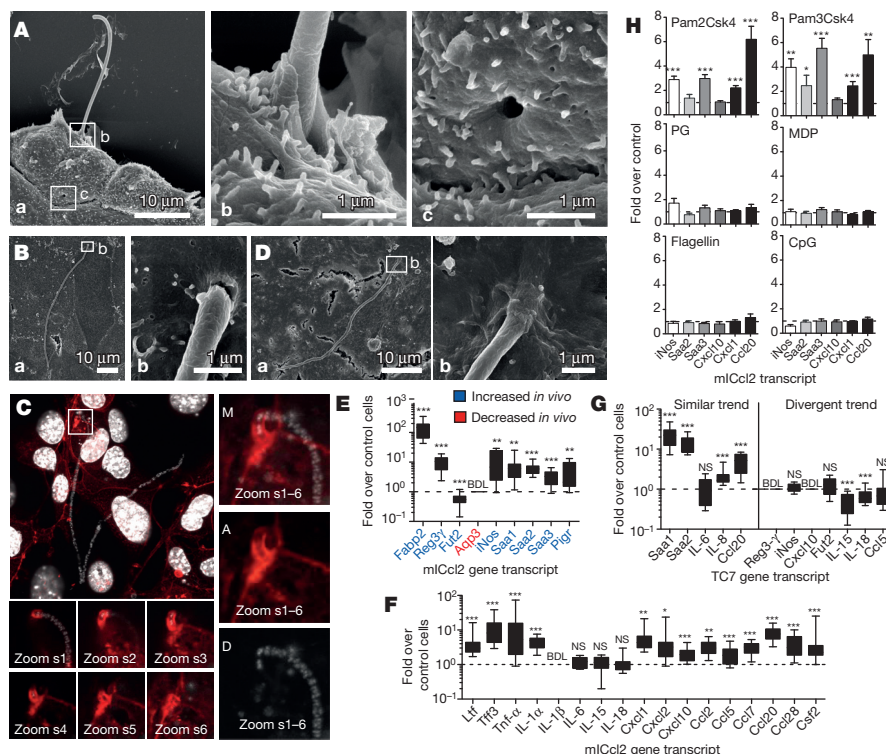


offspring grown *in vitro* were separated from filaments by filtration through a 5- μ m filter and added to newly plated cells, SFB numbers increased and the newly formed filaments differentiated into intracellular offspring at the filament tip (Fig. 3b, c), demonstrating filamentation and differentiation of *in vitro*-formed intracellular offspring. To assess whether SFB grown *in vitro* retained their ability to colonize mice and stimulate the characteristic innate and acquired immune responses, SFB grown *in vitro* for 3 days were divided into a filament/intracellular offspring fraction and a pure intracellular offspring fraction (Extended Data Fig. 1a, b) and gavaged into germ-free mice. Colonization was firmly established by both inputs at 5 days after gavage (Extended Data Fig. 1c) despite a 140-fold input difference for the filament/intracellular offspring and intracellular offspring fractions. However, unlike mice gavaged with SFB derived from faecal samples (SFBVivo), which generally showed good colonization of the ileum, mice gavaged with *in vitro*-grown SFB (SFBV_{itro}) had much lower numbers of SFB colonizing the ileum (Fig. 3d and Extended Data Fig. 1d); instead they showed heavy colonization of the caecum (Extended Data Fig. 1d). Thus, although SFBV_{itro} clearly can attach to the ileum, these results suggest that ileal colonization may be more efficient by intracellular offspring released from spores found in the faecal input, possibly because of the expression of flagella at this particular stage of the life cycle¹⁹. Notably, the magnitude of the innate host response (Fig. 3e) was proportional to the colonization level of the ileum (Fig. 3d) and not the overall SFB faecal load (Extended Data Fig. 1c), revealing the requirement for ileal attachment of SFB to induce the innate host response. Similar to SFBVivo, albeit with less potency, SFBV_{itro} were also able to stimulate the B-cell compartment in Peyer's patches (Fig. 3f, g), enhance IgA secretion in the faeces (Fig. 3h), and increase the number of Th17 cells and the level of IL-17A messenger RNA in the small intestine lamina propria (Fig. 3i–k).

Lastly, we investigated the SFB–host interaction and the host response to SFB growth. Despite the apparent requirement for close contact between host cells and SFB for efficient growth, a tight interaction was not readily observed. However, when the interaction was promoted by gently spinning intracellular offspring onto cells, SFB filaments were found attached to mICcl2 cells (Fig. 4A–C). This stable interaction was accompanied by actin accumulation surrounding the filament tip (Fig. 4C) and could leave structurally intact vacant attachment sites (Fig. 4A, c),

similar to those observed in the ileum of mice (Extended Data Fig. 1e). Attached filaments included both undifferentiated ones and those that had reached the final intracellular offspring stage. Contrary to *in vivo* results²³, attachment *in vitro* was not species specific (Fig. 4D). To assess the similarity in the host response to SFB *in vitro* and *in vivo*, we analysed the gene expression profile of epithelial-derived host factors known to be regulated by SFB colonization^{4,5,24–26}. We found that the gene regulation *in vitro* closely recapitulated gene regulation *in vivo* (Fig. 4E), thereby further supporting our *in vitro* model system. Going beyond previously implicated epithelial factors, we tested several additional cytokines, chemokines, and host defence genes (Fig. 4F). Our data show that SFB growth leads to a strong inflammatory host response, with the induction of pleiotropic inflammatory mediators such as tumour-necrosis factor- α (TNF- α), interleukin-1- α (IL1- α), and serum amyloid A 1–3 (Saa1–3), induction of several innate host defence mechanisms (Reg3 γ , iNos, and lactoferrin), and an immunological environment that is conducive for the recruitment of B cells, the transmigration of IgA, recruitment and activation of T cells, and recruitment of neutrophils, dendritic cells and monocytes. In agreement, we observed that the transcript level of most immune genes that are upregulated during co-culture with mICcl2 cells *in vitro* was also increased by SFB, and not by *Escherichia coli*, during colonization experiments *in vivo* (Extended Data Fig. 1f). Conversely, the transcriptional response in the human TC7 cell line was divergent from that observed in mICcl2 cells and less consistent with *in vivo* results (Fig. 4G). Lastly, by using an array of microbe-associated molecular patterns (MAMPs), we demonstrated that the inflammatory response to SFB *in vitro* is probably shaped by the activation of TLR2 (Fig. 4H).

We hereby demonstrate the successful culturing of SFB *in vitro* and provide new insights into SFB growth requirements and the host response to SFB challenge. Our data suggest that *in vivo*, attachment of SFB to the ileal surface is an important feature to elicit epithelial cell responses, whereas *in vitro*, where attachment remained infrequent, the close proximity of SFB and cells appears largely to bypass the need for attachment to deliver the stimulating signal(s). These findings highlight the importance of the privileged location of the replicative niche of SFB at the ileal epithelial surface in mediating the stimulatory potential of SFB. Future investigations using the *in vitro* culturing system will



be needed to dissect the contribution of bacterial factors, including MAMPs, and attachment per se to the unique immunostimulatory properties of this unusual and still enigmatic commensal.

Online Content Methods, along with any additional Extended Data display items and Source Data, are available in the online version of the paper; references unique to these sections appear only in the online paper.

Received 4 November 2013; accepted 3 November 2014.

Published online 19 January 2015.

- Round, J. L. & Mazmanian, S. K. The gut microbiota shapes intestinal immune responses during health and disease. *Nature Rev. Immunol.* **9**, 313–323 (2009).
- Cerf-Bensussan, N. & Gaboriau-Routhiau, V. The immune system and the gut microbiota: friends or foes? *Nature Rev. Immunol.* **10**, 735–744 (2010).
- Schnupf, P., Gaboriau-Routhiau, V. & Cerf-Bensussan, N. Host interactions with segmented filamentous bacteria: an unusual trade-off that drives the post-natal maturation of the gut immune system. *Semin. Immunol.* **25**, 342–351 (2013).
- Ivanov, I. I. *et al.* Induction of intestinal Th17 cells by segmented filamentous bacteria. *Cell* **139**, 485–498 (2009).
- Gaboriau-Routhiau, V. *et al.* The key role of segmented filamentous bacteria in the coordinated maturation of gut helper T cell responses. *Immunity* **31**, 677–689 (2009).
- Jepson, M. A., Clark, M. A., Simmons, N. L. & Hirst, B. H. Actin accumulation at sites of attachment of indigenous apathogenic segmented filamentous bacteria to mouse ileal epithelial cells. *Infect. Immun.* **61**, 4001–4004 (1993).
- Chase, D. G. & Erlandsen, S. L. Evidence for a complex life cycle and endospore formation in the attached, filamentous, segmented bacterium from murine ileum. *J. Bacteriol.* **127**, 572–583 (1976).
- Klaasen, H., Koopman, J. P. & Poelma, F. Intestinal, segmented, filamentous bacteria. *FEMS Microbiol.* **88**, 165–180 (1992).
- Yin, Y. *et al.* Comparative analysis of the distribution of segmented filamentous bacteria in humans, mice and chickens. *ISME J.* **7**, 615–621 (2012).
- Schnupf, P., Gaboriau-Routhiau, V. & Cerf-Bensussan, N. Host interaction with segmented filamentous bacteria: an unusual trade-off that drives the post-natal maturation of the gut immune system. *Semin. Immunol.* **25**, 342–351 (2013).
- Lee, Y. K., Menezes, J. S., Umesaki, Y. & Mazmanian, S. K. Proinflammatory T-cell responses to gut microbiota promote experimental autoimmune encephalomyelitis. *Proc. Natl Acad. Sci. USA* **108** (suppl. 1), 4615–4622 (2011).
- Wu, H. J., Ivanov, I. I., Darce, J., Hattori, K. & Shima, T. Gut-residing segmented filamentous bacteria drive autoimmune arthritis via T helper 17 cells. *Immunity* **32**, 815–827 (2010).
- Chappert, P., Bouladoux, N., Naik, S. & Schwartz, R. H. Specific gut commensal flora locally alters T cell tuning to endogenous ligands. *Immunity* **38**, 1198–1210 (2013).
- Kriegel, M. A. *et al.* Naturally transmitted segmented filamentous bacteria segregate with diabetes protection in nonobese diabetic mice. *Proc. Natl Acad. Sci. USA* **108**, 11548–11553 (2011).
- Yurkovetskiy, L. *et al.* Gender bias in autoimmunity is influenced by microbiota. *Immunity* **39**, 400–412 (2013).
- Prakash, T., Oshima, K., Morita, H., Fukuda, S. & Imaoka, A. Complete genome sequences of rat and mouse segmented filamentous bacteria, a potent inducer of Th17 cell differentiation. *Cell Host Microbe* **10**, 273–284 (2011).
- Szczesnak, A. *et al.* The genome of Th17 cell-inducing segmented filamentous bacteria reveals extensive auxotrophy and adaptations to the intestinal environment. *Cell Host Microbe* **10**, 260–272 (2011).
- Kuwahara, T. *et al.* The lifestyle of the segmented filamentous bacterium: a non-culturable gut-associated immunostimulating microbe inferred by whole-genome sequencing. *DNA Res.* **18**, 291–303 (2011).
- Pamp, S. J., Harrington, E. D., Quake, S. R., Relman, D. A. & Blainey, P. C. Single-cell sequencing provides clues about the host interactions of segmented filamentous bacteria (SFB). *Genome Res.* **22**, 1107–1119 (2012).
- Bolotin, A. *et al.* Genome sequence of “*Candidatus Arthromitus*” sp. strain SFB-mouse-NL, a commensal bacterium with a key role in postnatal maturation of gut immune functions. *Genome Announc.* **2**, 1–2 (2014).
- He, G. *et al.* Noninvasive measurement of anatomic structure and intraluminal oxygenation in the gastrointestinal tract of living mice with spatial and spectral EPR imaging. *Proc. Natl Acad. Sci. USA* **96**, 4586–4591 (1999).
- Ferguson, D. J. & Birch-Andersen, A. Electron microscopy of a filamentous, segmented bacterium attached to the small intestine of mice from a laboratory animal colony in Denmark. *Acta Pathol. Microbiol. Scand. B* **87**, 247–252 (1979).
- Tannock, G. W., Miller, J. R. & Savage, D. C. Host specificity of filamentous, segmented microorganisms adherent to the small bowel epithelium in mice and rats. *Appl. Environ. Microbiol.* **47**, 441–442 (1984).
- Goto, Y. *et al.* Innate lymphoid cells regulate intestinal epithelial cell glycosylation. *Science* **345**, 1254009 (2014).
- Shima, T. *et al.* Differential effects of two probiotic strains with different bacteriological properties on intestinal gene expression, with special reference to indigenous bacteria. *FEMS Immunol. Med. Microbiol.* **52**, 69–77 (2008).
- Lécuyer, E. *et al.* Segmented filamentous bacterium uses secondary and tertiary lymphoid tissues to induce gut IgA and specific T helper 17 cell responses. *Immunity* **40**, 608–620 (2014).

Acknowledgements We are grateful to B. Marteyn, F.-X. Campbell-Valois, and C. Parsot for discussions, M. Picard and S. Rakotobe for help with *in vivo* experiments, and T. Angélique for animal care. This work was supported by INSERM, Institut Pasteur, Collège de France, and INRA, and grants TORNADO-FP7-KBBE-2007-2A-222720, ANR-2010-BLAN1317, ERC-2009-AG-232798-HOMEOPITH, ERC-2013-AdG-339579-DECRYPT, and ERC-2013-AdG-339407-IMMUNOBIOTA and the Investissement d’Avenir ANR-10-IAHU-01 and LabEX IBEID. P.J.S. is a Howard Hughes Medical Institute Foreign Scholar.

Author Contributions N.C.-B., V.G.-R., P.J.S., and P.S. conceived the project and discussed experiments. P.S. designed and performed all *in vitro* experiments. V.G.-R. and M.G. performed the *in vivo* challenge experiments, V.G.-R. maintained SFB mice and M.G. analysed the TC7 and R.F. the mICI2 host response. M.M.-N. processed SEM samples and took images with P.S. G.N. assisted *in vitro* experiments. P.S. wrote the paper and P.J.S., N.C.-B. and V.G.-R. edited the manuscript.

Author Information Reprints and permissions information is available at www.nature.com/reprints. The authors declare no competing financial interests. Readers are welcome to comment on the online version of the paper. Correspondence and requests for materials should be addressed to P.J.S. (psanson@pasteur.fr) or N.C.-B. (nadine.cerf-bensussan@inserm.fr).

METHODS

Cell culture and SFB-specific culture medium. TC7, CMT93, and HeLa cells were cultured in DMEM (Gibco 31885) with 10% inactivated fetal calf serum (FCS; AbCys CVFV00-0U) and non-essential amino acids (Invitrogen 11140-035) while mICcl2 were maintained in DMEM/F12 advanced medium (Gibco 12634) with 2% inactivated FCS and Glutamax (Gibco 35050) and supplemented with 10 nM hEGF (Sigma E9644), 50 nM dexamethasone (Sigma D4902) and 1 nM triiodothyronine (Sigma T5516). HeLa cells were obtained from ATCC; CMT93 cells were provided by H. Blottière; TC7 cells were from A. Servin, and mICcl2 cells from the laboratory of A. Vandewalle. All cell lines were tested for mycoplasma every 2 weeks and always found to be negative. Cells were plated from 1 to 3 days before the experiment such that a monolayer was present at the start of the experiment. SFB medium was made up as follows: DMEM/F12 advanced medium with 2% FCS, Glutamax and 20 mM HEPES (Sigma H0887) with the following supplementation: 1 in 100 dilution of (1) brain-heart infusion (BD Difco 237500) 5× concentrated, (2) peptone/yeast (BBL Biosafe 211862) at 10% and casein amino acids at 5% (DIFCO 0320-01-1), (3) ribose/cellobiose/mannose (Sigma: R9629, C7252, M6020) at 200 mM; 1 in 1,000 dilution of (1) ferrous sulphate (Merck 3965) at 10 mM, (2) ferric ammonium citrate (LabGuard 0658) at 12.5 mM, (3) Hemin (Sigma 51280) at 1.5 mM in 50% ethanol with 1.4 N NH₄OH, (4) sodium ascorbate at 10 mg ml⁻¹ with 1-phosphoascorbate at 500 mM (Sigma: A4034, 49752); 1 in 10,000 dilution of retinoic acid (Sigma R2625) at 30 mg ml⁻¹ in DMSO; 1 in 500 dilution of (1) sperm DNA (Life Technologies 15632-011) at 10 mg ml⁻¹ digested for 1 h with 10 µl DNaseI (Roche 04716 728 001) at 37 °C and heat inactivated at 75 °C for 30 min, (2) RNA at 10 mg ml⁻¹ (Sigma R6750) undigested. SFB medium specific medium supplements, except for the nucleotides and hemin, were prepared fresh every 2 weeks and otherwise stored at 4 or -20 °C for retinoic acid and nucleotides. When mICcl2 cells were used, SFB medium was further supplemented with hEGF, dexamethasone, and triiodothyronine. Notably, additional supplementation with 0.2% yeast extract (BD 212750; 1/100 from 20%) has since further improved SFB growth and we now no longer add ascorbate, phosphoascorbate or hemin. Cells were plated either on regular 12-well tissue culture plates or on Costar transwell plates with 0.4-µm filters (Sigma CLS3460 and Fisher Scientific W2127P).

Purification of intracellular offspring from SFB-monoassociated mice and infection protocol. All liquids used for the isolation of intracellular offspring were pre-equilibrated overnight in an anaerobic chamber set to 0% oxygen. SFB-monoassociated JH^{-/-} mice were killed aseptically in a tissue culture hood and then placed in an anaerobic cabinet for dissection. The ileal, caecal, and colonic contents were resuspended in 50 ml PBS and homogenized by vortexing. Homogenates were passed through a 100-µm mesh to remove large faecal debris. The filtrate was spun at 8,000g for 5 min to pellet bacteria and insoluble material, and the pellet was resuspended in 3 ml PBS per mouse killed, layered onto 3 ml 50% and 2 ml 30% Nycodenz (AbCys 1002424) solution made with PBS in 15-ml Falcon tubes and spun for 10 min at 4,000g. SFB within the 30% fraction were collected, diluted in PBS, and bacteria were pelleted for 10 min at 8,500g. Pellets were resuspended in 15 ml pre-equilibrated PBS by pipetting/vortexing and filtered through a 5-µm filter (Sigma Z612502). The filtrate was again centrifuged for 5 min at 8,000g and the pellet was resuspended in an appropriate amount of pre-equilibrated culture medium. Usually one mouse was killed for every four 12-well plates used, and 50 µl of bacterial suspension was added to each well. To facilitate adhesion, cells challenged with SFB were sealed in ziplock bags within the cabinets, removed from the cabinet, and spun for 10 min at 300g.

SFB recovery, and quantification and analysis of SFB growth. To recover SFB, the culture supernatant was collected and centrifuged for 4 min at 8,000g and the pellet was resuspended in 100 µl PBS, of which 20 µl was spotted on glass slides for the Gram stain, 30 µl was mixed with an equal volume of 50% glycerol and frozen at -80 °C, and the remaining 50 µl was used for DNA extraction. The DNA was isolated with a Qiagen stool kit (51504; without the use of the inhibitor tablet) and diluted 1 in 20. SFB growth was enumerated by qPCR analysis of the 16S rRNA genes using the following primer pairs: the SFB specific F: 5'-AGGAGGAGTCTGCGG CACATTAGC-3'; and the universal R: 5'-TCCCCACTGCTGCCCTCCGTAG-3'. For qPCR, 6 µl of diluted SFB DNA was mixed with 1.5 µl of a 4 mM primer mix and 7.5 µl of Power SybrGreen Master mix (Applied 4368708) and run on an ABI 7900HT machine in a 384-well plate. Statistical analysis used a two-tailed Student's *t*-test (**P* < 0.05, ***P* < 0.01, ****P* < 0.001). SFB segment length analysis used ImageJ. For SEM analysis, SFB-containing supernatants were washed with PBS and suctioned onto 0.1-µm filters (Watman 110405) and fixed in 0.1 M cacodylate buffer containing 2.5% glutaraldehyde before being processed. Cells for SEM were fixed in PHEM buffer (18.14 g PIPES, 6.5 g HEPES, 3.8 g EGTA, 0.99 g MgSO₄ per litre with 10 M KOH to pH 7.0) containing 4% sucrose and 2.5% glutaraldehyde, and processed for SEM. For fluorescence, cells were fixed in PBS/3.7% PFA, permeabilized with PBS/0.1% Triton X-100, stained with DAPI and A568-phalloidin, and stacks of 0.4-µm slices were taken on a Leica SP5 confocal microscope.

Colonization of germ-free mice with *in vitro*-grown SFB. This experiment was done independently twice with similar results; one experiment is shown. SFB grown *in vitro* for 3 days on TC7 and mICcl2 cells on transwells were divided in equal parts and one half was filtered through a 5-µm filter to obtain a fraction containing intracellular offspring only. Bacteria were concentrated by centrifugation to obtain 0.25 ml of bacteria in PBS per mouse. The number of animals used followed availability of animals, isolators, and input quantities. Randomization or blinding was otherwise not performed. Two groups of four 11-week-old C57BL/6 male and female mice maintained at the germ-free facility at Institut Pasteur were starved for one night, gavaged with 0.25 ml 400 mM sodium bicarbonate, followed by 0.25 ml of *in vitro*-grown SFB. Age-matched control mice were colonized with *in vivo*-derived SFB as described below. Faecal samples were collected for each mouse at various times during a 3 week period, SFB DNA was extracted using a Qiagen stool kit and quantified on the basis of qPCR analysis of 16S rDNA and comparison with a SFB DNA sample of known SFB genome concentration as determined by Illumina sequencing. To monitor SFB associated with the ileum, DNA was extracted from frozen ileal biopsies using the method in ref. 27.

Isolation and staining of lamina propria lymphocytes from C57BL/6 mice. Age-matched germ-free C57BL/6 mice and mice colonized with either *in vitro*- or *in vivo*-grown SFB for 3 weeks were analysed for their innate and adaptive immune response as described in ref. 5. Briefly, after excision of Peyer's patches, the mouse small intestine was washed in PBS, and ileal samples were placed in RNeasy lysis buffer for RNA extraction, complementary DNA (cDNA) synthesis, and qPCR analysis using SYBR or Taqman technologies (Applied Biosystems) and a QuantStudio7 qPCR machine. Values were normalized to TfrC.

Lamina propria lymphocytes (LPL) were prepared as previously described⁵. The remaining small intestine was incubated four times in 60 ml of PBS-3 mM EDTA (Sigma) for 10 min at 37 °C, and digested in 60 ml of RPMI 1640 with 20% FCS (Gibco), 100 U ml⁻¹ collagenase (Sigma), and 175 U ml⁻¹ DNase I (Sigma) for 40 min at 37 °C. LPL were then purified on a 40–80% Percoll gradient run for 15 min at 2,000g and resuspended in DMEM-Glutamax with 8% FCS, 1 mM HEPES, 0.02 mM folic acid, 0.67 mM L-arginine, and 0.27 mM L-asparagine (all from Sigma).

Analysis of LPL for surface antigens and intracellular expression of IL-17 and IL-10 was by flow cytometry as described⁵. Briefly, LPL were stimulated for 4 h with 100 ng ml⁻¹ phorbol 12-myristate 13-acetate and 1 µg ml⁻¹ ionomycin, in the presence of Brefeldin A (10 µg ml⁻¹) (all from Sigma). Cells used for surface analysis were left unstimulated. For surface staining, LPL were labelled for 20 min at 4 °C with a cocktail of the following antibodies: FITC-anti-GL7 (clone GL7), PerCP-anti-CD8a (clone 53-6.7), APC-H7-anti CD4 (clone GK1.5), AF647-anti-B220 (clone RA3-6B2) (all from BD Pharmingen), PE-anti-IgA (Southern Biotech), and eFluor450-anti-CD45 (clone 30-F11) and PECy7-anti-CD3 (clone 145-2C11) (both from eBioscience).

For intracellular cytokine staining, cells were further fixed in 2% PFA for 20 min at room temperature (~24 °C), and washed and stained overnight at 4 °C with PE-anti-IL-17 (clone TC11-18H10) and APC-anti-IL-10 (clone JES5-16E3) (BD Pharmingen) diluted in PBS-1% FCS-0.5% saponin (Sigma). Labelled cells were analysed with a FACSCanto II and FACSDiva software (BD Biosciences). Gates were set on living cells after Aqua live/dead dye exclusion (Invitrogen).

For qPCR analysis, the median value of germ-free mice was calculated and used as the reference value of 1 for comparison of the median value of the test samples. **Colonization of germ-free mice with SFB from faeces and *E. coli*.** Germ-free male and female C3H/HeN mice were obtained from INRA (ANAXEM platform) germ-free facilities. Eight- to nine-week-old germ-free mice were gavaged with 0.5 ml of either fresh anaerobic cultures of *E. coli* MG1655 or faecal homogenate from SFB-monoassociated mice⁵. Colonization by SFB was monitored in faeces through bacterial DNA extraction and 16S rDNA amplification by qPCR using specific primer pairs for SFB. Values were normalized to Ccl25, a constitutively expressed epithelial cell marker, and compared with the median value from germ-free control mice. Germ-free and gnotobiotic mice were maintained in plastic isolators and fed *ad libitum* on a commercial diet sterilized by γ-irradiation (40 kGy). The numbers of animals used followed availability of animals, isolators, and were obtained from two independent experiments. Randomization or blinding was otherwise not performed. Gnotobiotic mice were killed on day 21 after colonization in parallel with age-matched germ-free controls. All animal procedures were performed in accordance with French legislation and EEC regulations for the care and use of laboratory animals, approved by the local ethics committee and authorized by the French Ministry of Research (license 01308.01).

Host response *in vitro* to SFB growth and MAMP stimulation. Host response to SFB and MAMPs included pooled results from four independent experiments with three technical samples. Generally a minimum of triplicate biological replicates were used and increased if trends were clear but significance not. After 3 days of *in vitro* growth of SFB on either mICcl2 or TC7 cells on transwells in SFB medium lacking hemin and sodium ascorbate, at 1–2.5% oxygen, cells were lysed and

RNA was extracted using a Nucleospin RNA kit (Macherey-Nagel). cDNA was synthesized using RNA superscript II, oligo dT, RNaseout, and dNTPs (Invitrogen), and qPCR was performed on an ABI 7900HT and QuantStudio7 (Life Technologies) qPCR machine using the protocol described in ref. 28. TaqMan assays were performed as suggested by the supplier. Values were normalized to B2M and cycle threshold (Ct, the number of cycles required for reaching mid-exponential levels) values for Reg3 γ , Tnf α , and Fabp2 were set to 41 in control cells owing to the lack of transcript detection. MAMP stimulation used the following agonists at the highest concentrations recommended by the supplier (Invivogen): Pam2CSK4 (tlrl-pm2 s-1) at 100 ng ml⁻¹, Pam3CSK4 (tlrl-pms) at 300 ng ml⁻¹, peptidoglycan of *E. coli* K12 (Tlr-ksspgn) at 10 μ g ml⁻¹, MDP (tlrl-mdp) at 10 μ g ml⁻¹, CpG (tlr-1584) at 3 μ g ml⁻¹, flagellin (tlrl-pstfla-5) at 100 ng ml⁻¹. Excess for flagellin (10 \times) was also tested and found to be similar.

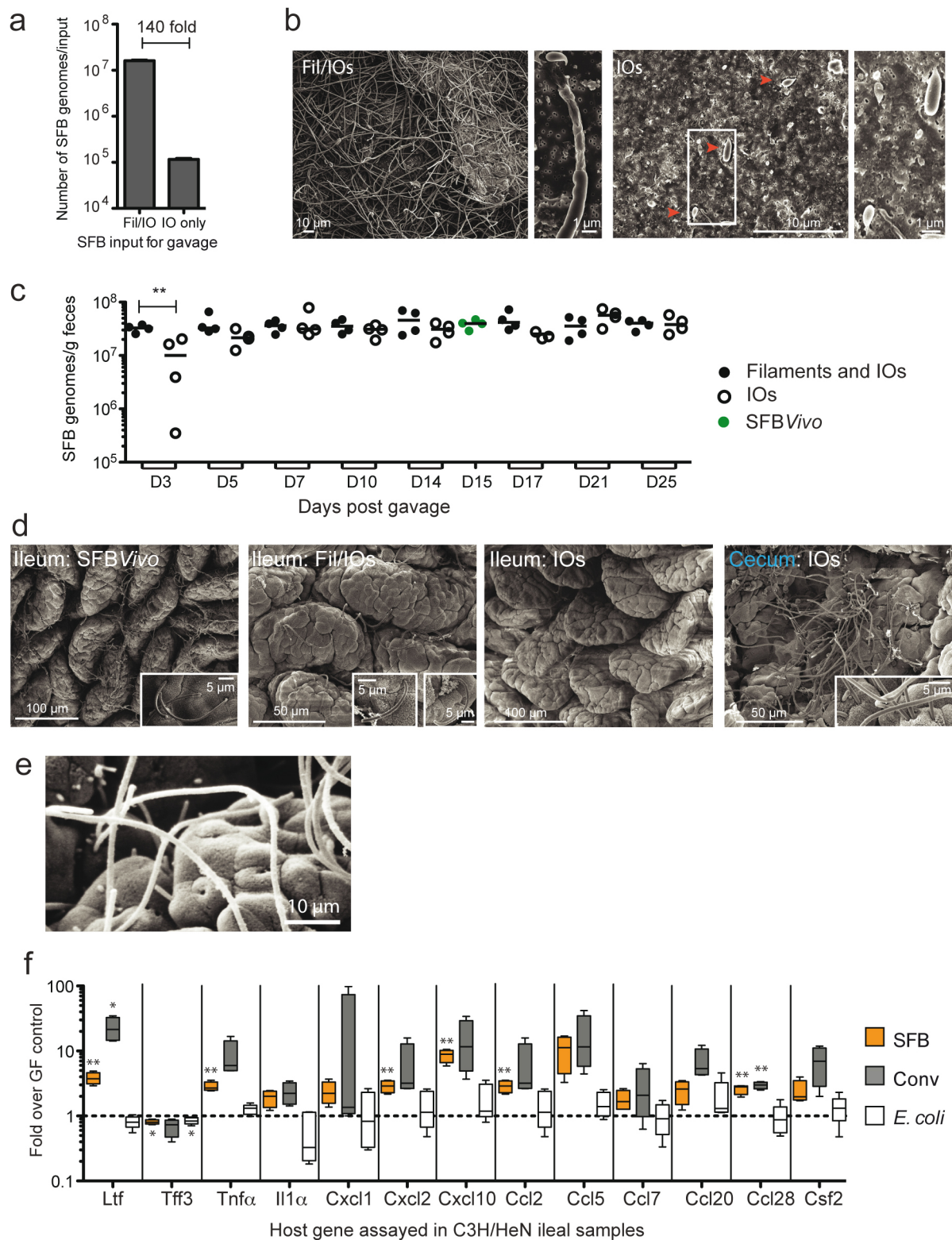
Mouse and human qPCR primers used. Mouse Taqman® assays were as follows: B2M Mm00437762_m1, TfrC Mm00441941_m1, Ccl25 Mm00436443_m1, Fabp2 Mm00433188_m1, Reg3g Mm01181783_g1, Fut2 Mm00490152_S1, Aqp3 Mm01208559_m1, Pigr Mm00465049_m1, Ltf Mm00434787_m1, Tff3 Mm00495590_m1, Tnfa Mm00443258_m1, IL1a Mm00439620_m1, IL1b Mm00434228_m1, IL6 Mm00446190_m1, IL15 Mm00434210_m1, IL18 Mm00434225_m1, Cxcl2 Mm00436450_m1, Ccl2 Mm00436450_m1, Ccl5

Mm01302428_m1, Ccl7 Mm01308393_g1, Ccl20 Mm01268754_m1, Ccl28 Mm00445039_m1, Csf2 Mm01290062_m1.

Mouse Sybr® primers were as follows: B2M (F:tcagtcgtcagcatggctcgc; R:tcgggtgggtggcgtgagtatac), iNos (F:cagctgggctgtacaaacctt; R:cattggaagtgaagcgtttcg), Saa1 (F:cattgttcacgaggctttcc; R:gttttccagttagcttcctcatgt), Saa2 (F:tgtgtatcccacaaggtttcaga; R:ttattaccctctctcctcaagca), Saa3 (F:cgcagcagcagcaggat; R:ccaggatcaagatgcaaaagatg), Cxcl1 (F:tggtctgggattcacctcaag; R:caagcctcgcgaccattct), Cxcl10 (F:gccgtcattttcgcctcat; R:gcttcctatgccctcatt).

Human Taqman® assays were as follows: B2M Hs00984230_m1, Saa1 Hs00761940_s1, Saa2 Hs01667582_m1, IL6 Hs00985639_m1, IL8 Hs99999034_m1, Ccl20 Hs01011368_m1, Reg3g Hs00417999_m1, iNos Hs01075529_m1, Cxcl10 Hs00171042_m1, Fut2 Hs00382834_m1, IL15 Hs01003716_m1, IL18 Hs01038788_m1, Ccl5 Hs00982282_m1.

27. Godon, J. J., Zumstein, E., Dabert, P., Habouzit, F. & Moletta, R. Molecular microbial diversity of an anaerobic digester as determined by small-subunit rDNA sequence analysis. *Appl. Environ. Microbiol.* **63**, 2802–2813 (1997).
28. Schnupf, P. & Sansonetti, P. J. Quantitative RT-PCR profiling of the rabbit immune response: assessment of acute *Shigella flexneri* infection. *PLoS ONE* **7**, e36446 (2012).



Extended Data Figure 1 | Intestinal colonization of *in vitro*-grown SFB and host response. **a, b**, qPCR quantification (**a**) and SEM (**b**) of *in vitro*-grown SFB used for gavage. **c**, qPCR quantification of SFB in faecal samples. **d**, SEM of SFB attachment *in vivo* at 25 days after gavage of C57BL/6 mice with SFBVivo or SFBVivo. **e**, SEM of 21-day SFB-colonized germ-free C3H/HeN mouse ileum showing vacant attachment sites. **f**, Host gene expression in the ileal lamina propria in conventional or germ-free mice colonized with either

SFB or *E. coli* for 21 days. Images and values are representatives from one of two experiments (**a–e**) or are cumulative values from two experiments performed with a total of seven germ-free, four SFB, five *E. coli*, and four conventional mice (**f**), showing box plots of 25–75% centiles with median and minimum/maximum whiskers. **c, f**, Two-tailed *t*-test statistical analysis (* $P < 0.05$, ** $P < 0.01$).

Commensal–dendritic–cell interaction specifies a unique protective skin immune signature

Shruti Naik^{1,2,†*}, Nicolas Bouladoux^{1,2,*}, Jonathan L. Linehan^{1,2}, Seong-Ji Han^{1,2}, Oliver J. Harrison^{1,2}, Christoph Wilhelm^{1,2}, Sean Conlan³, Sarah Himmelfarb^{1,2}, Allyson L. Byrd^{1,2,3}, Clayton Deming³, Mariam Quinones⁴, Jason M. Brenchley^{1,5}, Heidi H. Kong⁶, Roxanne Tussiwand⁷, Kenneth M. Murphy⁷, Miriam Merad⁸, Julia A. Segre³ & Yasmine Belkaid^{1,2}

The skin represents the primary interface between the host and the environment. This organ is also home to trillions of microorganisms that play an important role in tissue homeostasis and local immunity^{1–4}. Skin microbial communities are highly diverse and can be remodelled over time or in response to environmental challenges^{5–7}. How, in the context of this complexity, individual commensal microorganisms may differentially modulate skin immunity and the consequences of these responses for tissue physiology remains unclear. Here we show that defined commensals dominantly affect skin immunity and identify the cellular mediators involved in this specification. In particular, colonization with *Staphylococcus epidermidis* induces IL-17A⁺ CD8⁺ T cells that home to the epidermis, enhance innate barrier immunity and limit pathogen invasion. Commensal-specific T-cell responses result from the coordinated action of skin-resident dendritic cell subsets and are not associated with inflammation, revealing that tissue-resident cells are poised to sense and respond to alterations in microbial communities. This interaction may represent an evolutionary means by which the skin immune system uses fluctuating commensal signals to calibrate barrier immunity and provide heterologous protection against invasive pathogens. These findings reveal that the skin immune landscape is a highly dynamic environment that can be rapidly and specifically remodelled by encounters with defined commensals, findings that have profound implications for our understanding of tissue-specific immunity and pathologies.

We first assessed whether individual commensal species could modulate immunity in the context of pre-existing microbial communities. Despite the presence of a diverse microbiota, the skin of specific pathogen free (SPF) mice was permissive to long-term colonization with *S. epidermidis*⁵ at all skin sites analysed (Fig. 1a, b). At 2 weeks post topical association with as low as 1.3×10^6 colony-forming units (c.f.u.) per cm², levels of IL-17A- and IFN- γ -expressing T cells but not Foxp3⁺ regulatory T cells were significantly increased at several skin sites analysed (Fig. 1c, d and Extended Data Fig. 1a–d). Long-term accumulation of IL-17A-expressing T cells was not observed at sites distal to the skin and required colonization with live bacteria (Fig. 1c, d, h and Extended Data Fig. 1b). Furthermore, in contrast to responses to intradermal inoculation of *S. epidermidis*, commensal responses were not associated with inflammation (Fig. 1e–h and Extended Data Fig. 1e–h). Thus, an encounter with a new commensal can lead to a robust but non-inflammatory accumulation of effector T cells in the skin.

We next assessed the capacity of other constituents of the human (*Corynebacterium pseudodiphtheriticum*, *Propionibacterium acnes* and *Staphylococcus aureus*) and murine (*Staphylococcus xylosus*, *Staphylococcus lentus*, *Rothia nasimurium* and *S. epidermidis* 42E03) skin microbiota

to influence T-cell responses (Extended Data Fig. 2a). Six out of eight bacteria tested increased the number of skin IL-17A⁺ T cells and half of the commensals also increased the number of IFN- γ -expressing T cells (Fig. 2a and Extended Data Fig. 2a, b). Thus, the induction of cytokines, and in particular IL-17A, is a relatively conserved response of the skin to an encounter with a new commensal.

The majority of $\alpha\beta$ T cells found in murine skin are CD4⁺ T cells with few resident CD8⁺ T cells⁸ (Fig. 2b, c). Notably, *S. epidermidis* isolates were uniquely able to increase the number and frequencies of CD8⁺ T cells in the skin in both SPF and germ-free conditions and in response to an application dose as low as 1.3×10^6 c.f.u. per cm² (Fig. 2c and Extended Data Fig. 2c–h). Similarly to tissue-resident memory (TREM) cells induced by viral challenges⁹, clusters of CD8⁺ T cells preferentially localized to the basal epidermis or in close proximity to the epithelial layer and expressed CD103 and CD69 (Fig. 2c, d and Extended Data Fig. 3a, b). On the other hand, commensal-evoked CD8⁺ T cells have a distinct cytokine profile characterized by the production of either IL-17A or IFN- γ and in contrast to virally induced TREM cells that localize to the site of injury, commensal-induced CD8⁺ T cells accumulated at all skin sites analysed (Fig. 2c and Extended Data Fig. 1b). Although rarely seen at other body sites, Tc17 cells (a subset of CD8⁺ T cells) can be found in healthy non-human primate and human skin (Fig. 2e and Extended Data Fig. 3c). This discrete response provided us with the opportunity to explore the factors controlling a commensal-driven immune specification.

In germ-free mice, commensals promote T-cell responses through IL-1 (ref. 2). Consistently, mice deficient in IL-1R1 contained significantly fewer skin IL-17A⁺ CD8⁺ T cells post *S. epidermidis* association, and *in vitro* stimulation of purified *S. epidermidis*-evoked CD8⁺ T cells with IL-1 boosted IL-17A release (Fig. 2f and Extended Data Fig. 3d). CD8⁺ T-cell response peaked at 2 weeks post association, at which point the number of cells slowly contracted, although increased frequencies were maintained up to 6 months post application (Fig. 2g, h).

Dendritic cells are exquisite sensors of their environment and previous studies uncovered a functional specialization of defined dendritic cell subsets in their capacity to drive unique immune modules¹⁰. What remains unexplored is how this specialization could account for the capacity of the host to regulate defined aspects of its relationship with the microbiota. In the skin, dendritic cells could potentially be exposed to the microbiota via emission of dendrites through epithelial cells and/or to commensal products passively diffusing at invaginations such as hair follicles, which have more permissive cell adhesions¹¹. Supporting the idea that CD8⁺ T-cell accumulation post association depends on migratory dendritic cells¹², the response was largely abolished in *Ccr7*^{−/−} mice (Fig. 3a). Frequencies of skin dendritic cell subsets¹³ were not affected

¹Immunity at Barrier Sites Initiative, National Institute of Allergy and Infectious Diseases, NIH, Bethesda 20892, USA. ²Mucosal Immunology Section, Laboratory of Parasitic Diseases, National Institute of Allergy and Infectious Diseases, NIH, Bethesda, Maryland 20892, USA. ³Translational and Functional Genomics Branch, National Human Genome Research Institute, Bethesda, Maryland 20892, USA. ⁴Bioinformatics and Computational Bioscience Branch, National Institute of Allergy and Infectious Diseases, NIH Bethesda, Maryland 20892, USA. ⁵Immunopathogenesis Section, Laboratory of Molecular Microbiology, National Institute of Allergy and Infectious Diseases, NIH Bethesda, Maryland 20892, USA. ⁶Dermatology Branch, National Cancer Institute, NIH Bethesda, Maryland 20892, USA. ⁷Howard Hughes Medical Institute, Department of Pathology and Immunology, Washington University School of Medicine, St Louis, Missouri 63110, USA. ⁸Department of Oncological Sciences, Tisch Cancer Institute and Immunology Institute, Icahn School of Medicine at Mount Sinai, New York, New York 10029, USA. ⁹Present addresses: Howard Hughes Medical Institute, Laboratory of Mammalian Cell Biology and Development, The Rockefeller University, New York, New York 10065, USA.

*These authors contributed equally to this work.

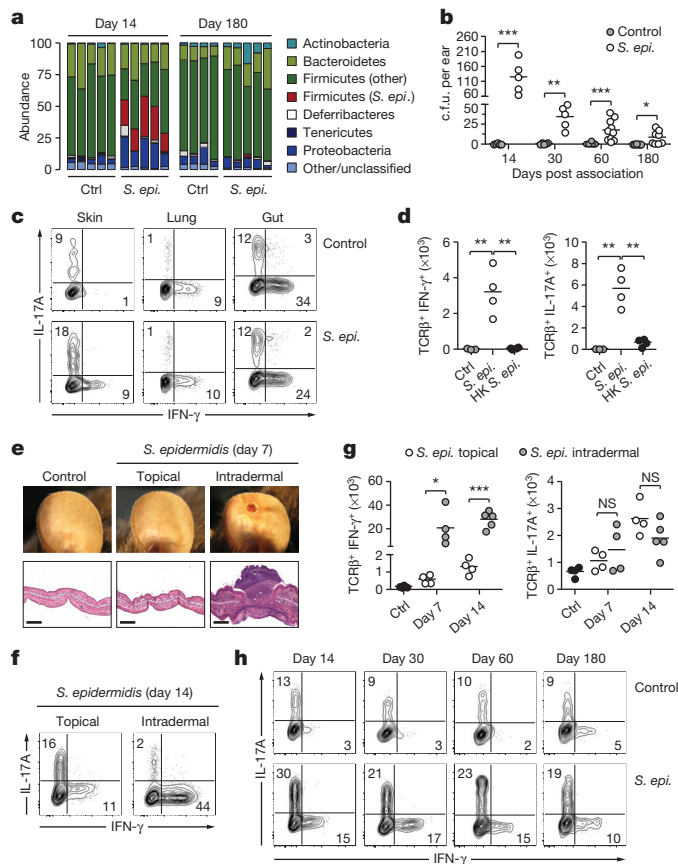


Figure 1 | Remodelling of skin immunity by commensal colonization. **a**, Relative abundance of bacterial phyla in mouse skin 14 and 180 days after *S. epidermidis* topical application. Each bar represents the percentage of sequences in operational taxonomic units (OTUs) assigned to each phylum for an individual mouse. Ctrl, control. **b**, Enumeration of colony-forming units (c.f.u.) from the ears after *S. epidermidis* application ($n = 5$ – 10 per group). **c**, IFN- γ and IL-17A production by skin, lung or gut effector (CD45 $^{+}$ TCR β^{+} Foxp3 $^{-}$) T cells in unassociated (control) and *S. epidermidis* (*S. epi.*)-associated mice at day 14. **d**, Absolute numbers of skin IFN- γ^{+} or IL-17A $^{+}$ effector T cells in unassociated mice (control, $n = 3$) and mice topically associated with live (*S. epi.*, $n = 4$) or heat-killed (HK *S. epi.*, $n = 4$) *S. epidermidis* at day 14. **e**, Representative images and histopathological comparison of the ear pinnae of unassociated (control), topically associated (topical) or intradermally inoculated (intradermal) mice at day 7. Scale bars, 250 μ m. **f**, **g**, Frequencies and absolute numbers of skin IFN- γ^{+} or IL-17A $^{+}$ effector T cells after topical application ($n = 4$) or intradermal inoculation ($n = 4$ – 5) of *S. epidermidis*. **h**, IFN- γ and IL-17A production by skin effector T cells in unassociated and *S. epidermidis*-associated mice at different time points. Results are representative of 2–3 independent experiments. * $P < 0.05$, ** $P < 0.01$, *** $P < 0.001$ as calculated by Student's *t*-test.

by *S. epidermidis* application, indicating that the induction of Tc17 cells did not result from altered dendritic cell frequencies (Extended Data Fig. 4a, b).

Mice constitutively deficient in Langerhans cells¹⁴ mounted T-cell responses to *S. epidermidis* in a manner comparable to their littermate controls (Fig. 3b and Extended Data Fig. 4c, and data not shown). Cross-presenting CD103 $^{+}$ dendritic cells¹⁵ depend on the expression of IRF8 and BATF3 for their development^{10,16} while CD11b $^{+}$ dendritic cells require CSF1 for their development and maintenance^{17,18} and IRF4 for the formation of peptide–MHC (major histocompatibility complex) class II complexes¹⁹. Making use of this differential requirement for transcription or survival factors, we assessed the relative contribution of these two dendritic cell subsets to CD8 $^{+}$ T-cell responses. The selective defect in skin-resident CD103 $^{+}$ dendritic cells (but not lymph-node-resident CD8 α^{+} dendritic cells; Extended Data Fig. 4d) in our *Batf3* $^{-/-}$ colony

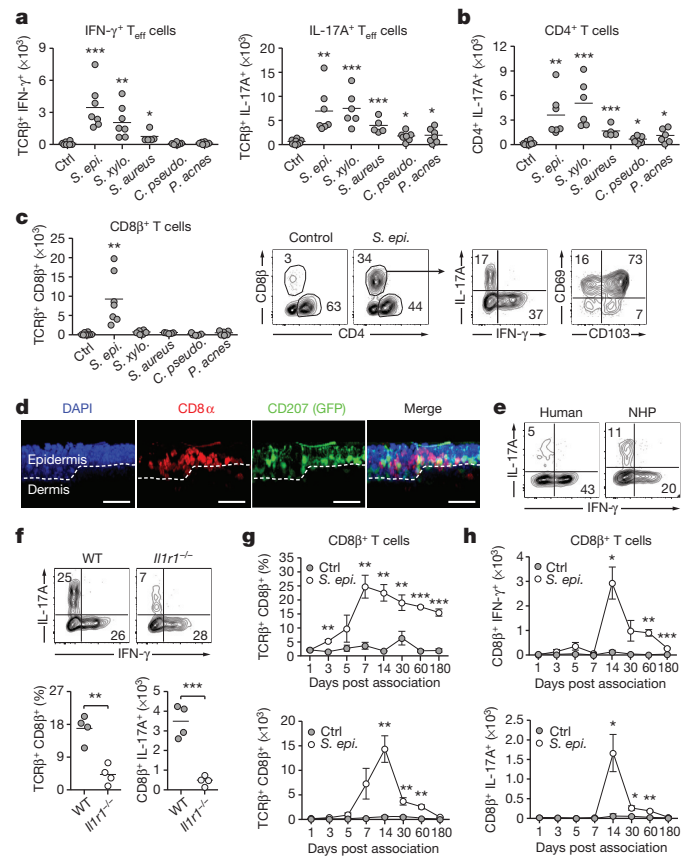


Figure 2 | Distinct commensal species impose specific immune signatures in the skin. **a**, Mice were left unassociated (Ctrl, $n = 8$) or topically associated with *S. epidermidis* ($n = 7$), *S. xylosum* ($n = 7$), *S. aureus* ($n = 5$), *C. pseudodiphtheriticum* ($n = 7$) or *P. acnes* ($n = 6$). Absolute numbers of skin IFN- γ^{+} or IL-17A $^{+}$ effector T cells are shown 2 weeks after first association. **b**, Absolute numbers of skin IL-17A $^{+}$ CD4 $^{+}$ effector T cells from mice in **a**. **c**, Absolute numbers of skin CD8 β^{+} effector T cells from mice in **a**. Flow plots show the frequencies of CD4 $^{+}$ and CD8 β^{+} effector T cells in unassociated and *S. epidermidis*-associated mice, the IFN- γ and IL-17A production, and the expression of CD69 and CD103 by CD8 β^{+} T cells in associated mice. **d**, Representative imaging volume projected along the *x* axis of ears from Langerin–GFP (green fluorescent protein) reporter mice 14 days post *S. epidermidis* application. Scale bars, 30 μ m; DAPI, 4',6'-diamidino-2-phenylindole. **e**, CD3 $^{+}$ CD8 $^{+}$ IFN- γ^{+} and CD3 $^{+}$ CD8 $^{+}$ IL-17A $^{+}$ T cells in normal human ($n = 1$) and non-human primate (NHP) skin ($n = 8$). **f**, Frequencies and absolute numbers of total CD8 β^{+} or IL-17A $^{+}$ CD8 β^{+} effector T cells in the skin of wild-type (WT, $n = 4$) and *Il1r1* $^{-/-}$ ($n = 4$) mice after *S. epidermidis* application. **g**, **h**, Frequencies and absolute numbers (mean \pm s.e.m.) of total CD8 β^{+} , IFN- γ^{+} CD8 β^{+} and IL-17A $^{+}$ CD8 β^{+} effector T cells in the skin over time following *S. epidermidis* application ($n = 3$ – 5 per time point). Results in **a**–**c** are a compilation of 2–3 experiments. Results in **d**–**h** are representative of two independent experiments. * $P < 0.05$, ** $P < 0.01$, *** $P < 0.001$ as calculated by Student's *t*-test.

allowed us to evaluate the direct contribution of these cells. *Batf3* $^{-/-}$ and *Ir8* $^{-/-}$ mice failed to develop CD8 $^{+}$ T-cell responses following colonization compared to control mice, highlighting a non-redundant role for CD103 $^{+}$ dendritic cells in the induction of CD8 $^{+}$ T-cell responses to *S. epidermidis* (Fig. 3c and Extended Data Fig. 4c, e).

Treatment of mice with an anti-CSF1R antibody led to a marked reduction in Langerhans cells and skin CD11b $^{+}$ dendritic cells, as well as in skin IL-17A $^{+}$ CD8 $^{+}$ T cells (Fig. 3d and Extended Data Fig. 4c). As the specific deletion of Langerhans cells had no consequence on T-cell responses to commensals (Fig. 3b), these results suggest that the immune effect observed was due to CD11b $^{+}$ dendritic cells. A large fraction of *S. epidermidis*-evoked CD8 $^{+}$ T cells were in close contact with CSF1R $^{+}$ CD11c $^{+}$ cells in the skin and these cells were the most transcriptionally

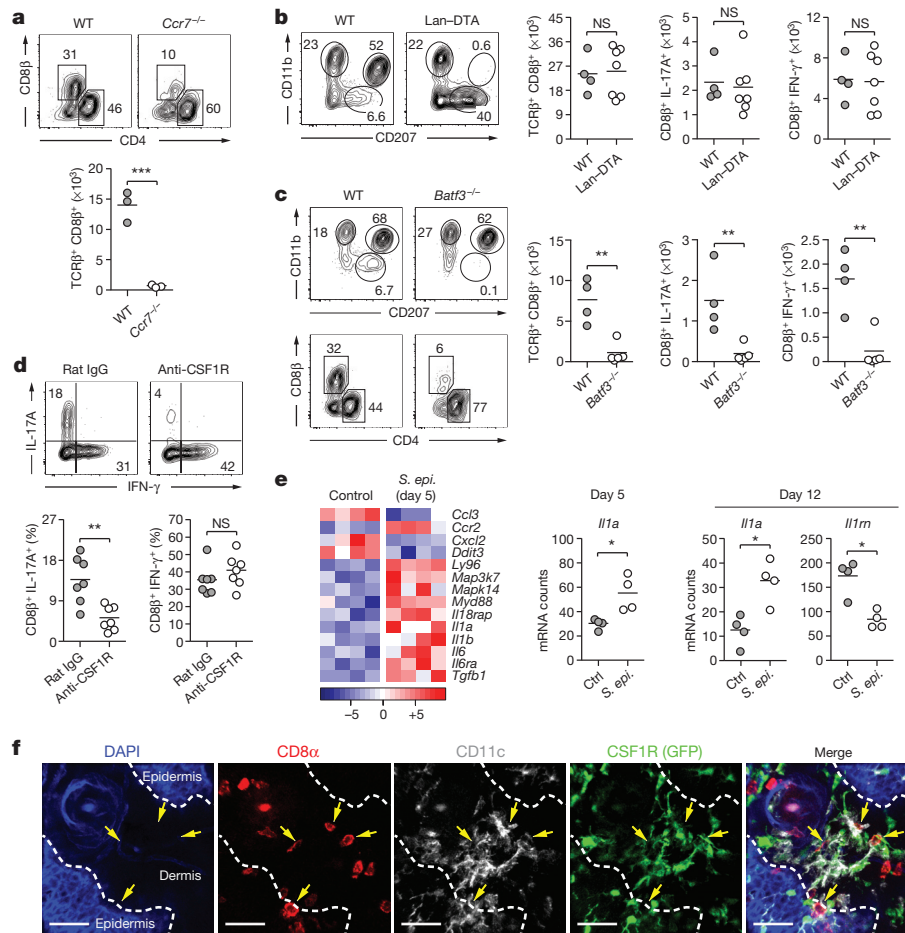


Figure 3 | Distinct dendritic cell subsets cooperate to mediate host-commensal interaction in the skin. **a**, Frequencies and absolute numbers of skin CD8β⁺ effector T cells in wild-type (WT, *n* = 3) and *Ccr7*^{-/-} (*n* = 3) mice 2 weeks post first *S. epidermidis* topical application. **b**, Phenotypic analysis of skin MHCII⁺ CD11c⁺ cells and absolute numbers of skin total CD8β⁺, IFN-γ⁺ CD8β⁺ and IL-17A⁺ CD8β⁺ effector T cells in wild-type (*n* = 4) and Langerin-diphtheria toxin subunit A (Lan-DTA, *n* = 7) mice after *S. epidermidis* application. NS, not significant. **c**, Phenotypic analysis of MHCII⁺ CD11c⁺ cells and effector T cells in the skin of wild-type (*n* = 4) and *Batf3*^{-/-} (*n* = 5) mice after *S. epidermidis* application. Graphs illustrate the absolute numbers of skin total CD8β⁺, IFN-γ⁺ CD8β⁺ and IL-17A⁺ CD8β⁺ effector T cells. Results shown in **a–c** are representative of 2–3 experiments. ***P* < 0.01, ****P* < 0.001 as calculated by Student's *t*-test. **d**, Frequencies of

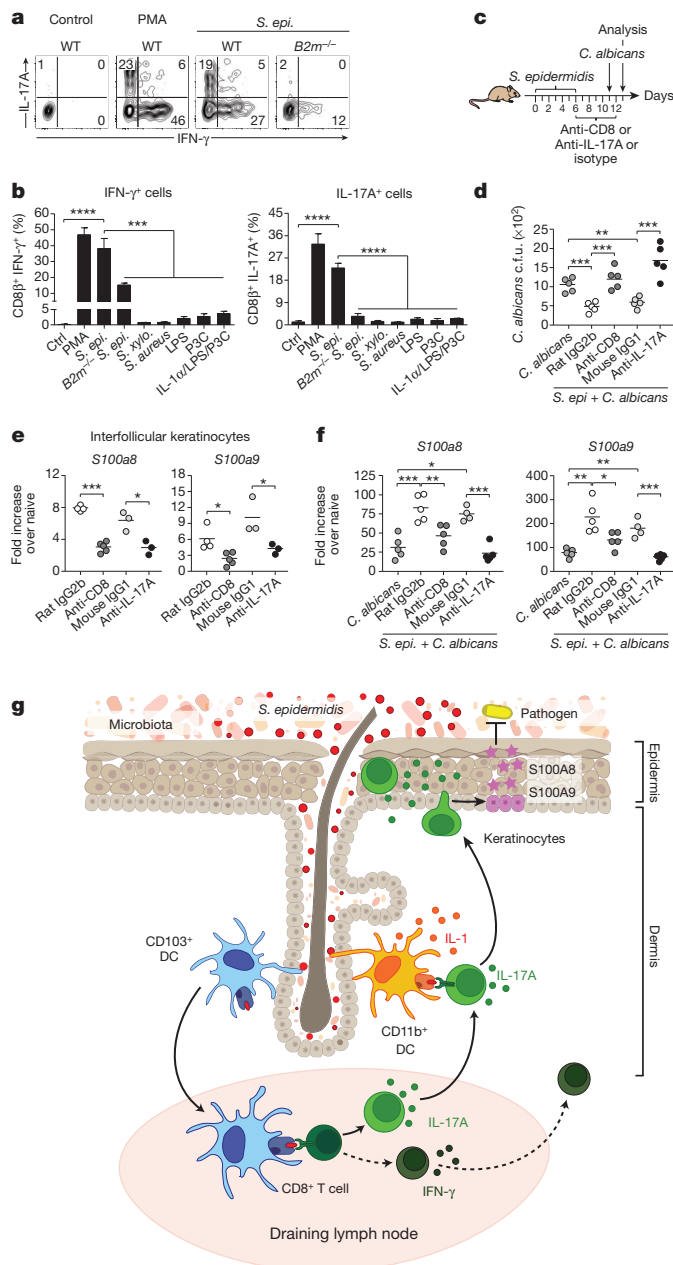
IFN-γ⁺ CD8β⁺ and IL-17A⁺ CD8β⁺ effector T cells in *S. epidermidis*-associated mice treated with anti-CSF1R (*n* = 7) or rat IgG isotype control (*n* = 7). Graphs are a compilation of the results of two independent experiments. ***P* < 0.01 by Student's *t*-test. **e**, Heat map of genes statistically differentially expressed in skin CD11b⁺ CD103⁻ dendritic cells from topically associated versus unassociated mice. Graphs summarize *Il1a* and *Il1rn* mRNA counts at day 5 and/or day 12 in CD11b⁺ CD103⁻ dendritic cells. Each column of the heat map and each dot of the graph represent gene expression from a biological replicate comprised of skin cells pooled and purified from 5 mice (*n* = 4 biological replicates, **P* < 0.05). **f**, Representative imaging volume projected along the *z* axis of ears from CSF1R GFP reporter mice 14 days post application, showing contact (arrows) between CD8α⁺ and CD11c⁺ CSF1R⁺ cells. Scale bars, 40 μm.

altered (including increases in *Il1a* and *Il1b* transcripts and a decrease in *Il1rn* transcripts) following *S. epidermidis* application (Fig. 3e, f and data not shown). Furthermore, anti-CSF1R antibody treatment significantly reduced skin IL-1 levels post association (Extended Data Fig. 4f). In mice conditionally depleted of IRF4 in their dendritic cell compartment¹⁹, CD8⁺ T cells accumulated in the skin but failed to produce IL-17A (Extended Data Fig. 4g). Together, these results support the idea that through their capacity to produce IL-1, CD11b⁺ dendritic cells could promote the induction and/or maintenance of IL-17A expression by CD8⁺ T cells. Thus, cooperation between skin-resident dendritic cells promotes and tunes responses to a defined commensal (Fig. 4g).

Of note, healthy human skin contains approximately 20 billion effector lymphocytes of unknown specificity²⁰. To address the possibility that T cells accumulating in murine skin in response to *S. epidermidis* were commensal specific, CD8⁺ T cells were purified from the skin or regional lymph nodes and exposed to dendritic cells loaded with *S. epidermidis* antigens. Exposure of *S. epidermidis*-loaded dendritic cells to CD8⁺ T cells promoted potent IL-17A and IFN-γ production (Fig. 4a, b and Extended Data Fig. 5a). In contrast, stimulation with IL-1α

or other bacterial antigens or ligands failed to induce cytokine production, and *S. epidermidis*-loaded dendritic cells did not promote cytokine release by activated T cells of irrelevant specificity (Fig. 4b and data not shown). A fraction of IFN-γ production by CD8⁺ T cells was still detectable in the absence of β2-microglobulin-dependent MHC class I presentation (Fig. 4a, b and Extended Data Fig. 5b), suggesting that some of the IFN-γ-producing CD8⁺ T cells may be responding in a bystander manner or in a β2-microglobulin-independent manner²¹. However, IL-17A was not observed following exposure to *B2m*^{-/-} dendritic cells loaded with *S. epidermidis*, demonstrating that Tc17 cells are commensal specific (Fig. 4a, b). Commensal-specific IL-17A⁺ cells were also found in the CD4⁺ T-cell compartment in both the skin and regional lymph nodes following *S. epidermidis* or *S. xyloso* application (Extended Data Fig. 5c–e). Our present results support the idea that, as in the gut^{22–24}, the majority of IL-17A-producing T cells in the skin may be commensal specific.

To assess the consequence of adaptive immune responses to commensals for skin immunity we employed a model of epicutaneous infection with the fungal pathogen *Candida albicans*. Prior association with



S. epidermidis significantly improved innate protection against *C. albicans*, an effect that was abolished by depletion of CD8⁺ T cells or neutralization of IL-17A (Fig. 4c, d). Microarray analysis of gene expression following *S. epidermidis* association revealed a significant upregulation of the alarmins S100A8 and S100A9 (data not shown), known to elicit microbicidal effects and as potent chemoattractants for neutrophils²⁵. Upregulation of these molecules was still detectable at an application dose as low as 1.3×10^6 c.f.u. per cm², and 2 weeks past the peak of CD8⁺ T-cell response in the skin (Extended Data Fig. 5f and data not shown). In keratinocytes, induction of these molecules can be mediated by IL-17A²⁶. Analysis of gene expression by interfollicular keratinocytes²⁷ from *S. epidermidis*-associated mice revealed a CD8⁺ T-cell- and IL-17A-dependent upregulation of S100A8 and S100A9 expression (Fig. 4e, f). Thus, *S. epidermidis* induces CD8⁺ T-cell responses able to promote skin innate responses in such a way that promotes heterologous protection against invasive microbes (Fig. 4g).

The skin immune system has evolved in the context of its constitutive exposure to a diverse microbiota that can be remodelled over time or in response to environmental challenges^{5–7,28}. Here we show that the skin

Figure 4 | Commensal-driven CD8⁺ T cell response is specific for *S. epidermidis* antigen. **a**, CD8⁺ effector T cells from the skin of *S. epidermidis*-associated mice were co-cultured with wild-type (WT) or B2m^{-/-} splenic dendritic cells (SpDC) untreated (Ctrl) or pre-incubated with heat-killed *S. epidermidis*, *S. xyloso* or *S. aureus*; LPS, Pam3Cys (P3C) or IL-1 α . Flow plots illustrate the frequencies of IFN- γ ⁺ CD8⁺ and IL-17A⁺ CD8⁺ T cells in overnight co-cultures. PMA, naive SpDC + PMA/ionomycin. **b**, Frequencies of IFN- γ ⁺ CD8⁺ and IL-17A⁺ CD8⁺ T cells in overnight co-cultures as described in **a** (mean \pm standard deviation of triplicate cultures). Data are representative of 2–3 independent experiments. *** P < 0.001, **** P < 0.0001 as calculated by Student's *t*-test. **c**, Unassociated or *S. epidermidis*-topically associated mice were infected with *C. albicans* and treated with anti-CD8, anti-IL-17A or corresponding isotype control antibodies. **d**, Enumeration of *C. albicans* colony-forming units from dorsal skin biopsies from mice in **c** 2 days post *C. albicans* infection. **e**, S100A8 and S100A9 gene expression (fold increase over naive unassociated) by interfollicular keratinocytes purified from the ears of mice 2 weeks after *S. epidermidis* application. **f**, S100A8 and S100A9 gene expression (fold increase over naive unassociated and uninfected) in dorsal skin biopsies from mice in **c** 2 days post *C. albicans* infection. Results in **d–f** are representative of two independent experiments. * P < 0.05, ** P < 0.01, *** P < 0.001 as calculated by Student's *t*-test. **g**, Model of the response of the skin immune system to colonization with a new commensal. Skin-resident CD103⁺ dendritic cells (DC) may acquire commensals or commensal-derived antigens by reaching into skin appendages or via capture of soluble factors. CD8⁺ T cells primed by CD103⁺ dendritic cells in the lymph node, migrate to the skin and are locally tuned by IL-1 produced by CD11b⁺ dendritic cells. Commensal-specific CD8⁺ T cells can enhance antimicrobial defence of keratinocytes in an IL-17 dependent manner. Dotted lines indicate points that are not addressed in this work.

is a highly dynamic immune environment that can be finely calibrated by defined commensals. In light of our present findings, it is intriguing to speculate that microbial diversity may also be required as a means to trigger and educate distinct aspects of the immune system. For instance, the capacity of defined commensals to promote CD8⁺ T-cell responses that can home to the epidermis may have evolved as a means to specifically reinforce the barrier function of this compartment. Here, we uncovered that tissue-resident dendritic cells are primary sensors of fluctuations in the commensal community and that these cells act in a highly coordinated manner to orchestrate the formation of commensal-specific T-cell responses. The result of this evolving interaction may represent a powerful protective mechanism of host defence by providing heterologous immunity against invasive microbes. In the context of highly perturbed communities, the cumulative cost of these responses may have severe consequences on tissue homeostasis. Indeed, commensal-specific responses are characterized by the production of IL-17A, a cytokine known to contribute to the aetiology and pathology of various skin inflammatory disorders, including psoriasis²⁹. Our work also presents a possible explanation for how variation in microbial communities at different skin sites^{5,6} may contribute to the site-specificity of dermatological disorders.

Online Content Methods, along with any additional Extended Data display items and Source Data, are available in the online version of the paper; references unique to these sections appear only in the online paper.

Received 7 March; accepted 11 November 2014.

Published online 5 January 2015.

- Grice, E. A. & Segre, J. A. The skin microbiome. *Nature Rev. Microbiol.* **9**, 244–253 (2011).
- Naik, S. *et al.* Compartmentalized control of skin immunity by resident commensals. *Science* **337**, 1115–1119 (2012).
- Chehoud, C. *et al.* Complement modulates the cutaneous microbiome and inflammatory milieu. *Proc. Natl Acad. Sci. USA* **110**, 15061–15066 (2013).
- Sanford, J. A. & Gallo, R. L. Functions of the skin microbiota in health and disease. *Semin. Immunol.* **25**, 370–377 (2013).
- Grice, E. A. *et al.* Topographical and temporal diversity of the human skin microbiome. *Science* **324**, 1190–1192 (2009).
- Costello, E. K. *et al.* Bacterial community variation in human body habitats across space and time. *Science* **326**, 1694–1697 (2009).
- Kong, H. H. *et al.* Temporal shifts in the skin microbiome associated with disease flares and treatment in children with atopic dermatitis. *Genome Res.* **22**, 850–859 (2012).

8. Belkaid, Y. *et al.* CD8⁺ T cells are required for primary immunity in C57BL/6 mice following low-dose, intradermal challenge with *Leishmania major*. *J. Immunol.* **168**, 3992–4000 (2002).
9. Mueller, S. N., Gebhardt, T., Carbone, F. R. & Heath, W. R. Memory T cell subsets, migration patterns, and tissue residence. *Annu. Rev. Immunol.* **31**, 137–161 (2013).
10. Murphy, K. M. Transcriptional control of dendritic cell development. *Adv. Immunol.* **120**, 239–267 (2013).
11. Mittal, A. *et al.* Non-invasive delivery of nanoparticles to hair follicles: a perspective for transcutaneous immunization. *Vaccine* **31**, 3442–3451 (2013).
12. Caux, C. *et al.* Regulation of dendritic cell recruitment by chemokines. *Transplantation* **73**, S7–S11 (2002).
13. Tamoutounour, S. *et al.* Origins and functional specialization of macrophages and of conventional and monocyte-derived dendritic cells in mouse skin. *Immunity* **39**, 925–938 (2013).
14. Igyártó, B. Z. *et al.* Skin-resident murine dendritic cell subsets promote distinct and opposing antigen-specific T helper cell responses. *Immunity* **35**, 260–272 (2011).
15. Bedoui, S. *et al.* Cross-presentation of viral and self antigens by skin-derived CD103⁺ dendritic cells. *Nature Immunol.* **10**, 488–495 (2009).
16. Hildner, K. *et al.* *Batf3* deficiency reveals a critical role for CD8 α ⁺ dendritic cells in cytotoxic T cell immunity. *Science* **322**, 1097–1100 (2008).
17. Merad, M., Sathe, P., Helft, J., Miller, J. & Mortha, A. The dendritic cell lineage: ontogeny and function of dendritic cells and their subsets in the steady state and the inflamed setting. *Annu. Rev. Immunol.* **31**, 563–604 (2013).
18. Hashimoto, D. *et al.* Pretransplant CSF-1 therapy expands recipient macrophages and ameliorates GVHD after allogeneic hematopoietic cell transplantation. *J. Exp. Med.* **208**, 1069–1082 (2011).
19. Vander Lugt, B. *et al.* Transcriptional programming of dendritic cells for enhanced MHC class II antigen presentation. *Nature Immunol.* **15**, 161–167 (2014).
20. Clark, R. A. *et al.* The vast majority of CLA⁺ T cells are resident in normal skin. *J. Immunol.* **176**, 4431–4439 (2006).
21. Lehmann-Grube, F., Dralle, H., Utermohlen, O. & Lohler, J. MHC class I molecule-restricted presentation of viral antigen in beta 2-microglobulin-deficient mice. *J. Immunol.* **153**, 595–603 (1994).
22. Yang, Y. *et al.* Focused specificity of intestinal T_H17 cells towards commensal bacterial antigens. *Nature* **510**, 152–156 (2014).
23. Goto, Y. *et al.* Segmented filamentous bacteria antigens presented by intestinal dendritic cells drive mucosal Th17 cell differentiation. *Immunity* **40**, 594–607 (2014).
24. Lécuyer, E. *et al.* Segmented filamentous bacterium uses secondary and tertiary lymphoid tissues to induce gut IgA and specific T helper 17 cell responses. *Immunity* **40**, 608–620 (2014).
25. Gebhardt, C., Nemeth, J., Angel, P. & Hess, J. S100A8 and S100A9 in inflammation and cancer. *Biochem. Pharmacol.* **72**, 1622–1631 (2006).
26. Mose, M., Kang, Z., Raaby, L., Iversen, L. & Johansen, C. TNF α - and IL-17A-mediated S100A8 expression is regulated by p38 MAPK. *Exp. Dermatol.* **22**, 476–481 (2013).
27. Nowak, J. A. & Fuchs, E. Isolation and culture of epithelial stem cells. *Methods Mol. Biol.* **482**, 215–232 (2009).
28. Oh, J., Conlan, S., Polley, E. C., Segre, J. A. & Kong, H. H. Shifts in human skin and nares microbiota of healthy children and adults. *Genome med.* **4**, 77 (2012).
29. Martin, D. A. *et al.* The emerging role of IL-17 in the pathogenesis of psoriasis: preclinical and clinical findings. *J. Invest. Dermatol.* **133**, 17–26 (2013).

Acknowledgements This work was supported by the Division of Intramural Research of the National Institute of Allergy and Infectious Diseases (NIAID) and by the Human Frontier Science Program (C.W.). We thank the NIAID animal facility staff, in particular A. Gozalo (isolation of *S. xylosum*); D. Trageser-Cesler and C. Acevedo (NIAID gnotobiotic facility); K. Holmes, C. Eigsti and E. Stregovsky (NIAID sorting facility); K. Frank and F. Stock (MALDI-TOF analysis); B. Malissen (Langerin-GFP reporter mice); H. C. Morse (*Irf8*^{-/-} mice); D. Kaplan (Langerin-DTA mice); R. Bosselut (*B2m*^{-/-} mice); S. B. Hopping (collection of human skin tissue samples); J. Oh, K. Loré, and the Brenchley laboratory (technical advice and reagents); and K. Becht and L. Martins dos Santos for technical assistance. We also thank the Belkaid laboratory for critical reading of the manuscript.

Author Contributions S.N., N.B., and Y.B. designed the studies. S.N. and N.B. performed the experiments and analysed the data. J.L.L. assisted with *in vitro* co-culture studies and S.-J.H. with innate cell analysis and imaging. O.J.H. and C.W. provided technical assistance. S.C. and C.D. provided technical advice and performed 454 pyrosequencing. S.C. and M.Q. analysed 454 pyrosequencing data. S.H. assisted in processing of human and non-human primate skin tissue samples. A.L.B. performed NanoString data analysis. J.M.B. and H.H.K. provided technical advice and skin tissue samples from non-human primates and human patients, respectively. R.T., K.M.M. and M.M. assisted with design of dendritic cell depletion strategies. J.A.S. helped to design sequencing studies and provided guidance on bacterial isolates. S.N., N.B. and Y.B. wrote the manuscript.

Author Information 454 sequencing data are deposited in the Sequence Read Archive under accession number SRP039428. Reprints and permissions information is available at www.nature.com/reprints. The authors declare no competing financial interests. Readers are welcome to comment on the online version of the paper. Correspondence and requests for materials should be addressed to Y.B. (ybelkaid@niaid.nih.gov).

METHODS

Mice. C57BL/6 and BALB/c specific pathogen free (SPF) mice were purchased from Taconic Farms. Germ-free C57BL/6 mice were bred at Taconic Farms and maintained in the NIAID gnotobiotic facility. B6.SJL, C57BL/6-[KO]IL1r1 (*Il1r1*^{-/-}) and C57BL/6J-[KO]B2m-[KO]Abb (*Abb*^{-/-} B2m^{-/-}) mice were obtained through the NIAID-Taconic exchange program. C57BL/6-Tg(Csflr-EGFP-NGFR/FKBP1A/TNFRSF6)2Bck/J (CSF1R GFP reporter)³⁰, B6.129P2(C)-*Ccr7*^{tm1Rfor}/J (*Ccr7*^{-/-}), B6.129P2(C)-*Batf3*^{tm1Kmm}/J (*Batf3*^{-/-}) mice and their C57BL/6 wild-type controls were purchased from The Jackson Laboratory. B6(Cg)-*Irf8*^{tm1.2Hm}/J (*Irf8*^{-/-}), B6.FVB-Tg(CD207-Dta)312Dhka/J (Lan-DTA), B6.129S2-*Cd207*^{tm3(DTR/GFP)Mal}/J (Lan-GFP) mice were obtained from H. C. Morse (National Institute of Allergy and Infectious Diseases, NIH), D. Kaplan (University of Minnesota) and B. Malissen (Centre d'immunologie de Marseille Luminy, France), respectively. Congenic B2m^{-/-} (B6.129-B2m^{tm1Jae} N12 x B6-LY5.2/Cr) mice were provided by R. Bosselut (National Cancer Institute, NIH). *Irf4*^{fl/fl} × *Cd11c*^{cre} mice were obtained by breeding B6.129S1-*Irf4*^{tm1Rdf}/J (*Irf4*^{fl/fl}) mice with B6.Cg-Tg(Igax-Cre)1-1Reiz/J (Igax-Cre) mice (both strains from The Jackson Laboratory). All mice were bred and maintained under pathogen-free conditions at an American Association for the Accreditation of Laboratory Animal Care (AAALAC)-accredited animal facility at the NIAID and housed in accordance with the procedures outlined in the Guide for the Care and Use of Laboratory Animals. All experiments were performed at the NIAID under an animal study proposal approved by the NIAID Animal Care and Use Committee. Gender- and age-matched mice between 6 and 12 weeks of age were used for each experiment. When possible, preliminary experiments were performed to determine requirements for sample size, taking into account resources available and ethical, reductionist animal use. In general, each mouse of the different experimental groups is reported. Exclusion criteria such as inadequate staining or low cell yield due to technical problems were pre-determined. Animals were assigned randomly to experimental groups.

Human and non-human primate skin tissue. Healthy human skin samples from anonymous patients were obtained as discarded material after cosmetic surgery according to a protocol approved by the Institutional Review Board of NIAID, NIH. All subjects gave informed consent. Non-human primate skin tissue was obtained from the glabella of eight healthy rhesus (*Macaca mulatta*) or pigtail (*Macaca nemestrina*) macaques immediately post euthanasia. All monkeys were housed and cared in accordance with AAALAC standards in AAALAC-accredited facilities, and all animal procedures performed according to protocols approved by the NIAID Animal Care and Use Committee.

Topical association and intradermal infection. *S. epidermidis* strain 42E03³¹ and *R. nasimurium* were isolated from mouse colonies. *S. epidermidis* strain NIHL087³², *S. epidermidis* strain 42E03, *S. lentus*, *S. xylosum* (isolated from mice as previously described³³), *S. aureus* strain NCTC 8325, *C. pseudodiphtheriticum* strain NIHL086⁵ and *R. nasimurium* were cultured for 18 h in tryptic soy broth at 37 °C. *P. acnes* ATCC 11827 was cultured for up to 72 h in tryptic soy broth in an anaerobic chamber. Bacteria were enumerated before topical application by assessing colony-forming units using traditional bacteriology techniques and by measuring optical density (OD) at 600 nm using a spectrophotometer.

For topical association of bacteria, each mouse was associated with bacteria by applying bacterial suspension (approximately 10⁹ ml⁻¹, 5 ml or for Extended Data Figs 1c, d, 2d and 5f, 10⁸ or 10⁷ c.f.u. per ml as indicated) across the entire skin surface (approximately 36 cm²) using a sterile cotton swab. Application of bacterial suspension was repeated every other day a total of four times. In experiments involving topical application of various bacterial species or strains, 18-h cultures were normalized using OD₆₀₀ to achieve similar bacterial density (approximately 10⁹ c.f.u. per ml). In some experiments, mice were infected intradermally in the ear pinnae with 10⁷ c.f.u. of *S. epidermidis* strain LM087. Mice were euthanized at different time points after the first topical association or intradermal inoculation with bacteria.

Tissue processing. *Murine tissues.* Cells from the lung, the small intestine lamina propria, the skin draining lymph nodes, the ear pinnae or flank tissue were isolated as previously described^{23,34}. Isolation of cells from epidermal and dermal compartments of the ear skin tissue were performed as previously reported³⁵.

Human and non-human primate skin. Subcutaneous fat tissue was scrapped off with a number 10 scalpel. Skin tissue was then weighted and perfused with 100–500 µl of digestion media (RPMI 1640 media supplemented with 2 mM L-glutamine, 1 mM sodium pyruvate and nonessential amino acids, 20 mM HEPES, 100 U ml⁻¹ penicillin, 100 µg ml⁻¹ streptomycin and 0.25 mg ml⁻¹ Liberase Cl purified enzyme blend (Roche)). Perfused skin tissue was placed in 5 ml of digestion media dermal side down and incubated for 1 h at 4 °C. Tissue was then minced with scissors in 5 ml of fresh digestion media and incubated at 37 °C with shaking. After 1 h, digestion was stopped by adding 100 µl of 0.5 M EDTA and 1 ml of fetal bovine serum. Digested tissue was then smashed on a 70 µm cell strainer to obtain a single-cell suspension.

Immunofluorescence/confocal microscopy. Ear pinnae were split, fixed in 1% paraformaldehyde solution (Electron Microscopy Sciences) overnight at 4 °C and

blocked in 1% BSA 0.25% Triton X blocking buffer for 2 h at room temperature. Tissues were first stained with anti-CD8α (clone 53-6.7, eBioscience), anti-CD11c (clone N418, eBioscience) and/or rabbit anti-GFP (Life Technologies) antibodies overnight at 4 °C, washed three times with PBS and then stained with 4',6'-diamidino-2-phenylindole (DAPI, Sigma-Aldrich) for 5 min at room temperature and before being mounted with ProLong Gold (Life Technologies) anti-fade reagent. Images were captured on a Leica TCS SP8 confocal microscope with a 40× oil objective (HC PL APO 40×/1.3 oil). Images were analysed using Imaris Bitplane software.

In vivo antibody administration. Mice were treated intraperitoneally (i.p.) with anti-CSF1R antibody (clone AFS98, BioXCell) or Rat IgG2a isotype control antibody (clone 2A3, BioXCell). Treatment schedule was as follows: 2 mg of either antibody was injected i.p. in each mouse 5 and 3 days before the first *S. epidermidis* topical application (days -5 and -3); each mouse then received 0.5 mg of either antibodies on days -2, -1 and days 0, 2, 4, 6, 9, 11 and 13 post topical application¹⁸. Mice were analysed two weeks after the first *S. epidermidis* topical application (or 19 days after the first antibody injection).

For CD8⁺ T-cell depletion, mice were treated i.p. with 0.5 mg of anti-CD8 antibody (clone 2.43) or rat IgG2b isotype control antibody (clone LTF-2, BioXCell) every 2–3 days starting at day 6 after the first topical application of *S. epidermidis*. For IL-17A neutralization, mice were treated i.p. with 0.5 mg of anti-IL-17A antibody (clone 17F3, BioXCell) or mouse IgG1 isotype control antibody (clone MOPC-21, BioXCell) every 2 days starting at day 6 after the first topical application of *S. epidermidis*.

In vitro re-stimulation. For detection of basal cytokine potential, single-cell suspensions from various tissues were cultured directly *ex vivo* in a 96-well U-bottom plate in complete medium (RPMI 1640 supplemented with 10% fetal bovine serum (FBS), 2 mM L-glutamine, 1 mM sodium pyruvate and nonessential amino acids, 20 mM HEPES, 100 U ml⁻¹ penicillin, 100 µg ml⁻¹ streptomycin, 50 mM β-mercaptoethanol) and stimulated with 50 ng ml⁻¹ phorbol myristate acetate (PMA) (Sigma-Aldrich) and 5 µg ml⁻¹ (mouse) or 1 µg ml⁻¹ (human and monkey) ionomycin (Sigma-Aldrich) in the presence of brefeldin A (GolgiPlug, BD Biosciences) for 2.5 h at 37 °C in 5% CO₂. After stimulation, cells were assessed for intracellular cytokine production as described below.

Phenotypic analysis. Murine single-cell suspensions were incubated with fluorochrome-conjugated antibodies against surface markers CD3 (145-2C11), CD4 (clone RM4-5), CD8α (53-6.7), CD8β (eBioH35-17.2), CD11b (M1/70), CD11c (N418 or HL3), CD19 (6D5), CD45.2 (104), CD45R (RA3-6B2), CD49b (DX5), CD69 (H1.2F3), CD103 (2E7), DEC205 (NLDC-145), KLRG1 (2F1), MHCII (M5/114.15.2) and/or TCRβ (H57-597) in Hank's buffered salt solution (HBSS) for 20 min at 4 °C and then washed. LIVE/DEAD Fixable Blue Dead Cell Stain Kit (Invitrogen Life Technologies) was used to exclude dead cells. Cells were then fixed for 15 min at 4 °C using 2% paraformaldehyde solution (Electron Microscopy Sciences) and washed twice. For simultaneous Foxp3 and intracellular cytokine staining, cells were stained with fluorochrome-conjugated antibodies against Foxp3 (FJK-16 s), IFN-γ (XMG-1.2) and IL-17A (eBio17B7) in HBSS containing 0.5% saponin (Sigma-Aldrich) for 45 min at 4 °C. For detection of Langerin, cells were incubated with a fluorochrome-conjugated antibody against CD207 (929F3.01) in permeabilization buffer supplied with the BD Cytofix/Cytoperm kit (BD Biosciences) for 1 h at 4 °C. Each staining was performed in the presence of purified anti-mouse CD16/32 (93), 0.2 mg ml⁻¹ purified rat IgG and 1 mg ml⁻¹ of normal mouse serum (Jackson Immunoresearch). Staining of cells from human or non-human primate skin tissue was performed using a similar protocol and the following antibodies against human proteins: anti-CD3 (SP34-2), anti-CD4 (L200), anti-CD8α (RPA-T8), anti-IFN-γ (4S.B3) and anti-IL-17A (eBio64DEC17). All antibodies were purchased from eBioscience, BD Biosciences, Miltenyi Biotec or Dendritics. Cell acquisition was performed on an LSRII flow cytometer using FACSDiVa software (BD Biosciences) and data were analysed using FlowJo software (TreeStar).

Analysis of skin microbiota after topical association. *DNA extraction from skin and 454 pyrosequencing.* Mouse ear skin samples were sterilely obtained and processed using a protocol adapted from ref. 31. For 16S rRNA amplicon sequencing, the DNA from each sample was amplified using Accuprime High Fidelity Taq polymerase (Invitrogen Life Technologies) with universal primers flanking variable regions V1 (primer 27 F; 5'-AGAGTTTGTATCTGGCTCAG-3') and V3 (primer 534 R; 5'-ATTACCGCGGCTGCTGG-3'). For each sample, the universal primers were tagged with unique sequences ('barcodes') to allow for multiplexing/demultiplexing³⁶. PCR products were then purified using the Agencourt Ampure XP kit (Beckman Coulter Genomics) and quantitated using the QuantIT dsDNA High-Sensitivity Assay kit (Invitrogen Life Technologies). Approximately equivalent amounts of each PCR product were then pooled and purified on a column from the MinElute PCR Purification Kit (Qiagen) into 30 µl TE buffer before sequencing at the NIH Intramural Sequencing Center on a 454 GS FLX (Roche) instrument using titanium chemistry. Sequencing data were analysed as previously described².

Bacteria quantitation. The ear skin of topically associated or unassociated control mice was swabbed with a sterile cotton swab previously soaked in tryptic soy broth. Swabs were streaked on either tryptic soy agar or blood agar plates. Plates were then placed at 37 °C under aerobic or anaerobic conditions for 18 h. Colony-forming units on each plate were enumerated and the identity of the isolates was confirmed by matrix-assisted laser desorption/ionization time of flight (MALDI-TOF) mass spectrometry.

Purification of skin dendritic cell subsets. Dendritic cell subsets were purified from the epidermis and dermis compartment of the ear skin tissue of unassociated mice and *S. epidermidis*-associated mice at days 5 and 12 post topical application. In brief, cell suspensions obtained from the dermis compartment were incubated with a mixture of antibodies containing anti-CD16/32 (93), anti-CD11b (M1/70), anti-CD11c (N418), anti-CD45.2 (104), anti-CD103 (2E7), anti-MHCII (M5/114.15.2) in the presence of DAPI (Sigma-Aldrich). Cells from the epidermis compartment were incubated with anti-CD16/32, anti-CD45.2, anti-MHCII and DAPI. The following two subsets of dendritic cells were sorted from the dermis by flow cytometry on a FACSria (BD Biosciences): CD45.2⁺ CD11c⁺ MHCII⁺ CD11b⁺ CD103⁺ cells (CD103⁺ dendritic cells) and CD45.2⁺ CD11c⁺ MHCII⁺ CD11b⁺ CD103⁺ cells (CD11b⁺ dendritic cells). Langerhans cells were sorted from the epidermis as CD45.2⁺ MHCII⁺ cells.

Gene expression analysis by NanoString. The nCounter analysis system (NanoString Technologies) was used to screen for the expression of signature genes associated with inflammation pathway in the different dendritic cell subsets⁵⁷. Two specific probes (capture and reporter) for each gene of interest were employed. In brief, RNA from each dendritic cell subset was obtained by lysing the sorted cells (10⁵ cells per µl) in RLT buffer (Qiagen) and then hybridized with the customized Reporter CodeSet and Capture ProbeSet of the Mouse Inflammation Panel including 150 selected genes (NanoString Technologies), according to the manufacturer's instructions. Messenger RNA molecules were counted on a NanoString nCounter, as previously described⁵. Data analysis was performed according to NanoString Technologies recommendations. mRNA counts were processed to account for hybridization efficiency, background noise and sample content using the R package NanoStringNorm with arguments: CodeCount = 'geo.mean', Background = 'mean.2sd', SampleContent = 'housekeeping.geo.mean'. Each sample profile was normalized to geometric mean of two housekeeping genes, *Ctct* and *Pgk1*. Post normalization, genes with mean counts less than 20 were disregarded and differential expression of remaining genes was determined using a nonparametric Welch *t*-test with correction for multiple testing using the Benjamini–Hochberg false discovery rate (FDR) controlling procedure in the *multtest* package in R. Based on genes with a FDR < 0.05, a heat map was rendered using the R package *gplots*.

Dendritic cell and T-cell co-culture assay. CD45⁺ CD90.2⁺ CD8β⁺ or CD45⁺ CD90.2⁺ CD4⁺ effector T cells (>95% purity) were sorted by flow cytometry from the ear skin tissue of C57BL/6 mice 2 weeks after topical association with *S. epidermidis* strain LM087 or *S. xyloso* using a FACSria cell sorter. For CD8β⁺ and CD4⁺ T-cell purification from the skin draining lymph nodes, single-cell suspension from the ear skin tissue of mice topically associated with *S. epidermidis* strain LM087 or *S. xyloso* were first magnetically enriched for CCR6⁺ cells by positive selection using PE-conjugated CCR6 antibody (clone 29-2L17), anti-PE MicroBeads and MACS separation columns (Miltenyi Biotec). The enriched fraction was further labelled with fluorochrome-conjugated antibodies against CD45, CD90.2, CD4 and/or CD8β and CD45⁺ CD90.2⁺ CD8β⁺ or CD45⁺ CD90.2⁺ CD4⁺ were sorted (>95% purity) by flow cytometry on a FACSria cell sorter. For splenic dendritic cell (SpDC) purification, single-cell suspensions from the spleen of congenic wild-type, *B2m*^{−/−} or *Abb*^{−/−} *B2m*^{−/−} mice were magnetically enriched for CD11c⁺ cells by positive selection using CD11c MicroBeads and MACS separation columns (Miltenyi Biotec). Purified SpDCs and CD8β⁺ or CD4⁺ T cells were co-cultured at a 15:1 ratio (5 × 10³ CD8β⁺ T cells) in a 96-well U-bottom plate in complete medium for 16 h at 37 °C in 5% CO₂. Brefeldin A (GolgiPlug) was added for the final 4 h of culture. SpDC were previously incubated for 3 h with or without heat-killed *S. epidermis*, heat-killed *S. xyloso* or heat-killed *S. aureus* (bacteria:SpDC ratio, 500:1) and washed before co-culture with CD8β⁺ T cells. In some experiments, co-cultures of CD8β⁺ T cells and naive SpDC were supplemented with 5 µg ml^{−1} ultra-pure lipopolysaccharide (LPS, InvivoGen), 100 nM *N*-α-palmitoyl-S-[2,3-bis(palmitoyloxy-(2R)-propyl)-L-cysteine (Pam3Cys, InvivoGen) and/or 10 ng ml^{−1} murine IL-1α (Peprotech). CD8β⁺ T cell cytokine production following co-culture was assessed by flow cytometry after intracellular cytokine staining using the following antibodies: anti-CD4, anti-CD8β, anti-CD45.1 (clone A20), anti-CD45.2, anti-TCRβ, anti-IFN-γ and anti-IL-17A.

Cytokine measurement. Leukocytes isolated from the skin of *S. epidermidis*-associated mice were cultured in 100 µl of complete medium for 3 h at 37 °C in 5% CO₂. FACS-purified CD8β⁺ T cells from the skin of *S. epidermidis*-associated mice were cultured overnight at 37 °C in 5% CO₂ in 30 µl of complete culture medium in a 96-well U-bottom plate coated with anti-CD3ε (1 µg ml^{−1}, clone 145-2C11, BD Biosciences) in the presence or absence of IL-1α and IL-1β (10 ng ml^{−1} each, Peprotech). Supernatants were collected and levels of inflammatory cytokines were assessed using a bead-based cytokine detection assay (FlowCytomix, eBioscience). Cytokine concentrations were adjusted to the plated density of 2 × 10⁴ cells in 100 or 30 µl culture volume.

Purification of keratinocytes. Interfollicular keratinocytes were purified by cell sorting from the ear skin tissue of unassociated mice and *S. epidermidis*-associated mice at 14 days post topical application. In brief, cell suspensions obtained from ear skin tissue were incubated with the following antibodies: anti-CD16/32 (93), anti-CD45 (30-F11), anti-CD49f (eBioGoH3), anti-CD117 (2B8), anti-CD140a (APA5) and anti-Sca-1 (D7) in the presence of DAPI. Interfollicular keratinocytes were sorted by flow cytometry on a FACSria (BD Biosciences) as CD45[−] CD117[−] CD140a[−] CD49f⁺ Sca-1⁺ cells.

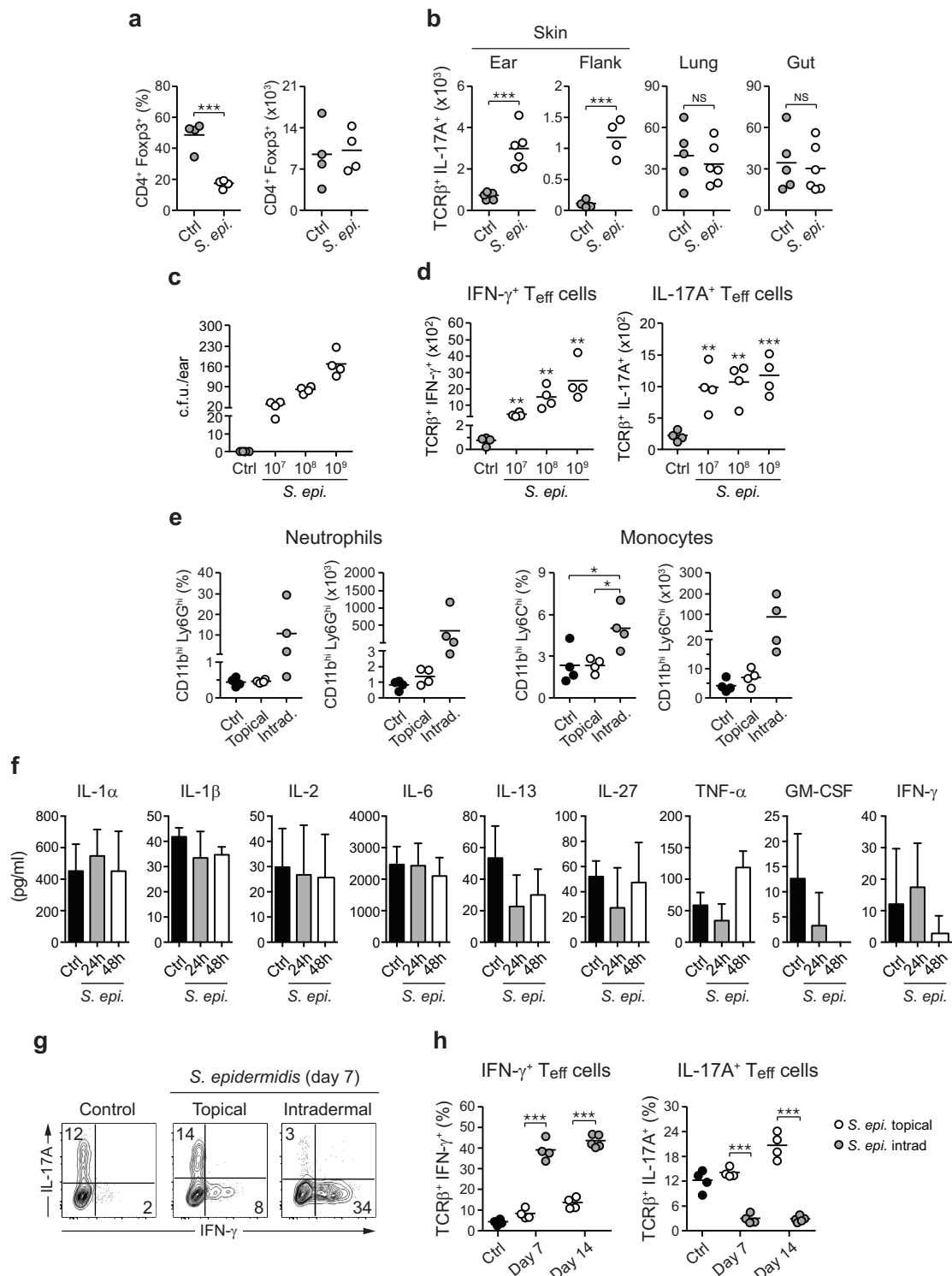
Candida albicans infection. Eleven days after the first topical application of *S. epidermidis*, mice were infected with *C. albicans* along the dorsal midline as previously described³⁸. In brief, *C. albicans* was grown in YPAD medium at 30 °C for 18 h and re-suspended at 10⁷ *C. albicans* yeast per 1 ml of sterile PBS. One hundred microlitres of this suspension was applied to sandpaper (100 grit)-treated dorsal skin to achieve an infectious dose of 10⁶ *C. albicans*. At 2 days post infection a 6 mm punch biopsy of skin was homogenized in sterile PBS containing penicillin and streptomycin before plating on YPAD plates. Colony-forming units were counted after culture at 30 °C for 48 h.

RNA purification and quantitative PCR. Total RNA was isolated from purified keratinocytes or skin tissue biopsies using the RNeasy Mini Kit (QIAGEN). Complementary DNA was prepared using the Omniscript Reverse Transcription Kit (QIAGEN) according to the manufacturer's instructions. Quantitative real-time PCR was performed on a Bio-Rad iCycler using the iQ SYBR Green Supermix (BioRad) and predesigned Quantitect primers (QIAGEN) specific for the following genes: *Hprt*, *S100a8* and *S100a9*.

Histology. Mice were euthanized 7 days after topical application or intraperitoneal injection of *S. epidermidis* LM087 in the ear. Unassociated mice were used as controls. The ears from each mouse were removed and fixed in PBS containing 10% formalin. Paraffin-embedded sections were cut at 0.5 mm, stained with haematoxylin and eosin and examined histologically.

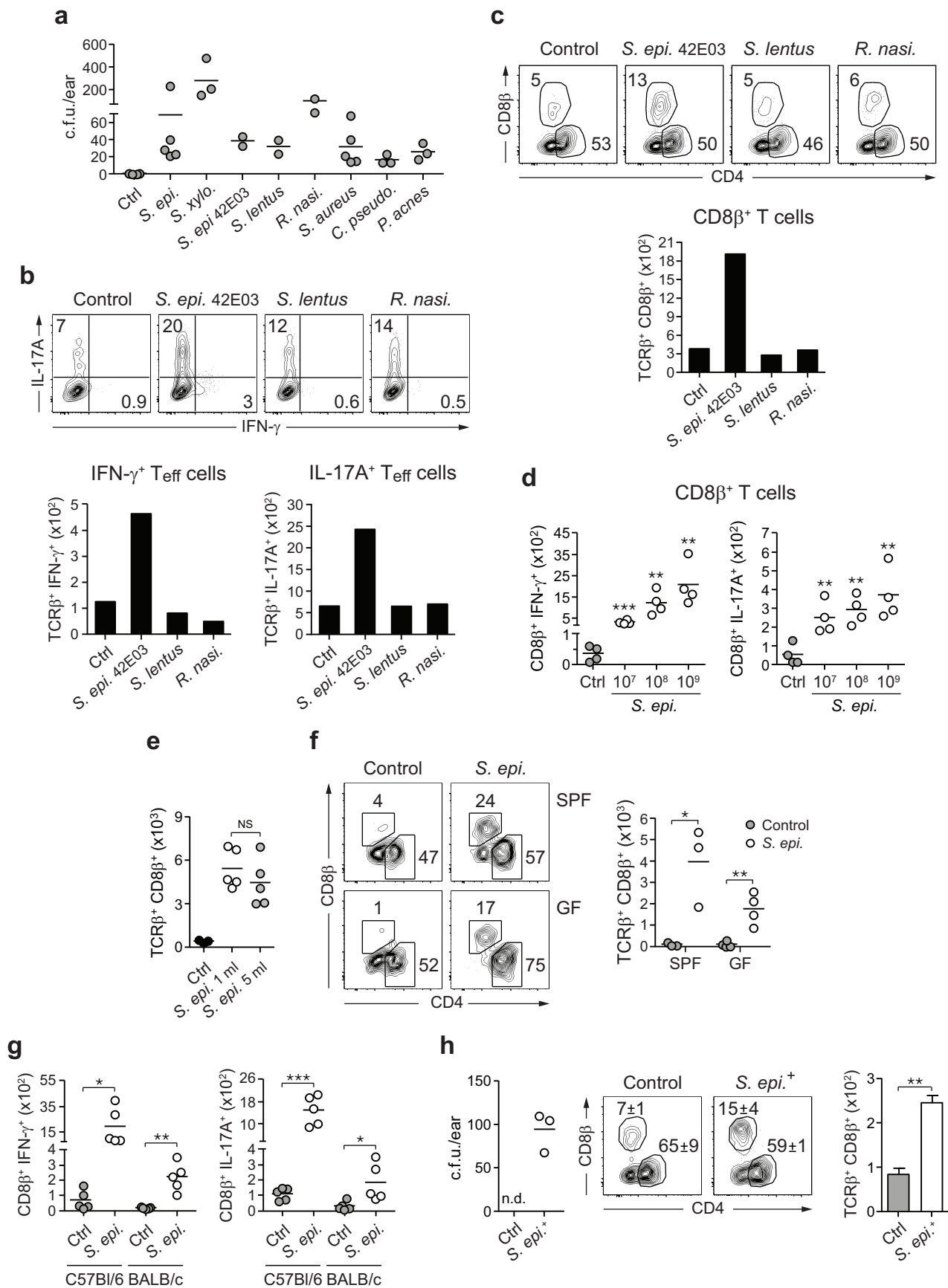
Statistics. Data are presented as mean ± standard error of the mean or mean ± standard deviation. Group sizes were determined based on the results of preliminary experiments. No statistical method was used to predetermine sample size. Mice were assigned at random to groups. Mouse studies were not performed in a blinded fashion. Generally, each mouse of the different experimental groups is reported. Statistical significance was determined with the two-tailed unpaired Student's *t*-test, under the untested assumption of normality. Within each group there was an estimate of variation, and the variance between groups was similar. All statistical analysis was calculated using Prism software (GraphPad). Differences were considered to be statistically significant when *P* < 0.05.

- Burnett, S. H. *et al.* Conditional macrophage ablation in transgenic mice expressing a Fas-based suicide gene. *J. Leukoc. Biol.* **75**, 612–623 (2004).
- Grice, E. A. *et al.* Longitudinal shift in diabetic wound microbiota correlates with prolonged skin defense response. *Proc. Natl Acad. Sci. USA* **107**, 14799–14804 (2010).
- Conlan, S. *et al.* *Staphylococcus epidermidis* pan-genome sequence analysis reveals diversity of skin commensal and hospital infection-associated isolates. *Genome Biol.* **13**, R64 (2012).
- Gozalo, A. S. *et al.* Spontaneous *Staphylococcus xyloso* infection in mice deficient in NADPH oxidase and comparison with other laboratory mouse strains. *J. Am. Assoc. Lab. Anim. Sci.* **49**, 480–486 (2010).
- Spencer, S. P. *et al.* Adaptation of innate lymphoid cells to a micronutrient deficiency promotes type 2 barrier immunity. *Science* **343**, 432–437 (2014).
- Helft, J. & Merad, M. Isolation of cutaneous dendritic cells. *Methods Mol. Biol.* **595**, 231–233 (2010).
- Lennon, N. J. *et al.* A scalable, fully automated process for construction of sequence-ready barcoded libraries for 454. *Genome Biol.* **11**, R15 (2010).
- Geiss, G. K. *et al.* Direct multiplexed measurement of gene expression with color-coded probe pairs. *Nature Biotechnol.* **26**, 317–325 (2008).
- Rittig, M. G. *et al.* Coiling phagocytosis of trypanosomatids and fungal cells. *Infect. Immun.* **66**, 4331–4339 (1998).



Extended Data Figure 1 | Assessment of Foxp3⁺ regulatory T cells and cytokine production by effector T cells after *S. epidermidis* topical application and/or intradermal inoculation. **a**, Frequencies and absolute numbers of skin regulatory (CD45⁺ TCR β ⁺ CD4⁺ Foxp3⁺) T cells in unassociated mice (Ctrl, *n* = 4) and mice associated with *S. epidermidis* (*n* = 4) at day 14 post first topical application. **b**, Absolute numbers of effector T cells producing IL-17A after PMA/ionomycin stimulation in the skin (ear pinnae and flank), the lung or the small intestine lamina propria (gut) at day 14 post topical association (Ctrl, *n* = 4–5; *S. epi.*, *n* = 4–5). **c**, **d**, Enumeration of colony-forming units and absolute numbers of effector T cells producing IFN- γ or IL-17A (PMA/ionomycin) from the skin 2 weeks post application with different doses (10⁷, 10⁸ or 10⁹ c.f.u. per ml) of *S. epidermidis* (*n* = 4 per group). **e**, Frequencies and absolute numbers of neutrophils and monocytes in the skin

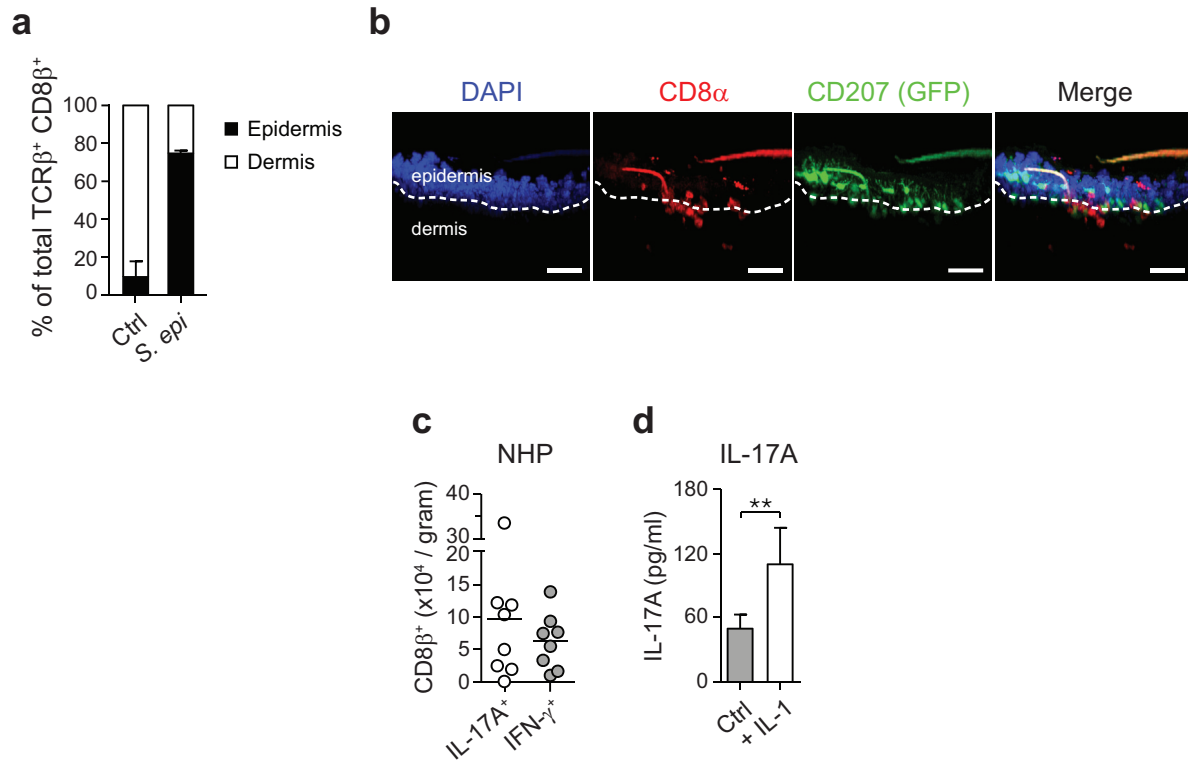
of mice 14 days after the first topical application or intradermal inoculation with *S. epidermidis* (*n* = 4 per group). **f**, Assessment of cytokine production (mean \pm s.e.m., *n* = 3 per time point) by leukocytes from the ear skin tissue 24 and 48 h after topical association with *S. epidermidis*. Unassociated mice were used as controls. No significant amounts of IL-4, IL-5, IL-17A, IL-18, IL-21 or IL-22 could be detected at the time of analysis. **g**, IFN- γ and IL-17A production by skin effector T cells in mice 7 days after *S. epidermidis* topical application or intradermal inoculation. **h**, Frequencies of IFN- γ and IL-17A-producing effector T cells in the skin of mice 7 and 14 days after the first topical application or intradermal inoculation of *S. epidermidis* (*n* = 4–5 mice per group). All results shown are representative of 2–3 experiments with similar results. **P* < 0.05; ***P* < 0.01; ****P* < 0.001; NS, not statistically significant as calculated by Student's *t*-test.



Extended Data Figure 2 | Assessment of CD8⁺ T-cell responses in the skin of specific pathogen-free and germ-free mice after topical application with skin commensals.

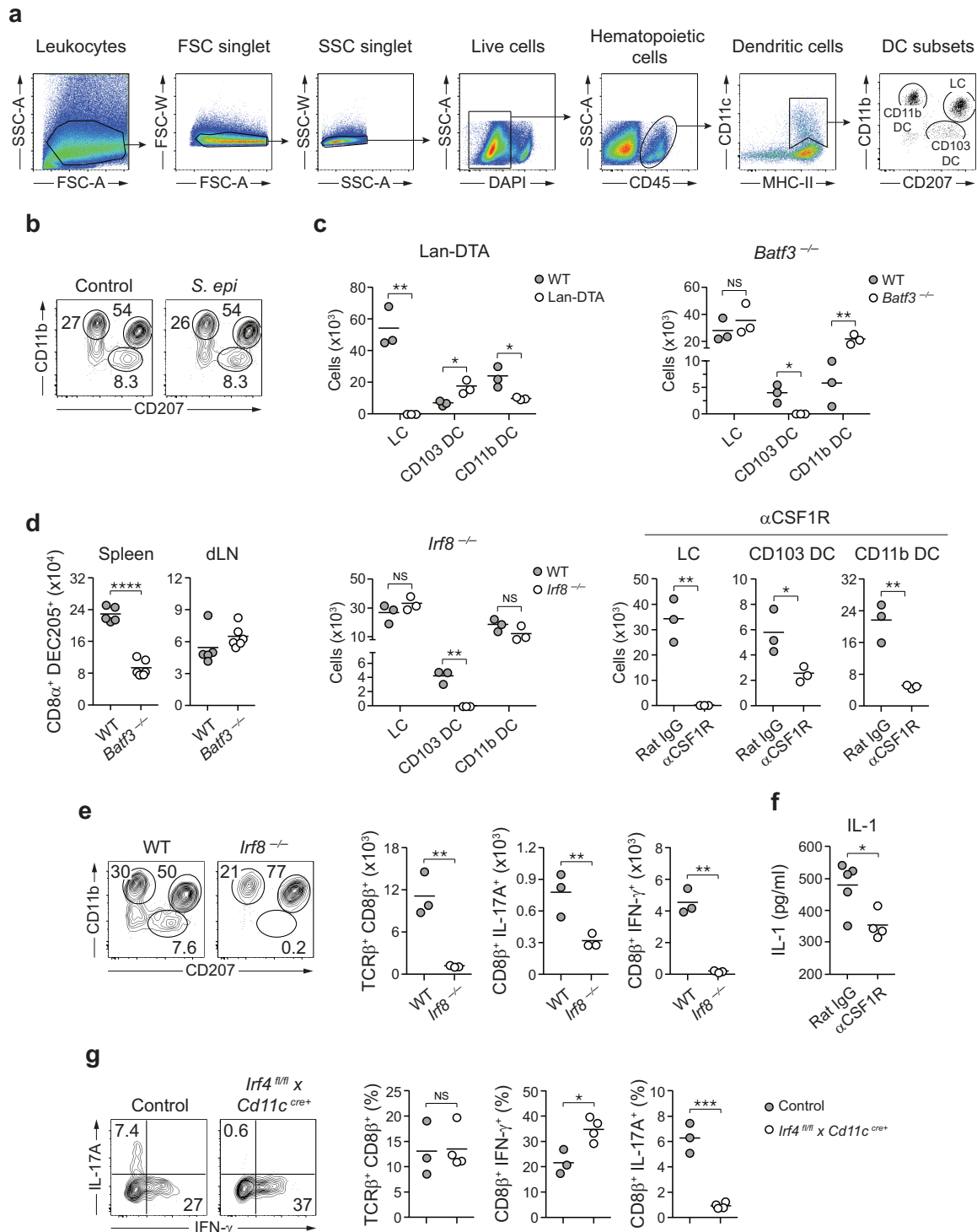
a, Mice were left unassociated (Ctrl, $n = 5$) or topically associated with *S. epidermidis* human isolate ($n = 5$), *S. xyloso* ($n = 3$), *S. epidermidis* murine isolate (*S.epi* 42E03, $n = 2$), *S. lentus* ($n = 2$), *R. nasimurium* ($n = 2$), *S. aureus* ($n = 5$), *C. pseudodiphtheriticum* ($n = 3$) or *P. acnes* ($n = 3$). Quantification of colony-forming units from the ears after topical application is shown 2 weeks after first association. **b**, Frequencies and numbers of effector (CD45⁺ TCRβ⁺ CD4⁺ Foxp3⁻) T cells producing IFN-γ or IL-17A after PMA/ionomycin stimulation in the skin of mice from **a** at day 14 post first topical application. Bar graphs represent the mean value from two mice. **c**, Frequencies of skin CD4⁺ and CD8β⁺ effector T cells in mice from **a** at day 14 post first topical application. **d**, Absolute numbers of IFN-γ- and IL-17A-producing CD8β⁺ effector T cells in the skin of unassociated (Ctrl) mice or mice associated with different doses (10^7 , 10^8 or 10^9 c.f.u. per ml) of *S. epidermidis* ($n = 4$ per group). **e**, Absolute numbers of skin CD8β⁺ effector T

cells in unassociated (Ctrl, $n = 3$) mice or mice associated with 1 ml ($n = 5$) or 5 ml ($n = 5$) of a suspension (10^9 c.f.u. per ml) of *S. epidermidis*. **f**, Flow cytometric assessment of the frequencies of CD4⁺ and CD8β⁺ effector T cells and absolute numbers of CD8β⁺ effector T cells in SPF ($n = 3$ per group) and germ-free (GF, $n = 4$ per group) mice 2 weeks after *S. epidermidis* topical application. **g**, Absolute numbers of IFN-γ- and IL-17A-producing CD8β⁺ effector T cells in the skin of unassociated (Ctrl) or *S. epidermidis*-associated C57BL/6 and BALB/c mice at 14 days post first topical application ($n = 5$ per group). For **d–g**, all results shown are representative of 2–3 independent experiments with similar results. * $P < 0.05$; ** $P < 0.01$; *** $P < 0.001$; NS, not statistically significant as calculated with Student's *t*-test. **h**, Quantification of colony-forming units from the ears of adult mice born from *S. epidermidis*-associated (*S. epi*⁺, $n = 3$) or unassociated (Ctrl, $n = 3$) breeder pairs. Flow plots and bar graphs (mean ± s.e.m.) illustrate the frequencies of CD4⁺ and CD8β⁺ effector T cells and absolute numbers of CD8β⁺ effector T cells, respectively. n.d., not detected; ** $P < 0.01$ as calculated with Student's *t*-test.



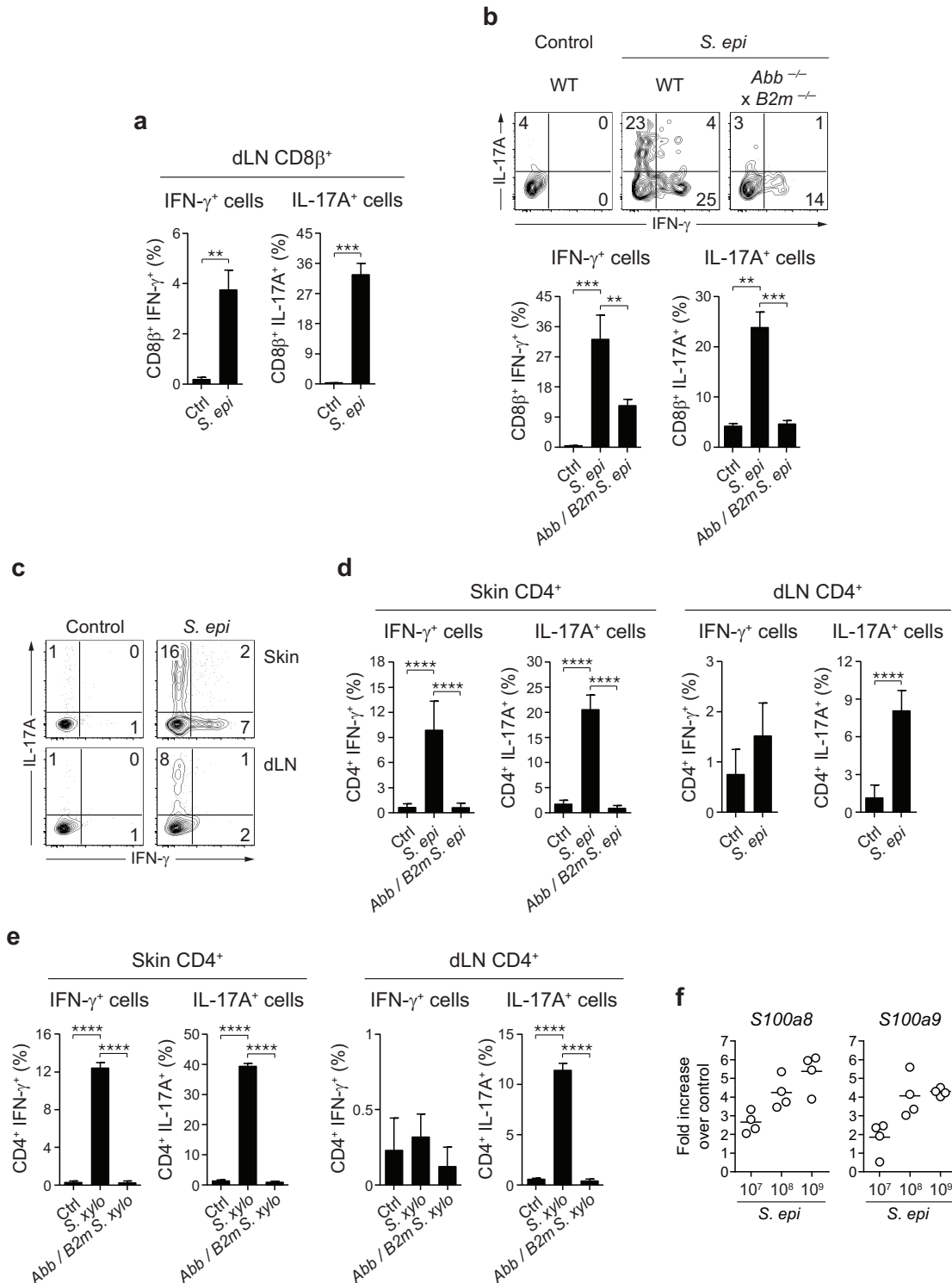
Extended Data Figure 3 | CD8 $^+$ T cells accumulate preferentially in the epidermis after topical application of *S. epidermidis*. **a**, Proportion of effector (CD45 $^+$ TCR β^+ Foxp3 $^-$) CD8 β^+ T cells in the epidermal and dermal compartments of the ear skin tissue 2 weeks after the first *S. epidermidis* topical application. **b**, Representative imaging volume projected along the x axis of ears from Langerin-GFP reporter mice at 14 days post first topical application with *S. epidermidis*. Scale bars, 30 μ m. **c**, Numbers of CD3 $^+$ CD8 β^+ cells

producing IFN- γ or IL-17A (after PMA/ionomycin stimulation) from normal nonhuman primate (NHP) skin ($n = 8$). **d**, Assessment of IL-17A production in the supernatant of CD8 β^+ T cells purified from the skin of mice topically associated with *S. epidermidis* and cultured overnight in presence of anti-CD3 ϵ alone (Ctrl) or with IL-1 α and IL-1 β (+ IL-1). Bars represent the mean value \pm s.e.m. ($n = 3$, $^{**}P < 0.01$ as calculated with Student's t -test). Results shown in **a**, **c** and **d** are representative of 2–3 experiments with similar results.



Extended Data Figure 4 | Depletion strategies for the different subsets of skin dendritic cells. **a**, Gating strategy for various dendritic cell subsets in the skin. Cells are first gated on live CD45⁺ CD11c⁺ MHCII⁺. Subsets of dendritic cells are then defined as follows: Langerhans cells (LC) are gated on CD11b⁺ CD207(Langerin)⁺ cells, CD103⁺ dendritic cells (CD103 DC) on CD11b⁺ CD207⁺ cells and CD11b⁺ dermal dendritic cells (CD11b DC) on CD11b⁺ CD207⁺ cells. **b**, Comparative assessment by flow cytometry of Langerhans cell, CD103 DC and CD11b DC in the ear skin of unassociated mice (control) and mice first topically associated with *S. epidermidis* 2 weeks earlier. **c**, Absolute numbers of Langerhans cell, CD103 DC and CD11b DC 2 weeks after the first topical application of *S. epidermidis* in wild-type (WT, *n* = 3), Langerin-DTA (Lan-DTA, *n* = 3), *Batf3*^{-/-} (*n* = 3) or *Irf8*^{-/-} (*n* = 3) mice and in mice treated with anti-CSF1R (*n* = 3) or isotype control (rat IgG, *n* = 3) antibodies. **d**, Absolute numbers of CD11c^{hi} MHCII⁺ CD8⁺ DEC205⁺

dendritic cells in the spleen and the skin draining lymph node (dLN) of wild-type (*n* = 5) and *Batf3*^{-/-} (*n* = 6) mice. **e**, Phenotypic analysis of CD45⁺ MHCII⁺ CD11c⁺ cells by flow cytometry and absolute numbers of effector (CD45⁺ TCRβ⁺ Foxp3⁻) CD8β⁺ T cells and IL-17A- or IFN-γ-producing CD8β⁺ T cells in wild-type (*n* = 3) and *Irf8*^{-/-} (*n* = 3) mice 2 weeks after the first topical application of *S. epidermidis*. **f**, Assessment of IL-1 production by leukocytes from the ear skin tissue of *S. epidermidis*-associated mice treated with anti-CSF1R (*n* = 4) or isotype control (rat IgG, *n* = 5) antibodies. **g**, Frequencies of total and IFN-γ- or IL-17A- producing CD8β⁺ effector T cells in *S. epidermidis*-associated *Irf4*^{fl/fl} × *Cd11c*^{Cre+} (*n* = 3) and littermate control (*n* = 3) mice. All data shown in this figure are representative of 2–3 experiments with similar results. **P* < 0.05; ***P* < 0.01; ****P* < 0.001; NS, not statistically significant as calculated with Student's *t*-test.



Extended Data Figure 5 | Commensal-driven CD4⁺ and CD8⁺ T-cell responses in the skin tissue and the skin draining lymph nodes are specific for commensal antigens. **a**, Frequencies of IFN- γ - or IL-17A-producing CD8 β ⁺ T cells in overnight co-cultures of splenic dendritic cells (SpDC) and CD8 β ⁺ T cells purified from the skin draining lymph node (dLN) of mice first topically associated with *S. epidermidis* 2 weeks earlier. **b**, Frequencies of IFN- γ - and IL-17A-producing CD8 β ⁺ T cells in overnight co-cultures of SpDC and CD8 β ⁺ T cells purified from the skin of mice 14 days after the first *S. epidermidis* application. Dendritic cells were purified from either wild-type (WT) or *Abb*^{-/-} *B2m*^{-/-} mice. **c**, **d**, Frequencies of IFN- γ - and IL-17A-producing CD4⁺ T cells in overnight co-cultures of SpDC and CD8 β ⁺ T cells purified from the skin ear tissue or the skin dLN of mice 14 days after the first *S. epidermidis* application. For **a**, **b** and **d**, Ctrl, naive SpDC; *S. epi*,

SpDC + heat-killed *S. epidermidis*; *Abb/B2m S. epi*, *Abb*^{-/-} *B2m*^{-/-} SpDC + heat-killed *S. epidermidis*. **e**, Frequencies of IFN- γ - and IL-17A-producing CD4⁺ T cells in overnight co-cultures of SpDC and CD8 β ⁺ T cells purified from the skin ear tissue or the skin dLN of mice 14 days after the first *S. xylo* application. Ctrl, naive SpDC; *S. xylo*, SpDC + heat-killed *S. xylo*; *Abb/B2m S. xylo*, *Abb*^{-/-} *B2m*^{-/-} SpDC + heat-killed *S. xylo*. All data shown in **a**–**d** are representative of three independent experiments. Graph bars represent the mean \pm standard deviation of triplicate cultures. ** P < 0.01, *** P < 0.0001, **** P < 0.0001 as calculated with Student's *t*-test. **f**, *S100a8* and *S100a9* gene expression in dorsal skin biopsies of mice associated with different doses (10^7 , 10^8 or 10^9 c.f.u. per ml) of *S. epidermidis* 2 weeks after the first topical application (n = 4 per group). Data are expressed as fold increase over gene expression in unassociated control mice.

Recognition determinants of broadly neutralizing human antibodies against dengue viruses

Alexander Rouvinski^{1,2*}, Pablo Guardado-Calvo^{1,2*}, Giovanna Barba-Spaeth^{1,2*}, Stéphane Duquerroy^{1,2,3}, Marie-Christine Vaney^{1,2}, Carlos M. Kikuti^{1,2†}, M. Erika Navarro Sanchez^{1,2†}, Wanwisa Dejnirattisai⁴, Wiyada Wongwiwat⁴, Ahmed Haouz⁵, Christine Girard-Blanc⁵, Stéphane Petres⁵, William E. Shepard⁶, Philippe Desprès^{7†}, Fernando Arenzana-Seisdedos⁸, Philippe Dussart^{9†}, Juthathip Mongkolsapaya^{4,10}, Gavin R. Screaton⁴ & Félix A. Rey^{1,2,5}

Dengue disease is caused by four different flavivirus¹ serotypes, which infect 390 million people yearly with 25% symptomatic cases² and for which no licensed vaccine is available. Recent phase III vaccine trials showed partial protection, and in particular no protection for dengue virus serotype 2 (refs 3, 4). Structural studies so far have characterized only epitopes recognized by serotype-specific human antibodies^{5,6}. We recently isolated human antibodies potentially neutralizing all four dengue virus serotypes⁷. Here we describe the X-ray structures of four of these broadly neutralizing antibodies in complex with the envelope glycoprotein E from dengue virus serotype 2, revealing that the recognition determinants are at a serotype-invariant site at the E-dimer interface, including the exposed main chain of the E fusion loop⁸ and the two conserved glycan chains. This ‘E-dimer-dependent epitope’ is also the binding site for the viral glycoprotein prM during virus maturation in the secretory pathway of the infected cell⁹, explaining its conservation across serotypes and highlighting an Achilles’ heel of the virus with respect to antibody neutralization. These findings will be instrumental for devising novel immunogens to protect simultaneously against all four serotypes of dengue virus.

Exposed at the surface of infectious mature dengue virus (DENV) particles, protein E is the sole target of neutralizing antibodies. It displays an icosahedral arrangement in which 90 E dimers completely coat the viral surface^{10,11} and which is sensitive to the environmental pH. Upon entry of DENV into cells via receptor-mediated endocytosis, the acidic endosomal environment triggers an irreversible fusogenic conformational change in protein E that leads to fusion of viral and endosomal membranes¹. A large fragment of E (termed sE for ‘soluble E’) lacking the C-terminal transmembrane anchor and a segment immediately preceding it (termed ‘stem’), crystallizes as a dimer mimicking the organization of protein E on virions. The structure of the sE dimer has been determined by X-ray crystallography^{8,12}. Protein E is relatively conserved, displaying about 65% amino-acid sequence identity when comparing the most distant DENV serotypes. In particular, there are two conserved N-linked glycosylation sites at positions N67 and N153. To examine its interaction with the antibodies, we selected four highly potent broadly neutralizing antibodies (bnAbs) identified in the accompanying work: 747(4) A11 and 747 B7 (‘E-dimer-dependent epitope 2’ (EDE2) group, requiring glycosylation at position N153 for efficient binding) and 752-2 C8 and 753(3) C10 (EDE1 group, binding regardless of the glycosylation at N153)⁷—referred to as A11, B7, C8 and C10 from hereon. The EDE2 bnAbs were isolated from the same patient (who had a secondary infection with serotype 2 (DENV-2)), and are

somatic variants of the same immunoglobulin-G (IgG) clone, derived from the *IGHV3-74* and *IGLV2-23* germ lines. The heavy chain has a very long (26 amino acids, international ImMunoGeneTics information system (IMGT) convention) complementarity-determining region 3 (CDR H3). The EDE1 bnAbs were isolated from different patients and derive from VH and VL genes *IGHV3-64* and *IGKV3-11* (EDE1 C8, the patient appeared to have a primary infection of undetermined serotype) and *IGHV1-3* and *IGLV2-14* (EDE1 C10, from a patient with secondary DENV-1 infection). The analysis of the genes coding for these antibodies is summarized in Table 1.

Although it crystallizes as dimer^{8,12,13}, recombinant sE is mainly monomeric in solution. Interaction with the Fab or single-chain Fv (scFv) of the four bnAbs shifted the equilibrium to dimer. The crystal structures of the antibody/antigen complexes were determined as described in the Methods section, to a resolution between 3.0 and 3.2 Å for the complexes with B7, C10 and C8; and 3.85 Å for the complex with A11 (Extended Data Table 1). They show that all four bnAbs bind in a similar way (Fig. 1), interacting with both subunits and leaving a similar footprint on the sE dimer (Extended Data Fig. 1).

The antibody/antigen contacts are centred in a valley lined by the *b* strand on the domain II side, and by the ‘150 loop’ of domain I of the adjacent subunit on the opposite side (Fig. 1), with the heavy chain contacting both N67 and N153 glycans across the E-dimer interface (Fig. 1a, e–g). The 150 loop spans residues 148–159, connecting β -strands E₀ and F₀ of domain I¹⁴, and carries the N153 glycan. The total buried surface area per epitope ranges between 1,050 and 1,400 Å², and the surface complementarity coefficient¹⁵ is between 0.67 and 0.74 (Extended Data Table 2), which are values typical for antibody/antigen complexes. The surface electrostatic potentials of epitope and paratopes are mildly charged (Extended Data Fig. 2), with a relatively complementary charge distribution. The EDE2 antibodies recognize sE essentially via the heavy chain, with the light chain involved only in contacts with the N153 glycan. The heavy chain buries nearly 85% of the total buried surface area—63% belonging to the long EDE2 CDR H3, which forms a protrusion matching the concave surface of the sE dimer. This protrusion is preformed in the antibody, as shown by the 1.7 Å resolution structure of the unliganded EDE2 A11 scFv (Extended Data Fig. 3), indicating no entropic cost for binding. In contrast, the EDE1 antibodies engage a substantial amount of light chain contacts from all three CDR and framework regions, contributing in total 40% in C8 and 47% in C10 of the buried surface area in the complex with sE. Although the germ lines are different between EDE1 C8 and C10 and the CDRs contribute

¹Institut Pasteur, Département de Virologie, Unité de Virologie Structurale, 75724 Paris Cedex 15, France. ²CNRS UMR 3569 Virologie, 75724 Paris Cedex 15, France. ³Université Paris-Sud, Faculté des Sciences, 91405 Orsay, France. ⁴Division of Immunology and Inflammation, Department of Medicine, Hammersmith Hospital Campus, Imperial College London, London W12 0NN, UK. ⁵Institut Pasteur, Protéopôle, CNRS UMR 3528, 75724 Paris Cedex 15, France. ⁶Synchrotron SOLEIL, L’Orme des Merisiers, Saint Aubin, BP48, 91192 Gif-sur-Yvette, France. ⁷Institut Pasteur, Département de Virologie, Unité des Interactions Moléculaires Flavivirus-Hôtes, 75724 Paris Cedex 15, France. ⁸Institut Pasteur, Département de Virologie, Unité de Pathogénie Virale, INSERM U1108, 75724 Paris Cedex 15, France. ⁹Institut Pasteur de Guyane, BP 6010, 97306 Cayenne, French Guiana. ¹⁰Dengue Hemorrhagic Fever Research Unit, Office for Research and Development, Faculty of Medicine, Siriraj Hospital, Mahidol University, Bangkok 10700, Thailand. [†]Present addresses: Institut Curie, 75248 Paris Cedex 05, France (C.M.K.); Altravax, Inc., 725 San Aleso Avenue, Suite 2, Sunnyvale, California 94085, USA (M.E.N.S.); U1157 INSERM GIP-CYROI, 97491 Saint Clotilde, La Réunion, France (P.De.); Institut Pasteur du Cambodge, 5 Monivong Boulevard, PO Box 983, Phnom Penh, Cambodia (P.Du).

*These authors contributed equally to this work.

Table 1 | Germline analysis of bnAbs EDE1 and EDE2

Heavy chain	V-H allele	V-H diverg [‡]	V-H aa ch/tot [§]	J-H allele	D-H allele	CDR length [1:2:3]	BSA (%)	
							CDR [1:2:3]	[CDR:FWR]
EDE2 A11	IGHV3-74*01†	8.68%	14/98	IGHJ6*02	IGHD3-22*01	[8:8:26] [5:17:24]¶	[6:11:62] [6:13:61]¶	[79:3] [80:3]¶
EDE2 B7	IGHV3-74*01	6.94%	9/98	IGHJ6*02	IGHD3-22*01	[8:8:26] [5:17:24]¶	[2:11:63] [2:14:62]¶	[76:8] [78:6]¶
EDE1 C8	IGHV3-64D*06	6.94%	12/98	IGHJ6*02	IGHD2-21*01	[8:8:15] [5:17:13]¶	[0:14:23] [0:22:23]¶	[37:24] [45:16]¶
EDE1 C10	IGHV1-3*01	2.78%	4/98	IGHJ4*02	IGHD4-17*01	[8:8:21] [5:17:19]¶	[0:9:44] [0:9:44]¶	[53:0] [53:0]¶
Light chain	V-L allele	V-L	V-L aa	J-L allele	D-L allele	CDR length [1:2:3]	BSA (%)	
							CDR [1:2:3]	[CDR:FWR]
EDE2 A11	IGL2-23*01†	6.94%	14/98	IGLJ3*02†	—	[9:3:10] [14:7:10]¶	[0:0:4] [0:10:4]¶	[4:13] [14:3]¶
EDE2 B7	IGLV2-23*01†	4.51%	10/98	IGLJ3*02†	—	[9:3:10] [14:7:10]¶	[0:0:4] [0:10:4]¶	[4:11] [14:2]¶
EDE1 C8	IGKV3-11*01	5.02%	9/95	IGKJ2*01	—	[6:3:10] [11:7:10]¶	[10:5:15] [10:9:15]¶	[30:9] [34:5]¶
EDE1 C10	IGLV2-14*01	3.82%	10/98	IGLJ3*02	—	[9:3:10] [14:7:10]¶	[17:8:14] [17:13:14]¶	[39:8] [44:3]¶

V-H, J-H, D-H, V-L, J-L represent the putative *Homo sapiens* genes and alleles corresponding to the given bnAb, predicted by IMGT analysis (see Methods).

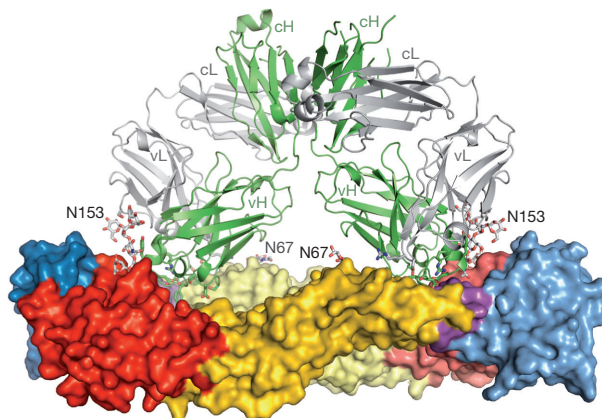
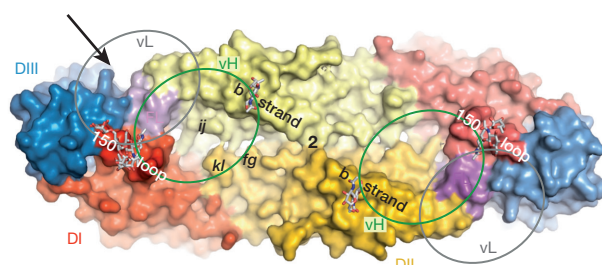
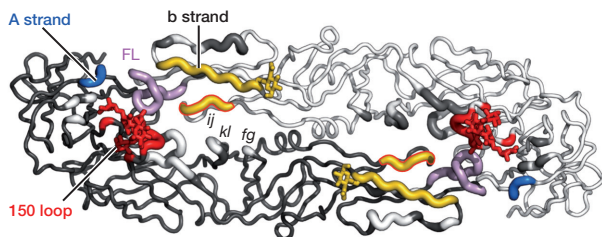
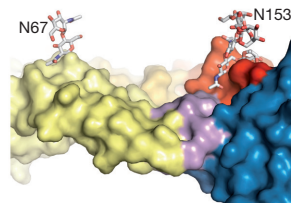
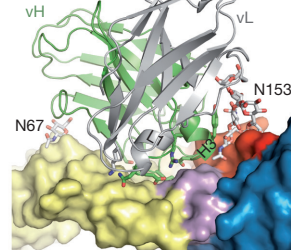
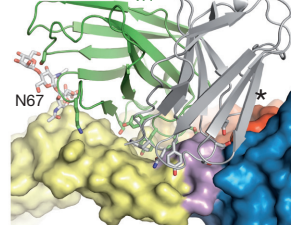
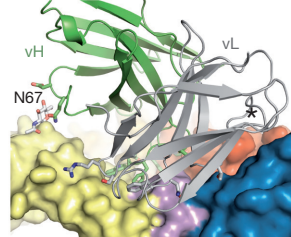
† Additional possibilities were also predicted by IMGT (not shown).

‡ Nucleotide (nt) divergence (diverg). The total length for all V-H and V-L alleles is 288 nucleotides except for EDE1 C8 V-L (279 nucleotides).

§ Number of amino-acid (aa) changes out of total V-H/V-L amino-acid length (ch/tot).

¶ Buried surface area (BSA) for CDR and framework regions. Buried surface area per CDR or framework region (FWR) are shown as percentage of the total BSA of Fab or ScFv within the complex with DENV-2 sE. Buried surface areas are represented per individual H-CDRs [1:2:3] and L-CDRs [1:2:3] or as a sum for light/heavy chain CDRs and framework regions [CDR:FWR].

|| IMGT and ¶ Kabat definitions of CDR and framework regions.

a DENV-2 sE - EDE2 A11 (side view)**b** DENV-2 sE (top view)**c** DENV-2 sE (top view)**d** DENV-2 sE**e** EDE2 B7**f** EDE1 C8**g** EDE1 C10**Figure 1 | DENV-2 sE in complex with four EDE**

bnAbs. **a**, Complex with Fab EDE2 A11. The sE dimer is in surface representation in side view, with the viral membrane-facing side below, coloured according to domains as labelled in **b**, with foreground and background subunits in bright and pale colours, respectively. The two N-linked glycan chains at N67 and N153 are shown as ball-and-stick and labelled. The A11 Fab is shown as ribbon with heavy and light chains in green and grey, respectively. **b**, The unliganded DENV-2 FGA02 sE dimer seen down the twofold axis (labelled '2'). Green and grey empty ovals (labelled vH and vL) show roughly the contact sites of heavy and light chains, respectively. Polypeptide segments relevant to the description of the epitopes are labelled. **c**, 'Worm' representation of the sE dimer, with the two subunits in different greys. Polypeptide segments in contact with the antibodies (either EDE1 or EDE2) are shown thicker, with the main segments of the epitope colour coded as boxed in Extended Data Fig. 4a, with additional contact segments in white or dark grey, depending on the subunit background. **d**, View down the arrow shown in **b**, highlighting the fusion loop 'valley' encased between two ridges, the *b* strand on one subunit and the 150 loop on the other. **e–g**, Same view as in **d** showing the complexes with bnAbs EDE2 B7 (**e**), EDE1 C8 (**f**) and EDE1 C10 (**g**) (only variable domains are shown). A black asterisk in **f** and **g** marks the region of the 150 loop, disordered in those complexes. Note that in the B7 and A11 complexes, the light chain is too far up to reach domain III.

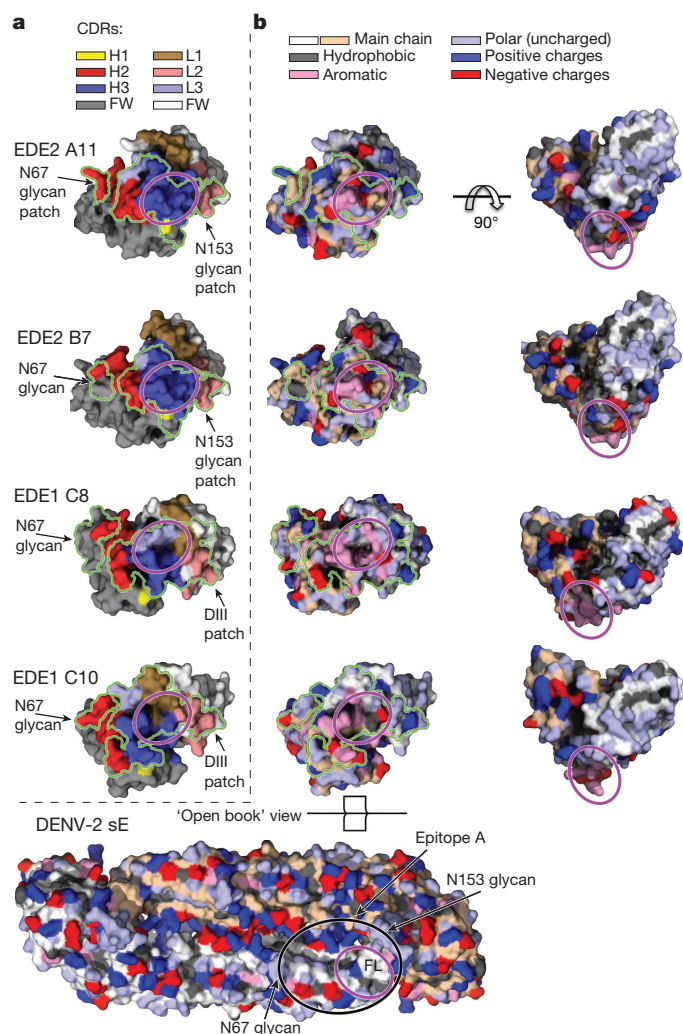


Figure 2 | Comparison of paratopes. **a**, The paratopes (outlined in green) on the antibody surface colour-coded by CDRs. The oval marks the region in contact with the E fusion loop. Note that the patch interacting with the N153 glycan (labelled) in EDE2 bnAbs corresponds to that interacting with domain III in EDE1 bnAbs. **b**, Chemical nature of paratope side chains. The left column corresponds to the same orientation as in **a**, with the surface coloured according to the side chain type. Exposed main-chain atoms of heavy and light chain are in sand and white, respectively. The bottom panel shows the sE dimer in the same rendering in an 'open book' orientation with respect to the antibodies. The epitope area is indicated with a black ellipse, with the fusion loop within the magenta oval corresponding to the one drawn on the antibodies.

differently to the paratope (Fig. 2a), the chemical nature of the residues involved is similar, including a clear clustering of aromatic side chains—a feature shared with the EDE2 bnAbs (Fig. 2b).

The bnAb contacts cluster on residues at the dimer interface (Fig. 1c) that are conserved across the four serotypes (Extended Data Fig. 4a), explaining their cross-reactivity. On domain II, both EDE1 and EDE2 bnAbs target the same residues (Extended Data Figs 4 and 5), which map to three main polypeptide segments: the *b* strand (amino acids 67–74, bearing the N67 glycan), the fusion loop and residues immediately upstream (amino acids 97–106), and the *ij* loop (amino acids 246–249). In contrast, on the opposite subunit the residues targeted are different: the EDE2 bnAbs interact with the 150 loop and the N153 glycan chain, whereas EDE1 bnAbs target domains I and III and induce disorder of the 150 loop. The structure of unliganded DENV-2 sE of the same strain (FGA-02, Fig. 1b–d), determined in parallel, was useful in assessing that EDE1 antibody binding indeed displaces the 150 loop.

This is relevant because a previous structure of DENV-4 sE in complex with an antibody that binds away from the EDE also had the 150 loop disordered¹³, highlighting an intrinsic mobility in this area depending on the E amino-acid sequence. Displacement of the 150 loop allows the EDE1 light chain to come closer to sE and interact with domain III (compare panel e with f and g in Fig. 1) in the region of the 'A strand' epitope, which has been structurally characterized previously for murine DENV cross-reactive antibodies^{16,17}. These domain III contacts are centred on the conserved E residue K310, the side chain of which makes a lid covering the indole ring of W101 of the fusion loop (Extended Data Fig. 6a), in an important stabilizing E-dimer contact.

The bnAbs make extensive interactions with the glycan chains, both at positions N67 and N153 of protein E (Extended Data Figs 6 and 7), using opposite sides of the paratope (Fig. 2a). The complex of sE with EDE1 C8 displays the highest-ordered N67 glycan structure (Extended Data Fig. 7), with interactions with CDR H2 (Fig. 2a). The distal mannose residues contact the framework region 3 (framework H3; Extended Data Figs 4b and 7). Except for EDE1 C10 (which is very close to its germ line; Table 1), several framework H3 residues in the other bnAbs analysed have undergone changes (Extended Data Fig. 4b), suggesting affinity maturation to recognize the sugars. With respect to the N153 glycan, the structure of sE in complex with the EDE2 bnAbs displays clear electron density for the 6 sugar residues closest to the apurine side chain (including in omit maps, as shown in Extended Data Fig. 7). A short α -helix in A11 and B7 CDR H3 projects aromatic side chains that pack against the sugar residues 1, 3 and 4 of the N153 glycan. The most distant residues of the glycan, mannoses 4, 5 and 6, are in contact with the light chain, via residues from CDR L2, including several hydrogen bonds (Extended Data Fig. 7 and Supplementary Information).

The glycine-rich fusion loop in the E dimer is such that it essentially exposes main-chain atoms, while the hydrophobic side chains are mostly buried. Together with the main chain of the *ij* loop, main-chain atoms make a large surface patch that is augmented by the exposed edge of the *b* strand (Fig. 3). The bnAbs make several specific hydrogen bonds to the sE main chain (Extended Data Fig. 6, see also list of interactions in Supplementary Information). Furthermore, the exposed side chains in this area are mostly conserved, resulting in a core region of the EDE that is serotype invariant, with non-conserved residues essentially at the periphery. The principal binding determinants of the EDE bnAbs thus appear to be the conformation of the main chain of the fusion

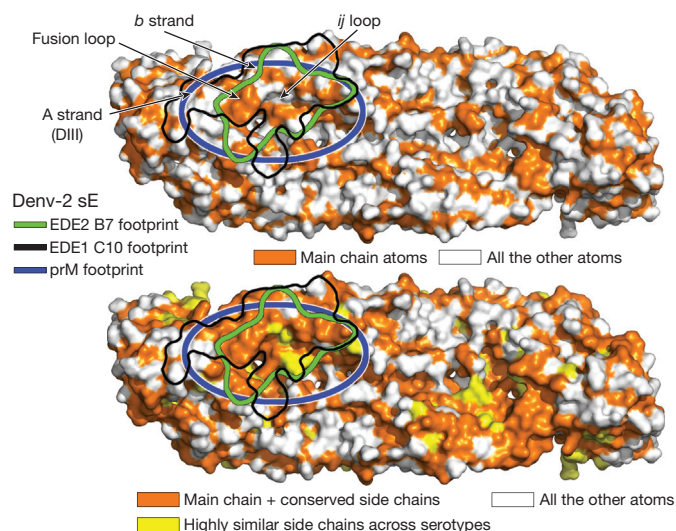


Figure 3 | Exposed main-chain atoms in the epitope. Surface representation of DENV-2 sE as viewed from outside the virion, with exposed main-chain atoms orange (top) or with main-chain atoms plus conserved side chains in orange, and highly similar side chains in yellow (bottom). The epitopes of EDE1 bnAb C10 (black outline) and EDE2 bnAb B7 (green outline) are indicated, with the prM footprint outlined in blue.

loop and its immediate neighbours in the context of an intact E dimer. This contrasts with the other major class of antibodies isolated from humans, which recognize the fusion loop sequence in a context independent of the quaternary organization⁷. The latter are cross reactive but poorly neutralizing and have a strong infection enhancing potential¹⁸.

What is the reason for the strong conservation of this site across serotypes? In the infected cell, newly synthesized immature DENV virions bud into the endoplasmic reticulum lumen, where the pH is neutral. These particles contain 180 copies of a heterodimer of protein E with the precursor membrane glycoprotein prM at their surface^{19,20}. As they are subsequently transported to the external medium across the Golgi apparatus, where the pH is acidic, the interaction with prM protects E from undergoing a premature acid-induced fusogenic conformational change¹. The E/prM heterodimers reversibly associate as 60 trimers or 90 dimers at neutral or acidic pH, respectively^{9,21}. Upon cleavage of its viral membrane tether by the TGN resident furin protease, prM remains bound to E dimers as long as the environment is acidic but it is released when the particle reaches the exterior of the cell (where the pH is neutral), thereby activating the virion to become fusogenic upon re-encountering the acidic endosomal environment of a new cell. The binding site of prM on the E dimer^{9,21} maps precisely to the EDE (Fig. 3), explaining the high conservation of this site. As the E-dimer conformation with bound prM was observed on immature particles at low pH only⁹, at neutral pH the EDE is not formed, and accordingly bnAbs do not bind to particles that are 100% immature⁷, which are formed exclusively of E/prM trimers¹⁹. But the efficient binding of the bnAbs to particles that have more than 60% uncleaved prM⁷, which have been shown to display patches of immature E/prM trimers at their surface^{22,23}, shows that these trimers must undergo a dynamic exchange with dimers. As the bnAbs have a higher affinity, they outcompete uncleaved prM on partly immature virions from its interaction with E dimers, binding by conformational selection²⁴. This process effectively displaces the equilibrium towards dimers, similar to the bnAb-induced shift towards dimers of the sE monomer–dimer equilibrium in solution (data not shown). Because the degree of prM cleavage is variable and depends on the particular cell in which the virus was replicated, the fact that these bnAbs bind efficiently partly mature particles is expected to be important for protection in humans.

The EDE is totally circumscribed to the E dimer and therefore it does not depend on the higher-order arrangement of dimers, as recently suggested for other quaternary epitopes on the DENV particle²⁵ on the basis of studies on a different flavivirus, the West Nile virus²⁶. Recent studies on DENV-2 detected a particle expansion at physiological temperatures of humans, causing the E dimers to reorient with respect to each other and presenting a different surface pattern as in mosquito-grown viruses^{27,28}. bnAbs targeting the EDE will neutralize regardless of the surface arrangement of E dimers. These results are in line with a recent study on the tick-borne encephalitis flavivirus, in which the corresponding recombinant sE dimer efficiently depleted human serum from neutralizing activity²⁹.

As a corollary, our results suggest that, similar to vaccine approaches against the respiratory syncytial virus³⁰, a viable strategy would consist of presenting a single stabilized pre-fusion E dimer to the immune system, designed to focus the B-cell response on the EDE, instead of the multivalent vaccines that are currently under development.

Online Content Methods, along with any additional Extended Data display items and Source Data, are available in the online version of the paper; references unique to these sections appear only in the online paper.

Received 30 April; accepted 1 December 2014.

Published online 12 January 2015.

1. Lindenbach, B., Thiel, H. & Rice, C. *Flaviviridae: the Viruses and their Replication* 5th edn, Vol. 1, 1101–1152 (Lippincott Williams & Wilkins, 2007).
2. Bhatt, S. *et al.* The global distribution and burden of dengue. *Nature* **496**, 504–507 (2013).

3. Capeding, M. R. *et al.* Clinical efficacy and safety of a novel tetravalent dengue vaccine in healthy children in Asia: a phase 3, randomised, observer-masked, placebo-controlled trial. *Lancet* **384**, 1358–1365 (2014).
4. Normile, D. Tropical diseases. Dengue vaccine trial poses public health quandary. *Science* **345**, 367–368 (2014).
5. Fibriansah, G. *et al.* A potent anti-dengue human antibody preferentially recognizes the conformation of E protein monomers assembled on the virus surface. *EMBO Mol. Med.* **6**, 358–371 (2014).
6. Teoh, E. P. *et al.* The structural basis for serotype-specific neutralization of dengue virus by a human antibody. *Sci. Translat. Med.* **4**, 139–183 (2012).
7. Dejnirattisai, W. *et al.* A new class of highly potent broadly neutralizing antibodies isolated from dengue viremic patients. *Nature Immunol.* <http://dx.doi.org/10.1038/ni.3058> (15 December 2014).
8. Modis, Y., Ogata, S., Clements, D. & Harrison, S. C. A ligand-binding pocket in the dengue virus envelope glycoprotein. *Proc. Natl Acad. Sci. USA* **100**, 6986–6991 (2003).
9. Yu, I. M. *et al.* Structure of the immature dengue virus at low pH primes proteolytic maturation. *Science* **319**, 1834–1837 (2008).
10. Kuhn, R. J. *et al.* Structure of dengue virus: implications for flavivirus organization, maturation, and fusion. *Cell* **108**, 717–725 (2002).
11. Zhang, X. *et al.* Cryo-EM structure of the mature dengue virus at 3.5-Å resolution. *Nature Struct. Mol. Biol.* **20**, 105–110 (2013).
12. Zhang, Y. *et al.* Conformational changes of the flavivirus E glycoprotein. *Structure* **12**, 1607–1618 (2004).
13. Cockburn, J. J. *et al.* Structural insights into the neutralization mechanism of a higher primate antibody against dengue virus. *EMBO J.* **31**, 767–779 (2012).
14. Rey, F. A., Heinz, F. X., Mandl, C., Kunz, C. & Harrison, S. C. The envelope glycoprotein from tick-borne encephalitis virus at 2 Å resolution. *Nature* **375**, 291–298 (1995).
15. Lawrence, M. C. & Colman, P. M. Shape complementarity at protein/protein interfaces. *J. Mol. Biol.* **234**, 946–950 (1993).
16. Cockburn, J. J. *et al.* Mechanism of dengue virus broad cross-neutralization by a monoclonal antibody. *Structure* **20**, 303–314 (2012).
17. Lok, S. M. *et al.* Binding of a neutralizing antibody to dengue virus alters the arrangement of surface glycoproteins. *Nature Struct. Mol. Biol.* **15**, 312–317 (2008).
18. Rodenhuis-Zybert, I. A. *et al.* A fusion-loop antibody enhances the infectious properties of immature flavivirus particles. *J. Virol.* **85**, 11800–11808 (2011).
19. Zhang, Y. *et al.* Structures of immature flavivirus particles. *EMBO J.* **22**, 2604–2613 (2003).
20. Kostyuchenko, V. A., Zhang, Q., Tan, J. L., Ng, T. S. & Lok, S. M. Immature and mature dengue serotype 1 virus structures provide insight into the maturation process. *J. Virol.* **87**, 7700–7707 (2013).
21. Li, L. *et al.* The flavivirus precursor membrane-envelope protein complex: structure and maturation. *Science* **319**, 1830–1834 (2008).
22. Plevka, P. *et al.* Maturation of flaviviruses starts from one or more icosahedrally independent nucleation centres. *EMBO Rep.* **12**, 602–606 (2011).
23. Plevka, P., Battisti, A. J., Sheng, J. & Rossmann, M. G. Mechanism for maturation-related reorganization of flavivirus glycoproteins. *J. Struct. Biol.* **185**, 27–31 (2014).
24. Changeux, J. P. & Edelstein, S. Conformational selection or induced fit? 50 years of debate resolved. *F1000 Biol. Rep.* **3**, 19 (2011).
25. de Alwis, R. *et al.* Identification of human neutralizing antibodies that bind to complex epitopes on dengue virions. *Proc. Natl Acad. Sci. USA* **109**, 7439–7444 (2012).
26. Kaufmann, B. *et al.* Neutralization of West Nile virus by cross-linking of its surface proteins with Fab fragments of the human monoclonal antibody CR4354. *Proc. Natl Acad. Sci. USA* **107**, 18950–18955 (2010).
27. Fibriansah, G. *et al.* Structural changes of dengue virus when exposed to 37 °C. *J. Virol.* **87**, 7585–7592 (2013).
28. Zhang, X. *et al.* Dengue structure differs at the temperatures of its human and mosquito hosts. *Proc. Natl Acad. Sci. USA* **110**, 6795–6799 (2013).
29. Jarmer, J. *et al.* Variation of the specificity of the human antibody responses after tick-borne encephalitis virus infection and vaccination. *J. Virol.* **88**, 13845–13857 (2014).
30. McLellan, J. S. *et al.* Structure-based design of a fusion glycoprotein vaccine for respiratory syncytial virus. *Science* **342**, 592–598 (2013).

Supplementary Information is available in the online version of the paper.

Acknowledgements This work was made possible by a Pediatrics Dengue Vaccine Initiative grant to F.A.R., allowing the set up of a production facility of recombinant DENV sE. The co-crystallization with the bnAbs was done with European Union funding (DenFree consortium) to F.A.R. and G.R.S./J.M. F.A.R. acknowledges support from Institut Pasteur, from the French Government's 'Investissements d'Avenir' program: Laboratoire d'Excellence 'Integrative Biology of Emerging Infectious Diseases' (grant number ANR-10-LABX-62-IBED) and the CNRS. G.S.R. and J.M. were supported by the Medical Research Council, UK, the Wellcome Trust, UK, the National Institute for Health Research Biomedical Research Centre, Funding Scheme. G.R.S. is a Wellcome Trust Senior investigator. We thank staffs at beam lines PROXIMA-1 and PROXIMA-2 at the SOLEIL synchrotron (St Aubin, France) and ID23-2 and ID29 at the European Synchrotron Radiation Facility (Grenoble, France). We thank A. Sakuntabhai for coordination of the DenFree grant, G. Bricogne for advice on diffraction data collection strategies, J. Cockburn and P.-Y. Lozach for help with the initial sE constructs, and S. Halstead and S. Kilks for support through the Pediatrics Dengue Vaccine Initiative.

Author Contributions J.M., G.R.S. and F.A.R. conceived the experiments. W.W. and W.D. made the constructs for production of antibody fragments in S2 cells. M.E.N.S. and C.M.K. made the constructs for production of recombinant sE, and crystallized the unliganded form of DENV-2 FGA02 sE. C.G.B. and S.P. produced large amounts of sE

protein for crystallization. A.R. and G.B.S. prepared the recombinant bnAb fragments and sE for crystallization. A.R. and A.H. optimized the crystals of the complexes. P.G.C., W.E.S., S.D., M.C.V. and A.R. collected and processed the diffraction data. P.G.C., M.C.V. and S.D. determined the structures and refined the atomic models. P.De., F.A.S. and F.A.R. conceived the protocols for production of recombinant sE. P.Du. provided a plasmid containing the envelope protein of DENV-2 FGA02 strain circulating in French Guiana in 2002. F.A.R. wrote the paper with the help of A.R., P.G.C., G.B.S., M.C.V. and S.D.

Author Information Coordinates and structure factor amplitudes have been deposited in the Protein Data Bank under accession numbers 4UTC, 4UTA, 4UT9,

4UTB and 4UT6 respectively for the structures of DENV-2 sE unliganded and in complex with EDE1 C8, EDE1 C10, EDE2 A11 and EDE2 B7, and 4UT7 for the structure of the unliganded scFv of EDE2 A11. The sequence of prM/sE fragment from Den2_FGA-02 has been deposited in GenBank under accession number KM087965. Patent application (UK 1413086.8) was deposited. Reprints and permissions information is available at www.nature.com/reprints. The authors declare no competing financial interests. Readers are welcome to comment on the online version of the paper. Correspondence and requests for materials should be addressed to F.A.R. (rey@pasteur.fr), G.R.S. (g.screaton@imperial.ac.uk) or J.M. (j.mongkolsapaya@imperial.ac.uk).

METHODS

No statistical methods were used to predetermine sample size.

Recombinant sE protein production. Recombinant DENV-2 FGA02 sE (1–395) was cloned into a vector pMT/BIP/V5-His with a carboxy (C)-terminal His-tag and produced in *Drosophila* S2 cells³¹, performed essentially as described earlier for DENV-4 sE (Den4_Burma/63632/1976)¹³, with some modifications (see below). Briefly, sE expression was driven by the metallothionein promoter and was induced by 5 μ M of CdCl₂ in Insect-XPRESS medium (Lonza). The constructs had a *Drosophila* BiP signal sequence fused at the amino (N)-terminal end of a prM/sE construct for efficient translocation into the endoplasmic reticulum of the transfected S2 cells. prM was present N-terminal to sE, as in the DENV polyprotein precursor, with the N termini of prM and sE generated by signalase cleavage in the endoplasmic reticulum, where prM (which remains membrane-anchored) plays a chaperone role by masking the fusion loop of sE. The prM/sE complex is transported across the acidic compartments, where prM is cleaved by furin into pr (N-terminal half, bound to sE) and M (membrane-anchored C-terminal half). Upon reaching the external milieu, sE and pr dissociate, and the sE component is purified by affinity chromatography from the cells' supernatant fluid. Clarified cell supernatants were concentrated 20-fold using Vivaflow tangential filtration cassettes (Sartorius, cut-off 10 kDa) and adjusted to pH 8.0, Tris 20 mM and 500 mM NaCl before purification in an AKTA FPLC system by HisTrap-HP chromatography. The protein was de-salted after elution of the HisTrap column and further purified by ion exchange chromatography on MonoQ. A final purification gel filtration step used a Superdex 200/1000 GL column equilibrated in 50 mM Tris pH8, 500 mM NaCl.

Note that the last four residues (392–395) were inadvertently replaced by a 'vector' sequence 'LRPL' instead of 'FKKG' as in the correct DENV-2 sequence (see Extended Data Fig. 4a). Fortunately, the 'vector' residues correctly completed the β -strand G of domain III and did not introduce any detectable difference in conformation there compared with the other available structures of DENV-2 sE. This discrepancy in the amino-acid sequence has been explicitly indicated in the deposited Protein Data Bank file.

Production of antigen-binding (Fab) and single-chain Fv (scFv) fragments of the bnAbs. The bnAb fragments were cloned into plasmids for expression as Fab³² and scFv³¹ in *Drosophila* S2 cells. The constructs contain a twin strep tag fused at the C terminus (only of the heavy chain in the case of the Fab) for affinity purification. The purification protocol included a streptactin affinity column followed by gel filtration as described above.

Immune complex formation and isolation. The purified DENV-2 sE protein was mixed with Fabs or scFvs (in approximately twofold molar excess) in standard buffer (500 mM NaCl, Tris 50 mM pH 8.0). The volume was brought to 0.2 ml by centrifugation in a Vivaspin 10 kDa cutoff; after 30 min incubation at 4 °C, the complex was separated from excess Fab or scFv by size-exclusion chromatography except when a clear peak for the complex was not obtained. In this case, a molar ratio 1:2 antigen:antibody mixture (that is, with an excess of antibody) was directly used for crystallization. In all cases, the buffer was exchanged to 150 mM NaCl, 15 mM Tris, pH 8 for crystallization trials. The protein concentrations used for crystallization, determined by measuring the absorbance at 280 nm and using an extinction coefficient estimated from the amino-acid sequences, are listed in Extended Data Table 1.

Crystallization and three-dimensional structure determinations. Crystallization trials were performed in sitting drops of 400 nl. Drops were formed by mixing equal volumes of the protein and reservoir solution in the format of 96 Greiner plates, using a Mosquito robot, and monitored by a Rock-Imager. Crystals were optimized with a robotized Matrix Maker and Mosquito setups on 400 nl sitting drops, or manually in 24-well plates using 2–3 μ l hanging drops. The crystallization and cryo-cooling conditions for diffraction data collection are listed in Extended Data Table 1.

X-ray diffraction data were collected at beam lines PROXIMA-1 and PROXIMA-2 at the SOLEIL synchrotron (St Aubin, France), and ID23-2 and ID29 at the European Synchrotron Radiation Facility (Grenoble, France) (Extended Data Table 1). Diffraction data were processed using the XDS package³³ and scaled with SCALA or AIMLESS³⁴ in conjunction with other programs of the CCP4 suite³⁵. The structures

were determined by molecular replacement with PHASER³⁶ and/or AMoRe³⁷ using the search models listed in Extended Data Table 1.

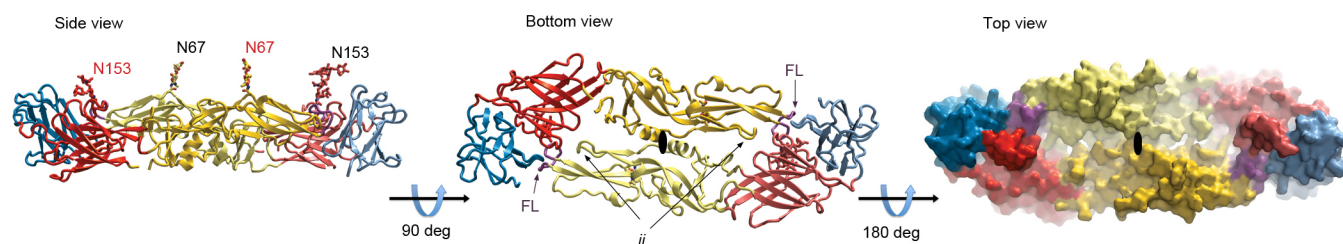
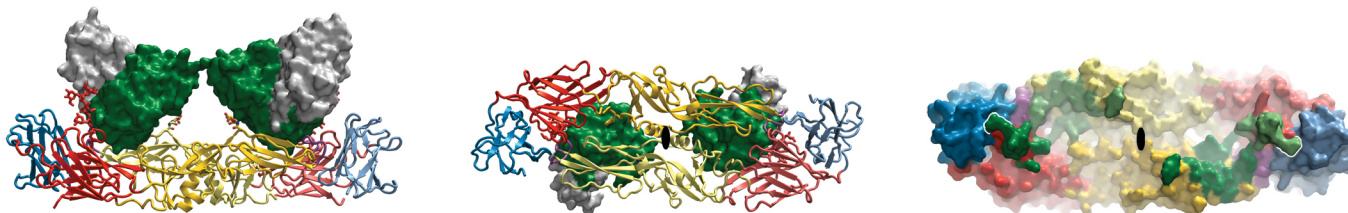
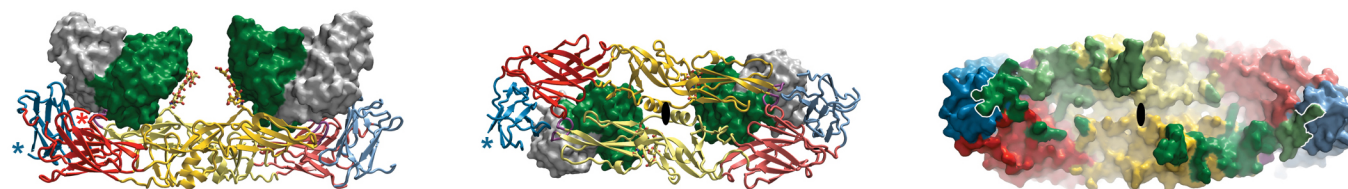
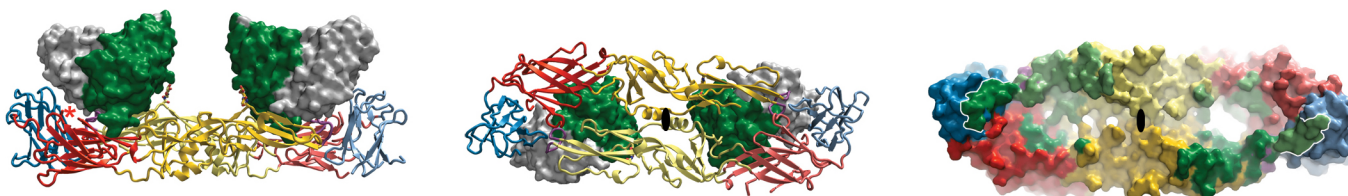
Subsequently, careful model building with COOT³⁸, alternating with cycles of crystallographic refinement with the program BUSTER/TNT³⁹, led to a final model. Refinement was constrained to respect non-crystallographic symmetry, and used target restraints (with high-resolution structures of parts of the complexes) and TLS refinement⁴⁰ depending on the resolution of the crystal (see Extended Data Table 1). Final omit maps were calculated using Phenix.Refine⁴¹ (Extended Data Fig. 7).

Analysis of the atomic models and Illustrations. Each complex was analysed with the CCP4 suite of programs³⁵. For intermolecular interactions, the maximal cutoff distance used for the interactions was 4.75 Å. Then the contacts of each residue of the Fab/ScFv or of DENV sE proteins were counted and plotted as a proportional bar above the corresponding residue.

The Ab sequences were analysed by Abysis (<http://www.bioinf.org.uk/software>) and IMGT (<http://www.imgt.org>)⁴² websites for mapping CDR/framework regions according to Kabat⁴³ and IMGT⁴² conventions, respectively. The analysis of the putative germline and somatic maturation events was done with the IMGT website (www.imgt.org).

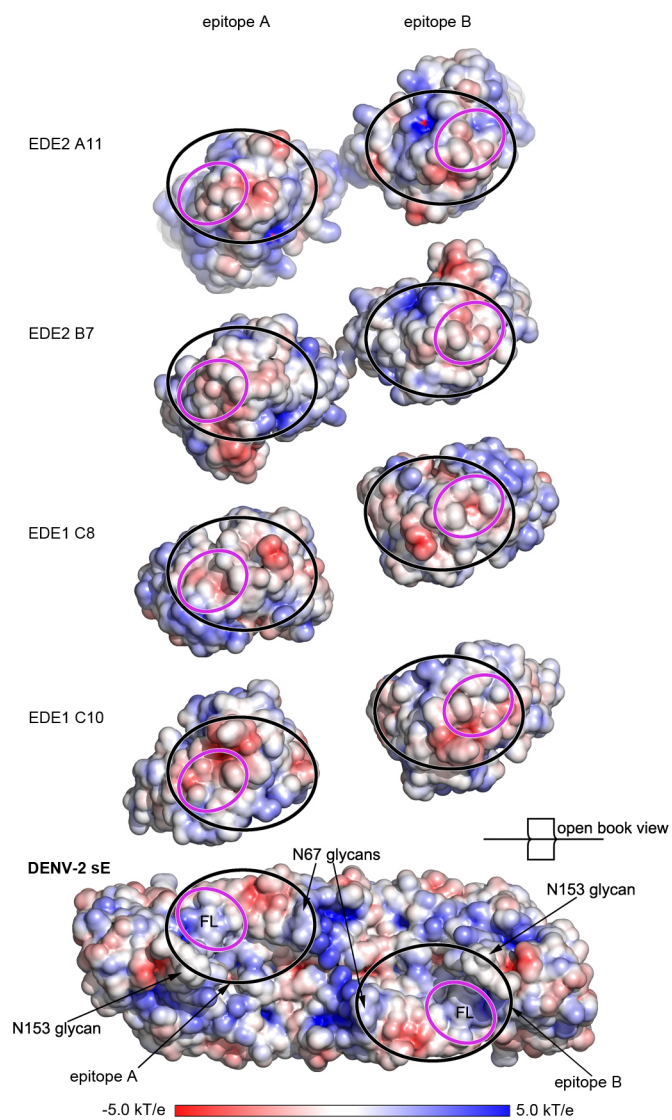
Multiple sequence alignments were calculated using Clustal W and Clustal X version 2 (ref. 44) on the EBI server⁴⁵. The figures were prepared using ESPript⁴⁶ and the PyMOL Molecular Graphics System, version 1.5.0.4 (Schrödinger) (pymol.sourceforge.net) with APBS⁴⁷ and PDB2PQR tools⁴⁸. For analysis, we created an atomic model for the DENV-2 sE dimer on the basis of chain A of sE from the complex with B7 (PDB 4UT6), which had no density breaks, to calculate the surface of the sE dimer presented in the corresponding panels in Figs 2b and 3 and Extended Data Fig. 2.

- Gilmartin, A. A. et al. High-level secretion of recombinant monomeric murine and human single-chain Fv antibodies from *Drosophila* S2 cells. *Protein Eng. Des. Sel.* **25**, 59–66 (2012).
- Backovic, M. et al. Efficient method for production of high yields of Fab fragments in *Drosophila* S2 cells. *Protein Eng. Des. Sel.* **23**, 169–174 (2010).
- Kabsch, W. XDS. *Acta Crystallogr. D* **66**, 125–132 (2010).
- Evans, P. R. & Murshudov, G. N. How good are my data and what is the resolution? *Acta Crystallogr. D* **69**, 1204–1214 (2013).
- Winn, M. D. et al. Overview of the CCP4 suite and current developments. *Acta Crystallogr. D* **67**, 235–242 (2011).
- McCoy, A. J. et al. Phaser crystallographic software. *J. Appl. Cryst.* **40**, 658–674 (2007).
- Navaza, J. Implementation of molecular replacement in AMoRe. *Acta Crystallogr. D* **57**, 1367–1372 (2001).
- Emsley, P., Lohkamp, B., Scott, W. G. & Cowtan, K. Features and development of Coot. *Acta Crystallogr. D* **66**, 486–501 (2010).
- Blanc, E. et al. Refinement of severely incomplete structures with maximum likelihood in BUSTER-TNT. *Acta Crystallogr. D* **60**, 2210–2221 (2004).
- Winn, M. D., Murshudov, G. N. & Papiz, M. Z. Macromolecular TLS refinement in REFMAC at moderate resolutions. *Methods Enzymol.* **374**, 300–321 (2003).
- Afonine, P. V. et al. Towards automated crystallographic structure refinement with phenix.refine. *Acta Crystallogr. D* **68**, 352–367 (2012).
- Lefranc, M. P. et al. IMGT, the international Immunogenetics information system. *Nucleic Acids Res.* **37**, D1006–D1012 (2009).
- Wu, T. T. & Kabat, E. A. An analysis of the sequences of the variable regions of Bence Jones proteins and myeloma light chains and their implications for antibody complementarity. *J. Exp. Med.* **132**, 211–250 (1970).
- Larkin, M. A. et al. Clustal W and Clustal X version 2.0. *Bioinformatics* **23**, 2947–2948 (2007).
- Goujon, M. et al. A new bioinformatics analysis tools framework at EMBL-EBI. *Nucleic Acids Res.* **38**, W695–699 (2010).
- Gouet, P., Courcelle, E., Stuart, D. I. & Metz, F. ESPript: analysis of multiple sequence alignments in PostScript. *Bioinformatics* **15**, 305–308 (1999).
- Baker, N. A., Sept, D., Joseph, S., Holst, M. J. & McCammon, J. A. Electrostatics of nanosystems: application to microtubules and the ribosome. *Proc. Natl Acad. Sci. USA* **98**, 10037–10041 (2001).
- Dolinsky, T. J., Nielsen, J. E., McCammon, J. A. & Baker, N. A. PDB2PQR: an automated pipeline for the setup of Poisson-Boltzmann electrostatics calculations. *Nucleic Acids Res.* **32**, W665–W667 (2004).
- Chen, V. B. et al. MolProbity: all-atom structure validation for macromolecular crystallography. *Acta Crystallogr. D* **66**, 12–21 (2010).

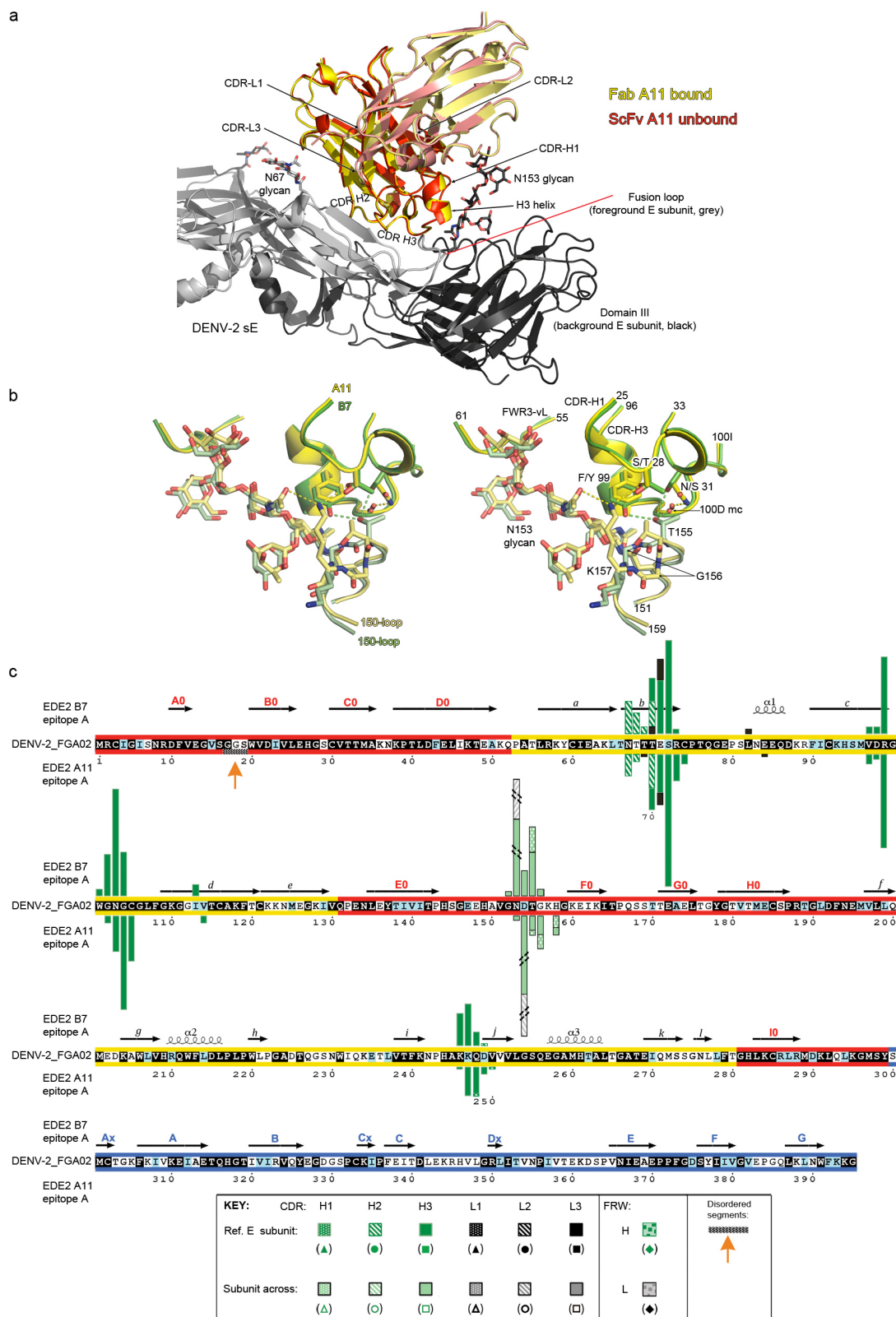
a - DENV-2 sE**b - DENV-2 sE / EDE2 B7****c - DENV-2 sE / EDE1 C8****d - DENV-2 sE / EDE1 C10**

Extended Data Figure 1 | Overall complexes and footprints of the bnAbs on the sE dimer. **a–d**, Each row corresponds to a different sE/bnAb complex (except for the first one, which shows the unliganded sE dimer) and each column displays the same orientation, as labelled. In the first two columns the sE dimer is depicted as ribbons and the bnAb variable domains as surface coloured as in Fig. 1. In the side view (left column) the viral membrane would be underneath, whereas the bottom view (middle column) corresponds to the sE dimer seen from the viral membrane with the antibodies visible across the sE ribbons. The top view (right column) shows the sE surface as presented to the immune system on the viral particle, showing the footprint of the antibodies (green) with a white depth-cuing fog. For clarity, a white outline delimits the green footprint on the blue surface of domain III. As a guide, in the top-left panel the glycan chains of foreground and background subunits are

labelled in red and black respectively. In the middle and right columns, the two-fold axis of the sE dimer is marked by a black ellipse at the centre. The fusion loop and the *ij* loop are labelled on the top-middle panel, and can be seen in the other rows in contact with the bnAbs. A red star in the left panels of rows **c** and **d** marks the location of the 150 loop, which is disordered in the complexes with the EDE1 bnAbs. This loop bears the N153 glycan recognized by the EDE2 bnAbs, as seen in row **b**, left panel (glycan shown as sticks with carbon atoms coloured red). In contrast, all the bnAbs are seen contacting the N67 glycan, with C8 displaying the most contacts (row **c**, left panel, N67 glycan as sticks with carbon atoms yellow). A blue star in row **c** shows a disordered loop in domain III. Note that EDE1 C10 (row **d**) inserts deeper into the sE dimer than the others bnAbs.



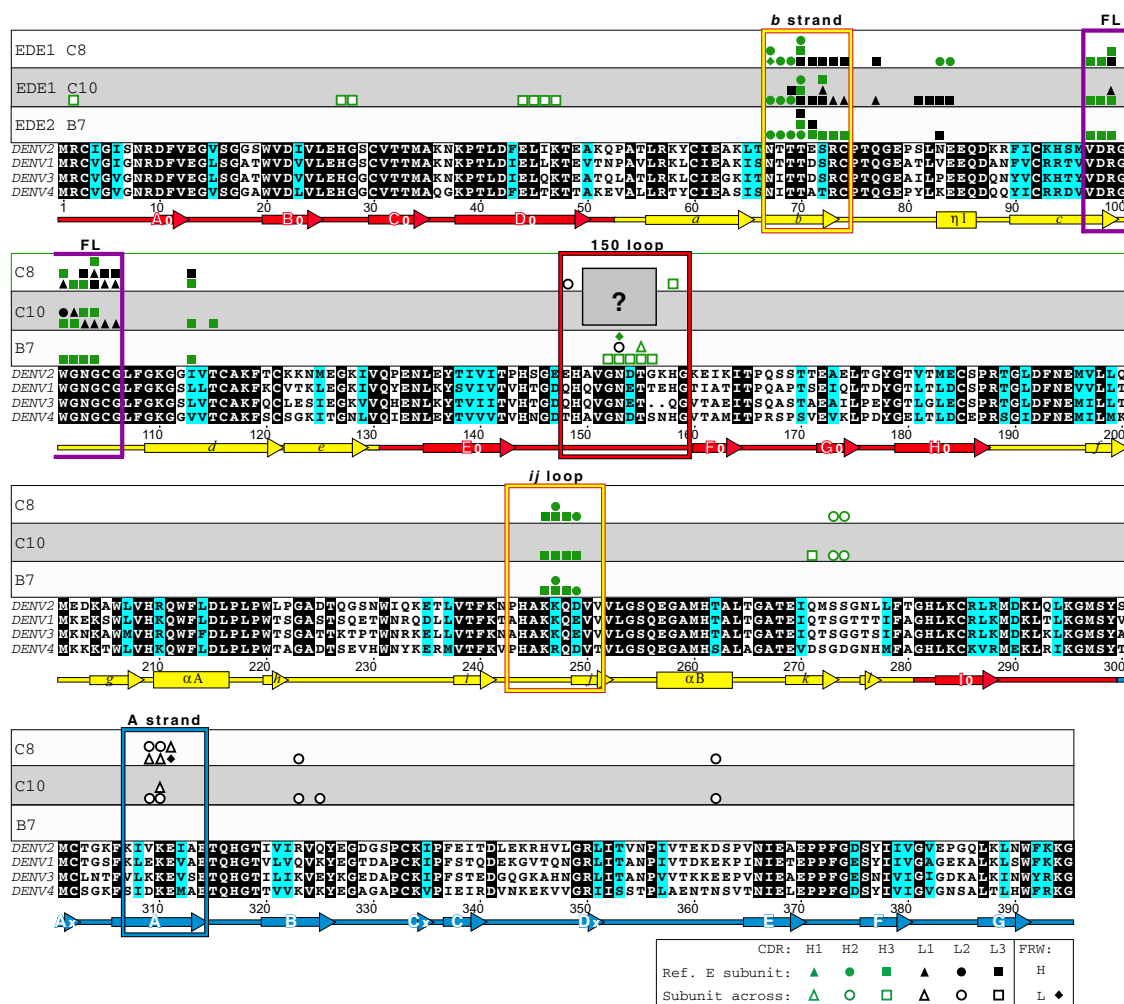
Extended Data Figure 2 | Electrostatic potential of paratopes and epitope. ‘Open book’ representation of the complexes, with negative and positive potential displayed and coloured according to the bar underneath. Because certain regions are disordered in the complexes, the unliganded DENV-2 sE dimer model, generated as described in the Methods section, was used to calculate the surface electrostatic potential of the sE dimer. Corresponding areas in contact are indicated by ovals as in Fig. 2.



Extended Data Figure 3 | Unliganded bnAb A11 and EDE2 bnAbs in interactions with DENV-2 sE. **a**, The structure of the unliganded EDE2 A11 scFv (red, 1.7 Å resolution) superposed to the variable domain of Fab A11 in complex with DENV-2 sE (yellow, 3.8 Å resolution), to show that the same conformation is retained in the sE/Fab fragment complex. **b**, Stereo view showing the superposed B7 (green) and A11 (yellow) variable domains, together with the 150 loop extracted from the structures of the corresponding Fab/DENV-2 sE complexes. Note that the main chain of the 150 loop

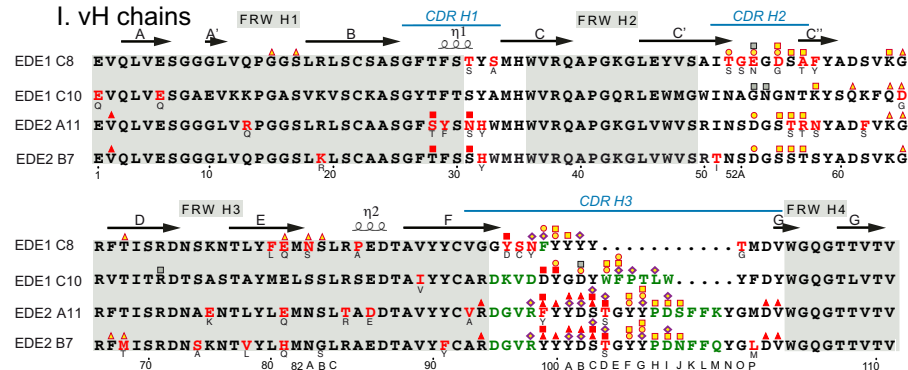
adopts different conformations in the two complexes, mainly because of the hydroxyl group the Y99 side chain in the CDR H3 of B7 makes a hydrogen bond with sE T155. A11 has a phenylalanine at this position, and so lacks the hydroxyl group. The sE protein in the complex with A11 displays the same conformation as the unliganded sE (not shown). **c**, Histograms of the atomic contacts of B7 (above the sE sequence) and A11 (below the sequence) according to the key at the bottom (see also detailed data and explanations in Supplementary Information). The secondary structure elements of the

a



b

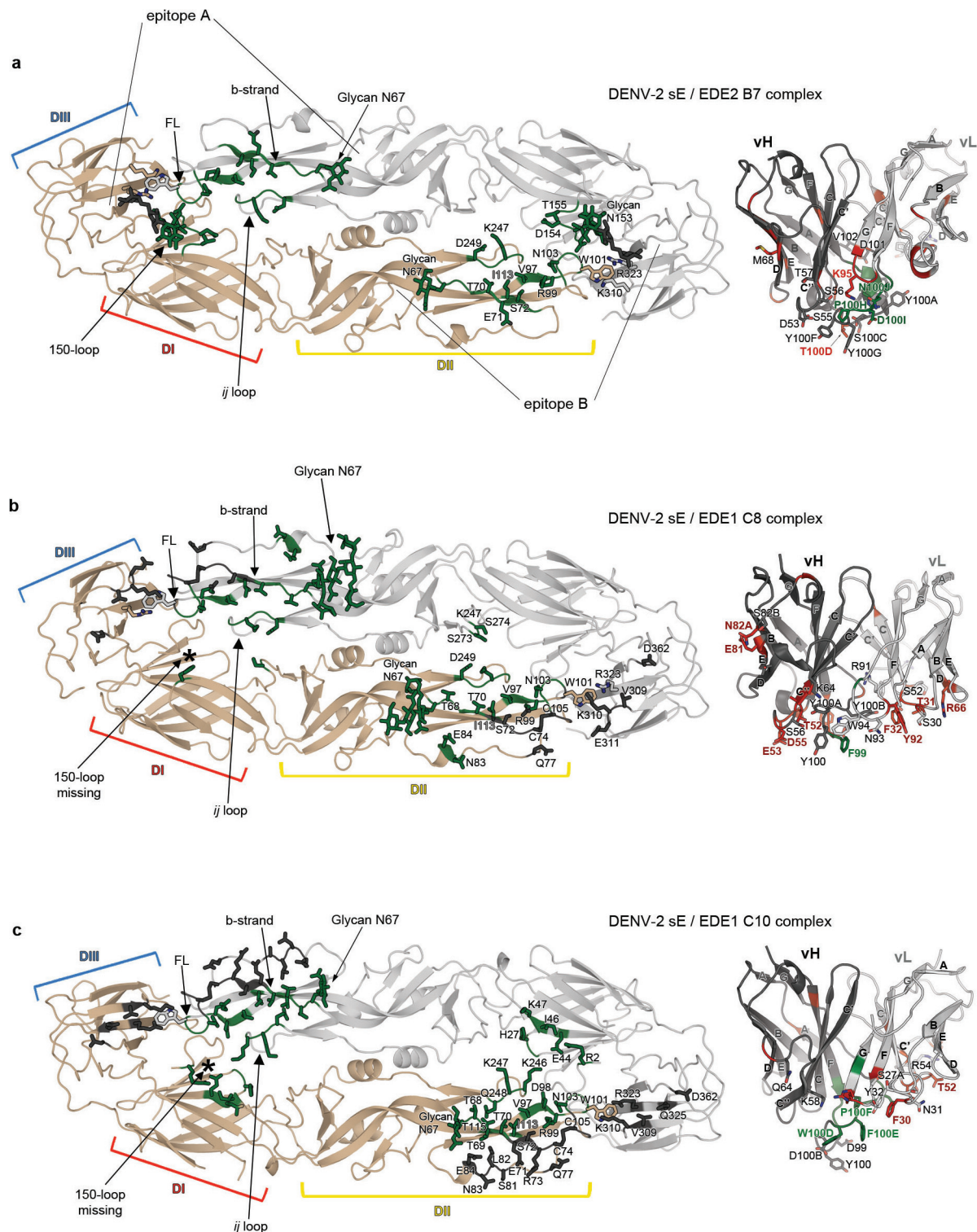
I. vH chains



Extended Data Figure 4 | Residues involved in bnAb/antigen interactions.

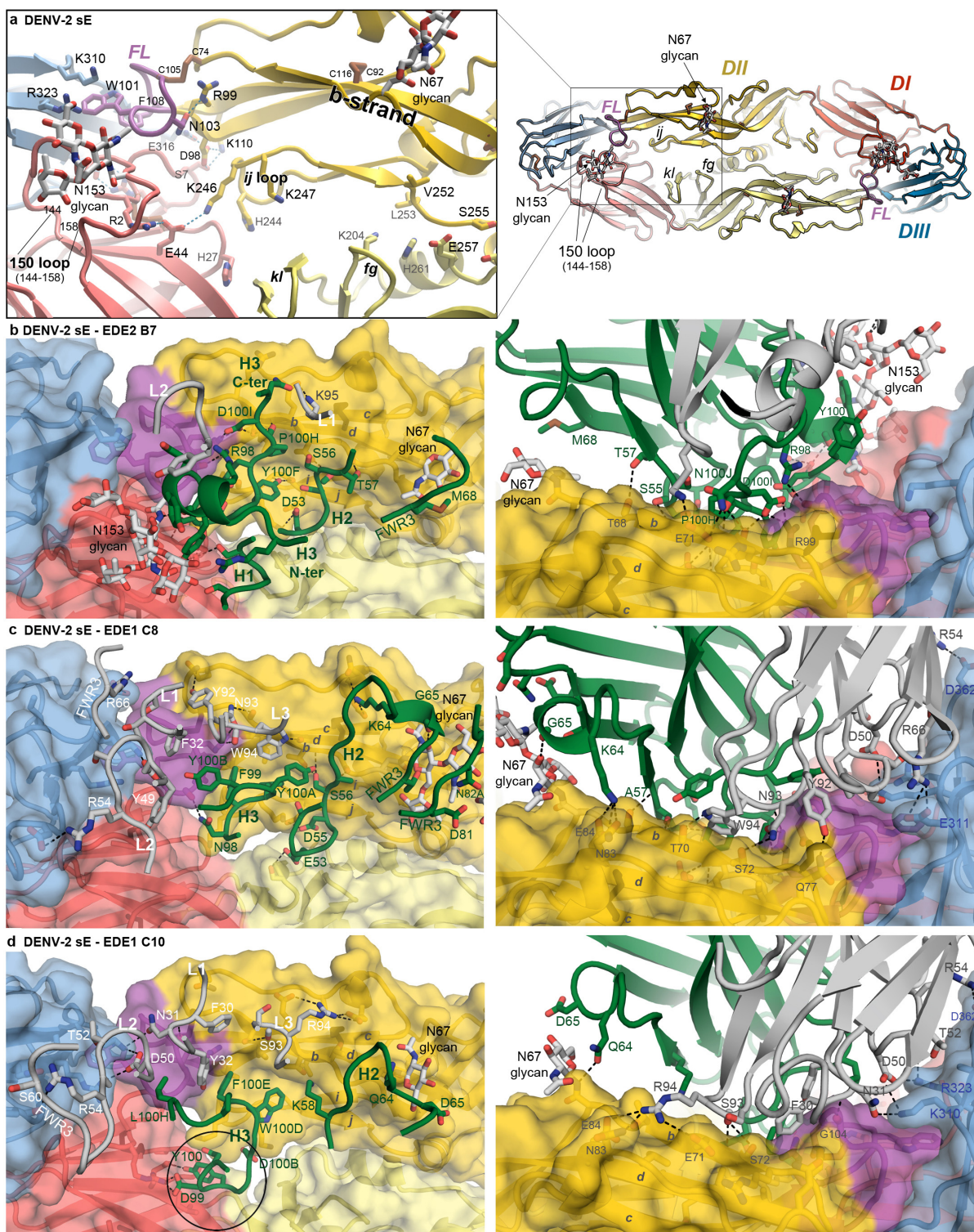
a, Amino-acid sequence alignment of sE from the four DENV serotypes, with residues in black or light blue background highlighting identity and similarity, respectively, across serotypes. Secondary structure elements are indicated underneath, with tertiary organization given by colours as in Fig. 1. DENV-2 sE residues contacted by the bnAbs are marked above, according to the code of the key (bottom-right insert). Full and empty symbols correspond to contacts on the reference subunit (defined as the one contributing the fusion loop to the epitope) and opposite subunit, respectively. Coloured boxes highlight the five distinct regions of sE making up the epitopes, matching Fig. 1c. The histogram displaying the number of atomic contacts per sE residue by each bnAb is provided as Supplementary Information. Because the EDE2 B7 and

A11 contacts are very similar, only the B7 contacts are shown here. The question mark on the 150 loop indicates residues likely to contact the EDE1 bnAbs, but which are not visible in the structure because the loop is disordered. **b**, Sequence alignment of the four bnAbs crystallized and with the framework and CDR regions in grey and white background (in Kabat numbering⁴³), respectively. Blue lines over the sequence mark the CDRs in the IMGT convention⁴². Somatic mutations are in red with germline residues in smaller font underneath. Residues arising from the recombination process are in green. A symbol above the sequence indicates the sE segment contacted, according to the key of the bottom-right inset. The secondary structure elements of the EDE1 C8 Ig β -barrels are indicated above the sequence, as guide.



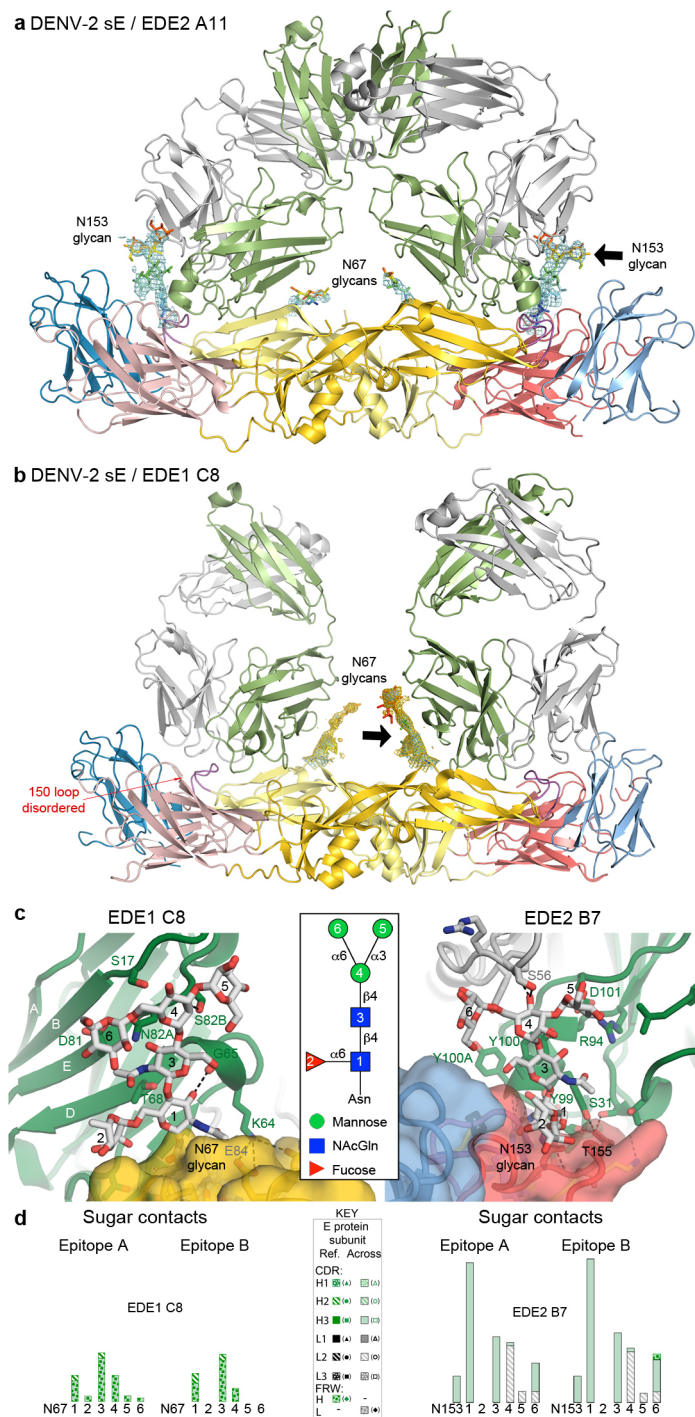
Extended Data Figure 5 | Epitopes and paratopes. The epitope area of DENV-2 sE from three different complexes is highlighted in green and dark grey, with relevant side chains as sticks, corresponding to residues interacting with the heavy and light chain, respectively (left panels). The variable domain of the corresponding bnAb is shown in side view, with interacting side chains

labelled. Heavy and light chains are in dark and light grey, respectively, with somatic mutations in red and residues that arose through the recombination process (third CDR in each chain) in green. **a**, EDE2 B7 complex; **b**, EDE1 C8 complex; **c**, EDE1 C10 complex.



Extended Data Figure 6 | Key interactions of the bnAbs with sE. **a**, The right panel shows the sE dimer in ribbons, with the framed area enlarged in the left panel to show the epitope, with main features labelled. **b**, sE dimer in complex with bnAb EDE2 B7, **c** with EDE1 C8 and **d** with EDE1 C10. The sE dimer surface is shown in a semi-transparent representation with the ribbons visible through. The glycan residues were not included in the surface, and are displayed as sticks. The relevant CDR loops of the bnAbs are shown as

ribbons with side chains as sticks on top of the sE protein, coloured as in Fig. 1. The orientation of the left panel in rows b–d corresponds to the enlargement of row a, and the right panel is a view along the arrow in Fig. 1b (main text). Hydrogen bonds are displayed as dotted lines. The circle in the left panel of **d** highlights a deep contact of EDE1 C10 CDR-H3 into the DENV-2 sE dimer (see also Extended Data Fig. 1d, left panel).



Extended Data Figure 7 | Interactions with the glycan chains. Ribbon representation of **a** the EDE2 A11 Fab and **b** the EDE1 C8 Fab in complex with DENV-2 sE, coloured as in Fig. 1. The simulated annealing omit maps contoured at 1σ (cyan) or 0.6σ (gold) show clear density for the N153 (in **a**) and N67 glycans (in **a** and **b**) (black arrows). To create an unbiased map, all glycan atoms were removed from the structures, all B factors were reset to 20 Å

and the structures were re-refined using torsion dynamics simulated annealing. Note that the antibody spans the two glycans across the dimer interface (as also shown in Fig. 1). **c**, Views down the black arrow in **a** (left panel) and the arrow in **b** (right panel), through the glycan chain. The key to the sugar connectivity and nomenclature is framed at the centre. **d**, Contacts of the sugar residues with the antibodies, coded according to the key.

Extended Data Table 1 | Crystallization conditions, data collection and refinement statistics

Crystal	DENV-2 sE	EDE2 A11 ScFv fragment	DENV-2 sE / EDE2 B7 Fab fragment	DENV-2 sE / EDE2 A11 Fab fragment	DENV-2 sE / EDE1 C8 Fab fragment	DENV-2 sE / EDE1 C10 ScFv fragment
PDB ID	4UTC	4UT7	4UT6	4UTB	4UTA	4UT9
Maximum resolution (Å)	3.1	1.7	3.2	3.85	3.0	3.2
Crystallization conditions						
Protein conc. (mg/ml)*	8	1.5	0.7	0.5	0.7	1.5
Crystallization buffer	100mM Tris pH 8.0 86 mM NaFormate 16% PEG 3,350	100mM MES pH 6.5 25% (v/v) PEG MME550 10mM ZnSO ₄ No additional cryoprotectant	100mM Tris pH 8.5 16% (w/v) PEG 400 200mM MgCl ₂ 22% Glycerol in 67% of crystallization solution	100mM Hepes pH 7.5 10% (w/v) PEG 6,000 5% (v/v) MPD Mix of Paratone-N with Paraffin Oil (1:1)	100mM Tris pH 8.5 18% (w/v) PEG 8,000 200mM Li ₂ SO ₄ 22% Glycerol in 67% of crystallization solution	100mM HEPES pH7.5 20% (w/v) PEG 8,000 22% PEG 400 in 67% of crystallization solution
Cryo-protectant solution	100 mM NaFormate 18% PEG 3,350 15% glycerol 10% PEG 400					
Crystallization method	Hanging drop	Sitting drop	Hanging drop	Sitting drop	Hanging drop	Hanging drop
Data Collection[†]						
Beamline	ESRF, ID23-2	SOLEIL, PX1	ESRF, ID29	ESRF, ID29	ESRF, ID29	SOLEIL, PX2
Space group	P 4 ₃ , 2	C 2	P 2	P 2 ₁ , 2 ₁	P 2 ₁ , 2 ₁	P 1
Unit cell a, b, c (Å)	105.4, 105.4, 165.8	62.9, 47.7, 90.7	101.3, 59, 191.6	58.8, 181.9, 204.8	59.6, 191.3, 203.6	57.5, 102.2, 131.1
α, β, γ (°)	90, 90, 90	90, 102.4, 90	90, 96.2, 90	90, 90, 90	90, 90, 90	91.5, 85.7, 96.1
Resolution (Å)	30-3.1 (3.26-3.1)	30-1.7 (1.73-1.7)	30-3.2 (3.34-3.2)	30-3.85 (4.22-3.85)	30-3.0 (3.11-3.0)	30-3.2 (3.3-3.2)
Measured reflections	301113 (15609)	91989 (2744)	136737 (16536)	102269 (22119)	204824 (20833)	89842 (8410)
Unique reflections	17615 (2395)	28835 (1467)	37500 (4534)	21168 (4997)	45639 (4492)	46477 (4332)
Completeness (%)	99.3 (96.0)	99.3 (95.5)	99.3 (99)	98.3 (98.3)	96.2 (97.6)	95.2 (96.7)
Mn(I) half-set correlation <I / σI>	ND	0.996 (0.811)	0.993 (0.716)	0.981 (0.727)	0.993 (0.560)	0.977 (0.541)
Rmerge (%)	23.9 (2.5)	8.9 (1.6)	9.2 (1.6)	5.8 (1.4)	7.9 (1.2)	5.0 (1.2)
	9.7 (60.9)	7.2 (43.6)	10.9 (64.0)	27.1 (92.5)	12.9 (101.1)	18.7 (55.5)
Structure Determination						
MR search models	1OAN	DENV-2 sE / bnAb EDE2 A11 Fab	DENV-2 sE / bnAb EDE2 A11 Fab	3KDM, 3H0T, 1OKE	3KDM, 3EYF, DENV-2 sE	1OKE
NCS	2	None	2	2	2	4
Targeting	1OAN	None	None	3H0T, 3TJE, DENV-2 sE, bnAb EDE2 A11 ScFv, DENV-2 sE / bnAb EDE2 B7 Fab	3KDM, 3EYF, DENV-2 sE, 1OAN	1OAN
Use of TLS	No	Yes	Yes	No	No	Yes
Refinement[‡]						
Rcryst. (%) / Rfree (%)	21.1 / 27.9	16.0 / 19.1	21.2 / 25.0	23.0 / 25.7	21.35 / 24.9	20.0 / 24.9
N° of Work/Test reflections	17453 / 882	28441 / 1428	37165 / 1984	21007 / 1070	45462 / 2306	46344 / 2343
N° of protein atoms	6072	2007	9681	12518	12496	19085
N° of heteroatoms	177	214	222	200	252	56
Rms deviation from ideal						
Bond lengths (Å)	0.010	0.010	0.008	0.008	0.010	0.008
Bond angles (°)	1.33	1.03	1.13	1.18	1.28	1.10
Ramachandran plot [§]						
Favoured (%)	92.1	98.0	91.3	96.1	94.9	91.5
Allowed (%)	6.7	2.0	7.0	3.8	4.8	7.2
Outliers (%)	1.2	0.0	1.7	0.1	0.3	1.3

One crystal was used to collect each of the diffraction data sets used to determine each crystal structure. DENV-2 sE: Den2_FGA-02 (GenBank KM087965). The DENV sE buffer used for all the crystallization experiments was 150 mM NaCl and 15 mM Tris pH 8. Proteins were crystallized at 18 °C.

* Protein concentration was estimated using theoretical extinction coefficients of the complexes (DENV sE + Fab or scFv). Absorbance at 280 nm ($A_{280\text{ nm}}$) of the protein solution was measured before crystallization. The theoretical extinction coefficients for individual component are as follows: DENV-2 sE-His, 1.03; bnAb EDE2 A11 ScFv, 2.08; bnAb EDE2 B7 Fab, 1.65; bnAb EDE2 A11 Fab, 1.68; bnAb EDE1 C8 Fab, 1.52; bnAb EDE1 C10 ScFv, 2.43 (see Methods for more details). Extinction coefficients were calculated without taking into account carbohydrate moieties.

† Highest-resolution shell is shown in parenthesis.

‡ Low resolution for refinements was truncated to 20 Å.

§ Ramachandran statistics were calculated with MolProbity⁴⁹.

PEG MME, poly-ethylene glycol monomethyl ether; MPD, 2-methyl-2,4-pentanediol; ND, non-determined; MR, molecular replacement; NCS, non-crystallographic symmetry; TLS, parametrization describing translation, libration and screw-rotation to model anisotropic displacements.

Extended Data Table 2 | Buried surface areas and surface complementarity in the various DENV sE–EDE complexes

	BSA Fab or ScFv			BSA DENV-2 sE					Complex	
	vH	vL	Total	Reference subunit (glycans)	Opposite subunit (glycans)	Total (Å ²)	Main chain atoms (Å ²) [†]	Total glycan BSA (Å ²)	BSA / molecule (Å ²)	SC
DENV-2 sE / EDE2 B7										
Epitope A	992.1	180.8	1172.9	621.1 (83.6)	478.4 (358.0)	1099.5	233 (21.2%)	442 (40%)	1136.2	0.728
Epitope B	1010.4	181.5	1191.9	501.8 (358.0)	604.1 (68.2)	1105.9	234 (21.2%)	426 (39%)	1148.9	0.721
DENV-2 sE / EDE2 A11										
Epitope A	945.1	199.4	1144.5	544.2 (17.80)	491.9 (359.1)	1036.1	224 (21.6%)	377 (36%)	1090.3	0.706
Epitope B	984.8	183.2	1168.0	473.4 (351.4)	587.5 (64.4)	1060.9	221 (20.8%)	416 (39%)	1114.5	0.668
DENV-2 sE / EDE1 C8										
Epitope A	744.2	492.3	1236.5	944.9 (204.9)	234.6	1197.6	362 (30.2%)	204.9 (17%)	1217.1	0.693
Epitope B	855.7	559.2	1414.9	366.4	963.3 (239.2)	1329.4	352 (26.5%)	239.2 (18%)	1372.2	0.687
DENV-2 sE / EDE1 C10[‡]										
Epitope A	706.6	623.3	1329.9	781.3 (84.5)	366.9	1148.2	351 (31%)	84.5 (7.3%)	1239.1	0.681
Epitope B	706.0	644.4	1350.4	373.2	778.3 (94.20)	1151.5	320 (28%)	94.2 (8.2%)	1251.0	0.681
Epitope C	823.7	562.6	1386.3	717.8 (90.6)	465.6	1183.4	374 (32%)	90.6 (7.6%)	1284.9	0.742
Epitope D	718.1	635.5	1353.6	374.9	788.7 (99.1)	1163.6	341 (29%)	99.1 (8.5%)	1258.6	0.668

BSA, buried surface area (in Å²) of sE protein by the Fabs or ScFv (calculated with the program 'areaimol' in CCP4); SC, shape complementarity coefficient (calculated with the program 'sc' in CCP4).

* Contribution of glycan chain to buried surface area (in Å² and as percentages).

† Contribution of main-chain atoms to buried surface area (in Å² and as percentages).

‡ There are two sE dimer-(bnAb C10 ScFv)₂ complexes in the asymmetric unit.

Tel1^{ATM}-mediated interference suppresses clustered meiotic double-strand-break formation

Valerie Garcia¹, Stephen Gray¹, Rachal M. Allison¹, Tim J. Cooper¹ & Matthew J. Neale¹

Meiotic recombination is a critical step in gametogenesis for many organisms, enabling the creation of genetically diverse haploid gametes. In each meiotic cell, recombination is initiated by numerous DNA double-strand breaks (DSBs) created by Spo11, the evolutionarily conserved topoisomerase-like protein¹, but how these DSBs are distributed relatively uniformly across the four chromatids that make up each chromosome pair is poorly understood. Here we employ *Saccharomyces cerevisiae* to demonstrate distance-dependent DSB interference in *cis* (in which the occurrence of a DSB suppresses adjacent DSB formation)—a process that is mediated by the conserved DNA damage response kinase, Tel1^{ATM}. The inhibitory function of Tel1 acts on a relatively local scale, while over large distances DSBs have a tendency to form independently of one another even in the presence of Tel1. Notably, over very short distances, loss of Tel1 activity causes DSBs to cluster within discrete zones of concerted DSB activity. Our observations support a hierarchical view of recombination initiation where Tel1^{ATM} prevents clusters of DSBs, and further suppresses DSBs within the surrounding chromosomal region. Such collective negative regulation will help to ensure that recombination events are dispersed evenly and arranged optimally for genetic exchange and efficient chromosome segregation.

We sought to elucidate the mechanisms that regulate the spatial patterning of meiotic DSBs. The conserved DNA damage response (DDR) kinase ataxia-telangiectasia mutated (ATM) inhibits excessive DSB formation in a number of organisms^{2–5}, suggesting that it might influence this process. While increased DSB formation in ATM mutants might arise from a loss of *trans*-interference^{3,4} (between chromatids), or from global derepression of Spo11 catalytic activity, some observations in *S. cerevisiae*^{6,7} can be explained by the loss of *cis*-interference^{3,5} (within chromatids; see Supplementary Discussion for further details).

To test the idea that ATM activity functions in *cis* to suppress additional DSBs within broken chromosomes^{3,5}, we employed *S. cerevisiae* to assess the frequency with which four test chromosomes are cleaved multiple times in the presence and absence of Tel1 (the budding yeast orthologue of the human ATM protein) using strains that accumulate meiotic DSBs due to deletion of *DMC1*, the meiosis-specific RecA/Rad51 paralogue⁸. Fragmented chromosomes were separated by pulsed-field gel electrophoresis (PFGE) and detected with a probe positioned in the centre of each chromosome. Fragments shorter than the distance between the probe and the closest telomere must arise from at least two DSBs on the same chromatid. In line with our predictions, such molecules increased 1.3- to 1.7-fold upon deletion of *TEL1* (Fig. 1a, b and Extended Data Fig. 1a). Moreover, we noted a nonlinear inverse correlation between the fold-increase and the fragment length (Fig. 1c), which, because there were only minor increases in the apparent frequency of broken chromosomes as measured by indirect end-labelling (Fig. 1d and Extended Data Fig. 1b), cannot solely be explained by an increase in DSBs (Extended Data Fig. 2). These data instead suggest that the closer two DSBs are, the more likely that coincident cleavage is derepressed in the *tel1Δ* strain—as expected for loss of *cis*-interference.

DSB interference has not previously been demonstrated. To investigate further the idea that Tel1 mediates DSB interference, for each of the

following analyses we compared the observed frequency of coincident DSB formation ('double-cuts') to that expected if DSBs were arising independently within the tested regions. We also used the ratio of these

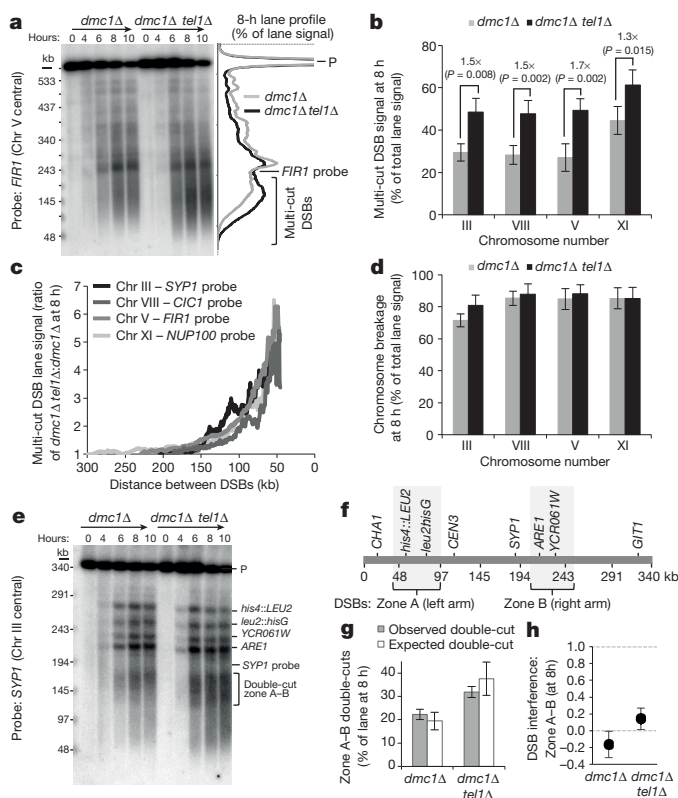


Figure 1 | Tel1 mediates distance-dependent suppression of DSB formation in *cis*. **a**, Agarose-embedded genomic DNA isolated at the indicated time points was fractionated by PFGE, transferred to nylon membrane and hybridized with a probe recognizing a central position on chromosome V. Example lane profiles depict the relative signal density for the 8-h time points. **b**, Quantification of multi-cut DSB signals, as depicted in **a**, for chromosomes III, VIII, V and XI (see Extended Data Fig. 1). Fold enrichment and statistical differences in average signal are indicated (*t*-test). **c**, Ratio of *dmc1Δ tel1Δ* versus *dmc1Δ* lane signal corresponding to multi-cut DSBs measured at 8 h (**a** and Extended Data Figs 1 and 2) plotted as a function of size. **d**, Average chromosome breakage for all four chromosomes (see Extended Data Fig. 1). **e–h**, Tel1-mediated DSB suppression spans less than 150 kb (see Extended Data Fig. 3 for details). **e**, As in **a** but hybridized with a probe recognizing a central position on chromosome III. Main DSB sites are indicated. 'Double-cut zone A–B': double-cuts formed from DSBs arising in both zones A and B on the same molecule. **f**, Physical map of chromosome III showing relative position of DSB zones and probes. **g**, Summary of observed and expected frequencies (based on independent events) of zone A–B double-cuts using data from 8 h time points. **h**, Calculated DSB interference between DSB zones A and B. **a–h**, Error bars, s.d. *n* = 3. *P* values, *t*-test.

¹Genome Damage and Stability Centre, University of Sussex, Brighton BN1 9RQ, UK.

two values to calculate the strength of DSB interference between any two given DSB loci (see Methods). Positive values indicate strong DSB interference, whereas values close to zero indicate no DSB interference (that is, independence). Negative values indicate concerted DSB formation.

Long-range: the distribution of DSBs on chromosome III allowed us to assess whether DSBs separated by large distances (~150 kilobases) are subject to interference (Fig. 1e–h and Extended Data Fig. 3). In both *dmc1Δ* and *dmc1Δ tel1Δ* strains, the frequency of chromatids cut simultaneously within the major left-arm and right-arm DSB zones was very close to that expected for independent behaviour (Fig. 1g–h). We conclude that, at this large scale, DSB events arise independently of one another in the presence and in the absence of Tel1.

Medium range: we next probed the interval between two prominent Spo11-DSB hotspots separated by ~20 kb (the widely-characterized *HIS4::LEU2* hotspot⁹ and a second site that maps within the *leu2::hisG* locus¹; Fig. 2a,b). To improve signal detection we included a second recombination mutant (*sae2Δ*) which, owing to an inability to remove Spo11, accumulates DSBs without single-stranded DNA resection, causing

DSB molecules to migrate as discrete double-stranded DNA bands^{10–12}. In both *sae2Δ* and *dmc1Δ* cells, signals ranging from 16–60 kb—indicative of DSBs arising in the vicinity of *HIS4::LEU2* and the *leu2::hisG* region simultaneously (double-cuts)—although detectable, were present at frequencies significantly below those expected for independent cleavage within the two hotspot regions (that is, positive interference; Fig. 2b–d and Extended Data Fig. 4). By contrast, double-cutting increased in both strains upon *TEL1* deletion, arising at frequencies similar to those expected for independent cleavage (Fig. 2c), and indicating a loss of interference (Fig. 2d). By comparison, in both *sae2Δ* and *dmc1Δ* strains, upon downregulation of the *MEC1* (orthologue of the human *ATR* gene) branch of the DDR checkpoint pathway (achieved by deletion of *RAD24*, the orthologue of the human *RAD17* DDR clamp loader), double-cut frequencies remained lower than expected for independent DSB formation (Fig. 2c), suggesting that interference remained largely intact (Fig. 2d).

In *dmc1Δ tel1Δ* cells, although double-cut events plateaued after ~6 h (Extended Data Fig. 5a), they were first detectable at the earliest point that single DSBs were also detectable (2.5 h), suggesting that double-cuts do not arise from the accumulation of unrepaired DSBs in *dmc1Δ* and *sae2Δ* strains. Indeed, double-cuts were also readily detectable in the otherwise recombination-proficient *tel1Δ* single mutant (~1.2% of total lane signal)—a situation that was not observed in wild-type cells (Fig. 2e). Thus, over medium distances, Tel1 suppresses the formation of adjacent DSBs on the same chromatid in both recombination-deficient and recombination-proficient cells. *TEL1* deletion also caused coincident formation of DSBs separated by 10–70 kb at other genomic loci (Extended Data Fig. 5b). While the increase in double-cutting at these loci may partly be due to increased global DSB levels, our results collectively support the view that Tel1 mediates DSB interference in *cis* over domains spanning at least 70 kb, but that do not extend to 150 kb.

Short range: to investigate the role of Tel1 at closely-spaced DSBs we focused on the *HIS4::LEU2* locus, which consists of two strong DSB hotspots separated by only ~2.4 kb (Fig. 3a). Despite such spatial proximity, molecules of ~2.4 kb were visible in the *sae2Δ* single mutant (~0.35 ± 0.07% of lane signal)—indicative of simultaneous breakage at the two sites even in the presence of a functional *TEL1* pathway (Fig. 3b–d). Deletion of *TEL1* further increased the frequency of these molecules ~14-fold (4.71 ± 1.28% of lane signal). Such double-cut molecules were also detectable in the *tel1Δ* single mutant (~0.99 ± 0.19% of lane signal), albeit at appreciably lower signal intensity owing to the transient nature of DSBs in repair-proficient cells, and to ssDNA resection causing the DSB signals to migrate heterogeneously during electrophoresis, hampering detection (Fig. 3b–d). Double-cut molecules in wild-type cells were below the detection limit of our assays.

Surprisingly, both the *tel1Δ* and the *tel1Δ sae2Δ* strain displayed substantially greater levels of simultaneous Spo11-DSB formation than expected from the measured DSB frequencies at the two sites (Fig. 3d), a phenomenon referred to as negative interference (Fig. 3e). Furthermore, the two DSBs within *HIS4::LEU2* displayed no interference in the *sae2Δ* strain even though the suppressive Tel1 pathway is presumably active (Fig. 3d, e). Thus, in contrast to the more widely spaced DSB hotspots characterized above (medium-range), DSBs within *HIS4::LEU2* do not interfere, and actually appear to form concertedly in the absence of *TEL1*.

To investigate whether this phenomenon was unique to *HIS4::LEU2*, we measured the frequency of simultaneous cleavage arising between the natural *ARE1* hotspot and each of the many minor DSB sites that flank this locus (Fig. 4a, b). In absolute terms, loss of *TEL1* activity resulted in a 9.1-fold increase in the observed frequency of double-cutting across the *ARE1* locus (Extended Data Fig. 6a). We then calculated the strength of interference between the *ARE1* hotspot and each minor site using two methods to estimate the single-cut DSB frequencies: direct measurement using Southern blotting, and that calculated using three independent Spo11-oligo data sets (two from wild-type cells^{1,13} and one from *tel1Δ*; S. Keeney and N. Mohibullah, personal communication; Fig. 4c, d,

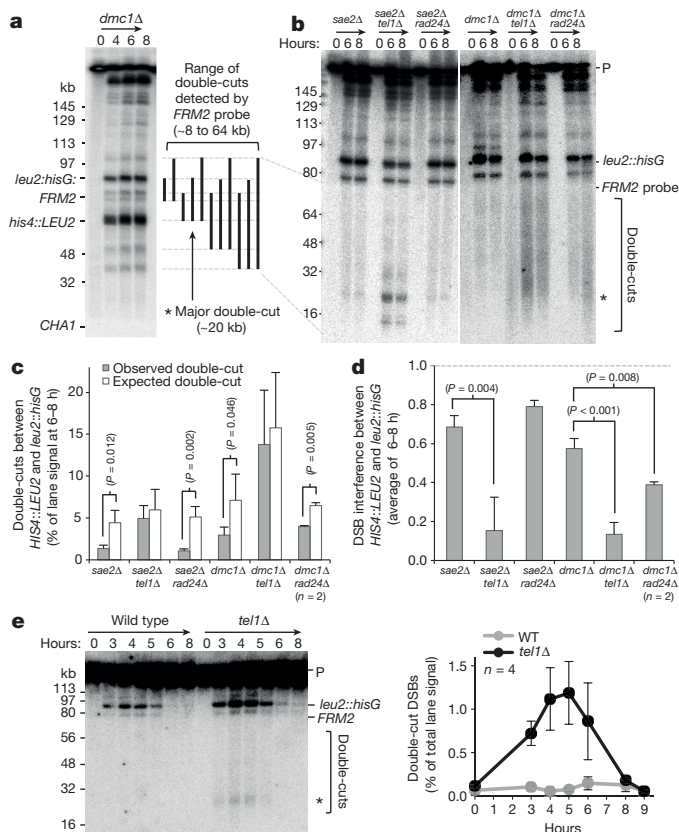


Figure 2 | Tel1 suppresses adjacent meiotic DSB formation within a 70-kb range. **a**, Example PFG with location of main DSBs (*HIS4::LEU2* and *leu2::hisG*) in left arm of chromosome III, detected by the *CHA1* probe, and diagram of the range of double-cuts detected by the *FRM2* probe in panels **b** and **e**. Major double-cut band is indicated with a star in **a**, **b**, **e**. **b–e**, Agarose-embedded genomic DNA isolated from the indicated time points and strains was fractionated by PFGE, transferred to nylon membrane and hybridized with *FRM2*. In *dmc1Δ* cells, the migration of the double-cut molecules was more variable and slightly retarded—at least in part owing to extensive ssDNA resection^{25,26}. **c**, Quantification of observed (**b**) and expected double-cut frequencies. Expected frequencies of double-cut molecules (as if forming independently) were calculated from measured single-cut frequencies (Extended Data Fig. 4). Statistically significant differences are indicated. **d**, Calculated DSB interference between *HIS4::LEU2* and *leu2::hisG* (see Extended Data Fig. 4). **e**, Detection of double-cuts by PFGE as in **b** (left panel) and quantification of double-cuts (right panel) in the indicated strains. Error bars, s.d. *n* = 3, unless indicated. *P* values, *t*-test.

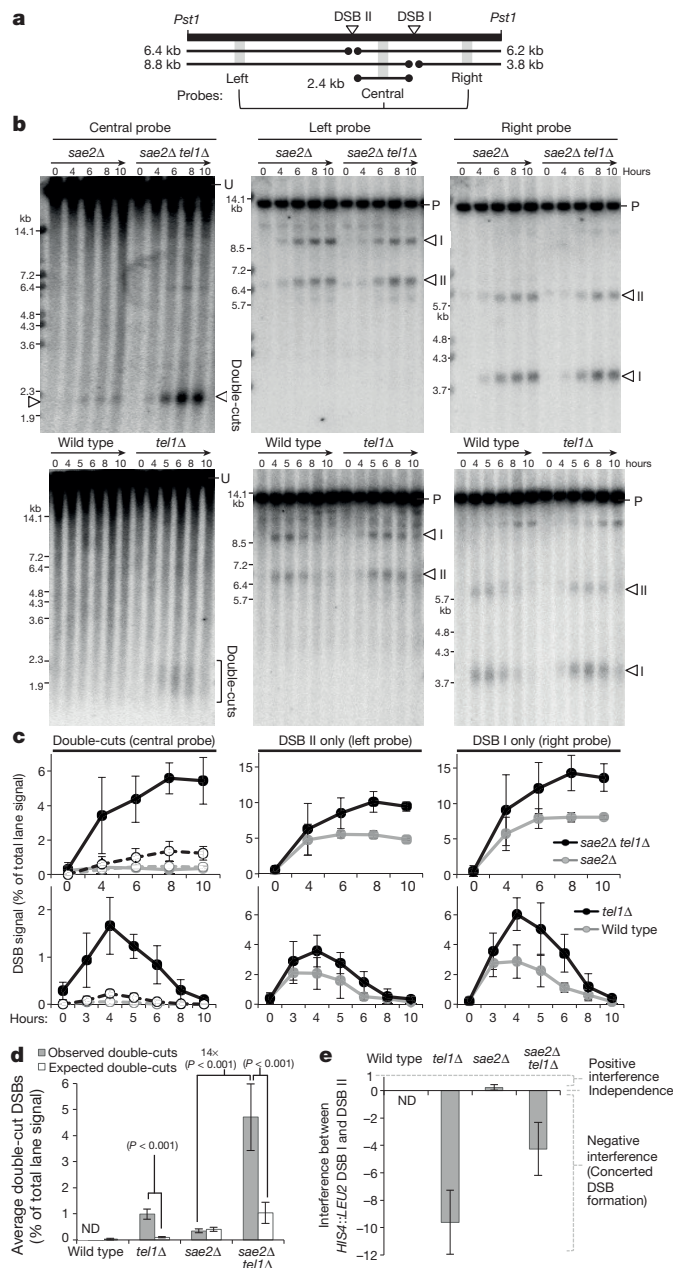


Figure 3 | Concerted DSB formation within the *HIS4:LEU2* hotspot.

a, Diagram of *HIS4:LEU2* locus showing location of DSBs, fragment sizes and probes used. **b**, Genomic DNA isolated from the indicated time points and strains was fractionated by electrophoresis, transferred to nylon membrane and hybridized with probes as indicated. U, uncut parental DNA; P, PstI-digested parental DNA. DSB signals are marked with open triangles or bracket. **c**, Quantification of DSB and double-cut signals in **b**. Left panels, for comparison, expected double-cuts frequencies (dashed lines) are plotted alongside measured double-cut frequencies (plain lines). **d**, **e**, Summary chart of observed and expected (based on independent events) double-cuts (**d**) and interference values (**e**) calculated by averaging the 3–8 h (wild type and *tel1Δ*) or 4–10 h (*sae2Δ* and *sae2Δ tel1Δ*) time points from each repeat. Wild-type double-cut data were omitted from panels **c–e** because the signal was below our detection limit. ND, not determined. **a–e**, Error bars, s.d. $n = 4$. P values, t -test.

Extended Data Fig. 6, Methods, and data not shown). In the *sae2Δ* control, sites greater than 3–4 kb from *ARE1* displayed significant positive interference, whereas a zone of reduced DSB interference was observed for those DSBs in close proximity to *ARE1* (Fig. 4c and Extended Data Fig. 6). In the absence of *TEL1*, this differential effect was dramatically

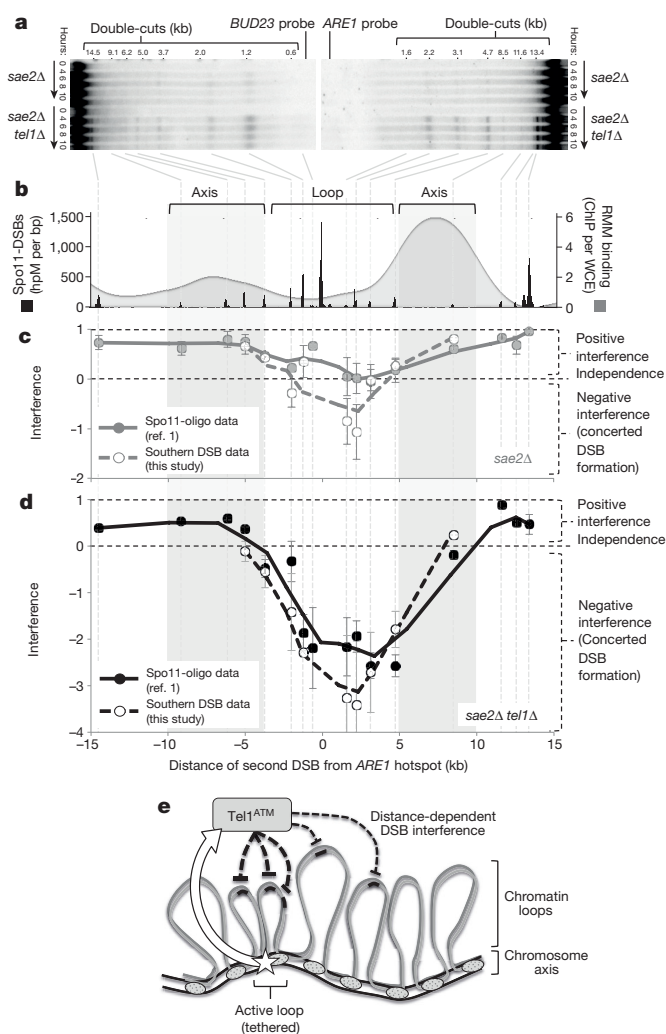


Figure 4 | Tel1 suppresses concerted DSB formation within chromatin loop domains.

a, Genomic DNA isolated from the indicated time points and strains was fractionated by electrophoresis, transferred to nylon membrane and hybridized with either *BUD23* or *ARE1* probes. **b**, Diagram of *ARE1* locus ± 15 kb showing relative RMM binding profile¹⁴ with Spo11-oligo (DSB) peaks overlaid. ChIP/WCE, chromatin immunoprecipitation/input signal; hpM/bp, hits per million reads per base pair. Inferred chromosome axes and loop sites are highlighted. **c**, **d**, The frequency of each double-cut species in **a** was quantified, and interference between each pair of DSBs plotted after using the normalized frequency of Spo11-oligos¹ at each site to estimate expected frequencies of double-cutting (solid line, see Supplementary Methods), or the measured frequency of DSB formation obtained for a subset of sites from Southern blotting experiments (dashed line, Extended Data Fig. 6). Plotted points show averages \pm standard deviation for two independent repeats (individual values within each repeat are averages of the 6–10 h time points). Plotted lines are 3-period moving averages. Comparable results were obtained when Spo11-oligo counts obtained from a second wild type¹³ or a *tel1Δ* strain were used (S. Keeney and N. Mohibullah, personal communication). Comparison of observed and expected frequencies and statistical analyses are provided in Extended Data Fig. 6. **e**, Cartoon highlighting how Tel1^{ATM} suppresses DSB formation within (heavy dashed lines) and adjacent to (light dashed lines) active loop domains.

increased: cleavage of sites greater than 5 kb from *ARE1* arose at a similar frequency to that expected (that is, no interference), whereas DSB sites much closer to *ARE1* were disproportionately elevated, with observed double-cut frequencies being \sim fourfold greater than expected if DSB formation was arising independently at each location (Fig. 4d and Extended Data Fig. 6). Collectively, we delimited a ~ 8 kb zone of strong negative DSB interference centred on the *ARE1* hotspot (Fig. 4d).

Our results suggest that the *ARE1* region is acting as a domain in which concerted DSB formation readily occurs, but which is to a large extent repressed by Tel1 activity. Recently a model for Spo11-DSB catalysis has gained favour in which short chromosomal domains, equal in size to individual chromatin loops, become tethered to the chromosome structural axis in order to trigger Spo11-DSB catalysis (the tethered loop–axis model^{14,15}). We superimposed the binding position of chromosome axis components (Rec114, Mer2 and Mei4 (RMM) profile¹⁴) onto our map of simultaneous Spo11-DSB events and observed that the peak of negative DSB interference mapped to a trough in axis-protein binding signal—indicative of the centre of a chromatin loop (Fig. 4b, c). Such a correlation between regions of strong negative DSB interference and putative loop DNA was also observed at other tested loci, *YCRO61W*, *SRB2* and *CCT6* (Extended Data Fig. 7).

We propose that our observation of negative DSB interference at close range, apparently confined within a chromatin loop domain, is a previously unconsidered expectation of the tethered loop model. Specifically, loop–axis tethering of a specific region (to create a DSB-permissive subchromosomal domain) within only a subpopulation of cells will mean that population average measures of DSB frequency become underestimates of the DSB frequency within the tethered (active) fraction. Consequently, negative interference can be explained by loss of interference within a loop that is tethered in only a fraction of the population (Extended Data Fig. 8 and Supplementary Discussion for further details). While we favour this view, it is also possible that short-range concerted DSB formation is simply a consequence of DSBs being formed in regions of increased local DSB potential that are present in only a subpopulation of cells, and which map within chromosome loop domains (because that is primarily where DSBs occur) but are not caused by them.

In summary, our observations suggest that Tel1 mediates DSB interference in *cis* over domains that span ~100 kb, via a process that may be modulated by the unique organizational structure of the meiotic chromosome (Fig. 4e). Consequently, when Tel1 activity is lost, DSBs separated by medium-to-large distances (>10 kb) form independently of each other, whereas at close range (<10 kb), Tel1 suppresses DSB clustering within domains that may be defined by the boundary of local chromatin loops.

Whereas our work strongly indicates that Tel1 mediates DSB interference in *cis*, previous work concluded that Tel1 suppresses DSB formation in *trans*⁴. We propose that these apparently distinct inhibitory roles are simply two consequences of a single process: distance-dependent inhibition of DSB formation, which—owing to their close association—is transmitted along the pair of sister chromatids (that is, in *cis* and in *trans*; see Supplementary Discussion for further details and analysis). In mouse and flies, *ATM* mutants appear to undergo increased rates of recombination initiation, failed DSB repair, and apoptosis^{2,3,16–18}. Our work predicts that these phenotypes may arise from an excess of DSBs within highly-localized active domains spanning a pair of sister chromatids³.

Recent work suggested that, in budding yeast, Rec114 (an evolutionarily conserved axis-associated accessory protein required for Spo11-DSB formation¹⁹) is negatively regulated by Tel1-dependent phosphorylation⁵. The meiosis-specific chromosomal checkpoint adaptor protein, Hop1 (similar to mouse HORMAD1-2) and histone H2A are two other targets of Mec1/Tel1-mediated regulation^{20,21}. However, double-cutting is not increased in strains harbouring non-phosphorylatable alleles of Rec114, Hop1 or H2A (V.G., R.M.A., M.J.N., unpublished observations), suggesting either that these factors act redundantly, or that DSB suppression is mediated via another target or function of Tel1.

Looking more broadly, our revelation that the strength of DSB interference varies non-uniformly with distance (Fig. 4) will have implications for the modelling of fine-scale recombination distributions in all sexually reproducing organisms, and particularly in mutants or under conditions that modulate ATM and ATR signalling. Furthermore, we note that clustered DSBs might behave as double-strand gaps—the initiators of recombination in the original model of DSB repair²².

Our study also allows us to draw a parallel with the ATM-dependent repression of programmed DSB formation during antigen receptor chain *VDJ* recombination²³. In both cases, potential cleavage sites are sequestered into active subdomains in which ATM activity suppresses concerted DSB formation²³. It is interesting to consider whether similar mechanisms regulate other types of programmed, yet ostensibly stochastic, biological events—such as firing of DNA replication origins, a process itself regulated by the ATR kinase²⁴.

Online Content Methods, along with any additional Extended Data display items and Source Data, are available in the online version of the paper; references unique to these sections appear only in the online paper.

Received 25 March 2014; accepted 27 October 2014.

Published online 5 January 2015.

- Pan, J. *et al.* A hierarchical combination of factors shapes the genome-wide topography of yeast meiotic recombination initiation. *Cell* **144**, 719–731 (2011).
- Joyce, E. F. *et al.* *Drosophila* ATM and ATR have distinct activities in the regulation of meiotic DNA damage and repair. *J. Cell Biol.* **195**, 359–367 (2011).
- Lange, J. *et al.* ATM controls meiotic double-strand-break formation. *Nature* **479**, 237–240 (2011).
- Zhang, L., Kleckner, N. E., Storlazzi, A. & Kim, K. P. Meiotic double-strand breaks occur once per pair of (sister) chromatids and, via Mec1/ATR and Tel1/ATM, once per quartet of chromatids. *Proc. Natl Acad. Sci. USA* **108**, 20036–20041 (2011).
- Carballo, J. A. *et al.* Budding yeast ATM/ATR control meiotic double-strand break (DSB) levels by down-regulating Rec114, an essential component of the DSB-machinery. *PLoS Genet.* **9**, e1003545 (2013).
- Blitzblau, H. G. & Hochwagen, A. ATR/Mec1 prevents lethal meiotic recombination initiation on partially replicated chromosomes in budding yeast. *Elife* **2**, e00844 (2013).
- Argunhan, B. *et al.* Direct and indirect control of the initiation of meiotic recombination by DNA damage checkpoint mechanisms in budding yeast. *PLoS ONE* **8**, e65875 (2013).
- Bishop, D. K., Park, D., Xu, L. & Kleckner, N. DMC1: a meiosis-specific yeast homolog of *E. coli* recA required for recombination, synaptonemal complex formation, and cell cycle progression. *Cell* **69**, 439–456 (1992).
- Cao, L., Alani, E. & Kleckner, N. A pathway for generation and processing of double-strand breaks during meiotic recombination in *S. cerevisiae*. *Cell* **61**, 1089–1101 (1990).
- Keeney, S. & Kleckner, N. Covalent protein-DNA complexes at the 5' strand termini of meiosis-specific double-strand breaks in yeast. *Proc. Natl Acad. Sci. USA* **92**, 11274–11278 (1995).
- Prinz, S., Amon, A. & Klein, F. Isolation of COM1, a new gene required to complete meiotic double-strand break-induced recombination in *Saccharomyces cerevisiae*. *Genetics* **146**, 781–795 (1997).
- McKee, A. H. & Kleckner, N. A general method for identifying recessive diploid-specific mutations in *Saccharomyces cerevisiae*, its application to the isolation of mutants blocked at intermediate stages of meiotic prophase and characterization of a new gene *SAE2*. *Genetics* **146**, 797–816 (1997).
- Thacker, D., Mohibullah, N., Zhu, X. & Keeney, S. Homologue engagement controls meiotic DNA break number and distribution. *Nature* **510**, 241–246 (2014).
- Panizza, S. *et al.* Spo11-accessory proteins link double-strand break sites to the chromosome axis in early meiotic recombination. *Cell* **146**, 372–383 (2011).
- Blat, Y., Protacio, R. U., Hunter, N. & Kleckner, N. Physical and functional interactions among basic chromosome organizational features govern early steps of meiotic chiasma formation. *Cell* **111**, 791–802 (2002).
- Barchi, M. *et al.* Surveillance of different recombination defects in mouse spermatocytes yields distinct responses despite elimination at an identical developmental stage. *Mol. Cell Biol.* **25**, 7203–7215 (2005).
- Di Giacomo, M. *et al.* Distinct DNA-damage-dependent and -independent responses drive the loss of oocytes in recombination-defective mouse mutants. *Proc. Natl Acad. Sci. USA* **102**, 737–742 (2005).
- Barchi, M. *et al.* ATM promotes the obligate XY crossover and both crossover control and chromosome axis integrity on autosomes. *PLoS Genet.* **4**, e1000076 (2008).
- Kumar, R., Bourbon, H. M. & de Massy, B. Functional conservation of Mei4 for meiotic DNA double-strand break formation from yeasts to mice. *Genes Dev.* **24**, 1266–1280 (2010).
- Downs, J. A., Lowndes, N. F. & Jackson, S. P. A role for *Saccharomyces cerevisiae* histone H2A in DNA repair. *Nature* **408**, 1001–1004 (2000).
- Carballo, J. A., Johnson, A. L., Sedgwick, S. G. & Cha, R. S. Phosphorylation of the axial element protein Hop1 by Mec1/Tel1 ensures meiotic interhomolog recombination. *Cell* **132**, 758–770 (2008).
- Szostak, J. W., Orr-Weaver, T. L., Rothstein, R. J. & Stahl, F. W. The double-strand-break repair model for recombination. *Cell* **33**, 25–35 (1983).
- Steinel, N. C. *et al.* The ataxia telangiectasia mutated kinase controls Ig κ allelic exclusion by inhibiting secondary V κ -to-J κ rearrangements. *J. Exp. Med.* **210**, 233–239 (2013).
- Toledo, L. I. *et al.* ATR prohibits replication catastrophe by preventing global exhaustion of RPA. *Cell* **155**, 1088–1103 (2013).

25. Westmoreland, J. *et al.* RAD50 is required for efficient initiation of resection and recombinational repair at random, gamma-induced double-strand break ends. *PLoS Genet.* **5**, e1000656 (2009).
26. Gray, S., Allison, R. M., Garcia, V., Goldman, A. S. & Neale, M. J. Positive regulation of meiotic DNA double-strand break formation by activation of the DNA damage checkpoint kinase Mec1(ATR). *Open Biol.* **3**, 130019 (2013).

Supplementary Information is available in the online version of the paper.

Acknowledgements V.G. was supported by an MRC New Investigator Grant to M.J.N. M.J.N. is supported by a University Research Fellowship from the Royal Society, a Career Development Award from the Human Frontiers Science Program Organisation,

and a Consolidator Grant from the European Research Council. We thank S. Keeney and N. Mohibullah for sharing unpublished observations.

Author Contributions V.G. and M.J.N. designed the experiments, analysed the data and wrote the paper. V.G., R.M.A., S.G. and M.J.N. performed the experiments. T.J.C. provided data analysis, mathematical modelling and bioinformatics support.

Author Information Reprints and permissions information is available at www.nature.com/reprints. The authors declare no competing financial interests. Readers are welcome to comment on the online version of the paper. Correspondence and requests for materials should be addressed to M.J.N. (m.neale@sussex.ac.uk) or V.G. (v.garcia@sussex.ac.uk).

METHODS

Yeast strains and culture methods. Meiotic cultures were prepared as described²⁶. Strains were derived from SK1 using standard techniques. *sae2Δ*, *exo1Δ*, *dmc1Δ* and *tel1Δ* are full replacements of the open reading frame with kanMX4 or hphNT2. A full strain list is provided in Extended Data Table 1.

Molecular techniques. DSB signals were detected via hybridization with specific DNA probes (detailed in Extended Data Table 2) after Southern blotting genomic DNA fractionated in agarose gels using standard techniques. For chromosome-scale analysis, genomic DNA was isolated in agarose plugs^{26,27}. Radioactive signals were collected on phosphor screens, scanned with a Fuji FLA5100, and quantified using ImageGauge software.

DSB analysis by Southern blotting. Genomic DNA was isolated from aliquots of synchronously sporulating cultures as described previously²⁸ but with minor modifications. Briefly, spheroplasts were prepared in 1 M sorbitol, 0.1 M EDTA, 0.1 M NaH₂PO₄ pH 7.5, 1% BME and 200 µg ml⁻¹ zymolyase 100T for 1 h at 37 °C, and lysed by adding SDS to 0.5% and proteinase K to 200 µg ml⁻¹ with incubation for 4 h to overnight at 60 °C. Protein was removed by mixing with an equal volume of phenol:chloroform:isoamyl alcohol (25:24:1), and nucleic acids precipitated by adding one-tenth volume of 3 M sodium acetate pH 5.2 and an equal volume of 100% ethanol. Precipitates were washed in 70% ethanol and dissolved in 1× TE overnight at 4 °C. RNase was added at 100 µg ml⁻¹, incubated for 60 min at 37 °C, genomic DNA was reprecipitated with ethanol/sodium acetate and DNA pellets were left to dissolve in 1× TE overnight at 4 °C. Signals were detected by Southern blotting of genomic DNA after fractionation on agarose gels as described previously²⁸.

For measuring the DSBs frequencies ('single-cuts') at various locations (for Figs 3, 4 and Extended Data Figs 6, 7), genomic DNA was digested with the appropriate restriction enzyme, fractionated on agarose in 1× TAE for ~18 h, transferred to nylon membrane under denaturing conditions, and hybridized with a probe allowing detection of DSBs to be quantified (as indicated in Extended Data Table 2).

For measuring the frequency of double-cuts (for Figs 3, 4 and Extended Data Figs 6, 7) undigested genomic DNA was fractionated and transferred using similar conditions. Membranes were hybridized with probes located between DSBs of interest (as indicated in figures and detailed in Extended Data Table 2).

Analysis of double-cutting at the *HIS4:LEU2* locus (Fig. 3) necessitated taking into account of the fact that the strains used in this study contain three copies of the *LEU2* gene: at the *his4X::LEU2*, *leu2::hisG* and *nuc1::LEU2* loci. Specifically, because the probe designed to detect double-cuts between sites I and II within the *his4X::LEU2* hotspot recognizes these three loci, numerous cross-reacting bands arise when probing DNA digested with restriction enzymes. Therefore undigested DNA was fractionated and transferred as for other loci. However, double-cut values recorded by this method were multiplied by three to correct for the fact that only ~1/3rd of the uncut parental DNA signal originated from the *HIS4:LEU2* locus. We note that double-cut frequencies measured using PstI-digested DNA were very similar to when using undigested DNA, but resulted in blots that were more complicated to analyse (data not shown). Radioactive signals were collected on phosphor screens, scanned with a Fuji FLA5100, and quantified (ImageGauge software, FujiFilm). Background subtraction was performed as described below.

DSB analysis by PFGE. DNA was prepared in agarose plugs as described^{26,27}. For PFGE on Fig. 1 and Extended Data Figs 1 and 3, chromosomes were fractionated using a CHEF-DRIII PFGE system (Bio-Rad) using the following conditions: 1.3% agarose in 0.5× TBE; 14 °C; 6 V cm⁻¹; switch angle 120°; switch time of 20–60 s for 28 h. For PFGE on Fig. 2a, b and Extended Data Fig. 4, the following conditions were changed: switch time of 30 s for 3 h and 3–6 s for 37 h. For PFG on Fig. 2e and Extended Data Fig. 5: switch time of 30 s for 3 h and 3–6 s for 22 h. After transfer to nylon membrane under denaturing conditions^{26,27}, membranes were hybridized with DNA probes specific to: central, left and right sub-telomeric regions of four chromosomes (Fig. 1, Extended Data Figs 1 and 3); the *FRM2* region between *HIS4:LEU2* and *leu2::hisG* (Fig. 2 and Extended Data Figs 4 and 5a); or to regions between specific DSB sites on chromosome V (*POL5*), chromosome IX (*DOT5*), or chromosome III (*CTR86* and *YCR061W*) (Extended Data Fig. 5b). Probe details are listed in Extended Data Table 2. We note that due to small differences in the length of chromosome IX between otherwise isogenic isolates, DSB signals migrate at slightly different positions in the panel of strains in Extended Data Fig. 5. The positions of expected double-cuts are not affected by these differences, however, because the relative distance between each DSB is unaltered regardless of absolute chromosome length. Radioactive signals were collected on phosphor screens, scanned with a Fuji FLA5100, and quantified (ImageGauge software, FujiFilm). Background subtraction was performed as described below.

DSB and double-cut quantification. Radioactive signals were collected on phosphor screens, scanned with a Fuji FLA5100, and quantified using ImageGauge software. Background signal caused by exposure fogging and non-specific membrane background (based on vacant areas of the blot) was removed using linear subtraction. The contribution of sheared parental DNA to DSB and double-cut signal was

removed using a gradient drawn along the lane profile starting from the base of the parental band down to the lane end. Signal above this cut-off were quantified as specific signal (DSBs or double-cuts). For quantification of double-cut molecules on membranes obtained from undigested DNA, signal that was retained in the wells (10–30% of the total lane signal) was added to, and treated as if it were, parental signal. This latter correction assumes that only parental DNA, and no double-cut DNA, is selectively retained in the well. In reality, some double-cut species probably do also get retained in the well, suggesting that our double-cut measurements may be slight underestimates.

Measurement of distance-dependent increases in multi-cut signal ratio. For Fig. 1c, for each chromosome, the signal intensity (expressed as a proportion of total lane signal) running through the multi-cut region (8 h time points from Extended Data Fig. 1a) of the *tel1Δ dmc1Δ* samples were each divided by the same signal obtained from the *dmc1Δ* control sample. The resulting ratio was plotted on the y axis against apparent double-cut length (in kb) on the x axis. The latter values were based on the approximate migration of the signal intensity on the PFG relative to lambda concatemer molecular weight markers. Due to the very low signal intensities towards the very bottom of the gels (and subsequently very erratic ratio calculations), the presented data was trimmed at ~50 kb. Double-cut signal length is indicative of the relative distance between any two given DSBs. Loss of Tel1 activity disproportionately increases the frequency of the shorter double-cut products (with little effect on fragments >100 kb), suggesting that Tel1 mediates distance-dependent DSB interference in *cis*. We note that owing to the fact that molecules with ssDNA regions migrate more slowly during PFGE²⁵ (that is, DSBs and double-cuts with resected DNA ends), the actual x axis (kb) values presented may be slight overestimates (perhaps +25%), and thus the distance that Tel1-dependent suppression is propagated may be somewhat shorter than the data make it appear.

To test whether the nonlinear increase in double-cutting frequency for shorter molecules could alternatively be explained by increases in DSB formation associated with any change in DSB interference, we developed a computer program that simulates DSB formation on a linear model of chromosome V (576 kb). This program was initially written in Sinclair BASIC using a plugin for the TextMate editor (<http://macromates.com/>) and the FUSE emulator for MacOSX (<http://fuse-emulator.sourceforge.net/>), and subsequently rewritten in MATLAB (<http://www.mathworks.co.uk/>). The simulation iterates 1 million times for each of the mean values of 2.5, 3, 3.5, and 4 DSBs per chromatid using DSB frequencies (per round of simulation) described by the Poisson distribution for the specified mean. To simulate the frequency distributions of fragments detected by an interstitial probe, tallies were made of only those fragments that include the simulated probe position (*FIR1* at position ~220 kb). Subsequently, ratios were calculated for each position within each of these simulated distributions and equivalent simulated distributions generated with mean DSB frequencies 1.5–4-fold greater. See Extended Data Fig. 2 for further details of our analysis. MATLAB code for this simulation is available on request.

Calculations of DSB interference. For calculations of interference between the left (zone A) and right (zone B) arm of chromosome III (Fig. 1e–h and as described in Extended Data Fig. 3), total DSB frequencies in each zone were measured using *CHA1* and *GIT1* probes, respectively. Expected frequencies of coincident cutting were obtained by multiplying these values. Observed frequencies of coincident cutting were estimated by measuring the total signal falling in a ~120–200 kb window (the approximate distance between zones A and B) after probing using the central, *SYPI* probe. Mean and standard deviation of the DSB frequencies for each time point are those of the three experimental repeats. A two-tailed *t*-test was used to compare the observed and expected samples. Although no time point showed statistically significant interference (neither positive nor negative), there were some notable trends: *dmc1Δ* cells display moderate negative interference at early time points, plateauing over time to display independence. Weak negative interference at early time points is actually expected, since at these time points, it is probable that only a subfraction of cells have initiated DSB formation, and thus expected double-cutting (calculated using the population average DSB frequency, which includes these inactive cells) will be an underestimate of that observed in the active fraction of cells. By contrast, *dmc1Δ tel1Δ* displays more positive interference than *dmc1Δ TEL1*⁺, also increasing with time. Although this might seem counterintuitive compared to the rest of the *tel1Δ* observations made in this study, we believe it is an artefact of the analysis, and is explained by the fact that in *dmc1Δ tel1Δ* cells the frequency of additional DSBs in the central zone (creating the smeared 50–100 kb zone towards the bottom of the gel in Extended Data Fig. 3g) are moderately increased at all time points compared to *dmc1Δ*, thus potentially cutting the 'zone A–B double-cuts' into smaller fragments. As a result, our calculation of interference moderately underestimates the frequency of double-cutting in zone A and zone B simultaneously—and more so over time as total DSB frequency increases. Although not perfect in numerical value, we believe that these analyses are sufficient to

demonstrate that there is little or no measureable interference between zone A and zone B on chromosome III.

For calculations of interference between *HIS4::LEU2* and *leu2::hisG* (Fig. 2, and as described in Extended Data Fig. 4), total DSB frequency across the entire *HIS4::LEU2* locus (both DSB sites plus two telomere-proximal DSBs) and across the *leu2::hisG* and two flanking minor hotspots (within ~10 kb) were measured using PFGE in the various strains and the resulting values were multiplied to obtain an expected frequency of double-cutting (see Extended Data Fig. 4 for all calculations and statistical analysis). DSB frequencies for each repeat were averages of the 6–10 h time points, and the mean and standard deviation are those of the three experimental repeats. A two-tailed *t*-test was used to compare the observed and expected samples.

For calculations of interference between the two DSBs within the *HIS4::LEU2* locus (Fig. 3), double-cut signals derived from the central (*LEU2*) probe were multiplied by three to take into account that this probe hybridizes to three parental genomic locations (*HIS4::LEU2*, *leu2::hisG*, *nuc1::LEU2*). Expected frequencies of double-cutting were calculated by multiplying the frequency of DSB I and DSB II as measured using probes on the right and left of the hotspot respectively (Fig. 3c). An independent method to estimate double-cutting frequency, based on the observed difference in the frequency of DSB site I or site II when using left versus right probes, yielded similar values (also yielding negative interference), but appeared more prone to quantification error. Details of this method are available on request.

For calculations of interference across the *ARE1* locus (Fig. 4 and Extended Data Fig. 6), two methods were employed to calculate expected double-cut frequencies. Primarily, we converted Spo11 oligo counts¹ (reads per million; RPM) at individual DSB sites to % DSBs by normalizing to the *BUD23-ARE1* DSB signal measured by Southern blotting analysis, where *BUD23-ARE1* (2,721 RPM) = $8.37 \pm 0.53\%$ DSBs (*sae2Δ*) or $13.2 \pm 0.39\%$ DSB (*sae2Δ tel1Δ*). Expected double-cut frequencies were then calculated by multiplying the frequencies of DSB formation at the test site and at the *ARE1* hotspot. Comparable DSB interference values were obtained when Spo11-oligo counts obtained from a second wild-type data set¹³ were used, and when unpublished Spo11-oligo counts from a *tel1Δ* strain were used (data not shown; S. Keeney and N. Mohibullah, personal communication), indicating the degree of robustness of our analysis, and highlighting the fact that DSB frequencies vary relatively uniformly in the presence or absence of *TEL1*. Nevertheless, to independently confirm these findings, we used Southern blotting to directly measure the individual DSB frequencies at nine of the DSB sites that flank *ARE1* and calculated expected double-cut frequencies as above. This latter method, which in principle is more accurate because it directly assesses DSB frequency at each site using the same genomic DNA samples used to also measure observed double-cutting (and therefore precisely estimates expected double-cutting in *sae2Δ* and *sae2Δ tel1Δ* strains), produced results that agreed very well with the analysis using normalized Spo11-oligo data sets (see Fig. 4 and Extended Data Fig. 6 for a comparison). DSB and double-cut frequencies for each repeat were averages of the 6–10 h time points, and the mean and standard deviation are those of the three experimental repeats. A two-tailed *t*-test was used to compare the observed and expected samples.

In Extended Data Fig. 7, where possible we used Southern blotting to directly measure the individual DSB frequencies at each DSB site in *sae2Δ* and *sae2Δ tel1Δ* strains (using the average value across the 6–10 h time points), and used this value to calculate expected frequencies of double-cutting. However, there were a few DSB sites that were either below signal detection by Southern blotting, or that proved refractory to probes/digest combinations. For these sites we converted the reported Spo11-oligo counts¹ to % DSB frequency as follows:

For the analysis of interval A in Extended Data Fig. 7d–f, the frequency of Spo11-oligos at the *BRL1-PUT2* locus (138 RPM) was converted to an estimated DSB frequency of $0.38 \pm 0.03\%$ in *sae2Δ* and $0.41 \pm 0.03\%$ in *sae2Δ tel1Δ* based on normalizing the frequency of Spo11-oligos at the main *SRB2-NCPI* hotspot (3,639 RPM) to $10.01 \pm 0.76\%$ DSBs (*sae2Δ*) or $10.8 \pm 0.68\%$ DSBs (*sae2Δ tel1Δ*) following direct measurement of DSB formation at the *SRB2-NCPI* hotspot using Southern analysis.

For the analysis of intervals B, C, and D in Extended Data Fig. 7g–i, the frequency of Spo11-oligos at the respective loci (177 RPM, 169 RPM, and 400 RPM) were converted to estimated DSB frequencies of 0.63%, 0.60%, and 1.42% in *sae2Δ* and 0.83%, 0.79%, and 1.87% in *sae2Δ tel1Δ* based on normalizing the frequency of

Spo11-oligos at the main *YDR186C-CCT6* hotspot (3,997 RPM) to 14.15% DSBs (*sae2Δ*) or 18.72% DSBs (*sae2Δ tel1Δ*) following direct measurement of DSB formation at the *YDR186C-CCT6* hotspot using Southern analysis.

Potential caveats with double-cut quantification using the methods described.

Our high-resolution analysis of interference in Fig. 4, Extended Data Figs 6, 7 assesses the frequency of coincident DSB formation at any pair of tested DSB sites (double-cuts) compared to the frequency of expected coincident cutting calculated by multiplying the measured single cut DSB frequencies at the pair of sites being tested. On any given side of a strong hotspot, double-cuts of increasing length are measured using the same probe (anchored close to a major DSB hotspot). A caveat of this method is that as the second site becomes more distant from the first (the anchor point), the ability to detect the assayed double-cut product will be impeded by the presence of any intervening additional DSB. However, for the genomic loci we have investigated, this small systematic error will have minimal impact on our data collection, as explained in detail below.

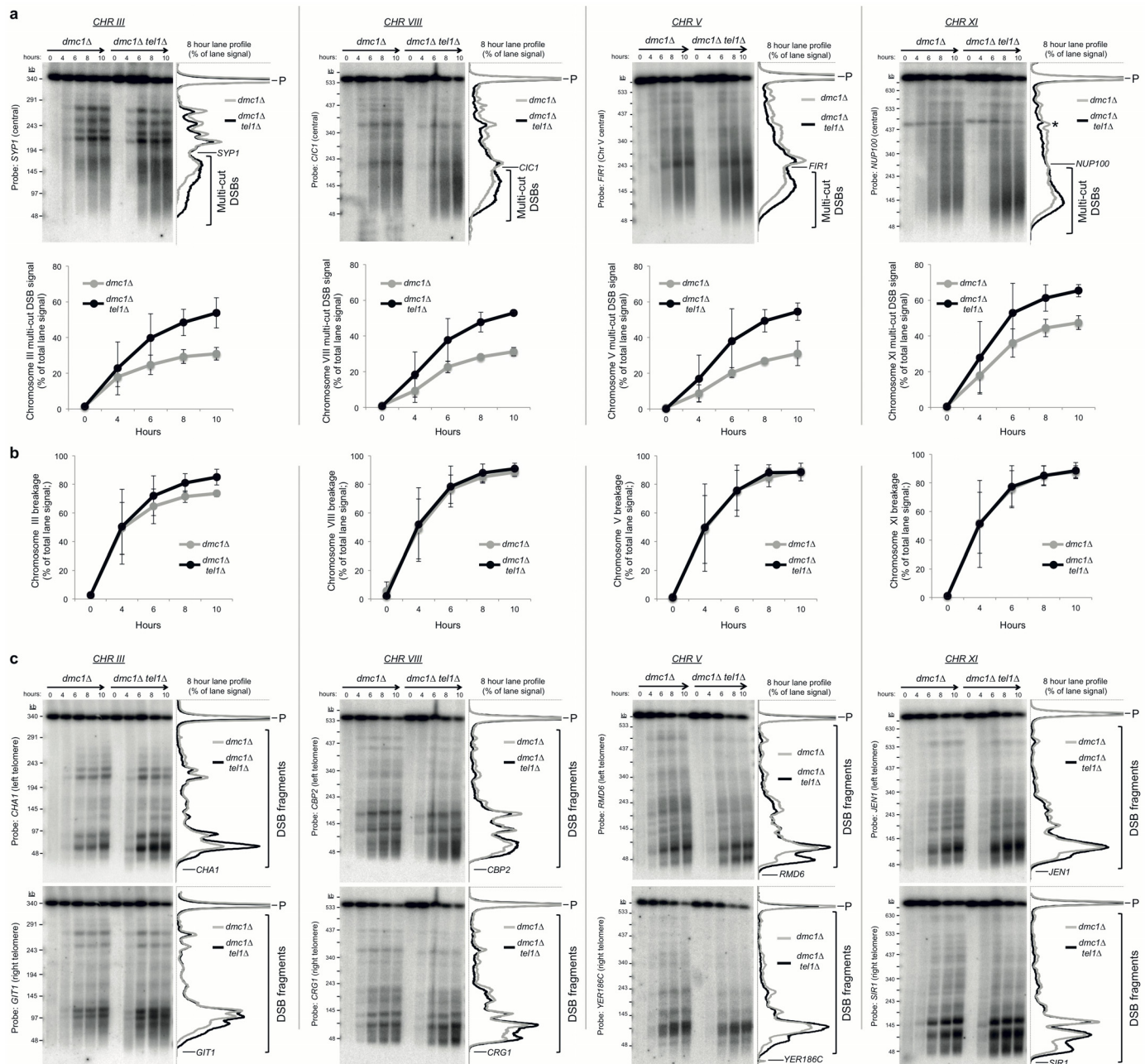
Given a molecule with DSBs arranged in linear order: A, B, C. If all DSBs form independently, the likelihood of an intervening DSB “B” cutting a molecule that has already been cut at site A and C, is directly proportional to the frequency of DSB formation at “B”. If DSB B = 5%, the observed frequency of A–C double-cuts will actually be only 95% of its actual value (5% of the time it is cut by B). Thus the corrected frequency of double-cut A–C is obtained by dividing the observed value by 0.95 (= multiplied by 1.053). Note that many interstitial DSBs are far weaker than 5%, and therefore will have an even lesser effect (see Extended Data Fig. 6 column D and N for examples of DSB frequencies across the *ARE1* locus). This means that larger double-cuts are only very weakly underestimated (unless the sum of all the intervening cuts is very large, which in general is not true; see comment earlier). Even if we were to attempt to correct for this systematic error, it would result in only a subtle increase in the frequency of double-cuts in the larger range, resulting in a slightly wider and stronger spread of reduced/negative interference in *tel1Δ*. Note that this correction will not fundamentally change our observation that negative interference is centred within a loop.

Alternatively, if DSBs are forming concertedly (as we propose occurs in loop domains), then the frequency that A–C is cut by B is not proportional to the population average frequency of DSBs at B, but instead, A–C will be cut at whatever frequency B cuts in situations when A (and/or C) are activated. In this scenario, A–C might be more severely underestimated. As above, while this might result in a pattern of negative interference that spreads more broadly and more strongly than depicted in Fig. 4, it again will not change the observation of negative interference in the loop. Moreover, if negative interference is indeed restricted to loops (as we propose in this manuscript), the apparently disproportionate underestimate in double-cuts due to intervening DSBs will only be true of DSBs within the activated region. Outside of this concerted region, we would expect DSBs to behave independently (and have less impact, as above).

We note that using both correction methods (independent DSBs or concerted DSBs) will actually strengthen the phenomenon of negative interference that we observe in the absence of *TEL1*. Our small underestimate of double-cutting might also explain why weak interference is still retained over moderate ranges (>10 kb) even in the absence of *TEL1* (that is, such weak interference that remains may be due to moderately underestimating long double-cuts, rather than actual retained interference; observed in both Fig. 2d and Fig. 4d).

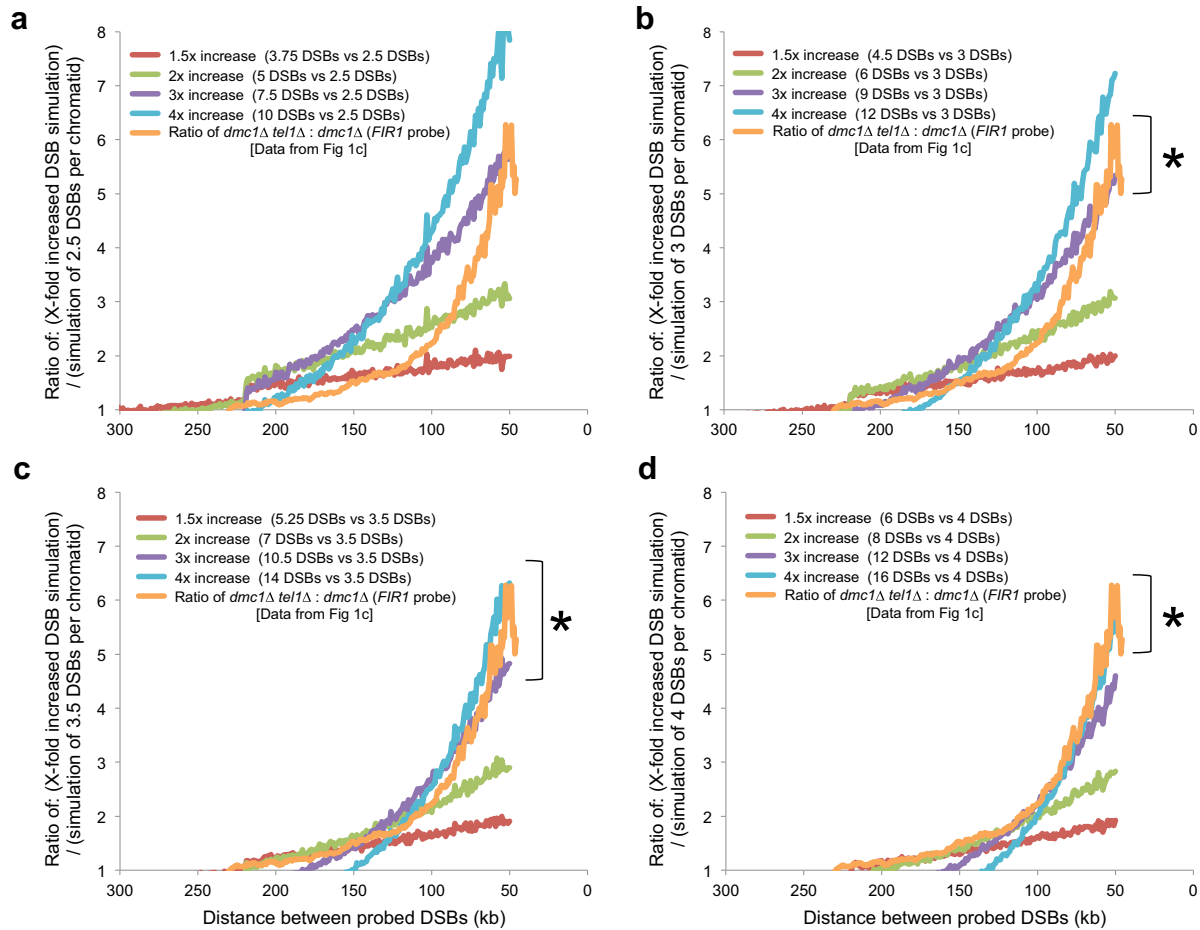
Bioinformatics. Raw Spo11-oligo data sets¹ containing signals at 1-bp step sizes were smoothed via Hann windows of varying size and zero values were filtered/removed to reduce file size via grep commands. Mei4-HA, Mer2-HA and Rec114-HA ChIP/WCE signals (sampled at *t* = 4 h and normalized by the authors¹⁴) were averaged with equal weighting and a continuous and smoothed data set was constructed via spline interpolation on MATLAB R2013+. Resulting data sets were exported directly into .bedGraph files and additional .BigWig files were created via the precompiled UCSC bedGraphToBigWig tool.

27. Murakami, H., Borde, V., Nicolas, A. & Keeney, S. Gel electrophoresis assays for analyzing DNA double-strand breaks in *Saccharomyces cerevisiae* at various spatial resolutions. *Methods Mol. Biol.* **557**, 117–142 (2009).
28. Garcia, V., Phelps, S. E., Gray, S. & Neale, M. J. Bidirectional resection of DNA double-strand breaks by Mre11 and Exo1. *Nature* **479**, 241–244 (2011).



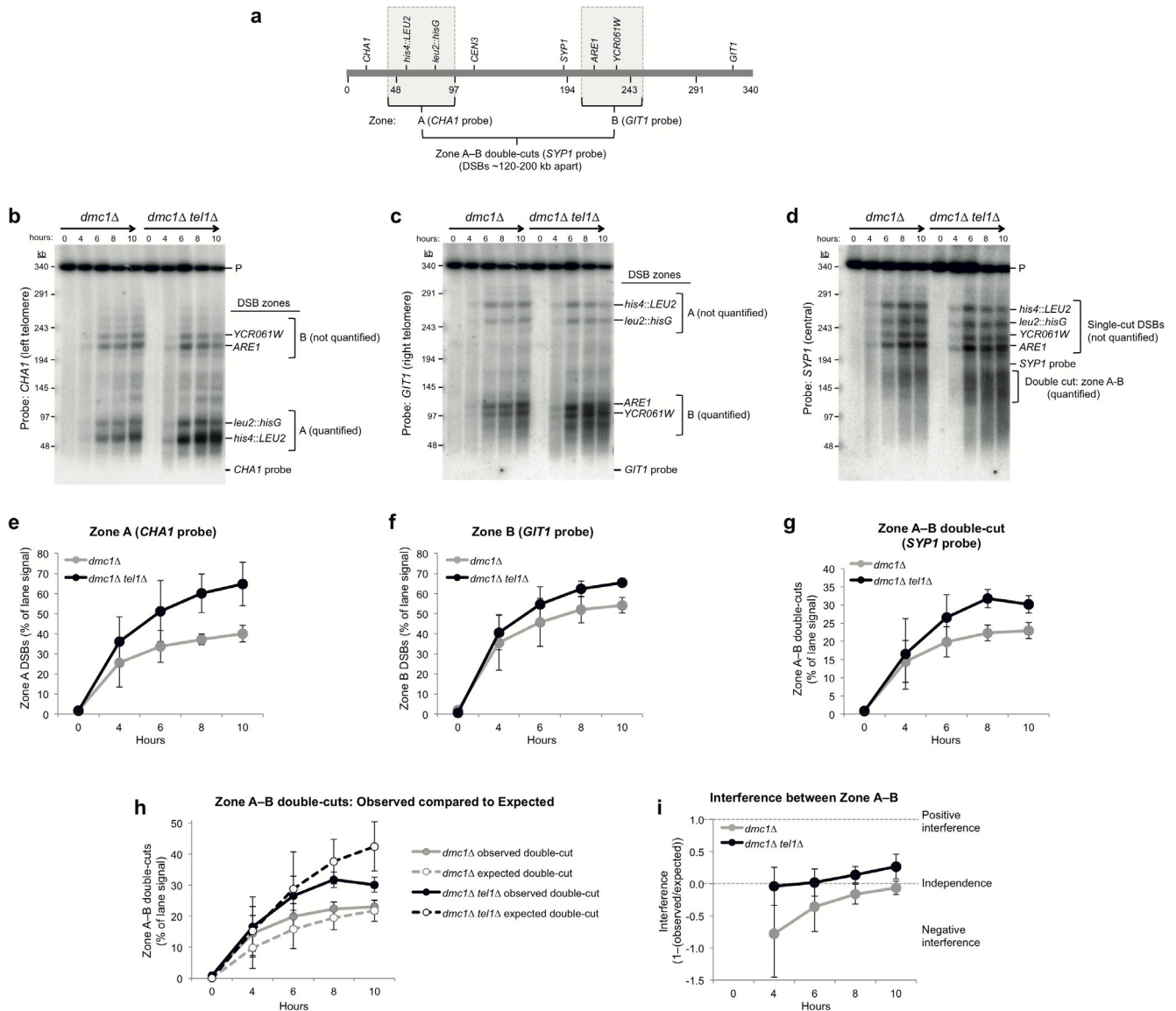
Extended Data Figure 1 | Tel1 suppresses the formation of multiple DSBs on the same chromatid. **a**, Top: agarose-embedded genomic DNA isolated at the indicated time points was fractionated by PFGE, transferred to nylon membrane and hybridized with probes recognizing a central position on chromosome III, VIII, V and XI. Example lane profiles depict the relative signal density for the 8 h time points. Representative blots are shown. Areas defined for quantification of multi-cut DSBs (bottom panel) are indicated. Asterisk: cross-hybridization band. **b**, Quantification of total chromosome breakage measured in **a**. **c**, As in **a** but using probes specific to the left (top panel), or right

(bottom panel) telomere. In agreement with more DSBs per chromatid being formed in the absence of Tel1, close inspection of the PFGE lane profiles revealed that *dmc1Δ tel1Δ* cells had an increased frequency of shorter chromosome fragments, yet also fewer large chromosome fragments. Because a similar shift in DSB distribution towards shorter molecules is also observed when chromosomes are probed from their opposite end (compare top and bottom panels), this apparent shift can be explained by an increase in the frequency of multiple DSBs arising on the same chromatid in *dmc1Δ tel1Δ* relative to *dmc1Δ*. **a–c**, Error bars, s.d. $n = 3$.



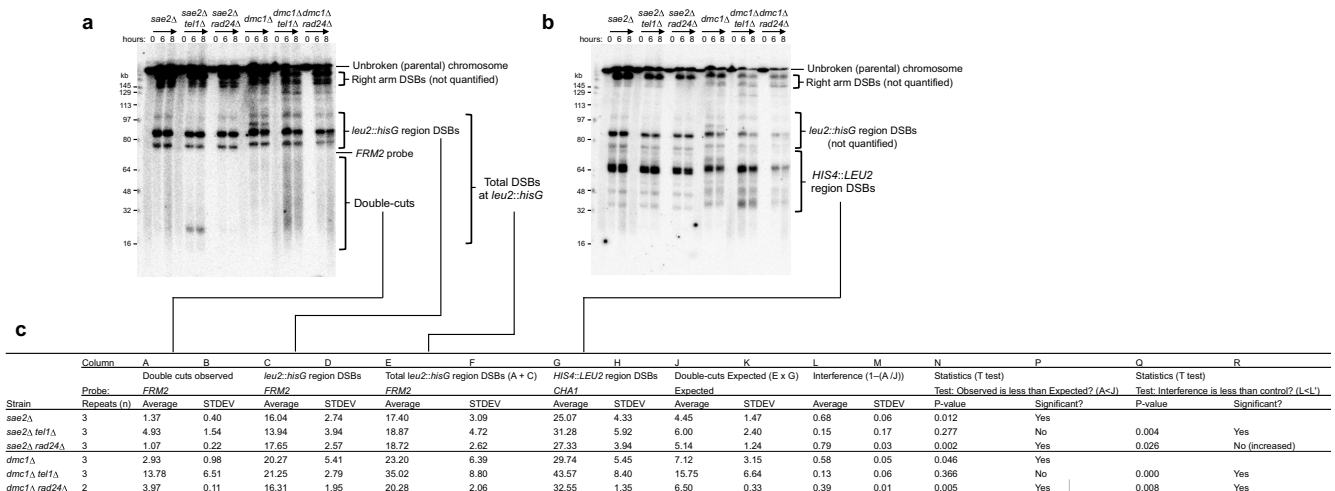
Extended Data Figure 2 | Nonlinear increases in the frequency of closely spaced DSBs that arise upon *TEL1* deletion cannot be explained by increases in absolute DSB frequency. **a–d**, To test whether the nonlinear increase in double-cutting frequency for shorter molecules (Fig. 1c) could alternatively be explained by increases in DSB formation unassociated with any change in DSB interference, DSB formation on chromosome V (576 kb) was simulated 1 million times for each of the mean values of 2.5, 3, 3.5 and 4 DSBs per chromatid using DSB frequencies (per round of simulation) described by the Poisson distribution for the specified mean. These frequencies are approximately equivalent to 217, 260, 304 and 347 DSBs per cell (~50 Mb). To simulate the frequency distributions of fragments detected by an interstitial probe, tallies were made of only those fragments that include the simulated probe position (*FIR1* at position ~220 kb). Subsequently, ratios were calculated for each position within each of these simulated distributions and equivalent simulated distributions generated with mean DSB frequencies 1.5× (red), 2× (green), 3× (purple), and 4× (blue) greater than the baseline. Finally, these data simulations were overlaid with the experimental observations made from chromosome V using the *FIR1* probe when comparing the ratio of the *dmc1Δ tel1Δ* : *dmc1Δ* (data from Fig. 1c; orange). In all cases, as in Fig. 1c, data has been trimmed for fragments shorter than 50 kb and greater than 300 kb.

The asterisks indicate instances of similarity between simulated and observed patterns. We note that in no circumstances do the simulations match the steep nonlinear curve, which is a hallmark of the experimental data caused by *TEL1* deletion. The closest match is arguably simulating the ratio between a starting mean DSB frequency of 3.5 and that obtained from a 3–4-fold increase (c). While these simulations create a potential match, they both require the relatively high initial frequency of DSB formation in *dmc1Δ* cells of 304 DSBs per cell (note that the wild-type average frequency is estimated at ~160 DSBs per cell¹), increasing to 900–1,200 DSBs per cell upon *TEL1* deletion. Moreover, in accord with the increased DSB frequency per cell, site-specific DSB frequencies would increase 3–4-fold in *dmc1Δ tel1Δ* cells relative to *dmc1Δ* cells to fit this simulation, something that we do not observe: average fold-changes in both *sae2Δ* and *dmc1Δ* strains are only ~1.5× upon *TEL1* deletion (Fig. 3c, Extended Data Fig. 4c and Extended Data Fig. 6a), a fold-change that is modelled by each of the red plots—all of which show very poor correlations with the observed data. Thus we conclude that the nonlinear inverse correlation between the fold-increase and the inter-DSB fragment length cannot solely arise from a global increase in DSB formation, but rather because the closer two DSBs are, the more likely that coincident cleavage is derepressed in the *tel1Δ* strain—as expected for a loss of *cis*-interference.



Extended Data Figure 3 | Tel1-mediated DSB interference spans less than 150 kb. **a**, Physical map of chromosome III showing relative position of DSB zones and probes. **b**, **d**, Agarose-embedded genomic DNA isolated at the indicated time points was fractionated by PFGE, transferred to nylon membrane and hybridized with probes recognizing a left (**b**), right (**c**) or central position (**d**) on chromosome III. Probes, main DSB sites and areas selected for quantification of DSBs arising in individual zones are indicated. **e–g**, Quantification of DSB formation in zone A (**e**), zone B (**f**) and double-cuts

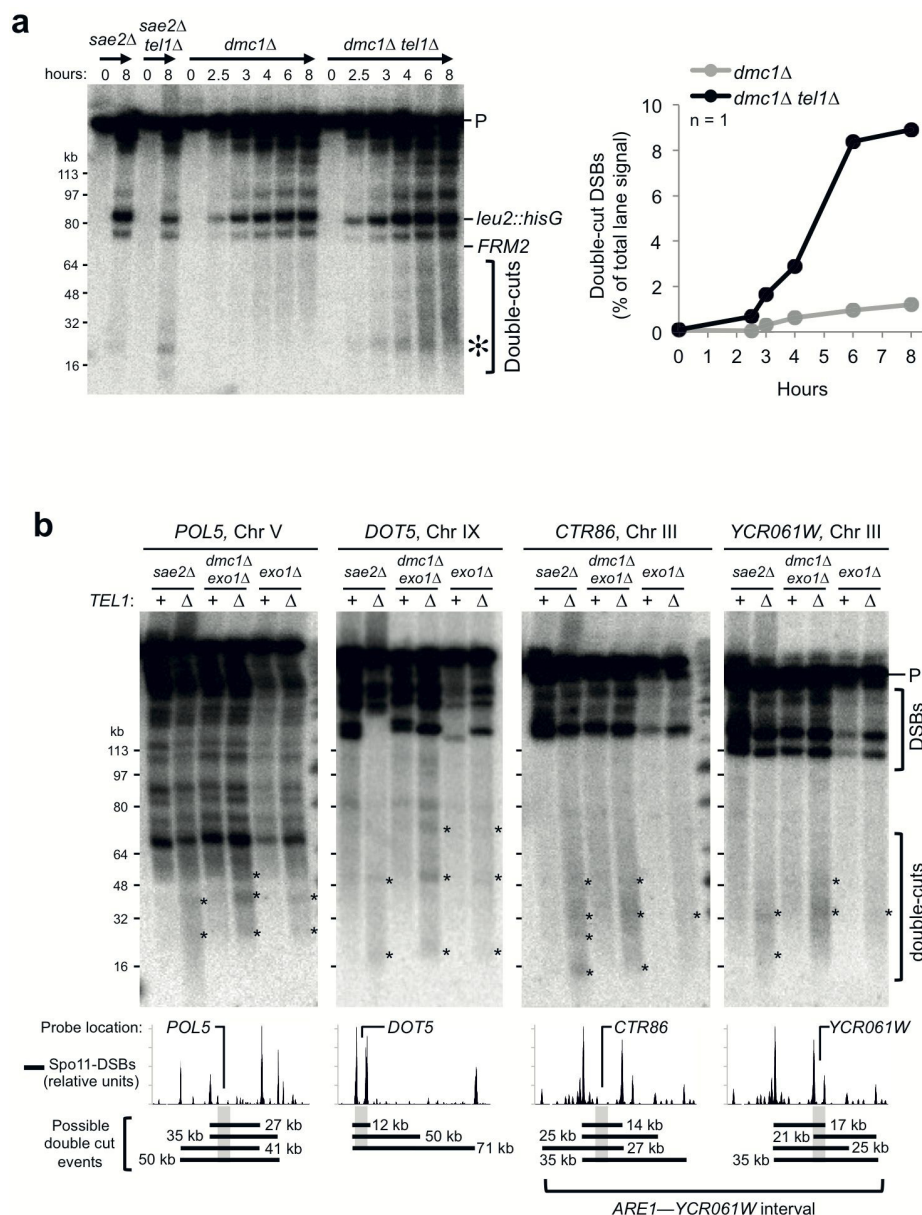
arising from DSBs occurring in both A and B on the same molecule (**g**). **h**, Comparison of observed zone A-B double-cuts (**g**) to expected zone A-B double-cuts (calculated from single cut frequencies measured in **e**, **f**). We observe no statistical difference between observed and expected values at any time point (*t*-test: *P* values all above 0.25 except *dmc1Δ tel1Δ* *t* = 10 h sample, 0.061). **i**, Calculated DSB interference between DSB zones A and B. **b–i**, Error bars, s.d. *n* = 3. See Supplementary Discussion for further details of this analysis.



Notes:
A-R: Column identifiers
A, C, E, G, J: Values are expressed as a percentage of total DNA. For each repeat, each measurement is an average of the 6 and 8 hour timepoint.
A: Double-cuts detected by *FRM2* probe are of variable length (~8-64 kb) depending which specific DSBs break within the *HIS4::LEU2* and *leu2::hisG* regions.
The major band at ~20 kb arises from double-cuts between the major hotspots within *HIS4::LEU2* (at position 66 kb) and *leu2::hisG* (at position 86 kb) as shown in panel b.
C: The *FRM2* probe is useful to estimate the frequency of DSBs in the *leu2::hisG* region, but will underestimate this value when a DSB forms telomere-proximal to the probe (i.e. at *HIS4::LEU2*) in the same molecule.
Thus total DSB formation in the *leu2::hisG* region can be calculated by adding the frequency of double-cuts (between *leu2::hisG* and *HIS4::LEU2*) to the measured *leu2::hisG* signal (E).
J: Expected frequency of double-cuts is calculated by multiplying total DSBs in the *leu2::hisG* region (E) by DSBs in *HIS4::LEU2* region (G).
L: Interference is calculated as $1 - (\text{observed double-cuts} / \text{expected double-cuts}) = 1 - (A/J)$
N: A one-tailed T-test was used to assess whether the observed frequency of double-cuts was less than expected (Is $A < J$?). Interference is present in all *TEL1+* strains, and is lost in *sae2Δ tel1Δ* and *dmc1Δ tel1Δ*.
Q: A one-tailed T-test was used to assess whether interference in the test strain (*sae2Δ tel1Δ* or *sae2Δ rad24Δ*, or *dmc1Δ tel1Δ* or *dmc1Δ rad24Δ*) was lower than in the control strain (*sae2Δ* or *dmc1Δ*, respectively).
sae2Δ rad24Δ displayed moderately and significantly stronger interference (0.79 vs 0.68 for *sae2Δ*), possibly due to slightly lower lane background in these samples allowing more accurate (lower) double-cut measurement

Extended Data Figure 4 | Analysis of DSB interference between *HIS4::LEU2* and *leu2::hisG*. a, b, Agarose-embedded genomic DNA isolated at the indicated time points was fractionated by PFGE, transferred to nylon membrane and hybridized with probes recognizing a, the *FRM2* locus located between the *HIS4::LEU2* and *leu2::hisG* DSB hotspots, and b, the *CHA1* locus on the left telomere of chromosome III. Areas selected for quantification are indicated. c, Analysis of DSB interference between *HIS4::LEU2* and *leu2::hisG* regions. The frequency of DSB formation within *HIS4::LEU2* and

leu2::hisG regions were measured in the various strains from PFGE using *CHA1* (b) and *FRM2* (a) probes, respectively, and the frequency of double-cuts were measured using the *FRM2* probe (a). Total DSBs arising within the *leu2::hisG* region were calculated by summing double-cuts and *leu2::hisG* DSBs. Standard deviation indicates the variation between repeat analyses ($n = 3$ for all samples except *rad24Δ dmc1Δ*: $n = 2$). See notes below table for further details.



Extended Data Figure 5 | Analysis of DSB double-cutting at various genomic loci. **a, b,** Agarose-embedded genomic DNA isolated from the indicated time points and strains was fractionated by PFGE, transferred to nylon membrane and hybridized with various probes: *FRM2* (**a**); *POL5*, *DOT5*, *CTR86*, *YCR061W* (**b**). **a,** Detection of double-cut (left panel) and quantification (right panel). Major double-cut band corresponding to

coincident DSBs at *HIS4::LEU2* and *leu2::hisG* is indicated with a star. **b,** Detection of double-cuts on different chromosomes following PFGE in strains fully (*dmc1Δ exo1Δ* and *sae2Δ*) or partially (*exo1Δ*) defective for DSB repair (top panel). Asterisks: *tel1Δ*-specific double-cut signals. Diagram depicts possible double-cuts (bottom panels).

a

Calculation using direct DSB measurement

sae2Δ										
COLUMN: A	B	C	D	E	F	G	H	J	K	L
bp from ARE1	Average	StDev	Average	StDev	Average	StDev	Average	StDev	P-value	Interference?
-14501	0.037	0.024								
-9139	0.010	0.005								
-6162	0.013	0.009								
-5009	0.020	0.009	0.695	0.064	0.058	0.002	0.657	0.153	0.030	POSITIVE
-3723	0.033	0.009	0.719	0.042	0.060	0.007	0.436	0.068	0.037	POSITIVE
-2004	0.083	0.005	0.795	0.177	0.066	0.011	-0.284	0.278	0.170	no
-1220	0.140	0.028	2.830	1.047	0.234	0.073	0.352	0.322	0.230	no
-633	0.007	0.000	nd	nd						
ARE1 DSB	8.366	0.528								
1592	0.017	0.005	0.108	0.011			-0.851	0.459	0.148	no
2205	0.100	0.019	0.585	0.011	0.049	0.004	-1.064	0.552	0.064	no
3128	0.047	0.009	0.548	0.028	0.046	0.001	-0.022	0.218	0.901	no
4737	0.053	0.009	0.871	0.048	0.073	0.001	0.267	0.135	0.101	no
8496	0.007	0.000	0.419	0.087	0.035	0.005	0.806	0.028	0.016	POSITIVE
11638	0.007	0.000								
12585	0.010	0.005								
13398	0.027	0.019								
Total ± StDev	0.610	0.148	15.926	2.038						

sae2Δ tel1Δ										
COLUMN: A	B	C	D	E	F	G	H	J	K	L
bp from ARE1	Average	StDev	Average	StDev	Average	StDev	Average	StDev	P-value	Interference?
-14501	0.200	0.019								
-9139	0.030	0.005								
-6162	0.070	0.005								
-5009	0.130	0.033	0.915	0.332	0.122	0.054	-0.111	0.221	0.882	no
-3723	0.233	0.009	1.170	0.212	0.155	0.041	-0.548	0.349	0.120	no
-2004	0.347	0.057	1.120	0.113	0.148	0.028	-1.416	0.838	0.047	NEGATIVE
-1220	1.543	0.052	3.570	0.184	0.469	0.016	-2.288	0.001	0.001	NEGATIVE
-633	0.163	0.071	nd	nd						
ARE1 DSB	13.178	0.387								
1592	0.143	0.052	0.254	0.071	0.033	0.002	-3.259	1.338	0.096	no
2205	0.750	0.042	1.350	0.047	0.180	0.066	-3.419	1.383	0.009	NEGATIVE
3128	0.400	0.038	0.711	0.057	0.112	0.036	-2.711	0.854	0.016	NEGATIVE
4737	0.583	0.061	1.603	0.255	0.213	0.052	-1.791	0.389	0.023	NEGATIVE
8496	0.050	0.005	0.500	0.000	0.066	0.006	0.241	0.007	0.092	no
11638	0.010	0.005								
12585	0.040	0.000								
13398	0.853	0.207								
Total ± StDev	5.547	0.660	24.500	1.658						
Fold increase	9.093		1.538							

Notes:

A-V Column identifiers

A Distance (in bp) of test DSB from ARE1-DSB (This equals the length of double-cut assayed.)

B-J & N-T Values (reported as % of lane signal) are the average and standard deviation of two independent repeats. Individual values from each repeat were averages of the 6-10 h timepoints.

B & C Average and standard deviation of observed double-cut frequencies as measured by Southern blotting using ARE1 and BUD23 probes

D & E Average and standard deviation of single-cut DSB frequencies as measured by Southern blotting using various AseI, BglII, and NgoMIV digests and TAF2, RSC6 and PWP2 probes (Extended Data Table 2)

F & G Average and standard deviation of expected double-cut frequencies calculated by multiplying % DSBs at ARE1 by the measured single-cut DSB frequency at each site (D)

H & J Average and standard deviation of interference calculated by the formula: 1-(B/F). These values are plotted in Figure 4

K & L 2-tailed T-test between the observed and expected datasets (B and F). Rows with P-values below 0.05 are coloured according to the type of (significant) interference: Red=Positive Blue=Negative Clear=Not significantly different from independence

M Relative Spo11-oligo counts obtained from Pan et al., Cell 2011. Qualitatively similar results were obtained using Spo11-oligo counts from a second WT dataset (Thacker et al., Nature 2014) and from an unpublished tel1Δ dataset (S.Keeney and N.Mohibullah, pers. comm.)

N & P Average and standard deviation of single-cut DSB frequencies as calculated by converting Spo11-oligo counts to DSB frequencies using the frequency of DSBs measured at ARE1 (highlighted in yellow)

Q & R Average and standard deviation of expected double-cut frequencies calculated by multiplying % DSBs at ARE1 by the single-cut DSB frequencies estimated from the converted Spo11-oligo counts (N)

S & T Average and standard deviation of interference calculated by the formula: 1-(Q/R). These values are plotted in Figure 4

U & V 2-tailed T-test between the observed and expected datasets (B and Q). Rows with P-values below 0.05 are coloured according to the type of (significant) interference: Red=Positive Blue=Negative Clear=Not significantly different from independence

nd Not determined (DSB frequency could not be assessed directly at this site due to contamination from strong flanking DSB peaks at ARE1)

Total ± StDev Refers to the aggregated frequency of double-cuts (B) or DSBs (D) observed across the ARE1 region

Fold increase Refers to the aggregated increase in frequency of double-cuts (B) or DSBs (D) observed across the ARE1 region in sae2Δ tel1Δ compared to sae2Δ

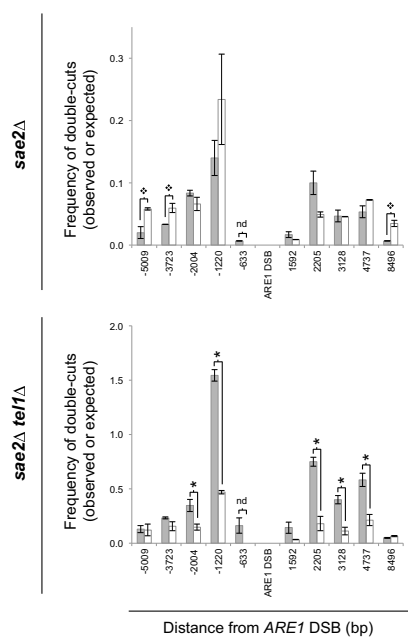
Calculation using Spo11-oligo data (Pan et al. 2011)

sae2Δ										
A	M	N	P	Q	R	S	T	U	V	
bp from ARE1	Spo11-oligos	Estimated DSBs	Expected double-cuts	Interference	Average	StDev	Average	StDev	P-value	Interference?
-14501	1087	1.603	0.101	0.134	0.017	0.736	0.142	0.041	POSITIVE	
-9139	208	0.307	0.019	0.026	0.003	0.620	0.136	0.060	no	
-6162	571	0.842	0.053	0.071	0.009	0.801	0.158	0.025	POSITIVE	
-5009	665	0.981	0.062	0.082	0.010	0.748	0.146	0.024	POSITIVE	
-3723	519	0.786	0.048	0.064	0.008	0.478	0.068	0.032	POSITIVE	
-2004	874	1.289	0.081	0.108	0.014	0.226	0.053	0.135	no	
-1220	1778	2.623	0.165	0.220	0.028	0.366	0.049	0.104	no	
-633	163	0.240	0.015	0.020	0.003	0.667	0.042	0.017	POSITIVE	
ARE1 DSB	5672	8.366	0.528							
1592	145	0.214	0.013	0.018	0.002	0.046	0.382	0.765	no	
2205	838	1.236	0.078	0.104	0.013	0.016	0.305	0.844	no	
3128	367	0.541	0.034	0.045	0.006	-0.050	0.339	0.884	no	
4737	534	0.788	0.049	0.066	0.008	0.177	0.246	0.289	no	
8496	138	0.204	0.013	0.017	0.002	0.606	0.049	0.020	POSITIVE	
11638	319	0.471	0.030	0.039	0.005	0.830	0.021	0.011	POSITIVE	
12585	266	0.392	0.025	0.033	0.004	0.685	0.183	0.035	POSITIVE	
13398	5435	8.017	0.503	0.672	0.084	0.958	0.033	0.009	POSITIVE	

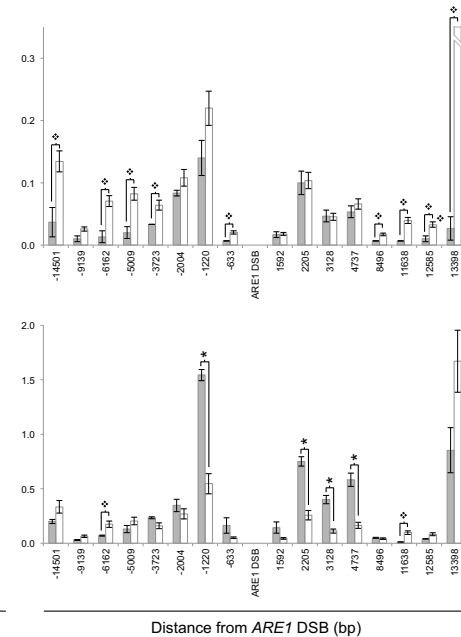
sae2Δ tel1Δ										
A	M	N	P	Q	R	S	T	U	V	
bp from ARE1	Spo11-oligos	Estimated DSBs	Expected double-cuts	Interference	Average	StDev	Average	StDev	P-value	Interference?
-14501	1087	2.525	0.215	0.334	0.057	0.397	0.048	0.087	no	
-9139	208	0.483	0.041	0.064	0.011	0.530	0.006	0.056	no	
-6162	571	1.327	0.113	0.175	0.030	0.597	0.042	0.039	POSITIVE	
-5009	665	1.545	0.132	0.204	0.035	0.368	0.054	0.159	no	
-3723	519	1.206	0.103	0.159	0.027	-0.480	0.192	0.068	no	
-2004	874	2.031	0.173	0.269	0.046	-0.328	0.436	0.288	no	
-1220	1778	4.131	0.352	0.546	0.093	-1.858	0.391	0.006	NEGATIVE	
-633	163	0.379	0.032	0.050	0.009	-2.187	0.870	0.153	no	
ARE1 DSB	5672	13.178	1.124							
1592	145	0.337	0.029	0.045	0.008	-2.164	0.626	0.117	no	
2205	838	1.947	0.166	0.257	0.044	-1.941	0.335	0.008	NEGATIVE	
3128	367	0.853	0.073	0.113	0.019	-2.570	0.273	0.011	NEGATIVE	
4737	534	1.241	0.106	0.164	0.028	-2.575	0.234	0.013	NEGATIVE	
8496	138	0.321	0.027	0.042	0.007	-0.187	0.091	0.338	no	
11638	319	0.741	0.063	0.098	0.017	0.892	0.066	0.019	POSITIVE	
12585	266	0.618	0.053	0.082	0.014	0.503	0.084	0.051	no	
13398	5435	12.627	1.077	1.670	0.284	0.471	0.214	0.082	no	

b

Calculation using direct DSB measurement

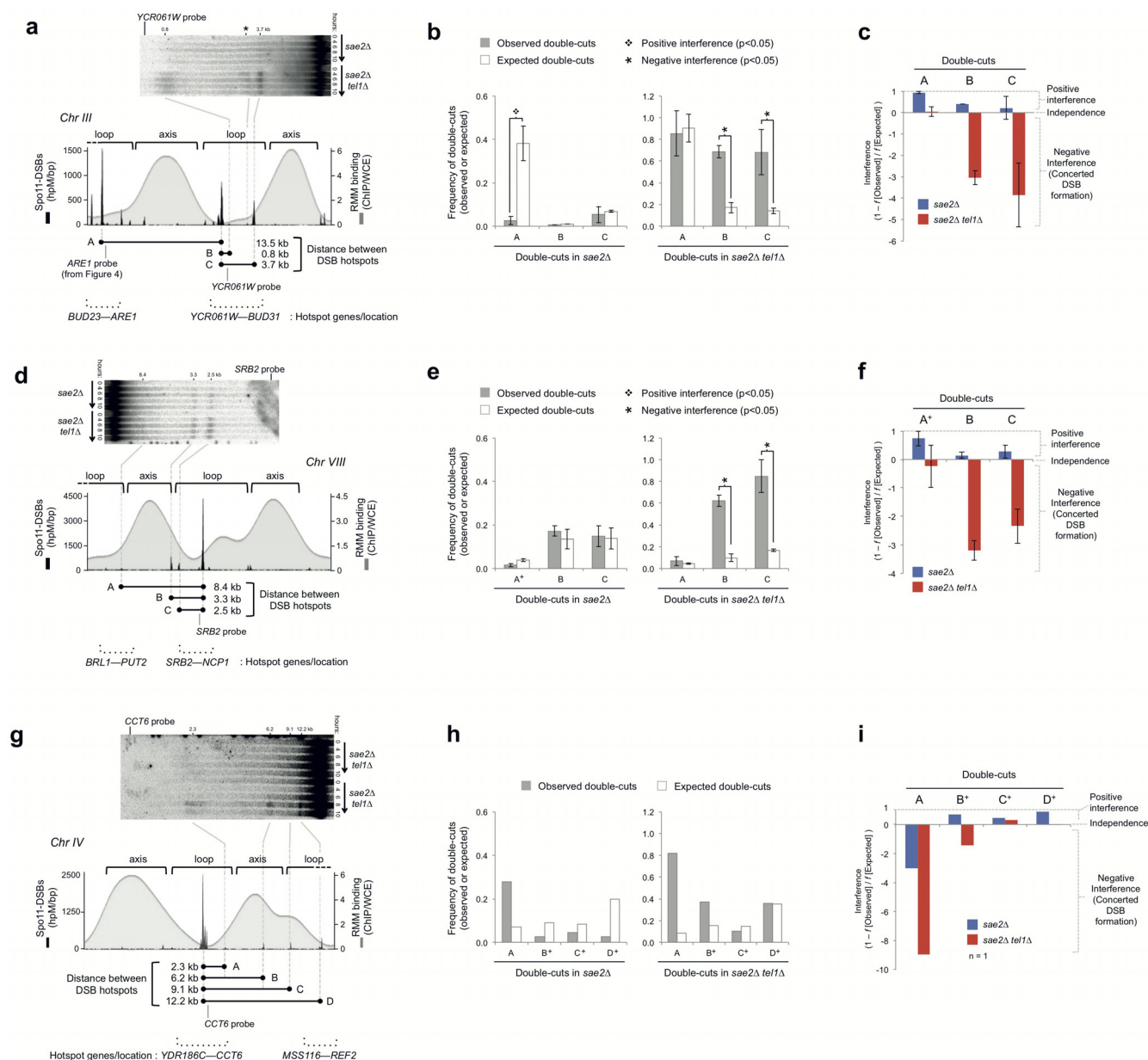


Calculation using Spo11-oligo data (Pan et al. 2011)



Extended Data Figure 6 | Analysis of DSB interference across the ARE1 region. **a**, DSB interference was calculated in *sae2Δ* (top) and *sae2Δ tel1Δ* (bottom) using the following formula: $1 - f(\text{observed double-cuts}) / f(\text{expected double-cuts})$, where the expected double-cut values were calculated using two methods. Left, single-cut frequencies were measured by Southern-blot using a TAF2 probe (for DSB sites on the left of ARE1) or a PWP2 and RSC6 probe (for the right-hand side of ARE1; Extended Data Table 2). Right, calculations were made after converting the measured Spo11-oligo frequency¹ at each DSB site to a % DSB \pm s.d. value by using the measured DSB frequency

at ARE1 in *sae2Δ* or *sae2Δ tel1Δ* for normalization (see Notes below table and Methods for further details). **b**, Chart of observed (column B) and expected (column F and Q) frequencies of double-cuts. Error bars, s.d. $n = 2$. *P* values, two-tailed *t*-test. Double-cut products that were present at a frequency that was statistically different from that for no interference (independence) were highlighted in **a** according to the type of interference present: red indicates positive DSB interference, blue indicates negative DSB interference (concerted DSB formation); in **b** the same statistical differences were indicated with open diamonds or asterisks, respectively.



Extended Data Figure 7 | Tel1 suppresses concerted DSB formation within chromatin loop domains at numerous chromosomal loci.

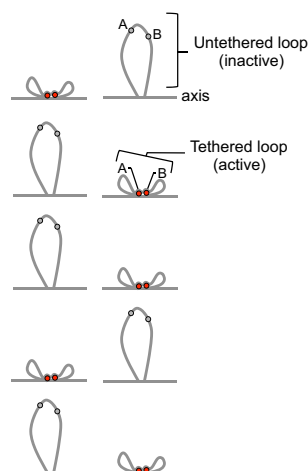
a–i, DSB interference was calculated across three DSB hotspot regions located on three different chromosomes: chromosome III, *BUD23-ARE1* to *YCR061W-BUD31* (**a–c**); chromosome VIII, *BRL1-PUT2* to *SRB2-NCP1* (**d–f**); and chromosome IV, *YDR186C-CCT6* to *MSS116-REF2* (**g–i**). **a, d, g**, Upper panels, genomic DNA isolated from *sae2Δ* or *sae2Δ tel1Δ* strains at the indicated time points was fractionated by agarose electrophoresis, transferred to nylon membrane and hybridized with the indicated probes: *YCR061W* (**a**), *SRB2* (**d**), *CCT6* (**g**). Lower panels, diagram of mean RMM binding profile¹⁴ overlaid with Spo11-DSB hotspot peaks¹. Intervals between various detectable double-cut events are indicated below and specified with the letters A to D. Probes used for detecting double-cuts by Southern blotting are indicated. **b, e, h**, Chart of observed and expected double-cuts for each of the indicated intervals, calculated as an average (per repeat) across the 4–10 h time points. Expected double-cut frequencies for each interval were calculated by multiplying the DSB frequencies (average across 4–10 h) at the two sites. Single-cut frequencies were measured by Southern-blot (see Extended Data Table 2 and Methods for details). For some intervals (superscript with a “+”), due to no Southern DSB data being available at the minor DSB site, calculations

were made using the normalized Spo11-oligo frequency¹ at the minor DSB site (as was performed in Fig. 4 and described in Methods). Asterisks and open diamonds indicate significant negative and positive interference, respectively. **c, f, i**, DSB interference was calculated by the following formula: $1 - f(\text{observed double-cuts}) / f(\text{expected double-cuts})$. Values above zero indicate positive DSB interference. Values below zero indicate negative DSB interference (concerted DSB formation). Conclusion: In addition to *ARE1* (Fig. 4), at all three additional loci tested, concerted DSB formation is localized predominantly within a domain approximately demarcated by the RMM binding profile (see **a, d** and **g**, lower panels). Notably, coincident formation of two DSBs, one within the *BUD23-ARE1* domain and one within the *YCR061W-BUD31* domain, arise independently in *sae2Δ tel1Δ* despite coincident DSB formation within each interval displaying negative interference. In **a**, double-cuts in interval A were measured using the *ARE1* probe (Fig. 4a). Asterisk in **a** upper panel denotes a band that is a mixture of two *tel1Δ*-dependent double-cuts, which owing to the relative location of the *YCR061W* probe and DSB sites cannot be unambiguously assigned and therefore were not analysed. Error bars, s.d. $n = 2$, except **g–i** where only one experiment was performed. *P* values, two-tailed *t*-test.

a

COLUMN:	a	b	c	d	e	f	g	h	i
Tethering frequency	DSB	Measured frequency of DSB formation (population average)	Expected double-cutting frequency of A x B within population (using population average DSB frequencies) i.e. column c: [A x B]	DSB	DSB frequency within the tethered loop i.e. [c/a]	Expected double-cutting frequency of A x B within tethered loop (using the DSB frequencies within the tethered loop) i.e. column f: [A x B]	Corrected expected double-cutting frequency of A x B within population (using the double-cut frequencies within the tethered loop) i.e. [g x a]	Apparent interference i.e. 1-[h/d]	
All the time:	1.00	A 0.10 B 0.05	0.005	A 0.10 B 0.05	0.005	0.005	0.005	0.0	
Half the time: (see "b" below)	0.50	A 0.10 B 0.05	0.005	A 0.20 B 0.10	0.020	0.010	-1.0		
1/4 of the time:	0.25	A 0.10 B 0.05	0.005	A 0.40 B 0.20	0.080	0.020	-3.0		
1/5th of the time: (see "c" below)	0.20	A 0.10 B 0.05	0.005	A 0.50 B 0.25	0.125	0.025	-4.0		
1/6th of the time:	0.167	A 0.10 B 0.05	0.005	A 0.60 B 0.30	0.180	0.030	-5.0		

b

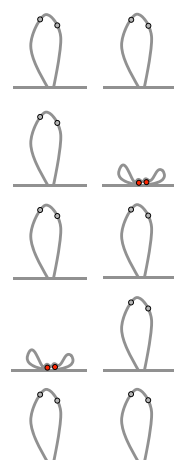


In this worked example, 50% of chromatids in the population are active/tethered at this locus

Observed population average DSB frequencies: A = 0.1, B = 0.05
Expected double-cut frequency: A x B = 0.005
Probability of loop tethering: 0.5 (i.e. on average 50% of loops tether/prime)
Probability of DSB formation per tethered loop: A* = 0.2, B* = 0.1
Probability of double-cut per tethered loop: A* x B* = 0.02
Observed population average double-cut frequencies: (A* x B*) x 0.5 = 0.01
If DSBs form independently, apparent interference: 1 - (0.01 / 0.005) = -1

Thus, loss of an interference signal, within a loop domain that is active/tethered in only a subpopulation of chromosomes will result in observed negative interference proportional to: 1 - (1 / loop tethering frequency) = 1 - (1 / 0.5), in this example.

c



In this worked example, 20% of chromatids in the population are active/tethered at this locus

Observed population average DSB frequencies: A = 0.1, B = 0.05
Expected double-cut frequency: A x B = 0.005
Probability of loop tethering: 0.2 (i.e. on average 20% of loops tether/prime)
Probability of DSB formation per tethered loop: A* = 0.5, B* = 0.25
Probability of double-cut per tethered loop: A* x B* = 0.125
Observed population average double-cut frequencies: (A* x B*) x 0.20 = 0.025
If DSBs form independently, apparent interference: 1 - (0.025 / 0.005) = -4.0

Thus, loss of an interference signal, within a loop domain that is active/tethered in only a subpopulation of chromosomes will result in observed negative interference proportional to: 1 - (1 / loop tethering frequency) = 1 - (1 / 0.20), in this example.

Extended Data Figure 8 | Stochastic loop tethering (activation) predicts apparent short-range negative interference. **a**, In this model, DSBs A and B reside within a single loop domain (subject to tethering-dependent DSB formation), which is active in only a subpopulation of cells. The expected frequency of coincident DSB formation (double-cutting), assuming no DSB interference, is calculated for different frequencies of loop activation/tethering per chromatid assuming a model where DSB formation is wholly dependent on loop activation/tethering. In summary, loop activation/tethering at a

frequency of X, will result in apparent negative interference of 1 - 1/X. See text for further details. **b, c**, Cartoons (left) and worked examples (right) for situations in which 50% (**b**) or 20% (**c**) of the chromatids within the assayed population are active/tethered at the test locus. The cartoons depict the tethering state of an average sample of 10 chromatids from the population. It is also possible that loop tethering and loop activation are not synonymous processes. In principle, activation of a loop might precede and enable tethering, but not be caused by it.

Extended Data Table 1 | Table of strains used in this study

Strains	Genotype	Reference
SG147	<i>MATa/alpha</i> , <i>ho::LYS2⁺</i> , <i>lys2⁻</i> , <i>ura3⁻</i> , <i>arg4-nspl⁻</i> , <i>leu2::hisG⁺</i> , <i>his4X::LEU2⁺</i> , <i>nuc1::LEU2⁺</i> , <i>dmc1Δ::LEU2⁺</i>	Gray et al, 2013
SG343	<i>MATa/alpha</i> , <i>ho::LYS2⁺</i> , <i>lys2⁻</i> , <i>ura3⁻</i> , <i>arg4-nspl⁻</i> , <i>leu2::hisG⁺</i> , <i>his4X::LEU2⁺</i> , <i>nuc1::LEU2⁺</i> , <i>dmc1Δ::HphMX⁺</i> , <i>tel1Δ::HphMX⁺</i>	This study
MJ781	<i>MATa/alpha</i> , <i>ho::LYS2⁺</i> , <i>lys2⁻</i> , <i>ura3⁻</i> , <i>arg4-nspl⁻</i> , <i>leu2::hisG⁺</i> , <i>his4X::LEU2⁺</i> , <i>nuc1::LEU2⁺</i> , <i>dmc1Δ::LEU2⁺</i> , <i>rad24Δ::Hyg⁺</i>	Gray et al, 2013
MJ315	<i>MATa/alpha</i> , <i>ho::LYS2⁺</i> , <i>lys2⁻</i> , <i>ura3⁻</i> , <i>arg4-nspl⁻</i> , <i>leu2::hisG⁺</i> , <i>his4X::LEU2⁺</i> , <i>nuc1::LEU2⁺</i> , <i>sae2Δ::KanMX6⁺</i>	Gray et al, 2013
SG346	<i>MATa/alpha</i> , <i>ho::LYS2⁺</i> , <i>lys2⁻</i> , <i>ura3⁻</i> , <i>arg4-nspl⁻</i> or <i>bgl1⁻</i> , <i>leu2::hisG⁺</i> or <i>leu2Δ⁺</i> , <i>his4X::LEU2⁺</i> , <i>nuc1::LEU2⁺</i> , <i>tel1Δ::HphMX4⁺</i> , <i>sae2Δ::KanMX6⁺</i>	This study
SG103	<i>MATa/alpha</i> , <i>ho::LYS2⁺</i> , <i>lys2⁻</i> , <i>ura3⁻</i> , <i>arg4-nspl⁻</i> , <i>leu2::hisG⁺</i> , <i>his4X::LEU2⁺</i> , <i>nuc1::LEU2⁺</i> , <i>rad24Δ::Hyg⁺</i> , <i>sae2Δ::KanMX⁺</i>	Gray et al, 2013
VG402	<i>MATa/alpha</i> , <i>ho::LYS2⁺</i> , <i>lys2⁻</i> , <i>ura3⁻</i> , <i>arg4-nspl⁻</i> , <i>leu2::hisG⁺</i> , <i>his4X::LEU2⁺</i> , <i>nuc1::LEU2⁺</i> , <i>sae2Δ::KanMX4⁺</i> , <i>tel1Δ::HphMX4⁺</i>	This study
MJ6	<i>MATa/alpha</i> , <i>ho::LYS2⁺</i> , <i>lys2⁻</i> , <i>ura3⁻</i> , <i>arg4-nspl⁻</i> , <i>leu2::hisG⁺</i> , <i>his4X::LEU2⁺</i> , <i>nuc1::LEU2⁺</i>	Neale et al, 2005
SG344	<i>MATa/alpha</i> , <i>ho::LYS2⁺</i> , <i>lys2⁻</i> , <i>ura3⁻</i> , <i>arg4-nspl⁻</i> , <i>leu2::hisG⁺</i> , <i>his4X::LEU2⁺</i> , <i>nuc1::LEU2⁺</i> , <i>tel1Δ::HphMX4⁺</i>	This study
VG392	<i>MATa/alpha</i> , <i>ho::LYS2⁺</i> , <i>lys2⁻</i> , <i>ura3⁻</i> , <i>arg4-nspl⁻</i> , <i>leu2::hisG⁺</i> , <i>his4X::LEU2⁺</i> , <i>nuc1::LEU2⁺</i> , <i>exo1Δ::KanMX4⁺</i>	This study
VG393	<i>MATa/alpha</i> , <i>ho::LYS2⁺</i> , <i>lys2⁻</i> , <i>ura3⁻</i> , <i>arg4-nspl⁻</i> , <i>leu2::hisG⁺</i> , <i>his4X::LEU2⁺</i> , <i>nuc1::LEU2⁺</i> , <i>exo1Δ::KanMX4⁺</i> , <i>tel1Δ::HphMX4⁺</i>	This study
VG376	<i>MATa/alpha</i> , <i>ho::LYS2⁺</i> , <i>lys2⁻</i> , <i>ura3⁻</i> , <i>arg4-nspl⁻</i> , <i>leu2::hisG⁺</i> , <i>his4X::LEU2⁺</i> , <i>nuc1::LEU2⁺</i> , <i>dmc1Δ::HphMX4⁺</i> , <i>tel1Δ::HphMX4⁺</i> , <i>exo1Δ::KanMX4⁺</i>	This study
VG377	<i>MATa/alpha</i> , <i>ho::LYS2⁺</i> , <i>lys2⁻</i> , <i>ura3⁻</i> , <i>arg4-nspl⁻</i> , <i>leu2::hisG⁺</i> , <i>his4X::LEU2⁺</i> , <i>nuc1::LEU2⁺</i> , <i>dmc1Δ::HphMX4⁺</i> , <i>exo1Δ::KanMX4⁺</i>	This study

All strains are of the SK1 background. Genetic modifications were generated by transformation or intercrossing using standard methods. Laboratory origin of strains is indicated.

Extended Data Table 2 | Table of primers/probes used in this study for DSB and double-cut detection

Probe	ORF chromosome coordinates	primers	Digestion	Comments
Figure 1 and Extended Data Figure 1				
<i>RMD6</i>	L ChrV: 13720 to 14415	RMD6_F@+13 CTTGGAAATGCTTTACTACCCAG RMD6_R@+592 GAACCTTTGAACCTTTGCACCTCTAC	NA	
<i>YER186C</i>	R ChrV: 562625 to 561705	YER186C_F@+4 TGTGGATCTCGTATGCTTACGAGC YER186C_R@+674 TCTCTATGCTATCACCCACCTCTCG	NA	
<i>FIR1</i>	R ChrV: 215063 to 217693	FIR1_F@+1 ATGAGCCCTCCGTGTACACCTGTCAA FIR1_R@+944 ATCCGAAGAAGCTTATCAGCATCTGC	NA	
<i>CHA1</i>	L ChrIII: 16880 to 15798	CHA1_F@-9 ACGAGCGAGATGTCGATAGTCTAC CHA1_R@+1052 TCTGGAATATGAATTTGTGACGCG	NA	Also Extended Data Figure 3 & 4
<i>GIT1</i>	R ChrIII: 298605 to 297049	GIT1_F@+35 GGAAGTGAAGAGAACTAATCC GIT1_R@+891 AAGGGAACCTGATAATTGTGAACCTG	NA	Also Extended Data Figure 3
<i>SYP1</i>	R ChrIII: 176438 to 173829	SYP1_F@+1015 ACACCTTAGATCTAAAGTGGGCTC SYP1_R@+1754 GGAATTAGTCTCTAGCTCGCCAG	NA	Also Extended Data Figure 3
<i>CBP2</i>	L ChrVIII: 25509 to 23617	CBP2_F@+715 CGCCACTTTGCACCTTGAATGAA CBP2_R@+1358 TTTCGATTGTGTGACAGCGTTTG	NA	
<i>CRG1</i>	R ChrVIII: 519437 to 520312	CRG1_F@+177 TTTAAAGAACTGATTGGGATTGAT CRG1_R@+749 GGAATTATCTCTAGCCCAAGAGAGTG	NA	
<i>CIC1</i>	ChrVIII: 210848 to 211978	CIC1_F@+478 CTTAAAGACCTTTTCAAGGCATATGAG CIC1_R@+1116 CTTGACAGCTCTGACTCGTAGATTC	NA	
<i>JEN1</i>	L ChrXI: 22234 to 24084	JEN1_F@+2 ATATGCTGCTGCTCAATTACAGATGAG JEN1_R@+620 GGCCACTTTCTGGAAGACTTATC	NA	
<i>SIR1</i>	R ChrXI: 640540 to 642504	SIR1_F@+14 CTCCAGGCTTGCAGTATTGATG SIR1_R@+981 CATTTGTTAAGCCAACTGACTC	NA	
<i>NUP100</i>	ChrXI: 310199 to 313078	NUP100_F@+128 ATTCACACATACAAATGCCCAATCAG NUP100_R@+895 GAGTCTGCTGTTCATCGAGTTTGTG	NA	
Figure 2 and Extended Data Figure 4 & 5				
<i>FRM2</i>	L ChrIII: 75285 to 74704	FRM2_F@+27 GCTATTACAACCGCTGTACCATC FRM2_R@+645 CATCGCTGAGGTATCTACTTTCAT	NA	Figure 2a, b, and c, Extended Data Figure 4a & 5a
<i>POLV</i>	L ChrV: 51539 to 48471	POL5_F@+1 ATGACAGGGAAGTCAACAGAGACCT POL5_R@+900 ACCAACAAAGCTTAGCAGACACTC	NA	Extended Data Figure 5b
<i>DOT5</i>	R ChrIX: 334882 to 335529	DOT5_F@+1 ATGGGTGAAGCACTACGTAGATCAAC DOT5_R@+892 AATAGTCCCGTCTCAATGTAACCC	NA	Extended Data Figure 5b
<i>YCR061W (i)</i>	R ChrIII: 225563 to 227458	YCR061W_F@+58 CCCATGATGACATGGACATGGAC YCR061W_R@+884 GGTATGCTCTTGAAGAAGCAGAGG	NA	Extended Data Figure 5b Also Extended Data Figure 7a
<i>CTR86</i>	R ChrIII: 220067 to 218376	CTR86_F@+50 TACCATGATGAAGAACGCCATGTTG CTR86_R@+898 ATTGCAATATCTGCAACAAAGTGTTG	NA	Extended Data Figure 5b
Figure 3				
<i>Leu2</i>		LEU2_F ATATACCATTCTAATGTCTGC LEU2_R AAGGATTTTCTTAAGTCTTCGGGG	NA	Central probe
<i>Leu2LH</i>		LEU2LH_F GTACGTACAGACCGTCTGACGG LEU2LH_R CTTGTCTGGGAAGCCTTCACACACCTCC	PstI	Left probe
<i>MRX2</i>	ChrIII: 63282 to 62776	HIS4_F@+5170 CGTGAAGTGGAAAGATGCC HIS4_R@+5495 GCAACTGTTCCAGCCTTCACC	PstI	Right probe
Figure 4				
<i>BUD23</i>	R ChrIII: 211545 to 210718	BUD23_F@+1 ATGTCAGTCTGAGAGGTTGG BUD23_R@+800 GTGAACCTGGAGTCTTCGCAAC	NA	Quantification of DC between ARE1 and hotspots on the left of ARE1
<i>ARE1</i>	R ChrIII: 211929 to 213761	ARE1_F@+4 ACTCAATTCGCGAAGCCCA ARE1_R@+715 TTGCCAAGTCCACATTGCG	NA	Quantification of DC between ARE1 and hotspots on the right of ARE1
<i>TAI2</i>	R ChrIII: 205397 to 201174	TAI2_F@+23 CCACTCTAGAGCCATTGTTAG TAI2_R@+93 TCATCAAGCAATCGACACATGG	AseI NcoMIV	Quantification of DSB% at ARE1 and hotspots on the left of ARE1
<i>PWP2</i>	R ChrIII: 223228 to 220457	PWP2_F@+35 GTACGGTCTAGAGGCAAGGTAC PWP2_R@+815 TTGCTGATGGAAGGTGACACAC	NcoMIV	Quantification of DSB% at ARE1 and hotspots on the right of ARE1
<i>RSC8</i>	R ChrIII: 214994 to 216445		BglII	Quantification of DSB% at ARE1 and hotspots on the right of ARE1
<i>CTR86</i>	R ChrIII: 220067 to 218376	CTR86_F@+50 TACCATGATGAAGAACGCCATGTTG CTR86_R@+898 ATTGCAATATCTGCAACAAAGTGTTG	BglII	Quantification of DSB% at YCR054W
<i>YCR061W (i)</i>	R ChrIII: 225563 to 227458	YCR061W_F@+58 CCCATGATGACATGGACATGGAC YCR061W_R@+884 GGTATGCTCTTGAAGAAGCAGAGG	BglII	Quantification of DSB% at YCR061W
<i>YCR061W (ii)</i>	R ChrIII: 225563 to 227458	YCR061W_F@+1283 GGTCCACCAACATCTCTTGGAG YCR061W_R@+2176 TCAGAGAGAACCCTCCAGTAGAGTC	BglII PstI EcoRI	Quantification of DSB% at YCR061W
Extended Data Figure 7				
<i>YCR061W (i)</i>	R ChrIII: 225563 to 227458	YCR061W_F@+58 CCCATGATGACATGGACATGGAC YCR061W_R@+884 GGTATGCTCTTGAAGAAGCAGAGG	NA	Quantification of DC between YCR061W and YCR065W
<i>YCR061W (ii)</i>	R ChrIII: 225563 to 227458	YCR061W_F@+1283 GGTCCACCAACATCTCTTGGAG YCR061W_R@+2176 TCAGAGAGAACCCTCCAGTAGAGTC	PstI EcoRI	Quantification of DC between YCR061W and YCR065W DSB% at YCR061W and weak hotspot within YCR061W DSB% at YCR063W and YCR065W
<i>PUT2</i>	R ChrVIII: 181977 to 183704	PUT2_F@+1 ATGCTATGACGAAGTGCCTC PUT2_R@+989 GCACCTGGGTGAAGTAGATGG	StuI	Quantification of DSB% at YHR039W, YHR040W and YHR042W
<i>SRB2</i>	R ChrVIII: 189131 to 189864	NCP1_F@+512 TTCTTCTGCTCAATTGCACTTTCCC NCP1_R@+56 CCACTACAGGACGCAACCTTAAGC	NA	Quantification of DC between SRB2/NCP1 and YHR039W, YHR040W and YHR042W
<i>CCT8</i>	R ChrIV: 836421 to 838061	CCT8_F@+20 TCGGAAGCTGGAATGCTGGAG CCT8_R@+1025 CTTCCACAGAGTTCTGAGCTTC	PstI	Quantification of DC between CCT8 and SLY1 DSB% at CCT8
<i>SLY1</i>	R ChrIV: 838392 to 840392	SLY1_F@+1 ATGCTGTGAGGAATGCTGCTCC SLY1_R@+1025 TTCTCTGAGCTCTGGAATGGC	EcoRI	DSB% at SLY1

Indicated columns: location of probes (gene locus) for Southern blots, primer sequences used to generate these probes (by PCR), and reference to figure(s) within this manuscript in which probes were used for data collection. For quantification of PFGE and double-cuts (DC), no DNA digestion was performed before electrophoresis. For quantification of single-cut DSB frequencies at specific loci, DNA was first digested to completion with the indicated restriction enzyme before electrophoresis.

TOOLBOX RATE THAT JOURNAL

Consumer-oriented websites allow researchers to compare the merits of scientific journals and review their publishing experiences.

ILLUSTRATION BY THE PROJECT TWINS



BY JEFFREY M. PERKEL

What if scientific journals were like hotels, restaurants and holiday operators — easy to compare online and reviewed by those who use them? That thought occurred to conservation biologist Neal Haddaway two years ago: frustrated by a bad experience publishing his work with a journal he prefers not to name, he decided to launch Journalysis.org, a journal-review

site that he likens to TripAdvisor. “I wanted to basically reward the journals that were doing a good job and, within reason, name and shame the ones that weren’t doing so well,” he says.

Haddaway, now a project manager at the Mistra Council for Evidence-based Environmental Management in Stockholm, was not alone in his thinking. His site is one of a handful of

NATURE.COM
For more on scientific software, apps and online tools, visit: nature.com/toolbox

comparison websites that have sprung up in the past few years. Those developing these tools say that, although the practice of rating journals online has been slow to take hold, the sites help authors to become discriminating consumers of publishing services, choosing the journals that suit them and dodging questionable operators.

Journal-comparison tools allow authors to search or filter journals by various dimensions of performance, from prestige to publishing ►

THE RIGHT ONE FOR ME

How to pick a journal that fits your research

With tens of thousands of journals to choose from, some researchers might have trouble working out which journal best suits their article — perhaps their cross-disciplinary research falls outside conventional venues. Some tools allow researchers to identify suitable publications on the basis of the title or abstract. The earliest example of this is JANE, the Journal/Author Name Estimator, which is built on a database of millions of Medline records. Given an article title or abstract, JANE suggests related journals, authors or articles.

Created in 2007, JANE now fields about 20,000 queries a month, says Martijn Schuemie, who designed the tool and is now an associate director at Johnson & Johnson, working in Hong Kong. He uses JANE himself, he says, especially to pinpoint journals closely aligned with his research. Even journal editors use it, notes *PeerJ* web developer Alf Eaton, to identify potential peer reviewers. Other sites that suggest suitable journals on the basis of the title

include Journal Selector from the Edanz Group in Fukuoka, Japan, and JournalGuide from Research Square in Durham, North Carolina.

Inexperienced users might also have trouble recognizing predatory or counterfeit outfits that do no legitimate peer review and little, if any, editing for the money they charge (see *Nature* **495**, 433–435; 2013). Publishing in such journals not only wastes authors' money; it can even damage a career, says Jeffrey Beall, scholarly communications librarian at the Auraria Library at the University of Colorado Denver. He has compiled on his website (<http://scholarlyoa.com>) blacklists of publishers and journals that he considers predatory. Others, such as the Directory of Open Access Journals (<http://doaj.org/>), have compiled 'whitelists' of trustworthy publishers (see *Nature* **512**, 17; 2014). JournalGuide has a built-in whitelist that highlights reputable (or 'verified') journals. **J.M.P.**

► speed. Many of these tools are free to use, created by consultancy firms that make their money from related services for researchers, such as English-language editing and advice on publishing. Among those websites are Journal Selector, created by the London-based firm Cofactor, collating several hundred journals; JournalGuide, from Research Square in Durham, North Carolina, covering more than 46,000 journals; and the Edanz Journal Selector, a site designed by the Edanz Group in Fukuoka, Japan, compiling some 28,000 titles.

These comparison websites might seem unnecessary: researchers tend to identify the best destinations for their work by checking where studies they admire have been published, or by asking colleagues for advice. But Keith Collier, chief operating officer at Research Square, says that his company sees a market in researchers who may be unfamiliar with English-language journals, especially those located outside the United States and Western Europe.

Even Western researchers might feel overwhelmed by the rapid growth in the scientific literature, finding it hard to keep track of the number of journals sprouting up. Online comparison tools could help them to select the best journal for interdisciplinary work — or steer them away from predatory publishers that take researchers' money, but offer little in return (see 'The right one for me').

Most sites provide an indicator of prestige, such as a score that denotes how many citations on average an article in that journal accrues.

But there is much more to picking journals than this one measure, says James Maclaurin, a philosopher at the University of Otago in Dunedin, New Zealand. He has developed a mobile app called HelpMePublish (available on Apple's iOS operating system, with an Android version in development), which indexes more than 6,000 journals.

THE CONSUMER PSYCHE

Some researchers want only open-access journals; others care more about the acceptance rate, fees and time to publication. For Maclaurin, a killer detail is whether a journal allows 'double-blind' peer review, in which the authors' and peer reviewers' identities are withheld from each other to prevent prejudice.

Often, sites are simply aggregating data from individual journals' webpages. But the relevant information is not always available: Maclaurin randomly selected 300 journals from his database, and found that nearly half of their websites made no mention of peer-review policies and only one specified the journal's acceptance rate. To get information for his database, he surveys journal editors, giving him access to details not available online.

Maclaurin's app allows people to search for free, but charges for access to certain data such as a journal's acceptance rate: individual subscriptions are US\$4.99 a year, and institutional ones \$1,250. He says that the app has been downloaded by "thousands of people" from 28 countries. JournalGuide shows similar

success, hosting, at present, 13,500 users per month, according to product-management director Laura Stemmler.

The emergence of such tools reflects a shift in the dynamic between publisher and researcher, argues Peter Binfield, co-founder and publisher of the open-access journal *PeerJ*. As long as an outlet is of reasonable quality, he says, researchers are starting to recognize that the content of their article matters more than esteem garnered from the reputation of the journal. "It's not where you publish; it's what you publish," he says. As such, authors are shifting towards a more transactional, consumer-like attitude to publishing, Binfield thinks — they are looking for the best deals on fees and time to publication (even though many still also hanker after prestige).

If that is true, consumer-oriented researchers might relish the chance to read reviews and leave ratings of their own — "a Yelp restaurant review for journals", as Binfield puts it. HelpMePublish restricts users to numerical ratings — on a scale of 1 to 5 — on topics such as refereeing practice and communication. But some websites enhance the experience even further. Journalysis and SciRev — both of which are free — provide space for free-form comments. Created by economists Jeroen Smits of Radboud University in Nijmegen, the Netherlands, and Janine Huisman of the Centre for International Development Issues Nijmegen, SciRev boasts some 14,000 journals in its database and has received more than 1,000 user reviews in its one year of operation.

In theory, a lot of bad reviews might push publishers to change their procedures. But scientists have been slow to embrace the feature. Inexplicably, some publishers have received many reviews on SciRev, whereas others have received few. For example, the *Open Access Macedonian Journal of Medical Sciences* has 38 reviews (all accompanied by positive ratings), yet *Science* has 6 and *Nature* only 2, none of which includes ratings.

JournalGuide initially accepted user reviews, but dropped them due to a poor response rate. Journalysis is faring little better; few researchers have left ratings. "That's where we're all falling down really — users aren't submitting enough data," Haddaway says. This is despite the fact that reviewing sites allow user anonymity. Typically, these tools require registration only with a validated academic e-mail address.

"I think there is just a reluctance to say something about a journal you may need to go back and try to submit something later on," says Collier. If that is true, perhaps it is not surprising that review features have yet to achieve critical mass. Even so, the lack of engagement so far has not jolted Haddaway's conviction that the tools are needed. "I think there needs to be more transparency," he says. ■

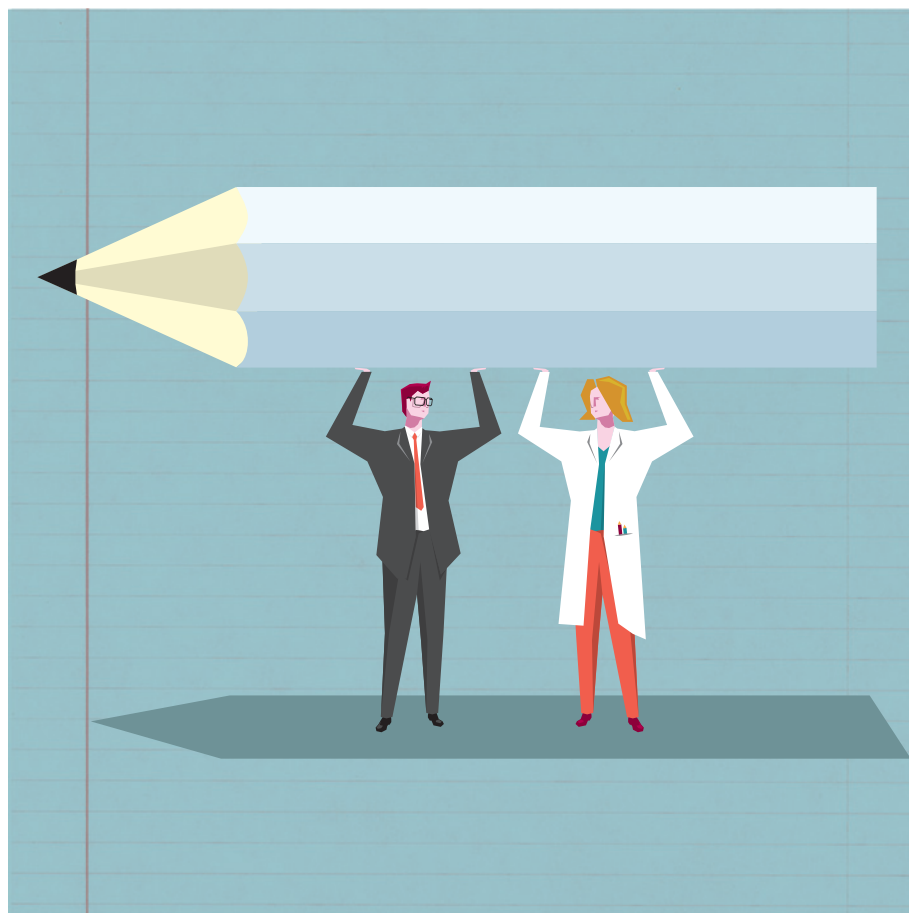
Jeffrey M. Perkel is a writer based in Pocatello, Idaho.

CAREERS

TOUGH DECISIONS When accepting a job means declining a prestigious award **p.123**

POSTDOCS Advice and resources for those post-PhD go.nature.com/9Z95KW

NATUREJOBS For the latest career listings and advice www.naturejobs.com



ADAPTED FROM HONG LU/GETTY

AUTHORSHIP

Dynamic duos

Partnering with a writer on a book can bring literary panache to scientific stories.

BY ROBERTA KWOK

If any researchers ever seemed well-equipped to write a popular book, they would be neuroscientists Stephen Macknik and Susana Martinez-Conde. Ten years ago, the husband-wife team launched the ‘Best Illusion of the Year Contest’, which honours magic tricks and other perceptual illusions. In 2007–08, they wrote two feature articles for *Scientific American* and started a monthly online column there about the neuroscience

of illusions. A few publishing companies took note and contacted the pair about writing a book.

But Macknik and Martinez-Conde, now at the State University of New York Downstate Medical Center in Brooklyn, were hesitant. They felt comfortable producing 2,000-word articles, but the idea of writing 8,000-word chapters, braiding multiple narratives and developing an overarching structure was intimidating. “We didn’t know if we could handle a book,” says Macknik.

Then, at a conference, the pair met Dan Ariely, a best-selling author and a behavioural economist at Duke University in Durham, North Carolina. He introduced them to his literary agent — who, in turn, suggested that they work with freelance science writer Sandra Blakeslee, who had co-authored several books, including one with a noted neuroscientist.

The three hashed out a plan for a book about the neuroscience of magic, and the proposal garnered interest from more than a dozen publishers. The team eventually went with Henry Holt and Company (part of Macmillan Publishers, which owns *Nature*). Over the next 9 months, the scientists wrote 500- to 2,000-word chunks and sent them to Blakeslee, who pushed for clearer explanations, revised the text, wrote additional sections and assembled the vignettes.

The result — *Sleights of Mind: What the Neuroscience of Magic Reveals About Our Everyday Deceptions* — hit the shelves in 2010. Although not a huge commercial success in the United States, it sold well in the United Kingdom and Spain, led to more speaking engagements for the scientists and won positive reviews and an award. Their confidence boosted, they are now on book number two.

Many scientists eager to write a book similarly wonder if they can do it on their own. Partnering with a professional writer, often a science journalist, can ease the pressure and vastly improve the manuscript. Writers can help to translate complex concepts for the public, construct compelling narratives and organize tens of thousands of words into a clear structure. Many also do a good deal of the required research. And the use of a co-author can also motivate the scientist to meet deadlines.

GOOD WITH THE BAD

But co-authorship comes with challenges. The scientist will not necessarily save time: working with writers requires extensive discussions and review of many drafts. The co-authors may disagree on what phrasing or details to include. And a skilled co-author is not cheap: the writer usually expects a flat fee (which can run as high as a couple of hundred thousand dollars), a share of payments from the publisher, or both. Still, it can be a rewarding — if not highly remunerative — experience. To best protect their interests and to streamline and smooth the process, scientists who aim to pursue this route should seek an experienced writer with a compatible personality, explicitly plan the

► schedule and division of labour before the project begins, consider the pros and cons of sharing a literary agent and line up a lawyer to review the contract.

STRONG STARTS

If the scientist brings a co-author on board early, the writer can help to prepare a marketable book proposal and craft an enticing sample chapter. Usually, a writer charges about US\$5,000–10,000 for this work, which can take a few months. Although some researchers may hesitate to invest that amount up front, the ultimate deal — and amount of the advance — hinge on a strong proposal. “It’s what will sell the book,” says Blakeslee.

To find a co-author, scientists can contact journalists who have interviewed them, written about similar topics or been recommended by colleagues. Whether candidates must have experience in writing books is debatable — Blakeslee believes that it is not essential, but Macknik argues that since the project will be time-consuming and risky, scientists should seek writers with a strong track record in book authorship.

If the scientist’s first choices are not available, those writers can often recommend others, says Thomas Hayden, a science

communication lecturer at Stanford University in California who has co-authored two books. Researchers can also post ads with writers’ organizations, such as the US National Association of Science Writers (www.nasw.org) or the Association of British Science Writers (www.absw.org.uk). Blakeslee recommends that a would-be scientist-author interview four or five candidates face to face, look for a good personality fit and evaluate samples of their work for accuracy and flair. It will not be clear how heavily the writer’s work was revised by an editor, but an interview will help the scientist to gauge the candidate’s intelligence and capabilities.

The writer with the most recognizable name is not always the best choice, says Hayden. Instead, the scientist should consider whether the writer asked thought-provoking questions during their meeting or previous interviews. “You want somebody who can go as deep as you can into the material,” he says.

Scientist and writer also should agree on the approach to the subject. That was important to David Spiegelhalter, a statistician at the University of Cambridge, UK, who co-wrote *The Norm Chronicles* (Profile, 2013), a book about risk assessment in everyday life. He and his co-author, UK journalist Michael

Blastland, had previously given joint lectures about how to communicate statistics and shared the view that experts should not belittle the public’s understanding of risk. So when the two decided to write a book together, they knew that they agreed on an approach: both wanted to respect readers’ gut feelings about risk but to help them to balance instinct and analytical thinking. The collaboration was smooth, and the book won acclaim for its avoidance of a patronizing tone.

The scientist will also need to find an agent (who typically takes a 15% commission on payments from the publisher). To find one, they can search the acknowledgements pages

of similar books or ask scientist-authors for recommendations. The website Publishers Marketplace sells reports about which agents have recently sold books, including those on science, around the world.

Sharing an agent with the co-author can simplify matters by reducing negotiation time and the number of people involved in decisions — but it also carries risks. If the relationship later falls apart, the agent is likely to take the side of the most important client, which might be the writer, says Madeleine Morel, a literary agent at 2M Communications in New York City. The scientist should also retain a lawyer who specializes in publishing to review the collaboration contract, which should spell out issues such as payment (see ‘Dividing the spoils’), cover credits, division of labour and deadlines.

Once the contract and book deal are in place, the real work begins. Sometimes, the scientist provides most of the ideas and resources for content — such as the subtopics each chapter should cover, lists of studies, articles or videos of lectures. And the writer may spend many hours interviewing the scientist to learn key concepts and gather anecdotes.

But the division of labour varies widely, and writers, too, can bring scientific expertise to the collaboration. Blakeslee had more than two decades of experience covering brain science when she began working with Macknik and Martinez-Conde, and she was more familiar with some neuroscience concepts — such as peripersonal space, the space around our bodies that can be reached by our arms — than the scientists were. Because following the news is part of a journalist’s job, the writer may also be better at keeping up with the latest research in the field. This skill impressed Douglas Emlen, an evolutionary biologist at the University of Montana in Missoula, during his collaboration on the textbook *Evolution: Making Sense of Life* (Roberts, 2012) with Carl Zimmer, a science writer in Guilford, Connecticut. “He brings examples to the table that never in a million years would I even be aware of,” says Emlen.

FINANCIAL DECISIONS

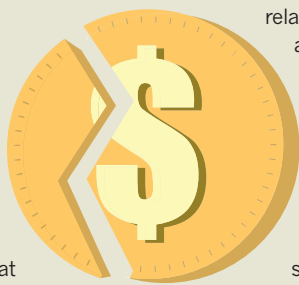
Dividing the spoils

Several types of payment scheme are possible for co-authored books. The writer’s portion will depend on his or her level of experience, the project’s complexity, the division of labour and the book’s expected sales. Scientists also should keep in mind that freelance writers do not receive a separate salary — they live on what they earn from their writing.

“This is what pays the mortgage,” says Catherine Dold, a freelance science and health writer in Boulder, Colorado, who spent 14 months working full-time on a co-authored book. “You can’t expect them to do it on the side, or just for the glory of it.”

Some writers charge a flat fee, which typically ranges from US\$40,000 to \$200,000; the researcher often pays the fee out of the advance or from a grant. Other co-authors ask for a percentage of payments from the publisher, and the writer’s share is usually 30–50% of the advance and 15–50% of royalties.

A hybrid approach that combines a flat fee with a share of payments from the publisher often sets up the best working



relationship, says Thomas Hayden, a science communication lecturer at Stanford University in California.

A writer who receives only a percentage of the advance and royalties may want to sell the book to the highest bidder, but the scientist might prefer a more prestigious publishing house with

a lower offer. And writers who receive only a flat fee may feel less motivated to help with marketing — by promoting the book on social media, for instance, or asking journalists in their network to review the book.

Generally, the less credit the writer receives, the higher the fee. A writer may charge more if his or her name appears in smaller type on the cover than the scientist’s or is not mentioned on the cover at all (for a ghostwritten book) than if all co-authors receive equal billing. A young journalist who is eager to write a first book might offer a discount in exchange for cover credit. But seasoned writers with several books under their belts may not value credit as highly and will want a larger slice of the financial pie. **R.K.**

Yet even if the journalist is responsible for all the writing, a scientist cannot expect him or her to produce a book alone. “It doesn’t happen by magic,” says Catherine Dold, a freelance science and health writer in Boulder, Colorado. In addition to interviewing the scientist for concepts and anecdotes, the writer will need frequent feedback on chapters. Blakeslee recommends that the co-authors meet in person regularly to work on the book, maintain rapport and ensure clear communication. If the scientist weighs in only at the end, the writer may focus on points that the scientist would not have chosen to highlight, or might neglect areas that the scientist considers important.

It is also crucial to stick to the schedule because book-publishing schedules tend to be less flexible than those many scientists are used to. If one partner falls behind, the other team member or members may have trouble adjusting their schedule. And the publisher may cancel the book if the manuscript is late. Spiegelhalter found that having a co-author made him less likely to procrastinate.

“You’ve just got to get on with it,” he says. “Teamwork is very effective at driving it along.”

Researchers should expect disagreements to arise, especially over wording or the appropriate level of technical detail. They must ensure that the text is accurate, but should also recognize the writer’s expertise in communicating to a lay audience. Writing engaging chapters that would maintain a reader’s attention “required shattering a lot of the conventions that I’m comfortable with,” says Emlen. Zimmer used more active verbs and shorter sentences than Emlen was used to, for example.

But if the scientist begins to feel that the relationship is foundering, it is better to terminate sooner than later, says Morel. The collaboration agreement should contain a termination clause that specifies what will happen if the partnership dissolves. The scientist might keep the copyright to the text, for example, while the writer keeps any payment received so far.

Well-matched co-authors can avoid such pitfalls. Emlen says that it was “a dream” to work with Zimmer on the evolution textbook: Emlen provided deep background knowledge of the field, and Zimmer conveyed the material with compelling stories and clean, accessible language. “I spent a lot of the past few years realizing just how hard it is to write like that,” says Emlen. At the end of the day, whatever the bumps along the way, both parties want the same thing: to write a great book. “You’re in this together,” says Blakeslee. ■

Roberta Kwok is a freelance science writer in Seattle, Washington.

TURNING POINT

Danielle Edwards



Evolutionary biologist Danielle Edwards faced a difficult choice last autumn. She could either accept a prestigious 3-year Discovery Early Career Research Award (DECRA) from the Australian Research Council and return to her home country or she could continue her efforts to secure tenure-track positions for herself and her husband at the University of California (UC) Merced. She chose the latter.

You grew up in Australia. Is it still the site of your fieldwork?

Yes, I maintain some research on Australian reptiles. I grew up north of Sydney with a national forest as my back yard. After exploring the reproductive biology of amphibians as an undergraduate at the University of Newcastle, Australia, I did a PhD at the University of Western Australia in Perth studying how environmental processes drive patterns of speciation in this biodiversity hotspot. I then spent more than five years in the United States studying Galapagos tortoises, but still do work on Australian reptiles and continue to expand my collaborations around the world.

Why did you move to the United States?

I never thought I would leave Australia. In 2009, I finished a postdoc at the Australian National University in Canberra. When that funding ran out, I tried for other grants in Australia, but was unsuccessful, so I took an offer for a postdoc at the University of Michigan. My now-husband eventually joined me a year later, and by 2011, we had both secured postdocs at Yale University in New Haven, Connecticut.

Did you look for permanent jobs in Australia?

Yes, since 2010. I applied for pretty much every Australian job I could — but, given the dismal state of funding in Australia, I was applying for US positions too. I’ve been interviewed several times for US jobs, and made it onto many

short lists — but could not do the same in Australia, where the odds are even worse than in the United States. In early 2013, I was ready to give up on academia. I was in my mid-30s, and wanted to have a child and settle down. When I applied for the DECRA, I had lots of US applications out. I was interviewed last May at UC Merced, and got the job offer a few days later. Last October, I found out I got the DECRA.

How did you respond?

When the DECRA came through, I was in a state of shock — I never thought I would get it. It was a huge thing for my family when I moved to the United States, especially once we learned that I am expecting our first child in April. Finding out about the award was an emotional time. On the one hand, we had an opportunity to go back to Australia where I would be able to raise my child near my extended family. On the other hand, UC Merced was in the process of interviewing my husband for a tenure-track faculty position, which he will begin this summer. However, we felt that there was no opportunity for long-term employment for us in Australia — particularly for both of us in the same place. Australian universities are struggling under funding cuts and only one has a spousal-hire policy. I never really felt that I had the option to take the DECRA.

Your declining the DECRA made headlines. What was that like?

Honestly, it’s a bit weird. There was a misperception that I had turned down the DECRA in protest, but it was much more complex than that. There were ten DECRA offers in evolutionary biology last year, but there were only three permanent academic positions in the field. If this grant is designed to keep or bring bright minds to Australia, there are no follow-on funding opportunities. Several people wrote to thank me for raising awareness about Australia’s funding situation.

Do you hope to make it back to Australia?

I wouldn’t rule it out, but I’m deeply committed to my new institution. We’ve landed in a pretty idyllic place. We’ll be able to afford to buy property and raise our child the way we grew up — something we wouldn’t be able to do in Australia. Plus, UC Merced is assembling a great group of people with a spectacular gender balance. I feel very positive about my decision and happy that I now have a direction. ■

INTERVIEW BY VIRGINIA GEWIN

MARK SISTROM

MORT'S LAWS

Ten commandments for a New Dawn.

BY JACEY BEDFORD

“Shut up! All of you!” Morton’s bellow silenced the squabbling voices in the cellar of the burned-out building. “You asked me here — now talk. One at a time.”

He perched on the edge of the squared-off pile of rubble that passed for a table. *Kids*, he thought. *I used to see ‘em as troops, but they’re no more than kids. When I was their age ...*

He stopped himself from heading down the nostalgia route. He’d never been their age. He’d grown up in the days of cars and air conditioning, Wal-Mart and cheap Chinese footwear. He’d lived in a house with a roof on it and had a real high school to drop out of. He’d even had a father, though the surly sot hadn’t taught him more than how to dial for pizza delivery.

His father had probably been killed in the first wave of the invasion, but Mort would never know. He’d been in the Marines by that time. Found himself a family he could rely on. He’d stayed loyal to that family until he was the last man standing, then he’d gathered a new family, teaching the survivors what he knew about fighting aliens.

The slow and the old had died a long time ago, except for Mort. He was a living tribute to his drill sergeant’s training, and a walking advert for good luck.

Andi Ferriby stood up to speak. At 28 she was her squad’s matriarch, savvy, sassy and as tough as they came. Mort had trained her to field-strip and reassemble the clumsy MM49s back in the days when they’d still had ammo. Even then the damn things were better used as a club. You could pump five rounds into a grom and they wouldn’t falter, but they were fragile in the brain-pan. Left temple was the place to whack for best effect.

But that was over now. The fighting had finished.

Had they won? Mort hadn’t a clue, but they’d survived in scattered groups. Was it enough? It had to be. They could rebuild communities, relearn skills.

It had started suddenly, with an armada of alien vessels raining down destruction on missile silos, oil supplies and communications towers simultaneously. The groms themselves, named after the only recognizable sound they made,

didn’t seem to have any weapons other than blades, but kill one and two would



take its place. A seemingly endless supply of alien cannon-fodder, millions of them. Billions. And in the end, sheer numbers won out over artillery and projectile weapons.

Inexplicably the squat, muscular aliens had stopped short of genocide, having knocked the planet back into the dark ages, country by country, town by town. Perhaps it was sport to them. Perhaps teaching upstart humans their place in the Universe had been their objective all along. Who could tell? They’d never been able to communicate.

Mort figured it had taken 40 years of offensive and counter-offensive to reduce eight billion people to a few ragged survivors. None of these kids remembered what it was like before.

Thirteen of them now stared at him expectantly. “OK. You talk first.” He pointed to Andi.

She nodded. “Gran’er Mort, we know about fighting and hiding, but we don’t know how to live peaceful. Just yesterday, Ainley’s bunch came at us for supplies, but we don’t hardly have any more than they do. They had nothing to trade. We had to send ‘em off, but there was hurting on both sides. Now the groms have gone, we shouldn’t be fighting each other.”

Mort shook his head. How could they rebuild what they’d never known?

“Time was, there was rules about that. My ma said so.” Jimmy York held out something small in his strong, brown hand.

Mort took it and felt his fingers tremble as he recognized a tightly folded page from a book. Reverently he opened it out.

“Where’d you get this?”

“Ma,” Jimmy said. “She said if we was gonna ever be civilized again we’d need to be able to read an’ write. She tried to teach me, but ... no time.” He shrugged. “She’s gone now. Ain’t no one can read in our squad.”

There was nothing left to read. Books all gone three decades ago; pages ripped out for arsepaper or burnt for winter warmth.

Mort squinted at the rubbed print on the worn paper, only gradually making out the words ...

Hills of the North, Rejoice.

Immortal, Invisible, God Only Wise.

Hell! An index page from a hymn book!

The long-dead military chaplain’s voice echoed in his head, but only the sermon’s tune remained — the words had evaporated.

No matter, he’d never believed anyway.

But these kids needed some basic rules to build on. If only he could remember the Ten Commandments. He dredged dim memory, found gaping holes, and invented what he’d forgotten.

That’s how the New Dawn got Mort’s Laws:

1. **Worship no gods.**
2. **Don’t kill what you can’t eat.**
3. **Treat others kindly, as you would be tret.**
4. **Honour your family and your squad.**
5. **No thieving, ask nicely or offer trade.**
6. **No lusting after your neighbour’s ass.**
7. **Learn all you can learn, and teach others for free.**
8. **Tell the truth and shame the devil.**
9. **Always wash your hands after using the latrine.**
10. **Never start a fight, but always finish it.**

In later years the lawmakers built a statue of Mort in the square of Newtown City. Every Saturday morning the philosophers would gather to teach anyone who would learn, talk to anyone who would listen, and debate with anyone who would speak. Always, the most hotly argued point was number six. ■

Jacey Bedford has had short stories published on both sides of the Atlantic and her first novel *Empire of Dust* is out now with the sequel due in August 2015.

ILLUSTRATION BY JACEY